

Fakultät für Physik und Astronomie, Universität Würzburg, Germany

Hyperfine Interactions in Lanthanide-Organic Complexes for Quantum Information Processing

For obtaining the academic degree of

Doktor der Naturwissenschaften (Dr. rer. nat.)

by the KIT-Faculty of Chemistry and Biosciences of the
Karlsruhe Institute of Technology (KIT)

and

Docteur de l'Université de Strasbourg en Physique

Approved

Dissertation

by

Denis Jankovic

Date of Oral Examination : 18.11.2024

Reviewer : Prof. Dr. Mario Ruben, KIT-INT and KIT-IQMT

Second reviewer : Prof. Dr. Paul-Antoine Hervieux, IPCMS, Université de Strasbourg

To my other half, Chloé, for her unwavering support and love.

To my family for everything they have done for me and that allowed me to do what I do.

To my friends for their support and good times.

Acknowledgements

Thank you to Paul-Antoine for his guidance, the people I met and the places I visited thanks to him, his trust and his unwavering good mood. Thank you to Mario for the opportunities he opened for me, for his trust, and for his time and patience. This thesis would not have been as enjoyable and eye-opening without you two. I had the amazing opportunity to meet and discuss with Nobel Laureate Steven Chu, and one thing he said stuck with me : "The most important thing when joining a team, is to make sure you will have a good supervisor". In this regard, I was lucky enough to not only have one, but two great supervisors.

I am grateful to the members of the jury for their time and effort in evaluating this thesis. I would like to thank Prof. Dr. Fernando Luis and Prof. Dr. Anja Metelmann for accepting to be the assessors of this thesis. I would like to thank Prof. Dr. Vincent Robert, Prof. Dr. Philip Willke, and Prof. Dr. Adriana Pálffy-Buß for accepting to be the jury members of this thesis.

I would like to thank my colleagues at the IPCMS, first, my comrade in arms, Jean-Gabriel "Gabe" Hartmann, for his friendship, his support, and his amazing capability to bare with me for such a long time and on such a regular basis. I wanted to extend my thanks to Rémi Pasquier, Vincent Hardel, Adrien Andoche, Benjamin Bakri and Patrick Lawes, who also had to endure years of being stuck together in the same office, even when it wasn't their office to begin with. I have known Rémi for almost 7 years now, and we did quite a long stretch of our higher education together, so I must particularly thank you for your friendship and neverending knowledge of the most obscure mathematical theorems, that almost always proved useful. Moreover, Samiul, Giovanni, Pierre, Lorry, Wilfried, and all the other members of QDyno and DON I interacted with on an almost-daily basis, you contributed to have such a good work environment, I really hope to be able to find another one even remotely as good as this one. I want to thank two of our interns, Julian Mayr, who helped us kickstart the part of the work on the Maximum Principle and did an amazing work with neural networks, and Gustavo Kuffaty, who also was primordial in the first simulations we did with Average Gate Fidelities and pulse generations. I can also only be grateful to the Ruben group team members in KIT, who have always been helpful and so nice, special thanks to Patrick again, but also Sai, Jo, Senthil and Svetlana !

I am so grateful to have had the opportunity to collaborate with so many people, Harry, Luca, and all the other members of the CRC 4f4future and also members of the Wernsdorfer group, as well as people from QUSTEC I was able to meet. I am also happy to have worked with Jonny and Hervé from IPHC, as well as Killian, Yannick, Emmanuel from IRMA, Claude from Fribourg, Fernando and Sergio from Madrid. Throughout this work I was able to travel around Europe, and even the world by the end, and I am grateful for all the opportunities I had to meet so many people and to learn so much from them. In particular, one of the most important things I learned is that science is a collaborative effort, and that it is important to be able to work with others, to learn from them, and to teach them what you know. Special hello to Saad and Vincent, who I met during such a trip.

A highlight of this thesis was attending the 73rd Lindau Nobel Laureate Meeting, where I met incredible people, including many Nobel Laureates, and had the chance to discuss with them. I hope to stay in touch with some of these inspiring individuals. I am deeply grateful to those who made this possible :

the Lindau Foundation, UDICE, Aziz Dinia for the nomination, Dr. Marko Rančić for his support and recommendation, and Paul-Antoine for both recommending me and making my participation possible.

I must have special thanks for all my friends I made since coming to Strasbourg, Flo, who was the first person I befriended in Strasbourg almost 10 years ago, and who has been a great friend since then. Antoine, Bleuenn, Alex, Oussama, and all the others who I met when starting the Magistère – the first one I met one year earlier even – you have made my studies in Strasbourg a great experience. I also want to thank my friend from before Strasbourg, Masha, we went to high school and started our adult lives when we arrived in Strasbourg together, even though we both took different paths in lives that led us to different places, I am grateful for the time we spent together and I value that we are able to still stay in touch for the past 12+ years.

To my parents and my brother, Мамо, Тато, Дане, хвала вам од срца што сте ме учинили особом која сам данас, хвала вам што сте неговали моју радозналост, што сте ми омогућили да студирам, што сте ме волели и штитили. Данијеле, ти си мој вољени млађи брат и поносан сам на тебе. Мама, Тата, посветили сте свој живот Данијелу и мени, и на крају, ова теза је подједнако ваша колико и моја. Волим вас. To my family as a whole бако Живадинко, бако Светлано, деко Лепомире, деко Зоране, Ани, Ацо, Мими, Зоки, Мајо, Лаки, и сви остали, ако урадим целу листу, нече имати краја. Поносан сам члан обе породице, и хвала вам свима.

Bisous à Murphy le meilleur des toutous, mascotte (in)officielle des Q-Dynos.

And finally, Chloé, mon cœur, tu m'as accompagné depuis le début de cette thèse, mais aussi avant. Aucun mot ne suffira pour te remercier dans ce simple paragraphe, et finalement, ils seront toujours tous contenus dans le plus simple, mais le plus sincère, des "je t'aime".

RESOURCES & FUNDING



This work was funded by the **French National Research Agency (ANR)** through the **Programme d'Investissement d'Avenir** under contract **ANR-11-LABX-0058_NIE** and **ANR-17-EURE-0024** within the **Investissement d'Avenir** program **ANR-10-IDEX-0002-02**.



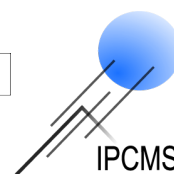
The author gratefully acknowledges financial support from the **Deutsche Forschungsgemeinschaft (DFG, German Research Foundation)** through the **Collaborative Research Centre "4f for Future"** (CRC 1573, project number 471424360) project B3.



Université
franco-allemande
Deutsch-Französische
Hochschule

This work has received financial support as a cotutelle from the **Franco-German University**, for which the author is grateful.

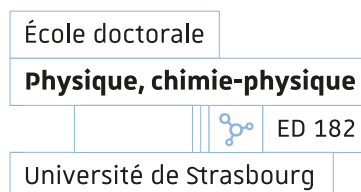
The French supervision of this thesis was carried out on the premises and with the resources of the **Institut de Physique et de Chimie de Matériaux de Strasbourg (IPCMS)**.



The German supervision of this thesis was carried out on the premises and with the resources of the **Institute of Nanotechnology** of the KIT (INT-KIT).

The author would also like to acknowledge the **High Performance Computing Center** of the **University of Strasbourg** for supporting this work by providing scientific support and access to computing resources. Part of the computing resources were funded by the **Equipex Equip@Meso project** (Programme Investissements d'Avenir) and the **CPER Alsacalcul/Big Data**.

Finally, this research was made possible thanks to the financial support provided by the ED182 Doctoral School.



Scientific Output

Publications

1. **Noisy qudit vs multiple qubits : conditions on gate efficiency for enhancing fidelity.**
Janković, D., Hartmann, JG., Ruben, M., Hervieux, PA.
npj Quantum Inf 10, 59 (2024).
2. **Nonlinearity of the Fidelity in Open Qudit Systems : Gate and Noise Dependence on High-dimensional Quantum Computing.**
Hartmann, JG., Janković, D., Pasquier, R., Ruben, M., Hervieux, PA
[Submitted to Quantum, in review]
3. ***Ab initio* Modelling of Lanthanide Nuclei and Study of the Hyperfine Anomaly.**
Hervieux, PA., Hartmann, JG., Janković, D., Bartel, J., Molique, H., Bonneau, L.
[Manuscript in preparation for submission to PRX]
4. **Elucidating the Physical and Mathematical Properties of the Prouhet-Thue-Morse Sequence in Quantum Computing.**
Janković, D., Hartmann, JG., Hervieux, PA.
[Manuscript in preparation for submission to J. Phys. A : Math. Theor.]
5. **Benchmarking Quantum Optimal Control Techniques for Qudit Gate Synthesis.**
Hartmann, JG., Janković, D., Ruben, M., Hervieux, PA.
[Manuscript in preparation]
6. **Full- and low-rank exponential Euler integrators for the Lindblad equation.**
Chen, H., Borzi, A., Janković, D., Hartmann, JG., Hervieux, PA.
[Submitted to SIAM Journal on Scientific Computing]

Posters

1. **Computation of the hyperfine structure of lanthanide-organic complexes used for Quantum Information Processing.**
Paris International School on Advanced Computational Materials Science 2021 (29/08-05/09/2021)
Sorbonne Université, Campus de Jussieu, Paris, France
Best Poster Awards : 2nd Place
2. **Computation of the hyperfine structure of lanthanide-organic complexes used for Quantum Information Processing.**
39th edition of the Joliot Curie International School (03/10-08/10/2021)
Saint-Pierre d'Oléron, France
3. **Computation of the hyperfine structure of lanthanide-organic complexes used for Quantum Information Processing.**

European Spring School in Quantum Science and Technology (10/04-14/04/2022)
Strasbourg, France

4. **Hyperfine Interactions in Lanthanide-Organic Complexes for Quantum Information Processing.**
Quantum Information Spring School (02/05-13/05/2022)
Ecole de Physique des Houches, les Houches, France
5. **Hyperfine Interactions in Lanthanide-Organic Complexes for Quantum Information Processing.**
molecule based Quantum Science and Technology (molQueST) (21/08-25/08/2022)
Monte Verità, Ascona, Switzerland
6. **Qudits vs Qubits : Faster and More Reliable Quantum Gates ?**
ED182 PhD Day 2023 (23/03/2023)
Collège Doctoral Européen, Strasbourg, France
Best Poster Awards : 2nd Place
7. **Qudits vs Qubits : Faster and More Reliable Quantum Gates ?**
US-Switzerland Quantum Symposium 2023 (27-28/03/2023)
uptownBasel Infinity AG, Arlesheim by Basel, Switzerland
8. **Qudits vs Qubits : Faster and More Reliable Quantum Gates ?**
Presented by my colleague J-G. Hartmann
ITI QMat Scientific Day (15/06/2023)
IPCMS, Strasbourg, France
Best Poster Awards : 2nd Place
9. **Qudits vs Qubits : Faster and More Reliable Quantum Gates ?**
EGAS 54 Strasbourg (18-22/06/2023)
Faculté de Chimie/Institut Le Bel, Strasbourg, France
10. **Qudits vs Qubits : Faster and More Reliable Quantum Gates ?**
KSQM MSCA QUSTEC EUCOR Summer School 2023 - European Summer School in Quantum Science and Technology (17-22/09/2023)
Durbach, Germany
Best Poster Award
11. **Electrical Addressing and Readout of Nuclear Spins in Ln-SMMs for Quantum Information Processing.**
CRC 4f4future Fall Workshop (11-13/10/2023)
Bühl, Germany
12. **Molecular Qudits vs Qubits : Faster and More Reliable Quantum Gates ?**
Asian Conference on Molecular Magnetism 2024 (01-04/09/2024)
Busan, Republic of Korea

Talks

1. **Hyperfine interactions in molecules : Quantum Computing with nuclei.**
ED182 PhD Day 2022 (21/03/2022)
Collège Doctoral Européen, Strasbourg, France
2. **Computation of the hyperfine structure of lanthanide-organic complexes used for Quantum Information Processing.**
ITI QMat Scientific Day (01/06/2022)
IPCMS, Strasbourg, France
3. **Quantum Computing with nuclei and molecules.**
PDI Seminars (07/04/2022)
Collège Doctoral Européen, Strasbourg, France

4. **Hyperfine interactions in lanthanide-organic complexes for Quantum Information Processing.**
QuantMOCOTE - Modelling, Optimization and Control of Quantum systems in Technology and Education (06-08/03/2023)
Institute of Mathematics, Würzburg, Germany
5. **Controlling molecular qudits : from pulses to quantum gates.** (05 - 06/10/2023)
Workshop on Optically Addressable Molecular Lanthanide Qubits for Quantum Devices
Baden-Baden, Germany
6. **Isotopically Enriched Lanthanide Nuclear Spin Qudits**
CRC 4f4future Spring Days (21-22/03/2024)
Pforzheim, Germany
7. **Controlling molecular qudits : from pulses to quantum gates.**
Invited by Dr. Saad Yalouz (19/05/2024)
Quantum Chemistry Laboratory, Strasbourg, France
8. **Controlling Ln-based qudits : A theoretical framework**
Workshop on Immobilization of Molecular Quantum Bits (12/06/2024)
Hirschegg, Austria
9. **Controlling Ln-based qudits : A theoretical framework**
Invited by Prof. Andreas Heinrich (05/09/2024)
Center for Quantum Nanosciences (QNS), Seoul, South Korea

"Преко прече, наоколо брже."

— *The shortcut is longer, the roundabout way is quicker*, **Serbian proverb**

"천 리 길도 한 걸음부터"

— *A journey of a thousand miles begins with a single step*, **Korean proverb**

Hyperfine Interactions in Lanthanide-Organic Complexes for Quantum Information Processing

Interfacing Quantum Realms: A Lanthanide Perspective

A thesis submitted by

Denis Janković

approved by the KIT-Faculty of Chemistry and Biosciences and the
University of Strasbourg in fulfilment of the requirements for the
titles of

Doktor der Naturwissenschaften (Dr. rer. nat.) by the KIT-Fakultät für Chemie
und Biowissenschaften des Karlsruher Instituts für Technologie (KIT)

and

Docteur de l'Université de Strasbourg en Physique

Under the supervision of
Prof. Dr. Paul-Antoine Hervieux

Prof. Dr. Mario Ruben

IPCMS, Université de Strasbourg, UMR 7504 CNRS, France

INT & IQMT, Karlsruhe Institute of Technology (KIT), Germany

CESQ, ISIS, Université de Strasbourg, UMR 7006 CNRS, France

Summary

In this manuscript titled "Hyperfine Interactions in Lanthanide-Organic Complexes for Quantum Information Processing," we explore the intricate interplay between atomic physics and quantum computing, focusing on hyperfine interactions in lanthanide-organic complexes and their applications in quantum information processing. The work bridges multiple disciplines, including quantum computing, optimal control theory, nuclear structure, hyperfine interactions, f -elements, crystal field theory, and molecular magnetism.

We begin by examining the Hamiltonian of free lanthanide ions, deriving matrix elements that account for electronic structure, spin-orbit coupling, and hyperfine interactions. Utilizing hydrogen-like wavefunctions and Slater determinants, we ensure antisymmetry in multi-electron systems, adhering to the Pauli exclusion principle. The spin-orbit coupling is treated perturbatively, leading to fine-structure splitting, with matrix elements derived using angular momentum coupling schemes. Hyperfine interactions, including magnetic dipole and electric quadrupole contributions, are formulated to account for energy level splitting due to nuclear spin states, which are essential for precision spectroscopy and quantum information applications.

Transitioning to ligand field theories, we elaborate on how surrounding organic ligands influence the electronic structure of lanthanide ions in complexes. We contrast Crystal Field Theory (CFT), which models ligands as point charges, with Ligand Field Theory (LFT), which considers covalency and orbital overlap. The ligand field Hamiltonian is expressed through multipolar expansions, and matrix elements are derived using advanced angular momentum theory. Selection rules based on ligand symmetry are established, reducing the complexity of the problem. These concepts are crucial for understanding the electronic structure and spectroscopy of lanthanide-organic complexes used in quantum computing.

In exploring configuration interaction, we delve into the Judd-Ofelt theory and its generalizations, which describe electric dipole transitions in lanthanide complexes. We address how odd ligand field parameters facilitate configuration mixing between different parity states, such as $4f^n$ and $4f^{n-1}5d$, and how this mixing is essential for understanding the hyperfine Stark effect observed in experiments. Perturbation theory is employed to derive effective operators that account for these transitions, providing a theoretical framework for hyperfine-induced transitions in lanthanide complexes.

Relativistic corrections are addressed through the Dirac equation, providing a foundation for understanding the hyperfine interaction and calculating hyperfine constants. We consider the finite mass, size, and magnetic characteristics of atomic nuclei, and how these nuclear properties influence the hyperfine structure in lanthanide ions. Calculations of hyperfine constants include corrections for finite nuclear charge and current distributions, using the Bohr-Weisskopf and Breit-Rosenthal corrections.

A significant portion of the work involves using electrons and muons as nuclear probes in hydrogen-like lanthanide ions, such as dysprosium. By calculating energy levels and hyperfine constants for different isotopes and nuclear models, we demonstrate that muonic ions provide enhanced sensitivity to nuclear properties due to greater wavefunction penetration into the nucleus. Hyperfine anomalies are calculated, revealing the ability to discriminate between different nuclear models and isotopes, which is valuable

for designing qudits with desired properties.

Transitioning to quantum computing, we focus on the use of nuclear spins in lanthanide ions as qudits for quantum information processing. We provide an overview of qubits, qudits, and essential quantum concepts such as state representations, quantum gates, and critical timescales. We discuss the differences between qubits and qudits, illustrating how qudits, as d -level quantum systems, can represent more information and potentially offer advantages over qubits. The scaling of noise with the dimension of the Hilbert space is analyzed, and conditions under which qudits outperform qubits are derived.

We explore the dynamics of open quantum systems interacting with an environment under the Markovian assumption, employing the Lindblad equation to model these systems. Using perturbation theory on the Lindblad master equation, we study the effects of decoherence on quantum operations in qudits. Beyond the first-order approach, higher-order corrections are considered, revealing the nonlinearity of fidelity in open qudit systems and the necessity of accounting for these corrections in high-dimensional systems.

To address the implementation of quantum gates on nuclear spins, we employ optimal control theory to optimize gate generation and reduce gate times, thereby improving system performance. Techniques such as the rotating wave approximation, Givens rotation decomposition, and optimal control algorithms like GRAPE and MAGICARP are utilized to minimize the time and energy costs of implementing quantum gates in high-dimensional systems. These methods are crucial for overcoming the challenges associated with longer gate times and increased decoherence in qudits.

Finally, the manuscript explores the applications of the Prouhet-Thue-Morse sequence in quantum computing. This mathematical sequence is shown to have significant utility in error correction, the design of noise-resistant quantum memories, and the analysis of quantum chaos. Its properties allow for the construction of logical states that satisfy the Knill-Laflamme conditions for error detection and correction, providing robustness against certain types of errors and dephasing.

Overall, the manuscript presents a comprehensive study that bridges atomic physics and quantum computing, with a specific focus on hyperfine interactions in lanthanide-organic complexes for quantum information processing. The work provides theoretical insights into the complex interactions within these systems and practical considerations for advancing quantum computational technologies using lanthanide-based qudits.

Zusammenfassung

In diesem Manuskript mit dem Titel "Hyperfeinwechselwirkungen in Lanthanid-Organischen Komplexen für die Quanteninformationsverarbeitung" untersuchen wir das komplexe Zusammenspiel zwischen Atomphysik und Quantencomputing, mit Schwerpunkt auf Hyperfeinwechselwirkungen in lanthanid-organischen Komplexen und deren Anwendungen in der Quanteninformationsverarbeitung. Die Arbeit schlägt eine Brücke zwischen mehreren Disziplinen, einschließlich Quantencomputing, Optimalsteuerungstheorie, Kernstruktur, Hyperfeinwechselwirkungen, f -Elementen, Kristallfeldtheorie und Molekülmagnetismus.

Wir beginnen mit der Untersuchung des Hamiltonoperators freier Lanthanidionen und leiten Matrixelemente her, die die elektronischen Strukturen, Spin-Bahn-Kopplung und Hyperfeinwechselwirkungen berücksichtigen. Durch die Verwendung von wasserstoffähnlichen Wellenfunktionen und Slater-Determinanten gewährleisten wir die Antisymmetrie in Viel-Elektronensystemen unter Beachtung des Pauli-Ausschlussprinzips. Die Spin-Bahn-Kopplung wird perturbativ behandelt, was zur Feinstrukturaufspaltung führt, wobei die Matrixelemente mithilfe von Drehimpulskopplungsschemata abgeleitet werden. Hyperfeinwechselwirkungen, einschließlich magnetischer Dipol- und elektrischer Quadrupolbeiträge, werden formuliert, um die Energieaufspaltung aufgrund von Kernspinzuständen zu berücksichtigen, die für Präzisionsspektroskopie und Quanteninformationsanwendungen essentiell sind.

Im Übergang zu Ligandenfeldtheorien erläutern wir, wie umliegende organische Liganden die elektronische Struktur von Lanthanidionen in Komplexen beeinflussen. Wir kontrastieren die Kristallfeldtheorie (CFT), die Liganden als Punktladungen modelliert, mit der Ligandenfeldtheorie (LFT), die Kovalenz und Orbitalüberlappung berücksichtigt. Der Ligandenfeld-Hamiltonoperator wird durch multipolare Expansionen ausgedrückt, und Matrixelemente werden unter Verwendung fortgeschrittener Drehimpulstheorie abgeleitet. Basierend auf der Ligandensymmetrie werden Auswahlregeln aufgestellt, die die Komplexität des Problems reduzieren. Diese Konzepte sind entscheidend für das Verständnis der elektronischen Struktur und Spektroskopie von lanthanid-organischen Komplexen, die im Quantencomputing verwendet werden.

Bei der Erforschung der Konfigurationswechselwirkung vertiefen wir uns in die Judd-Ofelt-Theorie und ihre Verallgemeinerungen, die elektrische Dipolübergänge in Lanthanidkomplexen beschreiben. Wir erläutern, wie ungerade Ligandenfeldparameter die Konfigurationsmischung zwischen Zuständen unterschiedlicher Parität, wie $4f^n$ und $4f^{n-1}5d$, ermöglichen und wie diese Mischung essentiell für das Verständnis des in Experimenten beobachteten Hyperfein-Stark-Effekts ist. Die Störungstheorie wird verwendet, um effektive Operatoren abzuleiten, die diese Übergänge berücksichtigen und einen theoretischen Rahmen für hyperfeininduzierte Übergänge in Lanthanidkomplexen bieten.

Relativistische Korrekturen werden durch die Dirac-Gleichung behandelt, die eine Grundlage für das Verständnis der Hyperfeinwechselwirkung und die Berechnung von Hyperfeinkonstanten bietet. Wir berücksichtigen die endliche Masse, Größe und magnetischen Eigenschaften von Atomkernen und wie diese Kernmerkmale die Hyperfeinstruktur in Lanthanidionen beeinflussen. Berechnungen von Hyperfeinkonstanten beinhalten Korrekturen für endliche Kernladungs- und Stromverteilungen unter Verwendung der Bohr-Weisskopf- und Breit-Rosenthal-Korrekturen.

Ein bedeutender Teil der Arbeit beinhaltet die Verwendung von Elektronen und Myonen als Kernsonden in wasserstoffähnlichen Lanthanidionen wie Dysprosium. Durch die Berechnung von Energieniveaus und Hyperfeinkonstanten für verschiedene Isotope und Kernmodelle zeigen wir, dass myonische Ionen aufgrund der stärkeren Wellenfunktionseindringung in den Kern eine erhöhte Empfindlichkeit gegenüber Kerneigenschaften bieten. Hyperfeinanomalien werden berechnet, was die Fähigkeit zeigt, zwischen verschiedenen Kernmodellen und Isotopen zu unterscheiden, was wertvoll für die Gestaltung von Qudits mit gewünschten Eigenschaften ist.

Im Übergang zum Quantencomputing konzentrieren wir uns auf die Verwendung von Kernspins in Lanthanidionen als Qudits für die Quanteninformationsverarbeitung. Wir geben einen Überblick über Qubits, Qudits und wesentliche Quantenkonzepte wie Zustandsdarstellungen, Quantengatter und kritische Zeitskalen. Wir diskutieren die Unterschiede zwischen Qubits und Qudits und zeigen, wie Qudits als d -dimensionale Quantensysteme mehr Informationen darstellen und potenziell Vorteile gegenüber Qubits bieten können. Die Skalierung von Rauschen mit der Dimension des Hilbertraums wird analysiert, und Bedingungen, unter denen Qudits Qubits übertreffen, werden abgeleitet.

Wir untersuchen die Dynamik offener Quantensysteme, die unter der Annahme der Markow-Eigenschaft mit einer Umgebung interagieren, und verwenden die Lindblad-Gleichung zur Modellierung dieser Systeme. Durch Anwendung der Störungstheorie auf die Lindblad-Mastergleichung untersuchen wir die Auswirkungen von Dekohärenz auf Quantenoperationen in Qudits. Über den Erstordnungsansatz hinaus werden höhere Ordnungen betrachtet, die die Nichtlinearität der Fid

elität in offenen Qudit-Systemen aufzeigen und die Notwendigkeit betonen, diese Korrekturen in hochdimensionalen Systemen zu berücksichtigen.

Um die Implementierung von Quantengattern auf Kernspins anzugehen, verwenden wir die Optimalsteuerungstheorie, um die Gattererzeugung zu optimieren und Gatterzeiten zu reduzieren, wodurch die Systemleistung verbessert wird. Techniken wie die Rotierende-Wellen-Näherung, Givens-Rotationszerlegung und optimale Kontrollalgorithmen wie GRAPE und MAGICARP werden genutzt, um die Zeit- und Energiekosten bei der Implementierung von Quantengattern in hochdimensionalen Systemen zu minimieren. Diese Methoden sind entscheidend, um die Herausforderungen zu überwinden, die mit längeren Gatterzeiten und erhöhter Dekohärenz in Qudits einhergehen.

Abschließend untersucht das Manuskript die Anwendungen der Prouhet-Thue-Morse-Sequenz im Quantencomputing. Diese mathematische Sequenz zeigt erhebliche Nützlichkeit in der Fehlerkorrektur, dem Design von rauschresistenten Quanten-Speichern und der Analyse von Quantenchaos. Ihre Eigenschaften ermöglichen den Aufbau logischer Zustände, die die Knill-Laflamme-Bedingungen für Fehlererkennung und -korrektur erfüllen und somit Robustheit gegenüber bestimmten Fehlertypen und Dephasierung bieten.

Insgesamt präsentiert das Manuskript eine umfassende Studie, die Atomphysik und Quantencomputing verbindet, mit speziellem Fokus auf Hyperfeinwechselwirkungen in lanthanid-organischen Komplexen für die Quanteninformationsverarbeitung. Die Arbeit liefert theoretische Einblicke in die komplexen Wechselwirkungen innerhalb dieser Systeme und praktische Überlegungen für den Fortschritt von Quantencomputing-Technologien unter Verwendung von Lanthanid-basierten Qudits.

Résumé

Dans ce manuscrit intitulé "Interactions hyperfines dans les complexes organiques de lanthanides pour le traitement de l'information quantique", nous explorons l'interaction complexe entre la physique atomique et le calcul quantique, en nous concentrant sur les interactions hyperfines dans des complexes organiques de lanthanides et leurs applications dans le traitement de l'information quantique. Ce travail établit un lien entre plusieurs disciplines, y compris le calcul quantique, la théorie du contrôle optimal, la structure nucléaire, les interactions hyperfines, les éléments f , la théorie du champ cristallin et le magnétisme moléculaire.

Nous commençons par examiner le hamiltonien des ions lanthanides libres, en dérivant des éléments de matrice qui tiennent compte de la structure électronique, du couplage spin-orbite et des interactions hyperfines. En utilisant des fonctions d'onde de type hydrogénoïde et des déterminants de Slater, nous assurons l'antisymétrie dans les systèmes multi-électroniques, conformément au principe d'exclusion de Pauli. Le couplage spin-orbite est traité de manière perturbative, conduisant au dédoublement de la structure fine, avec des éléments de matrice dérivés en utilisant des schémas de couplage de moment angulaire. Les interactions hyperfines, y compris les contributions dipolaires magnétiques et quadrupolaires électriques, sont formulées pour rendre compte du dédoublement des niveaux d'énergie dû aux états de spin nucléaire, essentiels pour la spectroscopie de précision et les applications en information quantique.

En passant aux théories du champ de ligands, nous élaborons sur la manière dont les ligands organiques environnants influencent la structure électronique des ions lanthanides dans les complexes. Nous contrastons la théorie du champ cristallin (CFT), qui modélise les ligands comme des charges ponctuelles, avec la théorie du champ de ligands (LFT), qui considère la covalence et le recouvrement orbitalaire. Le hamiltonien du champ de ligands est exprimé à travers des expansions multipolaires, et les éléments de matrice sont dérivés en utilisant une théorie avancée du moment angulaire. Des règles de sélection basées sur la symétrie des ligands sont établies, réduisant la complexité du problème. Ces concepts sont cruciaux pour comprendre la structure électronique et la spectroscopie des complexes organiques de lanthanides utilisés en calcul quantique.

En explorant l'interaction de configuration, nous approfondissons la théorie de Judd-Ofelt et ses généralisations, qui décrivent les transitions dipolaires électriques dans les complexes de lanthanides. Nous abordons comment les paramètres impairs du champ de ligands facilitent le mélange de configurations entre des états de parité différente, tels que $4f^n$ et $4f^{n-1}5d$, et comment ce mélange est essentiel pour comprendre l'effet Stark hyperfin observé dans les expériences. La théorie des perturbations est employée pour dériver des opérateurs effectifs qui rendent compte de ces transitions, fournissant un cadre théorique pour les transitions induites hyperfines dans les complexes de lanthanides.

Les corrections relativistes sont abordées à travers l'équation de Dirac, fournissant une base pour comprendre l'interaction hyperfine et calculer les constantes hyperfines. Nous considérons la masse finie, la taille et les caractéristiques magnétiques des noyaux atomiques, et comment ces propriétés nucléaires influencent la structure hyperfine dans les ions lanthanides. Les calculs des constantes hyperfines incluent des corrections pour la distribution finie de charge et de courant nucléaire, en utilisant les

corrections de Bohr-Weisskopf et de Breit-Rosenthal.

Une partie significative du travail implique l'utilisation d'électrons et de muons comme sondes nucléaires dans des ions hydrogénoïdes de lanthanides, tels que le dysprosium. En calculant les niveaux d'énergie et les constantes hyperfines pour différents isotopes et modèles nucléaires, nous démontrons que les ions muoniques fournissent une sensibilité accrue aux propriétés nucléaires en raison d'une plus grande pénétration de la fonction d'onde dans le noyau. Des anomalies hyperfines sont calculées, révélant la capacité à discriminer entre différents modèles nucléaires et isotopes, ce qui est précieux pour concevoir des qubits avec des propriétés désirées.

En passant au calcul quantique, nous nous concentrons sur l'utilisation des spins nucléaires dans les ions lanthanides comme qubits pour le traitement de l'information quantique. Nous fournissons un aperçu des qubits, des qudits et des concepts quantiques essentiels tels que les représentations d'états, les portes quantiques et les échelles de temps critiques. Nous discutons des différences entre les qubits et les qudits, illustrant comment les qudits, en tant que systèmes quantiques à d niveaux, peuvent représenter plus d'informations et potentiellement offrir des avantages par rapport aux qubits. La mise à l'échelle du bruit avec la dimension de l'espace de Hilbert est analysée, et des conditions dans lesquelles les qudits surpassent les qubits sont dérivées.

Nous explorons la dynamique des systèmes quantiques ouverts interagissant avec un environnement sous l'hypothèse markovienne, en employant l'équation de Lindblad pour modéliser ces systèmes. En utilisant la théorie des perturbations sur l'équation maîtresse de Lindblad, nous étudions les effets de la décohérence sur les opérations quantiques dans les qudits. Au-delà de l'approche de premier ordre, des corrections d'ordre supérieur sont considérées, révélant la non-linéarité de la fidélité dans les systèmes de qudits ouverts et la nécessité de prendre en compte ces corrections dans les systèmes de haute dimension.

Pour aborder l'implémentation des portes quantiques sur les spins nucléaires, nous employons la théorie du contrôle optimal pour optimiser la génération des portes et réduire les temps de porte, améliorant ainsi les performances du système. Des techniques telles que l'approximation de l'onde tournante, la décomposition en rotations de Givens et les algorithmes de contrôle optimal comme GRAPE et MAGICARP sont utilisées pour minimiser les coûts en temps et en énergie lors de l'implémentation des portes quantiques dans des systèmes de haute dimension. Ces méthodes sont cruciales pour surmonter les défis associés aux temps de porte plus longs et à l'augmentation de la décohérence dans les qudits.

Enfin, le manuscrit explore les applications de la séquence de Prouhet-Thue-Morse dans le calcul quantique. Cette séquence mathématique s'est avérée avoir une utilité significative dans la correction d'erreurs, la conception de mémoires quantiques résistantes au bruit et l'analyse du chaos quantique. Ses propriétés permettent la construction d'états logiques qui satisfont aux conditions de Knill-Laflamme pour la détection et la correction d'erreurs, offrant une robustesse contre certains types d'erreurs et de déphasage.

Dans l'ensemble, le manuscrit présente une étude complète qui relie la physique atomique et le calcul quantique, avec un accent spécifique sur les interactions hyperfines dans les complexes organiques de lanthanides pour le traitement de l'information quantique. Le travail fournit des aperçus théoriques sur les interactions complexes au sein de ces systèmes et des considérations pratiques pour faire progresser les technologies de calcul quantique en utilisant des qudits à base de lanthanides.

Contents

1	Introduction	1
1.1	Converging Paths: A multidisciplinary historical prelude	1
1.1.1	Quantum Computing	2
1.1.2	Optimal Control Theory	3
1.1.3	Nuclear structure	4
1.1.4	Hyperfine Interactions	6
1.1.5	f-elements	7
1.1.6	Crystal Field Theory	9
1.1.7	Molecular magnetism	10
1.2	Bridging the gap via lanthanide-organic complexes	12
1.2.1	The poster child: TbPc ₂	13
1.2.2	A scale-encompassing Hamiltonian	14
1.2.3	Towards a molecular quantum processor	16
1.2.4	Where the theory is lacking	16
1.3	Thesis outline	19
I	Lanthanides in matter: atomically free yet chemically bound	21
2	Free atom/ion Hamiltonian	25
2.1	Non-interacting e ⁻ in a central potential	25
2.1.1	Solving the eigensystem	26
2.1.2	Configuration basis	27
2.2	Angular momenta coupling schemes	27
2.3	Matrix elements for the two-electrons case	29
2.4	Unit Tensor Operators	33
2.4.1	Single electron operators	33
2.4.2	Multi-electron operators	34
2.5	Coulomb interelectronic repulsion	35
2.5.1	The diagonal basis	36
2.5.2	Matrix element for the valence shell	37
2.5.3	Mean-field contribution	39
2.5.4	Matrix element of excited configurations	39
2.5.5	Example in the case of two electrons	40
2.5.6	Off-diagonal elements of the interelectronic repulsion	41
2.5.7	LSJ-coupling	42
2.6	Spin-orbit coupling	42
2.6.1	The diagonal basis	42
2.6.2	Matrix element for the valence shell	43

2.6.3	Matrix element for excited configurations	44
2.6.4	Example in the case of two electrons	45
2.7	Hyperfine coupling	45
2.7.1	Magnetic Hyperfine interaction	45
2.7.2	Electric Quadrupole Hyperfine interaction	47
2.7.3	Hyperfine Splitting	48
3	Ligand Field	51
3.1	From Crystal Field Theory to Ligand Field Theory	51
3.1.1	Crystal Field Theory	51
3.1.2	Matrix element in the valence shell	52
3.1.3	Matrix element for excited configurations	53
3.1.4	Selection rules for the crystal field parameters	54
3.1.5	Mean field contribution	58
3.1.6	Ligand Field Theory	58
3.2	Ligand Field DFT	59
3.2.1	The radial degrees of freedom	60
4	Configuration Interaction	65
4.1	Symmetry and odd Ligand Field Parameters	65
4.2	Judd-Ofelt theory and effective operators	65
4.2.1	Overview of the Judd-Ofelt theory	65
4.3	The hyperfine Stark effect	72
4.3.1	The modulation of the hyperfine constant by an electric field	72
4.3.2	Double perturbation applied to the hyperfine magnetic dipole interaction	73
4.4	Towards hyperfine-induced luminescence	77
II	The Hyperfine Interaction	87
5	The Dirac equation	91
5.1	Introducing relativity into the Schrödinger equation	91
5.1.1	The Klein-Gordon equation	91
5.1.2	The Dirac equation	92
5.2	Adding external fields: The single-electron ion	94
5.2.1	The Dirac equation with external electromagnetic fields	94
5.2.2	The Dirac equation for a single-electron ion	94
5.3	Beyond the Dirac equation	96
6	The finite nucleus	99
6.1	Mass corrections	99
6.2	Muonic ions	99
6.3	The nuclear charge distribution	100
6.3.1	Ab-initio computation of the nuclear charge distribution	100
6.3.2	Multipole expansion of the nuclear potential	104
6.3.3	Electric monopole moment	106
6.3.4	Electric quadrupole moment	108
6.4	The nuclear current distribution	110
6.4.1	Ab-initio computation of the nuclear current distribution	111
6.4.2	Multipole expansion of the nuclear magnetic vector potential	117
6.4.3	Magnetic dipole moment	119
6.5	Other effects of the nucleus	120

7	Hyperfine constants	125
7.1	The hyperfine dipole constant	125
7.2	The hyperfine quadrupole constant	130
7.3	Isotope Shifts	132
7.3.1	The hyperfine anomaly	132
7.3.2	The Breit-Rosenthal correction	133
7.3.3	The Bohr-Weisskopf correction	133
7.3.4	Quadrupole hyperfine anomaly	134
7.4	The non-relativistic limit	135
7.4.1	The Pauli approximation	135
7.4.2	The non-relativistic limit of the hyperfine dipole constant	137
7.4.3	Fermi contact term for a finite current distribution nucleus	139
7.5	Hyperfine constants in matter	141
8	The electron/muon as a nuclear probe: hydrogen-like Dy ions	143
8.1	Wavefunctions of the electron and muon in H-like ions	143
8.2	Muonic and electronic H-like energy levels	144
8.3	Hyperfine isotope shifts of $^{161/163}\text{Dy}^{65+}$	151
8.3.1	Breit-Rosenthal corrections to the hyperfine constants	151
8.3.2	Bohr-Weisskopf corrections to the hyperfine constants	154
8.3.3	Hyperfine anomaly between ^{161}Dy and ^{163}Dy	158
8.3.4	Quadrupole hyperfine anomaly	159
8.4	Additional examples of $^{159}\text{Tb}^{64+}$ and $^{165}\text{Ho}^{66+}$	163
8.4.1	Nuclear charge and current densities	163
8.4.2	Hyperfine constants	168
III	Quantum Computing with Nuclear Spins in Lanthanides	175
9	From bits to qubits to qudits	179
9.1	What is a qubit?	179
9.1.1	State Representation	179
9.1.2	Density matrix representation	179
9.1.3	Bloch Sphere Representation	180
9.1.4	Entanglement	181
9.2	Quantum gates	182
9.2.1	Characteristics of Quantum Gates	182
9.2.2	Types of Quantum Gates	182
9.2.3	Implementing Quantum Gates	182
9.2.4	Physical Realisation	184
9.3	Quantum algorithms	184
9.3.1	Quantum Circuit	184
9.3.2	Prominent Quantum Algorithms	185
9.4	What is a qudit?	189
9.4.1	State Representation	189
9.4.2	Density Matrix Representation	189
9.4.3	Generalized Bloch Representation	189
9.4.4	Quantum Gates for Qudits	190
9.4.5	Advantages of Qudits	190
9.5	Timescales	190
9.5.1	T_1 : Longitudinal Relaxation Time	190

9.5.2	T_2 : Decoherence Time	191
9.5.3	T_2^* : Dephasing time	191
10	Markovian open quantum systems	195
10.1	The Lindblad equation	195
10.2	Alternative way to model errors: Kraus operators	196
10.3	Link with T_1 and T_2 timescales	197
10.3.1	Pure dephasing	197
10.3.2	Longitudinal relaxation	197
10.3.3	Dephasing in qudits	197
10.4	Issues in solving the Lindblad equation numerically	198
11	Noisy qudits vs. qubits: First-order approach	201
11.1	The AGI: Definition and First-Order Approximation	201
11.1.1	Fluctuation-dissipation relation for a perturbed pure state	201
11.1.2	Average Gate Fidelity of a single qudit	202
11.1.3	Average Gate Infidelity for the Pure Dephasing Channel of one qudit	203
11.1.4	1 dephasing qudit vs N qubits: Different AGI scalings	204
11.1.5	Process fidelity & averaged fluctuation-dissipation relation	206
11.2	Numerical validation and deviation	207
11.2.1	Fit and deviation from the linear behaviour	208
11.2.2	Gate dependence	208
11.2.3	Other cases than pure dephasing	210
11.2.4	A single qudit vs an ensemble of qubits	211
11.2.5	Summary	213
11.3	Linear and exp. scalings from the perspective of the AGI	215
11.3.1	Scaling of the gate durations with the number of qudits	215
11.3.2	Scaling of the noise strength with the number of qudits	217
12	Noisy qudit: Beyond the first-order approach	221
12.1	The Lindblad equation as a superoperator	221
12.2	Perturbative expression of the AGI	224
12.2.1	First-order AGI	226
12.2.2	Second-order AGI	227
12.2.3	Pure dephasing example and error correction considerations	229
12.3	Universal bounds on the AGI for large noise and gate times	231
13	Optimal gate generation	237
13.1	Rotating Wave Approximation and Rotating Frame	237
13.1.1	Laboratory frame to rotating frame	237
13.2	Quantum Speed Limits	243
13.2.1	Example for a qubit	243
13.2.2	General case	247
13.3	An overview of gate generation methods	251
13.3.1	(GRD) Givens Rotation Decomposition	251
13.3.2	GRAPE Algorithm	253
13.4	Towards optimal qudit gates	258
13.4.1	Optimal Control and Cost Functions	258
13.4.2	Pontryagin's Maximum Principle	259
13.4.3	PMP-informed discrete gradient ascent: MAGICARP	263

IV	The Ubiquitous Prouhet-Thue-Morse Sequence	277
14	The Ubiquitous Prouhet-Thue-Morse Sequence	279
14.1	The multiple definitions of the Prouhet-Thue-Morse sequence	279
14.2	The T-M sequence in Quantum Computing	281
14.2.1	Definition of PTM (logical) states	281
14.2.2	Relations between the PTM states and the Hadamard gate	283
14.2.3	X - X Spin chain and the PTM states	283
14.2.4	PTM states as eigenvalues of S_x	284
14.2.5	The PTM sequence as the indicator function of the purely dephased X - X Ising chain	284
14.2.6	Initializing a spin system in a Thue-Morse state	285
14.2.7	Quantum Error Correction (QEC)	285
14.2.8	Noise-resistant quantum memories	288
14.3	Link to quantum chaos	288
14.4	Link with number theory	289
14.5	Conclusion	291
V	Conclusion	295
15	Overview and Perspectives	297
15.1	Current state of the art	297
15.1.1	A theoretical toolbox for lanthanide-based qudit engineering	297
15.1.2	A how-to guide for Ln-molecular QIP implementations	297
15.1.3	Nuclear and hyperfine structure of lanthanides	298
15.2	Areas left to explore	299
15.2.1	Ab-initio study of the decoherence	299
15.2.2	In-depth study of the effect of ligand composition and geometry	299
15.2.3	Calculating the hyperfine structure of multielectronic ions in molecules/crystals	300
15.2.4	A methodology for exploring the isotopologue quantum chemical space	301
15.2.5	Computational performance scalings with increased number of qudits	302
15.2.6	Quantifying the optimality of a qudit gate implementation	302
15.2.7	Towards noise-robust and error-corrected qudit quantum computing	303
VI	Appendix	315
A	Mathematical Prelude to Quantum Information Processing	317
A.1	Hilbert Spaces and States	317
A.1.1	Operators on Hilbert Spaces	317
A.1.2	Quantum Postulates	318
A.1.3	Finite Dimensional Hilbert Spaces and Basis Representation	318
A.1.4	Composite Systems and Tensor Products	318
A.2	Schrödinger Equation and Evolution Operator	319
A.2.1	Time-Dependent Schrödinger Equation	319
A.2.2	Time-Independent Schrödinger Equation	319
A.2.3	Evolution Operator	320
A.2.4	Time-Dependent Evolution Operator	320
A.2.5	Interaction picture	321
A.2.6	The Heisenberg Picture	321
A.3	Density matrices	322
A.4	Superoperators and vectorisation	323

A.5	Quantum channels and Kraus operators	324
B	Methods for the numerical simulations	327
B.1	Numerical noisy qudit/multiqubit simulation	327
B.2	Random gate and pulse Hamiltonian generation	328
C	Symmetries I: Spherical Harmonics and Multipoles	329
C.1	Spherical Harmonics	329
C.2	Multipolar expansion	331
D	Symmetries II: Tensor Operators and Racah-Wigner coefficients	335
D.1	Coordinate systems	335
D.1.1	Polar Coordinates	335
D.1.2	Spherical Coordinates (or circular polarization basis)	335
D.2	Irreducible Tensor Operators	335
D.2.1	Angular Momentum Operators	335
D.2.2	Definition	336
D.3	n_j symbols	337
D.3.1	3_j symbols	337
D.3.2	6_j and 9_j symbols	338
D.3.3	Wigner-Eckart theorem	340
D.3.4	Coupled tensor operators	341
E	Preprint summarized in the main text	343
E.1	Nonlinearity of the Fidelity in Open Qudit Systems	344
F	Proofs of the statements in the main text	373
.1	Proofs for Section 9.5 (Timescales)	374
.2	Proofs for Section 11.1 (The Average Gate Infidelity: Definition and First-Order Approximation)	375
.3	Proofs for Section 12.2 (Perturbative expression of the AGI)	376
.4	Proofs for Section 12.3 (Universal bounds on the AGI for large noise and gate times) . . .	382
.5	Proofs for Section 13.2 (Quantum Speed Limits)	383
.6	Proofs for Section 14.2 (The T-M sequence in Quantum Computing)	384
.7	Proofs for Section 15.2 (Areas left to explore)	388
VII	French summarized version	401
0^F	Introduction en français	I
0 ^F .1	Chemins convergents : Une introduction historique multidisciplinaire	I
0 ^F .2	Comblen les lacunes grâce aux complexes organiques de lanthanides	XIII
0 ^F .3	Plan de la thèse	XX
I^F	(Résumé) Les lanthanides dans la matière: libres atomiquement mais liés chimiquement	XXIII
I ^F .1	hamiltonien d'un atome/ion libre	XXIII
I ^F .2	Champ de Ligands	XXV
I ^F .3	Interaction de configurations	XXVII
II^F	(Résumé) L'interaction hyperfine	XXIX
II ^F .1	L'équation de Dirac	XXIX
II ^F .2	Le noyau fini	XXX
II ^F .3	Constantes hyperfines	XXXII
II ^F .4	L'électron/muon comme sonde nucléaire : ions hydrogéoïdes de Dy	XXXIV

III^F (Résumé) Informatique Quantique avec des spins nucléaire de lanthanides	XXXVII
III ^F .1 Des bits aux qubits aux qudits	XXXVII
III ^F .2 Systèmes quantiques ouverts markoviens	XXXVIII
III ^F .3 Qudit bruyant vs. plusieurs qubits : approche du premier ordre	XL
III ^F .4 Qudit bruyant : Au-delà de l’approche du premier ordre	XLI
III ^F .5 Génération optimale de portes	XLIII
IV^F (Résumé) La séquence omniprésente de Prouhet-Thue-Morse	XLV
IV ^F .1 La séquence omniprésente de PTM	XLV
V^F Conclusion en français – Aperçu et Perspectives	XLVII
V ^F .1 État de l’art actuel	XLVII
V ^F .2 Axes de recherche futurs	XLIX

Chapter Contents

1.1	Converging Paths: A multidisciplinary historical prelude	1
1.2	Bridging the gap via lanthanide-organic complexes	12
1.3	Thesis outline	19

CHAPTER 1

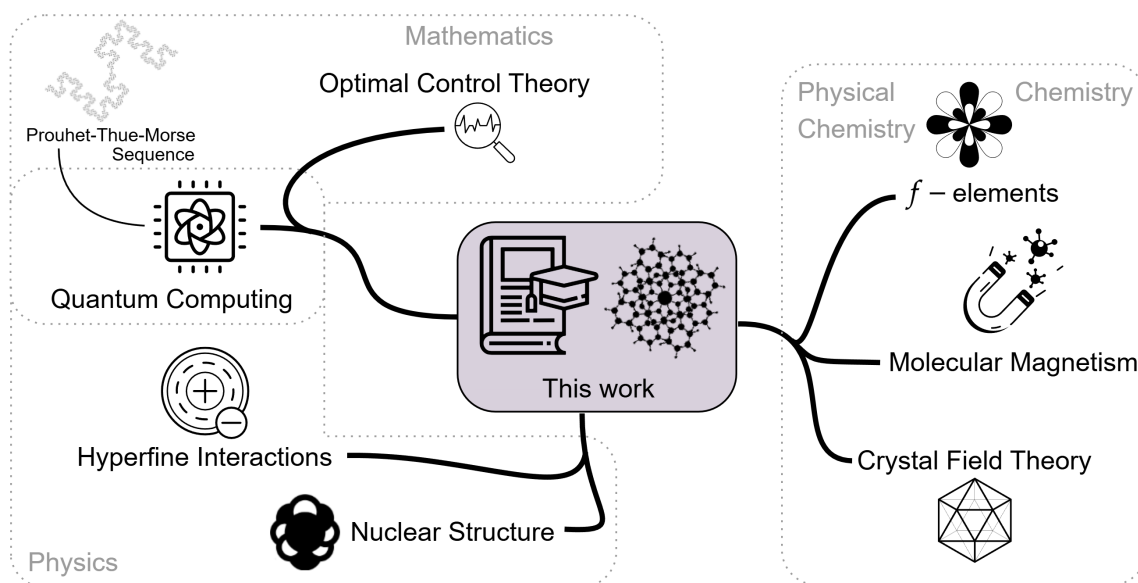
Introduction

"You have to know the past to understand the present."

— Carl Sagan

This introductory chapter aims to present all the different fields and how they relate to this thesis and endeavour. First, it will introduce the historical background and current state of the art of different formalisms. Then it will discuss how they weave together to form the theoretical foundation used for the systems of interest in this study.

1.1 Converging Paths: A multidisciplinary historical prelude



This work is at the intersection of several fields: quantum computing, optimal control theory, nuclear structure, hyperfine interactions, f -elements, crystal field theory, and molecular magnetism. The historical development of these fields has been intertwined, with each contributing unique insights and methodologies that have shaped our understanding of quantum systems and materials. This section

provides a brief overview of the evolution of these disciplines and their convergence, in this work, toward the study of lanthanide-organic complexes for quantum information processing.

1.1.1 Quantum Computing

The evolution of quantum computing is intimately connected with the quest to comprehend and manipulate the foundational principles of information processing. While classical computing has achieved remarkable advancements, the relentless miniaturization of transistors is approaching the physical limits imposed by quantum mechanics [1, 2]. This impending convergence has propelled the exploration of quantum computing as a new paradigm that leverages the unique properties of quantum mechanics.

The inception of quantum computing ideas can be traced back to the early 1980s. Yuri Manin first proposed the concept of harnessing quantum mechanics for computation in 1980 [3]. Shortly thereafter, Paul Benioff introduced a quantum mechanical model of a Turing machine [4], laying the groundwork for theoretical quantum computing models. Richard Feynman, in his seminal 1982 paper *Simulating physics with computers* [5], famously declared, "Nature isn't classical, dammit, and if you want to make a simulation of nature, you'd better make it quantum mechanical." David Deutsch further advanced the field in 1985 by proposing the first universal quantum computer model [6].

The development of quantum algorithms has been pivotal in demonstrating the potential advantages of quantum computers over their classical counterparts. Peter Shor's groundbreaking algorithm in 1994 for factoring large numbers and computing discrete logarithms [7] showcased that quantum computers could solve certain problems exponentially faster than classical computers. Lov Grover's 1996 algorithm provided a quadratic speedup for unstructured search problems [8], and Seth Lloyd's work on universal quantum simulators [9] highlighted the capability of quantum systems to efficiently simulate other quantum systems.

These theoretical advancements spurred extensive research into practical implementations of quantum computers. Various physical platforms have been explored, including superconducting circuits [10], trapped ions [11, 12], photonic systems [13, 14], neutral atoms [15, 16], and semiconductor quantum dots [17, 18]. Among these, superconducting qubits have emerged at the forefront due to their scalability and integration with existing technologies. Companies like IBM and Google have developed superconducting quantum processors with dozens to hundreds of qubits [19, 20], achieving significant milestones in coherence times and gate fidelities.

Despite rapid development, substantial technical challenges remain in achieving universal and fault-tolerant quantum computation. Issues related to decoherence, noise management, and error correction persist, particularly as systems scale up [21]. The DiVincenzo criteria [22] outline the essential requirements for a functional quantum computer, including scalable qubits, reliable initialization, long coherence times, a universal set of quantum gates, and efficient qubit readout. Meeting all these criteria simultaneously is a formidable task, and current qubit-based platforms (summarized in Fig. 1.1) often struggle with maintaining coherence and high-fidelity operations in larger systems.

In light of these challenges, alternative approaches such as qudits—quantum systems with more than two levels—have garnered increasing interest. By encoding information in higher-dimensional Hilbert spaces, qudits can potentially enhance computational efficiency and reduce the complexity of quantum circuits [23]. Although classical computing eventually standardized on binary bits, early computers explored ternary logic to increase computational capacity [24]. Similarly, qudits offer a way to encode more information per physical unit, which could be advantageous for scalability.

Nuclear spin systems, in particular, present an intriguing avenue due to their long coherence times and inherent isolation from environmental noise. The interplay between electronic and nuclear degrees of freedom in these systems offers unique advantages for quantum information processing [25]. While the strong isolation of nuclear spins poses challenges for control and manipulation, advancements in

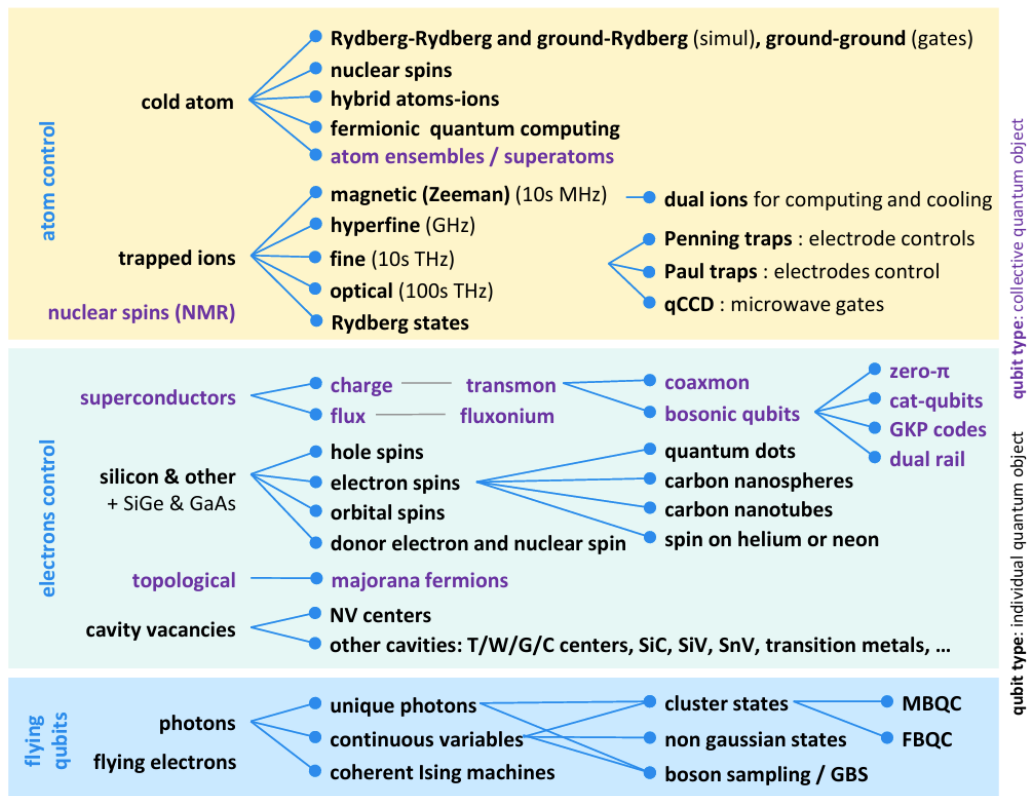


Figure 1.1: Rough zoology of qubit quantum computing platforms. Adapted from Ezratty [21].

platform design and control techniques [26] are making it increasingly feasible to harness these systems for quantum computing.

The exploration of qudit-based quantum computing represents a promising strategy to overcome some of the inherent limitations of qubit-based systems. By leveraging the natural properties of nuclear spins and high-dimensional quantum states, we may achieve more scalable and robust quantum computing architectures. As we continue to push the boundaries of technology and theory, the convergence of multiple disciplines—including physics, chemistry, and computer science—will be crucial in advancing toward the realization of practical quantum computers.

1.1.2 Optimal Control Theory

Optimal Control Theory is a mathematical discipline focused on finding control policies that optimize the performance of dynamical systems. Its origins trace back to the calculus of variations developed by Euler and Lagrange in the 18th century, which provided methods for finding functions that minimize or maximize functionals. This foundation set the stage for addressing more complex optimization problems in engineering and physics.

In the mid-20th century, the field experienced significant advancements with the introduction of the Pontryagin Maximum Principle by Lev Pontryagin and his collaborators in 1956 [27, 28]. This principle offered necessary conditions for optimality in control problems, enabling the determination of control laws that steer a system from an initial state to a final state while optimizing a given performance criterion. Around the same time, Richard Bellman developed the concept of dynamic programming, leading to the formulation of the Hamilton-Jacobi-Bellman equation [29], which provides a method for solving control problems by breaking them down into simpler subproblems.

Optimal Control Theory has been instrumental in various fields such as economics, where it aids in resource allocation; aerospace engineering, for trajectory optimization; and robotics, for motion

planning. In recent decades, its principles have been applied to quantum systems, giving rise to the field of quantum control. Quantum control involves manipulating quantum states and dynamics to achieve desired outcomes, which is essential for quantum computing and quantum information processing [30, 31].

In quantum computing, Optimal Control Theory is employed to design control pulses that drive qubits through specific quantum gates with high fidelity. Techniques like Gradient Ascent Pulse Engineering (GRAPE) have been developed to optimize control fields in systems with complex interactions [32]. These methods adjust control parameters iteratively to maximize the overlap between the desired and actual quantum states, effectively navigating the challenging control landscape of quantum systems.

As quantum systems become more intricate, especially with the introduction of qudits that have higher-dimensional state spaces, the application of Optimal Control Theory becomes increasingly vital. The complexity of controlling such systems requires sophisticated mathematical tools to ensure precise manipulation while mitigating errors due to decoherence and other quantum noise sources.

Integrating Optimal Control Theory with quantum technologies not only enhances the performance of quantum operations but also contributes to overcoming some of the scalability challenges faced by current quantum computing platforms. By optimizing control strategies, it's possible to improve gate fidelities and coherence times, bringing us closer to the realization of universal and fault-tolerant quantum computers.

1.1.3 Nuclear structure

The study of nuclear structure aims to understand the properties and behaviors of atomic nuclei by examining the interactions among protons and neutrons. This field has evolved significantly since Ernest Rutherford's gold foil experiment in 1911, which led to the discovery of the atomic nucleus [33]. Rutherford's work laid the foundation for subsequent models that sought to explain nuclear stability, binding energies, and other fundamental properties.

Early theoretical models, such as the liquid drop model proposed by George Gamow [34] and later refined by Niels Bohr and John Archibald Wheeler [35], treated the nucleus as an incompressible fluid drop. This macroscopic approach successfully explained nuclear fission and bulk properties but could not account for the discrete energy levels observed in experiments. To address this, Maria Goeppert Mayer and J. Hans D. Jensen independently developed the nuclear shell model in 1949 [36, 37], which considered individual nucleons moving in a mean potential. The shell model explained the occurrence of "magic numbers" corresponding to exceptionally stable configurations. This model illuminated the importance of quantum mechanics in nuclear systems and earned its creators the Nobel Prize in Physics in 1963. For illustrative purposes Fig. 1.2 shows the nuclear shell model orbits with their respective quantum numbers and typical level ordering.

Understanding the strong nuclear force—the fundamental force responsible for binding protons and neutrons together—has been crucial in nuclear physics. The strong force is characterized by its short-range yet immensely powerful attraction, overcoming the electromagnetic repulsion between protons. However, directly solving the equations of quantum chromodynamics (QCD) for nuclei is computationally intractable due to the complexity of many-body interactions at low energies.

To circumvent this challenge, effective interactions and phenomenological models have been developed. One notable example is the Skyrme interaction, introduced by Tony Skyrme in 1958 [39]. The Skyrme interaction is a parameterized effective force used within the mean-field framework, allowing for simplified calculations of nuclear properties while capturing essential features of the strong force.

The Skyrme-Hartree-Fock (SHF) method combines the Skyrme interaction with the Hartree-Fock approach to model the nucleus as a collection of independent nucleons moving in self-consistent mean fields [40]. This method accounts for exchange and correlation effects crucial for an accurate description of nuclear systems. To include pairing correlations essential for open-shell nuclei, the Hartree-Fock-

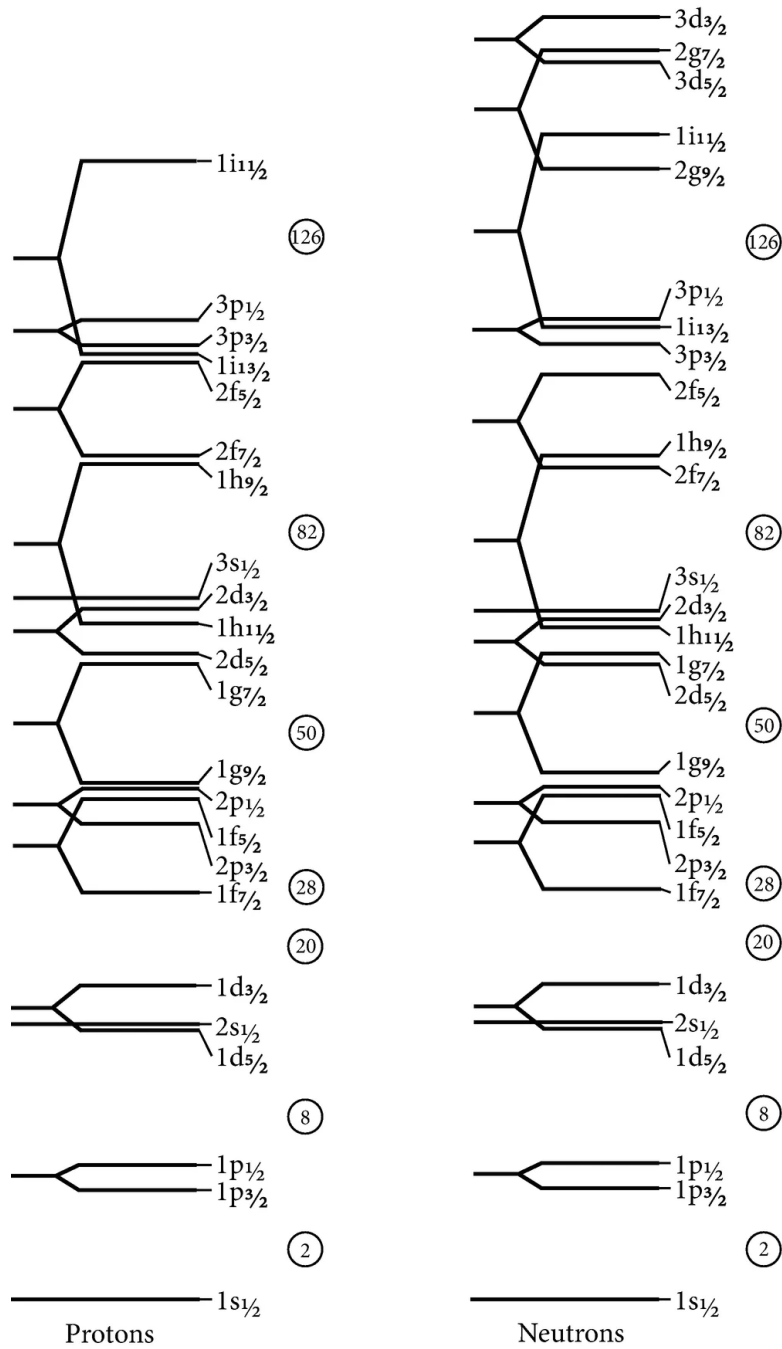


Figure 1.2: Nuclear shell-model orbits with their respective quantum numbers and typical level ordering. Magic numbers of protons and neutrons are shown encircled. Adapted from [38].

Bogoliubov (HFB) theory extends the SHF method by incorporating Bogoliubov transformations [41].

Deformed nuclei, particularly those in the lanthanide series, exhibit significant deviations from spherical symmetry due to their open-shell configurations and strong nucleon-nucleon interactions [42, 43]. The SHF and HFB models, employing Skyrme-type interactions, have been instrumental in predicting and explaining the properties of these deformed nuclei.

1.1.4 Hyperfine Interactions

The exploration of hyperfine interactions has been a cornerstone in the development of atomic and nuclear physics, providing profound insights into the internal structures of atoms and nuclei. The phenomenon was first observed in the late 19th - early 20th century when spectroscopists detected minute splittings in atomic spectral lines that extended beyond the fine structure explained by electron spin-orbit coupling. These additional splittings, termed hyperfine structure, were attributed to interactions between the electrons and the nucleus, specifically involving nuclear magnetic moments.

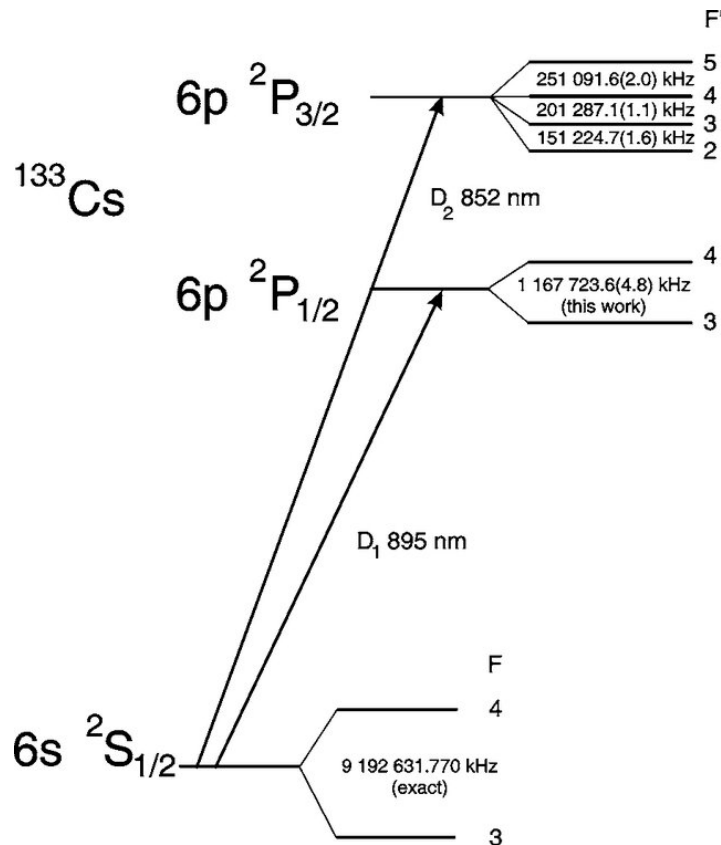


Figure 1.3: Neutral ^{133}Cs energy level diagram, not to scale. The hyperfine transition between the $F = 4$ and $F = 3$ ground states is used as the basis for atomic clocks. Adapted from [44].

The theoretical understanding of hyperfine interactions was significantly advanced by the introduction of the electron spin concept by George Uhlenbeck and Samuel Goudsmit [45]. Their proposal that electrons possess intrinsic angular momentum, or spin, was instrumental in explaining atomic fine structures. Paul Dirac's relativistic quantum theory of the electron further provided a comprehensive framework incorporating electron spin and magnetic moments [46], which was essential for accurately describing fine structure phenomena.

To account for hyperfine structures, it became necessary to consider the nuclear magnetic dipole moment arising from the intrinsic spin and orbital motion of protons and neutrons within the nucleus. The interaction between the nuclear magnetic moment and the magnetic field produced by the electrons at the nucleus leads to energy level splittings observable as hyperfine structure [47].

As experimental precision improved, it was discovered that certain nuclei exhibited hyperfine splittings that could not be fully explained by magnetic dipole interactions alone. In 1939, the existence of the nuclear electric quadrupole moment was proposed to address these discrepancies [48]. This quadrupole moment arises from a non-spherical charge distribution within deformed nuclei and interacts with the electric field gradients generated by surrounding electrons, leading to additional hyperfine splitting [49].

Further refinements in hyperfine interaction theory included corrections accounting for the finite size and structure of the nucleus. The Bohr-Weisskopf effect [50] considers the distribution of nuclear magnetization and its impact on the hyperfine interaction, which becomes particularly significant in heavy nuclei where the assumption of a point-like nucleus is inadequate. The Breit-Rosenthal correction [51] incorporates relativistic effects and the overlap of electron wavefunctions with the finite-sized nucleus, providing more precise calculations of hyperfine structures.

Muonic atoms have offered valuable insights into hyperfine interactions and nuclear properties. In these atoms, an electron is replaced by a muon, a lepton with the same charge but approximately 200 times the mass of an electron. The muon's closer proximity to the nucleus enhances sensitivity to nuclear charge distributions and deformations [52]. Studies of hyperfine splittings in muonic atoms have enabled detailed examinations of nuclear sizes, shapes, and the distribution of nuclear magnetization [53].

Hyperfine interactions have critical applications in modern technology and fundamental science. The hyperfine transition between the $F = 4$ and $F = 3$ ground states of cesium-133 is used to define the second in the International System of Units (SI) [54], as illustrated in Fig. 1.3. Atomic clocks based on this transition provide extremely stable frequency standards, essential for global positioning systems, telecommunications, and precision timekeeping [55].

In the realm of quantum computing, hyperfine levels are exploited for their long coherence times and robustness against environmental decoherence. Systems such as phosphorus-doped silicon use the nuclear spin states of phosphorus atoms as qubits, with hyperfine interactions facilitating the initialization and readout of quantum states through coupling with electron spins [56]. Trapped ion quantum computers, utilize hyperfine states of ions like $^{43}\text{Ca}^+$ and $^{171}\text{Yb}^+$ to achieve high-fidelity quantum operations and entanglement necessary for scalable quantum information processing [57, 58, 59].

Hyperfine interactions are also instrumental in nuclear physics research, particularly in studying nuclei with octupole deformation—nuclei that exhibit pear-shaped charge distributions. By analyzing hyperfine splitting patterns, researchers can infer the presence of such exotic shapes, which have implications for understanding fundamental symmetries and interactions within the nucleus [60]. These studies contribute to our knowledge of nuclear structure and inform models that predict nuclear behavior under various conditions.

In summary, the investigation of hyperfine interactions has profoundly influenced both theoretical and applied physics. From the initial observations of spectral line splittings to their utilization in cutting-edge technologies like atomic clocks and quantum computers, hyperfine interactions continue to be a vital area of study. They bridge our understanding of atomic and nuclear structures and facilitate advancements across multiple disciplines, including precision metrology, quantum information science, and fundamental physics research.

1.1.5 f-elements

The f -elements, represented in Fig. 1.4, are a group of elements that occupy the two rows at the bottom of the periodic table. This family encompasses the lanthanides and actinides, are characterized by the progressive filling of the $4f$ and $5f$ electron orbitals, respectively. Their discovery and subsequent exploration have been pivotal in advancing inorganic chemistry and materials science. The journey began in the late 18th and early 19th centuries with the isolation of yttrium and cerium. However, it was the work of Carl Gustav Mosander in the 1830s and 1840s that significantly expanded knowledge of the lanthanides by discovering lanthanum, erbium, and terbium [62].

The lanthanides posed a considerable challenge to chemists due to their similar chemical properties, which made separation and identification difficult. A phenomenon, often referred to as the "lanthanide contraction," arises from the shielding effect of the $4f$ electrons, leading to a gradual decrease in ionic

F Block Elements **Other Elements**

1	2	3	4	5	6	7	8	9	10	11	12	13	14	15	16	17	18	19	20	21	22	23	24	25	26	27	28	29	30	31	32	33	34	35	36	37	38	39	40	41	42	43	44	45	46	47	48	49	50	51	52	53	54	55	56	57	58	59	60	61	62	63	64	65	66	67	68	69	70	71	72	73	74	75	76	77	78	79	80	81	82	83	84	85	86	87	88	89	90	91	92	93	94	95	96	97	98	99	100	101	102	103	104	105	106	107	108	109	110	111	112	113	114	115	116	117	118
---	---	---	---	---	---	---	---	---	----	----	----	----	----	----	----	----	----	----	----	----	----	----	----	----	----	----	----	----	----	----	----	----	----	----	----	----	----	----	----	----	----	----	----	----	----	----	----	----	----	----	----	----	----	----	----	----	----	----	----	----	----	----	----	----	----	----	----	----	----	----	----	----	----	----	----	----	----	----	----	----	----	----	----	----	----	----	----	----	----	----	----	----	----	----	----	----	----	----	-----	-----	-----	-----	-----	-----	-----	-----	-----	-----	-----	-----	-----	-----	-----	-----	-----	-----	-----

Lanthanides: La, Ce, Pr, Nd, Pm, Sm, Eu, Gd, Tb, Dy, Ho, Er, Tm, Yb, Lu

Actinides: Ac, Th, Pa, U, Np, Pu, Am, Cm, Bk, Cf, Es, Fm, Md, No, Lr

Figure 1.4: The f -block of the periodic table, encompassing the lanthanides and actinides. Adapted from [61].

radii across the series and slight variations in chemical properties of lanthanide complexes [63]. This latter point, coupled to the development of advanced separation techniques, such as ion-exchange and solvent extraction during the mid-20th century, eventually allowed for the isolation of pure lanthanide elements.

Actinides, on the other hand, gained prominence with the discovery of uranium and thorium in the late 18th and early 19th centuries. The synthesis of neptunium and plutonium in the 1940s marked the expansion of the actinide series, driven largely by research related to nuclear energy and weaponry [64]. The actinides are notable for their radioactive properties and a greater variety of oxidation states compared to lanthanides, attributed to the participation of $5f$ electrons in bonding.

The unique electronic configurations of f -elements result in distinctive magnetic, optical, and chemical properties. The partially filled f -orbitals are shielded by outer s and p electrons, leading to narrow absorption and emission bands. Their valence electrons therefore behave a lot like the electrons of a free ion, weakly perturbed by the environment. This property is harnessed in various luminescent materials and devices. The strong spin-orbit coupling and large magnetic moments make f -elements particularly interesting for magnetic applications as we will see in just a minute regarding single molecular magnetism.

In contemporary technology, lanthanides have found extensive use across multiple industries due to these exceptional properties. They are critical components in the production of high-strength permanent magnets, such as neodymium-iron-boron (NdFeB) magnets, which are essential in electric vehicle motors, wind turbine generators, and various electronic devices [65]. Dysprosium and terbium are often added to these magnets to improve performance at high temperatures.

Lanthanides also play a vital role in lighting and display technologies. Europium and terbium are key activators in red and green phosphors used in fluorescent lamps and color television tubes [66]. The sharp emission lines and high quantum efficiencies of lanthanide ions are exploited in lasers and optical amplifiers, particularly in fiber-optic communication systems where erbium-doped fibers amplify signals over long distances [67].

A comprehensive review by Bünzli and Eliseeva [68] details the multifaceted applications of lanthanides in modern technology, emphasizing their roles in material sciences, electronics, and medicine. The continued exploration of f -element chemistry not only enhances our fundamental understanding of these elements but also drives innovation in various high-tech industries.

However, it is worth noting that the widespread use of lanthanides has raised ecological and geopolitical concerns. Mining and processing often cause environmental damage, including soil erosion, habitat destruction, and water contamination from toxic byproducts like radioactive thorium [69]. This is worsened by the low concentrations of lanthanides in ores, requiring large-scale material processing. Efforts are underway to develop sustainable mining practices and recycling technologies to reduce environmental impact [70], with recycling from electronic waste gaining attention as a supplement [71]. As demand for lanthanides grows with green technologies, addressing environmental impact and ensuring access remain crucial for sustainable development and innovation.

In summary, the *f*-elements, once considered chemically enigmatic due to their similar properties and complex electron configurations, have become indispensable in contemporary technology. Their magnetic, optical, and catalytic properties are central to advancements in energy, communication, healthcare, and environmental sustainability. Ongoing research into the *f*-elements promises to unlock new applications and address some of the critical challenges facing modern society.

1.1.6 Crystal Field Theory

Crystal Field Theory (CFT) was developed in the early 20th century to explain the electronic structures and spectral properties of transition metal complexes. The foundational work was conducted by Hans Bethe in 1929, who introduced the concept of crystal field splitting to describe how the degeneracy of the metal ion's *d*-orbitals is lifted due to the electrostatic fields produced by surrounding ligands [72, 73]. John Hasbrouck Van Vleck further advanced the theory by applying it to paramagnetic salts and elucidating the magnetic and spectral behaviors of transition metal ions in different coordination environments [74].

CFT models the metal-ligand interaction as a purely ionic bond where the ligands are treated as point charges or dipoles that create an electrostatic field, perturbing the energy levels of the metal ion's *d*-orbitals. In an octahedral field, for instance, the five degenerate *d*-orbitals split into two sets: the lower-energy t_{2g} orbitals and the higher-energy e_g orbitals. This splitting, known as the crystal field splitting energy (Δ_0), and shown in Fig. 1.5, explains the absorption of specific wavelengths of light, resulting in the characteristic colors of many transition metal complexes [75].

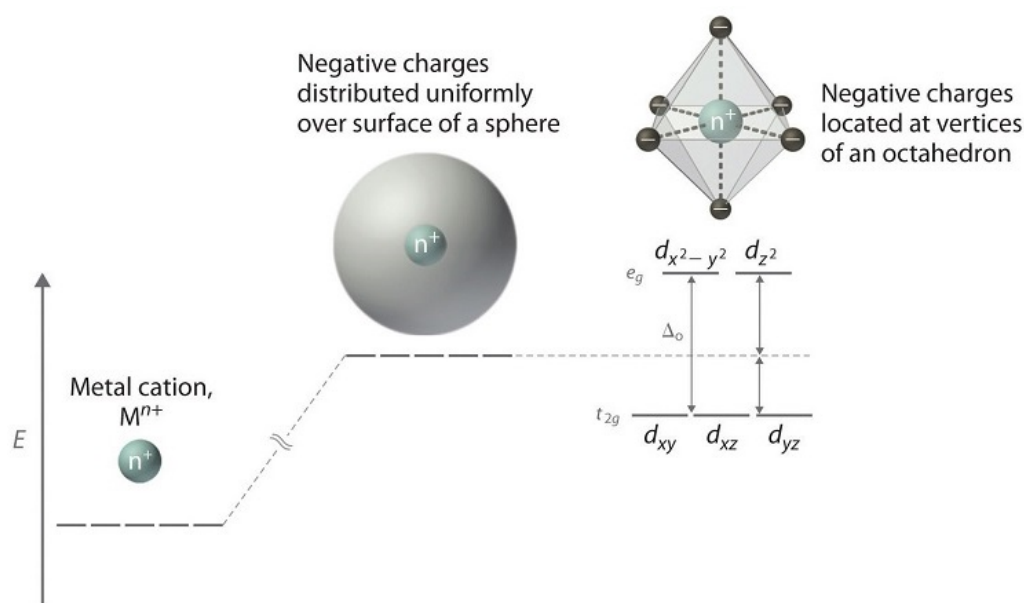


Figure 1.5: Crystal field splitting of *d*-orbitals in an octahedral field. The degenerate *d*-orbitals split into lower-energy t_{2g} and higher-energy e_g sets. Adapted from [76].

While initially formulated for *d*-block elements, CFT was later extended to the *f*-block elements—the lanthanides and actinides—to account for their unique electronic and magnetic properties. Due to the deeply buried nature of *f*-orbitals beneath the outer *s* and *p* orbitals, the crystal field effects in *f*-elements are generally weaker than in transition metals but are nonetheless crucial for understanding their spectroscopic behavior. The limitations of treating metal-ligand interactions purely electrostatically led to the development of Ligand Field Theory (LFT), which incorporates covalent character and molecular orbital considerations into the framework of CFT. LFT provides a more comprehensive understanding of bonding and electronic structures in coordination compounds, acknowledging that metal-ligand interactions often have significant covalent contributions [66, 77, 78].

In the field of molecular magnetism, CFT and LFT are indispensable tools for designing molecules with specific magnetic properties. By manipulating the ligand environment around a metal center, chemists can fine-tune the crystal field splitting to maximize magnetic anisotropy and stabilize particular spin states. This is particularly important in the development of single-molecule magnets (SMMs), where the goal is to achieve high blocking temperatures and slow magnetic relaxation [79, 80]. For example, increasing the axial crystal field splitting in dysprosium-based SMMs has led to significant enhancements in magnetic hysteresis and operating temperatures [81].

Understanding crystal field effects is also crucial in the context of quantum computing, especially when utilizing molecular systems as qubits or qudits. Precise control over the electronic energy levels through ligand design allows for the engineering of molecules with desired quantum properties, such as long coherence times and well-defined transition energies necessary for qubit manipulation[82]. The ability to tailor the crystal field can lead to improved performance of molecular spin qubits by minimizing decoherence pathways and enhancing spin relaxation times. In this work, we will also see how the symmetry of the complexes, via ligand field parameters, also play a role in the addressing speed of molecular qudits.

In conclusion, Crystal Field Theory has been a fundamental concept in inorganic chemistry, providing critical insights into the electronic structures and properties of metal complexes. Its applications extend beyond explaining colors and magnetism to enabling the rational design of materials for advanced technologies, including catalysis, luminescent devices, and quantum information processing. The ongoing refinement and application of CFT continue to be central to advancements in chemistry and materials science.

1.1.7 Molecular magnetism

The early 20th century saw the foundational understanding of magnetism at the atomic and molecular levels, with significant contributions from scientists like Pierre Curie and Paul Langevin, who explored magnetic susceptibilities and paramagnetism [83, 84]. The conceptual framework for understanding magnetic interactions in molecules was further developed with the introduction of quantum mechanics. Linus Pauling's work on the nature of the chemical bond provided insights into how unpaired electron spins contribute to magnetic properties in molecules [85]. The concept of exchange interactions, where electron spins on adjacent atoms or ions influence each other, became central to explaining magnetic coupling in molecular systems [86].

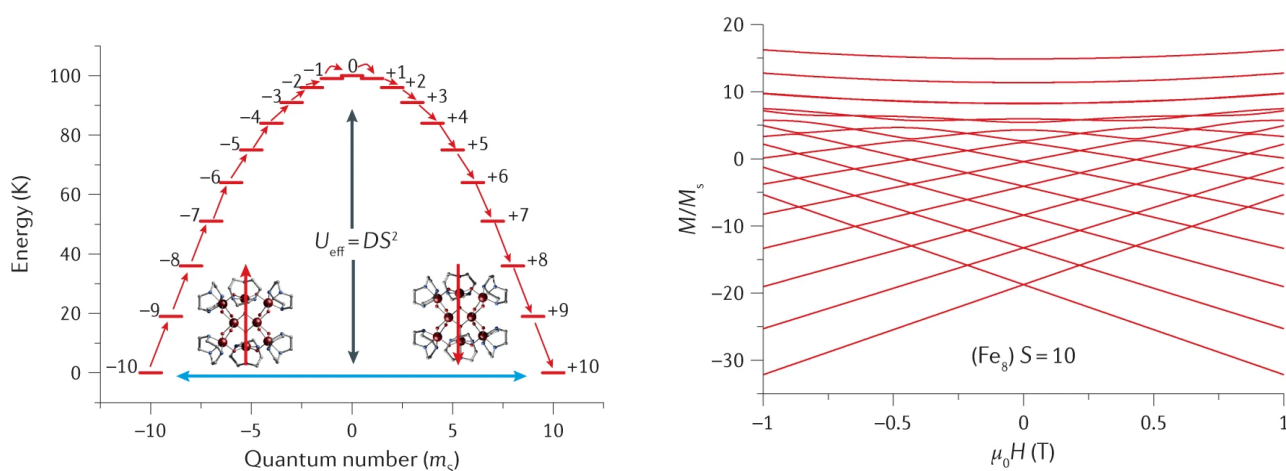
Molecular magnetism is a field that explores magnetic phenomena at the molecular level, bridging the gap between quantum chemistry and condensed matter physics. The origins of molecular magnetism can be traced back to the early 20th century with the study of paramagnetic and diamagnetic properties of coordination compounds [87]. However, it was not until the latter half of the century that significant advancements were made, fueled by the development of sophisticated spectroscopic techniques and a deeper understanding of electronic structures.

The foundational work by Olivier Kahn in the 1980s and 1990s played a crucial role in establishing molecular magnetism as a distinct discipline. Kahn's research focused on the design and synthesis

of molecular materials exhibiting cooperative magnetic behaviors, such as ferromagnetism and anti-ferromagnetism, through superexchange interactions mediated by bridging ligands [88]. This work demonstrated that magnetic ordering could be achieved in purely molecular systems without the need for extended lattices found in traditional magnetic materials.

A landmark discovery in the field was the identification of single-molecule magnets (SMMs) in 1993 by Dante Gatteschi and Roberta Sessoli [79]. They reported a manganese-based cluster, Mn_{12} -acetate, which exhibited slow relaxation of magnetization and magnetic hysteresis of purely molecular origin at low temperatures. This behavior was attributed to a high-spin ground state combined with significant magnetic anisotropy, resulting in an energy barrier for the reversal of magnetization—a phenomenon previously observed only in bulk magnetic materials.

SMMs are characterized by a large ground-state spin multiplicity and significant magnetic anisotropy, leading to an energy barrier for magnetization reversal. This barrier allows the molecule to maintain its magnetic orientation over time, a property essential for potential applications in high-density data storage and quantum computing [89]. The quantum tunneling of magnetization (QTM) observed in SMMs, and illustrated in Fig. 1.6, provided experimental evidence of macroscopic quantum phenomena in molecular systems [90]. This led on to the work of Ishikawa and Wernsdorfer, *et. al.* in the early-mid 2000s, where they studied the magnetic properties of TbPc_2 , observing slow magnetic relaxation and QTM [91, 92].



a) Schematic representation of the energy diagram for a single-molecule magnet with $S = 10$ with energy equal to DS^2 , where S is the spin state and D is the zero-field splitting parameter. The reversal of the magnetization occurs through m_S states (red arrows) via phonon absorption (to excite the spin system to the top of the barrier) and emission (deexcitation to the bottom of the other side of the barrier). Reversal of the magnetization can also occur through quantum tunnelling of magnetization through the barrier with the states that are in resonance.

b) Zeeman diagram for Fe_8 , a single-molecule magnet with $S = 10$ ground state. Quantum tunnelling of magnetization can occur for certain crossing of electronic states (m_S), providing a relaxation pathway for the magnetization.

Figure 1.6: Examples of QTM processing for two different SMMs. Adapted from [25].

The discovery of SMMs opened new avenues for research, with implications for data storage, quantum computing, and spintronics. SMMs act as nanoscale magnets where each molecule can potentially store a bit of information, leading to the concept of molecule-based memory devices with ultra-high density proposed by Bogani and Wernsdorfer [93]. The quantum tunneling of magnetization observed in these systems also provided a platform for studying quantum phenomena at the macroscopic scale.

In the context of quantum computing, SMMs present a promising platform for qubits and qudits due to their discrete energy levels and the potential for quantum coherence, as proposed by Leuenberger and Loss in 2001 [94]. The ability to manipulate the spin states of individual molecules using external stimuli, such as magnetic fields or light, opens avenues for information processing at the molecular scale. Challenges remain in achieving long coherence times and coherent control, but strategies like chemical modification to reduce decoherence pathways and integrating SMMs into solid-state devices are under active investigation [95, 96]. One of the most popular measurement techniques for observing the QTM is with superconducting quantum interference device (SQUID) magnetometers, which can measure the magnetisation of a sample with high sensitivity and resolution. With Wernsdorfer's development of nano-SQUIDs in 2009 [97] refining the capabilities of the micro-SQUID devices, the increased sensitivity enabled the direct electronic readout of the individual nuclear spin states of Tb^{3+} in TbPc_2 [98] that can be used as qudits, and will be the subject of the next subsection.

In summary, molecular magnetism has evolved from fundamental studies of magnetic properties in molecules to a vibrant field with significant implications for technology. The discovery and development of Single-Molecule Magnets have not only deepened the understanding of quantum magnetic phenomena but also paved the way for potential applications in quantum computing, high-density data storage, and spintronics. The continued interdisciplinary efforts combining synthetic chemistry, theoretical modeling, and advanced characterization techniques promise to further unlock the potential of molecular magnets in the years to come.

1.2 Bridging the gap via lanthanide-organic complexes

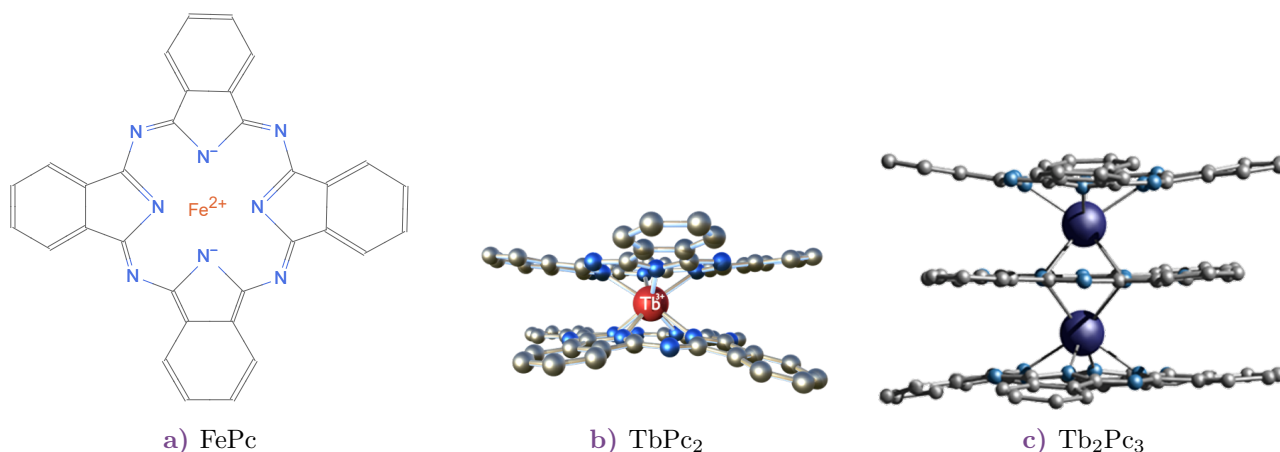


Figure 1.7: Examples of phthalocyanine-based molecular complexes, including: (a) FePc, (b) TbPc₂ and (c) Tb₂Pc₃.

The fields of quantum computing, optimal control theory, nuclear structure, hyperfine interactions, f -elements, crystal field theory, and molecular magnetism are interconnected through the study of lanthanide-organic complexes. In the collaboration between the chemists of our group in KIT and physicists of the Wernsdorfer Group in Grenoble and now KIT, the nuclear spin states of lanthanide ions was studied, specifically dysprosium and terbium, embedded in single-molecule magnets. The most successful of these have been the phthalocyanine-based (Pc) double-decker complexes with a single lanthanide ion (LnPc_2) at the center, most notably, they have used TbPc₂ (terbium bis-phthalocyanine, see Fig. 1.7 for visual examples). In 2012, the first direct electronic readout of the nuclear spin states of Tb^{3+} in a single molecule was demonstrated [98]. This work was soon followed in 2014 by the first demonstration of an electrically-driven nuclear spin in a single molecule, still TbPc₂ [26]. Finally, in 2018, on the same system, the first implementation of a quantum algorithm in a single molecule

was demonstrated [99]. In 2019, Wernsdorfer and Ruben published a strategy for a scalable qudit quantum processor based on $\text{Ln}_n\text{Pc}_{n+1}$ complexes [100], the idea being to use isotopologue chemistry to engineer the Hilbert Space of the nuclear spins of the lanthanide ions. For example, replacing the ^{159}Tb with the isotopically selected ^{161}Dy or ^{163}Dy would increase the number of nuclear levels, and therefore the dimension d of the qudit. Synthesizing in turn "multiple decker" phthalocyanines would increase the number of lanthanide ions, and therefore the number of qudits n . This in turn provides (i) a linear scaling of the Hilbert space dimension d with the choice of isotope and (ii) an exponential scaling of the Hilbert space dimension d^n with the number of qudits n . This thesis aims to explore the theoretical foundations of this topic of research, and to provide a roadmap from theoretical insights on the development of a molecular quantum processor based on lanthanide-organic complexes. This scheme is illustrated in Fig. 1.8.

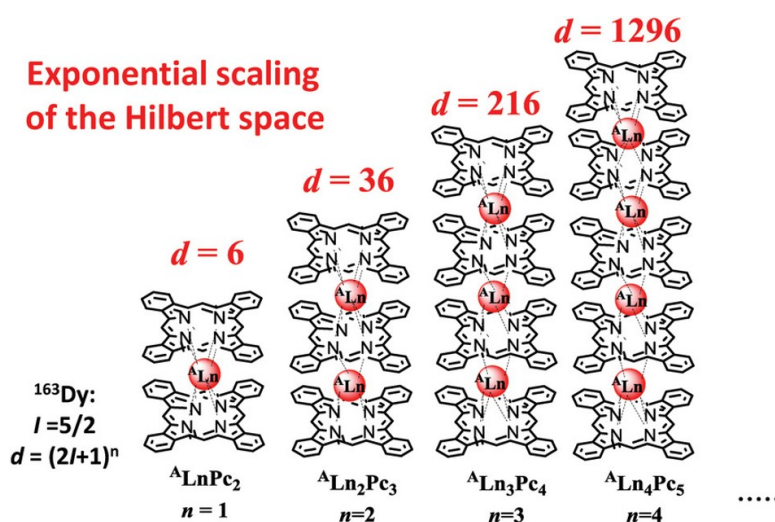


Figure 1.8: Conceptual scaling of the Hilbert space of the $\text{A Ln}_n\text{Pc}_{n+1}$ spin qudit ($I = 5/2$) with the example of $^{163}\text{Dy}_n\text{Pc}_{n+1}$ with $n = 1-4$ leading to exponential increase by $d = (2I + 1)^n$. Adapted from [100].

Finally, the work of Kumar *et al.* [101] that stems from a collaboration between our group in KIT and the group of Phillipe Goldner in Paris, shows the potential of more general lanthanide-organic complexes beyond the SMM approach, with the demonstration, in binuclear europium complexes in crystals, of triggered nuclear spin transitions by optical means instead of electrical means. This opens then also the possibility of using the optical transitions of the lanthanide ions to trigger the nuclear spin transitions.

1.2.1 The poster child: TbPc_2

Let us present in detail the physical system on which these previously mentioned experiments were performed, the TbPc_2 molecule. The TbPc_2 molecule is a single-molecule magnet (SMM) that consists of a Tb^{3+} ion coordinated to two phthalocyanine ligands. The experiments were done at cryogenic temperatures of 1.2 K, where the molecule exhibits slow magnetic relaxation due to the presence of a large energy barrier between the ground and first excited states. The molecule is placed on a gold surface and connected to gold electrodes, forming a break junction, as illustrated in Fig. 1.9. The valence electrons of the central Tb^{3+} ion are coupled via exchange interaction to the delocalised electron in the radical, this is the source of changes in conductance depending on the orientation of the ground Ising-like spin of the valence electrons, which will prove quite useful a bit later.

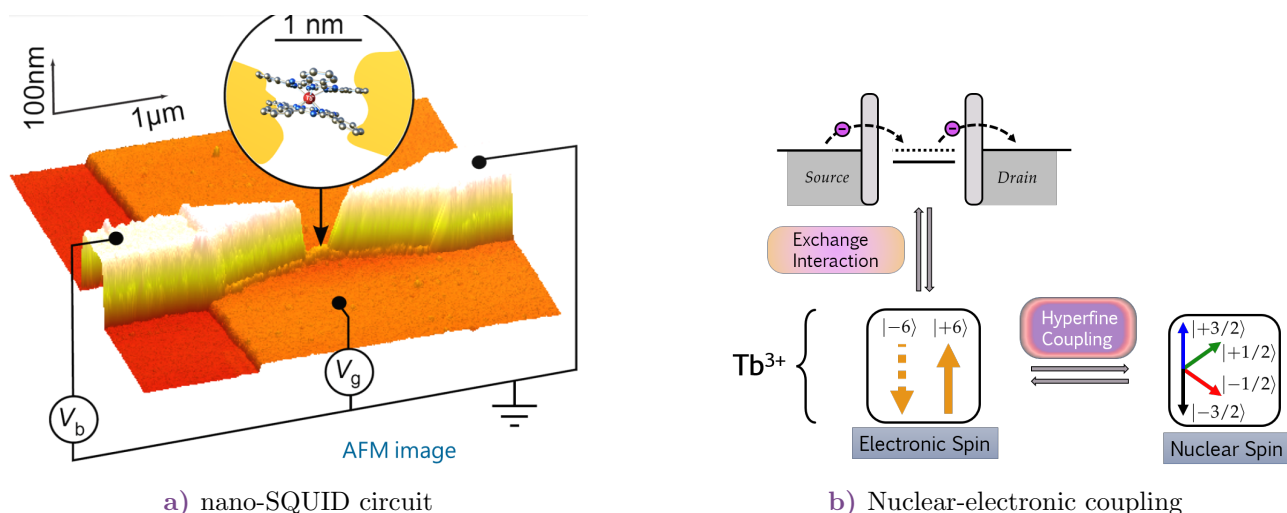


Figure 1.9: Schematic illustration of the TbPc₂ spin readout setup. (a) AFM coloured image of a TbPc₂ SMM connected to gold source and drain electrodes through tunnelling barriers, within a break junction on top of an Au/HfO₂ layer. (b) Schematic of the coupling procedure from the nuclear to the electronic spin states of Tb³⁺ via the hyperfine interaction, then to the delocalised electron of the tunnelling current via exchange interaction. Adapted from [26].

1.2.2 A scale-encompassing Hamiltonian

The Hamiltonian of the system is composed of several terms, each of which is responsible for a different energy splitting of the system. The central field Hamiltonian H_0 provides the separation of energy of the ground $4f^8$ and the $4f^7 5d^1$ excited electronic configurations. Then the ground spectroscopic term is 7F_6 , which is due to the interelectronic repulsion H_{e-e} and spin-orbit coupling H_{so} . The ligand field H_{LF} then splits the 7F_6 term into 7 energy levels, relatively well defined by $|M_J|$ the projection of the total angular momentum J on the quantization axis, with a very large energy gap between the ground $M_J = \pm 6$ and the first excited $M_J = \pm 5$ doublets, leading to a quasi-Ising spin behaviour of this doublet at cryogenic temperatures. Finally, the hyperfine interaction H_{hf} splits the levels into 4 hyperfine levels since the nuclear spin of the Tb³⁺ ion is $I = 3/2$, the hyperfine levels of the ground $M_J = \pm 6$ term are then $|4f^8 \ ^7F_6 \ M_J = \pm 6 \ M_I \rangle$, which are 4 doubly degenerate energy levels, for each pair of $M_J = \pm 6$ and $M_I = \pm 1/2, \pm 3/2$. The different energy splittings are represented in Fig. 1.10. Note the different scales of energy of the different terms of the Hamiltonian, note also the different physical origins of the different terms of the Hamiltonian, from purely atomic, to chemical in nature for the ligand field, to nuclear in nature for the hyperfine interaction.

Note: These considerations, and the quantum numbers indexing each state discussed in Fig. 1.10 are only true to first order, as each one of this state is an admixture of other states, with a majority of the weight on the state it is designated by. The admixtures comes from different selection rules and the fact that not all the terms of the Hamiltonian are diagonal in the same bases of quantum numbers. This will be discussed in more detail in Part I of this thesis.

The slight twist angle of the two phthalocyanines relative to each other, making the environment of the Tb³⁺ ion slightly deviating from the D_{4d} symmetry of the crystal, leads to the appearance of crystal field parameters B_q^k with $q \neq 0$ but with $q = \pm 4$ (See Section 3.1.1). This leads to, via the application of Wigner-Eckart's theorem, mixings between states with $\Delta M_J = 4$. Via third order perturbation theory, it is possible to show that a mixing between the states $M_J = -6$ and $M_J = 6$ is possible, as such corrections to the wavefunction would contain terms of the form

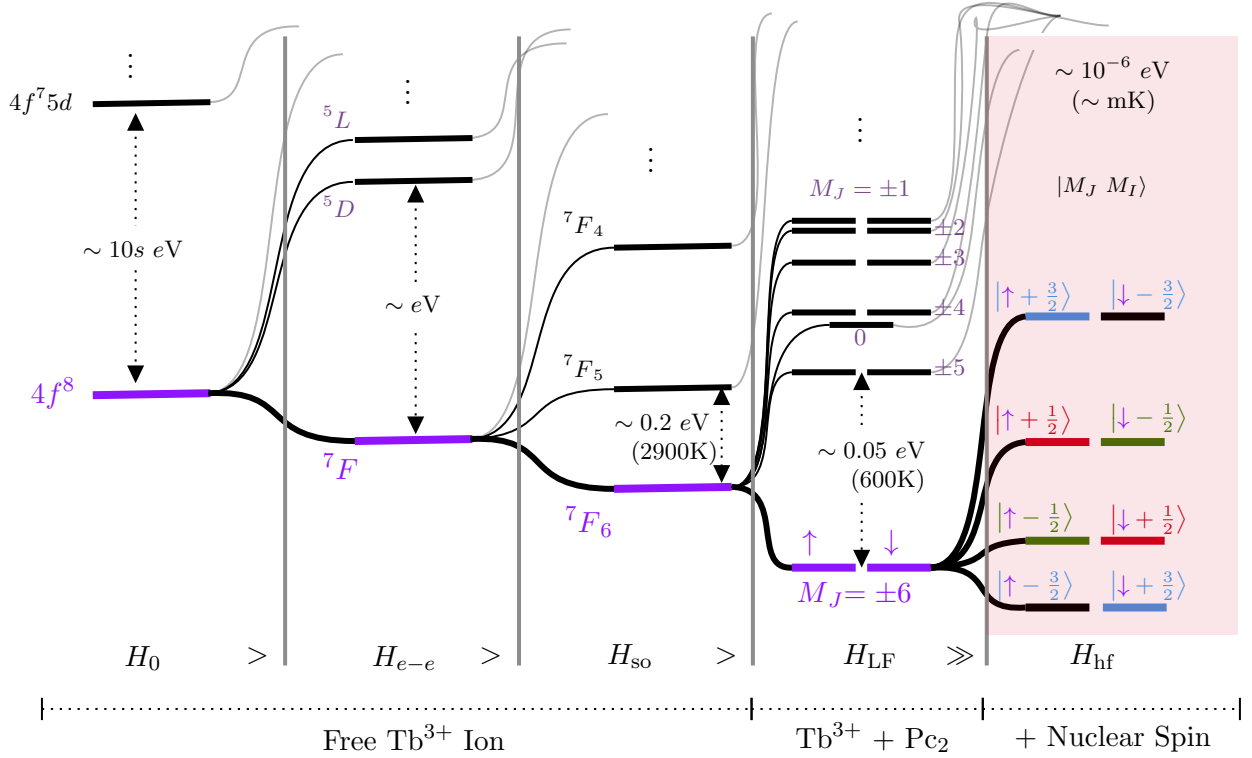
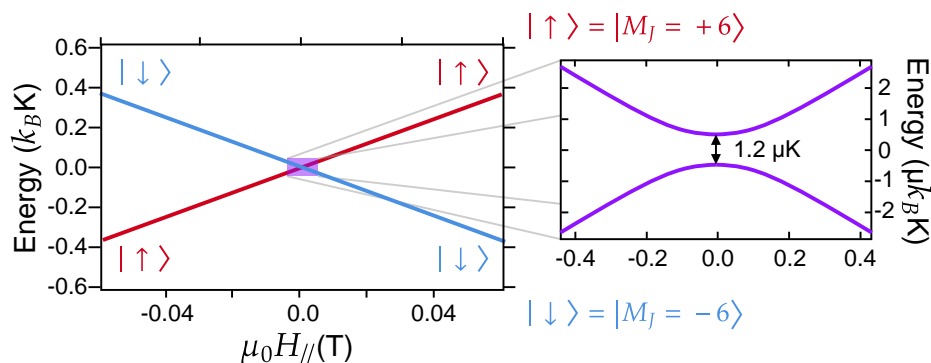


Figure 1.10: Iterative spectrum of each term of the Hamiltonian of TbPc₂ in decreasing order of energy amplitude. The computational Hilbert space is spanned by the 4 hyperfine levels of the ground state of the system. Represented here on the right.

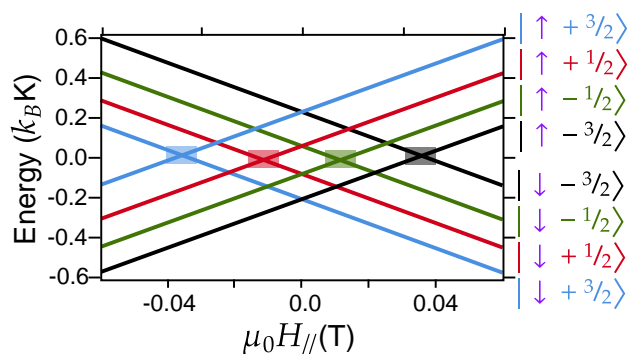
$\langle M_J = +6 | H_{LF} | M_J = +2 \rangle \langle M_J = +2 | H_{LF} | M_J = -2 \rangle \langle M_J = -2 | H_{LF} | M_J = -6 \rangle$, where the energy denominators have been neglected. This mixing is responsible for a zero field splitting between the two doublets, this in turn is responsible for the Quantum Tunneling of Magnetization (QTM) observed in the complex [26, 99, 102].

Ignoring the hyperfine structure, the Zeeman diagram, i.e. the energy levels of the system as a function of the magnetic field, presents then an avoided crossing between the two doublets, around $B = 0$ T. As represented in Fig. 1.11a), this anticrossing is of the order of $1.2 \times 10^{-6} k_B K$, which, refereing back to Fig. 1.10, is much smaller than the energy gap between hyperfine levels, which is of the order of $10^{-3} k_B K$. This means that, accounting for the hyperfine levels of the system, there will be 4 avoided crossing, one per value of the nuclear spin, each one will happen at a different critical value of the magnetic field, see Fig. 1.11b).

It is then possible to read in which nuclear spin state the Terbium nucleus is by measuring at which value of the magnetic field does the avoided crossing happen. When sweeping the magnetic field at a constant rate, the electronic spin will flip at the anticrossing, and this flip will then influence the conductance of the molecule as a whole [103], see Fig. 1.12. This makes it then possible to read the nuclear spin state of the Terbium nucleus, and therefore, provided it is possible to coherently manipulate the nuclear spin state, to use it as a qudit with $d = 4$ levels. This is exactly what was demonstrated by Thiele *et al.* in 2014 [26], where they showed that it was possible to drive coerently and therefore perform quantum operations on the nuclear spin of the Terbium nucleus. With the use of an AC electric field applied to the molecule, one can then drive Rabi oscillations, signature of coherent manipulation of the nuclear spin state, and perform quantum gates on the nuclear spin state of the Terbium nucleus [99, 104], as seen in Fig. 1.12.



a) Zeeman diagram of the ground $M_J = \pm 6$ doublet, neglecting the hyperfine splitting. The avoided crossing between the two doublets is highlighted. The energy of the avoided crossing is of the order of $1.2 \times 10^{-6} k_B K$.



b) Zeeman diagram of the ground $M_J = \pm 6$ doublet, with the hyperfine splitting. The avoided crossings for each value of the nuclear spin M_I are highlighted.

Figure 1.11: Zeeman diagram of the ground $M_J = \pm 6$ doublet, a) neglecting the hyperfine splitting b) with the hyperfine splitting. The energy levels are represented in units of $k_B K$, where k_B is the Boltzmann constant. The parallel magnetic field applied $\mu_0 H_{//}$ is given in Tesla. Re-adapted from [99].

1.2.3 Towards a molecular quantum processor

As stated at the beginning of this section, Godfrin *et al.* (2017) [99] demonstrated that coherence times were sufficiently long and Rabi oscillations were coherent enough to implement both the superposition (generalized-Hadamard) gate and Grover's search algorithm on qudit states (see Fig. 1.13).

This experiment was inspired by the theoretical framework laid out by Leuenberger and Loss, who, in the early 2000s, proposed general methods for quantum computing with large nuclear spins. They also presented a specific example involving a novel implementation of Grover's algorithm on a single, large qudit [94, 105, 106].

1.2.4 Where the theory is lacking

By commenting this last experiment, there are mainly four points where the theory is lacking in the current state of research.

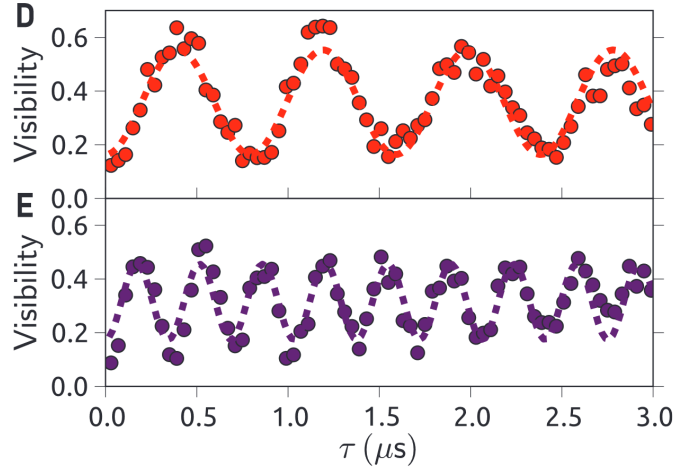
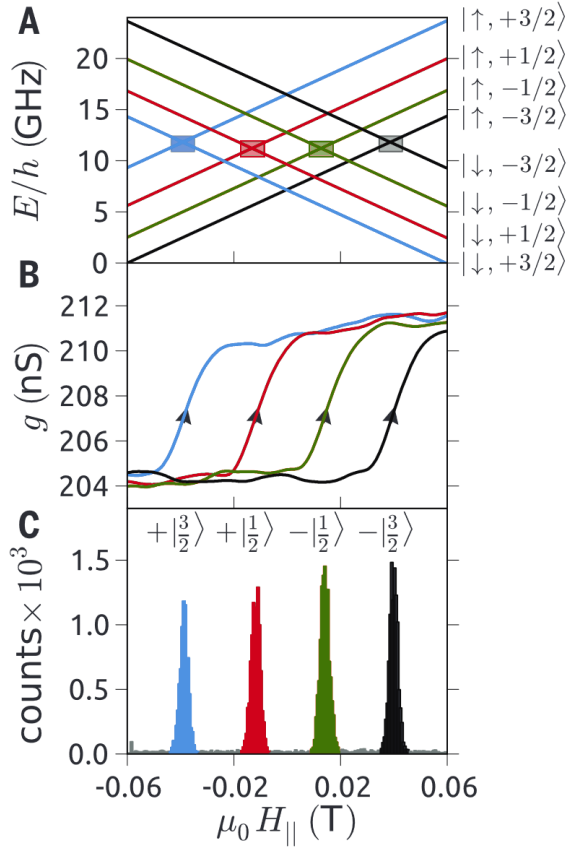


Figure 1.12: Panel A shows the Zeeman diagram from Fig. 1.11b). Panel B shows the conductance jumps due to the magnetic reversal occurring at the respective anti-crossings. Panel C shows a histogram of the counts of observed magnetic reversals occurring as a function of magnetic field strength. Panels D and E show the intermediate state populations undergoing Rabi oscillations at two different electric field strengths. Adapted from [26].

The hyperfine Stark effect

First, the electrical addressing of the nuclear spin transitions that was observed by Thiele *et al.* in 2014 [26]. The application of a DC electric field to the molecule was shown to change the resonance frequency of the nuclear spin transitions. An electric field of the order of ~ 0.1 mV/Å was shown to shift the resonance frequency of the nuclear spin by ~ 5 MHz. Moreover, an AC electric field was shown to drive Rabi oscillations on the nuclear spin transitions, with a Rabi frequency proportional to the amplitude of the AC electric field [103], as can be seen in Fig. 1.14, result corroborated by Godfrin *et al.* in 2017 [104].

This so-called **hyperfine Stark effect** is not yet well understood, and the current theoretical framework is lacking a proper description of this effect. While it is quite certain the effect is due to an interplay between the hyperfine interaction, the electric field and the ligand field of the phthalocyanines, the exact nature of this interplay is not yet well understood. We propose to investigate this effect in more detail in this thesis, via an atomistic approach and the introduction of effective operators obtained via multiperturbation theory. We will also show how the theoretical framework used can also be applied to study hyperfine-induced transitions in other systems, such as the binuclear europium complexes studied by Kumar *et al.* [101].

Quantum gates on the nuclear spin

Although Godfrin made considerable advances in the development of a qudit-based quantum computing platform, the implementation of Grover's algorithm was restricted to three out of the four nuclear spin states of the terbium nucleus. This raised an important theoretical question regarding qudit universality: whether the nuclear spin states of the terbium ion could be employed to implement a universal set of quantum gates, thereby enabling the execution of any arbitrary quantum algorithm. A subsequent question is then, given a desired gate, how to implement it in the system. This will be

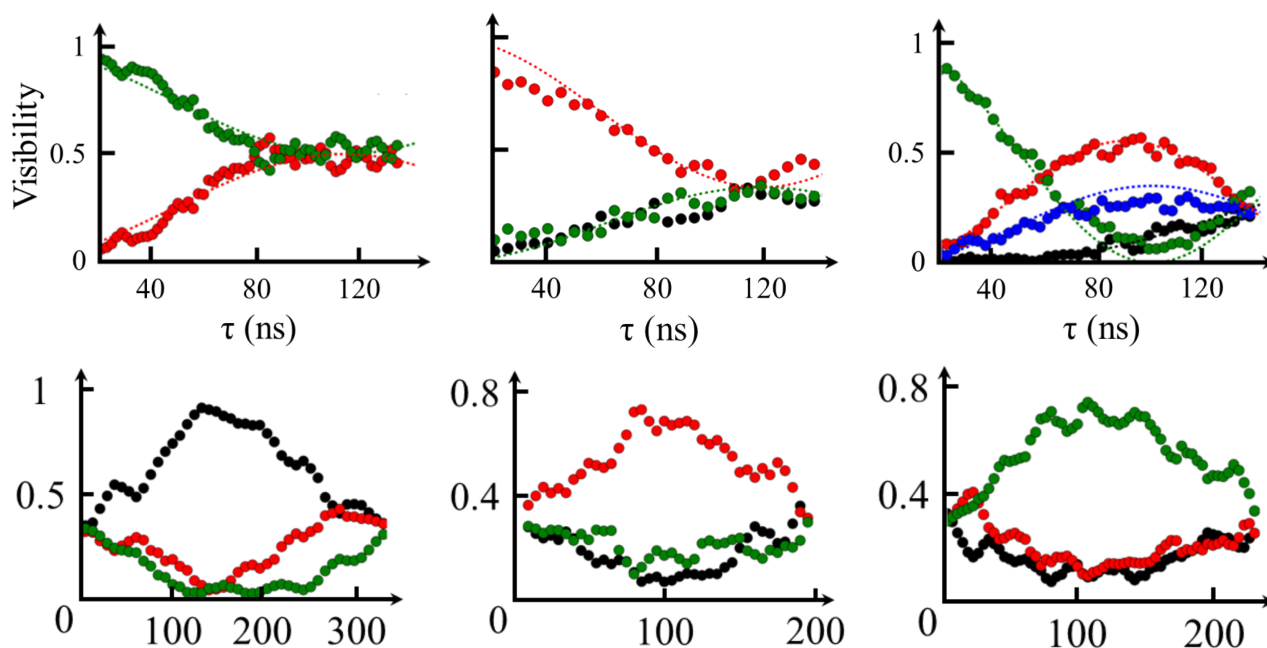


Figure 1.13: Experimental realization of Grover's algorithm in TbPc₂. Each plot shows the populations of individual nuclear spin states of TbPc₂ (represented by red, green, black, and blue) as a function of time (in ns). The top row illustrates the implementation of the Quantum Fourier Transform (QFT) superposition gate (generalized-Hadamard) in a qudit system with $d = 4$, where the first, second, and third columns represent 2, 3, and all 4 levels, respectively. The bottom row displays two cycles of the Grover diffusion operator applied to the marked state (black in the left, red in the center, and green in the right), showing the amplification of the amplitude before returning to the original superposition. Adapted from [99].

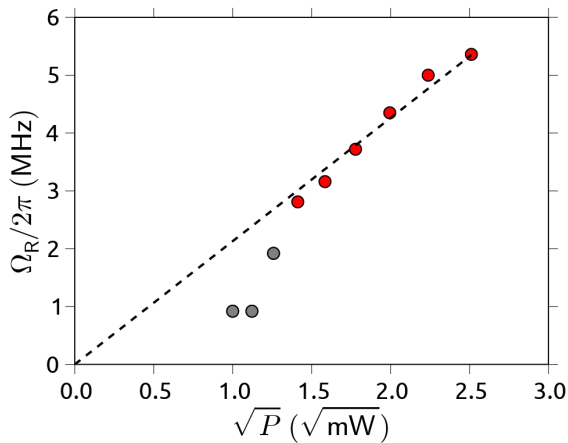
tackled in this thesis through the use of optimal control theory and an in-depth study of the system's control Hamiltonians.

Scaling of the noise with the dimension of the Hilbert space

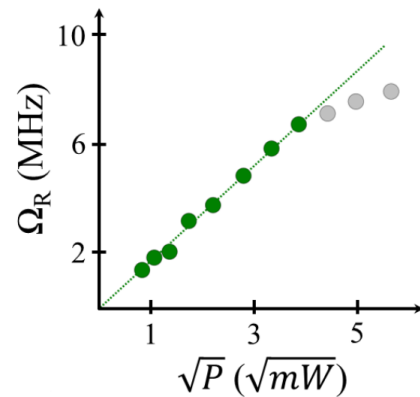
As proposed in [100], the idea is to scale the Hilbert space of the nuclear spins of the lanthanide ions by using isotopologue chemistry. This will lead to a linear scaling of the Hilbert space dimension d with the choice of isotope, however, it can be inferred that as the number of nuclear levels increases, the number of error channels will also increase. This will lead to a scaling of the noise with the dimension of the Hilbert space, and it is important to understand how this scaling will affect the performance of the quantum processor. Moreover, is it possible to quantify an upper limit on the dimension of the qudit in order to stay competitive with qubit platforms, given the noise level of the system? Finally, how does the computational performance of the system scale with the number of qudits? This will be studied in this thesis through the use of perturbation theory on the Lindblad master equation.

The nuclear degree of freedom

Finally, to come back to the isotopologue engineering of the Hilbert Space suggested by Wernsdorfer and Ruben [100], it is important to understand how the simple addition of one proton and one neutron to go from ¹⁵⁹Tb to ¹⁶¹Dy affects the hyperfine structure so as to transition from a 4 level system to a 6 level system. Moreover, the hyperfine splittings of ¹⁶¹Dy and ¹⁶³Dy have been observed to be quite different, albeit the number of hyperfine levels stay the same. How can a difference in two neutrons with zero charge lead to such a difference in the hyperfine structure? This will be studied in this thesis



a) Adapted from [103].



b) Adapted from [104].

Figure 1.14: Rabi frequency $\Omega_R/2\pi$ as a function of the square root of the microwave power P of the electric field driving the transition.

too and will provide a detour into the nuclear structure of the isotopes of different lanthanides, heavily charged ions and exotic muonic ions.

1.3 Thesis outline

This thesis is divided into three parts, each addressing a different aspect of the highlighted theoretical challenges regarding hyperfine interactions in lanthanide-organic complexes. An additional fourth part is present to provide an overview of a side project on the ubiquity of the Thue Morse sequence in the quantum computing world and its link to quantum chaos.

Lanthanides in matter: atomically free yet chemically bound

Part I will focus on the theoretical framework used to describe the the valence electrons of atomic systems. Using **Racah algebra**, we will formally derive the analytical expressions of the matrix elements of the different Hamiltonians presented in Fig. 1.10 and show how they can be evaluated non-empirically using Hartree-Fock or DFT codes. In particular we will present the **LFDF** method, that we consider the most appropriate to use in this context of Hilbert space engineering in lanthanides. We will also show how the interplay between the hyperfine interaction, the electric field and the ligand field of the phthalocyanines can be described using effective operators obtained via a generalisation of the **Judd-Ofelt theory** that we will introduce.

The Hyperfine Interaction

Part II will focus on the hyperfine interaction as well as the nuclear structure of different isotopes of lanthanides. We will start from the **Dirac equation** and derive the hyperfine interaction and the **hyperfine constants** through a perturbation of the electronic Hamiltonian. We will then show how the internal nuclear structure influences the hyperfine constants of the electrons, by calculating finite size effects such as the **Bohr-Weisskopf** or **Breit-Rosenthal** corrections. We will particularly dwell on highly charged hydrogen-like ions and **muonic ions**, and show how the electron or muon can be used as a probe of the nuclear structure.

Quantum Computing with Nuclear Spins in Lanthanides

Part III will focus on the quantum computing aspect of lanthanide-organic complexes, and more generally qudits. We will first remind basics in quantum computing and open quantum systems theory, and then apply these to qudits. We will first focus on the effect of the noise on qudits via perturbation theory on the **Lindblad master equation**. In particular, in a first chapter, using only a first-order approach, we will compare the scalings of computational infidelities of **qubits vs. qudits**, and show how the noise scales with the dimension of the Hilbert space. In a second chapter, we will generalize the perturbation to any order, and consider the effect of the Hamiltonian/gate on the computational performance as the duration of the operations and the noise amplitude increases. Following this, in a last chapter, we will focus on **how to implement quantum gates** on a **pulse-level** in the system, and show how **optimal control theory** can be used to tackle the necessity for shorter gate times to reduce the effect of the noise derived in the previous chapters.

The Ubiquitous Prouhet-Thue-Morse Sequence

Part IV will focus on a side project on the **Prouhet-Thue-Morse sequence**, whose appearance we notices while benchmarking some numerical simulations. We want therefore to point out its ubiquity in the quantum computing world. We will first introduce the sequence and its properties, and then show how it is related to **quantum chaos** and the quantum baker's map. We will then show how it appears naturally as an interaction of the Quantum Fourier Transform and the Hadamard transform of N qubits. Finally, we will show its link with **number theory** and the Riemann hypothesis.

PART I

Lanthanides in matter: atomically free yet chemically bound

2	Free atom/ion Hamiltonian	25
2.1	Non-interacting e^- in a central potential	25
2.2	Angular momenta coupling schemes	27
2.3	Matrix elements for the two-electrons case	29
2.4	Unit Tensor Operators	33
2.5	Coulomb interelectronic repulsion	35
2.6	Spin-orbit coupling	42
2.7	Hyperfine coupling	45
3	Ligand Field	51
3.1	From Crystal Field Theory to Ligand Field Theory	51
3.2	Ligand Field DFT	59
4	Configuration Interaction	65
4.1	Symmetry and odd Ligand Field Parameters	65
4.2	Judd-Ofelt theory and effective operators	65
4.3	The hyperfine Stark effect	72
4.4	Towards hyperfine-induced luminescence	77

Lanthanides in matter: atomically free yet chemically bound

"There is in all things a pattern that is part of our universe. It has symmetry, elegance, and grace - these qualities you find always in that the true artist captures. [...] We try to copy these patterns in our lives and in our society, seeking the rhythms, the dances, the forms that comfort. Yet, it is possible to see peril in the finding of ultimate perfection. It is clear that the ultimate pattern contains its own fixity."

— Frank Herbert, *Dune*

This part focuses on the atomistic aspect of this thesis. It presents the theoretical groundwork necessary for obtaining the key components of the Hamiltonians used to describe the physical systems of interest in this field. Lanthanides pose a unique challenge in quantum chemistry due to their complex electronic structure. Thus, we aim to introduce the theoretical tools needed to describe the electronic structure of lanthanides from an atomistic point of view, treating the atom or ion as being perturbed by its environment. This approach is valid because triply-ionized lanthanides possess a $4f$ valence shell that is shielded from the environment by the $5s$ and $5p$ shells. This section is divided into three chapters.

The first chapter begins by addressing the physics of a single atom or ion in isolation, without interactions with the external environment. It introduces mathematical tools for describing the angular degrees of freedom of the electronic Slater determinants, which represent the electronic states of the atom or ion. These tools incorporate the antisymmetrization of wavefunctions to respect the fermionic nature of electrons.

The second chapter introduces crystal field theory, which is essential for understanding the interaction of the electrons in the atom or ion with surrounding ligands. Additionally, we introduce ligand field theory, a more general framework that, when combined with quantum chemistry methods, provides a comprehensive model of the electronic structure of the atom or ion in a molecular environment.

The third and final chapter introduces the concept of effective operators that thanks to the use of Racah algebra derive selection rules for highly forbidden transitions in lanthanide ions. This is achieved through perturbation theory with excited states. This part is crucial for understanding the hyperfine Stark effect, which is observed and exploited by our collaborators in Grenoble and Karlsruhe to perform a qudit quantum algorithm using the TbPc_2 single-molecule magnet. As described in the introduction, in this system, the four hyperfine levels of the central Tb^{3+} ion act as the qudit. Understanding the **hyperfine Stark effect** reveals the underlying mechanism that controls the qudit and lays the groundwork for optimizing its addressability. By identifying the key parameters that need to be controlled in experiments, we aim to achieve optimal performance.

Chapter Contents

2.1	Non-interacting e^- in a central potential . .	25
2.2	Angular momenta coupling schemes	27
2.3	Matrix elements for the two-electrons case	29
2.4	Unit Tensor Operators	33
2.5	Coulomb interelectronic repulsion	35
2.6	Spin-orbit coupling	42
2.7	Hyperfine coupling	45

CHAPTER 2

Free atom/ion Hamiltonian

The aim of this section is to calculate the Hamiltonian matrix elements. More precisely, the Hamiltonian of the electrons in the atom/ion is presented, and the effects of the nucleus are included in the last part. For a more in-depth discussion of the nucleus, the reader is referred to the next part that delves in much more details about the structure of the nucleus and its interaction with valence electrons.

Since the electronic wavefunctions can be decomposed into radial and angular parts, Hamiltonian matrix elements will generally consist of a radial integral and a term depending on the angular quantum numbers and accounting for the antisymmetrization due to the fermionic nature of the electrons. The latter will be calculated using mathematical tools from **Racah algebra** discussed in [Appendix D](#).

Starting from the Schrödinger equation, the Hamiltonian of a free atom/ion is given by

$$H = \sum_{i=1}^N \left(-\frac{\hbar^2}{2m} \nabla_i^2 - \frac{Ze^2}{4\pi\epsilon_0 r_i} \right) + \sum_{i<j} \frac{e^2}{4\pi\epsilon_0 r_{ij}} + H_{\text{so}} + H_{\text{hf}}, \quad (2.1)$$

where the first term is the kinetic energy of the electrons, the second term is the Coulomb interaction between the electrons and the nucleus, the third term is the Coulomb interaction between the electrons, the fourth term is the spin-orbit coupling, and the fifth term is the hyperfine coupling. The spin-orbit coupling is a relativistic effect that couples the spin of the electron with its orbital angular momentum. The hyperfine coupling is the result of the interaction between the magnetic moment and the electric quadrupole of the nucleus with the magnetic moment of the electron.

2.1 Non-interacting electrons in a central potential

Let us consider the Hamiltonian

Definition: (*Central potential Hamiltonian for non-interacting electrons*)

$$H_0 = \sum_{i=1}^N \left(-\frac{\hbar^2}{2m} \nabla_i^2 - \frac{Ze^2}{4\pi\epsilon_0 r_i} \right) = \sum_{i=1}^N h_i \quad (2.2)$$

it represents the energy of N independent electrons of charge $-|e|$ under the influence of a central point-like infinitely massive nucleus of charge Ze , where Z would be the element number i.e. number of protons in the nucleus. Note that $N = Z$ in the case of neutral atoms, but $N < Z$ in the case of positively charged ions.

2.1.1 Solving the eigensystem

Solving for the eigenenergies and eigenfunctions of any h would simply yield the hydrogen-like wavefunctions $\psi_{n\ell m_l m_s}(\vec{r})$ of energy $\epsilon_{n\ell}$. The shorthand notation $\mathbf{n} \equiv n\ell m_l m_s$ will be used.

Since $H_0 = \sum_{i=1}^N h_i$, if $\psi_{\mathbf{n}}$ is an eigenfunction of h of eigenenergy $\epsilon_{\mathbf{n}}$, then

$$\Psi_{\vec{\mathbf{n}}}(\vec{\mathbf{r}}) = \prod_{i=1}^N \psi_{\mathbf{n}_i}(\vec{r}_i) \quad (2.3)$$

is an eigenfunction of H_0 of eigenenergy

$$E_{\vec{\mathbf{n}}} = \sum_{i=1}^N \epsilon_{\mathbf{n}_i}. \quad (2.4)$$

with $\vec{\mathbf{n}} = \{\mathbf{n}_1, \mathbf{n}_2, \dots, \mathbf{n}_N\}$.

Note that therefore all $N!$ wavefunctions obtained by permutations of the n_i 's are degenerate in energy. This means that since electrons are fermions, the wavefunction obtained by antisymmetrizing all degenerate product wavefunctions of the form (2.3) such that $\sum_{i=1}^N \epsilon_{\mathbf{n}_i}$ are equal is the correct, physical, eigenfunction of H_0 for N electrons, mathematically such a wavefunction is given by the Slater determinant

Definition: (*Slater determinant*)

$$\Psi_{\vec{\mathbf{n}}}(\vec{r}_1, \vec{r}_2, \dots, \vec{r}_N) = \frac{1}{\sqrt{N!}} \begin{vmatrix} \psi_{\mathbf{n}_1}(\vec{r}_1) & \psi_{\mathbf{n}_2}(\vec{r}_1) & \cdots & \psi_{\mathbf{n}_N}(\vec{r}_1) \\ \psi_{\mathbf{n}_1}(\vec{r}_2) & \psi_{\mathbf{n}_2}(\vec{r}_2) & \cdots & \psi_{\mathbf{n}_N}(\vec{r}_2) \\ \vdots & & \ddots & \vdots \\ \psi_{\mathbf{n}_1}(\vec{r}_N) & \psi_{\mathbf{n}_2}(\vec{r}_N) & \cdots & \psi_{\mathbf{n}_N}(\vec{r}_N) \end{vmatrix}. \quad (2.5)$$

Note: The Pauli exclusion principle in atoms and ions can be inferred immediately from the mathematical form of (2.5), since if any of the \mathbf{n} 's are the same, the determinant would be vanishing.

Note: The ground state for an idealized atomic system of non-interacting electrons can be obtained straightforwardly from energetic considerations in (2.4). For a bosonic system, the eigenenergy with the lowest energy would be $N\epsilon_{1s}$. That would however require all electrons to be in the $1s$ state, which comprises the two states characterized by the quantum numbers $n = 1, \ell = 0, m_\ell = 0, m_s = \pm \frac{1}{2}$. Therefore only two electrons can occupy an $1s$ orbital, any supplementary electron would need to populate the $2s$ orbital on behalf of Pauli's exclusion principle. Following this logic, one ends up with the well-known *aufbau* principle, or Klechkowsky rule stating that electrons in an atomic system in its ground state, electrons first fill subshells of the lowest available energy, then fill subshells of higher energy, with each shell having a degeneracy

of $4l + 2$, corresponding to the number of possible values of m_ℓ and m_s .

Example: One can consider a two-electron state. With $\tilde{\mathbf{n}} = (n_1 \ell_1 m_{l_1} m_{s_1}, n_2 \ell_2 m_{l_2} m_{s_2})$, the Slater determinant of the two-electron system is given by

$$\begin{aligned}\Psi_{\tilde{\mathbf{n}}}(\vec{r}_1, \vec{r}_2) &= \frac{1}{\sqrt{2}} \begin{vmatrix} \psi_{\mathbf{n}_1}(\vec{r}_1) & \psi_{\mathbf{n}_2}(\vec{r}_1) \\ \psi_{\mathbf{n}_1}(\vec{r}_2) & \psi_{\mathbf{n}_2}(\vec{r}_2) \end{vmatrix} \\ &= \frac{1}{\sqrt{2}} (\psi_{\mathbf{n}_1}(\vec{r}_1) \psi_{\mathbf{n}_2}(\vec{r}_2) - \psi_{\mathbf{n}_2}(\vec{r}_1) \psi_{\mathbf{n}_1}(\vec{r}_2)).\end{aligned}\quad (2.6)$$

2.1.2 Configuration basis

Under the reasonable assumption that H_0 is the term in the Hamiltonian with the largest eigenvalues and contribution to the final spectrum of the electrons, one can define a new basis in which to work going forward thanks to the ground state configuration of the atomic system at study. Since H_0 is diagonal in the base determined by \mathbf{n} , the latter quantum numbers will characterize the newly defined basis.

Notation-wise, with respect to suitably chosen closed-shells (generally all the shells filled according to the *aufbau* principle) the electronic configuration of the ground state is uniquely characterized by the $n\ell$ quantum numbers of the p valence electrons and the corresponding states are denoted $|n\ell^p\rangle$. If the state is in an excited configuration, with an electron from shell $n_c \ell_c^{k_c}$ promoted to the shell $n_e \ell_e$ for example, one can refer to the excited state as $|n_c \ell_c^{k_c-1} n \ell^p n_e \ell_e^1\rangle$, or, if the electron is promoted from the valence shell, $|n \ell^{p-1} n_e \ell_e^1\rangle$. The basis of the configuration space is then given by the Slater determinants of the states $|n\ell^p\rangle$, $|n_c \ell_c^{k_c-1} n \ell^p n_e \ell_e^1\rangle$, etc... This notation can be used for more than one excitation of course, for example $|2s^1 4f^5 6s^2\rangle$ for the triply ionized Eu^{3+} ion whose ground configuration is $|4f^6\rangle$, represents the excited state where one electron from the core shell $2s$ and one from the valence shell $4f$ have been promoted to the previously unoccupied $6s$ shell. In essence, any shell that does not appear in the notation of a state is assumed to either be entirely filled or empty.

Note: Each actual single state is characterized not only by the n 's and ℓ 's of the N electrons, but also by their m_ℓ 's and m_s 's. For example, a completely uniquely defined Slater determinant for the C atom would be $|2p^2; m_{l_1} = 0, m_{s_1} = -1/2, m_{l_2} = -1, m_{s_2} = 1/2\rangle$, signifying one of the $2p$ electron has an $m_l = 0$ and $m_s = -1/2$ and the other has an $m_l = -1$ and $m_s = 1/2$. Notably, if a shell is almost full, expliciting which quantum numbers are not occupied can also uniquely define a Slater determinant, for example for the F atom, $|2p^5; \bar{m}_l = 0, \bar{m}_s = 1/2\rangle$ denotes the Slater determinant where none of the $2p$ electrons are in the $m_l = 0, m_s = 1/2$ state, meaning the 5 other $2p$ states are occupied. The reason only $n\ell$'s are specified here is because H_0 is degenerate with respect to the other quantum numbers.

2.2 Angular momenta coupling schemes

The total angular momentum of a system of N electrons is given by the sum of the individual angular momenta of the electrons. The total angular momentum \vec{J} is then given by

$$\vec{J} = \sum_{i=1}^N \vec{l}_i + \sum_{i=1}^N \vec{s}_i = \sum_{i=1}^N (\vec{l}_i + \vec{s}_i), \quad (2.7)$$

where \vec{l}_i is the orbital angular momentum and \vec{s}_i is the spin angular momentum of the i -th electron. The total angular momentum of the system can be decomposed into the orbital angular momentum \vec{L} and the spin angular momentum \vec{S} of the electrons. The total angular momentum \vec{J} is then given by

$$\vec{J} = \sum_{i=1}^N \vec{l}_i + \sum_{i=1}^N \vec{s}_i = \vec{L} + \vec{S}. \quad (2.8)$$

The total angular momentum \vec{J} can also be decomposed into the sum of all the individual angular momenta of the electrons \vec{j}_i . The total angular momentum \vec{J} is then given by

$$\vec{J} = \sum_{i=1}^N (\vec{l}_i + \vec{s}_i) = \sum_{i=1}^N \vec{j}_i. \quad (2.9)$$

An example of the two different ways to decompose the total angular momentum of a system of 2 electrons is given in Section 2.2.

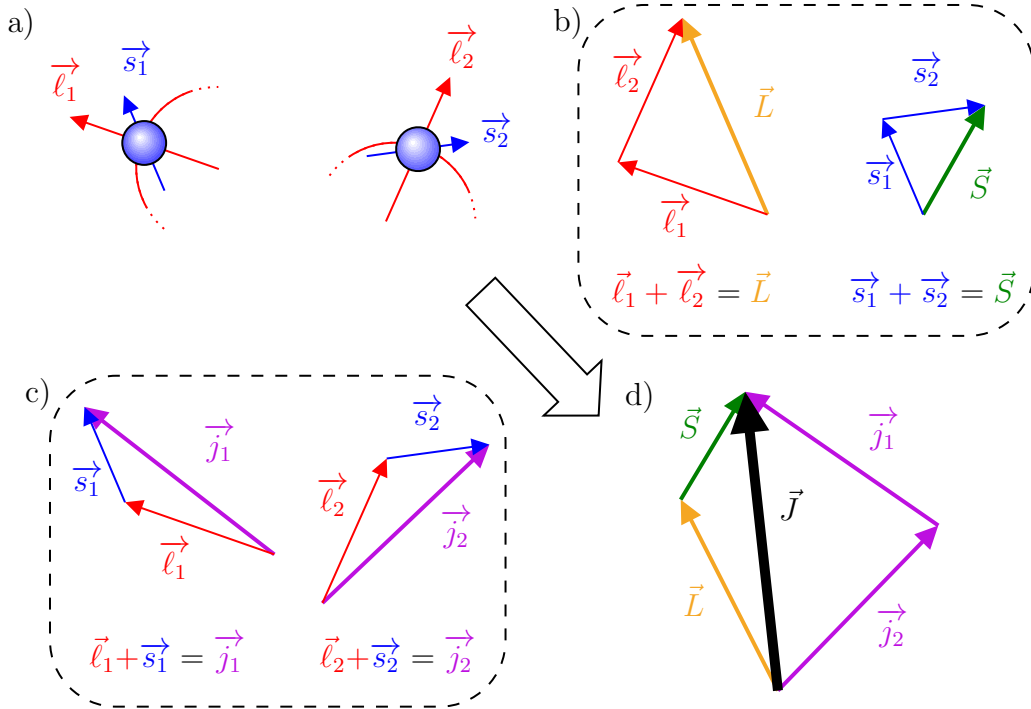


Figure 2.1: Geometric representation of the two traditional coupling schemes for the total angular momentum of a two-electron system. a) Two electrons with an orbital angular momentum \vec{l} and spin \vec{s} , b) The $L - S$ coupling scheme, where the two orbital angular momenta \vec{l}_1 and \vec{l}_2 are added to form the total orbital angular momentum \vec{L} and the two spins \vec{s}_1 and \vec{s}_2 are added to form the total spin \vec{S} , c) The $j - j$ coupling scheme, where the total angular momentum of each electron is constructed by adding the orbital and spin angular momenta of each electron individually d) The total angular momentum of the system \vec{J} is the sum of the total orbital angular momentum \vec{L} and the total spin \vec{S} or the sum of the total angular momentum of each electron \vec{j}_1 and \vec{j}_2 .

In the case of $L - S$ coupling, the wavefunction corresponding to a certain projection of the total angular momentum J is given by

$$|\alpha LSJM_J\rangle = (-1)^{J-M_J} \sqrt{2J+1} \sum_{M_L, M_S} \begin{pmatrix} L & J & S \\ M_L & -M_J & M_S \end{pmatrix} |\alpha LM_L SM_S\rangle, \quad (2.10)$$

where α is a shorthand notation for the quantum numbers of the electrons.

While in the case of $j - j$ coupling, the wavefunction corresponding to a certain projection of the total angular momentum J is given by

$$|\alpha j_1 j_2 J M_J\rangle = (-1)^{J-M_J} \sqrt{2J+1} \sum_{m_1, m_2} \begin{pmatrix} j_1 & J & j_2 \\ m_1 & -M_J & m_2 \end{pmatrix} |\alpha j_1 m_1 j_2 m_2\rangle, \quad (2.11)$$

The choice of coupling schemes depends on the problem at hand, for example, the $L - S$ coupling scheme is more appropriate when the interaction between the electrons is stronger relative to the spin-orbit coupling and the $j - j$ coupling scheme is more appropriate when the spin-orbit coupling is stronger relative to the interaction between the electrons. The latter is the case for heavy, relativistic, highly-charged ions for example.

In most cases, the eigenstates of an atom are neither in the $L - S$ nor in the $j - j$ coupling scheme, but a mixture of both. It is possible to transform between the two coupling schemes using the $9 - j$ symbols, and one has

$$|n_a \ell_a n_b \ell_b (\ell_1 s_1) j_1 (\ell_2 s_2) j_2 L S J M_J\rangle = \mathcal{N} \sum_{LS} \langle (\ell_1 \ell_2) L (s_1 s_2) S J | (\ell_1 s_1) j_1 (\ell_2 s_2) j_2 J \rangle |n_a \ell_a n_b \ell_b (\ell_1 \ell_2) L (s_1 s_2) S J M_J\rangle, \quad (2.12)$$

where $\mathcal{N} = \begin{cases} 1 & \text{if } j_1 = j_2 \text{ and } \ell_1 = \ell_2 \\ \sqrt{2} & \text{else} \end{cases}$ and the generalized Clebsch-Gordan coefficients are given by

$$\langle (\ell_1 \ell_2) L (s_1 s_2) S J | (\ell_1 s_1) j_1 (\ell_2 s_2) j_2 J \rangle = \sqrt{[S][L][j_1][j_2]} \begin{Bmatrix} \ell_1 & \ell_2 & L \\ s_1 & s_2 & S \\ j_1 & j_2 & J \end{Bmatrix}. \quad (2.13)$$

Note: If the spin-orbit coupling is strong enough relatively to the interaction between the electrons, the $j - j$ coupling scheme, represented by c) in [Section 2.2](#), is more appropriate. [Figure 2.2](#) shows the evolution of the energy levels from the pure $L - S$ coupling with no spin-orbit coupling to the jj coupling with maximum spin-orbit coupling, in Pr^{3+} , where the radial integrals, energies, and spin-orbit constant were obtained from a Hartree-Fock (HF) code.

2.3 Matrix elements for the two-electrons case

To illustrate the complication arising from the antisymmetrization of the wavefunction, let us consider the general form of matrix elements of a single electron tensor operator¹ $\mathbf{t}_i^{(k)}$ acting on the position space of the electron i in the basis of the two-electron system.

The wavefunction of the two-electron system is given by the Slater determinant (2.6)

$$\Psi_{\mathbf{n}}(\vec{r}_1, \vec{r}_2) = \frac{1}{\sqrt{2}} (\psi_{\mathbf{n}_1}(\vec{r}_1) \psi_{\mathbf{n}_2}(\vec{r}_2) - \psi_{\mathbf{n}_2}(\vec{r}_1) \psi_{\mathbf{n}_1}(\vec{r}_2)). \quad (2.14)$$

In the $L - S$ basis, it can be written as (omitting the sums over m_ℓ and m_s for brevity)

¹See [Appendix D.2](#).

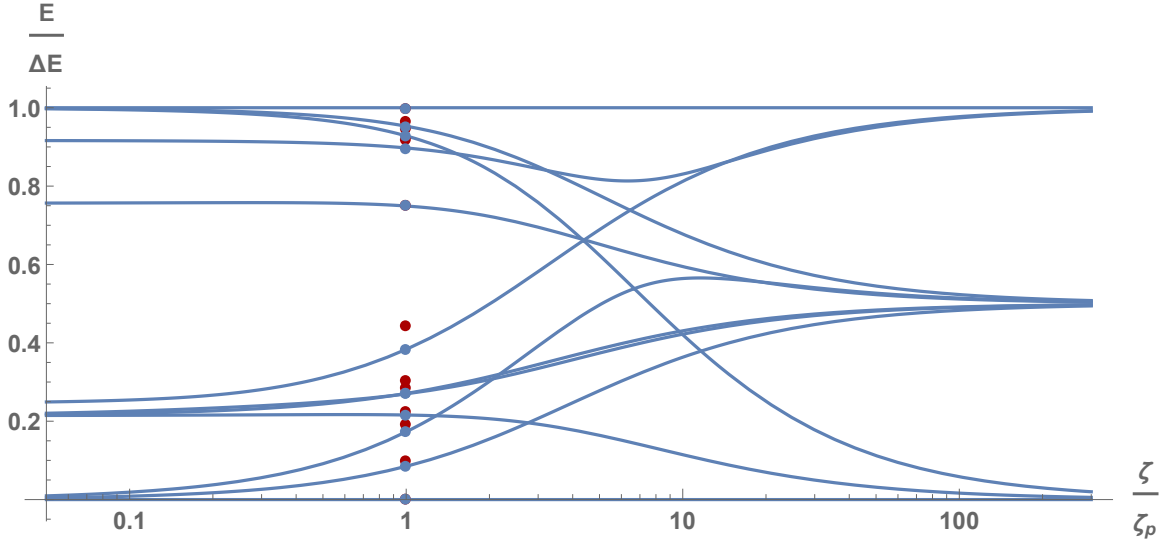


Figure 2.2: Evolution of the energies of the $4f^2$ configuration of free Pr^{3+} , from LS coupling ($\zeta = 0$, no spin-orbit, left) to jj coupling (right, spin-orbit maximum). Numerical values for R^k integrals were obtained from an Hartree-Fock (HF) wavefunctions and HF potential U . The red points are experimental data from [107], while the blue points are the energies obtained from the HF code with ζ_p the calculated spin-orbit coupling constant. ΔE is the difference between the minimum and maximum energies in the configuration. Obtained spin-orbit constant from the HF code : $\zeta_p = 1011 \text{ cm}^{-1}$.

$$|n_a \ell_a s_a n_b \ell_b s_b LSJM_J\rangle = \frac{1}{\sqrt{2}} (|(n_{a,1} \ell_{a,1} s_{a,1} n_{b,2} \ell_{b,2} s_{b,2}) LSJM_J\rangle - |(n_{a,2} \ell_{a,2} s_{a,2} n_{b,1} \ell_{b,1} s_{b,1}) LSJM_J\rangle), \quad (2.15)$$

where the subscripts 1 and 2 denote the electron to which the quantum numbers belong², it is important to note that when coupling two angular momenta j_1 and j_2 , the order of the coupling does matter, and the Clebsch-Gordan coefficients are not symmetric under the exchange of j_1 and j_2 , see (D.8). This can therefore be rewritten as

$$|n_a \ell_a s_a n_b \ell_b s_b LSJM_J\rangle = \frac{1}{\sqrt{2}} (|(n_{a,1} \ell_{a,1} s_{a,1} n_{b,2} \ell_{b,2} s_{b,2}) LSJM_J\rangle - (-1)^{s_a+s_b+l_a+l_b+L+S} |(n_{b,1} \ell_{b,1} s_{b,1} n_{a,2} \ell_{a,2} s_{a,2}) LSJM_J\rangle), \quad (2.16)$$

using the symmetry properties³ of the $3j$ -symbols/Clebsch-Gordan coefficients, considering $s = 1/2$, one can omit the spin quantum numbers for brevity, and write

$$|n_a \ell_a n_b \ell_b LSJM_J\rangle = \frac{1}{\sqrt{2}} (|(n_{a,1} \ell_{a,1} n_{b,2} \ell_{b,2}) LSJM_J\rangle + (-1)^{l_a+l_b+L+S} |(n_{b,1} \ell_{b,1} n_{a,2} \ell_{a,2}) LSJM_J\rangle). \quad (2.17)$$

²In essence $|(n_{a,1} \ell_{a,1} s_{a,1} n_{b,2} \ell_{b,2} s_{b,2}) LS\rangle = (|n_a \ell_a s_a\rangle \otimes |n_b \ell_b s_b\rangle)_{LS}$

³see (D.12)

Note: In the case where $\mathbf{n}_a = \mathbf{n}_b = \mathbf{n}$, it is then important to not omit m_ℓ and m_s in the ket notation since those have to be different for the two electrons and (2.17) becomes

$$|n\ell m_\ell m_s n\ell m'_\ell m'_s LSJM_J\rangle = \frac{1}{\sqrt{2}} (|(n_1\ell_1 m_{\ell,1} m_{s,1} n_2\ell_2 m'_{\ell,2} m'_{s,2}) LSJM_J\rangle + (-1)^{l_a+l_b+L+S} |(n_1\ell_1 m'_{\ell,1} m'_{s,1} n_2\ell_2 m_{\ell,2} m_{s,2}) LSJM_J\rangle). \quad (2.18)$$

Consider now that the previous expression is not physical since an LS state is generally not composed of two electrons of definite m_ℓ and m_s but is a superposition of all allowed m_ℓ and m_s states??.

Doing the formal calculation would simplify the expression to

$$|(n\ell)^2 LSJM_J\rangle = \frac{1}{2} (1 + (-1)^{L+S}) |(n_1\ell_1 n_2\ell_2) LSJM_J\rangle. \quad (2.19)$$

This means that L and S must be such that $L + S$ is even otherwise the wavefunction would vanish. This is generalizable to any number of electrons in the same electronic configuration.

We can therefore write to maintain generality:

Definition: (*Two-electron antisymmetrized wavefunction*)

$$|(n_a\ell_a n_b\ell_b) LSJM_J\rangle = \frac{\mathcal{N}_{a,b}}{\sqrt{2}} (|(n_{a,1}\ell_{a,1} n_{b,2}\ell_{b,2}) LSJM_J\rangle + (-1)^{l_a+l_b+L+S} |(n_{b,1}\ell_{b,1} n_{a,2}\ell_{a,2}) LSJM_J\rangle), \quad (2.20)$$

with $\mathcal{N}_{a,b}$ a normalization factor that depends on the quantum numbers of the two electrons, and is equal to 1 if the two electrons are not in the same state and $1/\sqrt{2}$ if they are.

The matrix elements of the q -th component of the single electron tensor operator $\mathbf{t}_i^{(k)}$ acting on the position space of the electron i in the basis of the two-electron system are then given by the Wigner-Eckart theorem (D.29)

$$\langle (n_a\ell_a n_b\ell_b) LSJM_J | \mathbf{t}_{i,q}^{(k)} | (n'_a\ell'_a n'_b\ell'_b) L'S'J'M_{J'} \rangle = (-1)^{J-M_J} \begin{pmatrix} J & k & J' \\ -M_J & q & M_{J'} \end{pmatrix} \times \langle (n_a\ell_a n_b\ell_b) LSJ || \mathbf{t}^{(k)} || (n'_a\ell'_a n'_b\ell'_b) L'S'J' \rangle. \quad (2.21)$$

Equation (D.43) states as a reminder

$$\langle \alpha j_1 j_2 J || \mathbf{T}^{(k)} || \alpha' j'_1 j'_2 J' \rangle = \delta_{j_2, j'_2} (-1)^{j_1+j_2+J'+k} ([J][J'])^{\frac{1}{2}} \begin{Bmatrix} J & k & J' \\ j'_1 & j_2 & j_1 \end{Bmatrix} \times \langle \alpha j_1 || \mathbf{T}^{(k)} || \alpha' j'_1 \rangle. \quad (2.22)$$

And it would be tempting to use it immediately to decouple L and S (resp. L' and S') from J (resp. J') and obtain

$$\begin{aligned} \langle (n_a \ell_a n_b \ell_b) L S J \| \mathbf{t}^{(k)} \| (n'_a \ell'_a n'_b \ell'_b) L' S' J' \rangle &= (-1)^{L+S+J'+k} \sqrt{2J+1} \sqrt{2J'+1} \begin{Bmatrix} J & k & J' \\ L' & S & L \end{Bmatrix} \delta_{S,S'} \\ &\times \langle (n_a \ell_a n_b \ell_b) L \| \mathbf{t}^{(k)} \| (n'_a \ell'_a n'_b \ell'_b) L' \rangle, \quad (2.23) \end{aligned}$$

Notice, one can not then immediately use the same decoupling formula to decouple l_a and l_b to calculate $\langle (n_a \ell_a n_b \ell_b) L \| \mathbf{t}^{(k)} \| (n'_a \ell'_a n'_b \ell'_b) L' \rangle$ since it would require to know the order of which is the first and second angular moment. This then requires to first express the antisymmetrized wavefunction as a function of the distinguishable states, as in (2.17). So, going one step back, before writing (2.23), one should first express the matrix element in the basis of the distinguishable states, as in (2.17). This leads to

$$\begin{aligned} \langle (n_a \ell_a n_b \ell_b) L S J \| \mathbf{t}^{(k)} \| (n'_a \ell'_a n'_b \ell'_b) L' S' J' \rangle &= \\ &\frac{\mathcal{N}_{a,b} \mathcal{N}_{a',b'}}{2} \left(\langle (n_{a,1} \ell_{a,1} n_{b,2} \ell_{b,2}) L S J \| \mathbf{t}_i^{(k)} \| (n'_{a,1} \ell'_{a,1} n'_{b,2} \ell'_{b,2}) L' S' J' \rangle \right. \\ &+ (-1)^{l'_a + l'_b + L' + S'} \langle (n_{a,1} \ell_{a,1} n_{b,2} \ell_{b,2}) L S J \| \mathbf{t}_i^{(k)} \| (n'_{b,1} \ell'_{b,1} n'_{a,2} \ell'_{a,2}) L' S' J' \rangle \\ &+ (-1)^{l_a + l_b + L + S} \langle (n_{b,1} \ell_{b,1} n_{a,2} \ell_{a,2}) L S J \| \mathbf{t}_i^{(k)} \| (n'_{a,1} \ell'_{a,1} n'_{b,2} \ell'_{b,2}) L' S' J' \rangle \\ &\left. + (-1)^{l_a + l_b + L + S + l'_a + l'_b + L' + S'} \langle (n_{b,1} \ell_{b,1} n_{a,2} \ell_{a,2}) L S J \| \mathbf{t}_i^{(k)} \| (n'_{b,1} \ell'_{b,1} n'_{a,2} \ell'_{a,2}) L' S' J' \rangle \right). \quad (2.24) \end{aligned}$$

Looking at diagonal matrix elements between two states in the same configuration ($\vec{\mathbf{n}} = \vec{\mathbf{n}}'$), (2.24) simplifies to

$$\begin{aligned} \langle (n_a \ell_a n_b \ell_b) L S J \| \mathbf{t}^{(k)} \| (n_a \ell_a n_b \ell_b) L' S' J' \rangle &= \\ &\frac{\mathcal{N}_{a,b}^2}{2} \left(\langle (n_{a,1} \ell_{a,1} n_{b,2} \ell_{b,2}) L S J \| \mathbf{t}_i^{(k)} \| (n_{a,1} \ell_{a,1} n_{b,2} \ell_{b,2}) L' S' J' \rangle \right. \\ &+ (-1)^{l_a + l_b + L + S} \langle (n_{a,1} \ell_{a,1} n_{b,2} \ell_{b,2}) L S J \| \mathbf{t}_i^{(k)} \| (n_{b,1} \ell_{b,1} n_{a,2} \ell_{a,2}) L' S' J' \rangle \\ &+ (-1)^{l_a + l_b + L + S} \langle (n_{b,1} \ell_{b,1} n_{a,2} \ell_{a,2}) L S J \| \mathbf{t}_i^{(k)} \| (n_{a,1} \ell_{a,1} n_{b,2} \ell_{b,2}) L' S' J' \rangle \\ &\left. + (-1)^{L+S+L'+S'} \langle (n_{b,1} \ell_{b,1} n_{a,2} \ell_{a,2}) L S J \| \mathbf{t}_i^{(k)} \| (n_{b,1} \ell_{b,1} n_{a,2} \ell_{a,2}) L' S' J' \rangle \right). \quad (2.25) \end{aligned}$$

Each reduces matrix element in (2.24) can be decoupled to obtain terms of the form (2.23). Meaning the prefactor $(-1)^{L+S+J'+k} \sqrt{2J+1} \sqrt{2J'+1} \begin{Bmatrix} J & k & J' \\ L' & S & L \end{Bmatrix} \delta_{S,S'}$ can be factored out and the reduced matrix element $\langle (n_a \ell_a n_b \ell_b) L \| \mathbf{t}^{(k)} \| (n'_a \ell'_a n'_b \ell'_b) L' \rangle$ takes the same form as in (2.24) but with the additional condition that $S = S'$

$$\begin{aligned} \langle (n_a \ell_a n_b \ell_b) L \| \mathbf{t}^{(k)} \| (n'_a \ell'_a n'_b \ell'_b) L' \rangle &= \frac{\mathcal{N}_{a,b} \mathcal{N}_{a',b'}}{2} \left(\langle (n_{a,1} \ell_{a,1} n_{b,2} \ell_{b,2}) L \| \mathbf{t}_i^{(k)} \| (n'_{a,1} \ell'_{a,1} n'_{b,2} \ell'_{b,2}) L' \rangle \right. \\ &+ (-1)^{l'_a + l'_b + L' + S'} \langle (n_{a,1} \ell_{a,1} n_{b,2} \ell_{b,2}) L \| \mathbf{t}_i^{(k)} \| (n'_{b,1} \ell'_{b,1} n'_{a,2} \ell'_{a,2}) L' \rangle \\ &+ (-1)^{l_a + l_b + L + S} \langle (n_{b,1} \ell_{b,1} n_{a,2} \ell_{a,2}) L \| \mathbf{t}_i^{(k)} \| (n'_{a,1} \ell'_{a,1} n'_{b,2} \ell'_{b,2}) L' \rangle \\ &\left. + (-1)^{l_a + l_b + L + l'_a + l'_b + L'} \langle (n_{b,1} \ell_{b,1} n_{a,2} \ell_{a,2}) L \| \mathbf{t}_i^{(k)} \| (n'_{b,1} \ell'_{b,1} n'_{a,2} \ell'_{a,2}) L' \rangle \right). \quad (2.26) \end{aligned}$$

The order of coupling of the 2 ℓ 's is now clear in every term of (2.26) and one has for $i = 1$

$$\begin{aligned} \langle (n_{x,1}\ell_{x,1}n_{y,2}\ell_{y,2})L \| \mathbf{t}_1^{(k)} \| (n'_{z,1}\ell'_{z,1}n'_{w,2}\ell'_{w,2})L' \rangle &= (-1)^{\ell_x+\ell_y+L'+k} \sqrt{2L+1} \sqrt{2L'+1} \times \\ &\times \begin{Bmatrix} L & k & L' \\ \ell'_z & \ell_y & \ell_x \end{Bmatrix} \delta_{\ell_y, \ell'_w} \langle n_x \ell_x \| \mathbf{t}^{(k)} \| n_z \ell_z \rangle, \end{aligned} \quad (2.27)$$

where $(x, y), (z, w) \in \{(a, b), (b, a)\}$, and a similar expression for $i = 2$.

As an illustrative example, one can look at the diagonal elements between two configurations of equivalent electrons, starting from (2.17), one can write

$$\langle n\ell^2 L \| \mathbf{t}^{(k)} \| n\ell^2 L' \rangle = (-1)^{L'+k} \sqrt{2L+1} \sqrt{2L'+1} \begin{Bmatrix} L & k & L' \\ \ell & \ell & \ell \end{Bmatrix} \langle n\ell \| \mathbf{t}^{(k)} \| n\ell \rangle, \quad (2.28)$$

and (2.23) then yields

$$\langle n\ell^2 LSJ \| \mathbf{t}^{(k)} \| n\ell^2 L'S'J' \rangle = k(\ell, L, S, J, L', S', J') \langle n\ell \| \mathbf{t}^{(k)} \| n\ell \rangle, \quad (2.29)$$

with

$$k(\ell, L, S, J, L', S', J') = (-1)^{L'+L+S+J'} \delta_{S, S'} \sqrt{[J][J'] [L][L']} \begin{Bmatrix} J & k & J' \\ L & S & L' \end{Bmatrix} \begin{Bmatrix} L & k & L' \\ \ell & \ell & \ell \end{Bmatrix}. \quad (2.30)$$

As a reminder $[x] \equiv \sqrt{2x+1}$. Similar expressions can be derived if one considers the matrix elements of the tensor operator acting on the spin space of the electrons, or the tensor operator acting on the position space of one electron and the spin space of the other, etc...

2.4 Unit Tensor Operators

The computations of the previous section show how the antisymmetrization of the wavefunction can complicate the calculation of matrix elements of operators acting on the position space of the electrons. Moreover, this was only in the case of 2 electrons only. Is there a way to simplify the calculation of matrix elements of operators while considering the wavefunction of more than even 2 electrons? The answer is yes, and it is to use the unit tensor operators, which this section introduces. A more in-depth derivation and explanation of the computations methods to obtain the values of the reduced matrix elements of the unit tensor operators can be found in [108, 109, 110] for example.

2.4.1 Single electron operators

Introducing the single electron operator whose reduced matrix element is normalized to unity i.e. $\forall |\ell - \ell'| \leq k \leq \ell + \ell'$,

$$\langle \alpha \ell \| \mathbf{u}^{(k)}(l, l') \| \alpha' \ell' \rangle = \delta_{\alpha, \alpha'} \delta_{\ell, l} \delta_{\ell', l'}, \quad (2.31)$$

and thank to the Wigner-Eckart theorem, one can express the matrix elements of any single-electron operator $\mathbf{t}_i^{(k)}$ acting on the position space of electron i in the basis of the multi-electronic system as

$$\langle \alpha \cdots \ell_i \cdots | \mathbf{t}_i^{(k)} | \alpha' \cdots \ell'_i \cdots \rangle = \langle \alpha \ell_i \| \mathbf{t}_i^{(k)} | \alpha' \ell'_i \rangle \langle \alpha \cdots \ell_i \cdots | \mathbf{u}^{(k)} | \alpha' \cdots \ell'_i \cdots \rangle, \quad (2.32)$$

or for reduced matrix elements

$$\langle \alpha \cdots \ell_i \cdots \ell_i \| \mathbf{t}_i^{(k)} \| \alpha' \cdots \ell'_i \cdots \ell'_i \rangle = \langle \alpha \ell_i \| \mathbf{t}_i^{(k)} | \alpha' \ell'_i \rangle \langle \alpha \cdots \ell_i \cdots \ell_i \| \mathbf{u}^{(k)} \| \alpha' \cdots \ell'_i \cdots \ell'_i \rangle. \quad (2.33)$$

It becomes highly non-trivial to calculate $\langle \alpha \cdots \ell_i \cdots \ell_i \| \mathbf{u}^{(k)} \| \alpha' \cdots \ell'_i \cdots \ell'_i \rangle$ as it requires doing the operation done in [Section 2.3](#) recursively and while conserving the antisymmetry of the wavefunction to odd permutations of the electrons. But this has been done in [\[109, 111\]](#) and the results are tabulated. And thanks to the last relations, only the reduced matrix elements of $\mathbf{u}^{(k)}$ are needed to calculate the matrix elements of any single-electron operator.

One can also generalize the expression for coupled basis states and p equivalent electrons

$$\langle \alpha \ell^p LSJ \| \mathbf{t}_i^{(k)} \| \alpha' \ell'^p L'S'J' \rangle = \langle \alpha \ell \| \mathbf{t}^{(k)} | \alpha' \ell' \rangle \langle \alpha \ell^p LSJ \| \mathbf{u}^{(k)} \| \alpha' \ell'^p L'S'J' \rangle. \quad (2.34)$$

Note: For the case $p = 2$, we have computed the reduced matrix elements of the unit tensor operators in [\(2.29\)](#) and [\(2.30\)](#). Therefore, in this case, we can write

$$\langle \alpha \ell^2 LSJ \| \mathbf{u}^{(k)} \| \alpha' \ell'^2 L'S'J' \rangle = (-1)^{L'+L+S+J'} \delta_{\alpha, \alpha'} \delta_{S, S'} \sqrt{[J][J'] [L][L']} \begin{Bmatrix} J & k & J' \\ L & S & L \end{Bmatrix} \begin{Bmatrix} L & k & L' \\ \ell & \ell & \ell \end{Bmatrix}. \quad (2.35)$$

One can also define the double unit tensor operator $\mathbf{v}^{(k1)}$ as the product of the unit tensor operator on the position space of the electron and $\vec{s} = \mathbf{s}^{(1)}$ on the spin space of the electron.

$$\mathbf{v}^{(k1)} = \mathbf{u}^{(k)} \mathbf{s}^{(1)}. \quad (2.36)$$

Finally, one can define the double unit tensor operator $\mathbf{w}^{(k\kappa)}$ as the product of the unit tensor operator of rank k on the position space of the electron and the unit tensor operator of rank κ on the spin space of the electron. Since $\langle s \| \mathbf{s}^{(1)} \| s' \rangle = \delta_{s, s'} \frac{\sqrt{3}}{2}$, $\mathbf{v}^{(k1)} = \frac{\sqrt{3}}{2} \mathbf{w}^{(k1)}$.

We have then

$$\langle \alpha s \ell \| \mathbf{v}^{(k1)} (l, l') \| \alpha' s' \ell' \rangle = \delta_{\alpha, \alpha'} \delta_{\ell, l} \delta_{\ell', l'} \delta_{s, s'} \frac{\sqrt{3}}{2}, \quad (2.37)$$

and

$$\langle \alpha s \ell \| \mathbf{w}^{(k\kappa)} (l, l') \| \alpha' s' \ell' \rangle = \delta_{\alpha, \alpha'} \delta_{\ell, l} \delta_{\ell', l'} \delta_{s, s'}. \quad (2.38)$$

2.4.2 Multi-electron operators

Finally, one can define, for a shell of p equivalent electrons, the unit tensor operator $\mathbf{U}^{(k)}$ as the sum of the unit tensor operators acting on each electron of the shell

$$\mathbf{U}^{(k)} = \sum_{i=1}^p \mathbf{u}_i^{(k)}. \quad (2.39)$$

And thus

$$\langle \alpha \ell^p \| \sum_{i=1}^p \mathbf{t}_i^{(k)} \| \alpha' \ell^p \rangle = \langle \ell \| \mathbf{t}_i^{(k)} \| \ell \rangle \langle \alpha \ell^p \| \mathbf{U}^{(k)} \| \alpha' \ell^p \rangle. \quad (2.40)$$

This can also be expressed in a coupled basis as

$$\langle \alpha \ell^p LSJ \| \sum_{i=1}^p \mathbf{t}_i^{(k)} \| \alpha' \ell^p L' S' J' \rangle = \langle \ell \| \mathbf{t}_i^{(k)} \| \ell \rangle \langle \alpha \ell^p LSJ \| \mathbf{U}^{(k)} \| \alpha' \ell^p L' S' J' \rangle. \quad (2.41)$$

And, similarly, one can define the double unit tensor operators $\mathbf{V}^{(k1)}$ and $\mathbf{W}^{(k\kappa)}$ as the sum of the double unit tensor operators acting on each electron of the shell.

All these operators have an implicit dependence on the number of electrons in the shell, and the antisymmetry of the wavefunction to odd permutations of the electrons is conserved.

The reduced matrix elements of the unit tensor operators $\mathbf{u}^{(k)}$, $\mathbf{v}^{(k1)}$, $\mathbf{U}^{(k)}$, $\mathbf{V}^{(k1)}$ and $\mathbf{W}^{(k\kappa)}$ can all be found in the tables of Tuszynski or Nielson and Koster [109, 111].⁴ And any multi-electron operator can be expressed in terms of these reduced matrix elements.

2.5 Coulomb interelectronic repulsion

Consider the next term in the total Hamiltonian

Definition: (*Interelectronic repulsion Hamiltonian*)

$$H_{e-e} = \sum_{i < j} \frac{e^2}{4\pi\epsilon_0 r_{ij}}, \quad (2.42)$$

which can also be written as

$$H_{e-e} = \frac{1}{2} \sum_{i \neq j} \frac{e^2}{4\pi\epsilon_0 r_{ij}}, \quad (2.43)$$

where $r_{ij} = |\vec{r}_i - \vec{r}_j|$ is the distance between the electrons i and j .

In order to calculate the matrix elements H_{e-e} , it would be more practical to express it in terms of tensor operators, which can be done thanks to the expansion (C.24)

$$\frac{1}{r_{ij}} = \sum_{k=0}^{\infty} \sum_{q=-k}^k \frac{r_{<}^k}{r_{>}^{k+1}} (-1)^q C_q^{(k)}(\theta_i, \phi_i) C_{-q}^{(k)}(\theta_j, \phi_j), \quad (2.44)$$

where $r_{<}$ and $r_{>}$ are the smallest and largest of r_i and r_j respectively. The matrix elements of H_{e-e} in the valence shell are then given by

⁴The reduced matrix elements might be computed in the uncoupled basis LS , one can then use the recoupling formulae in Appendix D.3.4, for example

$$\langle \alpha LSJ \| \mathbf{U}^{(k)} \| \alpha' L' S' J' \rangle = \delta_{S,S'} (-1)^{L+S+J'+k} ([J][J'])^{\frac{1}{2}} \left\{ \begin{matrix} J & k & J' \\ L' & S & L \end{matrix} \right\} \times \langle \alpha LS \| \mathbf{U}^{(k)} \| \alpha' L' S \rangle.$$

$$\begin{aligned}
\langle \Psi_{\vec{n}} | H_{e-e} | \Psi_{\vec{n}} \rangle &= \langle n\ell^p | H_{e-e} | n\ell^p \rangle \\
&= \frac{1}{2} \sum_{i \neq j} \langle n\ell^p | \frac{e^2}{4\pi\epsilon_0 r_{ij}} | n\ell^p \rangle \\
&= \frac{1}{2} \sum_{i \neq j} \frac{e^2}{4\pi\epsilon_0} \sum_{k=0}^{+\infty} \langle n\ell^p | \frac{r_{ij}^k}{r_{ij}^{k+1}} \underbrace{\sum_{q=-k}^k (-1)^q C_q^{(k)}(\theta_i, \phi_i) C_{-q}^{(k)}(\theta_j, \phi_j)}_{\equiv \mathbf{C}_i^{(k)} \cdot \mathbf{C}_j^{(k)}} | n\ell^p \rangle \quad (2.45) \\
&= \frac{1}{2} \sum_{i \neq j} \frac{e^2}{4\pi\epsilon_0} \sum_{k=0}^{+\infty} \langle n\ell^p | \frac{r_{ij}^k}{r_{ij}^{k+1}} | n\ell^p \rangle \langle \ell^p | \mathbf{C}_i^{(k)} \cdot \mathbf{C}_j^{(k)} | \ell^p \rangle
\end{aligned}$$

2.5.1 The diagonal basis

Ideally it would simplify things if one finds the basis in which H_{e-e} is diagonal. First, since the interelectronic repulsion is spin-independent, the total spin momentum of the p electrons in the valence shell $S = \sum_{i=1}^p m_{\ell,i}$ can be used as a quantum number for a diagonal basis. Similarly then, one would be tempted to use $L = \sum_{i=1}^p m_{s,i}$ as another quantum number. To confirm if H_{e-e} is diagonal in L , the Wigner-Eckart theorem can be of great use

Definition: (*Wigner-Eckart theorem*)

$$\langle LM_L | T_q^{(k)} | L'M_{L'} \rangle = (-1)^{L-M_L} \begin{pmatrix} L & k & L' \\ -M_L & q & M_{L'} \end{pmatrix} \langle L || T^{(k)} || L' \rangle, \quad (2.46)$$

since H_{e-e} is a sum of scalar operators acting on the electrons, it is a tensor operator of rank $k = 0$, and the selection rules on the $3j$ -symbol then impose that $L = L'$ and

$$\langle LM_L | H_{ee} | L'M_{L'} \rangle = \frac{\delta_{L,L'} \delta_{M_L,M_{L'}}}{2L+1} \langle L || H_{e-e} || L' \rangle. \quad (2.47)$$

The good quantum numbers are then L and S , and H_{e-e} is degenerate in M_L and M_S , and

$$\langle LSM_L M_S | H_{e-e} | L'S' M_{L'} M_{S'} \rangle = \frac{1}{2L+1} \langle L || H_{e-e} || L \rangle \delta_{L,L'} \delta_{M_L,M_{L'}} \delta_{S,S'} \delta_{M_S,M_{S'}}. \quad (2.48)$$

Definition: (*Spectroscopic term*) Traditionally, one denotes

$${}^{2S+1}L \quad (2.49)$$

the spectroscopic term i.e. the eigenstate of H_{e-e} whose quantum numbers are L and S . L is generally written in spectroscopic notation, which is a letter corresponding to the value of L ($S, P, D, F, G, H, I, K, L, M, \dots$)^a with $L = 0, 1, 2, 3, 4, 5, 6, 7, 8, 9, 10, 11, \dots$

^aThe letters after M are in alphabetic order.

Note: Equation (2.48) seems to infer that H_{e-e} only depends on L , and is degenerate in S . This is formally the case, but it can be proven that $L + S$ is necessarily even. Therefore, the choice of L

also imposes some conditions on S .

2.5.2 Matrix element for the valence shell

Rewriting the matrix element in the newly chosen basis (assuming arbitrary M_L and M_S , since H_{e-e} is degenerate in M_L and M_S , an implicit $\delta_{M_L, M'_L} \delta_{M_S, M'_S}$ is present in the expressions of the matrix elements for the rest of this section) yields

$$\langle n\ell^p LS | H_{e-e} | n\ell^p LS \rangle = \frac{1}{2} \sum_{i \neq j} \frac{e^2}{4\pi\epsilon_0} \sum_{k=0}^{+\infty} \langle n\ell^p | \frac{r_{>}^k}{r_{<}^{k+1}} | n\ell^p \rangle \langle \ell^p LS | \mathbf{C}_i^{(k)} \cdot \mathbf{C}_j^{(k)} | \ell^p LS \rangle. \quad (2.50)$$

In order to calculate $\langle \ell^p L | \mathbf{C}_i^{(k)} \cdot \mathbf{C}^{(k)} | \ell^p L \rangle$, one can use the following expression in terms of unit tensor operators \mathbf{u} and \mathbf{U}

$$\sum_{i \neq j}^p (\mathbf{t}_i^{(k)} \cdot \mathbf{t}_j'^{(k)}) = \left(\frac{\langle \ell \| \mathbf{t}^{(k)} \| \ell \rangle \langle \ell \| \mathbf{t}'^{(k)} \| \ell \rangle}{\langle \ell \| \mathbf{u}^{(k)} \| \ell \rangle^2} \right) \left[(\mathbf{U}^{(k)} \cdot \mathbf{U}^{(k)}) - \sum_{i=1}^p (\mathbf{u}_i^k \cdot \mathbf{u}_i^k) \right], \quad (2.51)$$

where the tensor operator $\mathbf{t}_i^{(k)}$ acts on the electron i and $\mathbf{t}_j'^{(k)}$ acts on the electron j .

Using

$$\frac{1}{\langle \ell \| \mathbf{u}^{(k)} \| \ell \rangle^2} \langle n\ell^p LS | \sum_{i=1}^p (\mathbf{u}_i^k \cdot \mathbf{u}_i^k) | n\ell^p LS \rangle = \frac{p}{2\ell + 1} \quad (2.52)$$

one gets ⁵

$$\langle n\ell^p LS | H_{e-e} | n\ell^p LS \rangle = \frac{e^2}{4\pi\epsilon_0} \sum_{k=0}^{+\infty} F_k(n\ell, n\ell) f_k(\ell^p LS, \ell^p LS), \quad (2.53)$$

with

$$F_k(n\ell, n'\ell') \equiv \int_{r_1=0}^{+\infty} \int_{r_2=0}^{+\infty} P_{n\ell}^2(r_1) \frac{r_{>}^k}{r_{<}^{k+1}} P_{n'\ell'}^2(r_2) dr_1 dr_2, \quad (2.54)$$

$$f_k(\ell^p LS, \ell^p LS) \equiv \frac{\langle \ell \| \mathbf{C}^{(k)} \| \ell \rangle^2}{2} \left(\frac{\langle \ell^p LS | (\mathbf{U}^{(k)} \cdot \mathbf{U}^{(k)}) | \ell^p LS \rangle}{\langle \ell \| \mathbf{u}^{(k)} \| \ell \rangle^2} - \frac{p}{2\ell + 1} \right). \quad (2.55)$$

Equation (2.55) can be further explicitated in terms of a product of reduced matrix elements of single unit tensor see [110] for a detailed derivation.

Note that

$$\langle \ell \| \mathbf{C}^{(k)} \| \ell \rangle = (-1)^\ell (2\ell + 1) \begin{pmatrix} \ell & k & \ell \\ 0 & 0 & 0 \end{pmatrix}, \quad (2.56)$$

using selection rules on the $3j$ -symbol, one gets that for (2.56) not to be zero, $0 \leq k \leq 2\ell$ and k needs to be even, and one can rewrite the matrix element without loss of generality as

⁵See [112, 113] for a detailed derivation of the matrix element of the interelectronic repulsion inside one shell.

Definition: (Matrix element of H_{e-e} for the valence shell)

$$\begin{aligned}\langle n\ell^p LS | H_{e-e} | n\ell^p LS \rangle &= \frac{e^2}{4\pi\epsilon_0} \sum_{k=0}^{2\ell} F_k(n\ell, n\ell) f_k(\ell^p LS, \ell^p LS) \\ &= \frac{e^2}{4\pi\epsilon_0} \sum_{q=0}^{\ell} F_{2q}(n\ell^p, n\ell^p) f_{2q}(\ell^p LS, \ell^p LS).\end{aligned}\quad (2.57)$$

Note: The form of (2.57) means it is possible to describe the effect on the valence shell of the interelectronic Coulomb repulsion with a finite number of parameters. More precisely, for the valence shell $n\ell^p$, only $2\ell + 2$ parameters are needed, namely the $\ell + 1$ radial integrals $F_k(n\ell, n\ell)$ and the $\ell + 1$ angular matrix elements $f_k(\ell^p LS, \ell^p LS)$.

Since L and S are resulting from the coupling of the p orbital and p spin angular momenta of the valence electrons, there are only a finite number of possible values of L and S per valence shell, and the number of energy levels due to the interelectronic repulsion can be calculated. Moreover, (2.17) states that $L + S$ is even. Tables 2.1 to 2.3 and 4.2 show the possible spectroscopic terms for the s, p, d and f shells respectively. One can see that some spectroscopic terms are share the same L and S quantum numbers, and are thus degenerate in energy, but to disambiguate them, one can use a supplementary α quantum number, which comes from group theory, see [110, 114].

Configuration	Number of Terms	Spectroscopic Terms
s^0, s^2	1	1S
s^1	1	2S

Table 2.1: Spectroscopic terms for $\ell = 0$

Configuration	Number of Terms	Spectroscopic Terms
p^0, p^6	1	1S
p^1, p^5	1	2P
p^2, p^4	3	$^1D, ^3P, ^1S$
p^3	3	$^2D, ^2P, ^4S$

Table 2.2: Spectroscopic terms for $\ell = 1$

Configuration	Number of Terms	Spectroscopic Terms
d^0, d^{10}	1	1S
d^1, d^9	1	2D
d^2, d^8	5	$^1G, ^3F, ^1D, ^3P, ^1S$
d^3, d^7	8	$^2H, ^2G, ^4F, ^2F, ^2D, ^2D, ^4P, ^2P$
d^4, d^6	16	$^1I, ^3H, ^3G, ^5D, ^1G, ^1G, ^3F, ^3F, ^3D, ^1F$ $^1D, ^1D, ^3P, ^3P, ^1S, ^1S$
d^5	16	$^2I, ^2H, ^4G, ^2G, ^2G, ^4F, ^4D, ^2F, ^2F, ^4P$ $^6S, ^2D, ^2D, ^2D, ^2P, ^2S$

Table 2.3: Spectroscopic terms for $\ell = 2$

2.5.3 Mean-field contribution

One last simplification of the matrix element is worth considering.

The term $k = 0$ in the sum is

$$\frac{e^2}{4\pi\epsilon_0} F_0(n\ell^p, n\ell^p) f_0(\ell^p LS, \ell^p LS), \quad (2.58)$$

with

$$f_0(\ell^p LS, \ell^p LS) = \frac{\langle \ell \| \mathbf{C}^{(0)} \| \ell \rangle^2}{2} \left(\frac{\langle \ell^p LS | (\mathbf{U}^{(0)} \cdot \mathbf{U}^{(0)}) | \ell^p LS \rangle}{\langle \ell \| \mathbf{u}^{(0)} \| \ell \rangle^2} - \frac{p}{2\ell + 1} \right), \quad (2.59)$$

the latter has been computed in [113], and is equal to

$$f_0(n\ell^p LS, n\ell^p LS) = \frac{p(p-1)}{2}, \quad (2.60)$$

it is independent of both L and S . Therefore the term of H_{e-e} for $k = 0$ is only a term dependent on n , ℓ and p , and does not split the electronic configuration's degeneracy (namely in L and S). It is thus just a mean-field addition to the energy of the electronic configuration as obtained from the study of H_0 . It is quite standard to ignore the term $k = 0$ if one only considers the energy levels within the same electronic configuration. It is sometimes even included in H_0 as it has the same effect on the degeneracy of the electronic spectrum.

Definition: (Mean-field contribution of the interelectronic repulsion in the $n\ell^p$ configuration)

$$\frac{e^2}{4\pi\epsilon_0} \frac{p(p-1)}{2} \int_{r_1=0}^{+\infty} \int_{r_2=0}^{+\infty} P_{n\ell}^2(r_1) \frac{1}{r_{>}} P_{n\ell}^2(r_2) dr_1 dr_2 \quad (2.61)$$

If however one considers interconfigurational effects, albeit one of the shells' $k = 0$ term can be incorporated in the chosen energy origin (generally the valence shell), it is primordial to consider the mean-field contribution of the other shell, as it contributes significantly to the energy splitting between the two shells.

Note: For a closed shell, note that since all $4\ell + 2$ electronic states are occupied, $L = S = 0$ necessarily (there is only one spectroscopic term), and one can compute (2.57). This would yield [113]

$$f_k(\ell^{4\ell+2} {}^1S, \ell^{4\ell+2} {}^1S) = -\langle \ell \| \mathbf{C}^{(k)} \| \ell \rangle. \quad (2.62)$$

2.5.4 Matrix element of excited configurations

If one were to consider the configuration $|n\ell^{p-1}n_e\ell_e^1\rangle$ where an electron has been promoted from the valence shell to an excited one, the electron in $n_e\ell_e$ would (i) Necessarily be in the state $L = \ell_e$ and $S = 1/2$ (ii) Interact with the $p-1$ electrons in the valence shell.

Note: The matrix element be calculated similarly to the calculation of matrix elements for the two electron cases, by conceptualizing the $n\ell^{p-1}$ electrons as a single electron with an effective angular momentum L_1 and spin S_1 .

The matrix element of the interelectronic repulsion in this case is given by [112, 113]

$$\begin{aligned}
& \langle (n\ell^{p-1}L_1S_1) (n_e\ell_e^1\ell_e1/2) LS | H_{e-e} | (n\ell^{p-1}L'_1S'_1) (n_e\ell_e^1\ell_e1/2) L'S' \rangle = \\
& \delta_{L,L'}\delta_{S,S'}\delta_{L_1,L'_1}\delta_{S_1,S'_1}\frac{e^2}{4\pi\epsilon_0}\sum_{k=0}^{2l}F_k(n\ell,n\ell)f_k(\ell^{p-1}L_1S_1,\ell^{p-1}L_1S_1) \\
& + \delta_{L,L'}\delta_{S,S'}\delta_{S_1,S'_1}\frac{e^2}{4\pi\epsilon_0}\sum_{k=0}^{2l}F_k(n\ell,n_e\ell_e)f'_k(\ell^{p-1}L_1S_1\ell_eLS,\ell^{p-1}L'_1S_1\ell_eLS) \quad (2.63) \\
& - \delta_{L,L'}\delta_{S,S'}\frac{e^2}{4\pi\epsilon_0}\sum_{k=0}^{2l}G_k(n\ell,n_e\ell_e)g'_k(\ell^{p-1}L_1S_1\ell_eLS,\ell^{p-1}L'_1S_1\ell_eLS),
\end{aligned}$$

where f_k and F_k are defined in (2.54) and (2.55), while F_k is called the direct radial integral, G_k is the exchange radial integral and is given by

$$G_k(n\ell,n'\ell') = \int_{r_1=0}^{+\infty} \int_{r_2=0}^{+\infty} P_{n\ell}(r_1)P_{n'\ell'}(r_1)\frac{r_1^k}{r_1^{k+1}}P_{n\ell}(r_2)P_{n'\ell'}(r_2)dr_1dr_2, \quad (2.64)$$

while f'_k and g'_k are given by

$$\begin{aligned}
& f'_k(\ell^{p-1}L_1S_1\ell_eLS,\ell^{p-1}L'_1S'_1\ell_eLS) = \\
& (-1)^{L+L'_1+\ell_e}\delta_{S_1,S'_1}\langle\ell\|\mathbf{C}^{(k)}\|\ell\rangle\langle\ell_e\|\mathbf{C}^{(k)}\|\ell_e\rangle\left\{\begin{matrix}L_1 & \ell_e & L \\ \ell_e & L'_1 & k\end{matrix}\right\}\left\langle\ell^{p-1}S_1L_1\left\|\mathbf{U}^{(k)}\right\|\ell^{p-1}S_1L'_1\right\rangle \quad (2.65)
\end{aligned}$$

and

$$\begin{aligned}
& g'_k(\ell^{p-1}L_1S_1\ell_eLS,\ell^{p-1}L'_1S'_1\ell_eLS) = \\
& \left|\langle\ell\|\mathbf{C}^{(k)}\|\ell_e\rangle\right|^2\sum_r(-1)^r(2r+1)\left\{\begin{matrix}l_a & l_a & r \\ \ell_e & \ell_e & k\end{matrix}\right\}\left[(-1)^{L+L'_1+\ell_e}\frac{\delta_{S_1,S'_1}}{2}\left\{\begin{matrix}L_1 & \ell_e & L \\ \ell_e & L'_1 & r\end{matrix}\right\}\right. \\
& \times\left\langle\ell^{p-1}S_1L_1\left\|\mathbf{U}^{(r)}\right\|\ell^{p-1}S_1L'_1\right\rangle+2(-1)^{L+S+L'_1+S'_1+\ell_e+1/2} \\
& \times\left[\frac{3}{2}\right]^{1/2}\left\{\begin{matrix}L_1 & \ell_e & L \\ \ell_e & L'_1 & r\end{matrix}\right\}\left\{\begin{matrix}S_1 & 1/2 & S \\ 1/2 & S'_1 & 1\end{matrix}\right\}\left\langle\ell^{p-1}S_1L_1\left\|\mathbf{V}^{(1r)}\right\|\ell^{p-1}S'_1L'_1\right\rangle\right] \quad (2.66)
\end{aligned}$$

Note: F_k and G_k are oftentimes referred to as the **direct** and **exchange Slater integrals/parameters**, respectively.

2.5.5 Example in the case of two electrons

For the case of two electrons, one can use (2.24) with $\mathbf{t}^{(k)} = (\mathbf{C}^{(k)} \cdot \mathbf{C}^{(k)})$ to compute the matrix element of the interelectronic repulsion. The result is, for example for the Pr^{3+} ion, where the valence shell is a $4f$ orbital ($\ell = 3$) and the excited shell is just denoted by $n\ell$ (it can also represent a $4f$ orbital, in which case it is the matrix element in the valence shell).

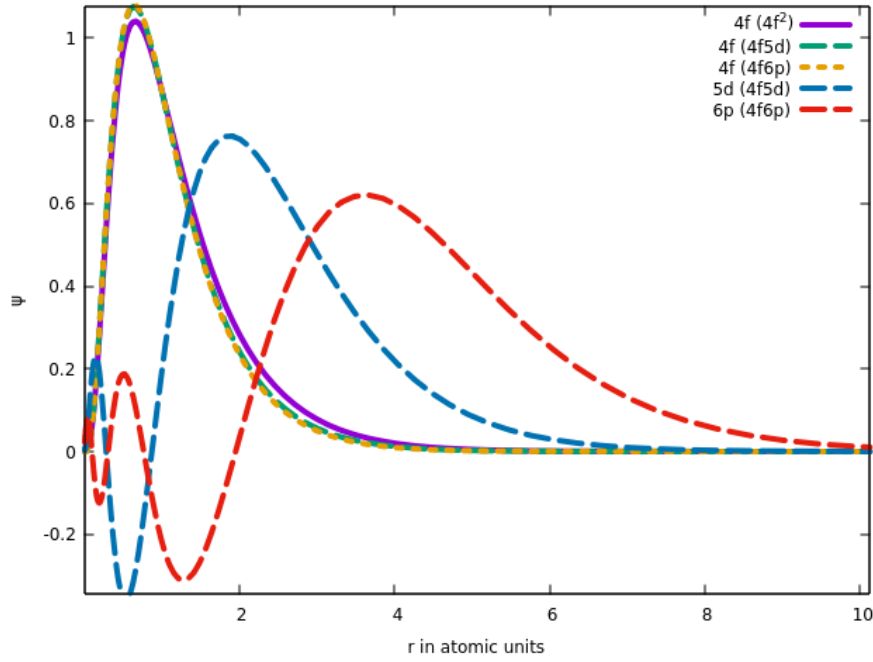


Figure 2.3: Radial wavefunctions for the 4f, 5d and 6p orbital of Pr^{3+} for different configurations ($4f^2$, $4f5d$ and $4f6p$). The radial wavefunctions are computed using a Hartree-Fock code.

$$\langle 4fn\ell LS | H_{e-e} | 4f'n'\ell'LS \rangle = \frac{e^2}{4\pi\epsilon_0} \mathcal{N}_{3,\ell} \mathcal{N}_{3,\ell'} 7\sqrt{[\ell][\ell']} \times$$

$$\times \sum_k \left(\begin{matrix} (-)^L \left\{ \begin{matrix} 3 & \ell' & L \\ \ell & 3 & k \end{matrix} \right\} \begin{pmatrix} 3 & k & 3 \\ 0 & 0 & 0 \end{pmatrix} \begin{pmatrix} \ell & k & \ell' \\ 0 & 0 & 0 \end{pmatrix} R^k(4f, n\ell, 4f', n'\ell') \\ + (-)^S \left\{ \begin{matrix} \ell' & 3 & L \\ \ell & 3 & k \end{matrix} \right\} \begin{pmatrix} 3 & k & \ell' \\ 0 & 0 & 0 \end{pmatrix} \begin{pmatrix} \ell & k & 3 \\ 0 & 0 & 0 \end{pmatrix} R^k(4f, n\ell, n'\ell', 4f') \end{matrix} \right). \quad (2.67)$$

With

$$R^l(i, j, k, p) := \int_0^\infty dr_1 P_{n_i \ell_i}(r_1) P_{n_k \ell_k}(r_1) \int_0^\infty dr_2 P_{n_j \ell_j}(r_2) P_{n_p \ell_p}(r_2) \left(\frac{r_<^l}{r_>^{l+1}} \right) \quad (2.68)$$

which can be equal to the direct or exchange Slater integral, depending on the values of i, j, k, p .

Note: Note the notation $4f'$ that signifies that the radial wavefunctions are not necessarily the same for both $4f$ orbitals, since having different number of electrons in the orbital leads to slightly different radial wavefunctions. This is illustrated in Fig. 2.3 for Pr^{3+} wavefunctions for different configurations computed using a Hartree-Fock code.

2.5.6 Off-diagonal elements of the interelectronic repulsion

Off-diagonal elements of the interelectronic repulsion of the form

$$\langle n\ell^p LS | H_{e-e} | (n\ell^{p-1} L'_1 S'_1) (n_e \ell_e^1 \ell_e 1/2) LS \rangle \quad (2.69)$$

do exist, they are for example computed in [110, 115]. The main selection rules are that it is still diagonal in L and S but also that ℓ_e and ℓ need to be of the same parity. The particular form of the matrix element will not be given here, as it is not as useful as the diagonal elements for the study of interest in this work.

2.5.7 LSJ-coupling

In the next section we will see that an additional quantum number, arising from the coupling of the orbital angular momentum L and the spin angular momentum S , is useful to describe the energy levels of the atom. This quantum number is the total angular momentum $J = L + S$.

The LSJ wavefunctions are related to the LS wavefunctions by the Clebsch-Gordan coefficients since it is a standard coupling of two angular momenta L and S . See Appendix D.2.1.

Knowing that

$$|\alpha LSJM_J\rangle = (-1)^{L-S-M_J} \sqrt{2J+1} \sum_{M_L, M_S} \begin{pmatrix} L & J & S \\ M_L & -M_J & M_S \end{pmatrix} |\alpha LM_L SM_S\rangle, \quad (2.70)$$

where α is a shorthand for all the other quantum numbers, and (D.15), one can easily show that, since $H_{e-e} \propto \delta_{M_L, M_{L'}} \delta_{M_S, M_{S'}}$,

$$\langle \alpha LSJM_J | H_{e-e} | \alpha L'S'J'M_{J'} \rangle = \langle LSM_L M_S | H_{e-e} | L'S'M_{L'} M_{S'} \rangle \delta_{J, J'} \delta_{M_J, M_{J'}}. \quad (2.71)$$

2.6 Spin-orbit coupling

Consider the term in the Hamiltonian

Definition: (*Spin-orbit coupling Hamiltonian*)

$$H_{so} = \sum_{i=1}^N \xi(r_i) \vec{l}_i \cdot \vec{s}_i, \quad (2.72)$$

it represents the interaction between the spin and the orbital angular momentum of the electrons and is a consequence of the relativistic effects on the electrons, as a matter of fact it can be derived from the relativistic Dirac equation as a first order correction in $\frac{1}{c^2}$ to the non-relativistic Hamiltonian with a scalar potential V . $\xi(r_i)$ is the spin-orbit coupling constant, such that, if V is a central potential, $\frac{1}{2m_e c^2 r} \frac{dV}{dr}$ is the order of magnitude of the relativistic correction to the Hamiltonian.

2.6.1 The diagonal basis

Just as in the previous subsection, it is useful to find the basis in which H_{so} is diagonal.

The selection rules for H_{so} can be computed [112], and are:

$$\begin{aligned} \Delta S &= 0, \pm 1, \\ \Delta L &= 0, \pm 1, \\ \Delta J &= 0. \end{aligned} \quad (2.73)$$

Where J is the total angular momentum of the electrons, $J = L + S$. The good quantum numbers is then J , and H_{so} is degenerate in M_J .

However, it becomes clear that H_{so} is not diagonal in L and S , but if one considers that H_{e-e} has a much larger effect on the energy levels than H_{so} , one can continue labelling the states with L and S , with the addition of J as a quantum number. One should then keep in mind that the states are an actual mixture of L and S states, whose relative importance is determined by the ratio of the amplitude of the matrix elements of H_{so} and H_{e-e} .

Definition: (*Spectroscopic term with spin-orbit*) The spectroscopic term with spin-orbit coupling is denoted by

$$^{2S+1}L_J, \quad (2.74)$$

i.e. the eigenstate of H_{e-e} and H_{so} that are mostly characterized by the quantum numbers L , S and J .

To obtain the number of spin-orbit spectroscopic terms and therefore the number of energy levels due to H_{so} , and H_{e-e} , one can refer to Tabs. 2.1 to 2.3 and 4.2 and to the fact that J takes all integer (if S is an integer), or half-integer (if S is a half-integer), values such that $|L - S| \leq J \leq L + S$. The number of $^{2S+1}L_J$ terms for each ℓ is given in Tabs. 2.4 to 2.7.

	s^0, s^2	s^1
N° of $^{2S+1}L_J$	1	1

Table 2.4: Number of spectroscopic terms for $\ell = 0$

	p^0, p^6	p^1, p^5	p^2, p^4	p^3
N° of $^{2S+1}L_J$	1	2	5	5
Excited configuration		p^0s^1	p^1s^1	p^2s^1
N° of excited $^{2S+1}L_J$		1	4	8
Total (valence + excited)		3	9	13
Excited configuration	p^5s^1	p^4s^1	p^3s^1	
N° of excited $^{2S+1}L_J$	4	8	10	
Total (valence + excited)	5	10	15	

Table 2.5: Number of spectroscopic terms for $\ell = 1$ with excited configurations

	d^0, d^{10}	d^1, d^9	d^2, d^8	d^3, d^7	d^4, d^6	d^5
N° of $^{2S+1}L_J$	1	2	9	19	34	37
Excited configuration		d^0p^1	d^1p^1	d^2p^1	d^3p^1	d^4p^1
N° of excited $^{2S+1}L_J$		2	12	45	110	180
Total (valence + excited)		4	21	64	144	217
Excited configuration	d^9p^1	d^8p^1	d^7p^1	d^6p^1	d^5p^1	
N° of excited $^{2S+1}L_J$	12	45	110	180	214	
Total (valence + excited)	13	47	119	199	248	

Table 2.6: Number of spectroscopic terms for $\ell = 2$ with excited configurations

2.6.2 Matrix element for the valence shell

The matrix element of H_{so} in the basis of the spectroscopic terms is given by

	f^0, f^{14}	f^1, f^{13}	f^2, f^{12}	f^3, f^{11}	f^4, f^{10}	f^5, f^9	f^6, f^8	f^7
N° of $^{2S+1}L_J$	1	2	13	41	107	198	295	327
Excited configuration		$f^0 d^1$	$f^1 d^1$	$f^2 d^1$	$f^3 d^1$	$f^4 d^1$	$f^5 d^1$	$f^6 d^1$
N° of excited $^{2S+1}L_J$		2	20	107	386	977	1878	2725
Total (valence + excited)		4	33	148	493	1175	2173	3052
Excited configuration	$f^{13} d^1$	$f^{12} d^1$	$f^{11} d^1$	$f^{10} d^1$	$f^9 d^1$	$f^8 d^1$	$f^7 d^1$	
N° of excited $^{2S+1}L_J$	20	107	386	977	1878	2725	3106	
Total (valence + excited)	21	109	399	1018	1985	2923	3401	

Table 2.7: Number of spectroscopic terms for $\ell = 3$ with excited configurations

$$\begin{aligned}
\langle n\ell^p LSJ | H_{so} | n\ell^p L' S' J \rangle &= \sum_{i=1}^p \langle n\ell | \xi(r_i) | n\ell \rangle \langle LSJ | \vec{l}_i \cdot \vec{s}_i | L' S' J \rangle \\
&= \langle n\ell | \xi(r) | n\ell \rangle \langle n\ell^p LSJ | \sum_{i=1}^p \vec{l}_i \cdot \vec{s}_i | n\ell^p L' S' J \rangle,
\end{aligned} \tag{2.75}$$

with

$$\langle n\ell^p LSJ | \sum_{i=1}^p \vec{l}_i \cdot \vec{s}_i | n\ell^p L' S' J \rangle = (-1)^{L+S+J+1} \left\{ \begin{matrix} L & S & J \\ S' & L' & 1 \end{matrix} \right\} \langle \ell^p LS || \sum_{i=1}^p \vec{l}_i \cdot \vec{s}_i || \ell^p L' S' \rangle, \tag{2.76}$$

and (see Section 2.4.2)

$$\langle \ell^p LS || \sum_{i=1}^p \vec{l}_i \cdot \vec{s}_i || \ell^p L' S' \rangle = \sqrt{\ell(\ell+1)(2\ell+1)} \langle \ell^p LS || \mathbf{V}^{(11)} || \ell^p L' S' \rangle. \tag{2.77}$$

In conclusion,

Definition: (Matrix element of H_{so} for the valence shell)

$$\begin{aligned}
\langle n\ell^p LSJ | H_{so} | n\ell^p L' S' J \rangle &= (-1)^{L'+S'+J+1} \left\{ \begin{matrix} L & S & J \\ S' & L' & 1 \end{matrix} \right\} \times \\
&\times \langle n\ell | \xi(r) | n\ell \rangle \sqrt{\ell(\ell+1)(2\ell+1)} \langle \ell^p LS || \mathbf{V}^{(11)} || \ell^p L' S' \rangle.
\end{aligned} \tag{2.78}$$

2.6.3 Matrix element for excited configurations

If one considers again the configuration $|n\ell^{p-1} n_e \ell_e^1\rangle$, the matrix element of H_{so} is easily obtainable if one splits the matrix element in two parts, one for the electrons in the valence shell and one for the electron in the excited shell. The matrix element is then given by [109, 115, 116].

$$\begin{aligned}
\langle (n\ell^{p-1} L_1 S_1) (n_e \ell_e^1 \ell_e 1/2) LSJ || H_{so} || (n\ell^{p-1} L'_1 S'_1) (n_e \ell_e^1 \ell_e 1/2) L' S' J \rangle &= \\
&\chi(\ell^p, \ell_e, L_1 S_1 L'_1 S'_1, L S L' S', J) \langle n\ell | \xi(r) | n\ell \rangle \\
&+ \delta_{L_1, L'_1} \delta_{S_1, S'_1} \chi_e(\ell^p, \ell_e, L_1 S_1, L S L' S', J) \langle n_e \ell_e | \xi(r) | n_e \ell_e \rangle
\end{aligned} \tag{2.79}$$

with

$$\begin{aligned} \chi(\ell^p, \ell_e, L_1 S_1 L'_1 S'_1, L S L' S', J) = \\ (-1)^{L_1 + S_1 + \ell_e + 1/2 + S + S' + J} \sqrt{\ell(\ell+1)(2\ell+1)(2L+1)(2L'+1)(2S+1)(2S'+1)} \times \\ \times \langle \ell^p L_1 S_1 \| \mathbf{V}^{(11)} \| \ell^p L'_1 S'_1 \rangle \begin{Bmatrix} L_1 & L & \ell_e \\ L' & L'_1 & 1 \end{Bmatrix} \begin{Bmatrix} S_1 & S & 1/2 \\ S' & S'_1 & 1 \end{Bmatrix} \begin{Bmatrix} L & S & J \\ S' & L' & 1 \end{Bmatrix}, \end{aligned} \quad (2.80)$$

and

$$\begin{aligned} \chi_e(\ell^p, \ell_e, L_1 S_1, L S L' S', J) = \\ (-1)^{L_1 + S_1 + \ell_e + 1/2 + L + L' - J} \sqrt{\ell_e(\ell_e+1)(2\ell_e+1)(2L+1)(2L'+1)(2S+1)(2S'+1)} \times \\ \times \underbrace{\langle \ell_e 1/2 \| \mathbf{V}^{(11)} \| \ell_e 1/2 \rangle}_{=\sqrt{3}/2} \begin{Bmatrix} \ell_e & L & L_1 \\ L' & \ell_e & 1 \end{Bmatrix} \begin{Bmatrix} 1/2 & S & S_1 \\ S' & 1/2 & 1 \end{Bmatrix} \begin{Bmatrix} L & S & J \\ S' & L' & 1 \end{Bmatrix}. \end{aligned} \quad (2.81)$$

2.6.4 Example in the case of two electrons

Let's consider the two-electron case of Pr^{3+} ion again as in [Section 2.5.5](#), the valence shell being the $4f$ orbital. The matrix element of H_{so} in the basis of the spectroscopic terms is then given by

$$\begin{aligned} \langle 4f n \ell, (LS) J M_J | H_{\text{SO}} | 4f' n' \ell' (L' S') J' M_{J'} \rangle \\ = \hbar^2 \mathcal{N}_{3,\ell} \mathcal{N}_{3,\ell'} 2\delta_{\ell,\ell'} (-1)^{J+1+\ell_1+\ell_2} \delta_{JJ'} \delta_{M_J, M_{J'}} \delta_{\ell,\ell'} \\ \frac{\sqrt{3}}{2} \sqrt{[L][L'] [S][S']} \begin{Bmatrix} L & S & J \\ S' & L' & 1 \end{Bmatrix} \begin{Bmatrix} S & 1 & S' \\ \frac{1}{2} & \frac{1}{2} & \frac{1}{2} \end{Bmatrix} \left((-1)^{S+S'} \langle 4f | \xi(r) | 4f \rangle 2\sqrt{21} \begin{Bmatrix} 3 & L & 3 \\ L' & \ell & 1 \end{Bmatrix} \right. \\ \left. + (-1)^{L+L'} \langle n \ell | \xi(r) | n \ell \rangle \sqrt{\ell(\ell+1)(2\ell+1)} \begin{Bmatrix} \ell & L' & 3 \\ L' & \ell & 1 \end{Bmatrix} \right). \end{aligned} \quad (2.82)$$

2.7 Hyperfine coupling

A detailed study of the microscopic (and relativistic) origins of the hyperfine interaction is done in the next part of this manuscript, starting at [Chapter 5](#).

In this subsection, we will start from the nonrelativistic limit of the hyperfine interaction and we will derive the matrix elements of the hyperfine interaction in the basis of the spectroscopic terms.

2.7.1 Magnetic Hyperfine interaction

From a nonrelativistic point of view, the magnetic hyperfine interaction has its origin in the interaction between the nuclear magnetic moment $\mu_I = g_I \mu_N \vec{I}$ and the magnetic moment of the electrons $\vec{\mu}_e$. \vec{I} is the nuclear spin, μ_N is the nuclear magneton, and g_I is the nuclear g-factor. The Hamiltonian of the magnetic hyperfine interaction is then given by [\[108\]](#)

$$H_{\text{hf,dip}} = \mathcal{A} \sum_i \frac{\vec{N}_i}{r_i^3} \cdot \vec{I} + \mathcal{A} \left(\frac{8\pi}{3} \delta(\vec{r}_i) \vec{S}_i \right) \cdot \vec{I}, \quad (2.83)$$

With :

$$\vec{N}_i = \vec{L}_i - \vec{S}_i + \frac{3(\vec{s}_i \cdot \vec{r}_i) \vec{r}_i}{r_i^2} \quad \text{and} \quad \mathcal{A} = \frac{2\mu_0}{4\pi} \frac{g_I \mu_N \mu_B}{\hbar^2}. \quad (2.84)$$

The second term in (2.92) is the Fermi contact term, which is a consequence of the non-relativistic limit of the Dirac equation, and it will be derived in Chapter 7. It is only relevant for the s electrons, and is not considered in the following.

It is then possible to compute the matrix elements of $\sum_i \vec{N}_i / r_i^3$:

Using the equality $\vec{e}_r = \mathbf{C}^{(1)}$

$$\frac{3(\vec{s}_i \cdot \vec{r}_i) \vec{r}_i}{r_i^2} = 3(\vec{s}_i \vec{e}_{r_i}) \vec{e}_{r_i} = 3 \left(((\mathbf{s}_i)^{(1)} \cdot \mathbf{C}_i^{(1)}) \mathbf{C}_i^{(1)} \right). \quad (2.85)$$

Then using (D.35) and (D.39) and the definition of the $6j$ symbol (D.20):

$$\begin{aligned} \frac{3(\vec{s}_i \cdot \vec{r}_i) \vec{r}_i}{r_i^2} &= -3\sqrt{3} \left\{ \{(\mathbf{s}_i)^{(1)} \mathbf{C}_i^{(1)}\}^{(0)} \mathbf{C}_i^{(1)} \right\}^{(1)} \\ &= -3\sqrt{3} \sum_k ((1, 1) 0, 1; 1 | 1, (1, 1) k; 1) \left\{ (\mathbf{s}_i)^{(1)} \{ \mathbf{C}_i^{(1)} \mathbf{C}_i^{(1)} \}^{(k)} \right\}^{(1)} \\ &= -3\sqrt{3} \sum_k \sqrt{2k+1} \begin{Bmatrix} 1 & 1 & k \\ 1 & 1 & 0 \end{Bmatrix} \left\{ (\mathbf{s}_i)^{(1)} \{ \mathbf{C}_i^{(1)} \mathbf{C}_i^{(1)} \}^{(k)} \right\}^{(1)}. \end{aligned} \quad (2.86)$$

We first have $\begin{Bmatrix} 1 & 1 & k \\ 1 & 1 & 0 \end{Bmatrix} \neq 0$ only if $k = 0, 1, 2$, and then $\begin{Bmatrix} 1 & 1 & k \\ 1 & 1 & 0 \end{Bmatrix} = \frac{(-1)^k}{3}$. Moreover, evaluating $\langle l || \{ \mathbf{C}_i^{(1)} \mathbf{C}_i^{(1)} \}^{(K)} || l' \rangle$, we find :

$$\{ \mathbf{C}_i^{(1)} \mathbf{C}_i^{(1)} \}^{(0)} = -\sqrt{\frac{1}{3}}, \quad \{ \mathbf{C}_i^{(1)} \mathbf{C}_i^{(1)} \}^{(1)} = 0, \quad \{ \mathbf{C}_i^{(1)} \mathbf{C}_i^{(1)} \}^{(2)} = \sqrt{\frac{2}{3}} \mathbf{C}_i^{(2)}. \quad (2.87)$$

Finally, this means that

$$\mathbf{N}_i^{(1)} = \mathbf{L}_i^{(1)} - \sqrt{10} \left\{ (\mathbf{S}_i^{(1)})^{(1)} \mathbf{C}_i^{(2)} \right\}^{(1)} \quad (2.88)$$

This means that taking the matrix element of $\sum_i \vec{N}_i / r_i^3$ yields

$$\begin{aligned} &\langle \alpha J M_J I M_I | \mathbf{N}^{(1)} \cdot \mathbf{I}^{(1)} | \alpha J' M_{J'} I M_{I'} \rangle \\ &= \sum_{q=-1}^1 (-1)^q \langle \alpha J M_J I M_I | N_q^{(1)} I_{-q}^{(1)} | \alpha J' M_{J'} I M_{I'} \rangle \\ &= \sum_{q=-1}^1 (-1)^q (-1)^{J-M_J} \begin{pmatrix} J & 1 & J' \\ -M_J & q & M_{J'} \end{pmatrix} \langle \alpha J || \mathbf{N}^{(1)} || \alpha J' \rangle (-1)^{I-M_I} \begin{pmatrix} I & 1 & I \\ -M_I & -q & M_{I'} \end{pmatrix} \langle I || \mathbf{I}^{(1)} || I \rangle. \end{aligned} \quad (2.89)$$

If one considers that,

$$\begin{aligned} &\langle 4f n l, (LS) J M_J, I M_I | (\vec{I} \cdot \vec{J}) | 4f' n' l' (L' S') J M_{J'}, I' M_{I'} \rangle = \\ &\sum_q (-1)^q (-1)^{J-M_J} \begin{pmatrix} J & 1 & J \\ -M_J & q & M_J \end{pmatrix} \underbrace{\langle J || \vec{J} || J \rangle}_{=\sqrt{J(J+1)(2J+1)}} (-1)^{I-M_I} \begin{pmatrix} I & 1 & I \\ -M_I & -q & M_I \end{pmatrix} \langle I || \vec{I} || I \rangle. \end{aligned} \quad (2.90)$$

We can write, when $J = J'$, effectively:

Definition: (*Effective magnetic hyperfine interaction within a J multiplet*)

$$H_{\text{hf,dip}} = a \vec{I} \cdot \vec{J} \quad \text{and} \quad a = \frac{2\mu_0 g_I \mu_N \mu_B}{4\pi \hbar^2} \frac{\langle (LS) J || \sum_{i=v,w} (\mathbf{N}_i)^{(1)} / r_i^3 || (LS) J \rangle}{\sqrt{J(J+1)(2J+1)}}. \quad (2.91)$$

Note: In Chapter 7, we will also derive the same expression as the non-relativistic limit of the magnetic hyperfine interaction treated as a perturbation of the spherically-symmetric relativistic Dirac equation. Interestingly, it will be in the coupled basis of J and I , while here it was done in the decoupled basis.

There exist off-diagonal terms with $\langle \alpha J M_J I M_I | \mathbf{N}^{(1)} \cdot \mathbf{I}^{(1)} | \alpha J \pm 1 M_J' I M_I' \rangle$, contrary to \vec{J} which is diagonal in J , these can be found in [108] for example.

2.7.2 Electric Quadrupole Hyperfine interaction

On top of the interaction between the nuclear and electronic magnetic dipoles, the nuclei of lanthanides are quite deformed [43], and this deviation from the sphericity of the electrostatic potential that was assumed in H_0 can be described by the electric quadrupole interaction. The Hamiltonian of the electric quadrupole interaction is then given by [108]

$$H_{\text{hf,quad}} = \mathcal{B} \sum_i \left(\frac{I(I+1)}{r_i^3} + \frac{3(\vec{r}_i \cdot \vec{I}_i)^2}{r_i^5} \right) \quad (2.92)$$

with $\mathcal{B} = \frac{e^2 Q}{4I(2I-1)}$ and $Q = \sqrt{\frac{4I(2I-1)}{(I+1)(2I+1)(2I+3)}} \langle I || R^2 \mathbf{C}^{(2)}(\Theta, \Phi) || I \rangle^6$.

Similarly to the magnetic hyperfine interaction, the matrix elements of $\sum_i \left(\frac{I(I+1)}{r_i^3} + \frac{3(\vec{r}_i \cdot \vec{I}_i)^2}{r_i^5} \right)$ can be re-expressed in term of spherical tensor operators.

Starting with (D.35), we can write

$$\vec{r} \cdot \vec{I} = r \left(\mathbf{C}^{(1)} \cdot \mathbf{I}^{(1)} \right) = -\sqrt{3} \left[\mathbf{C}^{(1)} \cdot \mathbf{I}^{(1)} \right]_0^{(0)}. \quad (2.93)$$

Then, using the definition of the $9j$ symbol (D.21), we can write

$$\begin{aligned} (\vec{r} \cdot \vec{I}) &= 3r^2 \left(\mathbf{C}^{(1)} \mathbf{I}^{(1)} \right)_0^{(0)} \left(\mathbf{C}^{(1)} \mathbf{I}^{(1)} \right)_0^{(0)} \\ &= 3r^2 \left(\left(\mathbf{C}^{(1)} \mathbf{I}^{(1)} \right)_0^{(0)} \left(\mathbf{C}^{(1)} \mathbf{I}^{(1)} \right)_0^{(0)} \right) \\ &= 3r^2 \sum_k \langle (11)0(11)0; 0 | (11)k(11)k; 0 \rangle \left(\left(\mathbf{C}^{(1)} \mathbf{C}^{(1)} \right)^{(k)} \left(\mathbf{I}^{(1)} \mathbf{I}^{(1)} \right)^{(k)} \right)_0^{(0)} \\ &= 3r^2 \sum_k (2k+1) \begin{Bmatrix} 1 & 1 & 0 \\ 1 & 1 & 0 \\ k & k & 0 \end{Bmatrix} \left(\left(\mathbf{C}^{(1)} \mathbf{C}^{(1)} \right)^{(k)} \left(\mathbf{I}^{(1)} \mathbf{I}^{(1)} \right)^{(k)} \right)_0^{(0)} \end{aligned} \quad (2.94)$$

⁶ $\vec{R} = (R, \Theta, \Phi)$ is the nuclear position operator in spherical coordinates, the reduced matrix element is of the nuclear charge quadrupole

The $9j$ -symbol is non-zero only for $k = 0, 1, 2$, and thanks to (2.87), only two of those $(\mathbf{C}^{(1)}\mathbf{C}^{(1)})^{(k)}$ are non-zero. Computing the corresponding $(\mathbf{I}^{(1)}\mathbf{I}^{(1)})^{(k)}$ and the $9j$ -symbol, we find that the $11(0)$ term perfectly cancels the $\frac{I(I+1)}{r^3}$ term, the $11(1)$ term vanishes, and one is left with the $11(2)$ term, which means

$$H_{\text{hf,quad}} = \mathcal{B} \sum_i \frac{1}{r_i^3} \sqrt{6} (-1)^q C_q^{(2)} \left(\mathbf{I}^{(1)} \mathbf{I}^{(1)} \right)_{-q}^{(2)}. \quad (2.95)$$

Just as previously for the magnetic dipole, it is possible to derive an effective electric quadrupole interaction within a J multiplet, which is given by

Definition: (*Effective electric quadrupole hyperfine interaction within a J multiplet*)

$$H_{\text{hf,quad}} = \frac{b}{2} \frac{3(\vec{I} \cdot \vec{J})^2 + \frac{3}{2} \vec{I} \cdot \vec{J} - I^2 J^2}{I(2I-1)J(2J-1)}. \quad (2.96)$$

with

$$b = -\frac{e^2 Q}{4I(2I-1)} \sqrt{\frac{J(2J-1)}{(J+1)(2J+1)(2J+3)}} \langle \alpha J \| \mathbf{C}^{(2)}(\theta, \phi) \| \alpha' J \rangle. \quad (2.97)$$

Note: In Chapter 7, we will also derive the same expression, in the coupled basis.

2.7.3 Hyperfine Splitting

Considering the diagonal matrix elements, the hyperfine energy correction is given by

$$\langle \alpha J M_J I M_I | H_{\text{HF}} | \alpha J M_J I M_I \rangle = a M_I M_J + \frac{b}{2} \frac{3M_I^2 - I(I+1)}{I(2I-1)} \frac{3M_J^2 - J(J+1)}{J(2J-1)}. \quad (2.98)$$

Note: It is not uncommon to find in the literature the following effective Hamiltonian for the hyperfine interaction, which is a simplification of the effective Hamiltonians we derived in (2.91) and (2.97) for $M_J = \pm J$:

$$H_{\text{HF}} = a \vec{I} \cdot \vec{J} + P \left(M_I^2 - \frac{I(I+1)}{3} \right), \quad (2.99)$$

in which case $P = \frac{b}{2} \frac{3}{I(2I-1)}$.

Equation (2.98) means that the hyperfine splitting between two adjacent M_I and $M_I = M_I + 1$ states in the same J, M_J multiple is given by

$$\Delta E_{\text{HF}} = a M_J + \frac{b}{2} \frac{6M_I + 3}{I(2I-1)} \frac{3M_J^2 - J(J+1)}{J(2J-1)}. \quad (2.100)$$

Note: We observe that in the absence of a quadrupole term, the hyperfine splitting is identical between any two M_I states, and it is proportional to M_J . The quadrupole term introduces a dependence on M_I in the hyperfine splitting, which is proportional to M_I . **The latter is primordial for nuclear spin qubits**, as it allows for the individual and discriminative addressing of the different transitions between the nuclear spin states.

Main takeaways from Chapter 2

- **Hamiltonian of Free Atoms/Ions:**

- Total Hamiltonian includes kinetic energy, electron-nucleus and electron-electron Coulomb interactions, spin-orbit coupling, and hyperfine coupling.
- Expressed as:

$$H = \sum_{i=1}^N \left(-\frac{\hbar^2}{2m} \nabla_i^2 - \frac{Ze^2}{4\pi\epsilon_0 r_i} \right) + \sum_{i<j} \frac{e^2}{4\pi\epsilon_0 r_{ij}} + H_{\text{so}} + H_{\text{hf}} \quad (2.101)$$

- **Non-Interacting Electrons:**

- Solutions yield hydrogen-like wavefunctions.
- Multi-electron states are constructed using Slater determinants to ensure antisymmetry.

- **Angular Momentum Coupling:**

- L - S coupling and j - j coupling schemes describe total angular momentum.
- Choice depends on the relative strengths of electron-electron interactions and spin-orbit coupling.

- **Coulomb Interelectronic Repulsion:**

- Leads to energy level splitting into spectroscopic terms labeled by ^{2S+1}L .
- Energy depends on total orbital (L) and spin (S) angular momenta.

- **Spin-Orbit Coupling:**

- Relativistic effect coupling electron spin and orbital angular momentum.
- Further splits energy levels, introducing total angular momentum $J = L + S$ and spectroscopic terms $^{2S+1}L_J$.

- **Hyperfine Coupling:**

- Interaction between nuclear moments and electrons, including magnetic dipole and electric quadrupole terms.
- Causes uneven hyperfine splitting of energy levels, important for nuclear spin qubits.
- Effective Hamiltonians for hyperfine interactions can be derived for electrons in the same J multiplet. Exact expressions will be derived in the next part of this manuscript.

Chapter Contents

3.1 From Crystal Field Theory to Ligand Field Theory	51
3.2 Ligand Field DFT	59

CHAPTER 3

Ligand Field

This section will be dedicated to the study of the ligand field, which is the effect of the surrounding ligands on the electronic structure of the central atom. The ligand field is a consequence of the electrostatic interaction between the electrons of the ligands and the electrons of the central atom. The ligand field is a perturbation of the atomic Hamiltonian, and can be treated as such. The ligand field is a very important concept in the study of transition metal complexes, as it is the origin of the color of many of these compounds. In the case of lanthanides and actinides, the ligand field is also of great importance, as it is the origin of the magnetic and optical properties of these elements in molecular and solid-state compounds.

3.1 From Crystal Field Theory to Ligand Field Theory

3.1.1 Crystal Field Theory

The Crystal Field Theory (CFT) is a model that describes the effect of the ligands on the electronic structure of the central atom. The CFT is based on the electrostatic interaction between the electrons of the ligands and the electrons of the central atom. The CFT is a very simple model that assumes that the ligands are point charges, and that the electrons of the central atom are spherically symmetric. The CFT is a qualitative model that is very useful for understanding the electronic structure of transition metal complexes. It was first proposed by Hans Bethe [72, 73] and John Van Vleck [74] in the 1930s.

The CFT is based on the following assumptions:

- The ligands are point charges.
- The electrons of the central atom do not overlap with the ligand charges and are contained inside a sphere of radius smaller than the distance to the ligands.
- The ligands are arranged in a regular geometry around the central atom.
- The ligands interact with the electrons of the central atom through electrostatic interactions.
- The ligands are non-polarizable.
- The ligands are non-magnetic.
- The ligands are non-relativistic.
- The ligands are static.

Based on those assumptions and the multipolar expansion of the electrostatic interaction between the ligands and the central atom, see (C.26), the potential of the ligand on N electrons can be written as

$$H_{\text{CF}}(\vec{r}_1 \dots \vec{r}_N) = -|e| \sum_{i=0}^N \sum_{l=0}^{+\infty} \sum_{m=-l}^l (-1)^m V_{-m}^{(l)}(r_i) C_m^{(l)}(\theta_i, \phi_i), \quad (3.1)$$

where $V_m^{(l)}(r)$ are the multipolar expansion coefficients of the potential of the ligand on the electrons, and $C_m^{(l)}(\theta, \phi)$ are the normalized spherical harmonics.

Since the electrons of the central atom do not overlap with the ligand, the expression of $V_m^{(l)}(r)$ is given by (see (C.27))

$$V_m^{(l)}(r) = r^l \int \frac{\rho_L(\vec{r}_L)}{r_L^{l+1}} C_m^{(l)}(\theta_L, \phi_L) d^3 \vec{r}_L, \quad (3.2)$$

with the subscript L indicating that the integral is over the ligands, and $\rho_L(\vec{r}_L)$ is the charge density of the ligands. Which, if one assumes point charges for the ligands, is given by

$$\rho(\vec{r}_L) = \sum_{i=1}^{N_L} q_\lambda \delta(\vec{r}_L - \vec{r}_\lambda), \quad (3.3)$$

where q_λ is the charge and \vec{r}_λ is the position of the λ -th ligand charge, out of N_L . This then simplifies (C.27) to

$$V_m^{(l)}(r) = r^l \sum_{i=\lambda}^{N_L} \frac{q_i}{r_\lambda^{l+1}} C_m^{(l)}(\theta_\lambda, \phi_\lambda). \quad (3.4)$$

The main advantage of CFT becomes apparent when computing the matrix elements of the crystal field Hamiltonian.

3.1.2 Matrix element in the valence shell

The matrix element of the crystal field Hamiltonian in the basis of the spectroscopic terms is given by

$$\langle n\ell^p LSJM_J | H_{\text{CF}} | n\ell^p L'S'J'M_{J'} \rangle = \sum_{l=0}^{+\infty} \sum_{m=-l}^l (-1)^m \langle n\ell | e V_{-m}^{(l)}(r) | n'\ell' \rangle \langle \ell^p LSJM_J | \sum_{i=0}^p C_m^{(l)}(\theta_i, \phi_i) | \ell^p L'S'J'M_{J'} \rangle, \quad (3.5)$$

obtaining the matrix element of the crystal field Hamiltonian in the basis of the spectroscopic terms is then a matter of computing the matrix elements of the spherical harmonics

$$\langle \ell^p LSJM_J | \sum_{i=0}^p C_m^{(l)}(\theta_i, \phi_i) | \ell^p L'S'J'M_{J'} \rangle = \langle \alpha\ell || \mathbf{C}^{(l)} || \alpha'\ell' \rangle \langle \ell^p LSJM_J | \sum_{i=0}^p U_m^{(l)} | \ell^p L'S'J'M_{J'} \rangle. \quad (3.6)$$

Since, using the Wigner-Eckart theorem, one can write

$$\langle \ell^p LSJM_J | U_m^{(l)} | \ell^p L'S'J'M_{J'} \rangle = (-1)^{J-M_J} \begin{pmatrix} J & l & J' \\ -M_J & m & M_{J'} \end{pmatrix} \langle \ell^p LSJ \| \mathbf{U}^{(l)} \| \ell^p L'S'J' \rangle, \quad (3.7)$$

one can see that while the reduced matrix elements of \mathbf{U} are diagonal in S , no other selection rules are generally present, not even regarding M_J .

On another note, we remind the reader that the reduced matrix element of the spherical harmonics is given by (D.33)

$$\langle \alpha \ell \| \mathbf{C}^{(l)} \| \alpha' \ell' \rangle = \delta_{\alpha, \alpha'} (-1)^l ([\ell][\ell'])^{\frac{1}{2}} \begin{pmatrix} \ell & l & \ell' \\ 0 & 0 & 0 \end{pmatrix}. \quad (3.8)$$

The $3j$ -symbol implies that the multipoles $V_m^{(l)}$ of order $l \geq \ell + \ell'$ are not needed, as the corresponding $\langle \alpha \ell \| \mathbf{C}^{(l)} \| \alpha' \ell' \rangle$ would be zero, the same can be said of the parameters whose order l is of a different parity than $\ell + \ell'$. In that regard, one can define the Crystal Field Parameters as

Definition: (*Crystal Field Parameters*)

$$A_m^l(n\ell, n'\ell') \equiv B_m^l \langle n\ell | r^l | n'\ell' \rangle \equiv (-1)^m \langle n\ell | eV_{-m}^{(l)}(r) | n'\ell' \rangle, \quad (3.9)$$

or, effectively, with the assumptions of CFT, one can write

$$B_m^l = (-1)^m \int \frac{e\rho_L(\vec{r}_L)}{r_L^{l+1}} C_{-m}^{(l)}(\theta_L, \phi_L) d^3\vec{r}_L = (-1)^m \sum_{\lambda=1}^{N_L} \frac{eq_\lambda}{r_\lambda^{l+1}} C_{-m}^{(l)}(\theta_\lambda, \phi_\lambda). \quad (3.10)$$

The form of the matrix element of the crystal field Hamiltonian in the basis of the spectroscopic terms is then given by

Definition: (*Matrix element of the crystal field Hamiltonian for the valence shell*)

$$\begin{aligned} \langle n\ell^p LSJM_J | H_{\text{CF}} | n\ell^p L'S'J'M_{J'} \rangle &= (-1)^{J-M_J} \delta_{S,S'} \sum_{q=0}^{\ell} \sum_{m=-2q}^{2q} \begin{pmatrix} J & 2q & J' \\ -M_J & m & M_{J'} \end{pmatrix} \times \\ &B_m^{2q}(n\ell, n\ell) \langle n\ell | r^{2q} | n\ell \rangle \langle n\ell \| \mathbf{C}^{(2q)} \| n\ell \rangle \langle \ell^p LSJ \| \mathbf{U}^{(2q)} \| \ell^p L'S'J' \rangle. \end{aligned} \quad (3.11)$$

3.1.3 Matrix element for excited configurations

If one considers the singly excited configuration $|n\ell^{p-1}n_e\ell_e^1\rangle$, the matrix element of the crystal field Hamiltonian is easily obtainable if one splits the matrix element in two parts, one for the electrons in the valence shell and one for the electron in the excited shell. The matrix element can then be computed using the methodology described in [109, 116], with the abuse of notation that the m -th component of $B_m^{2q}(n\ell, n\ell)$ still being present in a reduce matrix element, this needs to be understood as a term only really appearing back in (3.11), but is still used here to insist on the orbital dependence of the crystal field parameters.

$$\begin{aligned}
& \langle (n\ell^{p-1}L_1S_1) (n_e\ell_e^1\ell_e1/2) LSJ \| H_{CF} \| (n\ell^{p-1}L'_1S'_1) (n_e\ell_e^1\ell_e1/2) L'S'J' \rangle = \sum_{q=0}^{\ell} \sum_{m=-2q}^{2q} \\
& (-1)^{L'+L'_1+S'+S_1+s+\ell} B_m^{2q}(n\ell, n\ell) \langle n\ell | r^{2q} | n\ell \rangle \langle n\ell \| \mathbf{C}^{(2q)} \| n\ell \rangle \langle \ell^{p-1}L_1S_1 \| \mathbf{U}^{(2q)} \| \ell^{p-1}L'_1S'_1 \rangle \times \\
& \quad \times \begin{Bmatrix} L_1 & L & \ell_e \\ L' & L'_1 & 2q \end{Bmatrix} \begin{Bmatrix} S_1 & S & 1/2 \\ S' & S'_1 & 0 \end{Bmatrix} \begin{Bmatrix} L & S & J \\ S' & L' & 2q \end{Bmatrix} \\
& + \sum_{q_e=0}^{\ell_e} \sum_{m=-2q_e}^{2q_e} \delta_{L_1, L'_1} \delta_{S_1, S'_1} (-1)^{L_1+S_1+L+S+s+\ell} \sqrt{(2L+1)(2S+1)(2L'+1)(2S'+1)} \times \\
& \times B_m^{2q_e}(n_e\ell_e, n_e\ell_e) \langle n_e\ell_e | r^L | n_e\ell_e \rangle \langle n_e\ell_e \| \mathbf{C}^{(2q_e)} \| n_e\ell_e \rangle \begin{Bmatrix} \ell_e & L & L_1 \\ L' & \ell_e & 2q_e \end{Bmatrix} \begin{Bmatrix} 1/2 & S & S_1 \\ S' & 1/2 & 0 \end{Bmatrix} \begin{Bmatrix} L & S & J \\ S' & L' & 2q_e \end{Bmatrix} \\
& \quad \quad \quad (3.12)
\end{aligned}$$

Off-diagonal matrix elements

The final term of the matrix element of the crystal field Hamiltonian for excited configurations is the off-diagonal matrix element, mixing the valence and excited shells. It is probably the most interesting term as it is the origin of a lot of the interesting physical properties of lanthanide-based materials, in particular the ones of interest in this manuscript. Assuming ℓ and ℓ_e are of different parity, the matrix element is given by

$$\begin{aligned}
& \langle n\ell^p LSJ \| H_{CF} \| (n\ell^{p-1}L'_1S'_1) (n_e\ell_e^1\ell_e1/2) L'S'J' \rangle = \sum_{t=\frac{|\ell-\ell_e|-1}{2}}^{\frac{\ell+\ell_e-1}{2}} \sum_{m=-2t-1}^{2t+1} \\
& (-1)^{L+S+L_1+S_1+1/2+\ell+1} \sqrt{(2L+1)(2S+1)(2L'+1)(2S'+1)} (\ell^N LS \{ | \ell^{N-1}L_1S_1\ell \rangle \times \\
& \times B_m^{2t+1}(n\ell_e, n_e\ell_e) \langle n\ell | r^{2t+1} | n_e\ell_e \rangle \langle n\ell \| \mathbf{C}^{(2t+1)} \| n_e\ell_e \rangle \begin{Bmatrix} \ell_e & L & L_1 \\ L' & \ell_e & 2t+1 \end{Bmatrix} \begin{Bmatrix} 1/2 & S & S_1 \\ S' & 1/2 & 0 \end{Bmatrix} \begin{Bmatrix} L & S & J \\ S' & L' & 2t+1 \end{Bmatrix} \Big\}, \\
& \quad \quad \quad (3.13)
\end{aligned}$$

with $(\ell^N LS \{ | \ell^{N-1}L_1S_1\ell \rangle$ the coefficient of fractional parentage, as defined in [110] and that are tabulated in [111].

If ℓ and ℓ_e are of the same parity, the matrix element is the same, except that the sum over t is from $\frac{|\ell-\ell_e|}{2}$ to $\frac{\ell+\ell_e}{2}$, and the occurrences of $2t+1$ are replaced by $2t$.

For simplicity, and using the generalized inter-shell unit tensor operator defined in (2.31), this can be rewritten in a form similar to the one of the matrix element for the valence shell

$$\begin{aligned}
& \langle (n\ell^p LSJ) \| H_{CF} \| (n\ell^{p-1}L'_1S'_1) (n_e\ell_e^1\ell_e1/2) L'S'J' \rangle = \sum_{t=\frac{|\ell-\ell_e|-1}{2}}^{\frac{\ell+\ell_e-1}{2}} \sum_{m=-2t-1}^{2t+1} B_m^{2t+1}(n\ell_e, n_e\ell_e) \\
& \times \langle n\ell | r^{2t+1} | n_e\ell_e \rangle \langle n\ell \| \mathbf{C}^{(2t+1)} \| n_e\ell_e \rangle \langle (n\ell^p LSJ) \| \mathbf{U}^{(2t+1)}(4f^n, 4f^{n-1}5d) \| (n\ell^{p-1}L'_1S'_1) (n_e\ell_e^1\ell_e1/2) L'S'J' \rangle. \\
& \quad \quad \quad (3.14)
\end{aligned}$$

3.1.4 Selection rules for the crystal field parameters

The main advantage of CFT is that only a finite number of crystal field parameters are sufficient to characterise the effect of the ligand on the electrons.

Consequences of the spherical harmonics selection rules

It was already stated that as a consequence of (3.8), only the parameters B_m^l with $l \leq \ell + \ell'$ and with l of the same parity as $\ell + \ell'$ are necessary, the others can simply be considered null. This means that if one considers only one shell with $\ell = \ell'$, there will be only $\ell + 1$ orders l of non-zero parameters B_m^l , the even ones between 0 and 2ℓ included. For each one of those orders, there will be $2l + 1$ possible values of m , so in total there will be $\sum_{k=0}^{\ell} (2(2k) + 1) = 2\ell^2 + 3\ell + 1$ non-zero parameters B_m^l .

If one were to consider two shells this time, with $\ell \neq \ell'$, the number of non-zero parameters B_m^l would be the sum of the number of non-zero parameters for each shell – $B_m^l(n\ell, n\ell)$ and $B_m^l(n'\ell', n'\ell')$ – $2(\ell^2 + \ell'^2) + 3(\ell + \ell') + 2$, plus the off-diagonal elements between the two shells $B_m^l(n\ell, n'\ell')$. The number of the latter can be computed to be $2\ell\ell' + 3\min(\ell, \ell') + 2 - (-1)^{\ell+\ell'}$.

Note: The number of non-zero crystal field parameters for one shell with $\ell = \ell'$ is given by

$$N_{\text{CF}}(\ell) = 2\ell^2 + 3\ell + 1, \quad (3.15)$$

while the number of non-zero crystal field parameters for two shells, including the off-diagonal ones, with $\ell \neq \ell'$ is given by

$$N_{\text{CF}}(\ell, \ell') = 2(\ell^2 + \ell\ell' + \ell'^2) + 3(\ell + \ell' + \min(\ell, \ell')) + 4 - (-1)^{\ell+\ell'}. \quad (3.16)$$

This is summarized in Tab. 3.1.

$\ell \backslash \ell'$	s (0)	p (1)	d (2)	f (3)
s (0)	1	10	17	32
p (1)	10	6	31	44
d (2)	17	31	15	64
f (3)	32	44	64	28

Table 3.1: Total number of crystal field parameters necessary to model the crystal field in one ($\ell = \ell'$) and two shells ($\ell \neq \ell'$) if the ligand presents no symmetries C_1 .

Consequences of the geometry of the ligands

Moreover, depending on the finite point group symmetry of the ligands, the crystal field parameters A_m^l are zero for certain additional values of l and m . On top of that, in that situation, the crystal field parameters A_m^l are not all independent, as the symmetry of the ligands imposes additional constraints on the crystal field parameters, reducing the number of independent parameters [117].

The elements of the 32 point groups ?? transform any spherical harmonics $Y_m^{(l)}$ into a linear combination of spherical harmonics of the same order l and different m . This relations between the spherical harmonics the lead to the selection rules for the crystal field parameters.

For example:

- Choosing the p -fold rotation axis C_p along the z -axis implies that the potential remains invariant under rotations by $2\pi/p$. This rotational symmetry transforms the spherical harmonics $Y_m^{(l)}$ into $e^{im\frac{2\pi}{p}} Y_m^{(l)}$. For this to hold, m must be a multiple of p :

$$m = 0, \pm p, \pm 2p, \dots \quad (3.17)$$

- Inversion symmetry C_i causes $Y_m^{(l)}$ to transform into $(-1)^l Y_m^{(l)}$. Consequently, the coefficients A_m^l vanish for odd l :

$$A_m^l = 0 \quad \text{if } l \text{ is odd.} \quad (3.18)$$

- Reflecting through a plane containing the z -axis, such as the zx -plane, (C_s symmetry), transforms $Y_m^{(l)}$ into $(-1)^l Y_{-m}^{(l)}$. This symmetry requires that:

$$A_m^l = (-1)^l A_{-m}^l. \quad (3.19)$$

- A rotatory-reflection by $2\pi/2p$ (S_{2p}) transforms $Y_m^{(l)}$ into $e^{im(2\pi/p)} Y_{-m}^{(l)}$. For this operation, the condition is:

$$n + m + \frac{m}{p} = \text{even.} \quad (3.20)$$

Based on these conditions, the allowed combinations of n and m for S_{2p} are summarized in [Tab. 3.2](#):

n	m	m/p	
odd	odd	impossible, as m/p cannot be even.	
odd	even	odd	$p = 2; n \geq 3.$
even	odd	odd	$p = 3; n \geq 3.$
even	even	even	$p = 2 \text{ or } 3.$

Table 3.2: Allowed combinations of n and m for point group S_{2p} .

- The p -fold axis (C_{ph}) results in the relation (3.17). The inversion leads to relation (3.18) when $p = 4$ and 6 . A rotatory-reflection by $2\pi/p$ transforms $Y_m^{(l)}$ into $e^{im(1+2\nu/p)} Y_{-m}^{(l)}$, leading to the condition:

$$n + m + \frac{2m}{p} = \text{even.} \quad (3.21)$$

The allowed combinations of n and m for C_{ph} are listed in [Tab. 3.3](#):

n	m	$\frac{2m}{p}$	
odd	odd	even	$p = 3; n \geq 3.$
odd	even	odd	$p = 4; n \geq 3.$
even	odd	odd	$p = 2 \text{ or } 6.$
even	even	even	$p = 2, 3, 4, \text{ or } 6.$

Table 3.3: Allowed combinations of n and m for point group C_{pv} .

- For C_{pv} , the p -fold axis leads to relation (3.17). Reflection in the zx -plane leads to relation (3.19). When p is even, the yz -plane is also a symmetry plane; reflection in the yz -plane transforms $Y_m^{(l)}$ into $Y_{-m}^{(l)}$. Therefore,

$$A_m^l = A_{-m}^l. \quad (3.22)$$

- D_p : The p -fold axis leads to relation (3.17). If we choose one of the p twofold axes as the x -axis, the twofold rotation transforms $Y_m^{(l)}$ into $(-1)^n Y_{n-m}^{(l)}$. Therefore,

$$A_m^l = (-1)^n A_{-m}^l. \quad (3.23)$$

- For D_{ph} , the relations (3.17), (3.19), (3.21) and (3.23) hold.
- For D_{pv} , the relations (3.17), (3.19), (3.20) and (3.23) hold.

Number of energy levels

As can be seen from (3.7), in C_1 symmetry, the only quantum number that can be used to label the states is not even J but its projection M_J . This means that, at maximum, the number of energy levels due to the crystal field is $2J + 1$ for each $^{2S+1}L_J$ term, i.e. the number of Slater determinants. This number can obviously be greatly reduced if the ligand presents symmetries. Moreover, due to Kramers' theorem¹, that states that the energy levels of a system with time-reversal symmetry are at least doubly degenerate, the states will be degenerate with respect to the sign of M_J for any system with an odd number of electrons.

	s^0, s^2	s^1
N° of S.D.	1	2

Table 3.4: Number of $LSJM_J$ states/Slater Determinants for $\ell = 0$

	p^0, p^6	p^1, p^5	p^2, p^4	p^3
N° of S.D.	1	6	15	20
Excited configuration		p^0s^1	p^1s^1	p^2s^1
N° of excited S.D.		2	12	30
Total (valence + excited)		8	27	50
Excited configuration	p^5s^1	p^4s^1	p^3s^1	
N° of excited S.D.	12	30	40	
Total (valence + excited)	13	36	55	

Table 3.5: Number of $LSJM_J$ states/Slater Determinants for $\ell = 1$ with excited configurations

	d^0, d^{10}	d^1, d^9	d^2, d^8	d^3, d^7	d^4, d^6	d^5
N° of S.D.	1	10	45	120	210	252
Excited configuration		d^0p^1	d^1p^1	d^2p^1	d^3p^1	d^4p^1
N° of excited S.D.		6	60	270	720	1260
Total (valence + excited)		16	105	390	930	1512
Excited configuration	d^9p^1	d^8p^1	d^7p^1	d^6p^1	d^5p^1	
N° of excited S.D.	60	270	720	1260	1512	
Total (valence + excited)	61	280	765	1380	1722	

Table 3.6: Number of $LSJM_J$ states/Slater Determinants for $\ell = 2$ with excited configurations

	f^0, f^{14}	f^1, f^{13}	f^2, f^{12}	f^3, f^{11}	f^4, f^{10}	f^5, f^9	f^6, f^8	f^7
N° of S.D.	1	14	91	364	1001	2002	3003	3432
Excited configuration		f^0d^1	f^1d^1	f^2d^1	f^3d^1	f^4d^1	f^5d^1	f^6d^1
N° of excited S.D.		10	140	910	3640	10010	20020	30030
Total (valence + excited)		24	231	1274	4641	12012	23023	33462
Excited configuration	$f^{13}d^1$	$f^{12}d^1$	$f^{11}d^1$	$f^{10}d^1$	f^9d^1	f^8d^1	f^7d^1	
N° of excited S.D.	140	910	3640	10010	20020	30030	34320	
Total (valence + excited)	141	924	3731	10374	21021	32032	37323	

Table 3.7: Number of $LSJM_J$ states/Slater Determinants for $\ell = 3$ with excited configurations

¹Kramer's theorem, as well as multipolar expansion will, interestingly, both play a crucial role in the next part of this manuscript, regarding the description of the nucleus.

3.1.5 Mean field contribution

Similarly to the electrostatic interaction between the electrons in Section 2.5.3, the Crystal Field also induces a mean field contribution to the Hamiltonian. The term $l = 0, m = 0$ in the sum of (3.11) is independent of L, S, J and M_J , and can be computed to be

Definition: (Mean field contribution of the Crystal Field in the $n\ell^p$ shell)

$$ep \int P_{n\ell}^2(r) \int \frac{\rho(\vec{r}_L)}{r_L} d^3\vec{r}_L dr = p \frac{eQ_L}{R_L} \quad (3.24)$$

The last equality being valid if the ligands are point charges at the same distance R_L from the central atom, in which case Q_L is the total charge of the ligands.

3.1.6 Ligand Field Theory

The assumptions made in Section 3.1.1 can be considered reasonable for describing impurities in crystal matrices, for example. However, some of these assumptions are quite restrictive. Specifically, the assumption that the ligands are point charges is a strong one, and the idea that the electrons of the central atom do not overlap with the ligands is also quite limiting. In the case of molecular complexes, the covalency of the bonds between the ligands and the central atom plays a crucial role, and thus:

- The ligand/molecule is not composed of point charges.
- Electrons of the central atom are not necessarily confined within a sphere smaller than the distance to the ligands; they do overlap with the ligands, particularly in the case of hybridized molecular orbitals.
- The ligands are now polarizable, mainly by the central atom.

Crystal Field Theory (CFT) is therefore not suitable for describing the electronic structure of molecular complexes. **Ligand Field Theory (LFT)** is a generalization of CFT that accounts for the covalency of the bonds between the ligands and the central atom. It is based on the same principles as CFT, except for the three mentioned limitations.

The form of the Hamiltonian remains the same as in (3.1), but the expressions for $V_m^l(r)$ and, consequently, the Crystal Field Parameters $A_m^l(n\ell, n\ell')$ are different:

$$H_{\text{LF}}(\mathbf{r}) = e \sum_{i=0}^N \sum_{l=0}^{+\infty} \sum_{m=-l}^l (-1)^m V_m^{(l)}(r) C_m^{(l)}(\theta_i, \phi_i), \quad (3.25)$$

with $V_m^{(l)}(r)$ given by:

$$V_m^{(l)}(r) = r^l \int_{r_L=r}^{+\infty} \frac{\rho_L(\vec{r}_L)}{r_L^{l+1}} C_{-m}^{(l)}(\theta_L, \phi_L) d^3\vec{r}_L + \frac{1}{r^{l+1}} \int_{r_L=0}^r \frac{\rho_L(\vec{r}_L)}{r_L^{l+1}} C_{-m}^{(l)}(\theta_L, \phi_L) d^3\vec{r}_L. \quad (3.26)$$

Therefore, the Crystal Field Parameters $A_m^l(n\ell, n\ell')$ are given by:

$$A_m^l(n\ell, n'\ell') = (-1)^m \times \int_{r=0}^{\infty} \left(r^l \int_{r_L=r}^{+\infty} \frac{\rho_L(\vec{r}_L)}{r_L^{l+1}} C_{-m}^{(l)}(\theta_L, \phi_L) d^3\vec{r}_L + \frac{1}{r^{l+1}} \int_{r_L=0}^r \frac{\rho_L(\vec{r}_L)}{r_L^{l+1}} C_{-m}^{(l)}(\theta_L, \phi_L) d^3\vec{r}_L \right) P_{n\ell}(r) P_{n'\ell'}(r) dr. \quad (3.27)$$

We can observe that the radial integrals over the electronic and ligand parts are no longer separable. Additionally, other complications arise. First, it becomes non-trivial to define the density ρ_L of the ligands and to extract it from any calculation, as the charge density of the molecule consists of hybridized molecular orbitals of the ligands and the central atom. The ligand charge is also polarized by the central atom. The same applies to the radial wavefunctions of the central atom, which are now hybridized with and polarized by the ligands. A schematic representation of the complications in the density and wavefunctions calculations is given in Fig. 3.1.

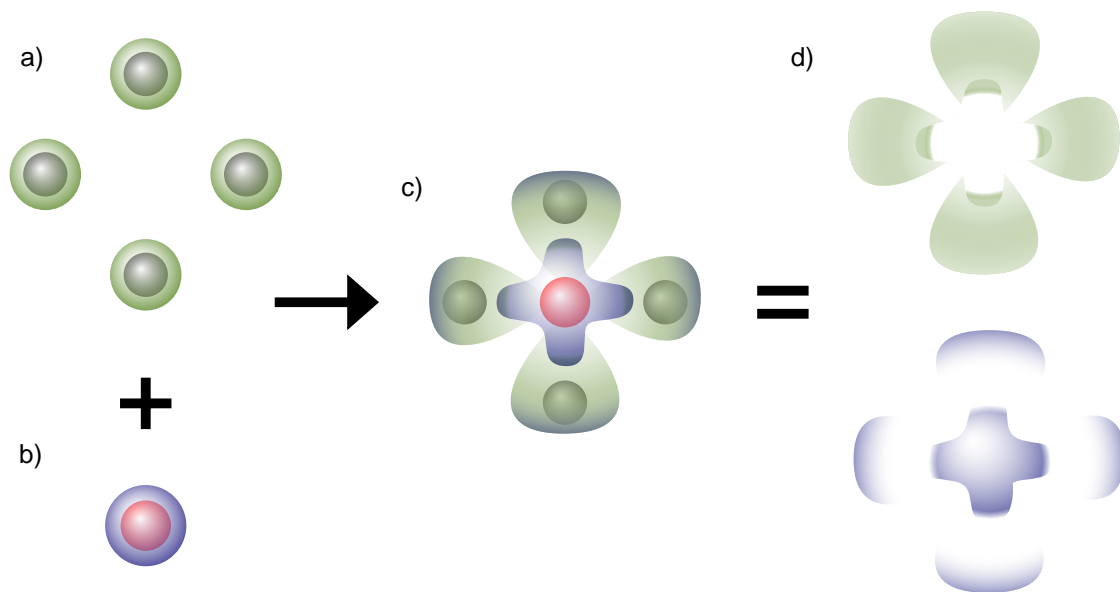


Figure 3.1: Schematic representation of the density mixings in a molecular complex. a) the densities of the ligand with no central ion. b) the spherical density of the free ion. c) the density of the molecular complex with hybridized orbitals. d) the extracted densities of the ligands and the central ion separately.

The second complication, related to this, is that even if one can extract the molecular orbitals and their related densities of the ligands and the central atom separately, the radial wavefunctions of the central atom are not necessarily orthogonal to each other anymore.

In the following section, we will discuss a method for the computation of the Crystal Field Parameters $A_m^L(n\ell, n\ell')$ using Density Functional Theory (DFT) that circumvents those complications.

3.2 Ligand Field DFT

The expressions for the Hamiltonian terms obtained in the previous sections all have a common structure. For the *valence shell*, we have:

$$\langle n\ell^p LSJM_J | H | n\ell^p L'S'J'M_{J'} \rangle = \sum_r C_r(n\ell) D_r(L, L', S, S', J, J', M_J, M_{J'}) \langle \ell^p LSJ || \mathbf{T}_r || \ell^p L'S'J' \rangle. \quad (3.28)$$

For the *singly excited configurations*:

$$\begin{aligned}
\langle (n\ell^{p-1}L_1S_1n_e\ell_e^1) (LS) JM_J | H | (n\ell^{p-1}L'_1S'_1n_e\ell_e^1) (L'S') J' M_{J'} \rangle = \\
\sum_r C_r(n\ell) D_r(\ell_e, L, L_1, L', L'_1, S, S_1, S', S'_1, J, J', M_J, M_{J'}) \langle \ell^p L_1 S_1 || \mathbf{T}_r || \ell^p L'_1 S'_1 \rangle \\
+ C_{r,e}(n_e\ell_e) D_{r,e}(\ell_e, L, L_1, L', L'_1, S, S_1, S', S'_1, J, J', M_J, M_{J'}), \quad (3.29)
\end{aligned}$$

And for the off-diagonal terms mixing the valence and excited shells:

$$\begin{aligned}
\langle (n\ell^{p-1}L_1S_1n_e\ell_e^1) (LS) JM_J | H | (n\ell^{p-1}L'_1S'_1n_e\ell_e^1) (L'S') J' M_{J'} \rangle = \\
\sum_r C_r(n\ell, n_e\ell_e) D_r(\ell_e, L, L_1, L', L'_1, S, S_1, S', S'_1, J, J', M_J, M_{J'}) (\ell^N LS \{ | \ell^{N-1} L_1 S_1 \ell \}). \quad (3.30)
\end{aligned}$$

Here, \mathbf{T}_r is generally a unit tensor operator (such as $\mathbf{U}^{(k)}$, $\mathbf{V}^{(k1)}$, or $\mathbf{W}^{(k\kappa)}$) whose matrix elements are tabulated in [109, 111]. It can also be an operator whose matrix elements can be expressed as a linear combination of the matrix elements of unit tensor operators. Both \mathbf{T}_r and the coefficients of fractional parentage, which are also tabulated in [111], contain the information related to the antisymmetrization of the wavefunctions.

All the remaining multi-electronic effects on the angular degrees of freedom are encapsulated in D_r . This takes the form of a product of nj -symbols and originates from decoupling formulas in the LSJ coupling scheme. It's noteworthy that these quantities depend only on the number of electrons in the valence shell and the nature of the shell. They do not depend on the specific atomic or ionic species under consideration, nor on the ligands. This universality applies to all systems with the same valence shell and excited configurations.

The radial degrees of freedom are described by the single-electron-like $C_r(n\ell)$ parameters. These parameters can be fitted from experimental data or computed from first principles. In this section, we will focus on the latter approach, specifically on the computation of the $C_r(n\ell)$ parameters using Density Functional Theory (DFT) or Hartree-Fock (HF)/Dirac-Fock (DF) methods. These parameters vary from one physical system to another and will be the focus of the following sections.

It is practical to tabulate the products of D_r 's and the reduced matrix elements in advance for all possible configurations of the valence shell. The matrix elements of the Hamiltonian can then be obtained by simply multiplying these precomputed values by the $C_r(n\ell)$ parameters.

We will consider these $C_r(n\ell)$ parameters in the following subsections.

3.2.1 The radial degrees of freedom

The LFDFT theoretical framework

Ramanantoanina describe the method they developed to bridge the gap between atomistic description and quantum chemistry calculations in [118]. We will summarize the main points of their method, called LFDFT, here.

The main point of interest here, is the methodology they deployed to compute the radial parameters $C_r(n\ell)$ from DFT calculations, which is based on extracting radial wavefunctions from the Kohn-Sham orbitals. The radial wavefunctions are then used to compute the radial parameters $C_r(n\ell)$.

By doing an Average of Configuration (AOC) method that forces fractional occupation of electrons within Kohn-Sham orbitals that are selectively chosen as the active subspace, they can extract the radial wavefunctions of the valence shell after convergence of the DFT calculations.

Depending on the geometry of the ligand, some slight m_ℓ variations in the radial wavefunctions of the valence shell can be observed. In order to consider a single radial wavefunction for each $n\ell$ orbital, they average the radial wavefunctions over the m_ℓ values.

Configuration energies

If one only considers the valence shell, one can set the origin of the energy to be the central-potential energy of the valence configuration $\langle n\ell | H_0 | n\ell \rangle$. Moreover, one can include in the origin of the energy all mean-field contributions discussed in Sections 2.5.3 and 3.1.5. This removes the need to calculate $F_0(n\ell, n\ell)$ for the interelectronic repulsion and $A_0^0(n\ell, n\ell)$ for the Ligand Field.

If one considers two configurations, the valence shell and the singly excited configuration, the origin of the energy can be still be chosen to the central-potential energy of the valence configuration $\langle n\ell | H_0 | n\ell \rangle$, and the mean-field contributions of the valence shell and the singly excited configuration. However, the energy difference between the valence shell and the singly excited configuration needs to be taken into account and calculated, but it can also be effectively included in the $F_0(n\ell, n_e\ell_e)$ parameter for example. In DFT, it simply takes the form of

$$\Delta(\ell\ell_e) = \Delta E_{n\ell, n_e\ell_e} = E^{\text{DFT}}(n\ell^{p-1}n_e\ell_e) - E^{\text{DFT}}(n\ell^p). \quad (3.31)$$

The Slater parameters

The first radial parameters to be considered are the Slater parameters, where C_r can represent either $F_k(n\ell, n'\ell')$ or $G_k(n\ell, n'\ell')$ from (2.57) and (2.63), which are the two particle matrix elements of the Coulomb operator in the basis of the radial wavefunctions.

$$\begin{aligned} F_k(n\ell, n'\ell') &= (\langle n\ell | \otimes \langle n\ell |) \frac{r_{>}^k}{r_{<}^{k+1}} (|n'\ell'\rangle \otimes |n'\ell'\rangle) \\ &= \int_{r_1=0}^{+\infty} \int_{r_2=0}^{+\infty} P_{n\ell}^2(r_1) \frac{r_{<}^k}{r_{>}^{k+1}} P_{n'\ell'}^2(r_2) dr_1 dr_2 \\ &= \int_{r_1=0}^{+\infty} P_{n\ell}^2(r_1) \left(\frac{1}{r_1^{k+1}} \int_{r_2=0}^{r_1} r_2^k P_{n'\ell'}^2(r_2) dr_2 + r_1^k \int_{r_2=r_1}^{+\infty} \frac{1}{r_2^{k+1}} P_{n'\ell'}^2(r_2) dr_2 \right) dr_1, \end{aligned} \quad (3.32)$$

and

$$\begin{aligned} G_k(n\ell, n'\ell') &= (\langle n\ell | \otimes \langle n'\ell' |) \frac{r_{<}^k}{r_{>}^{k+1}} (|n\ell\rangle \otimes |n'\ell'\rangle) \\ &= \int_{r_1=0}^{+\infty} \int_{r_2=0}^{+\infty} P_{n\ell}(r_1) P_{n'\ell'}(r_1) \frac{r_{<}^k}{r_{>}^{k+1}} P_{n\ell}(r_2) P_{n'\ell'}(r_2) dr_1 dr_2 \\ &= \int_{r_1=0}^{+\infty} P_{n\ell}(r_1) P_{n'\ell'}(r_1) \times \\ &\quad \left(\frac{1}{r_1^{k+1}} \int_{r_2=0}^{r_1} r_2^k P_{n\ell}(r_2) P_{n'\ell'}(r_2) dr_2 + r_1^k \int_{r_2=r_1}^{+\infty} \frac{1}{r_2^{k+1}} P_{n\ell}(r_2) P_{n'\ell'}(r_2) dr_2 \right) dr_1. \end{aligned} \quad (3.33)$$

They will be dependent on the radial wavefunctions of the valence shell and, if considered, the singly excited configuration. These can be obtained directly from the HF or DF calculations, or, more indirectly, from the DFT calculations, using the molecular orbitals as the radial wavefunctions. To be exact, in our case, they are the dominant part of the radial functions extracted from the active Kohn-Sham orbitals centered on the lanthanide ion that predominantly possess $n\ell$ and $n'\ell'$ characters.

The Spin-Orbit parameters

For the spin-orbit interaction, we have the Spin-Orbit parameters $\langle n\ell|\xi(r)|n\ell\rangle$ and $\langle n_e\ell_e|\xi(r)|n_e\ell_e\rangle$ from (2.78) and (2.79) are single-electron matrix elements of

$$\xi(r) = \frac{\hbar^2}{2m_e c^2} \frac{1}{r} \frac{dV(r)}{dr} \quad (3.34)$$

with $V(r)$ the electric potential felt by the electron. This quantity can be computed in a variety of ways, be it from atomistic calculations with the wavefunctions directly, or, again, indirectly from DFT calculations with the use of the ZORA (Zeroth-Order Regular Approximation) found in the seminal work of Van Lenthe [119] and $C_r(n\ell) = \zeta_{n\ell} = \langle n\ell|\xi(r)|n\ell\rangle$ can be readily computed from ZORA energies by

$$\zeta_{n\ell} = \frac{2}{2\ell + 1} \left(E_{n\ell, j=l+\frac{1}{2}}^{\text{ZORA}} - E_{n\ell, j=l-\frac{1}{2}}^{\text{ZORA}} \right). \quad (3.35)$$

The Ligand Field parameters

This is the most significant part of the LFDFT method. We will explain here how the LFDFT method can be used to compute the Ligand Field parameters.

We can define the $(2\ell + 1) \times (2\ell + 1)$ (or $(2(\ell + \ell_e) + 2) \times (2(\ell + \ell_e) + 2)$) matrix V_{LF} , the Ligand Field operator in the $n\ell$ basis, as

$$\langle n\ell\mu|H_{\text{CF}}|n\ell\nu\rangle = \sum_{q=0}^{\ell} \sum_{m=-2q}^{2q} A_m^{2q}(n\ell, n\ell) \langle n\ell\mu|C_m^{(2q)}|n\ell\nu\rangle, \quad (3.36)$$

$$\langle n_e\ell_e\mu|H_{\text{CF}}|n\ell\nu\rangle = \sum_{q=0}^{\ell} \sum_{m=-2q}^{2q} A_m^{2q}(n_e\ell_e, n_e\ell_e) \langle n_e\ell_e\mu|C_m^{(2q)}|n_e\ell_e\nu\rangle, \quad (3.37)$$

$$\langle n_e\ell_e\mu|H_{\text{CF}}|n\ell\nu\rangle = \sum_{q=0}^{\ell} \sum_{m=-2q}^{2q} A_m^{2q}(n_e\ell_e, n_e\ell_e) \langle n_e\ell_e\mu|C_m^{(2q)}|n\ell\nu\rangle. \quad (3.38)$$

The $A_m^l(n\ell, n\ell')$ as defined in (3.27) are the Ligand Field Parameters that need to be computed, for which one can use the *Angular Overlap Model* (AOM) that defines the e_σ , e_π and e_δ parameters, characterizing the overlap with ligand orbitals related to covalent σ , π and δ bonds, respectively.

The energy splitting in the $n\ell$ and $n_e\ell_e$ shells are then characterized by these parameters. For example, for the $4f$ and $5d$ shells, the AOM parameters are defined with respect to the energy splittings as depicted in Fig. 3.2.

The ligand-field reduced matrix V_{LF} is then obtained by the following relations that make use of *Wigner's Darstellungsmatrizen* $D_{m,m'}^{(k)}$ and where μ and ν are the magnetic quantum numbers of the $n\ell$ and $n'\ell'$ orbitals, respectively:

$$\langle f, \mu|V_{\text{LF}}|f, \nu\rangle = \sum_{k=1}^{\text{ligands}} \sum_{\lambda=\sigma,\pi} D_{\mu\lambda}^{4f}(k) \cdot D_{\nu\lambda}^{4f}(k) \cdot e_{\lambda,k}(f) \quad (3.39)$$

$$\langle d, \mu|V_{\text{LF}}|d, \nu\rangle = \sum_{k=1}^{\text{ligands}} \sum_{\lambda=\sigma,\pi} D_{\mu\lambda}^{5d}(k) \cdot D_{\nu\lambda}^{5d}(k) \cdot e_{\lambda,k}(d) \quad (3.40)$$

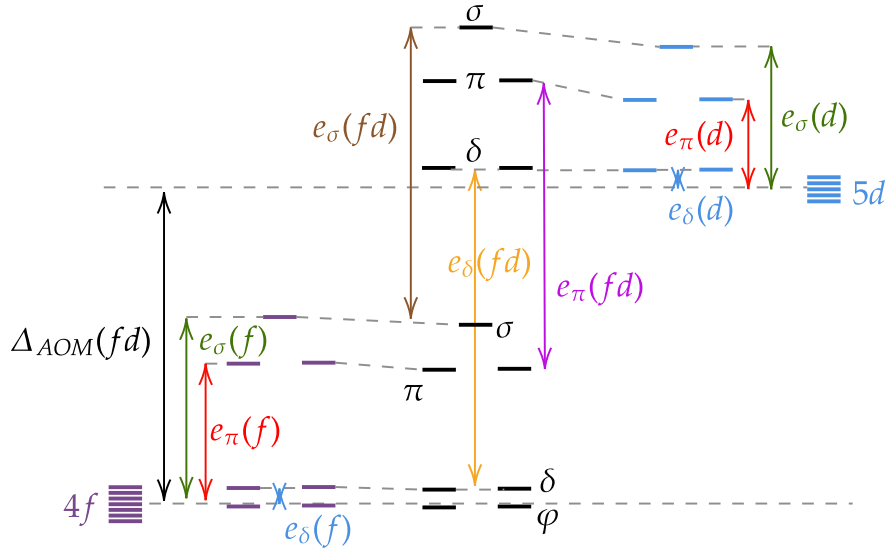


Figure 3.2: Representation of the AOM parameters adjusted from the interaction of a lanthanide ion with one ligand. The first order energy splitting of the $4f$ and $5d$ orbitals is presented in purple and blue respectively and the second order energy splitting is represented in black. Adapted from [120].

$$\langle f, \mu | V_{\text{LF}} | d, \nu \rangle = \sum_{k=1}^{\text{ligands}} \sum_{\lambda=\sigma,\pi} D_{\mu\lambda}^{4f}(k) \cdot D_{\nu\lambda}^{5d}(k) \cdot e_{\lambda,k}(fd), \quad (3.41)$$

with the additional condition that

$$\Delta_{\text{AOM}}(fd) = \Delta(fd) + \frac{1}{7} \text{Tr}(\langle f | V_{\text{LF}} | f \rangle) - \frac{1}{5} \text{Tr}(\langle d | V_{\text{LF}} | d \rangle) \quad (3.42)$$

where $\Delta(fd)$ is the energy splitting defined in (3.31).

It is then a matter of using (3.36) to (3.38) to identify each matrix element of V_{LF} with the corresponding sum of Ligand Field parameters $A_m^k(n\ell, n\ell)$, and then to solve the system of equations to obtain the $A_m^k(n\ell, n\ell)$. From Tab. 3.1, one can see that the number of parameters to be computed in the case of the $4f$ and $5d$ shells is 64, while there are $12 \times 12 = 144$ matrix elements in V_{LF} , leading to an overdetermined system of equations.

The method, including the formal procedure to obtain the AOM parameters from DFT are explained in more detail in [120, 121].

Noteably, it has successfully been applied with good agreement with experimental data to the study of the electronic structure and emissions of lanthanide complexes in [118, 122], moreover it was also successfully applied to the TbPc₂ SMM of interest in our work in [123], to predict $d - f$ core excitation energies, by working in the $3d$ and $4f$ active space.

Main takeaways from Chapter 3

- **Ligand Field and Crystal Field Concepts:**

- Both theories describe the effect of surrounding ligands on the electronic structure of a central atom.
- **Crystal Field Theory (CFT)** assumes ligands are point charges arranged in a regular geometry, with no overlap between ligand charges and central atom electrons.
- **Ligand Field Theory (LFT)** generalizes CFT by considering ligand electron densities and their overlap with central atom orbitals.
- LFT provides a more accurate description for molecular complexes, accounting for covalency and ligand polarizability.
- These concepts are crucial for understanding magnetic and optical properties of lanthanides and actinides.

- **Matrix Elements and Crystal Field Parameters:**

- The potential is expanded using spherical harmonics in terms of crystal field parameters $A_m^l(n\ell, n'\ell')$.
- Selection rules, based on symmetry and angular momentum, reduce the number of necessary parameters.
- Mean field contributions can be separated to simplify calculations.

- **Ligand Field Density Functional Theory (LFDFT):**

- Combines LFT with Density Functional Theory for computational studies.
- Radial parameters $C_r(n\ell)$ are extracted from DFT calculations using Kohn-Sham orbitals.
- Addresses challenges in calculating overlap between ligand and central atom electron densities.
- Facilitates computation of Slater parameters, spin-orbit parameters, and most importantly, ligand field parameters.

Chapter Contents

4.1 Symmetry and odd Ligand Field Parameters	65
4.2 Judd-Ofelt theory and effective operators	65
4.3 The hyperfine Stark effect	72
4.4 Towards hyperfine-induced luminescence	77

CHAPTER 4

Configuration Interaction

"Facts do not cease to exist because they are ignored."

– Aldous Huxley, *Complete Essays, Vol. II: 1926-1929*

4.1 Symmetry and odd Ligand Field Parameters

From the previous sections, we obtained that the only term of the Hamiltonian that can couple electronic configuration of different parities (such as $4f^n$ and $4f^{n-1}5d$ configurations) is the Ligand Field term. The amplitude of this mixing is determined by the off-diagonal matrix elements (3.13), and importantly, requires the presence of **odd Ligand Field Parameters** $A_m^l(n\ell, n\ell')$ with l odd. Moreover, from symmetry considerations, we know that such off-diagonal LFPs are only possible in complexes lacking inversion symmetry, since, otherwise, (3.18) holds

$$A_m^l(n\ell, n\ell') = (-1)^m A_{-m}^l(n\ell, n\ell'), \quad (4.1)$$

and the off-diagonal matrix elements would vanish.

4.2 Judd-Ofelt theory and effective operators

4.2.1 Overview of the Judd-Ofelt theory

The Judd-Ofelt theory is a method introduced by Brian Judd and George Ofelt in the 1960s to describe the intensity of the electric dipole transitions in rare-earth ions. As the $f - f$ transitions should be parity-forbidden, the method is based on the assumption that the electric dipole transitions are mainly due to the interaction of the rare-earth ion with the ligands, and in particular due to the configuration mixing it induces. It is based on the standard second-order perturbation theory applied to the Hamiltonian of the rare-earth ion in the presence of the ligands. The Hamiltonian is given by

$$H_{\text{tot}} = H + \varepsilon (PH_{\text{LF}}Q + QH_{\text{LF}}P), \quad (4.2)$$

where H is the unperturbed Hamiltonian of the rare-earth ion, H_{LF} is the Ligand Field Hamiltonian, and P and Q are the projection operators on the ground ($4f^n$) and excited ($4f^{n-1}5d$ among others)

states of the rare-earth ion, respectively, with $PQ = 0$. The parameter ε is a small parameter that allows for the perturbation theory to be applied.

Note: H is the unperturbed block diagonal Hamiltonian of the free ion ($PHP + QHQ$) including terms of the ligand field Hamiltonian within the same configuration, i.e. terms of the form $PH_{\text{LF}}P$.

The ground state wavefunctions perturbed to first order are then given by

$$|\Psi_i\rangle = |\Psi_i^{(0)}\rangle + \varepsilon \sum_{j \neq i} \frac{\langle \Psi_j^{(0)} | QH_{\text{LF}}P | \Psi_i^{(0)} \rangle}{\varepsilon(E_i^{(0)} - E_j^{(0)})} |\Psi_j^{(0)}\rangle \quad (4.3)$$

where $|\Psi_i^{(0)}\rangle$ are the unperturbed wavefunctions of the rare-earth ion, and i indexes states from the ground state configurations $P|\Psi_i^{(0)}\rangle = |\Psi_i^{(0)}\rangle$ and j indexes states from the excited configurations $Q|\Psi_j^{(0)}\rangle = |\Psi_j^{(0)}\rangle$.

From selection rules consideration in (3.13), and assuming the ground state is $4f^n$ and $4f^{n-1}5d$ spans the space Q projects on, we can rewrite $QH_{\text{LF}}P$ as

$$QH_{\text{LF}}P = \sum_{t=0}^2 \sum_{m=-2t-1}^{2t+1} B_m^{2t+1}(4f, 5d) \langle 5d | r^{2t+1} | 4f \rangle \Upsilon_m^{(2t+1)}. \quad (4.4)$$

Referring to (3.14),

$$\Upsilon^{(2t+1)} \equiv \langle 5d | \mathbf{C}^{(2t+1)} | 4f \rangle \mathbf{U}^{(2t+1)}(4f^{n-1}5d, 4f^n). \quad (4.5)$$

with (see (2.31))

$$P\Upsilon^{(2t+1)}P = 0, \quad Q\Upsilon^{(2t+1)}Q = 0, \quad P\Upsilon^{(2t+1)}Q = \Upsilon^{(2t+1)}. \quad (4.6)$$

. We thus have the perturbed wavefunctions

$$|\psi_i\rangle = |\Psi_i^{(0)}\rangle + \varepsilon \sum_{j \neq i} \sum_{t=0}^2 \sum_{m=-2t-1}^{2t+1} B_m^{2t+1}(4f, 5d) \langle 5d | r^{2t+1} | 4f \rangle \frac{\langle \Psi_j^{(0)} | \Upsilon_m^{(2t+1)} | \Psi_i^{(0)} \rangle}{\varepsilon(E_i^{(0)} - E_j^{(0)})} |\Psi_j^{(0)}\rangle. \quad (4.7)$$

It would be useful to define the first order correction to the wavefunction as

$$|\Psi_i^{(1)}\rangle = \sum_{j \neq i} \sum_{t=0}^2 \sum_{m=-2t-1}^{2t+1} B_m^{2t+1}(4f, 5d) \langle 5d | r^{2t+1} | 4f \rangle \frac{\langle \Psi_j^{(0)} | \Upsilon_m^{(2t+1)} | \Psi_i^{(0)} \rangle}{E_i^{(0)} - E_j^{(0)}} |\Psi_j^{(0)}\rangle. \quad (4.8)$$

Let's consider the electric dipole operator \mathbf{D} , which is given by

Definition: (*Electric dipole operator*)

$$\mathbf{D}^{(1)} = \sum_{i=1}^N -|e|\vec{r}_i = \sum_{i=1}^N -|e|r_i \mathbf{C}^{(1)}(\theta_i, \phi_i). \quad (4.9)$$

Without configuration mixing, the matrix elements of the electric dipole between two states in the $4f$ configuration, $|\Psi_i^{(0)}\rangle = |4f^n LSJM_J\rangle$ and $|\Psi_{i'}^{(0)}\rangle = |4f^n L'S'J'M_{J'}\rangle$, are given by

$$\langle 4f^n LSJM_J | D_q^{(1)} | 4f^n L'S'J'M_{J'} \rangle = (-1)^{J-M_J} e \begin{pmatrix} J & 1 & J' \\ -M_J & q & M_{J'} \end{pmatrix} \langle 4f || r || 4f \rangle \langle 4f || \mathbf{C}^{(1)} || 4f \rangle \langle 4f LSJ || \mathbf{U}^{(1)} || 4f L'S'J' \rangle, \quad (4.10)$$

this expression contains

$$\langle 4f || \mathbf{C}^{(1)} || 4f \rangle = -7 \begin{pmatrix} 3 & 1 & 3 \\ 0 & 0 & 0 \end{pmatrix}, \quad (4.11)$$

which, is actually vanishing [124] on account of $3 + 1 + 3 = \text{odd}$.

This is what is meant by the electric dipole transitions being parity-forbidden, since to zeroth order, the transition amplitude Γ is equal to (4.10), which is zero.

We can then write explicitly $\Psi_j^{(0)} = |4f^{n-1} 5dL'S'J'M_{J'}\rangle$, and the matrix elements of the electric dipole operator between the ground and excited states are given by

$$\langle 4f^n LSJM_J | D_q^{(1)} | 4f^{n-1} 5dL'S'J'M_{J'} \rangle = (-1)^{J-M_J} \begin{pmatrix} J & 1 & J' \\ -M_J & q & M_{J'} \end{pmatrix} e \langle 4f || r || 5d \rangle \langle 4f || \mathbf{C}^{(1)} || 5d \rangle \langle 4f LSJ || \mathbf{U}^{(1)} (4f^n, 4f^{n-1} 5d) || 4f L'S'J' \rangle, \quad (4.12)$$

this time $\langle 4f || \mathbf{C}^{(1)} || 5d \rangle$ is non-vanishing, and this also means we have the equalities

$$P\mathbf{D}^{(1)}P = 0, \quad Q\mathbf{D}^{(1)}Q = 0, \quad P\mathbf{D}^{(1)}Q = \mathbf{D}^{(1)}. \quad (4.13)$$

Moreover, effectively, in the subspace of the ground and excited states we are considering, we have

$$\mathbf{D}^{(1)} = \langle 4f || r || 5d \rangle \langle 4f || \mathbf{C}^{(1)} || 5d \rangle \mathbf{U}^{(1)}(4f^n, 4f^{n-1} 5d). \quad (4.14)$$

By considering the perturbed wavefunction (4.7), we can calculate the transition amplitude to first order in ε :

Definition: (*First order transition amplitude*)

$$\vec{\Gamma}(i, i') = \langle \Psi_i | \mathbf{D}^{(1)} | \Psi_{i'} \rangle = \langle \Psi_i^{(0)} | \mathbf{D}^{(1)} | \Psi_{i'}^{(1)} \rangle + \langle \Psi_i^{(1)} | \mathbf{D}^{(1)} | \Psi_{i'}^{(0)} \rangle = \langle \Psi_i^{(0)} | \mathbf{D}^{(1)} | \Psi_{i'}^{(1)} \rangle + \text{h.c.} \quad (4.15)$$

where we remind that i indexes the ground state configurations ($4f^n$) and j indexes the excited state configurations ($4f^{n-1} 5d$). The matrix elements of the electric dipole operator between the ground and excited states are given by

$$\begin{aligned} \langle \Psi_i^{(0)} | \mathbf{D}^{(1)} | \Psi_{i'}^{(1)} \rangle &= \sum_{j \neq i'}^2 \sum_{t=0}^2 \sum_{m=-2t-1}^{2t+1} B_m^{2t+1}(4f, 5d) \langle 5d || r^{2t+1} || 4f \rangle \frac{\langle \Psi_j^{(0)} | \Upsilon_m^{(2t+1)} | \Psi_{i'}^{(0)} \rangle}{E_i^{(0)} - E_j^{(0)}} \langle \Psi_i^{(0)} | \mathbf{D}^{(1)} | \Psi_j^{(0)} \rangle \\ &= \sum_{t=0}^2 \sum_{m=-2t-1}^{2t+1} B_m^{2t+1}(4f, 5d) \langle 5d || r^{2t+1} || 4f \rangle \sum_{j \neq i'} \frac{\langle \Psi_i^{(0)} | \mathbf{D}^{(1)} | \Psi_j^{(0)} \rangle \langle \Psi_j^{(0)} | \Upsilon_m^{(2t+1)} | \Psi_{i'}^{(0)} \rangle}{E_i^{(0)} - E_j^{(0)}} \end{aligned} \quad (4.16)$$

The key insight and assumptions of the Judd-Ofelt theory is that the energy denominator $E_i^{(0)} - E_j^{(0)}$ is (i) large relative to the numerator terms (ii) similar for all j states. The first is justified if the excited $4f^{n-1}5d$ configurations are far from the ground $4f^n$ configurations, and the second is justified if the excited configurations are close in energy to each other relatively to the difference in energy between the ground and excited configurations.

Note: Physically, this means we consider the excited configurations to be degenerate and far in energy from the ground configurations. The relative positions of the $4f^n$ and $4f^{n-1}5d$ configurations for triply ionized lanthanide ions are depicted in Fig. 4.1 for comparison. For most rare-earth ions, these assumptions are only moderately satisfied, but they provide a significant simplification in the analysis.

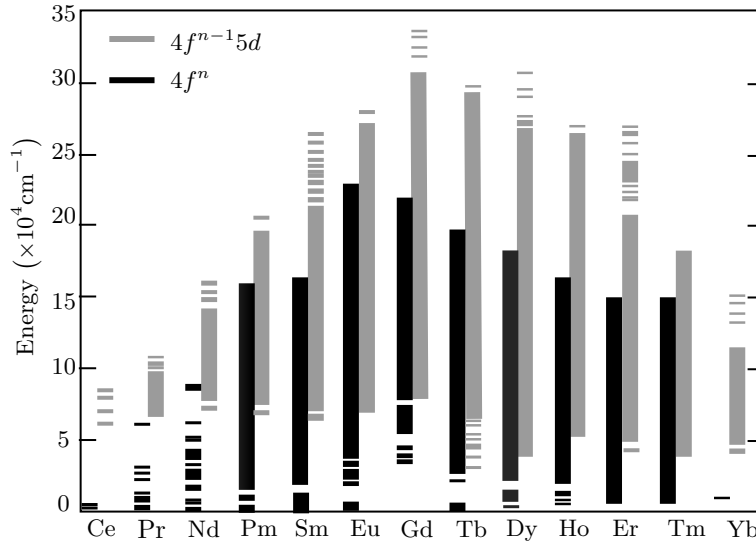


Figure 4.1: Energy levels of the $4f$ and $5d$ orbitals in the lanthanide series. The energy levels are in units of 10^4 cm^{-1} . The $4f^n$ and $4f^{n-1}5d$ configurations are indicated. Adapted from [125].

Thus by assuming that $E_i^{(0)} - E_j^{(0)} = \Delta E$ is constant, we can write (4.16) as

$$\begin{aligned}
 \langle \Psi_i^{(0)} | \mathbf{D}^{(1)} | \Psi_{i'}^{(1)} \rangle &= \\
 &= \sum_{t=0}^2 \sum_{m=-2t-1}^{2t+1} B_m^{2t+1}(4f, 5d) \langle 5d | r^{2t+1} | 4f \rangle \sum_{j \neq i'} \frac{\langle \Psi_i^{(0)} | \mathbf{D}^{(1)} | \Psi_j^{(0)} \rangle \langle \Psi_j^{(0)} | \Upsilon_m^{(2t+1)} | \Psi_{i'}^{(0)} \rangle}{\Delta E} \\
 &= \sum_{t=0}^2 \sum_{m=-2t-1}^{2t+1} B_m^{2t+1}(4f, 5d) \langle 5d | r^{2t+1} | 4f \rangle \langle \Psi_i^{(0)} | \mathbf{D}^{(1)} \frac{\sum_{j \neq i'} |\Psi_j^{(0)} \rangle \langle \Psi_j^{(0)}|}{\Delta E} \Upsilon_m^{(2t+1)} | \Psi_{i'}^{(0)} \rangle
 \end{aligned} \tag{4.17}$$

We note, referring to (4.6) and (4.13), that $\sum_{j \neq i'} |\Psi_j^{(0)} \rangle \langle \Psi_j^{(0)}|$ effectively acts as a closure relation between $\mathbf{D}^{(1)}$ and $\Upsilon_m^{(2t+1)}$. The assumptions of the Judd-Ofelt theory are precisely made to take advantage of this. Therefore, one has, using (4.5) and (4.12):

$$\begin{aligned}
\langle \Psi_i^{(0)} | \mathbf{D}^{(1)} | \Psi_{i'}^{(1)} \rangle &= \\
&= \frac{1}{\Delta E} \sum_{t=0}^2 \sum_{m=-2t-1}^{2t+1} B_m^{2t+1}(4f, 5d) \langle 5d | r^{2t+1} | 4f \rangle \langle \Psi_i^{(0)} | D_q^{(1)} \Upsilon_m^{(2t+1)} | \Psi_{i'}^{(0)} \rangle \\
&= \frac{e}{\Delta E} \sum_{t=0}^2 \sum_{m=-2t-1}^{2t+1} B_m^{2t+1}(4f, 5d) \langle 5d | r^{2t+1} | 4f \rangle \langle 4f | r | 5d \rangle \langle 4f | \mathbf{C}^{(1)} | 5d \rangle \langle 5d | \mathbf{C}^{(2t+1)} | 4f \rangle \times \\
&\quad \times \langle \Psi_i^{(0)} | U_q^{(1)}(4f^n, 4f^{n-1}5d) U_m^{(2t+1)}(4f^{n-1}5d, 4f^n) | \Psi_{i'}^{(0)} \rangle. \quad (4.18)
\end{aligned}$$

Using some property of Racah algebra, in particular regarding coupled tensor operators (D.35) and closure/orthogonality relations of coefficients of fractional parentages, we can write the product of $U_q^{(1)}(4f^n, 4f^{n-1}5d)$ and $U_m^{(2t+1)}(4f^{n-1}5d, 4f^n)$ as

$$\begin{aligned}
U_q^{(1)}(4f^n, 4f^{n-1}5d) U_m^{(2t+1)}(4f^{n-1}5d, 4f^n) &= \\
&= \sum_{\Lambda} (-1)^{q+m} \sqrt{2\Lambda+1} \begin{pmatrix} 1 & 2t+1 & \Lambda \\ q & m & -(q+m) \end{pmatrix} \left[\mathbf{U}_{q1}^{(1)} \times \mathbf{U}^{(2t+1)} \right]_{-(q+m)}^{(\Lambda)} \quad (4.19)
\end{aligned}$$

Simplifying $\left[\mathbf{U}_{q1}^{(1)} \times \mathbf{U}^{(2t+1)} \right]_{-(q+m)}^{(\Lambda)}$ further, we have

$$\begin{aligned}
U_q^{(1)}(4f^n, 4f^{n-1}5d) U_m^{(2t+1)}(4f^{n-1}5d, 4f^n) &= \\
&= \sum_{\Lambda} (-1)^{\Lambda+q+m} (2\Lambda+1) \begin{pmatrix} 1 & 2t+1 & \Lambda \\ q & m & -(q+m) \end{pmatrix} \begin{Bmatrix} 2t+1 & \Lambda & 1 \\ 3 & 2 & 3 \end{Bmatrix} U_{-(q+m)}^{(\Lambda)}. \quad (4.20)
\end{aligned}$$

These simplifications allow one to write the matrix element of the dipole operator as

$$\begin{aligned}
\langle \Psi_i^{(0)} | D_q^{(1)} | \Psi_{i'}^{(1)} \rangle &= \sum_{\Lambda} (-1)^{\Lambda} \langle \Psi_i^{(0)} | U_{\rho}^{(\Lambda)} | \Psi_{i'}^{(0)} \rangle \\
&\quad \times \left(\sum_{t=0}^2 \sum_{m=-2t-1}^{2t+1} (-1)^{\rho} B_m^{(2t+1)}(4f, 5d) \begin{pmatrix} \Lambda & 1 & 2t+1 \\ \rho & q & m \end{pmatrix} A_{2t+1}^{\Lambda}(4f, 5d) R(4f, 5d) \right) \quad (4.21)
\end{aligned}$$

with $\rho = -q - m$ and the angular term $A_{2t+1}^{\Lambda}(4f, 5d)$ given by

$$A_{2t+1}^{\Lambda}(4f, 5d) = (2\Lambda+1) \begin{Bmatrix} 2t+1 & \Lambda & 1 \\ 3 & 2 & 3 \end{Bmatrix} \langle 4f | \mathbf{C}^{(1)} | 5d \rangle \langle 5d | \mathbf{C}^{(2t+1)} | 4f \rangle, \quad (4.22)$$

and the radial term $R(4f, 5d)$ given by

$$R(4f, 5d) = e \frac{\langle 4f | r | 5d \rangle \langle 5d | r^{2t+1} | 4f \rangle}{\Delta E}. \quad (4.23)$$

The same calculation can be done for the hermitian conjugate of the matrix element, and the result is

$$\begin{aligned} \langle \Psi_i^{(1)} | D_q^{(1)} | \Psi_{i'}^{(0)} \rangle &= \sum_{\Lambda} (-1)^{\Lambda} \langle \Psi_i^{(0)} | U_{\rho}^{(\Lambda)} | \Psi_{i'}^{(0)} \rangle \\ &\times \left(\sum_{t=0}^2 \sum_{m=-2t-1}^{2t+1} (-1)^{\rho} B_m^{(2t+1)}(4f, 5d) \begin{pmatrix} \Lambda & 2t+1 & 1 \\ \rho & m & q \end{pmatrix} A_{2t+1}^{\Lambda}(4f, 5d) R(4f, 5d) \right). \end{aligned} \quad (4.24)$$

Note that $\begin{pmatrix} \Lambda & 2t+1 & 1 \\ \rho & m & q \end{pmatrix} = (-1)^{\Lambda} \begin{pmatrix} \Lambda & 1 & 2t+1 \\ \rho & q & m \end{pmatrix}$, so the terms in the sums of the two expression only differ by a factor of $(-1)^{\Lambda}$. This means that, in order to calculate (4.15), the terms with odd Λ will cancel out. Moreover, in order not to vanish, the $3j$ - and $6j$ -symbols containing Λ impose $1 \leq \Lambda \leq 2t+2 = 6$. Thus, posing $\Lambda = 2\lambda$, one is left with

$$\begin{aligned} \Gamma_q(i, i') &= \langle \Psi_i^{(1)} | D_q^{(1)} | \Psi_{i'}^{(1)} \rangle = 2 \sum_{\lambda} \langle \Psi_i^{(0)} | U_{\rho}^{(2\lambda)} | \Psi_{i'}^{(0)} \rangle \\ &\times \left(\sum_{t=0}^2 \sum_{m=-2t-1}^{2t+1} (-1)^{q+m} B_m^{(2t+1)}(4f, 5d) \begin{pmatrix} 2\lambda & 1 & 2t+1 \\ -(q+m) & q & m \end{pmatrix} A_{2t+1}^{2\lambda}(4f, 5d) R(4f, 5d) \right) \end{aligned} \quad (4.25)$$

Two important takeaways can be highlighted:

1. It is possible to express the matrix element of the dipole operator between two perturbed states as the matrix element of an *effective operator* between the two same unperturbed states, in the unperturbed basis, we have derived an effective dipole operator \tilde{D} such that

$$\langle \Psi_i^{(0)} | \tilde{D}_q | \Psi_{i'}^{(0)} \rangle = \langle \Psi_i^{(1)} | D_q^{(1)} | \Psi_{i'}^{(1)} \rangle$$

and

$$\tilde{D}_q = \sum_{\lambda} \tilde{D}_q^{2\lambda} \quad (4.26)$$

with

$$\tilde{D}_q^{\Lambda} = 2U_{\rho}^{(\Lambda)} \sum_{t=0}^2 \sum_{m=-2t-1}^{2t+1} (-1)^{q+m} B_m^{(2t+1)}(4f, 5d) \begin{pmatrix} \Lambda & 1 & 2t+1 \\ \rho & q & m \end{pmatrix} A_{2t+1}^{\Lambda}(4f, 5d) R(4f, 5d). \quad (4.27)$$

2. The linestrength of a $f - f$ transition from state i to i' is given by [125]

$$f(i, i') = \sum_{M_J M_{J'}} |\langle 4f^n LSJM_J | \vec{\Gamma}(i, i') | 4f^n L'S'J'M_{J'} \rangle|^2 \quad (4.28)$$

$$= \sum_{\Lambda \in \{2,4,6\}} \Omega_{\Lambda} |\langle 4f^n LSJ | \mathbf{U}^{(\Lambda)} | 4f^n L'S'J' \rangle|^2, \quad (4.29)$$

with the *Judd-Ofelt* parameters

$$\Omega_{\Lambda} = \sum_{t=0}^2 \sum_{m=-2t-1}^{2t+1} \frac{|B_m^{(2t+1)}(4f, 5d)|^2}{4t+3} |A_{2t+1}^{\Lambda}(4f, 5d)|^2 |R(4f, 5d)|^2. \quad (4.30)$$

From an experimental point of view, this expression is extremely useful as it allows to fit only 3 parameters that, by themselves determine (approximately) all the $4f - 4f$ transitions in a given

system, without the need to consider the excited $4f^{n-1}5d$ states. From a theoretical point of view, it involves the odd ligand field parameters, that are generally not considered, but proves they are primordial for understanding the behaviour of lanthanides in matter. For example, selection rules in the $6j$ -symbol in the definition of $A_{2t+1}^A(4f, 5d)$ impose that a ligand field parameter of rank $2t + 1 = 1$ only contributes to the $\Lambda = 2$ Judd-Ofelt parameter, imposing in turn, via $\mathbf{U}^{(2)}$, that ligand field parameters of rank 1 only affect the $\Delta J \leq 2$ transitions. However rank 1 ligand field parameters appear only in C_1, C_2, C_s or C_{2v} symmetries, meaning the $\Delta J \leq 2$ transitions are *hypersensitive* to the symmetry of the ligand field [126].

Selection rules and limitations of the Judd-Ofelt theory

While the Judd-Ofelt theory is quite resourceful and also successful in predicting the luminescence properties of lanthanides once the Judd-Ofelt parameters are extracted from the experimental data, it is not without its limitations. A study of the selection rules imposed by the $6j$ -symbols in $A_{2t+1}^A(4f, 5d)$ and the Wigner-Eckart theorem yields the following conditions for a transition to be allowed:

$$\Delta S = 0, \quad \Delta L \leq 6, \quad \Delta J \begin{cases} = 2, 4, 6 \text{ if } J \text{ or } J' \text{ is zero} \\ \leq 6 \text{ otherwise} \end{cases} \quad (4.31)$$

If one looks at the emission spectrum of Eu^{3+} starting in the 5D_0 state, presented in Fig. 4.2, one can observe transitions that are not allowed by the Judd-Ofelt theory, as they correspond to $\Delta S \neq 0$ transitions. The same observation can be done in the spectrum of Sm^{3+} [127], indicating that the Judd-Ofelt theory is not sufficient to describe the luminescence of lanthanides in its entirety.

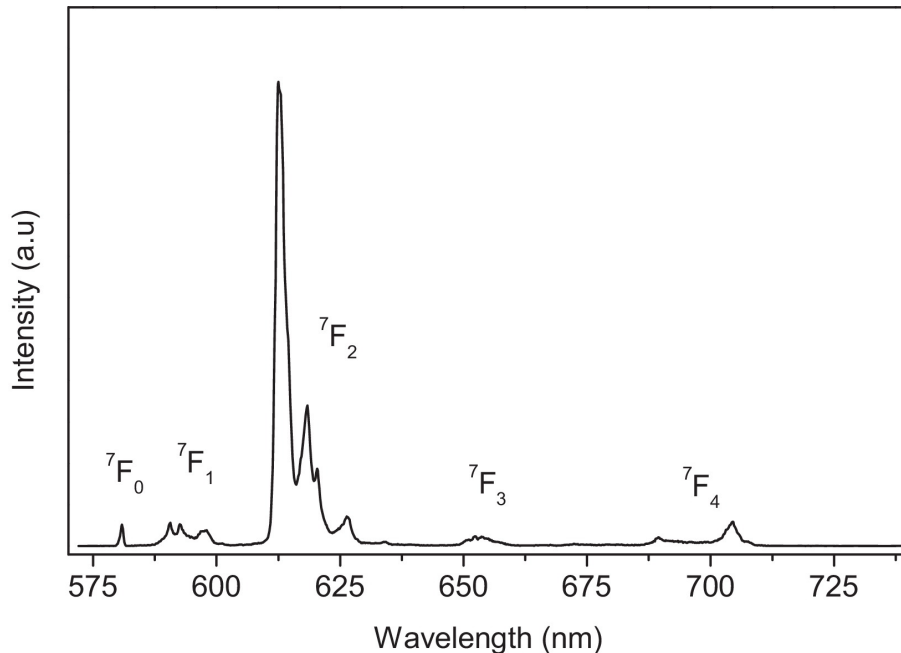


Figure 4.2: Luminescence spectrum $[\text{Eu}(\text{tta})_3(\text{phen})]$ at 77 K. The excitation wavelength is 396 nm. All the transitions start from the 5D_0 state. Adapted from [128].

The Wybourne-Downer theory and multiperturbation theory

The Wybourne-Downer theory is similar in idea to the Judd-Ofelt theory, but in place of (4.2), one considers the double perturbation expansion

$$H = H_0 + \varepsilon(PH_{\text{LF}}Q + QH_{\text{LF}}P) + \mu(PH_{\text{pert}}Q + QH_{\text{pert}}P + QH_{\text{pert}}Q), \quad (4.32)$$

choosing $H_{\text{pert}} = H_{\text{so}}$ yields what is called the Wybourne-Downer theory. But the multiperturbation framework is of course much more general, and can account for more than just the spin-orbit corrections [108].

The perturbed wavefunctions and energies are then both expanded in a double power series of ε and μ :

$$\Psi_i = \Psi_i^{(0)} + \varepsilon\Psi_i^{(10)} + \mu\Psi_i^{(01)} + \varepsilon\mu\Psi_i^{(11)} + \dots \quad (4.33)$$

$$E_i = E_i^{(0)} + \varepsilon E_i^{(10)} + \mu E_i^{(01)} + \varepsilon\mu E_i^{(11)} + \dots \quad (4.34)$$

Computing the transition amplitude to first non-vanishing orders yields

$$\begin{aligned} \vec{\Gamma}(i, i') = \varepsilon & \left(\langle \Psi_i^{(0)} | \mathbf{D}^{(1)} | \Psi_{i'}^{(10)} \rangle + \langle \Psi_i^{(10)} | \mathbf{D}^{(1)} | \Psi_{i'}^{(0)} \rangle \right) \\ & + \mu \left(\langle \Psi_i^{(0)} | \mathbf{D}^{(1)} | \Psi_{i'}^{(01)} \rangle + \langle \Psi_i^{(01)} | \mathbf{D}^{(1)} | \Psi_{i'}^{(0)} \rangle \right) \\ & + \varepsilon\mu \left(\langle \Psi_i^{(10)} | \mathbf{D}^{(1)} | \Psi_{i'}^{(01)} \rangle + \langle \Psi_i^{(01)} | \mathbf{D}^{(1)} | \Psi_{i'}^{(10)} \rangle \right. \\ & \quad \left. + \langle \Psi_i^{(0)} | \mathbf{D}^{(1)} | \Psi_{i'}^{(11)} \rangle + \langle \Psi_i^{(11)} | \mathbf{D}^{(1)} | \Psi_{i'}^{(0)} \rangle \right). \end{aligned} \quad (4.35)$$

If one considers the Wybourne-Downer theory with $H_{\text{pert}} = H_{\text{so}}$, between states not coupled via the Judd-Ofelt approach, $\vec{\Gamma}$ takes the form [127]

$$\begin{aligned} \vec{\Gamma}(i', i) = \sum_{j, j'} & \left[\frac{\langle \Psi_i^{(0)} | \mathbf{D}^{(1)} | \Psi_{j'}^{(0)} \rangle \langle \Psi_{j'}^{(0)} | H_{\text{so}} | \Psi_j^{(0)} \rangle \langle \Psi_j^{(0)} | H_{\text{LF}}^{\text{odd}} | \Psi_{i'}^{(0)} \rangle}{(E_{j'}^{(0)} - E_{i'})(E_j^{(0)} - E_{i'}^{(0)})} \right. \\ & \left. + \frac{\langle \Psi_i^{(0)} | H_{\text{LF}}^{\text{odd}} | \Psi_{j'}^{(0)} \rangle \langle \Psi_{j'}^{(0)} | H_{\text{so}} | \Psi_j^{(0)} \rangle \langle \Psi_j^{(0)} | \mathbf{D}^{(1)} | \Psi_{i'}^{(0)} \rangle}{(E_{j'}^{(0)} - E_i)(E_j^{(0)} - E_i^{(0)})} \right], \end{aligned} \quad (4.36)$$

with $H_{\text{LF}}^{\text{odd}}$, the ligand field Hamiltonian with only the odd rank parameters. j and j' both index excited states of the system in electronic configurations that are of the opposite parity to the ground state. The Wybourne-Downer correction allows to violate the spin selection rules as well as the J -selection rules, and can thus account for certain transitions observed in the luminescence spectra of Eu^{3+} and Sm^{3+} .

Accounting for more and more possible H_{pert} terms allows to complete the picture of the $4f - 4f$ transitions in lanthanides, and the multiperturbation theory is a powerful tool to do so.

4.3 The hyperfine Stark effect

The experiments of Godfrin *et al.* [99, 104, 129] and Thiele *et al.* [26, 103] have shown that the hyperfine transitions within the same manifold of a lanthanide ion (in this case, terbium in TbPc_2) can be driven by an electric field.

4.3.1 The modulation of the hyperfine constant by an electric field

The empirical tentative explanation for this effect is that the electric field modifies the hyperfine constant of the lanthanide ion, and thus the energy levels of the hyperfine transitions. Moreover, a

period modulation of the hyperfine transition leads to a Rabi driving of the hyperfine transitions, and thus a control of the populations and coherences of the hyperfine levels.

In mathematical form, the Hamiltonian of the hyperfine Stark effect can be written as

$$H_{\text{hf,dip}} = a(\vec{E})\vec{I} \cdot \vec{J} = a_0\vec{I} \cdot \vec{J} + \delta a(\vec{E})\vec{I} \cdot \vec{J}, \quad (4.37)$$

with a_0 the unperturbed hyperfine constant, and $\delta a(\vec{E})$ the Stark shift of the hyperfine constant.

Looking at the unperturbed states of the ground hyperfine multiplet, a Rabi driving of the hyperfine transitions should not be possible, as the electric field does not couple the states of the same electronic multiplet, much less in the same hyperfine multiplet, i.e. considering the particular case of Tb^{3+} in TbPc_2 , the electronic ground configuration is $^7F_6M_J = \pm 6$,

$$\langle 4f^8 \ ^7F_6M_J = \pm 6 | \vec{E} \cdot \vec{r} | 4f^8 \ ^7F_6M_J = \pm 6 \rangle \propto \langle 4f || \mathbf{C}^{(1)} || 4f \rangle = 0. \quad (4.38)$$

4.3.2 Double perturbation applied to the hyperfine magnetic dipole interaction

We can write the magnetic hyperfine interaction (2.88) as

$$H_{\text{hf,dip}} = \alpha \left({}^{\text{hf,dip,1}}\mathbf{h}^{(1)} - \sqrt{15} {}^{\text{hf,dip,2}}\mathbf{h}^{(1)} \right) \cdot \mathbf{I}^{(1)}, \quad (4.39)$$

where

$${}^{\text{hf,dip,1}}\mathbf{h}^{(1)} \equiv \frac{1}{r^3} \mathbf{L}^{(1)} = \frac{1}{r^3} \langle \ell || \mathbf{L}^{(1)} || \ell' \rangle \mathbf{U}^{(1)}, \quad (4.40)$$

and, using the sum of 2.38 over all electrons,

$${}^{\text{hf,dip,2}}\mathbf{h}^{(1)} \equiv \frac{1}{r^3} \langle \ell || \mathbf{C}^{(1)} || \ell' \rangle \mathbf{W}^{(12)1}. \quad (4.41)$$

The double perturbation theory approach from the previous subsection, can be applied with $H_{\text{pert}} = H_{\text{hf,dip},k}$ for $k = 1, 2$, and by calculating the matrix element of the dipole operator between two perturbed states, one obtains the effective operators for $\mathbf{D}^{(1)}$ [108].

Due to ${}^{\text{hf,dip,1}}h_q^{(1)}$, resulting from the contraction¹

$$\langle \Psi_i | \overbrace{U_q^{(1)}(4f, n''f)}^{\text{from } {}^{\text{hf,dip,1}}\mathbf{h}^{(1)}} \overbrace{U_\rho^{(1)}(n''f, n'\ell')}^{\text{from } \mathbf{er}^{(1)}} \overbrace{U_q^{(2t+1)}(n'\ell', 4f)}^{\text{from } \mathbf{H}_{\text{LF}}^{\text{odd}}} | \Psi_{i'} \rangle, \quad (4.42)$$

one has

$$\begin{aligned} {}^{\text{hf,dip,1}}\tilde{D}_{\rho,q}^{(1)} &= e \sum_k \sum_{t,m} B_m^{2t+1}(4f, 5d) \sum_{\ell' \in \text{even}} \langle \varrho^{2t+1}(4f \rightarrow \ell') | r | \varrho^{-3}(4f \rightarrow f) \rangle \\ &\times \sqrt{\ell(\ell+1)(2\ell+1)} \langle \ell || \mathbf{C}^{(2t+1)} || \ell' \rangle \langle \ell' || \mathbf{C}^{(1)} || \ell \rangle \\ &\times \sum_{\lambda,\mu} (-1)^{\lambda+m} [\lambda] \left(X_{qp\rho}^{1(2t+1)1}(\lambda\mu; \ell'\ell) + X_{pq\rho}^{(2t+1)11}(\lambda\mu; \ell'\ell) \right) U_\mu^{(\lambda)}(\ell\ell) \end{aligned} \quad (4.43)$$

with

¹ $\mathbf{L}^{(1)}$ is non-zero between two states of same ℓ only, hence the $n''f$ in $U_q^{(1)}(4f, n''f)$

$$X_{q_1 q_2 q_3}^{k_1 k_2 k_3}(\lambda \mu; \ell' \ell'') = \sum_{x\sigma} [x] \begin{pmatrix} k_1 & k_2 & x \\ q_1 & q_2 & -\sigma \end{pmatrix} \begin{pmatrix} x & k_2 & \lambda \\ \sigma & q_2 & -\mu \end{pmatrix} \quad (4.44)$$

$$\times \left\{ \begin{matrix} k_3 & x & k_1 \\ \ell & \ell' & \ell'' \end{matrix} \right\} \left\{ \begin{matrix} k_2 & \lambda & x \\ \ell & \ell'' & \ell \end{matrix} \right\}$$

and

$$\varrho^k(4f \rightarrow \ell'; r) = \sum_{n'}^{\text{exc}} \frac{\langle 4f | r^k | n' \ell' \rangle}{(E_{4f} - E_{n' \ell'})} P_{n' \ell'}(r). \quad (4.45)$$

Note: ϱ are the perturbed radial functions, and for ϱ^{2t+1} for example, one can use both the above definition, or the radial wavefunctions obtained from a molecular orbital for example, that would represent the exact perturbed (not only to first order) radial wavefunctions by the ligand field, different from the free atom ones, as illustrated in Fig. 4.3. In the latter case, $B_m^{2t+1}(4f, 5d) \sum_{\ell' \in \text{even}} \langle \varrho^{2t+1}(4f \rightarrow \ell') | r | \varrho^{-3}(4f \rightarrow f) \rangle$ can be identified as the $A_m^{2t+1}(4f, 5d)$ Ligand Field parameters obtained from LFDT for example.

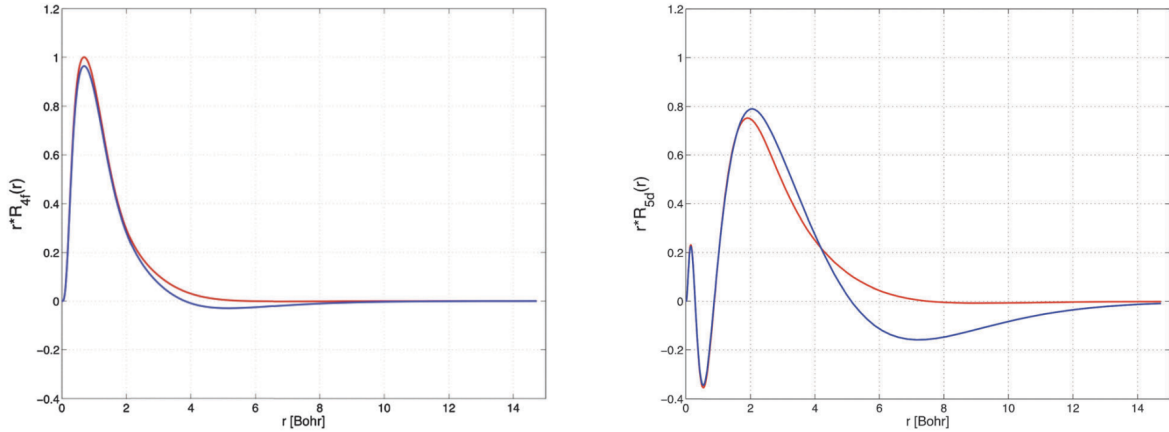


Figure 4.3: Radial functions of the 4f (left hand side) and 5d (right hand side) Kohn–Sham (DFT) orbitals of the free Pr^{3+} ion (in red) and Pr^{3+} in $\text{CaF}_2:\text{Pr}^{3+}$ (in blue). Adapted from [66].

Due to $\text{hf,dip}, 2h_q^{(1)}$, resulting from the contraction

$$\langle \Psi_i | \overbrace{W_q^{(0(2t+1))1}(4f, n' \ell')}^{\text{from } \mathbf{H}_{\text{LF}}^{\text{odd}}} \overbrace{W_\rho^{(01)1}(n' \ell', n'' \ell'')}^{\text{from } \text{er}^{(1)}} \overbrace{W_q^{(12)1}(n'' \ell'', 4f)}^{\text{from hf,dip}, 1\mathbf{h}^{(2)}} | \Psi_{i'} \rangle \quad (4.46)$$

thanks to the formula [108]

$$w_{\varrho}^{(\kappa_1 k_1)x}(s\ell, s\ell') w_{\eta}^{(\kappa_2 k_2)y}(s\ell', s\ell) = \sum_{z\zeta} \sum_{\kappa_3 k_3} (-1)^{x-y-\zeta+\kappa_3+k_3+2s} [z, x, y]^{1/2} [\kappa_3, k_3] \begin{pmatrix} x & y & z \\ \varrho & \eta & -\zeta \end{pmatrix} \quad (4.47)$$

$$\times \left\{ \begin{matrix} \kappa_2 & \kappa_3 & \kappa_1 \\ \frac{1}{2} & \frac{1}{2} & \frac{1}{2} \end{matrix} \right\} \left\{ \begin{matrix} k_2 & k_3 & k_1 \\ \ell & \ell' & \ell \end{matrix} \right\} \left\{ \begin{matrix} \kappa_1 & k_1 & x \\ \kappa_2 & k_2 & y \\ \kappa_3 & k_3 & z \end{matrix} \right\} w_{\zeta}^{(\kappa_3 k_3)z}(\ell\ell),$$

one has

$$\begin{aligned}
{}^{\text{hf,dip},2}\tilde{D}_{\rho,q}^{(1)} = & 2\sqrt{3} \sum_{\ell'} \sum_{\ell''} \sum_{tp}^{\text{odd}} B_p^{2t+1}(4f, 5d) \langle \varrho^{2t+1} (4f \rightarrow \ell') | r | \varrho^{-3} (4f \rightarrow \ell'') \rangle \\
& \times \langle \ell \| \mathbf{C}^{(2t+1)} \| \ell' \rangle \langle \ell' \| \mathbf{C}^{(1)} \| \ell'' \rangle \langle \ell'' \| \mathbf{C}^{(2)} \| \ell \rangle \sum_y^{\text{odd}} \sum_{\lambda,\mu}^{\text{even}} [y][\lambda]^{\frac{1}{2}} \sum_{x,\sigma} (-1)^{x+1} [x] \\
& \times \begin{pmatrix} 2t+1 & 1 & x \\ p & \rho & -\sigma \end{pmatrix} \begin{pmatrix} x & 1 & \lambda \\ \sigma & q & -\mu \end{pmatrix} \left\{ \begin{matrix} \ell'' & 2 & 1 & 2t+1 \\ \ell & \ell & 1 & x \\ \ell & y & \lambda & 1 \end{matrix} \right\} \\
& \times W_{\mu}^{(1y)\lambda}(s\ell, s\ell').
\end{aligned} \tag{4.48}$$

This last term contains a $12j$ -symbol [130].

A similar tensorial form is obtained for the effective operators for intra-shell correction due to $QH_{\text{hf}}Q$ in (4.32) and therefore they do not introduce new selection rules [108].

The effect we are looking to explain is not a transition between two different electronic manifolds as before however, but the energy modulation of the hyperfine transitions within the same electronic manifold.

Therefore, rewriting (4.39) in the form of the effective operator, we have

Definition: (*Effective hyperfine Stark operator between two unperturbed $4f^n$ states*)

$$H_{\text{hf,dip}} = a\vec{I} \cdot \vec{J} + \sum_{\rho=-1}^1 (-1)^{\rho+q} E_{-\rho} {}^{\rho}(D_{\text{eff}})^q I_{-q} = a\vec{I} \cdot \vec{J} + \vec{E} \cdot \overleftrightarrow{D}_{\text{eff}} \cdot \vec{I} \tag{4.49}$$

$$\text{with } {}^{\rho}(D_{\text{eff}})^q = \left\langle 4f^n LSJM_J \left| \left({}^{\text{hf,dip},1}\tilde{D}_{\rho,q}^{(1)} + {}^{\text{hf,dip},2}\tilde{D}_{\rho,q}^{(1)} \right) \right| 4f^n LSJM_J \right\rangle.$$

If one considers the only excited configuration to be $n'\ell' = 5d$, and $n''\ell'' = 4f$, we need to consider the expressions from intra-shell corrections that have the same tensorial form but with some permutation of indices [108].

The effective operator terms responsible for driving the hyperfine transitions are those represented by ${}^{\rho}(D_{\text{eff}})^{\pm 1}$, and $\delta a(\vec{E})$ defined in (4.37) is then given by

Definition: (*Stark shift of the hyperfine constant*)

$$\begin{aligned}
(\delta a(\vec{E})\vec{J})_q = & \frac{J_q}{\sqrt{J(J+1)(2J+1)}} \sum_{\rho=-1}^1 (-1)^{\rho+q} E_{-\rho} \left\langle 4f^n LSJM_J \left| \left({}^{\text{hf,dip},1}\tilde{D}_{\rho,q}^{(1)} + {}^{\text{hf,dip},2}\tilde{D}_{\rho,q}^{(1)} \right) \right| 4f^n LSJM_J \right\rangle.
\end{aligned} \tag{4.50}$$

In order to understand how the electric field influences the hyperfine transitions, and to quantify the role of odd ligand field parameters, it is necessary to undertake a detailed analysis of the selection rules imposed by the nj -symbols present in both ${}^{\text{hf,dip},1}\tilde{D}_{\rho,q}^{(1)}$ and ${}^{\text{hf,dip},2}\tilde{D}_{\rho,q}^{(1)}$. This analysis will also help determine how many parameters are required to accurately describe the hyperfine Stark effect in a particular case.

As an initial approach, we observe that each term of the effective operators involves a product of the following type:

$$\begin{pmatrix} k_1 & k_2 & x \\ q_1 & q_2 & -\sigma \end{pmatrix} \begin{pmatrix} x & k_3 & \lambda \\ \sigma & q_3 & -\mu \end{pmatrix}, \quad (4.51)$$

where (k_1, q_1) , (k_2, q_2) , and (k_3, q_3) represent any permutation of $(2t+1, p)$, $(1, q)$, and $(2t+1, \rho)$. This product is only non-zero when $\mu = q_1 + q_2 + q_3 = p + q + \rho$. Furthermore, applying the Wigner-Eckart theorem to evaluate the matrix elements of ${}^\rho(D_{\text{eff}})^q$ introduces an additional term of the form

$$\begin{pmatrix} J & \lambda & J \\ M_J & \mu & -M_J \end{pmatrix}, \quad (4.52)$$

which implies that only terms with $\mu = 0$ contribute to the hyperfine Stark effect.

Combining these two selection rules, we find that $p + q + \rho = 0$. Given that p and q can take values $0, \pm 1$, this necessitates the presence of non-zero odd-rank ligand field parameters with $p = 0, \pm 1, \pm 2$ in order to drive hyperfine transitions with an electric field.

Note: This observation confirms that the electrical driving of the nuclear qudit transitions in TbPc₂ arises from the presence of odd-rank ligand field parameters beyond those assumed under the D_{4d} symmetry of the ligand. Although D_{4d} symmetry allows odd-rank parameters with $2t+1 = 5$, they are restricted to having components with $p = \pm 4$, which do not contribute to the hyperfine Stark effect. This therefore implies the TbPc₂ system used for the experiments of Godfrin *et al.* [99, 104, 129] and Thiele *et al.* [26, 103] must have been deformed from the D_{4d} symmetry as was already hinted by the presence of Quantum Tunneling of Magnetization (QTM), that shouldn't be possible in D_{4d} [102], but rather in simple C_4 symmetry. The latter however would still not allow for the presence of odd-rank parameters with $p = \pm 1, \pm 2$, and thus the system must have a more complex symmetry.

Equation (4.49) is a general expression for the hyperfine Stark effect, while keeping in mind the exact expressions of (4.43) and (4.48) are very effective in nature, and rely on the Judd-Ofelt assumptions to contract the expressions to a manageable form. Moreover, it is impossible, without the exact computation of the different contributions, to obtain a hierarchy of which allowed terms are contributing the most to the hyperfine Stark effect. However, the angular selection rules obtained, coupled with the particular energy levels of the system, like for the Judd-Ofelt theory, provide a valuable insight into the effects of the odd ligand field parameters on the hyperfine transitions of lanthanides. It is, nonetheless, a more precise and quantitative approach than the previous empirical explanation [104] that was very similar in spirit to double perturbation theory but was not based on the exact expressions of the effective operators.

Note: The key takeaway from this complex form of the effective operators is that, for a given ligand geometry and thus known non-zero ligand-field parameters, (4.43) and (4.48) can indicate whether the hyperfine Stark effect is possible in a system just by considering the selection rules, and without requiring a full calculation of each term's value in both expressions.

In an attempt to quantify further the amplitude of the effective operators, the integral

$$\langle \varrho^{2t+1}(4f \rightarrow \ell') | r | \varrho^{-3}(4f \rightarrow f) \rangle$$

appearing in both (4.43) and (4.48) when one considers intra-shell contributions with excitations from $5d$, have been computed for the case of $\text{Pr}^{3+}(4f^2)$, $\text{Eu}^{3+}(4f^6)$, $\text{Gd}^{3+}(4f^7)$ and $\text{Tb}^{3+}(4f^8)$ in the seminal book of Wybourne [108]. The results are presented in Tab. 4.1.

$2t + 1$	Pr^{3+}	Eu^{3+}	Gd^{3+}	Tb^{3+}
1	5.5209	-2.4887	-2.1743	-1.9239
3	-25.3936	-10.3939	-8.7955	-7.5500
5	-175.6036	-62.8265	-51.6912	-43.2150

Table 4.1: Values of the integral $\langle \varrho^{2t+1}(4f \rightarrow \ell') | r | \varrho^{-3}(4f \rightarrow f) \rangle$ in atomic units for different lanthanide ions. Adapted from [108].

We can observe that the values increase with t quite substantially, and also seem to decrease in amplitude as the number of electrons in the $4f$ shell increases. While the relative amplitude of the angular part of the effective operators is not known, the values of the integrals provide a first insight into the relative importance of the different contributions to the hyperfine Stark effect and the absolute values of the hyperfine Stark effect in different lanthanide ions.

As a final note, the same approach can be applied to the quadrupole hyperfine interaction too, and the effective operator for the quadrupole can be taken into account. The quadrupole hyperfine interaction is generally weaker than the magnetic dipole interaction, but it can still be important in the context of the hyperfine Stark effect.

4.4 Towards hyperfine-induced luminescence

In a collaboration between our groups at KIT and Strasbourg and IRCP in Paris, Kumar, Serrano *et al.* [101] have recently studied the $^5D_0 \rightarrow ^7F_0$ luminescence transition in binuclear Eu^{3+} complexes in a crystal, and a selective control of the population of the hyperfine states of 7F_0 was demonstrated via Spectral Hole Burning (SHB) that is schematically presented in Fig. 4.4.

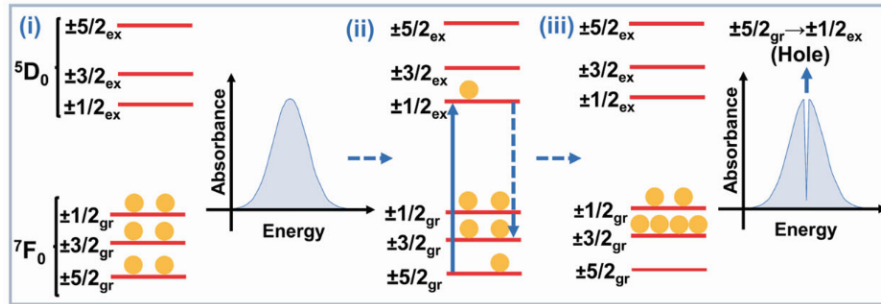


Figure 4.4: Schematic representation of the spectral hole burning experiment. Adapted from [101].

Note: SHB consists of burning a hole in the inhomogeneously broadened absorption spectrum of the material, by applying a resonant laser pulse at a particular frequency corresponding to a homogeneous peak in the absorption spectrum. This leads to a population transfer from the ground state to an excited state of a selected number of sites that are resonant with the laser frequency, and therefore contributing to the homogeneous peak. Those sites decay back to a state that is not resonant with the laser frequency, and therefore there are no more sites to absorb laser light at that frequency, leading to a hole in the absorption spectrum, that gets filled back as the sites relax back to the ground state.

Equation (4.48) contains a term that determines $0 \rightarrow 0$ transitions, since for $\lambda = 0$, $y = x = 1$, it simplifies to

$$\begin{aligned}
{}^{0\leftrightarrow 0}\mathcal{T}_{\rho,q} = \langle 4f^6 {}^7F_0 | {}^{\text{hf,dip},2}\tilde{D}_{\rho,q}^{(1)} | 4f^6 {}^5D_0 \rangle = & 6 \sum_{\ell'}^{\text{even}} \sum_{\ell''}^{\text{odd}} \sum_{tp}^{\text{odd}} B_p^t \langle \varrho^t (4f \rightarrow \ell') | r | \varrho^{-3} (4f \rightarrow \ell'') \rangle \\
& \times \langle \ell || \mathbf{C}^{(t)} || \ell' \rangle \langle \ell' | \mathbf{C}^{(1)} | \ell'' \rangle \langle \ell'' | \mathbf{C}^{(2)} | \ell \rangle \begin{pmatrix} t & 1 & 1 \\ p & \rho & -q \end{pmatrix} \\
& \times \left\{ \begin{matrix} t & 1 & 1 \\ \ell'' & \ell & \ell' \end{matrix} \right\} \left\{ \begin{matrix} 2 & 1 & 1 \\ \ell & \ell'' & \ell \end{matrix} \right\} \langle 4f^6 {}^7F_0 | W_0^{(11)0} | 4f^6 {}^5D_0 \rangle
\end{aligned} \tag{4.53}$$

This term, coupled back with the nuclear spin \vec{I} can allow to calculate the transition amplitude between the hyperfine states of the 7F_0 hyperfine multiplet, and the hyperfine states of the 5D_0 hyperfine multiplet (and reciprocally) since we have

$$\begin{aligned}
\Gamma_{\rho}(M_I, M'_I) &= \sum_q (-1)^q \langle 4f^6 {}^7F_0 M_I | {}^{0\leftrightarrow 0}\mathcal{T}_{\rho,q} I_{-q}^{(1)} | 4f^6 {}^5D_0 M'_I \rangle \\
&= \frac{\sqrt{210}}{2} (-1)^{5/2-M_I} \sum_q (-1)^q \begin{pmatrix} I & 1 & I \\ -M_I & q & M'_I \end{pmatrix} \langle 4f^6 {}^7F_0 M_I | {}^{0\leftrightarrow 0}\mathcal{T}_{\rho,q} | 4f^6 {}^5D_0 M'_I \rangle.
\end{aligned} \tag{4.54}$$

From this expression, one can observe there is a direct link between the hyperfine Stark effect and the hyperfine-induced luminescence, and that the effective operator formalism also provides a way to calculate nuclear-spin-dependent transition amplitudes between hyperfine states of different electronic manifolds.

One can envision, after careful consideration of the selection rules, and a characterisation of the interplay between ρ and q in the effective operators, a way to control the population of the hyperfine states of the 7F_0 and 5D_0 hyperfine multiplets, similarly to the control of the hyperfine states of the 7F_6 hyperfine multiplet in the case of Tb^{3+} in TbPc_2 .

Main takeaways from Chapter 4

- **Odd Ligand Field Parameters and Judd-Ofelt Theory:**

- Odd ligand field parameters (LFPs) are necessary to couple electronic configurations of different parities, such as $4f^n$ and $4f^{n-1}5d$.
- Such odd LFPs exist only in complexes lacking inversion symmetry.
- The Judd-Ofelt theory explains the intensity of electric dipole transitions in rare-earth ions by considering configuration mixing induced by ligand fields.
- It uses second-order perturbation theory to account for otherwise forbidden $f - f$ transitions.
- Introduces effective operators that allow calculation of transition amplitudes between perturbed states.

- **Hyperfine Stark Effect and Double Perturbation Theory:**

- Electric fields can modulate hyperfine transitions by affecting the hyperfine constant.
- Double perturbation theory extends the Judd-Ofelt framework to include hyperfine interactions.
- Effective operators are derived to describe the hyperfine Stark effect.
- The presence of certain odd ligand field parameters is crucial for enabling the hyperfine Stark effect.

- **Hyperfine-Induced Luminescence:**

- Effective operator formalism can be applied to hyperfine-induced luminescence.
- Allows calculation of nuclear-spin-dependent transition amplitudes.
- Demonstrates a connection between hyperfine Stark effect and hyperfine-induced luminescence.

- **Applicability to Lanthanide based Quantum Technologies:**

- Both Hyperfine Stark effect and Hyperfine-induced luminescence have been used or proposed as a way to control qubits.
- Theoretical framework developed in this chapter can be used to understand and predict the behavior of lanthanides in such systems.

Conclusion

In this part, we have laid out the theoretical foundation necessary to understand the behavior of lanthanides, starting from their atomistic characteristics to their interactions within molecular environments. The unique electronic configuration of lanthanides, particularly the shielding of the $4f$ valence shell by the $5s$ and $5p$ shells, allows us to treat them as atomically free yet chemically influenced entities—a central theme throughout the chapters. This shielding effect not only influences their chemical reactivity but also makes lanthanides a fascinating case study for understanding the delicate balance between isolated atomic properties and environmental interactions.

We began by exploring the physics of a single, isolated lanthanide atom or ion, focusing on the angular degrees of freedom of electronic Slater determinants. This foundational perspective provided insights into how antisymmetrization affects the wavefunctions due to the fermionic nature of electrons. The proper treatment of electronic wavefunctions and the careful consideration of symmetry are essential for capturing the quantum behavior of these complex elements. This allowed us to calculate the matrix elements of various operators, as well as the selection rules governing electronic transitions in free lanthanides. Understanding these individual atomic properties set the stage for describing more complex systems, particularly when lanthanides are embedded in environments where symmetry is broken or modified.

Building on this atomistic understanding, the second chapter introduced Crystal Field Theory (CFT) and Ligand Field Theory (LFT). CFT offered a simplified model of electrostatic interactions between the lanthanide ion and surrounding ligands by treating ligands as point charges. This model was instrumental in providing a qualitative picture of how the $4f$ free-atom orbital degeneracy is lifted by the presence of an electrostatic potential from surrounding ligands. However, the limitations of CFT, particularly its inability to account for the covalent nature of interactions, necessitated the use of Ligand Field Theory (LFT). LFT expanded upon CFT by incorporating the covalent aspects of bonding between the lanthanide ions and their ligands. This more sophisticated approach enabled a deeper understanding of the influence of covalency and orbital overlap on the electronic structure of lanthanides. The inclusion of computational methods, such as Density Functional Theory (DFT), demonstrated how theoretical constructs could be employed to simulate real-world properties effectively, and in particular we presented a theoretical framework to calculate the ligand field parameters for lanthanide complexes, and in particular odd-rank ligand field parameters that are crucial for the optical and electrical properties of lanthanides.

In the third chapter, we shifted our focus to the concept of effective operators and the utilization of Racah algebra to derive the selection rules for highly forbidden transitions in lanthanide ions and showed the ubiquity of odd-rank ligand field parameters in the understanding of those transitions. The use of Racah algebra and perturbation theory helped in deriving selection rules that dictate the conditions under which electronic transitions can occur. The introduction of effective operators allowed us to simplify the complex interactions within lanthanide systems, providing a practical means of calculating transition selection rules in otherwise intractable or barely-tractable systems. These methods were particularly useful for understanding transitions implying an external electric field.

These insights were introduced through discussions on the Judd-Ofelt and Wybourne-Downer theory. The Judd-Ofelt theory provided a framework for calculating the intensities of electric dipole transitions by considering configuration mixing, which allows otherwise forbidden transitions to occur. This theoretical framework was essential in quantifying the effects of ligand fields on transition intensities, thereby offering predictive power regarding the optical properties of lanthanide complexes. The Wybourne-Downer theory, on the other hand, extended this framework by considering additional perturbations such as spin-orbit coupling, thereby broadening the scope of allowed transitions and offering a more comprehensive picture of the behavior of lanthanide ions in various environments.

The chapter also examined the hyperfine Stark effect, an extremely important phenomenon observed by our collaborators from the Wernsdorfer group in Grenoble and Karlsruhe, which are the fundamental property allowing for fast and efficient control of the hyperfine levels, and that permitted for the first experimental implementation of a quantum algorithm in a molecular qubit. The hyperfine interactions are sensitive to external electric fields, which can modify the hyperfine constants and thus influence the energy levels of the ion. This analysis leveraged multi-perturbation theory to understand how electric fields drive hyperfine transitions by considering, again, odd ligand field parameters. The effective operator formalism is therefore instrumental in calculating the transition amplitudes between hyperfine states, thereby providing a theoretical basis for understanding the hyperfine Stark effect in lanthanides. This effect was further linked to the hyperfine-induced luminescence, where the population of hyperfine states could be selectively controlled through Spectral Hole Burning (SHB) experiments. While the derived form of the effective hyperfine Stark operator can only discriminate which transitions are allowed and which are not, the aim for future works is to couple this with the LFDFT method from the previous subsection to calculate the exact values of the effective operators, and thus the exact values of the hyperfine Stark effect in a given system.

Overall, this part of the thesis has provided a comprehensive view of lanthanides as atomic systems influenced by their chemical environment, starting from an isolated atom to more complex interactions with ligands and external fields. The theoretical tools developed here—ranging from angular momentum frameworks, ligand field interactions, to perturbative approaches—serve as a robust foundation for understanding the electronic structure and transitions in lanthanides. By combining a fundamental understanding of atomic structure with sophisticated models for environmental interactions, we have built a framework that captures the essential physics governing the behavior of lanthanide complexes.

These insights pave the way for practical applications in a variety of fields. The understanding of forbidden transitions and their enhancement through ligand interactions has implications for designing luminescent materials, which are central to applications in lighting, displays, and biological imaging. Furthermore, the detailed analysis of hyperfine interactions and electric field effects offers promising avenues for the development of quantum computing technologies, where lanthanide ions and their nuclei could serve as stable, optically addressable qubits.

References of this part

- [26] Thiele, S.; Balestro, F.; Ballou, R.; Klyatskaya, S.; Ruben, M.; Wernsdorfer, W. “Electrically driven nuclear spin resonance in single-molecule magnets”, *Science (New York, N.Y.)*, 2014, *344*:6188, 1135–1138.
- [43] Hartree-Fock-Bogoliubov results based on the Gogny force https://www-phynu.cea.fr/science_en_ligne/carte_potentiels_microscopiques/carte_potentiel_nucleaire_eng.htm (accessed 08/15/2024).
- [66] Ramanantoanina, H.; Urland, W.; García-Fuente, A.; Cimpoesu, F.; Daul, C. “Ligand field density functional theory for the prediction of future domestic lighting”, *Physical Chemistry Chemical Physics*, 2014, *16*:28, 14625–14634.
- [72] Bethe, H. “Termaufspaltung in kristallen”, *Annalen der Physik*, 1929, *395*:2, 133–208.
- [73] Bethe, H. “Zur Theorie des Zeemaneffektes an den Salzen der seltenen Erden”, *Zeitschrift für Physik*, 1930, *60*:3, 218–233.
- [74] Van Vleck, J. “Valence strength and the magnetism of complex salts”, *The Journal of Chemical Physics*, 1935, *3*:12, 807–813.
- [99] Godfrin, C.; Ferhat, A.; Ballou, R.; Klyatskaya, S.; Ruben, M.; Wernsdorfer, W.; Balestro, F. “Operating Quantum States in Single Magnetic Molecules: Implementation of Grover’s Quantum Algorithm”, *Physical Review Letters*, 2017, *119*:18, 187702.
- [101] Kumar, K. S.; Serrano, D.; Nonat, A. M.; Heinrich, B.; Karmazin, L.; Charbonnière, L. J.; Goldner, P.; Ruben, M. “Optical spin-state polarization in a binuclear europium complex towards molecule-based coherent light-spin interfaces”, *Nature Communications*, 2021, *12*:1, 2152.
- [102] Moreno-Pineda, E.; Godfrin, C.; Balestro, F.; Wernsdorfer, W.; Ruben, M. “Molecular Spin Qudits for Quantum Algorithms”, *Chemical Society Reviews*, 2018, *47*:2, 501–513.
- [103] Thiele, S. Read-out and coherent manipulation of an isolated nuclear spin using a single molecule magnet spin transistor, Ph.D. Thesis, Université de Grenoble, 2014.
- [104] Godfrin, C. Quantum information processing using a molecular magnet single nuclear spin qudit, These de doctorat, Université Grenoble Alpes (ComUE), 2017.
- [107] Dieke, G. H.; Crosswhite, H. M. “The Spectra of the Doubly and Triply Ionized Rare Earths”, *Applied Optics*, 1963, *2*:7, 675–686.
- [108] Wybourne, B. G.; Smentek, L., *Optical Spectroscopy of Lanthanides: magnetic and hyperfine interactions*. CRC Press: S.I., 2019.
- [109] Tuszynski, J. A., *Spherical tensor operators: tables of matrix elements and symmetries*; World Scientific: 1990.
- [110] Cowan, R. D., *The Theory of Atomic Structure and Spectra*; University of California Press: 2023; 764 pp.
- [111] Nielson, C.; Koster, G., *Spectroscopic Coefficients for the Pn, Dn, and Fn Configurations*; M.I.T. Press: 1963.
- [112] Condon, E. U.; Odabasi, H., *Atomic Structure*; CUP Archive: 1980; 684 pp.
- [113] Rudzikas, Z., *Theoretical Atomic Spectroscopy*; Cambridge University Press: 2007; 466 pp.

- [114] Judd, B. R., *Operator Techniques in Atomic Spectroscopy*; Princeton University Press: 2014; 302 pp.
- [115] Jucis, A. P.; Savukinas, A. J., *Matematicheskiye osnovi teorii atoma*; Izdat "Mintis": 1973; 479 pp.
- [116] Tuszyński, J. A. "The action of product tensor operators within and between pure and mixed configurations", *The Journal of Chemical Physics*, 1986, *85*:7, 3950–3963.
- [117] Watanabe, H., *Operator methods in ligand field theory*; Englewood Cliffs, N.J., Prentice-Hall: 1966; 218 pp.
- [118] Ramanantoanina, H. "A DFT-based theoretical model for the calculation of spectral profiles of lanthanide M4,5-edge x-ray absorption", *The Journal of Chemical Physics*, 2018, *149*:5, 054104.
- [119] Van Lenthe, E. The ZORA equation. Ph.D. Thesis, Vrije Universiteit Amsterdam, 1996.
- [120] Ramanantoanina, H.; Urland, W.; Cimpoesu, F.; Daul, C. "The angular overlap model extended for two-open-shell f and d electrons", *Physical Chemistry Chemical Physics*, 2014, *16*:24, 12282–12290.
- [121] Suta, M.; Cimpoesu, F.; Urland, W. "The angular overlap model of ligand field theory for f elements: An intuitive approach building bridges between theory and experiment", *Coordination Chemistry Reviews*, 2021, *441*, 213981.
- [122] Ramanantoanina, H.; Studniarek, M.; Daffé, N.; Dreiser, J. "Non-empirical calculation of X-ray magnetic circular dichroism in lanthanide compounds", *Chemical Communications*, 2019, *55*:20, 2988–2991.
- [123] Ramanantoanina, H.; Daul, C. "A non-empirical calculation of 2p core-electron excitation in compounds with 3d transition metal ions using ligand-field and density functional theory (LFDFT)", *Physical Chemistry Chemical Physics*, 2017, *19*:31, 20919–20929.
- [124] DLMF: Chapter 34 3j,6j,9j Symbols <https://dlmf.nist.gov/34> (accessed 08/11/2024).
- [125] Walsh, B. M. In *Advances in Spectroscopy for Lasers and Sensing*, ed. by Di Bartolo, B.; Forte, O., Springer Netherlands: Dordrecht, 2006, pp 403–433.
- [126] Jørgensen, C. K.; Judd, B. R. "Hypersensitive pseudoquadrupole transitions in lanthanides", *Molecular Physics*, 1964.
- [127] Tanaka, M.; Kushida, T. "Interference between Judd-Ofelt and Wybourne-Downer mechanisms in the $\{^5D\}_{-0} \rightarrow \{^7F\}_{-\mathit{J}}$ ($J=2,4$) transitions of $\{\mathrm{Sm}\}^{2+}$ in solids", *Physical Review B*, 1996, *53*:2, 588–593.
- [128] Binnemans, K. "Interpretation of europium(III) spectra", *Coordination Chemistry Reviews*, 2015, *295*, 1–45.
- [129] Godfrin, C.; Ballou, R.; Bonet, E.; Ruben, M.; Klyatskaya, S.; Wernsdorfer, W.; Balestro, F. "Generalized Ramsey interferometry explored with a single nuclear spin qudit", *npj Quantum Information*, 2018, *4*:1, 1–7.
- [130] Ord-Smith, R. J. "The Symmetry Relations of the $12j$ Symbol", *Physical Review*, 1954, *94*:5, 1227–1228.

Configuration	Number of Terms	Spectroscopic Terms
f^0, f^{14}	1	1S
f^1, f^{13}	1	2F
f^2, f^{12}	7	$^1I, ^3H, ^1G, ^3F, ^1D, ^3P, ^1S$
f^3, f^{11}	17	$^2L, ^2K, ^4I, ^2I, ^2H, ^2H, ^4G, ^2G, ^2G, ^4F$ $^2F, ^2F, ^4D, ^2D, ^2D, ^4S, ^2P$
f^4, f^{10}	47	$^1N, ^3M, ^3L, ^5I, ^1L, ^1L, ^3K, ^3K, ^1K, ^3I$ $^3I, ^5G, ^1I, ^1I, ^1I, ^3H, ^3H, ^3H, ^3H, ^3G$ $^3G, ^3G, ^5F, ^1H, ^1H, ^5D, ^1G, ^1G, ^1G, ^1G$ $^3F, ^3F, ^3F, ^3F, ^1F, ^3D, ^3D, ^5S, ^1D, ^1D$ $^1D, ^1D, ^3P, ^3P, ^3P, ^1S, ^1S$
f^5, f^9	73	$^2O, ^2N, ^4M, ^2M, ^2M, ^4L, ^2L, ^2L, ^2L, ^4K$ $^4K, ^6H, ^2K, ^2K, ^2K, ^2K, ^2K, ^4I, ^4I, ^4I$ $^4H, ^4H, ^4H, ^2I, ^2I, ^2I, ^2I, ^2I, ^6F, ^4G$ $^4G, ^4G, ^4G, ^2H, ^2H, ^2H, ^2H, ^2H, ^2H, ^2H$ $^4F, ^4F, ^4F, ^4F, ^2G, ^2G, ^2G, ^2G, ^2G, ^2G$ $^6P, ^4D, ^4D, ^4D, ^2F, ^2F, ^2F, ^2F, ^2F, ^2F$ $^2F, ^4P, ^4P, ^2D, ^2D, ^2D, ^2D, ^2D, ^2D, ^2P, ^2P$ $^2P, ^2P, ^4S$
f^6, f^8	119	$^1Q, ^3O, ^3N, ^5L, ^1N, ^1N, ^3M, ^3M, ^3M, ^5K$ $^1M, ^1M, ^3L, ^3L, ^3L, ^3K, ^3K, ^3K, ^3K, ^3K$ $^3K, ^5I, ^5I, ^1L, ^1L, ^1L, ^1L, ^5H, ^5H, ^1K$ $^1K, ^1K, ^3I, ^3I, ^3I, ^3I, ^3I, ^3I, ^7F, ^5G$ $^5G, ^5G, ^1I, ^1I, ^1I, ^1I, ^1I, ^1I, ^1I, ^3H$ $^3H, ^3H, ^3H, ^3H, ^3H, ^3H, ^3H, ^3H, ^5F, ^5F$ $^1H, ^1H, ^1H, ^1H, ^3G, ^3G, ^3G, ^3G, ^3G, ^3G$ $^3G, ^5D, ^5D, ^5D, ^1G, ^1G, ^1G, ^1G, ^1G, ^1G$ $^1G, ^1G, ^3F, ^3F, ^3F, ^3F, ^3F, ^3F, ^3F, ^3F$ $^3F, ^5P, ^1F, ^1F, ^1F, ^1F, ^3D, ^3D, ^3D, ^3D$ $^3D, ^5S, ^1D, ^1D, ^1D, ^1D, ^1D, ^1D, ^3P, ^3P$ $^3P, ^3P, ^3P, ^3P, ^1P, ^1S, ^1S, ^1S, ^1S$
f^7	119	$^2Q, ^2O, ^4N, ^2N, ^2N, ^4M, ^2M, ^2M, ^2M, ^2M$ $^4L, ^4L, ^4L, ^6I, ^4K, ^4K, ^4K, ^2L, ^2L, ^2L$ $^2L, ^2L, ^6H, ^4I, ^4I, ^4I, ^4I, ^2K, ^2K$ $^2K, ^2K, ^2K, ^2K, ^2K, ^6G, ^4H, ^4H, ^4H, ^4H$ $^4H, ^2I, ^2I, ^2I, ^2I, ^2I, ^2I, ^2I, ^2I$ $^6F, ^4G, ^4G, ^4G, ^4G, ^4G, ^4G, ^4G, ^2H, ^2H$ $^2H, ^2H, ^2H, ^2H, ^2H, ^2H, ^2H, ^6D, ^2G, ^2G$ $^2G, ^2G, ^2G, ^2G, ^2G, ^2G, ^2G, ^4F, ^4F$ $^4F, ^4F, ^4F, ^6P, ^8S, ^2F, ^2F, ^2F, ^2F, ^2F$ $^2F, ^2F, ^2F, ^2F, ^2F, ^4D, ^4D, ^4D, ^4D, ^4D$ $^4D, ^2D, ^2D, ^2D, ^2D, ^2D, ^2D, ^2D, ^4P, ^4P$ $^4S, ^4S, ^2P, ^2P, ^2P, ^2P, ^2P, ^2S, ^2S$

Table 4.2: Spectroscopic terms for $\ell = 3$

PART II

The Hyperfine Interaction

5	The Dirac equation	91
5.1	Introducing relativity into the Schrödinger equation	91
5.2	Adding external fields: The single-electron ion	94
5.3	Beyond the Dirac equation	96
6	The finite nucleus	99
6.1	Mass corrections	99
6.2	Muonic ions	99
6.3	The nuclear charge distribution	100
6.4	The nuclear current distribution	110
6.5	Other effects of the nucleus	120
7	Hyperfine constants	125
7.1	The hyperfine dipole constant	125
7.2	The hyperfine quadrupole constant	130
7.3	Isotope Shifts	132
7.4	The non-relativistic limit	135
7.5	Hyperfine constants in matter	141
8	The electron/muon as a nuclear probe: hydrogen-like Dy ions	143
8.1	Wavefunctions of the electron and muon in H-like ions	143
8.2	Muonic and electronic H-like energy levels	144
8.3	Hyperfine isotope shifts of $^{161/163}\text{Dy}^{65+}$	151
8.4	Additional examples of $^{159}\text{Tb}^{64+}$ and $^{165}\text{Ho}^{66+}$	163

The Hyperfine Interaction

*"To see a World in a Grain of Sand, And a Heaven in a Wild Flower
Hold Infinity in the palm of your hand, And Eternity in an hour."*

– William Blake, *Auguries of Innocence*

The characteristic length scale of an electron within an atom is on the order of the Bohr radius, $a_0 \sim 10^{-10}$ m, whereas the characteristic length scale of a nucleus is on the order of the Fermi radius, $r_0 \sim 10^{-15}$ m. This section aims to explore the intricate interplay between these two scales: the electron and the nucleus, using tools from both atomic physics and low-energy nuclear physics. By collaborating with nuclear physicists, who provided detailed magnetization and charge distributions for various lanthanide nuclei, we have applied these insights to the approach of isotopologue engineering of nuclear molecular qubits in our group. This work is an example of multiscale physics, where the hyperfine interaction is analyzed from the perspectives of atomic physics, nuclear physics, and, within the larger scope of this project, quantum chemistry. This part then offers a coherent understanding of this interaction across different scales.

The hyperfine interaction, a relativistic phenomenon, arises from the interaction between the electron's magnetic moment and the magnetic field generated by the nucleus. This interaction governs the energy levels of the ground-state lanthanides in the organic complexes studied throughout this PhD thesis. To lay the foundation for this exploration, we begin by revisiting the Dirac equation and introducing the hyperfine interaction, subsequently deriving the effective Hamiltonian that describes the hyperfine interaction in the atomic physics context.

In parallel, the study of highly charged electronic and muonic hydrogen-like ions presents a valuable approach for probing the internal structure of atomic nuclei. Here, we extend the discussion of hyperfine interactions to the realm of low-energy nuclear physics, demonstrating how these interactions can reveal valuable information about the hyperfine structure of selected hydrogen-like lanthanide ions. This analysis includes a focus on muonic ions, which are particularly effective for investigating nuclear charge distributions. By employing nuclear simulations based on a modified Skyrme-Hartree-Fock model with BCS corrections, we illustrate how small changes in nuclear charge, such as the addition of nucleons, significantly impact the hyperfine structure of lanthanides. This approach is especially useful in modeling highly deformed nuclei, with a focus on isotopes such as $^{161}\text{Dy}^{66+}$, $^{163}\text{Dy}^{65+}$, $^{159}\text{Tb}^{64+}$, and $^{165}\text{Ho}^{66+}$, all of which are promising candidates for nuclear qubits.

This work also involves calculating the hyperfine splitting of electronic and muonic hydrogen-like ions, while incorporating crucial finite volume corrections, such as the Bohr-Weisskopf and Breit-Rosenthal effects. These corrections refine our understanding of nuclear magnetic and quadrupole moments by accounting for how the electron and muon wavefunctions penetrate the nuclear charge and magnetic dipole densities.

Furthermore, the multipole expansion method, which has already proven useful in earlier chapters e.g. in Ligand Field Theory, plays a critical role in this analysis as well. It serves as a unifying mathematical

framework that can be applied across different domains, linking atomic and nuclear physics as well as quantum chemistry. Through this part, let us deepen our understanding of nuclear properties but also demonstrate how subtle changes within the nucleus can have profound effects on atomic behavior.

Chapter Contents

5.1	Introducing relativity into the Schrödinger equation	91
5.2	Adding external fields: The single-electron ion	94
5.3	Beyond the Dirac equation	96

CHAPTER 5

The Dirac equation

"The electron and its spin are like a rotating ball and its angular momentum, except the electron is neither a ball nor a rotating object."

– A spherical cow in a vacuum somewhere, probably

The Dirac equation, formulated by Paul Dirac in 1928 [46], is a relativistic quantum mechanical wave equation that describes the behavior of spin-1/2 fermions. It is a generalization of the Schrödinger equation that incorporates special relativity in its formulation. The Dirac equation of a free electron is given by

$$(i\hbar\gamma^\mu\partial_\mu - mc)\psi = 0, \quad (5.1)$$

where γ^μ are the Dirac matrices, ∂_μ is the four-gradient operator, m is the mass of the particle, c is the speed of light, and ψ is the wave function of the particle. The Dirac matrices are defined as

$$\gamma^0 = \begin{pmatrix} \mathbb{1} & 0 \\ 0 & -\mathbb{1} \end{pmatrix}, \quad \gamma^i = \begin{pmatrix} 0 & \sigma^i \\ -\sigma^i & 0 \end{pmatrix}, \quad (5.2)$$

where $\mathbb{1}$ is the identity matrix and σ^i are the Pauli matrices. One can also define $\alpha \equiv \begin{pmatrix} 0 & \sigma^i \\ \sigma^i & 0 \end{pmatrix}$ and $\beta \equiv \gamma^0$. The Dirac equation can be expanded as

$$(c\vec{\alpha} \cdot \vec{p} + mc^2\beta)\psi = \begin{pmatrix} mc^2 & c\vec{\sigma} \cdot \vec{p} \\ c\vec{\sigma} \cdot \vec{p} & -mc^2 \end{pmatrix} \begin{pmatrix} u \\ v \end{pmatrix} = i\hbar\frac{\partial}{\partial t} \begin{pmatrix} u \\ v \end{pmatrix}, \quad (5.3)$$

where $\vec{\sigma}$ are the Pauli matrices in a vector form, \vec{p} is the momentum operator, and u and v are the upper and lower components of the wave function, respectively.

5.1 Introducing relativity into the Schrödinger equation

5.1.1 The Klein-Gordon equation

To see how Dirac arrived at the Dirac equation, a brief overview of the Schrödinger equation and the Klein-Gordon equation is necessary. The Schrödinger equation is a non-relativistic quantum mechanical wave equation that describes the behavior of particles on the microscopic scale. It is given by

$$i\hbar\frac{\partial}{\partial t}\psi = H\psi, \quad (5.4)$$

with H being the Hamiltonian operator. The Hamiltonian operator for a free particle is given by

$$H = \frac{p^2}{2m}, \quad (5.5)$$

where $p \equiv -i\hbar\nabla$ is the momentum operator and m is the mass of the particle.

The Schrödinger equation is not compatible with special relativity, as it is not Lorentz invariant. To introduce relativity into the Schrödinger equation, one can use the Klein-Gordon equation, which is a relativistic wave equation that describes the behavior of spin-0 particles. The Klein-Gordon equation is given by

Definition: (*Klein-Gordon equation*)

$$\left(\frac{1}{c^2} \frac{\partial^2}{\partial t^2} - \nabla^2 + \frac{m^2 c^2}{\hbar^2} \right) \psi = 0. \quad (5.6)$$

Or, more compactly,

$$\left(\square + \frac{m^2 c^2}{\hbar^2} \right) \psi = 0, \quad (5.7)$$

where $\square \equiv \frac{1}{c^2} \frac{\partial^2}{\partial t^2} - \nabla^2$ is the d'Alembertian operator.

The Klein-Gordon equation is compatible with special relativity, but it has some issues, such as negative probabilities and the lack of a spin term. Moreover, it is a second-order differential equation, compared to the first-order Schrödinger equation.

A naive approach would be to do the identification between observables and operators in (5.6) and (5.7)

$$E^2 = (\vec{p})^2 c^2 + m^2 c^4 = c^2 \square + m^2 c^4, \quad (5.8)$$

and, therefore, one could find a first-order operator similar to the Hamiltonian operator in (5.5) by taking the square root of the Klein-Gordon operator. This approach, used in [131] for example, necessitates the application of advanced tools from linear algebra, which falls beyond the scope of this work.

5.1.2 The Dirac equation

Another approach to arrive at a first-order relativistic wave equation is, instead of calculating the square root directly, to find an operator Γ , that when squared gives the Klein-Gordon operator and

$$i\hbar \frac{\partial}{\partial t} \psi = \Gamma \psi. \quad (5.9)$$

Dirac postulated that Γ takes the form

$$\Gamma^\mu = \vec{\Gamma} \cdot \vec{p} + \Gamma_0 m c^2. \quad (5.10)$$

This expression can be squared to try and compute the components of Γ^μ , using (5.6) and (5.9):

$$(\Gamma^\mu)^2 \psi = (\vec{p})^2 c^2 \psi + m^2 c^4 \psi \quad (5.11)$$

i.e.

$$\sum_{j,k=1}^3 \frac{\{\Gamma_j, \Gamma_k\}}{2} p_j p_k + \sum_{k=1}^3 m c^2 \{\Gamma_0, \Gamma_k\} = \sum_{i=1}^3 p_i^2 c^2 + m^2 c^4 \quad (5.12)$$

this imposes conditions on the anticommutation relations of the components of Γ^μ , which are given by $\forall 1 \leq j, k \leq 3$,

$$\{\Gamma_k, \Gamma_j\} = 2c^2\delta_{kj}, \quad \{\Gamma_k, \Gamma_0\} = 0 \quad \text{and} \quad \Gamma_0^2 = 1. \quad (5.13)$$

No scalar operator can satisfy these conditions, therefore, the components of Γ must be matrices. Moreover, it can be demonstrated that the Γ matrices must be $4k \times 4k$ complex matrices, and for $k = 1$, the Γ matrices are given by

$$\Gamma_0 = \begin{pmatrix} \mathbb{1} & 0 \\ 0 & -\mathbb{1} \end{pmatrix} \equiv \beta, \quad \Gamma_i = \begin{pmatrix} 0 & c\sigma_i \\ c\sigma_i & 0 \end{pmatrix} \equiv c\alpha_i. \quad (5.14)$$

The Dirac equation is then obtained by considering that $k = 1$ solution, leading to

Definition: (*Dirac equation*)

$$(c\vec{\alpha} \cdot \vec{p} + \beta mc^2) \psi = i\hbar \frac{\partial}{\partial t} \psi. \quad (5.15)$$

The dimensions of the matrices requires that the wavefunction ψ is a statevector with 4 components, or bispinor. The 2×2 block diagonal form of the Dirac matrices allows one to write the Dirac equation as a system of two equations, coupling the upper and lower components of the wavefunction

$$\begin{aligned} (c(\vec{\sigma} \cdot \vec{p})v(\vec{r}, t) + mc^2u(\vec{r}, t)) &= i\hbar \frac{\partial}{\partial t} u(\vec{r}, t), \\ (c(\vec{\sigma} \cdot \vec{p})u(\vec{r}, t) - mc^2v(\vec{r}, t)) &= i\hbar \frac{\partial}{\partial t} v(\vec{r}, t), \end{aligned} \quad (5.16)$$

with $\psi \equiv \begin{pmatrix} u \\ v \end{pmatrix}$, both u and v being two-component statevectors, or spinors.

By looking for stationary solutions of the decoupled Dirac equation

$$\begin{aligned} (c(\vec{\sigma} \cdot \vec{p})v(\vec{r}) + mc^2u(\vec{r})) &= Eu(\vec{r}), \\ (c(\vec{\sigma} \cdot \vec{p})u(\vec{r}) - mc^2v(\vec{r})) &= Ev(\vec{r}), \end{aligned} \quad (5.17)$$

two solutions arise for the eigenenergy,

$$E = \pm \sqrt{c^2p^2 + m^2c^4}, \quad (5.18)$$

corresponding to the positive and negative energy solutions of the Dirac equation, with eigenvectors

$$\psi_+ = \begin{pmatrix} u \\ \frac{c(\vec{\sigma} \cdot \vec{p})}{E + mc^2} u \end{pmatrix} \quad \text{and} \quad \psi_- = \begin{pmatrix} \frac{c(\vec{\sigma} \cdot \vec{p})}{E - mc^2} v \\ v \end{pmatrix}. \quad (5.19)$$

The positive energy solutions correspond, in the non-relativistic limit, to the electron. The negative energy solutions were initially considered as unphysical, but Dirac showed that they correspond, in the non-relativistic limit, to the positron, the antiparticle of the electron. Moreover, the two components of the spinors correspond to the two possible spin states of the electron, with u and v corresponding to spin up and spin down, respectively.

The Dirac equation predicts therefore the existence of antiparticles, which were later discovered experimentally by Carl Anderson in 1932 [132] but also predicts the intrinsic property of the electron, the spin, which was confirmed earlier by the Stern-Gerlach experiment in 1922 [133].

5.2 Adding external fields: The single-electron ion

5.2.1 The Dirac equation with external electromagnetic fields

The Dirac equation can be extended to include the interaction of an electron with external fields through the minimal coupling principle. This principle involves replacing the momentum operator \vec{p} with $\vec{p} - e\vec{A}(\vec{r}, t)$, where $\vec{A}(\vec{r}, t)$ is the vector potential of the electromagnetic field, and $e < 0$ is the charge of the electron. Additionally, the scalar potential $\Phi(\vec{r}, t)$ can be incorporated into the Dirac equation. Thus, the Dirac equation with external electromagnetic fields is expressed as:

Definition: (*Dirac equation with external electromagnetic fields*)

$$\left(c\vec{\alpha} \cdot (\vec{p} - e\vec{A}(\vec{r}, t)) + \beta mc^2 + e\phi(\vec{r}, t) \right) \psi(\vec{r}, t) = i\hbar \frac{\partial}{\partial t} \psi(\vec{r}, t), \quad (5.20)$$

Note: This equation is invariant under the gauge transformation

$$\begin{aligned} \vec{A}(\vec{r}, t) &\rightarrow \vec{A}(\vec{r}, t) + \vec{\nabla} \frac{\hbar}{e} \theta(\vec{r}, t), \\ \phi(\vec{r}, t) &\rightarrow \phi(\vec{r}, t) - \frac{\hbar}{e} \frac{\partial}{\partial t} \theta(\vec{r}, t), \\ \psi(\vec{r}, t) &\rightarrow e^{i\theta(\vec{r}, t)} \psi(\vec{r}, t). \end{aligned} \quad (5.21)$$

Equation (5.20) now allows one to go beyond the free electron case and study the interaction of the electron with external fields. This is particularly important in the context of atomic physics, where the electron interacts with the electromagnetic field of, for example, the nucleus.

5.2.2 The Dirac equation for a single-electron ion

Let's consider the simple case of a single-electron ion, where the electron interacts with the electromagnetic field of a point nucleus. The only external field considered is the radial Coulomb field of the nucleus, which is given by

$$\begin{aligned} \vec{A}(\vec{r}, t) &= 0, \\ \Phi(\vec{r}, t) &= \phi(r), \end{aligned} \quad (5.22)$$

The Dirac equation for a single-electron ion is then given by

$$(c\vec{\alpha} \cdot \vec{p} + \beta mc^2 + e\phi(r)) \psi(\vec{r}, t) = i\hbar \frac{\partial}{\partial t} \psi(\vec{r}, t). \quad (5.23)$$

It can be shown [134], that since the electric potential is spherically symmetric, the eigenfunctions of the Dirac equation can be written as

$$\psi_{n\kappa, m_j}(\vec{r}) = \begin{pmatrix} g_{n\kappa}(r) \chi_{\kappa, m_j}(\theta, \phi) \\ i f_{n\kappa}(r) \chi_{-\kappa, m_j}(\theta, \phi) \end{pmatrix} \equiv \frac{1}{r} \begin{pmatrix} i P_{n\kappa}(r) \chi_{\kappa, m_j}(\theta, \phi) \\ Q_{n-\kappa}(r) \chi_{-\kappa, m_j}(\theta, \phi) \end{pmatrix}, \quad (5.24)$$

where $\chi_{\kappa, m_j}(\theta, \phi)$ are the two-component spin-angular eigenfunctions, $g_{n\kappa}$ (resp. $P_{n\kappa}$) and $f_{n\kappa}$ (resp. $Q_{n\kappa}$) are radial functions, n is the principal quantum number, and κ and m_j are the relativistic quantum numbers. The spin-angular eigenfunctions are related to the spinor spherical harmonics Ω_{κ, m_j} introduced by [135], and the spherical harmonics $Y_m^{(l)}$ by the relation

$$\chi_{\kappa, m_j}(\theta, \phi) = \Omega_{\kappa, m_j}(\theta, \phi) = \sum_{m_s} C(l, \frac{1}{2}j; m_j - m_s, m_s) Y_{m_j - m_s}^{(l)}(\theta, \phi) \chi_{m_s}, \quad (5.25)$$

where $C(l\frac{1}{2}j; m_j - m_s, m_s)$ are the Clebsch-Gordan coefficients defined in (D.8), l is the orbital quantum number, j is the total angular momentum quantum number, and m_s is the spin quantum number, the eigenvalue of the spin operator whose eigenfunctions are the spinors χ_{m_s} .

Assuming a point-like, infinitely massive nucleus, the electric potential energy is given by $e\phi(r) = -\frac{Ze^2}{4\pi\epsilon_0 r}$ where Z is the atomic number of the nucleus, e is the charge of the electron, r is the distance between the electron and the nucleus, and ϵ_0 is the vacuum permittivity. The Dirac equation for a single-electron ion then becomes

$$\left(c\vec{\alpha} \cdot \vec{p} + \beta mc^2 - \frac{Ze^2}{4\pi\epsilon_0 r} \right) \psi(\vec{r}, t) = i\hbar \frac{\partial}{\partial t} \psi(\vec{r}, t). \quad (5.26)$$

The radial functions $P_{n\kappa}(r)$ and $Q_{n-\kappa}(r)$ in (5.24), are then solutions of the radial Dirac equation, which can be obtained by substituting (5.19) into (5.23) and separating the radial and angular parts of the equation.

$$\begin{aligned} -\left(\frac{d}{dr} + \frac{\kappa}{r} \right) P_{n\kappa}(r) + \left(\frac{Z\alpha}{r} - \frac{mc^2}{\hbar c} \right) Q_{n\kappa} &= \frac{E_{n\kappa}}{\hbar c} Q_{n\kappa}(r), \\ \left(\frac{d}{dr} - \frac{\kappa}{r} \right) Q_{n\kappa}(r) + \left(\frac{Z\alpha}{r} + \frac{mc^2}{\hbar c} \right) P_{n\kappa} &= \frac{E_{n\kappa}}{\hbar c} P_{n\kappa}(r), \end{aligned} \quad (5.27)$$

where α is the fine-structure constant, and $E_{n\kappa}$ is the energy of the electron.

Note: κ emerges as the eigenvalue in the eigenfunction $\chi_{\kappa, m_j}(\theta, \phi)$, associated with the operator $\vec{L} \cdot \vec{\sigma}$. This is because $(\vec{\sigma} \cdot \vec{L} + \hbar)\chi_{\kappa, m_j}(\theta, \phi) = -\hbar\kappa\chi_{\kappa, m_j}(\theta, \phi)$, where \vec{L} is the orbital angular momentum operator.

In the works of [134] and [135], further analysis reveals the eigenenergies for a single-electron ion as:

$$E_{n\kappa} = \frac{mc^2}{\sqrt{1 + \frac{\alpha^2 Z^2}{\gamma + n - |\kappa|}}} \quad (5.28)$$

Here, $\gamma = \sqrt{\kappa^2 - (Z\alpha)^2}$, the principal quantum number is denoted by n , and κ serves as the relativistic quantum number. The relationship between κ and the orbital quantum number ℓ is defined as $\kappa = -\ell - 1$ for $j = \ell + \frac{1}{2}$ and $\kappa = \ell$ for $j = \ell - \frac{1}{2}$. Additionally, $|\kappa| = j + 1/2$, where j is the total angular momentum quantum number, resulting from the coupling of the orbital and spin angular momenta.

Note: Notably, the energy levels of a hydrogen-like ion with a point-like nucleus depend on n and j only, giving naturally rise to the spin-orbit splitting, which is a relativistic effect that can be modeled by an effective Hamiltonian in the Schrödinger equation. The form of that Hamiltonian will be recovered in latter sections.

Note: Expanding (5.28) in terms of the fine-structure constant α , yields both the electron's rest mass and the non-relativistic energy levels for a single-electron ion as the first two leading terms:

$$E_{n\kappa} = mc^2 - \frac{Z\alpha^2}{2n^2} mc^2 - \frac{Z^2\alpha^4}{2n^3} \left(\frac{1}{|\kappa|} - \frac{3}{4n} \right) mc^2 + \mathcal{O}(\alpha^6). \quad (5.29)$$

The term proportional to α^4 (α^2 relative to the non-relativistic hydrogen-like energy) represents the first relativistic correction to the energy levels, known as the fine-structure correction. The Dirac equation, which incorporates special relativity, accurately predicts the fine structure observed in the hydrogen atom. This fine structure was first observed by Albert A. Michelson and Edward

W. Morley in 1891 [136]. Notably, using the notation $n\ell_j$ to refer to an orbital via its quantum numbers, the energy difference between the $2p_{3/2}$ and $2p_{1/2}$ levels of the hydrogen atom, as given by (5.29), is $\Delta E = \frac{\alpha^4}{32}mc^2 \approx 0.37 \text{ cm}^{-1}$.

5.3 Beyond the Dirac equation

The Dirac equation is a powerful tool for describing the behavior of spin-1/2 fermions, such as the electron. However, it is not the end of the story. In order to account for interacting particles of different kind, one must consider the quantum field theory, and in particular, quantum electrodynamics (QED). QED is a quantum field theory that describes the interaction between charged particles and the electromagnetic field. It is based on the principles of quantum mechanics and special relativity, and it is one of the most successful theories in physics, with a precision of up to 10^{-12} in some cases in atomic physics [137].

QED effects for highly charged ions has been studied in [138] for example, where the author considered the self energy of the electron, which is the energy shift of the electron due to its interaction with its own electromagnetic field, or the vacuum polarization effect, which is the effect of the virtual electron-positron pairs that are created and annihilated in the vacuum. The latter has been studied both with regards to its effect on the electronic wavefunctions and the hyperfine structure.

Figure 5.1 shows the first-order-in- $(Z\alpha)$ Feynmann diagrams for both QED effects.

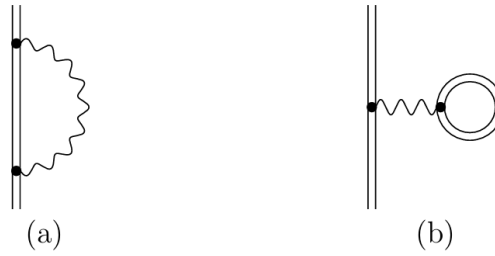


Figure 5.1: First-order-in- $(Z\alpha)$ Feynmann diagrams for the self energy (a) and the vacuum polarization (b) effects in QED. Taken from [138].

Finally relativistic effects have to be considered when multiple electronic systems are studied, as for example, the electron-electron interaction is no longer instantaneous, and the electron-electron interaction is mediated by the exchange of virtual photons. In this case, the usual term associated with the Coulombic potential energy must be replaced by the Breit interaction term [139].

QED or higher order relativistic corrections is however not within the scope of this work, and the Dirac equation will be the main tool used to study the hyperfine interaction of hydrogen-like ions in the following chapters.

Main takeaways from Chapter 5

- **The Dirac Equation:**

- A relativistic wave equation for spin- $\frac{1}{2}$ particles.
- Incorporates special relativity into quantum mechanics.
- Predicts electron spin and antiparticles.

- **Relativity in Quantum Mechanics:**

- The Schrödinger equation is not Lorentz invariant.
- The Klein-Gordon equation applies to spin-0 particles but has issues for electrons.
- The Dirac equation resolves these issues for spin- $\frac{1}{2}$ particles.

- **Application to Hydrogen-like Atoms:**

- Applies to electrons in the Coulomb potential.
- Predicts fine-structure splitting naturally.
- Spin-orbit interaction emerges without added terms.

- **External Electromagnetic Fields:**

- Included via minimal coupling $\vec{p} \rightarrow \vec{p} - e\vec{A}$.
- Gauge invariance is maintained.

- **Limitations and Extensions:**

- Does not account for electron-electron interactions or higher-order effects.
- Quantum Electrodynamics (QED) is needed for precise calculations.

Chapter Contents

6.1	Mass corrections	99
6.2	Muonic ions	99
6.3	The nuclear charge distribution	100
6.4	The nuclear current distribution	110
6.5	Other effects of the nucleus	120

CHAPTER 6

The finite nucleus

6.1 Mass corrections

Up until this point, the nucleus was assumed to be infinitely massive, but in reality, the nucleus has a finite mass M_N . Depending on the degree of precision required, the mass of the nucleus can be considered in different ways. The simplest approach is simply to consider the Normal Mass Shift (NMS). The NMS is the correction due to the incorporation of the reduced mass excluding the correction to the rest mass, of the electron-nucleus system in the Dirac equation., i.e. the substitution

$$m = m_e \rightarrow \mu = \frac{m_e M_N}{m_e + M_N}, \quad (6.1)$$

with M_N being the mass of the nucleus. This reduces to solving the Dirac equation in the center-of-mass frame, where the reduced mass is the mass of the electron. This also only accounts for the non-relativistic kinetic energy of the electron, therefore, to obtain relativistic corrections, a more sophisticated approach is required.

Assuming a single electron ion with a massive point-like nucleus, the Normal Mass Shift (NMS) affects both the energy and the wavefunctions. The energy is rescaled by the factor $\frac{M_N}{m_e + M_N}$ while the wavefunctions lengthscales are rescaled by the inverse factor.

However, in the case of multi-electronic atoms, the NMS is not sufficient, and one must consider the Specific Mass Shift (SMS), a mass polarization effect. The SMS can take the form of an effective Hamiltonian, given by

$$H_{\text{SMS}} = -\frac{\hbar^2}{M_N} \sum_{i < j} \vec{\nabla}_i \cdot \vec{\nabla}_j. \quad (6.2)$$

Finally, a more rigorous, relativistic, treatment of the finite mass of the nucleus requires the use of the Bethe-Salpeter equation for example [140], or more generally, a full QED treatment of the electron-nucleus interaction [141].

6.2 Muonic ions

Muonics ions are atoms where the electron is replaced by a muon, a particle with the same charge as the electron but with a mass 207 times larger. The muon is a lepton, and as such, it interacts with the nucleus through the electromagnetic force. The muon is also unstable, with a mean lifetime of $2.2\mu\text{s}$, which is long enough to form muonic atoms. The muon is also a point-like particle, and the muonic atom can be treated similarly to a single-electron ion with a massive nucleus. However, the

mass of the muon is not small enough to consider the nucleus as infinitely massive, and the finite mass of the nucleus must be taken into account. In this work, we will consider the reduced mass of the muon-nucleus system, given by

$$\mu = \frac{m_\mu M_N}{m_\mu + M_N}, \quad (6.3)$$

where m_μ is the mass of the muon. The energy levels and wavefunctions of a muonic ion can then be calculated by solving the Dirac equation with the reduced mass given by (6.3).

6.3 The nuclear charge distribution: Monopole and quadrupole

The nucleus, on top of not being infinitely massive, is also not a point-like particle. It has a finite size, moreover its charge distribution is not necessary spherically symmetric either.

6.3.1 Ab-initio computation of the nuclear charge distribution

In order to describe the nuclear charge distribution, one must consider the nuclear charge density $\rho(\vec{R})$, where \vec{R} will denote the spatial coordinates pertaining to the nucleus. The nuclear charge density can be computed ab-initio, by solving the Schrödinger equation for the nucleons. However, the nuclear force is not well understood outside the framework of Quantum ChromoDynamics (QCD), and the Schrödinger equation for the nucleons is not analytically solvable. Instead, one can use effective interactions, such as the Skyrme interaction, to model the nuclear force. The Skyrme interaction is a density-dependent effective interaction that can be used to compute the nuclear charge density. This is a methodology oftentimes used in low-energy nuclear physics theory. For that reason we have collaborated with nuclear physicists to obtain the nuclear charge distribution for the nucleus of interest and use it in our calculations. Low-energy nuclear theory aims to describe the structure and behavior of atomic nuclei, which consist of protons and neutrons, near their ground state. Since a nucleus involves many particles, solving this N body problem exactly is impossible. Instead, we use numerical solving methods, one of the most common being the Hartree-Fock (HF) method. In this approach, we assume that each nucleon (proton or neutron) moves independently in an average potential generated by all the others. I am grateful to my local collaborators Johann Bartel and Hervé Molique as well as Ludovic Bonneau, from Bordeaux, for providing the numerical code and the nuclear charge distribution data for the nuclei studied in this work. I am also grateful for the discussions we had that helped me understand the techniques used in low-energy nuclear theory. More details about the computational methods and the theory behind the nuclear structure can be found in the paper stemming from this collaboration **The hyperfine interaction as a probe of the microscopic structure of the nucleus**, to be submitted to PRX.

The Skyrme-effective interaction

The Skyrme interaction is a simplified model for the forces between nucleons in a nucleus. Instead of dealing with the exact strong force from QCD, we use an effective interaction that captures the essential features. This interaction includes terms representing different aspects of the force, like the short-range nature of the interaction and how it changes with the density of nucleons. The Skyrme-effective interaction serves as a practical model for approximating the nuclear force and is commonly used to compute nuclear charge densities. This phenomenological method has demonstrated significant success in low-energy nuclear physics, particularly when describing the structure and behavior of nuclei in or near the nuclear ground state.

The Skyrme interaction is a local effective nuclear interaction consisting of several terms, each capturing different facets of the nuclear force. These terms describe the short-range nature of the force, which becomes negligible beyond a distance of approximately 2 fm, is attractive within this range, and

exhibits strong repulsion at very short distances. In its original formulation by Skyrme [39] and later implemented by Vautherin and Brink [40], the interaction is expressed as a sum of two-body and three-body potential terms:

$$\mathcal{V}_{Sk} = \mathcal{V}_{Sk,2} + \mathcal{V}_{Sk,3}, \quad (6.4)$$

where the two-body potential is given by

$$\begin{aligned} \mathcal{V}_{Sk,2}(\vec{R}_i, \vec{R}_j) = & t_0 [1 + x_0 P_\sigma] \delta(\vec{R}_{ij}) + \frac{1}{2} t_1 [1 + x_1 P_\sigma] \left[\delta(\vec{R}_{ij}) k^2 + k'^2 \delta(\vec{R}_{ij}) \right] \\ & + t_2 [1 + x_2 P_\sigma] \vec{k}' \cdot \delta(\vec{R}_{ij}) \vec{k} + i W_0 (\sigma_i + \sigma_j) \cdot \left[\vec{k}' \times \delta(\vec{R}_{ij}) \vec{k} \right], \end{aligned} \quad (6.5)$$

and the three-body potential is described by

$$\mathcal{V}_{Sk,3}(\vec{R}_i, \vec{R}_j, \vec{R}_k) = t_3 [1 + x_3 P_\sigma] \delta(\vec{R}_{ij}) \delta(\vec{R}_{jk}). \quad (6.6)$$

In these expressions, the interaction is characterized by Dirac delta distributions acting on the relative distances $\vec{R}_{ij} = \vec{R}_i - \vec{R}_j$ between nucleons. The term P_σ represents the spin-exchange operator associated with the Pauli spin matrices σ , while \vec{k} and \vec{k}' denote the momentum operators of the nucleons. The parameter W_0 is the strength of the spin-orbit coupling. The constants t_i and x_i are Skyrme parameters, which are fitted to experimental data such as nuclear ground-state properties and nuclear matter characteristics (a fictitious system of $N = 2$ interacting nucleons without Coulomb interaction).

In the case of even-even nuclei, where time-reversal symmetry applies (as will be discussed later), the three-body term can be reformulated as a density-dependent two-body term:

$$\mathcal{V}_{Sk,3}(\vec{R}_i, \vec{R}_j, \rho) = \frac{1}{6} t_3 [1 + x_3 P_\sigma] \delta(\vec{R}_{ij}) \rho(\vec{R}_{ij}), \quad (6.7)$$

where $\vec{R}_{ij} = (\vec{R}_i + \vec{R}_j)/2$ is the center-of-mass vector of the interacting nucleons, and ρ represents the total nucleon density, $\rho = \rho_n + \rho_p$, comprising both protons (p) and neutrons (n).

This density-dependent term paves the way for discussions on the numerous refinements and extensions of Skyrme-type parameterizations that have been explored since the original formulation.

■ The Skyrme Hartree-Fock equations

The Hartree-Fock (HF) method offers a framework for addressing the N -body problem by modeling nucleons as independent particles moving within an averaged field generated by the other nucleons. This mean-field approach is a common approximation in quantum many-body systems, and the inclusion of the Skyrme potential allows for more detailed modeling of interactions between nearby nucleons.

The Hamiltonian of the system is given by

$$\mathcal{H}_\nu = T + \mathcal{V}_{Sk} + \mathcal{V}_{Coul} \quad (6.8)$$

where T represents the kinetic energy operator, \mathcal{V}_{Sk} is the Skyrme interaction, and \mathcal{V}_{Coul} accounts for the Coulomb interaction. The expectation value of this Hamiltonian for a nucleus in its ground state $|\Psi\rangle$, a Slater determinant, composed of single-particle (s.p.) states φ_j , is given by

$$\langle \Psi | \mathcal{H} | \Psi \rangle = \int H(\vec{R}) d^3 \vec{R}. \quad (6.9)$$

The Skyrme-Hartree-Fock equations are derived by minimizing the total energy with respect to the s.p. wavefunctions φ_j , leading to Schrödinger-like equations:

$$\left[-\vec{\nabla} \cdot \frac{\hbar^2}{2m_q^*(\vec{R})} \vec{\nabla} + U_q(\vec{R}) - i\vec{W}_q(\vec{R}) \cdot (\vec{\nabla} \times \vec{\sigma}) \right] \varphi_{q,j}(\vec{R}) = \varepsilon_{q,j} \varphi_{q,j}(\vec{R}) , \quad (6.10)$$

which the $\varphi_{q,j}(\vec{R})$ must satisfy under the normalization constraint:

$$\frac{\delta}{\delta \varphi_{q,j}} \left[E - \sum_j \varepsilon_{q,j} \int |\varphi_{q,j}(\vec{R})|^2 d^3r \right] = 0 . \quad (6.11)$$

In these equations, q indexes the nature of the nucleon (proton or neutron), $m_q^*(\vec{R})$ represents an effective mass term, $U_q(\vec{R})$ is the mean-field potential, $\varepsilon_{q,j}$ are the single-particle energies, and $\vec{W}_q(\vec{R})$ refers to the spin-orbit form factors.

The solution of the Skyrme-Hartree-Fock equations proceeds iteratively. Starting with an initial guess for the fields in the Schrödinger-like equations in (6.10), the s.p. wavefunctions for protons and neutrons, $\varphi_{p,j}(\vec{R})$ and $\varphi_{n,j}(\vec{R})$, are obtained by solving the equations. These wavefunctions are used to update the densities of the Skyrme interaction, thereby refining the fields in the Schrödinger-like equations. This process repeats until convergence is achieved, yielding the final local densities from the computed wavefunctions.

Symmetries in nuclei

In our work modeling the nuclear structure of lanthanide nuclei, we must account for the deformations of these nuclei away from spherical symmetry. It is well-known that these nuclei often exhibit either prolate or oblate deformations. This presents a challenge when solving the Skyrme-Hartree-Fock equations, as the assumption of spherical symmetry is no longer applicable, making it difficult to resolve the equations in configuration space. However, we can retain the assumption of axial symmetry in our model for lanthanides, as we do not consider higher multipole moments beyond the electric quadrupole.

An initial approach involves expanding the nucleon wavefunctions in a truncated basis of an axially deformed harmonic oscillator (HO) [142, 143]. In this method, the oscillator frequencies ω_z and ω_\perp define the nuclear deformation parameter β . This parameter indicates whether the nucleus is prolate ($\beta > 0$) or oblate ($\beta < 0$), and serves as a measure of the nuclear shape. As a result, an additional optimization step is required in the Skyrme-Hartree-Fock iterations, where the deformation parameter must be determined self-consistently by minimizing the total energy of the nucleus.

As a refinement, the constrained Hartree-Fock (CHF) method can be employed to examine the deformation energy of the nucleus as a function of β [144]. In this approach, a constraint is applied to the mass quadrupole moment of the nucleus, providing a more precise representation of nuclear shapes away from spherical symmetry. For instance, in the case of the nucleus ^{162}Dy , the deformation energy can be calculated as a function of β to demonstrate the transition between prolate and oblate shapes. Figure 6.1 illustrates the deformation energy of ^{162}Dy , showing how the nuclear energy changes with its shape parameter β .

Nuclear quadrupole moments

One can also check whether the structure of the deformed nucleus reproduces, indeed, the experimentally measured deformation of the studied nucleus as it is given e.g. by the charge rms radius $R_{\text{rms}} = \langle R^2 \rangle$ and the charge quadrupole moment¹ $Q_0^{(2,\text{int})}$. As far as the latter is concerned, one, however, needs to

¹Considering the symmetries of the nucleus, the latter has only one non-zero component, $Q_0^{(2)}$.

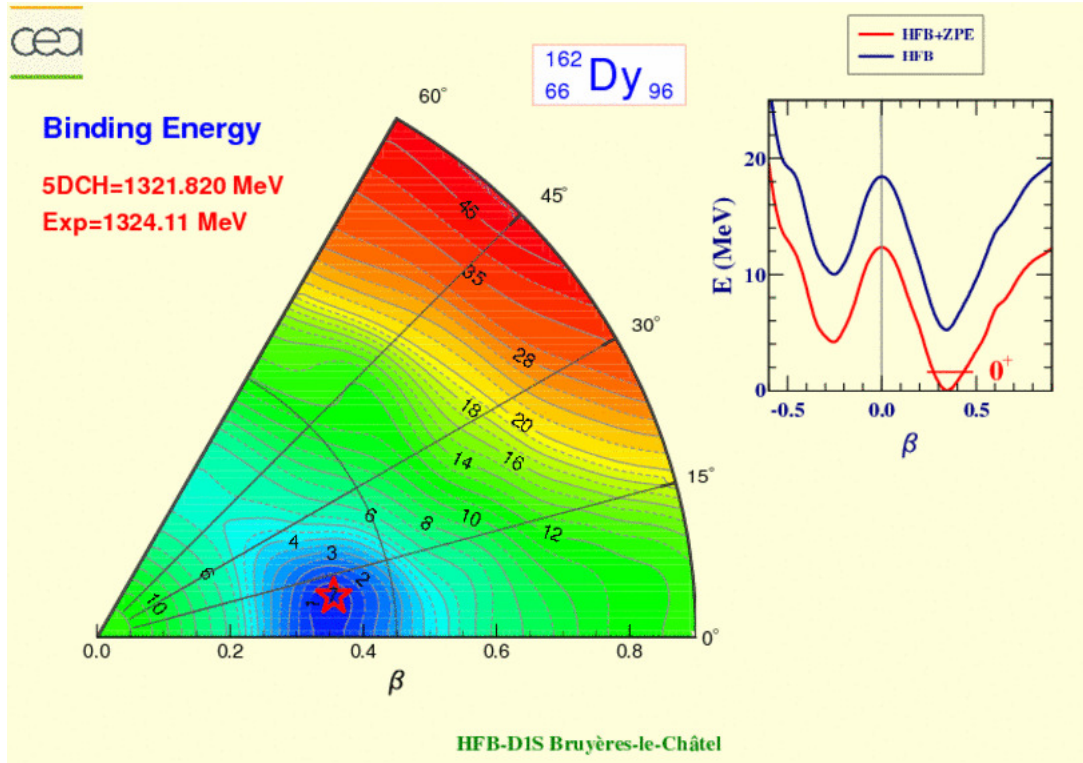


Figure 6.1: Deformation energy (left) of the nucleus ^{162}Dy as a function of the deformation parameter β . The right panel shows the energy in the $\beta\gamma$ -plane to explore possible triaxial (three-dimensional) deformation (taken from [43]).

convert the *intrinsic* charge quadrupole moment, as it is calculated in the mean-field method that is used in our approach, into the *spectroscopic* quadrupole moment which is the quantity that is measured in the experiment as tabulated by Stone [145]. This is done by use of the following equation [146, 147]

$$Q_0^{(2,\text{spec})} = \frac{3K^2 - I(I+1)}{(I+1)(2I+3)} \langle \Psi | Q_0^{(2)} | \Psi \rangle = \frac{3K^2 - I(I+1)}{(I+1)(2I+3)} Q_0^{(2,\text{int})}, \quad (6.12)$$

with K being the projection of the total angular momentum I on the symmetry axis of the nucleus, we assume the first is aligned with the latter and that $K = I$. The calculated rms radii and quadrupole moments for ^{161}Dy and ^{163}Dy are in good agreement with the experimental data, as shown in Table 6.1.

	$R_{\text{rms}}^{(\text{cal})}$	$R_{\text{rms}}^{(\text{exp})}$ [148]	$R_{\text{rms}}^{(\text{emp})}$	$Q_0^{(2,\text{spec},\text{cal})}$	$Q_0^{(2,\text{spec},\text{exp})}$ [145]
^{161}Dy	5.212	5.196	5.118	2.62	2.51
^{163}Dy	5.232	5.211	5.137	2.73	2.65

Table 6.1: Comparison with the experimentally obtained charge rms radii (in fm) and spectroscopic charge quadrupole moments (in ebarn) for ^{161}Dy and ^{163}Dy . $R_{\text{rms}}^{(\text{emp})} \equiv (0.836A^{1/3} + 0.57)^{1/2}$ [149].

Note: One notices that if $K = I \leq \frac{1}{2}$, the spectroscopic quadrupole moment vanishes. Moreover, looking back at (6.32), the magnetic moment vanishes for $K = I = 0$. Figure 6.2 shows a schematic representation of the nuclear charge and current distributions, illustrating the quadrupole deformation and its relation to the sign of Q_{20} . The quadrupole moment is a measure of the deviation of the charge distribution from a spherical shape, and a non-zero value indicates a

deformed nucleus, a positive value corresponds to a prolate (cigar-shaped) nucleus, and a negative value to an oblate (disc-shaped) nucleus.

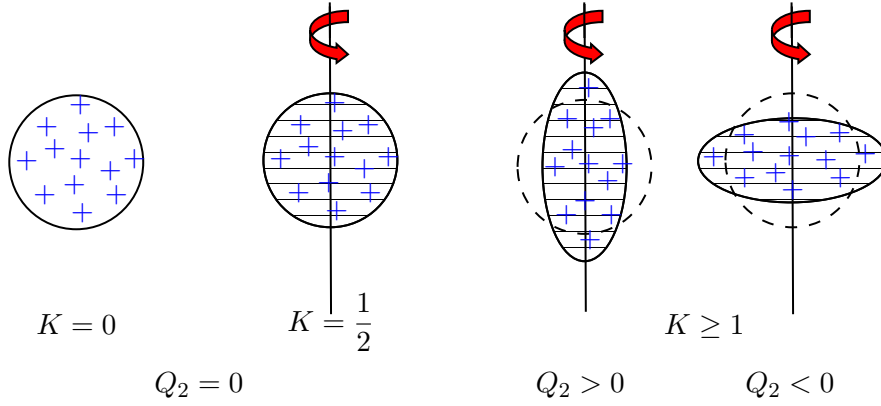


Figure 6.2: Schematic representation of the nuclear charge and current distributions. For nuclei with a spin $K \geq 1$, an electric quadrupole Q is allowed.

Summary

In summary, this Skyrme-Hartree-Fock BCS model (we also refer to as the **HFBCS** model, see [Section 6.4.1](#)), incorporating effective interactions and self-consistent blocking, provides a framework for understanding nuclear structure and properties. By simplifying the complex nucleon interactions into manageable forms, this approach successfully describes various nuclear phenomena, including shapes, pairing effects, and, as will be seen in [Section 6.4.1](#), magnetic moments.

One can use the nuclear charge distribution obtained from these computations to calculate the charge multipole moments of the nucleus and incorporate them into the Dirac equation for a single-electron ion, as we will see in the next subsection.

For indicative purposes, the obtained nuclear charge distributions for ^{161}Dy and ^{163}Dy can be seen in [Fig. 6.3](#). The proton (p) and neutron (n) density distributions are shown in cylindrical coordinates (z, ρ) on a planar slice along the z -axis. In these figures, lengths are normalized by considering the nucleus as a homogeneously charged sphere whose radius is given by $R_N = \sqrt{\frac{5}{3}} R_{\text{rms}}^2$ fm. In this last expression R_{rms} is the radius of the root mean square (RMS) charge of the nucleus given by the empirical formula $R_{\text{rms}} = (0.836A^{1/3} + 0.57)$ fm [149]. For the two isotopes considered in this work, this gives $R_N(^{161}\text{Dy}) = 6.607$ fm and $R_N(^{163}\text{Dy}) = 6.631$ fm. Moreover, the outer shell of the nucleus is indicated by the dashed curve, and chosen to be the full width at half maximum (FWHM) of the respective isotope's radial proton density.

6.3.2 Multipole expansion of the nuclear potential

The Laplace equation for the electric potential $\phi(\vec{r})$ in the presence of the nuclear charge distribution $\rho(\vec{R})$ is given by

$$\nabla^2 \phi = -\frac{\rho}{\epsilon_0}, \quad (6.13)$$

Using the multipole expansion of the potential of the nucleus to the electron (see [\(C.26\)](#)), one can write the potential as

$$\phi(\vec{r}) = \sum_{k=0}^{+\infty} \sum_{q=-k}^k (-1)^q \phi_{-q}^{(k)}(r) C_q^{(k)}(\theta, \phi) \quad (6.14)$$

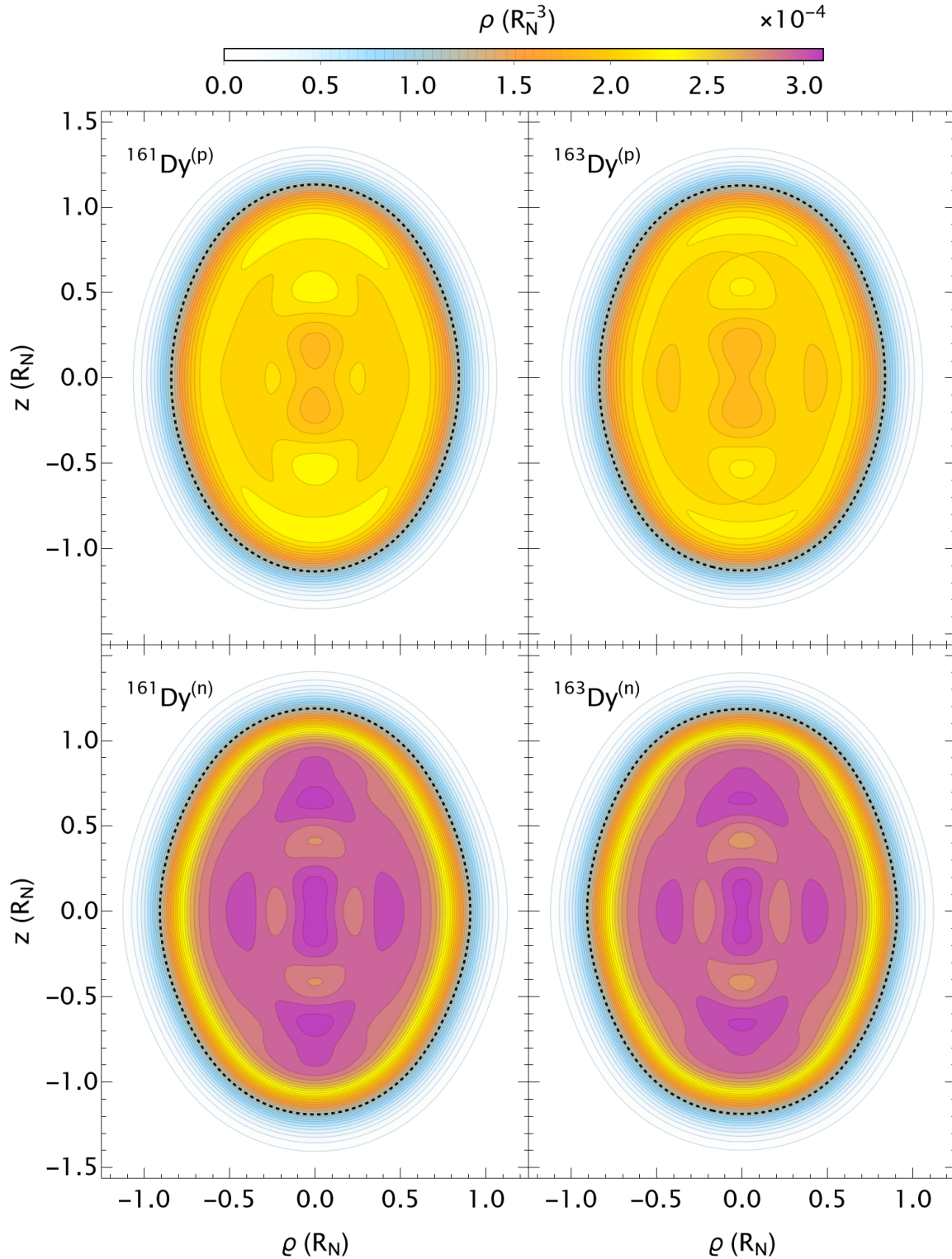


Figure 6.3: Nucleon density distributions of ^{161}Dy and ^{163}Dy with logarithmically spaced contour curves. (*p*) stands for the protons and (*n*) for neutrons. The figures are plotted in cylindrical coordinates (z, ρ) , on a planar slice through the z -axis. The spatial coordinates are in units of R_N , the empirical nuclear radius (see text) for each isotope, leading to a density distribution in units of R_N^{-3} . The contours represent curves of equivalent density, with numerical values as indicated by the legend above. The dashed curve indicates the contour line of the FWHM of the isotope's proton density, representing the outer shell of the nucleus.

where $\phi_q^{(k)}(r)$ are the multipole moments of the nucleus, and $C_q^{(k)}(\theta, \phi)$ and $Y_q^{(k)}(\theta, \phi)$ are the normalized and non-normalized spherical harmonics, respectively. The multipole moments of the nucleus can be written as (see (C.27))

$$\phi_q^{(k)}(\vec{r}) = \frac{1}{4\pi\epsilon_0} \int_{R=0}^{+\infty} \rho(\vec{R}) \frac{r_{>}^k}{r_{<}^{k+1}} C_q^{(k)}(\Theta, \Phi) d^3\vec{R}, \quad (6.15)$$

where \vec{R} is the nuclear radius vector, $\rho(\vec{R})$ is the charge distribution of the nucleus, $r_{<} = \min(r, R)$, $r_{>} = \max(r, R)^{k+1}$ and $C_q^{(k)}(\Theta, \Phi)$ are the normalized spherical harmonics defined in (C.1). The integral can be split in two regions, $r < R$ and $r > R$, and the multipole moments can be written as

$$\phi_q^{(k)}(\vec{r}) = \frac{1}{4\pi\epsilon_0 r^{k+1}} \int_{R=0}^r \rho(\vec{R}) R^k C_q^{(k)}(\Theta, \Phi) d^3\vec{R} + \frac{r^k}{4\pi\epsilon_0} \int_{R=r}^{+\infty} \frac{\rho(\vec{R})}{R^{k+1}} C_q^{(k)}(\Theta, \Phi) d^3\vec{R}. \quad (6.16)$$

6.3.3 Electric monopole moment

The first term of the multipole expansion ($k = 0$) is the electric monopole moment of the nucleus, and considering $C_0^{(0)}(\Theta, \Phi) = 1$, $\forall \Theta, \Phi$, it is given by

$$\phi_{0,0}(r) \equiv \phi_0^{(0)}(\vec{r}) = \frac{1}{4\pi\epsilon_0 r} \int_{R=0}^r \rho(\vec{R}) d^3\vec{R} + \frac{1}{4\pi\epsilon_0} \int_{R=r}^{+\infty} \frac{\rho(\vec{R})}{R} d^3\vec{R}. \quad (6.17)$$

We can define ${}^{\text{in}}\phi_0^{(0)}(\vec{r})$ and ${}^{\text{ex}}\phi_0^{(0)}(\vec{r})$ as the contributions of the nuclear region inside and outside the electron's orbit, respectively

$$\begin{aligned} {}^{\text{in}}\phi_0^{(0)}(\vec{r}) &\equiv \frac{1}{4\pi\epsilon_0 r} \int_{R=0}^r \rho(\vec{R}) d^3\vec{R} \equiv \frac{{}^{\text{in}}Q^{(0)}(r)}{4\pi\epsilon_0 r}, \\ {}^{\text{ex}}\phi_0^{(0)}(\vec{r}) &\equiv \frac{1}{4\pi\epsilon_0} \int_{R=r}^{+\infty} \frac{\rho(\vec{R})}{R} d^3\vec{R} \equiv \frac{{}^{\text{ex}}Q^{(0)}(r)}{4\pi\epsilon_0}. \end{aligned} \quad (6.18)$$

One notices that ${}^{\text{in}}Q^{(0)}(r)$ is the nuclear charge inside a sphere of radius r , while ${}^{\text{ex}}Q^{(0)}(r)$ has the dimensions of an electric potential and is the contribution of the nuclear charge outside the sphere of radius r to the electric monopole moment of the nucleus. A schematical representation of the appearance of the two electric monopole moments is shown in Fig. 6.4.

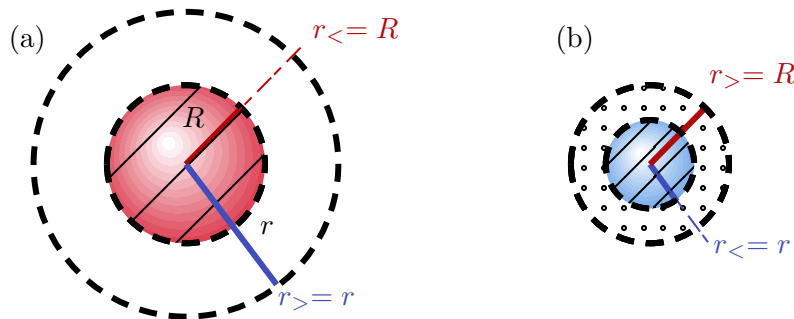


Figure 6.4: Schematic of the two integration regions: (a) the traditional case where the electronic wavefunction does not penetrate the nucleus, and (b) where it does, splitting the integration into $R < r$ and $R > r$, with the monopole moment divided into internal and external contributions as in (6.18).

Note: If one ignores the penetration of the electronic wavefunction inside the nucleus, i.e. consider only the $R < r$ region, then ${}^{\text{ex}}Q(r)$ is zero, and the electric monopole moment of the nucleus is

given by

$$\phi_{0,0}(r \rightarrow +\infty) = \frac{1}{4\pi\epsilon_0 r} \int_{R=0}^{+\infty} \rho(\vec{R}) d^3 \vec{R} = \frac{1}{4\pi\epsilon_0 r} {}^{\text{in}}Q(r \rightarrow +\infty) = \frac{Z|e|}{4\pi\epsilon_0 r}, \quad (6.19)$$

where Z is the atomic number of the nucleus.

The finite size and charge density distribution of the nucleus can still be taken into account in the radial Dirac equation by considering the monopole charge distribution of the nucleus. This is the spherically symmetric charge distribution that would yield the same electric monopole moment as the realistic nucleus.

If one considers the spherical average of the charge density of the nucleus:

Definition: (*Spherical average charge density*)

$$\rho_{0,0}(R) \equiv \frac{1}{4\pi R^2} \int_{\Omega} \rho(\vec{R}) d^2 \vec{\Omega} = \frac{1}{4\pi R^2} \int_{\Theta=0}^{\pi} \int_{\Phi=0}^{2\pi} \rho(\vec{R}) \sin(\Theta) d\Theta d\Phi, \quad (6.20)$$

then, by solving the Poisson equation for the spherical average charge density, one can obtain the electric monopole moment of the nucleus as:

$$\begin{aligned} {}^{\text{in}}Q^{(0)}(r) &= 4\pi \int_{R=0}^r \rho_{0,0}(R) R^2 dR = \int_{R=0}^r \rho(\vec{R}) d^3 \vec{R}, \\ {}^{\text{ex}}Q^{(0)}(r) &= 4\pi \int_{R=r}^{+\infty} \rho_{0,0}(R) R dR = \int_{R=r}^{+\infty} \frac{\rho(\vec{R})}{R} d^3 \vec{R}. \end{aligned} \quad (6.21)$$

Note: A simplistic approximation used for the spherical average charge density is a simple solid sphere model, where the charge density is constant inside the nucleus and zero outside. Where the radius of the nucleus R_N is given by the empirical formula $R_N = \sqrt{\frac{5}{3}} R_{\text{rms}}^2$ fm [149]. The spherical average charge density of the nucleus is then given by

$$\rho_{0,0}(R) = \begin{cases} \frac{3Ze}{4\pi R_N^3} & \text{if } R \leq R_N, \\ 0 & \text{if } R > R_N, \end{cases} \quad (6.22)$$

Note: Another case of interest for modelling the spherical average charge density is the Fermi distribution, which is a continuous step function that models the charge density of the nucleus as a uniform distribution inside the nucleus and decreases to zero outside. The Fermi distribution is given by

$$\rho(R) = \frac{\rho_0}{1 + \exp\left(\frac{R-\tilde{c}}{a}\right)}, \quad (6.23)$$

with

$$\rho_0 = \frac{3}{4\pi \tilde{c}^3 \left(1 + \left(\frac{\pi a}{\tilde{c}}\right)^2\right)}. \quad (6.24)$$

The parameters a , \tilde{c} have been taken from [149].

In the upper part of Fig. 6.5, the monopole electric potentials, $\phi_{0,0}$, are depicted, illustrating the

influence of the spatial distribution of protons within the nucleus of ^{161}Dy . As stated, due to the spherical symmetry of the monopole, these potentials are expressed in terms of the radial component r , averaged over the angular components. Here, r is measured in units of the nuclear radius, R_N , providing the potential in units of $R_N^{-1}e/4\pi\epsilon_0$. Each curve represents a different model for the monopole density distribution: (dashed) a point-like ($\frac{Z}{r}$) nuclear model, (blue) a uniformly distributed spherical model (see (6.22)), (black) a smooth Fermi distribution (see (6.23)), and (red) a more realistic model using the HFBCS code (the computed charge distribution is plotted in Fig. 6.3). Notice that outside the nuclear radius at $R/R_N = 1$, all potentials converge, and the variations in the HFBCS calculations for each isotope are minimal (refer to the green curve and the corresponding y -axis on the right).

The lower part of the figure illustrates the distributions of the monopolar nuclear charge densities, $\rho_{0,0}^{(0)}(R)$, associated with the spatial distribution of protons within the ^{161}Dy nucleus. Due to the monopole's spherical symmetry, these densities are given in terms of the radial component R , averaged over the angular components. R is expressed in units of the nuclear radius, R_N , resulting in the monopole density units of eR_N^{-3} . The HFBCS model indicates a lower proton density at the nucleus's center, which increases unevenly toward a peak at the outer edge. The outcomes are nearly identical for both isotopes, with only minor differences in the HFBCS model near $R = 0$ (refer to the green curve and the corresponding y -axis on the right). The dashed vertical line marks the nuclear surface at $R = 1 \times R_N$, to which the other curves are normalized.

Note: By solving numerically the Dirac equation with the radial electric potential $\phi_{0,0}(r) = \text{in}\phi_0^{(0)}(r) + \text{ex}\phi_0^{(0)}(r)$, one can obtain the correction in energy levels and wavefunctions due to the finite size of the nucleus up to a monopole approximation, this approach has the advantage of only requiring the solution of the radial Dirac equation, although it does not account for the higher multipoles of the nucleus. This is then done perturbatively in Chapters 7 and 8.

6.3.4 Electric quadrupole moment

In order to take into account the deformation of the nucleus, one must consider the electric quadrupole moment of the nucleus, but instead of solving the Dirac equation in a non-radial potential, one can treat the electric quadrupole moment perturbatively using the solutions of the Dirac equation in a spherically symmetric potential as a zeroth-order approximation, this can in turn allow to obtain an effective quadrupole Hamiltonian.

The electric quadrupole potential is obtained by looking at the next non-vanishing term in the multipole expansion (6.14), for $k = 2$.

$$\phi_{\text{quad}}(\vec{r}) = \sum_{q=-2}^2 (-1)^q \phi_{-q}^{(2)}(r) C_q^{(2)}(\theta, \phi), \quad (6.25)$$

with

$$\phi_q^{(2)}(\vec{r}) = \frac{1}{4\pi\epsilon_0 r^3} \int_{R=0}^r \rho(\vec{R}) R^2 C_q^{(2)}(\Theta, \Phi) d^3\vec{R} + \frac{r^2}{4\pi\epsilon_0} \int_{R=r}^{+\infty} \frac{\rho(\vec{R})}{R^3} C_q^{(2)}(\Theta, \Phi) d^3\vec{R}. \quad (6.26)$$

Or, in terms of non-normalized spherical harmonics

$$\phi_{\text{quad}}(\vec{r}) = \sum_{q=-2}^2 (-1)^q \tilde{\phi}_{-q}^{(2)}(r) Y_q^{(2)}(\theta, \phi), \quad (6.27)$$

with

$$\tilde{\phi}_q^{(2)}(\vec{r}) = \frac{1}{5\epsilon_0 r^3} \int_{R=0}^r \rho(\vec{R}) R^2 Y_q^{(2)}(\Theta, \Phi) d^3\vec{R} + \frac{r^2}{5\epsilon_0} \int_{R=r}^{+\infty} \frac{\rho(\vec{R})}{R^3} Y_q^{(2)}(\Theta, \Phi) d^3\vec{R}. \quad (6.28)$$

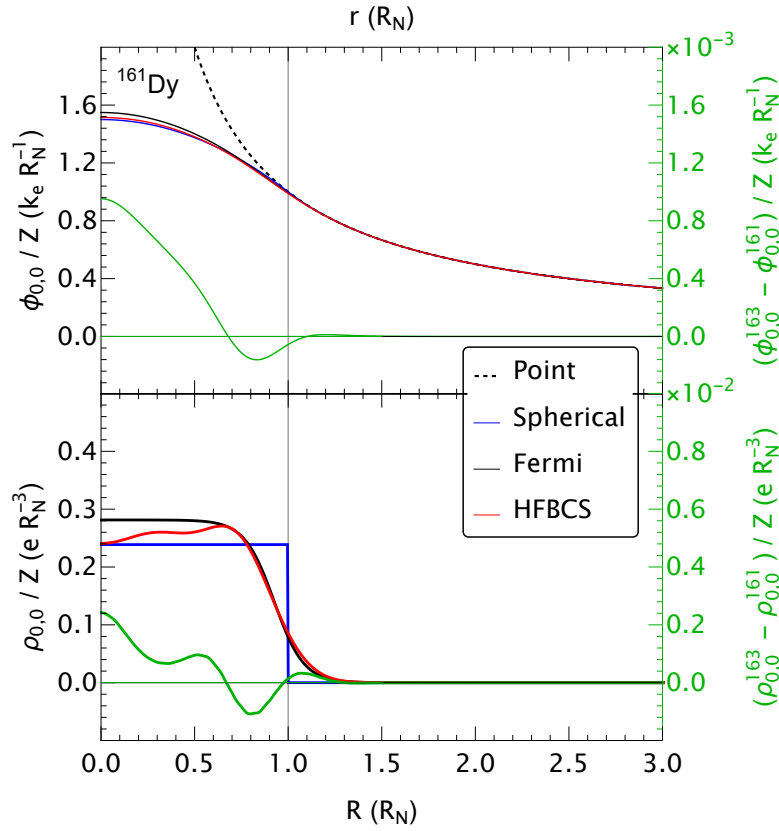


Figure 6.5: Z -normalized proton monopole density (bottom part) obtained for the ^{161}Dy nucleus from a uniform sharp-edge (blue), a Fermi-function type (black) and the distribution resulting from the here presented HFBCS type (red) calculation with self-consistent blocking and the Z -normalized monopole potential experienced by the electron resulting from the different approaches for the density (upper part). The Coulomb potential generated by a nuclear point-charge density is shown by the dotted line. The green lines show the difference in density and potential between the two dysprosium isotopes obtained with the HFBCS model. $k_e \equiv \frac{e}{4\pi\epsilon_0}$ is the Coulomb constant.

Similarly to the monopole moment, one can define two quantities, $^{\text{in}}Q^{(2)}(r)$ and $^{\text{ex}}Q^{(2)}(r)$, as the contributions to the nuclear region inside and outside the electron's orbit, respectively.

Definition: (*Quadrupole electric potential of the nucleus*) Let's define

$$\begin{aligned} ^{\text{in}}Q_q^{(2)}(r) &\equiv \int_{R=0}^r \rho(\vec{R}) R^2 C_q^{(2)}(\Theta, \Phi) d^3\vec{R}, \\ ^{\text{ex}}Q_q^{(2)}(r) &\equiv \int_{R=r}^{+\infty} \frac{\rho(\vec{R})}{R^3} C_q^{(2)}(\Theta, \Phi) d^3\vec{R}. \end{aligned} \quad (6.29)$$

The quadrupole potential then takes the form

$$\phi_{\text{quad}}(\vec{r}) = \sum_{q=-2}^2 \frac{{}^{\text{in}}Q_{-q}^{(2)}(r)}{4\pi\epsilon_0 r^3} C_q^{(2)}(\theta, \phi) + r^2 \frac{{}^{\text{ex}}Q_{-q}^{(2)}(r)}{4\pi\epsilon_0} C_q^{(2)}(\theta, \phi). \quad (6.30)$$

One can also write factor the quadrupole potential in terms of the radial component r and the spherical

harmonics $C_q^{(2)}(\theta, \phi)$,

$$\phi_{\text{quad}}(\vec{r}) = \left(\sum_{q=-2}^2 \frac{\text{in}Q_{-q}^{(2)}(r)}{4\pi\epsilon_0 r^3} + r^2 \frac{\text{ex}Q_{-q}^{(2)}(r)}{4\pi\epsilon_0} \right) C_q^{(2)}(\theta, \phi) = \phi_{-q}^{(2)}(r) C_q^{(2)}(\theta, \phi). \quad (6.31)$$

This radial part of the quadrupole potentials, converted to the spectroscopic referential frame (see (6.12)), $\phi_{2,0}(r)$ produced by the spatial distributions of protons within the deformed nuclei of isotopes ^{161}Dy (black) and ^{163}Dy (red) are shown on Fig. 6.6. r is in units of the nuclear radius, R_N , thus giving the potential in units of $eR_N^{-1}/4\pi\epsilon_0$. The vertical line represents the surface of the nucleus at $R = R_N$, to which the other curves are normalised. For indicative purposes, we also show the quadrupole potential of a point-like model ($\frac{Q_0^{(2)}}{r^3}$). Note the strong similarities in the curves for each isotope, since the neutrons do not contribute towards the quadrupole moment, and they have the same number of protons, yet a slightly higher maximum for ^{163}Dy , indicating a more pronounced deformation of the proton distribution. The values of $\text{in}Q_{-q}^{(2)}(r)$ and $\text{ex}Q_{-q}^{(2)}(r)$ are rescaled from their intrinsic values to their spectroscopic ones, according to (6.12).

Note: For information, $C_0^{(2)}(\Theta, \Phi) = \frac{1}{2} (\cos(\Theta)^2 - 1)$, which is oftentimes the form used in the literature.

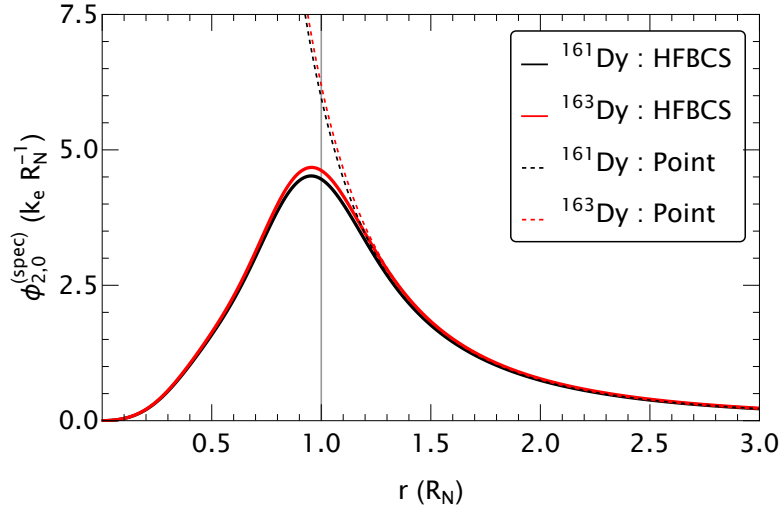


Figure 6.6: The radial part of the spectroscopic quadrupole contribution to the nuclear electric potential for ^{161}Dy (black) and ^{163}Dy (red), as obtained from our HFBCS calculation, compared with the corresponding potentials obtained for a point-quadrupole nucleus (dashed). $k_e \equiv \frac{e}{4\pi\epsilon_0}$ is the Coulomb constant.

6.4 The nuclear current distribution : Magnetic Dipole Moment

On top of the nucleus not being a point charge, it also has a magnetic (dipole) moment. The magnetic moment is due to the motion and spin of the protons and neutrons inside the nucleus, and is therefore not a point dipole either.

6.4.1 Ab-initio computation of the nuclear current distribution

Our collaboration with nuclear physicists has allowed us to obtain the nuclear magnetic dipole moments for the nuclei of interest on top of their charge distributions mentioned in [Section 6.3.1](#). Using the same numerical code, it is possible to extract the magnetic current distribution of the nucleus, which can be used to calculate the magnetic dipole moment of the nucleus.

■ Magnetic Dipole Moments in Nuclei

In atomic nuclei, the magnetic dipole moment is a fundamental property that arises from the motion and intrinsic spin of protons and neutrons. The magnetic dipole moment determines how the nucleus interacts with magnetic fields and is an important characteristic in understanding nuclear structure. It consists of contributions from both the orbital motion of nucleons and their intrinsic spin.

For an axially symmetric nucleus, just as it is the case for the electric quadrupole, the intrinsic magnetic dipole $\mu_z^{(\text{intr})}$ needs to be expressed in the spectroscopic referential frame (yielding $\mu_z^{(\text{spec})}$), the spectroscopic magnetic moment can be expressed as [\[146\]](#):

$$\mu_z^{(\text{spec})} = \frac{K}{K+1} \langle \Psi | \mu_z | \Psi \rangle \equiv \frac{K}{K+1} \mu_z^{(\text{intr})}, \quad (6.32)$$

where K is the projection of the nucleus's total angular momentum I along its symmetry axis, we assume the first is aligned with the latter and that $K = I$, and μ_z is the operator for the magnetic dipole moment in the direction of this axis. The wave function Ψ describes the quantum state of the nucleus.

■ Odd nuclei and time-reversal symmetry

As a final consideration in the development of our model, it is important to note that the standard BCS pairing correlation method relies on time-reversed pairs of nucleons. In this framework, each single-particle state $|k\rangle$ has a time-reversed partner $|\bar{k}\rangle = \mathcal{T}|k\rangle$, with both states having the same energy due to Kramer's degeneracy. This symmetry holds in systems where both proton and neutron numbers are even.

However, in systems where this symmetry is broken, such as in even-odd, odd-even or odd-odd nuclei² Kramer degeneracy no longer applies. In such cases, the unpaired nucleon (or odd particle) disrupts the time-reversal symmetry across the system, meaning that there is no true time-reversed partner for all nucleons. Since the time-reversal symmetry breaking caused by the odd particle leads to a core polarisation that affects all the particles of the nuclear system, the BCS method must then be modified to account for the unpaired nucleon, but also for the other nucleons, generally referred to as the core. The concept of a pseudo pair is introduced [\[150, 151\]](#), whereby for each single-particle state $|k\rangle$, a conjugate partner $|\tilde{k}\rangle$ is identified that has the largest overlap $\langle \tilde{k} | \bar{k} \rangle$ with the time-reversed state $|\bar{k}\rangle$. It turns out that there is no ambiguity in finding such a conjugate partner, but that rather the overlap of a given single-particle state $|k\rangle$ with its conjugate partner $|\tilde{k}\rangle$, what was formerly its Cooper-pair partner, is generally of the order of 99% or better. This extension allows the BCS pairing method to handle odd-even and odd-odd nuclei, ensuring pairing correlations are still included.

In odd-even nuclei, such as in the neighboring nucleus of an even-even core, the presence of an unpaired nucleon induces polarization effects in the core. This polarization, caused by the unpaired nucleon, is crucial for reproducing experimentally observed quantities such as magnetic dipole moments. The computational technique used to address these cases is called self-consistent blocking. In this method, the relevant single-particle state associated with the unpaired nucleon is considered fully occupied, effectively blocking it from participating in pairing interactions. Its conjugate partner, with

²For example ^{161,163}Dy are such even-odd nuclei, possessing an even number of protons and an odd number of neutrons.

opposite quantum numbers, is also blocked with zero occupation probability, preventing the pair from contributing to pair excitations. This method enables a consistent treatment of nuclear systems with broken time-reversal symmetry.

Understanding Magnetic Currents

The magnetic properties of the nucleus arise not just from the spin of the nucleons but also from their orbital motion. Two important components contribute to the magnetic current within the nucleus:

- **Convection Current (\vec{j}_ℓ):** This current is associated with the orbital motion of the nucleons, similar to how an electric current is generated by moving charges. Mathematically, it is given by:

$$\vec{j}_\ell(\vec{r}) = i\mu_N \sum_{q,j} v_{q,j}^2 g_\ell \left[\varphi_{q,j}(\vec{r}) \vec{\nabla} \varphi_{q,j}^*(\vec{r}) - \varphi_{q,j}^*(\vec{r}) \vec{\nabla} \varphi_{q,j}(\vec{r}) \right], \quad (6.33)$$

where μ_N is the nuclear magneton (a unit for magnetic dipole moments in nuclear physics), g_ℓ is the orbital g-factor, $\varphi_{q,j}(\vec{r})$ are the wave functions of the nucleons, q indexes the nature of the nucleon (proton or neutron), and $v_{q,j}^2$ are the occupation probabilities of these nucleons.

- **Spin Current (\vec{j}_s):** This current arises from the intrinsic spin of the nucleons and is given by [152]:

$$\vec{j}_s(\vec{r}) = \mu_N \sum_{q,j} v_{q,j}^2 g_s \vec{\nabla} \times [\varphi_{q,j}^*(\vec{r}) \vec{s} \varphi_{q,j}(\vec{r})], \quad (6.34)$$

where g_s is the spin g-factor, and \vec{s} is the spin operator. This expression captures how the intrinsic spin of nucleons contributes to the overall magnetic field.

Magnetic Dipole Moment Calculations

To calculate the total magnetic dipole moment of a nucleus in the nuclear numerical code, we consider contributions from both the intrinsic and collective motions. We also take into account how both the spin and orbital motion of protons and neutrons contribute:

$$\langle \mu_z \rangle = g_\ell \langle \ell_z \rangle + g_s \langle s_z \rangle, \quad (6.35)$$

where $\langle \ell_z \rangle$ and $\langle s_z \rangle$ are the expectation values of the orbital and spin angular momentum operators, respectively. Table 6.2 shows the Landé g factors for protons and neutrons used in these calculations.

	g_ℓ	$\langle \ell_z \rangle^{(\text{tot})}$	g_s	$\langle s_z \rangle^{(\text{tot})}$	$\langle \mu_z \rangle^{(\text{tot})}$
Neutron	0	2.238199	-3.8262	0.261801	-1.0017
Proton	1	-0.018104	5.58658	0.018104	0.0830

Table 6.2: Values of the Landé g factors for protons and neutrons needed to calculate the expectation value of the magnetic moment through Eq. (6.35). The expectation values of the orbital and spin angular momentum operators are also shown for ^{161}Dy .

In the context of axially symmetric nuclei, the magnetic dipole moment is evaluated by summing up the contributions from each nucleon. For nuclei like ^{161}Dy and ^{163}Dy , this involves considering how the unpaired neutron or proton affects the magnetic moment, which is a process known as "core polarization" (see Section 6.3.1).

Comparison with Experimental Data

The theoretical calculations of magnetic moments can be compared with experimental measurements to validate the models used. For the nuclei ^{161}Dy and ^{163}Dy , the calculated magnetic dipole moments are shown in table 6.3.

	$\langle \mu_z \rangle$	$\mu^{(\text{spec})}$	$\mu^{(\text{exp})}$ [145]
^{161}Dy	-0.91865	-0.6562	-0.480
^{163}Dy	0.92765	0.6626	0.673

Table 6.3: Intrinsic and spectroscopic contributions to the magnetic moments of ^{161}Dy and ^{163}Dy , compared with experimental values.

The comparison shows that while the model captures the general behavior of magnetic moments, some discrepancies with experimental data remain, indicating the need for further refinement in understanding the complex interplay of nuclear forces and motions.

Summary

Magnetic dipole moments in nuclei result from the complex interplay of nucleon spins and orbital motions. By using the Skyrme-Hartree-Fock model, which includes terms for these magnetic currents, we can gain insights into the structure of the nucleus and its interaction with magnetic fields. Although the calculated magnetic moments align reasonably well with experimental values, they highlight the intricacies involved in modeling nuclear properties. The obtained current and magnetic moment distributions for ^{161}Dy and ^{163}Dy can be seen in Fig. 6.7 for the protons and Fig. 6.8 for the neutron. The spatial coordinates are in units of R_N , the empirical nuclear radius, leading to a current distribution in units of $R_N^{-2} \cdot s^{-1}$. Moreover, the outer shell of the nucleus is indicated by the dashed curve, and chosen to be the full width at half maximum (FWHM) of the respective isotope's proton density.

Neutron current distributions are represented on Fig. 6.8. In comparison with the proton case shown in Fig. 6.7, the intensity of the currents is greater. From the symmetries of the currents, it can be seen that only the z -component of the magnetic dipole moment is non-zero, as expected for axially symmetric nuclei.

Note: The core polarization effect is particularly visible in Figs. 6.7 and 6.8. Since ^{161}Dy and ^{163}Dy have an odd number of neutrons, and assuming the core is the even-even nucleus ^{160}Dy or ^{162}Dy , respectively, that exhibits no intrinsic currents. Then it appears that the proton current densities mirror the structure of the neutron current densities, albeit with lower intensity, suggesting that the proton currents are induced by the neutron currents.

Although the single-particle model falls short in fully capturing the complex interactions between nucleons in the nucleus and the resulting currents, it offers a useful foundation for understanding the structure of current distributions. For instance, in the case of ^{163}Dy , which has 97 neutrons, simple predictions from the nuclear shell model suggest that the unpaired neutron occupies the $1h_{9/2}$ state [38]. Additionally, experimental data shows that the ground state of ^{163}Dy corresponds to a $K^\pi = 5/2^-$ band [145].

Figure 6.9 shows the normalized current distributions ^a calculated for the 3D spherical harmonic oscillator eigenstate, which corresponds to the quantum state $|n\ell_j m_j = -5/2\rangle$. This state can be expressed as a combination of orbital (m_l) and spin (m_s) components

$$|n\ell_j m_j = -5/2\rangle = \frac{1}{\sqrt{11}} \left(\sqrt{3} |n\ell m_l = -2 m_s = -1/2\rangle - 2\sqrt{2} |n\ell m_l = -3 m_s = +1/2\rangle \right). \quad (6.36)$$

In this expression, $n = 6$ and $\ell = 5$, which correspond to the $1h$ orbital state. The using Clebsch-Gordan coefficients (see (D.8)) in the equation represent the relative contributions of two specific combinations of the orbital angular momentum (m_l) and spin angular momentum (m_s) to form the total angular momentum state $m_j = -5/2$.

The current distribution closely resembles the one obtained for ^{163}Dy . Similar qualitative considerations can be applied to the other isotopes and elements investigated in this study, even though,

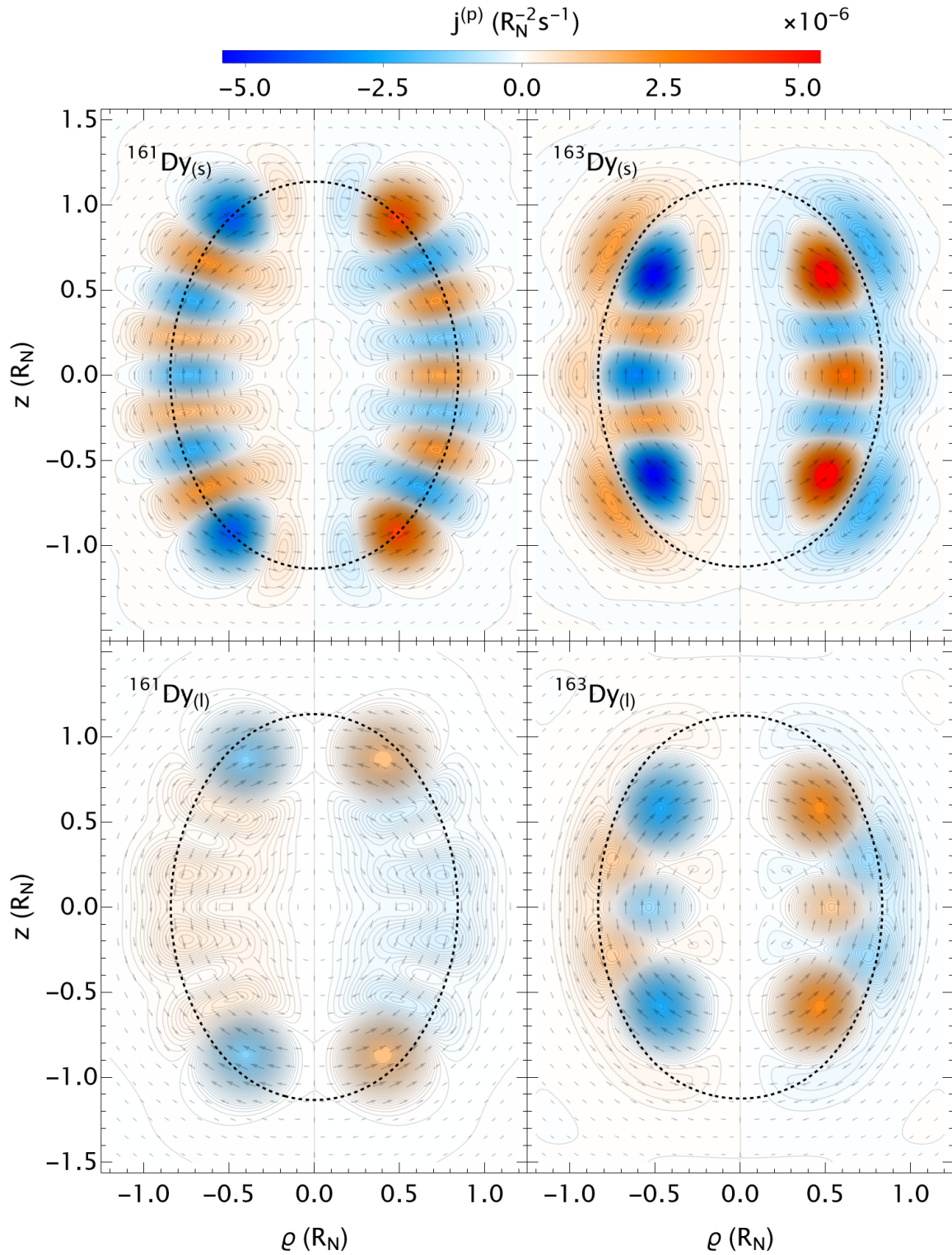


Figure 6.7: Proton current distributions, $\vec{j}^{(p)}(\vec{R})$ (upper : spin contributions, lower: orbital contributions), of ^{161}Dy (left) and ^{163}Dy (right) with associated magnetic dipole moments $\vec{R} \wedge \frac{1}{2} \left(\vec{j}^{(p)}(\vec{R}) \right)$ indicated by the arrow vectors. The figures are plotted in cylindrical coordinates (z, ϱ) , on a planar slice through the z -axis. The contours represent curves of equivalent density, with numerical values as indicated by the legend. The dashed curve indicates the contour line of the FWHM of the isotope's proton density, representing the outer shell of the nucleus.

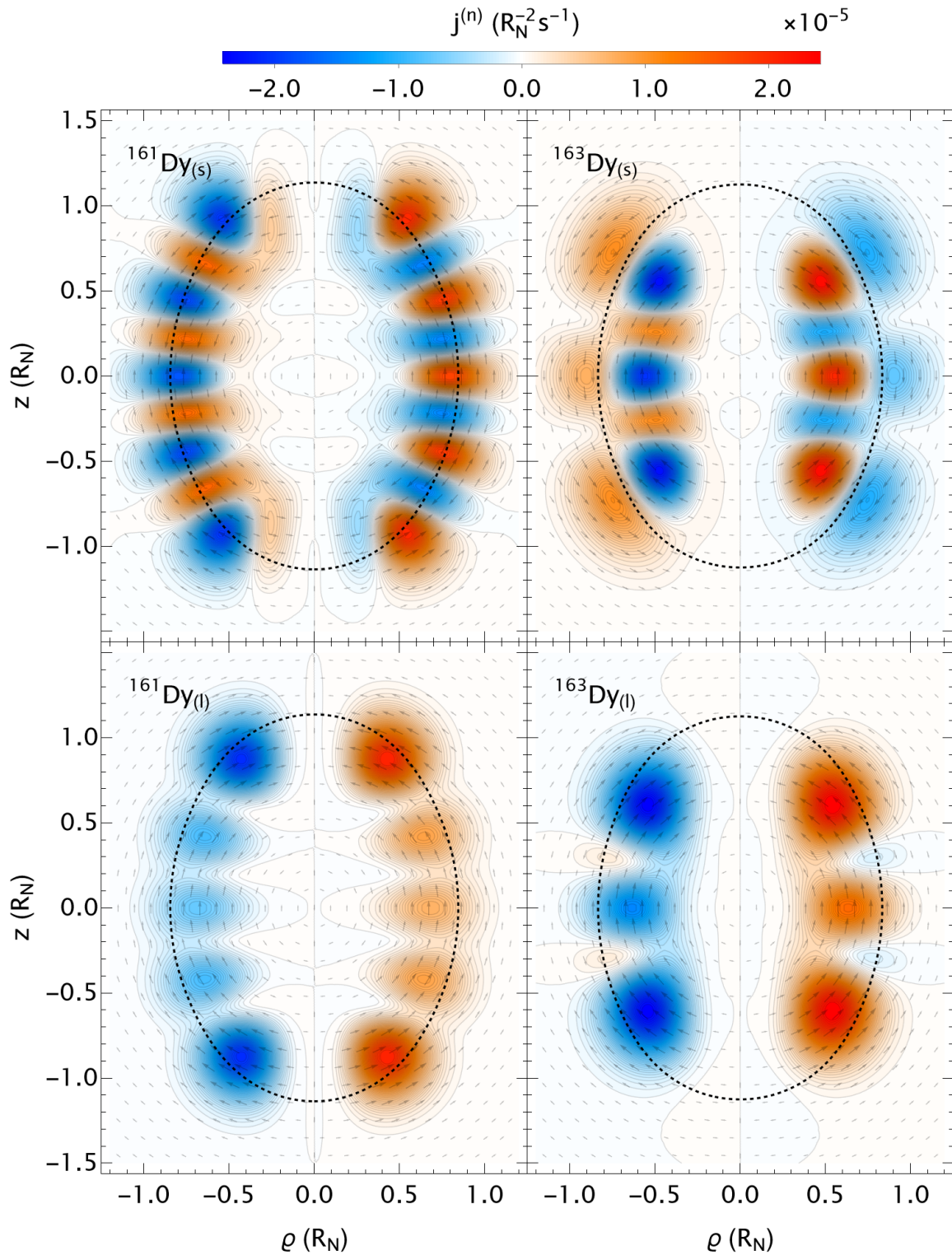


Figure 6.8: Neutron current distributions, $\vec{j}^{(n)}(\vec{R})$ (upper : spin contributions, lower: orbital contributions), of ^{161}Dy (left) and ^{163}Dy (right) with associated magnetic dipole moments $\vec{R} \wedge \frac{1}{2} \left(\vec{j}^{(n)}(\vec{R}) \right)$ indicated by the arrow vectors. The figures are plotted in cylindrical coordinates (z, ϱ) , on a planar slice through the z -axis. The contours represent curves of equivalent density, with numerical values as indicated by the legend. The dashed curve indicates the contour line of the FWHM of the isotope's proton density, representing the outer shell of the nucleus.

in some cases, one should also account for configuration mixing and other non-trivial effects. For example, the single particle spectra for both the neutrons and the protons in ^{162}Dy , obtained from the HFBCS calculations, are shown in Fig. 6.10. The Nilsson quantum numbers of the corresponding harmonic oscillator states are also indicated, along with the occupation probabilities of the states, and we can observe the configuration mixing in the single-particle states.

$$^a i (\psi_{n,\ell}^* \nabla \psi_{n,\ell} - \psi_{n,\ell} \nabla \psi_{n,\ell}^*)$$

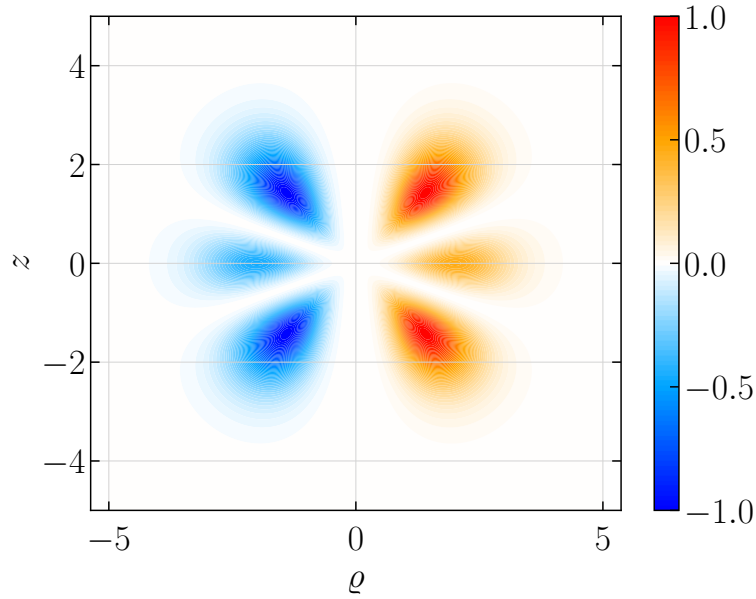


Figure 6.9: Normalized current distribution for the 3D spherical harmonic oscillator eigenstate corresponding to the quantum state $|1h_{9/2} m_j = -5/2\rangle$, which is a component of the single particle ground state of ^{163}Dy according to the shell model. The figure is plotted in cylindrical coordinates (z, ρ) , on a planar slice through the z -axis. The contours represent curves of equivalent density, with numerical values as indicated by the legend.

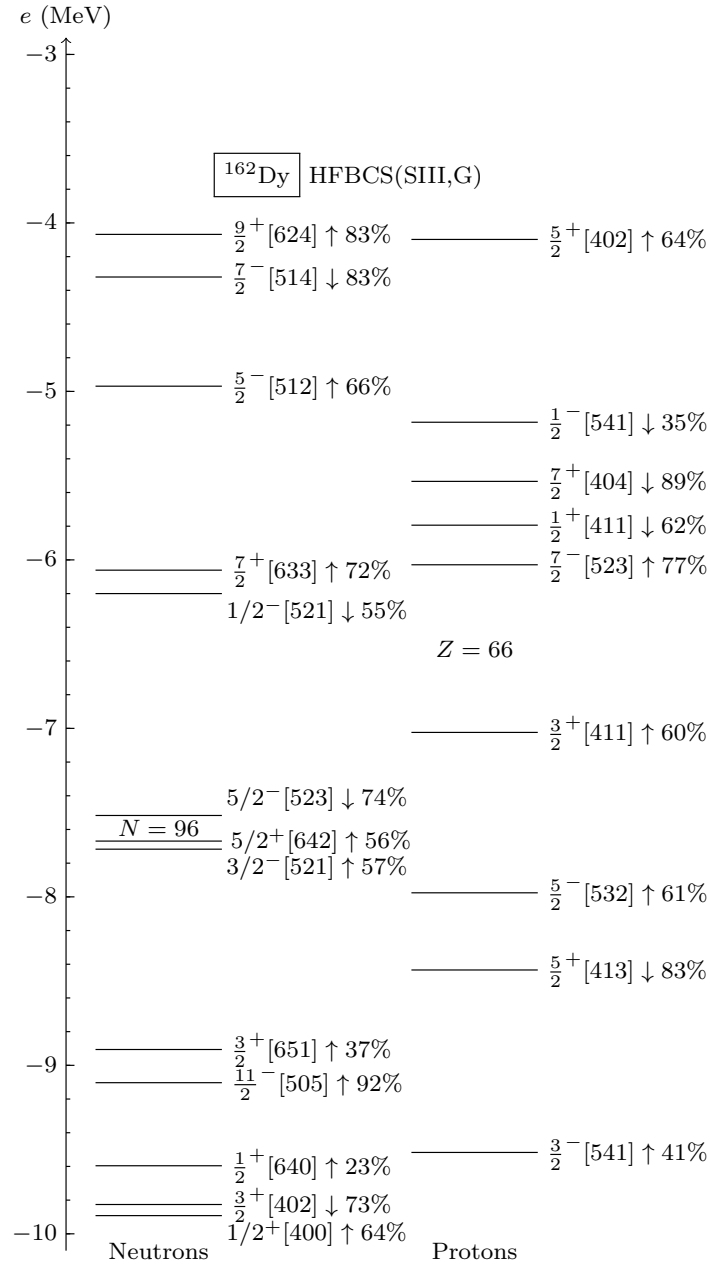


Figure 6.10: Single particle spectra for the ^{162}Dy nucleons near the Fermi level obtained from the HFBCS calculations. Each level is denoted by K^π quantum numbers, where K is the projection of the total angular momentum along the symmetry axis, and π is the parity. The numbers in square brackets indicate the Nilsson quantum numbers of the corresponding harmonic oscillator states, while the percentage values represent the contribution of the state to the multi-particle state of the ground state, the arrows indicate the spin

6.4.2 Multipole expansion of the nuclear magnetic vector potential

Considering a finite current density distribution in the nucleus, one starts from the form of the vector potential in the Coulomb gauge ($\vec{\nabla} \cdot \vec{A} = 0$), given by

$$\vec{A}(\vec{r}) = \frac{\mu_0}{4\pi} \int \frac{\vec{j}(\vec{R})}{|\vec{r} - \vec{R}|} d^3\vec{R}. \quad (6.37)$$

Given a set of normalized spherical harmonics $\{C_q^{(k)}(\theta, \phi)\}_{k,q}$, one can define the following normalized vector spherical harmonics, for $k \geq 1$,

$$\vec{Y}_q^{(k)} = \vec{e}_r C_q^{(k)}(\theta, \phi), \quad (6.38)$$

$$\vec{\Psi}_q^{(k)} = \frac{1}{\sqrt{k(k+1)}} \left[r \vec{\nabla} C_q^{(k)}(\theta, \phi) \right], \quad (6.39)$$

$$\text{and } \vec{\Phi}_q^{(k)} = \frac{i}{\hbar \sqrt{k(k+1)}} \left[\vec{L} C_q^{(k)}(\theta, \phi) \right]. \quad (6.40)$$

It should be emphasized that while the definition of \vec{Y} remains unchanged for $k = 0$, both $\vec{\Psi}^{(0)}$ and $\vec{\Phi}^{(0)}$ are identically zero.

Any vector field $\vec{V}(\vec{r})$ can be decomposed into a series of vector spherical harmonics

$$\vec{V}(\vec{r}) = \sum_{k=0}^{+\infty} \sum_{q=-k}^k \left({}^r V_q^{(k)}(r) \vec{Y}_q^{(k)} + {}^{(\Psi)} V_q^{(k)}(r) \vec{\Psi}_q^{(k)} + {}^{(\Phi)} V_q^{(k)}(r) \vec{\Phi}_q^{(k)} \right). \quad (6.41)$$

However,

$$\vec{\nabla} \vec{V} = \left(\frac{d^r V_q^{(k)}}{dr} + \frac{2}{r} {}^r V_q^{(k)} - \frac{k(k+1)}{r} {}^{(\Psi)} V_q^{(k)} \right) C_q^{(k)}(\theta, \phi), \quad (6.42)$$

and \vec{A} respects the Coulomb gauge condition $\vec{\nabla} \vec{A} = 0$, therefore, \vec{A} can be expressed into a series of $\vec{\Phi}_q^{(k)}$ only, taking the form

$$\vec{A}(\vec{r}) = \frac{\mu_0}{4\pi} \sum_{k=1}^{+\infty} \sum_{q=-k}^k \frac{i}{\hbar \sqrt{k(k+1)}} \left[\vec{L} C_q^{(k)}(\theta, \phi) \right] A_q^{(k)}(r). \quad (6.43)$$

Using the orthogonality relation

$$\frac{-1}{\hbar^2 k(k+1)} \int_{\theta, \phi} \left[\vec{L} C_{q'}^{(k')}(\theta, \phi) \right] \cdot \left[\vec{L} C_{-q}^{(k)}(\theta, \phi) \right] d^2 \vec{\Omega} = (-1)^q \delta_{k,k'} \delta_{q,q'}, \quad (6.44)$$

one obtains

$$A_q^{(k)}(r) = \frac{4\pi}{\mu_0} \frac{i}{\hbar \sqrt{k(k+1)}} (-1)^q \int_{\theta, \phi} \left[\vec{L} C_{-q}^{(k)}(\theta, \phi) \right] \cdot \vec{A}(\vec{r}) d^2 \vec{\Omega}. \quad (6.45)$$

The multipolar expansion of $\frac{1}{|\vec{r}-\vec{R}|}$ in (6.37),

$$\begin{aligned} A(\vec{r}) &= \frac{\mu_0}{4\pi} \sum_{k=0}^{+\infty} \frac{1}{r^{k+1}} \sum_{q=-k}^k (-1)^q C_q^{(k)}(\theta, \phi) \int_{R=0}^r C_{-q}^{(k)}(\Theta, \Phi) \vec{j}(\vec{R}) R^k d^3 \vec{R}, \\ &+ \frac{\mu_0}{4\pi} \sum_{k=0}^{+\infty} r^k \sum_{q=-k}^k (-1)^q C_q^{(k)}(\theta, \phi) \int_{R=r}^{+\infty} C_{-q}^{(k)}(\Theta, \Phi) \vec{j}(\vec{R}) \frac{1}{R^{k+1}} d^3 \vec{R}, \end{aligned} \quad (6.46)$$

can be inserted in (6.45), and, computing the effect of each component of \vec{L} on $C_{-q}^{(k)}$, one can prove that³

$$\left(\int_{\theta, \phi} (-1)^{q'} C_{q'}^{(k')}(\theta, \phi) \left[\vec{L} C_{-q}^{(k)}(\theta, \phi) \right] d^2 \vec{\Omega} \right) C_{-q'}^{(k')}(\Theta, \Phi) = \vec{L} C_{-q}^{(k)}(\Theta, \Phi), \quad (6.47)$$

³Note that $\vec{L} = \vec{r} \wedge \vec{\nabla}_r$ on the left side of this equality is acting on the electronic coordinates θ, ϕ while, $\vec{L} = \vec{R} \wedge \vec{\nabla}_R$, on the right side, is acting on the nuclear coordinates Θ, Φ .

therefore,

$$A_q^{(k)}(r) = \frac{i}{\hbar\sqrt{k(k+1)}} \frac{1}{r^{k+1}} (-1)^q \int_{R=0}^r \left[\vec{L}C_{-q}^{(k)}(\Theta, \Phi) \right] \cdot \vec{j}(\vec{R}) R^k d^3 \vec{R},$$

$$+ \frac{i}{\hbar\sqrt{k(k+1)}} r^k (-1)^q \int_{R=r}^{+\infty} \left[\vec{L}C_{-q}^{(k)}(\Theta, \Phi) \right] \cdot \vec{j}(\vec{R}) \frac{1}{R^{k+1}} d^3 \vec{R}. \quad (6.48)$$

To follow convention, we can write the multipolar expansion of the vector potential as

$$\vec{A}(\vec{r}) = \frac{\mu_0}{4\pi} \sum_{k=1}^{+\infty} \sum_{q=-k}^k (-1)^q \frac{(-i)}{\hbar k} \left[\vec{L}C_q^{(k)}(\theta, \phi) \right] {}^{in}M_{-q}^{(k)}(r) \frac{1}{r^{k+1}}$$

$$+ \frac{\mu_0}{4\pi} \sum_{k=1}^{+\infty} \sum_{q=-k}^k (-1)^q \frac{(-i)}{\hbar k} \left[\vec{L}C_q^{(k)}(\theta, \phi) \right] {}^{ex}M_{-q}^{(k)}(r) r^k, \quad (6.49)$$

with

$${}^{in}M_q^{(k)}(r) \equiv -\frac{i}{\hbar(k+1)} \int_{R=0}^r \left[\vec{L}C_q^{(k)}(\Theta, \Phi) \right] \cdot \vec{j}(\vec{R}) R^k d^3 \vec{R}, \quad (6.50)$$

and

$${}^{ex}M_q^{(k)}(r) \equiv -\frac{i}{\hbar(k+1)} \int_{R=r}^{+\infty} \left[\vec{L}C_q^{(k)}(\Theta, \Phi) \right] \cdot \vec{j}(\vec{R}) \frac{1}{R^{k+1}} d^3 \vec{R}. \quad (6.51)$$

6.4.3 Magnetic dipole moment

Truncating the previous expansion to the first non-vanishing term ($k = 1$) yields

$$\vec{A}(\vec{r}) = \frac{\mu_0}{4\pi} \sum_{q=-1}^1 (-1)^q \frac{(-i)}{\hbar} \left[\vec{L}C_q^{(1)}(\theta, \phi) \right] \frac{{}^{in}M_{-q}^{(1)}(r)}{r^2} + \frac{\mu_0}{4\pi} \sum_{q=-1}^1 (-1)^q \frac{(-i)}{\hbar} \left[\vec{L}C_q^{(1)}(\theta, \phi) \right] {}^{ex}M_{-q}^{(1)}(r) r. \quad (6.52)$$

For an arbitrary vector $\vec{v}^{(1)}$, one can show that

$$[\vec{r} \wedge \vec{v}^{(1)}]_\lambda = \frac{-i}{\hbar} \left[r \vec{L}C_\lambda^{(1)}(\theta, \phi) \right] \cdot \vec{v}^{(1)}. \quad (6.53)$$

We recall that for vectors \vec{v} , represented as first-rank tensors $\vec{v}^{(1)}$, the scalar product is defined as

$$\vec{v}^{(1)} \cdot \vec{u}^{(1)} = \sum_{\lambda} (-1)^\lambda v_\lambda^{(1)} u_{-\lambda}^{(1)}. \quad (6.54)$$

Moreover, it is important to remember \vec{L} commutes with any function of r , from there, one can look at the following scalar product:

$$\begin{aligned} & \vec{A}(\vec{r}) \cdot \vec{v}^{(1)} \\ &= \frac{\mu_0}{4\pi r^3} \frac{(-i)}{\hbar} \left(\sum_{q=-1}^1 (-1)^q \left[r \vec{L}C_q^{(1)}(\theta, \phi) \right] \frac{{}^{in}M_{-q}^{(1)}(r)}{r^3} \cdot \vec{v}^{(1)} + \sum_{q=-1}^1 (-1)^q \left[r \vec{L}C_q^{(1)}(\theta, \phi) \right] {}^{ex}M_{-q}^{(1)}(r) \cdot \vec{v}^{(1)} \right) \\ &= \frac{\mu_0}{4\pi r^3} \sum_{q=-1}^1 (-1)^q [\vec{r} \wedge \vec{v}^{(1)}]_q {}^{in}M_{-q}^{(1)}(r) + \frac{\mu_0}{4\pi} \sum_{q=-1}^1 (-1)^q [\vec{r} \wedge \vec{v}^{(1)}]_q {}^{ex}M_{-q}^{(1)}(r) \\ &= \frac{\mu_0}{4\pi r^3} {}^{in}\vec{M}^{(1)}(r) \cdot (\vec{r} \wedge \vec{v}^{(1)}) + \frac{\mu_0}{4\pi} {}^{ex}\vec{M}^{(1)}(r) \cdot (\vec{r} \wedge \vec{v}^{(1)}) \\ &= \left(\frac{\mu_0}{4\pi r^3} ({}^{in}\vec{M}^{(1)}(r) \wedge \vec{r}) + \frac{\mu_0}{4\pi} ({}^{ex}\vec{M}^{(1)}(r) \wedge \vec{r}) \right) \cdot \vec{v}^{(1)}. \end{aligned} \quad (6.55)$$

Therefore, one obtains

Definition: (*Dipole magnetic vector potential of the nucleus*)

$$\vec{A}(\vec{r}) = \frac{\mu_0}{4\pi} \frac{{}^{in}\vec{M}^{(1)}(r) \wedge \vec{r}}{r^3} + \frac{\mu_0}{4\pi} \left({}^{ex}\vec{M}^{(1)}(r) \wedge \vec{r} \right), \quad (6.56)$$

with, also using (6.53),

$${}^{in}\vec{M}^{(1)}(r) = \frac{1}{2} \int_{R=0}^r \vec{R} \wedge \vec{j}(\vec{R}) d^3\vec{R} \quad (6.57)$$

and

$${}^{ex}\vec{M}^{(1)}(r) = \frac{1}{2} \int_{R=r}^{+\infty} \frac{\vec{R} \wedge \vec{j}(\vec{R})}{R^3} d^3\vec{R}. \quad (6.58)$$

Note: One can define the magnetic dipole density as

$$\vec{m}(\vec{R}) \equiv \frac{1}{2} \vec{R} \wedge \vec{j}(\vec{R}). \quad (6.59)$$

Such that the magnetic dipole moment of the nucleus is given by

$$\vec{M}^{(1)} = {}^{in}\vec{M}^{(1)}(r \rightarrow \infty) = \int_{R=0}^{\infty} \vec{m}(\vec{R}) d^3\vec{R}. \quad (6.60)$$

Similarly, one can define the angular average of the magnetic dipole density as

$$\vec{\rho}_1(R) \equiv \frac{1}{4\pi R^2} \int_{\Omega} \vec{m}(\vec{R}) d\Omega, \quad (6.61)$$

such that the magnetic dipole moment of the nucleus is given by

$$\vec{M}^{(1)} = {}^{in}\vec{M}^{(1)}(r \rightarrow \infty) = \int 4\pi R^2 \vec{\rho}_1(R) dR. \quad (6.62)$$

Figure 6.11 shows the only non-zero component of $\vec{\rho}_1$, $\rho_{1,z} = \rho_{1,0}$, for the isotopes ${}^{161}\text{Dy}$ and ${}^{163}\text{Dy}$. It is normalized by the total magnetic dipole value $M_z^{(1)}$, that are shown in Tab. 6.3 and it thus in units of R_N^{-3} , with R_N being the nuclear radius. The dipole densities are dominated by the contributions from the neutron spins, particularly for isotope ${}^{163}\text{Dy}$ with an additional 2 neutrons. It is interesting to see that there are peaks in the curves lying close to the outer surface of the (spherically averaged) nuclear radius. Comparison of the curves for each isotope show that the difference in only 2 neutrons in the nucleus leads to a complete change of sign of the dipole densities contributing towards the dipole moment (as $M_z^{(1),161}$ and $M_z^{(1),163}$ are of opposite sign). Furthermore, it is interesting to see that there are peaks in the curves lying close to the outer surface of the (spherically averaged) nuclear radius. This is consistent with the expectation that the magnetic dipole moment of the nucleus is dominated by the contributions from the single unpaired neutron in the outer shell of the nucleus.

6.5 Other effects of the nucleus

Aside from the finite size, mass, and magnetization of the nucleus, atomic energy levels are influenced by other nuclear effects.

Parity violation One such effect is atomic parity violation, caused by the weak interaction between atomic electrons and nuclear constituents [153]. This interaction can mix atomic states of different parity, leading to phenomena like circular dichroism, where atoms interact differently with left and

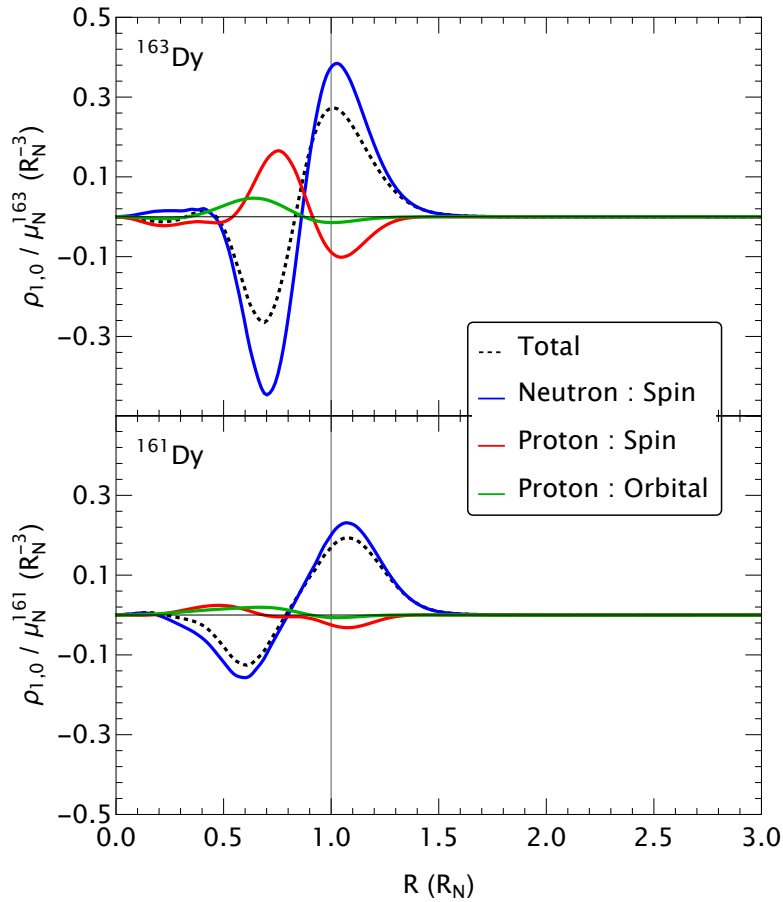


Figure 6.11: The distributions of the magnetic dipolar radial density contributions, normalized by the total magnetic moment of the isotope $A = 161, 163$ ($\mu_N^1 = {}^{(A)}M_z^{(1),\text{iso}}$), $\rho_{1,0}(R)$ within the nuclei of isotopes ${}^{163}\text{Dy}$ (upper) and ${}^{161}\text{Dy}$ (lower). R is used in units of the nuclear radius, R_N , thus giving the dipole in units of R_N^{-3} . The dashed vertical line represents the surface of the nucleus at $R = 1 \times R_N$, to which the other curves are normalised. Each curve describes a different contribution to the dipole density distribution: (dashed) the total dipole density, (blue) the neutron spins, (red) the proton spins, and (green) the proton orbital currents.

right-handed circularly polarized photons. This effect introduces an odd parity-violating potential, resulting in a slight asymmetry in atomic transitions.

Nuclear polarization Nuclear polarization is another effect, stemming from the interaction between the radiation field and intrinsic nuclear dynamics. The nucleus can undergo virtual transitions to excited states through the exchange of virtual photons, causing shifts in the energy levels of the atomic electrons. Although these polarization effects are generally small, they become significant in high-precision atomic structure calculations, particularly in heavy elements.

NEEC/NEET/BIC Other mechanisms involve direct interactions between atomic electrons and nuclear excited states. Nuclear Excitation by Electron Capture (NEEC) occurs when an electron is captured into an atomic bound state while simultaneously exciting the nucleus. Nuclear Excitation by Electron Transition (NEET) happens when the nucleus is excited during an atomic transition, given that the energies of the atomic and nuclear transitions match. Additionally, Bound Internal Conversion (BIC) involves a nuclear transition inducing an electron transition within the atom. These processes directly couple atomic and nuclear transitions, affecting atomic energy levels.

These other effects are discussed in greater detail in the review Pálffy [149], but will not be further elaborated on in this work. A complete and metrologically relevant study of the hyperfine structure must however consider these nuclear effects, as they can significantly impact the accuracy of the final calculations.

Main takeaways from Chapter 6

- **Finite Nuclear Mass and Mass Corrections:**

- The nucleus has finite mass, leading to mass corrections in atomic calculations.
- Normal Mass Shift (NMS) and Specific Mass Shift (SMS) account for these effects.

- **Muonic Ions:**

- Muonic ions involve muons replacing electrons, requiring adjusted reduced mass.
- Energy levels are calculated using the Dirac equation with this reduced mass.

- **Nuclear Charge and Magnetic Distributions:**

- Nuclei have finite size and may be deformed.
- Charge distributions affect electric monopole and quadrupole potentials.
- Magnetic dipole moments arise from nucleon spins and orbital motions.
- Both charge and current distributions were computed using the Skyrme-Hartree-Fock-Bogoliubov (HFBCS) model, in collaboration with nuclear physicists.
- Lanthanide nuclei exhibit complex current distributions, and a high deformation of the charge distribution.

- **Multipole Expansion of Nuclear Potentials:**

- Electric and magnetic potentials are expanded using multipole series.

- **Other Nuclear Effects not covered in the manuscript:**

- Parity violation and nuclear polarization can impact atomic energy levels.
- Important for high-precision measurements and metrological applications.

Chapter Contents

7.1	The hyperfine dipole constant	125
7.2	The hyperfine quadrupole constant	130
7.3	Isotope Shifts	132
7.4	The non-relativistic limit	135
7.5	Hyperfine constants in matter	141

CHAPTER 7

Hyperfine constants

We have seen in [Section 6.3.3](#) that the monopole electric field of the nucleus can be inserted in the Dirac equation for a central potential discussed in [Chapter 5](#), this will lead to a change in the atomic energy levels as well as the radial distribution of the wavefunctions. In this chapter, we will discuss the first order correction to the atomic energy levels due to the higher order multipoles of the nuclear magnetic and electric fields. This will allow to define the hyperfine constants, which are used to characterise the energy splittings of atomic levels due to the higher-than-monopole nuclear fields.

7.1 The hyperfine dipole constant

The effect of the dipole magnetic vector potential of the nucleus on the electron derived in [\(6.56\)](#) can be modeled as an effective Hamiltonian term in the Dirac equation. This subsection aims to show the derivation of that term.

One can rewrite [\(6.52\)](#) and [\(6.56\)](#) as

$$\vec{A}(\vec{r}) \equiv \frac{\mu_0}{4\pi} \sum_{q=-1}^1 (-1)^q \frac{(-i)}{\hbar} \left[\vec{L} C_q^{(1)}(\theta, \phi) \right] f_{M,-q}(r), \quad (7.1)$$

with

$$\vec{f}_M(r) = \frac{1}{2} \frac{1}{r^2} \int_{R=0}^r \left(\vec{R} \wedge \vec{j}(\vec{R}) d^3 \vec{R} + r \int_{R=r}^{+\infty} \frac{\vec{R} \wedge \vec{j}(\vec{R})}{R^3} d^3 \vec{R} \right), \quad (7.2)$$

and obtain the correction to the Dirac equation due to the magnetic dipole moment of the nucleus according to the minimal coupling principle (see [\(5.20\)](#))

Definition: (*Hyperfine magnetic dipole Hamiltonian*)

$$H_{\text{hf,dip}} = -ec\vec{\alpha} \cdot \vec{A}(\vec{r}). \quad (7.3)$$

We can define the total angular momentum operator of the electrons+nucleus system as $\vec{F} = \vec{J} + \vec{I}$, with \vec{J} and \vec{I} being the total angular momentum operators of the electrons and nucleus, respectively. Therefore, the energy correction due to the hyperfine dipole Hamiltonian in this basis is given by

first-order perturbation theory as

$$\begin{aligned} \langle n_a \kappa_a F M_F | H_{\text{hf,dip}} | n_b \kappa_b F M_F \rangle = \\ -iec \frac{\mu_0}{4\pi\hbar} \sum_{q=-1}^1 (-1)^q \langle n_a \kappa_a m_a F M_F | [\vec{\alpha} \cdot \vec{L} C_q^{(1)}(\theta, \phi)] f_{M,-q}(r) | n_b \kappa_b m_b F M_F \rangle \end{aligned} \quad (7.4)$$

The Wigner-Eckart theorem states that

$$\langle F M_F | T_q^{(k)} | F' M_{F'} \rangle = (-1)^{F-M_F} \begin{pmatrix} F & k & F' \\ -M_F & q & M_{F'} \end{pmatrix} \langle F || T^{(k)} || F' \rangle, \quad (7.5)$$

where $T_q^{(k)}$ is a tensor operator of rank k and q is the projection of the operator in the z -axis. $\langle F || T^{(k)} || F' \rangle$ is the reduced matrix element of the operator, independent of M_F and $M_{F'}$.

Using (7.5), one can obtain that

$$\begin{aligned} \langle I M_I | f_{M,-q}(r) | I M_I' \rangle &= (-1)^{I-M_I} \begin{pmatrix} I & 1 & I \\ -M_I & -q & M_{I'} \end{pmatrix} \langle I || f_M(r) || I \rangle \\ &= (-1)^{I-M_I} \begin{pmatrix} I & 1 & I \\ -M_I & -q & M_{I'} \end{pmatrix} \begin{pmatrix} I & 1 & I \\ -I & -q & I \end{pmatrix}^{-1} \langle II | f_{M,-q}(r) | II \rangle. \end{aligned} \quad (7.6)$$

Given two irreducible tensor operators $T^{(k)}$ and $U^{(k)}$ of rank k , acting, respectively on the electronic and nuclear spaces, one can compute the matrix element of their scalar product as

$$\begin{aligned} \langle (J_a I) F M_F | T^{(k)} \cdot U^{(k)} | (J_b I) F' M_{F'} \rangle = \\ (-1)^{J_b+I+F} \delta_{F,F'} \delta_{M_F,M_{F'}} \begin{Bmatrix} J_b & I & F \\ I & J_a & k \end{Bmatrix} \langle J_a || T^{(k)} || J_b \rangle \langle I || U^{(k)} || I \rangle. \end{aligned} \quad (7.7)$$

Therefore, since only $f_{M,0}(r)$ is non-zero (see Section 6.4.1), one can write

$$\begin{aligned} \langle n_a \kappa_a F M_F | [\vec{\alpha} \cdot \vec{L} C_q^{(1)}(\theta, \phi)] f_{M,0}(r) | n_b \kappa_b F' M_{F'} \rangle \times = (-1)^{J_b+I+F} \delta_{F,F'} \delta_{M_F,M_{F'}} \delta_{q,0} \\ \times \begin{Bmatrix} J_b & I & F \\ I & J_a & 1 \end{Bmatrix} \langle n_a \kappa_a || \vec{\alpha} \cdot \vec{L} C_q^{(1)}(\theta, \phi) || I I \rangle \langle II | f_{M,0}(r) | II \rangle \langle n_b \kappa_b || \begin{pmatrix} I & 1 & I \\ -I & 0 & I \end{pmatrix}^{-1} || I \rangle. \end{aligned} \quad (7.8)$$

Note: One notices that F and M_F are good quantum numbers indexing a diagonal basis for the hyperfine dipole interaction. It does not however mean that the perturbation provides an exact energy correction since, while it is exact on the angular degrees of freedom, it is only a first order perturbation on the radial degrees of freedom that remain unchanged from the unperturbed spherically symmetric Hamiltonian. This can be seen by the fact that the perturbation is not diagonal in n .

Let us note that

$$\begin{aligned} \langle (J_a I) F M_F | \vec{I} \cdot \vec{J} | (J_b I) F' M_{F'} \rangle = \\ (-1)^{J_b+I+F} \delta_{F,F'} \delta_{M_F,M_{F'}} \begin{Bmatrix} J_b & I & F \\ I & J_a & 1 \end{Bmatrix} \langle J_a || \vec{J} || J_b \rangle \langle I || \vec{I} || I \rangle. \end{aligned} \quad (7.9)$$

Since,

$$\langle j || \vec{J} || j' \rangle = \sqrt{j(2j+1)(j+1)} \delta_{jj'}, \quad (7.10)$$

one sees that (7.9) vanishes for states with different F , I or \mathcal{K} (equiv. J). Furthermore, comparing (7.9) and (7.8), one can see that for matrix elements diagonal in J , the magnetic dipole hyperfine interaction is proportional to $\vec{I} \cdot \vec{J}$,

$$\langle n_a \kappa_a F M_F | H_{\text{hf,dip}} | n_a \kappa_a F M_F \rangle = a \langle n_a \kappa_a F M_F | \vec{I} \cdot \vec{J} | n_a \kappa_a F M_F \rangle, \quad (7.11)$$

and

$$a \equiv -ie c \frac{\mu_0}{4\pi \hbar} \frac{\langle n_a \kappa_a || \vec{\alpha} \cdot \vec{L} C_0^{(1)} \langle II | f_{M,0}(r) | II \rangle || n_a \kappa_a \rangle}{\begin{pmatrix} I & 1 & I \\ -I & 0 & I \end{pmatrix} \langle J_a || \vec{J} || J_a \rangle \langle I || \vec{I} || I \rangle}. \quad (7.12)$$

This also allows to write the hyperfine dipole Hamiltonian as an effective one for states in the same J multiplet, and (7.12) gives the expression of the hyperfine constant a in terms of the reduced matrix elements of the magnetic dipole moments of the nucleus and the electron.

Definition: (*Effective dipole Hamiltonian*)

$$H_{\text{hf,dip}}^{\text{eff}} = a \vec{I} \cdot \vec{J}. \quad (7.13)$$

The expression in (7.12) can be readily computed in the case of a single electron. One can calculate the matrix element $\langle n_a \kappa_a m_a | [\vec{\alpha} \cdot \vec{L} C_0^{(1)}(\theta, \phi)]^I f_M(r) | n_b \kappa_b m_b \rangle$, where $^I f_M(r) \equiv \langle II | f_{M,0}(r) | II \rangle$, by noticing that \vec{L} commutes with any function of r , and by extension so does $\vec{\alpha} \cdot \vec{L}$

$$[\vec{\alpha} \cdot \vec{L} C_0^{(1)}(\theta, \phi)]^I f_M(r) = ^I f_M(r) [\vec{\alpha} \cdot \vec{L} C_0^{(1)}(\theta, \phi)] = \vec{\alpha} \cdot \vec{L} [C_0^{(1)I} f_M(r)], \quad (7.14)$$

and

$$\vec{\alpha} \cdot \vec{L} [C_0^{(1)}(\theta, \phi) | n \kappa m \rangle] = [\vec{\alpha} \cdot \vec{L} C_0^{(1)}(\theta, \phi)] | n \kappa m \rangle + C_0^{(1)}(\theta, \phi) [\vec{\alpha} \cdot \vec{L} | n \kappa m \rangle], \quad (7.15)$$

since \vec{L} is a differential this is simply the Leibniz product rule.

Thus,

$$\begin{aligned} \langle n_a \kappa_a m_a | \vec{\alpha} \cdot \vec{L} [C_0^{(1)}(\theta, \phi) f_M(r)] | n_b \kappa_b m_b \rangle = \\ \left[\langle n_a \kappa_a m_a | \vec{\alpha} \cdot \vec{L} \right] [C_0^{(1)}(\theta, \phi) f_M(r) | n_b \kappa_b m_b \rangle] - \left[\langle n_a \kappa_a m_a | f_M(r) C_0^{(1)}(\theta, \phi) \right] [\vec{\alpha} \cdot \vec{L} | n_b \kappa_b m_b \rangle] \end{aligned} \quad (7.16)$$

Moreover,

$$\vec{\alpha} \cdot \vec{L} | n \kappa m \rangle = \begin{pmatrix} 0 & \vec{\sigma} \cdot \vec{L} \\ \vec{\sigma} \cdot \vec{L} & 0 \end{pmatrix} \frac{1}{r} \begin{pmatrix} P_{n\kappa}(r) \chi_{\kappa m}(\theta, \phi) \\ i Q_{n\kappa}(r) \chi_{-\kappa m}(\theta, \phi) \end{pmatrix} = \frac{1}{r} \begin{pmatrix} \hbar(\kappa - 1) i Q_{n\kappa}(r) \chi_{-\kappa m}(\theta, \phi) \\ \hbar(-\kappa - 1) P_{n\kappa}(r) \chi_{\kappa m}(\theta, \phi) \end{pmatrix}, \quad (7.17)$$

since $(\vec{\sigma} \cdot \vec{L} + \hbar) \chi_{\kappa m}(\theta, \phi) = -\hbar \kappa \chi_{\kappa m}(\theta, \phi)$.

Hence, one can write

$$\begin{aligned} \langle n_a \kappa_a | [\vec{\alpha} \cdot \vec{L} C_0^{(1)}(\theta, \phi)]^I f_M(r) | n_b \kappa_b \rangle = \\ -i\hbar(\kappa_a + \kappa_b) \langle \kappa_a m_a | C_0^{(1)}(\theta, \phi) | -\kappa_b m_b \rangle \int_{r=0}^{+\infty} ^I f_M(r) (P_{n_a \kappa_a}(r) Q_{n_b \kappa_b}(r) + Q_{n_a \kappa_a}(r) P_{n_b \kappa_b}(r)) dr. \end{aligned} \quad (7.18)$$

Or, alternatively,

$$\begin{aligned} \langle n_a \kappa_a m_a || [\vec{\alpha} \cdot \vec{L} C_0^{(1)}(\theta, \phi)]^I f_M(r) || n_b \kappa_b m_b \rangle = \\ -i\hbar(\kappa_a + \kappa_b) \langle \kappa_a || C^{(1)}(\theta, \phi) || -\kappa_b \rangle \int_{r=0}^{+\infty} I f_M(r) (P_{n_a \kappa_a}(r) Q_{n_b \kappa_b}(r) + Q_{n_a \kappa_a}(r) P_{n_b \kappa_b}(r)) dr. \end{aligned} \quad (7.19)$$

One can now calculate the hyperfine splitting due to the magnetic dipole interaction, using (7.8),

$$\langle \kappa_a || C^{(k)} || \kappa_b \rangle = (-1)^{j_a} i \sqrt{[j_a][j_b]} \begin{pmatrix} j_a & j_b & k \\ -1/2 & 1/2 & 0 \end{pmatrix} \Pi(L_a + k + L_b) \quad (7.20)$$

with

$$[x] \equiv 2x + 1, \quad \Pi(l) \equiv \begin{cases} 1, & \text{if } l \text{ is even} \\ 0, & \text{if } l \text{ is odd} \end{cases}. \quad (7.21)$$

This means that

$$\langle \kappa_a || C^{(1)}(\theta, \phi) || -\kappa_a \rangle = -\frac{1}{2} \sqrt{\frac{[j_a]}{j_a(j_a + 1)}}. \quad (7.22)$$

Finally,

$$\begin{pmatrix} I & 1 & I \\ -I & 0 & I \end{pmatrix} = \sqrt{\frac{I}{(I+1)[I]}}, \quad (7.23)$$

thus, recalling (7.10) to (7.12),

Definition: (Hyperfine dipole constant for a single electron ion)

$$\begin{aligned} a &= ec \frac{\mu_0}{2\pi} \frac{\kappa_a}{I j_a(j_a + 1)} \int_{r=0}^{+\infty} \langle II | f_{M,0} | II \rangle P_{n_a \kappa_a}(r) Q_{n_a \kappa_a}(r) dr. \\ &= ec \frac{\mu_0}{2\pi} \frac{\kappa_a}{I j_a(j_a + 1)} \mathcal{I}_{\text{lab}}^M \int_{r=0}^{+\infty} \frac{1}{2} \left(\frac{1}{r^2} \int_{R=0}^r (\vec{R} \wedge \vec{j}(\vec{R}))_z d^3 \vec{R} + r \int_{R=r}^{+\infty} \frac{(\vec{R} \wedge \vec{j}(\vec{R}))_z}{R^3} d^3 \vec{R} \right) \times \\ &\quad \times P_{n_a \kappa_a}(r) Q_{n_a \kappa_a}(r) dr, \end{aligned} \quad (7.24)$$

where $\mathcal{I}_{\text{lab}}^M$ is the conversion factor from the intrinsic magnetic dipole to the laboratory one, it is given by (6.32) and is equal to $\frac{I}{I+1}$. We obtain the same result as in [154].

Ultimately, using (7.9) to (7.11), and

$$\begin{aligned} \left\{ \begin{matrix} J & I & F \\ I & J & 1 \end{matrix} \right\} &= (-1)^{F+I+J+1} \frac{2(I(I+1) + J(J+1) - F(F+1))}{\sqrt{2I(2I+1)(2I+2)2J(2J+1)(2J+2)}} \\ &= (-1)^{F+I+J} \frac{F(F+1) - I(I+1) - J(J+1)}{2\langle J || \vec{J} || J \rangle \langle I || \vec{I} || I \rangle}, \end{aligned} \quad (7.25)$$

one obtains that

Definition: (*Hyperfine dipole correction*)

$$W_{\text{hf,dip}} \equiv \langle n_a \kappa_a F M_F | H_{\text{hf,dip}} | n_a \kappa_a F M_F \rangle = \frac{a}{2} K_a \quad (7.26)$$

where $K_a \equiv F(F+1) - I(I+1) - J_a(J_a+1)$.

The splitting between two hyperfine levels F and $F' = F - 1$ in the same J multiplet is given by

$$\Delta E \equiv a F \quad (7.27)$$

While (7.26) is a general expression for the magnetic dipole hyperfine interaction, it is particularly useful for the case of a single electron, where a can be computed explicitly with relative ease. In the case of multiple electrons, the expression of a is more complex, but the general form remains the same, and referring to (7.5), (7.10), (7.12) and (7.23), one has

$$\begin{aligned} a &= -iec \frac{\mu_0}{4\pi\hbar} \frac{\langle n_a \mathcal{K}_a | \vec{\alpha} \cdot \vec{L} C_0^{(1)}(\theta, \phi) \langle II | f_{\text{M},0}(r) | II \rangle | n_a \mathcal{K}_a \rangle}{I \sqrt{J_a(2J_a+1)(J_a+1)}} \\ &= -iec \frac{\mu_0}{4\pi\hbar} \frac{\langle n_a \mathcal{K}_a(J_a) m_J = J_a | \vec{\alpha} \cdot \vec{L} C_0^{(1)}(\theta, \phi) \langle II | f_{\text{M},0}(r) | II \rangle | n_a \mathcal{K}_a(J_a) m_J = J_a \rangle}{I J_a} \\ &\equiv -iec \frac{\mu_0}{4\pi\hbar} \frac{\langle n_a J_a J_a II | T_{\text{M},0}^{(1)}(\vec{r}) | n_a J_a J_a II \rangle}{I J_a}. \end{aligned} \quad (7.28)$$

It can be seen that, in the case one does not consider the electronic penetration inside the nucleus (i.e. $r \gg R$), or equivalently, if one considers a point nuclear magnetic dipole, $f_{\text{M},0}(r)$ reduces to

$$f_{\text{M},0}(r) = \frac{1}{2r^2} \int_{R=0}^{+\infty} \left(\vec{R} \wedge \vec{j}(\vec{R}) \right)_z d^3\vec{R} = \frac{M_z^{(1)}}{r^2}, \quad (7.29)$$

with $\vec{M}^{(1)}$ the intrinsic nuclear magnetic moment, consequently,

Definition: (*Hyperfine dipole constant with no nuclear penetration*)

$$\begin{aligned} a_{\text{n.p.}} &= -iec \frac{\mu_0}{4\pi\hbar} \frac{\langle II | M_z^{(1)} | II \rangle \langle n_a \mathcal{K}_a(J_a) m_J = J_a | \vec{\alpha} \cdot \vec{L} C_0^{(1)}(\theta, \phi) r^{-2} | n_a \mathcal{K}_a(J_a) m_J = J_a \rangle}{I J_a} \\ &= -iec \frac{\mu_0 M_z^{(1,\text{spec})}}{4\pi\hbar} \frac{\langle n_a J_a J_a | \vec{\alpha} \cdot \vec{L} C_0^{(1)}(\theta, \phi) r^{-2} | n_a J_a J_a \rangle}{I J_a}, \end{aligned} \quad (7.30)$$

with $M_z^{(1,\text{spec})} = \langle II | M_z^{(1)} | II \rangle = \mathcal{I}_{\text{lab}}^{\text{M}} M_z^{(1)}$ the spectroscopic nuclear magnetic moment computed in (6.32).

Or, in the case of the single electron again, one can write,

Definition: (*Hyperfine dipole constant for a single electron ion with no nuclear penetration*)

$$a_{\text{n.p.}} = ec \frac{\mu_0}{2\pi} \frac{M_z^{(1)}}{I} \frac{\kappa_a}{j_a(j_a+1)} \int_{r=0}^{+\infty} \frac{1}{r^2} P_{n_a \kappa_a}(r) Q_{n_a \kappa_a}(r) dr. \quad (7.31)$$

Note this is the same result obtained in [135].

7.2 The hyperfine quadrupole constant

Starting from the multipole expansion of the quadrupolar nuclear potential (6.30), one can write the hyperfine quadrupole interaction hamiltonian as

Definition: (*Hyperfine quadrupole Hamiltonian*)

$$H_{\text{hf,quad}} = e\phi_{\text{quad}}(\vec{r}), \quad (7.32)$$

with ¹

$$\phi_{\text{quad}}(\vec{r}) = \frac{1}{4\pi\epsilon_0} C_0^{(2)}(\theta, \phi) f_{Q,0}(r) \quad (7.33)$$

and

$$f_{Q,0}(r) = \frac{1}{2r^3} \int_{R=0}^r \rho(\vec{R}) R^2 C_0^{(2)}(\Theta, \Phi) d^3\vec{R} + r^2 \int_{R=r}^{+\infty} \frac{\rho(\vec{R}) C_0^{(2)}(\Theta, \Phi)}{2R^3} d^3\vec{R}, \quad (7.34)$$

similarly to (7.8), one can write

$$\begin{aligned} \langle n_a \mathcal{K}_a F M_F | H_{\text{hf,quad}} | n_b \mathcal{K}_b F M_F \rangle &= -\frac{e}{4\pi\epsilon_0} (-1)^{J_b+I+F+1} \delta_{F,F'} \delta_{M_F,M_{F'}} \times \\ &\times \left\{ \begin{matrix} J_b & I & F \\ I & J_a & 2 \end{matrix} \right\} \langle n_a \mathcal{K}_a || C_0^{(2)}(\theta, \phi) \langle II | f_{Q,0}(r) | II \rangle || n_b \mathcal{K}_b \rangle \begin{pmatrix} I & 2 & I \\ -I & 0 & I \end{pmatrix}^{-1}, \quad (7.35) \end{aligned}$$

with, in the case of a single electron,

$$\begin{aligned} \langle n_a \kappa_a || C_0^{(2)}(\theta, \phi) \langle II | f_Q(r) | II \rangle || n_b \kappa_b \rangle &= \\ \langle \kappa_a || C^{(2)}(\theta, \phi) || \kappa_b \rangle \int_{r=0}^{+\infty} \langle II | f_{Q,0}(r) | II \rangle (P_{n_a \kappa_a}(r) P_{n_b \kappa_b}(r) + Q_{n_a \kappa_a}(r) Q_{n_b \kappa_b}(r)) dr. \quad (7.36) \end{aligned}$$

The use of the following relations

$$\left\{ \begin{matrix} I & J & F \\ J & I & 2 \end{matrix} \right\} = (-1)^{I+J+F} \begin{pmatrix} J & 2 & J \\ -J & 0 & J \end{pmatrix} \begin{pmatrix} I & 2 & I \\ -I & 0 & I \end{pmatrix} \frac{6K(K+1) - 8J(J+1)I(I+1)}{2I(2I-1)2J(2J-1)}, \quad (7.37)$$

$$\begin{pmatrix} I & 2 & I \\ -I & 0 & I \end{pmatrix} = \sqrt{\frac{2I(2I-1)}{[I](2I+2)(2I+3)}}, \quad (7.38)$$

$$\langle \kappa_a || C^{(2)}(\theta, \phi) || \kappa_a \rangle \stackrel{(7.20)}{=} -\frac{1}{4} \sqrt{\frac{(2j_a-1)[j_a](2j_a+3)}{j_a(j_a+1)}}, \quad (7.39)$$

allows one to write

¹The symmetries of the nuclei (see Section 6.3.1) are such that only one component of the quadrupole tensor is non-zero, and the quadrupole potential is scalar, given that the symmetry axis of the nucleus is chosen to be along z , only $f_{Q,0}$ is non-zero.

Definition: (*Hyperfine quadrupole correction*)

$$W_{\text{hf,quad}} \equiv \langle n_a \kappa_a F M_F | H_{\text{hf,quad}} | n_a \kappa_a F M_F \rangle = \frac{b}{2} \frac{3K_a(K_a + 1) - 4j_a(j_a + 1)I(I + 1)}{2I(2I - 1)2j_a(2j_a - 1)}, \quad (7.40)$$

with $K_a = F(F + 1) - I(I + 1) - j_a(j_a + 1)$, and with

Definition: (*Hyperfine quadrupole constant for a single electron*)

$$\begin{aligned} b &= \frac{|e|}{4\pi\epsilon_0} \frac{2j_a - 1}{j_a + 1} \int_{r=0}^{+\infty} \langle II | f_Q(r) | II \rangle (P_{n_a \kappa_a}^2(r) + Q_{n_a \kappa_a}^2(r)) dr \\ &= \frac{|e|}{4\pi\epsilon_0} \frac{2j_a - 1}{2j_a + 2} \mathcal{I}_{\text{lab}}^E \times \\ &\quad \int_{r=0}^{+\infty} \left(\frac{1}{r^3} \int_{R=0}^r \rho(\vec{R}) R^2 C_0^{(2)}(\Theta, \Phi) d^3 \vec{R} + r^2 \int_{R=r}^{+\infty} \frac{\rho(\vec{R}) C_0^{(2)}(\Theta, \Phi)}{R^3} d^3 \vec{R} \right) \times \\ &\quad (P_{n_a \kappa_a}^2(r) + Q_{n_a \kappa_a}^2(r)) dr, \end{aligned} \quad (7.41)$$

where $\mathcal{I}_{\text{lab}}^E$ is the conversion factor from the intrinsic quadrupole moment to the laboratory one, according to (6.12), it is given by $\frac{3I^2 - I(I+1)}{(I+1)(2I+3)}$.

Just as for the magnetic dipole hyperfine interaction, in the case of multiple electrons, (7.40) stays valid by replacing $j_a = J_a$ but the expression of b is more complex to compute,

$$\begin{aligned} b &= \frac{e}{4\pi\epsilon_0} \sqrt{\frac{2J_a(2J_a - 1)}{[J_a](2J_a + 2)(2J_a + 3)}} \langle \mathcal{K}_a || C^{(2)}(\theta, \phi) || \mathcal{K}_a \rangle \times \\ &\quad \int_{r=0}^{+\infty} \langle II | 4f_Q(r) | II \rangle (P_{n_a \kappa_a}^2(r) + Q_{n_a \kappa_a}^2(r)) dr. \end{aligned} \quad (7.42)$$

Finally, in the case one does not consider the electronic penetration inside the nucleus (i.e. $r \gg R$), $f_Q(r)$ reduces to

$$4f_Q(r) = \frac{2}{r^3} \int_{R=0}^{+\infty} \rho(\vec{R}) R^2 C_0^{(2)}(\Theta, \Phi) d^3 \vec{R} = \frac{2Q_0^{(2,\text{int})}}{r^3}, \quad (7.43)$$

where $Q_0^{(2,\text{int})}$ is the intrinsic nuclear quadrupole moment, and consequently

Definition: (*Hyperfine quadrupole constant with no nuclear penetration*)

$$\begin{aligned} b_{\text{n.p.}} &= \frac{e}{4\pi\epsilon_0} \sqrt{\frac{2J(2J - 1)}{[J](2J + 2)(2J + 3)}} \langle \mathcal{K}_a || C^{(2)}(\theta, \phi) || \mathcal{K}_a \rangle \langle II | 2Q_0^{(2,\text{int})} | II \rangle \left\langle \frac{1}{r^3} \right\rangle_{n_a \kappa_a} \\ &= \frac{2eQ_0^{(2,\text{spec})}}{4\pi\epsilon_0} \sqrt{\frac{2J(2J - 1)}{[J](2J + 2)(2J + 3)}} \langle \mathcal{K}_a || C^{(2)}(\theta, \phi) || \mathcal{K}_a \rangle \int_{r=0}^{+\infty} \frac{1}{r^3} (P_{n_a \kappa_a}^2(r) + Q_{n_a \kappa_a}^2(r)) dr, \end{aligned} \quad (7.44)$$

with $Q_0^{(2,\text{spec})} = \langle II | Q_0^{(2,\text{int})} | II \rangle = \mathcal{I}_{\text{lab}}^E Q_0^{(2,\text{int})}$ the spectroscopic nuclear quadrupole moment.

Or, in the case of the single electron again, one can write,

Definition: (*Hyperfine quadrupole constant for a single electron ion with no nuclear penetration*)

$$b_{\text{n.p.}} = \frac{|e|Q_0^{(2,\text{spec})}}{4\pi\epsilon_0} \frac{2j_a - 1}{2j_a + 2} \int_{r=0}^{+\infty} \frac{1}{r^3} (P_{n_a\kappa_a}^2(r) + Q_{n_a\kappa_a}^2(r)) dr. \quad (7.45)$$

Just as in the case of the magnetic dipole hyperfine interaction, the effect of the electric quadrupole hyperfine interaction can be written in the form of an effective Hamiltonian for states of the same J multiplet. Notice that

$$\langle \mathcal{K}_a F M_F | 12(\vec{I} \cdot \vec{J})^2 + 6\vec{I} \cdot \vec{J} - 4I^2 J^2 | \mathcal{K}_a F M_F \rangle = 3K(K+1) - 4J_a(J_a+1)I(I+1), \quad (7.46)$$

and therefore, referring to (7.40), one can write

Definition: (*Effective quadrupole Hamiltonian*)

$$H_{\text{hf,quad}}^{\text{eff}} = \frac{b}{2} \frac{3(\vec{I} \cdot \vec{J})^2 + \frac{3}{2}\vec{I} \cdot \vec{J} - I^2 J^2}{I(2I-1)J_a(2J_a-1)}. \quad (7.47)$$

7.3 The Isotope Shifts: Breit-Rosenthal and Bohr-Weisskopf

7.3.1 The hyperfine anomaly

If one considers the expression of the hyperfine dipole constant without taking into account the penetration of the nucleus by the electron given in (7.30) and (7.31) for multiple electrons and a single electron respectively, one can compute their ratio for two isotopes 1 and 2

$$\frac{{}^{(A)}a_{\text{n.p.}}}{{}^{(B)}a_{\text{n.p.}}} = \frac{{}^{(A)}M_z^{(1,\text{spec})}}{{}^{(B)}M_z^{(1,\text{spec})}} \frac{{}^{(B)}IJ_B}{\langle n_A J_A J_A | \vec{\alpha} \cdot \vec{L} C_0^{(1)}(\theta, \phi) r^{-2} | n_A J_A J_A \rangle} \frac{\langle n_B J_B J_B | \vec{\alpha} \cdot \vec{L} C_0^{(1)}(\theta, \phi) r^{-2} | n_B J_B J_B \rangle}{{}^{(A)}IJ_A}. \quad (7.48)$$

If one considers both isotopes are in the same electronic state i.e. $J_A = J_B$, this simplifies to

$$\frac{{}^{(A)}a_{\text{n.p.}}}{{}^{(B)}a_{\text{n.p.}}} = \frac{{}^{(A)}M_z^{(1,\text{spec})} / {}^{(A)}I}{{}^{(B)}M_z^{(1,\text{spec})} / {}^{(B)}I}. \quad (7.49)$$

Therefore the quantity

$$\frac{{}^{(A)}a_{\text{n.p.}}}{{}^{(B)}a_{\text{n.p.}}} \frac{{}^{(B)}M_z^{(1,\text{spec})} / {}^{(B)}I}{{}^{(A)}M_z^{(1,\text{spec})} / {}^{(A)}I} = 1 \quad (7.50)$$

for two isotopes with an infinitely massive, point-like nucleus with point dipole moments.

One can check experimentally if this equality holds [155], and it is found that it very rarely does. This discrepancy is known as the hyperfine anomaly, and is quantified by

Definition: (*Hyperfine anomaly*)

$$\Delta_B^A \equiv \frac{{}^{(A)}a}{{}^{(B)}a} \frac{{}^{(B)}M_z^{(1,\text{spec})} / {}^{(B)}I}{{}^{(A)}M_z^{(1,\text{spec})} / {}^{(A)}I} - 1. \quad (7.51)$$

Its origins are multiple, and are evidently due to the assumptions made to get (7.49), one of which is the point-like nature of the nucleus and its magnetic dipole.

7.3.2 The Breit-Rosenthal correction

One can first consider the effect due to the finite charge distribution of the nucleus, but still assuming a point-like magnetic dipole. This correction enters (7.49) through the electronic wavefunctions, in essence, the expression stays the same, but the expectation values of the electronic operators are modified. This correction is known as the Breit-Rosenthal effect ϵ_{BR} .

$$a_{p.d.} \equiv a_{pt}(1 - \epsilon_{BR}), \quad (7.52)$$

where $a_{p.d.}$ is the hyperfine constant for a point dipole nucleus with a finite charge distribution, and a_{pt} is the hyperfine constant for a point charge nucleus. By decomposing the expectation value in (7.30) into a radial and an angular part, one can write

$$\langle JJI | \vec{\alpha} \cdot \vec{L} C_0^{(1)}(\theta, \phi) r^{-2} | JJI \rangle = \langle nJ | \vec{\alpha} \cdot \vec{L} C_0^{(1)}(\theta, \phi) | nJ \rangle \int_{r=0}^{+\infty} \frac{1}{r^2} P_{n\kappa}(r) Q_{n\kappa}(r) dr. \quad (7.53)$$

Since the finite charge distribution of the nucleus is incorporated into the Dirac equation via its monopole charge distribution², that is spherically symmetric, the angular part of the expectation value remains the same, and only the radial wavefunctions are modified. This allows one to write

$$\frac{{}^{(A)}a_{n.p.} \, {}^{(B)}M_z^{(1,spec)} / {}^{(B)}I}{{}^{(B)}a_{n.p.} \, {}^{(A)}M_z^{(1,spec)} / {}^{(A)}I} = \frac{\int_{r=0}^{+\infty} \frac{1}{r^2} P_{n\kappa}^{(f.c.)}(r) Q_{n\kappa}^{(f.c.)}(r) dr}{\int_{r=0}^{+\infty} \frac{1}{r^2} P_{n\kappa}^{(pt.)}(r) Q_{n\kappa}^{(pt.)}(r) dr}, \quad (7.54)$$

where the superscripts f.c. and pt. refer to the electronic wavefunctions for a nucleus with a finite charge distribution and a point nucleus, respectively.

Therefore, the Breit-Rosenthal effect is given by

Definition: (*Breit-Rosenthal effect*)

$$\epsilon_{BR} = 1 - \frac{a_{p.d.}}{a_{pt}} = 1 - \frac{\int_{r=0}^{+\infty} \frac{1}{r^2} P_{n\kappa}^{(f.c.)}(r) Q_{n\kappa}^{(f.c.)}(r) dr}{\int_{r=0}^{+\infty} \frac{1}{r^2} P_{n\kappa}^{(pt.)}(r) Q_{n\kappa}^{(pt.)}(r) dr}. \quad (7.55)$$

7.3.3 The Bohr-Weisskopf correction

If one considers now the continuous and finite current distribution/magnetic dipole density distribution of the nucleus, one can write the hyperfine constant as

$$a_{f.d.} \equiv a_{p.d.}(1 - \epsilon_{BW}), \quad (7.56)$$

where $a_{f.d.}$ is the hyperfine constant for a **f**inite **d**ipole density distribution and ϵ_{BW} is the Bohr-Weisskopf effect. In this case, the electronic wavefunctions are not modified, but the integrals in the expectation values are. By separating $\langle n_a J_a J_a II | T_{M,0}^{(1)}(\vec{r}) | n_a J_a J_a II \rangle$ in (7.28) into a radial and an angular part, one can write

$$\langle n_a J_a J_a II | T_{M,0}^{(1)}(\vec{r}) | n_a J_a J_a II \rangle \propto \int_{r=0}^{+\infty} \frac{1}{2} \left(\frac{1}{r^2} \int_{R=0}^r \left(\vec{R} \wedge \vec{j}(\vec{R}) \right)_z d^3 \vec{R} + r \int_{R=r}^{+\infty} \frac{\left(\vec{R} \wedge \vec{j}(\vec{R}) \right)_z}{R^3} d^3 \vec{R} \right) \times P_{n_a \kappa_a}(r) Q_{n_a \kappa_a}(r) dr \quad (7.57)$$

with a proportionality constant that depends on the electronic angular quantum numbers, that are the same for the two isotopes. This allows to write

²See the discussion in Section 6.3.

Definition: (*Bohr-Weisskopf effect*)

$$\epsilon_{\text{BW}} = 1 - \frac{a_{\text{f.d.}}}{a_{\text{p.d.}}} \quad (7.58)$$

$$= 1 - \frac{\int_{r=0}^{+\infty} \left(\frac{1}{2r^2} \int_{R=0}^r \left(\vec{R} \wedge \vec{j}(\vec{R}) \right)_z d^3 \vec{R} + r \int_{R=r}^{+\infty} \frac{\left(\vec{R} \wedge \vec{j}(\vec{R}) \right)_z d^3 \vec{R}}{2R^3} \right) P_{n_a \kappa_a}^{(\text{f.c.})}(r) Q_{n_a \kappa_a}^{(\text{f.c.})}(r) dr}{M_z^{(1)} \int_{r=0}^{+\infty} \frac{1}{r^2} P_{n\kappa}^{(\text{f.c.})}(r) Q_{n\kappa}^{(\text{f.c.})}(r) dr}.$$

If one considers only those two corrections to the hyperfine constant as the origin of the hyperfine anomaly, one can write

$$1 + \Delta_B^A = \frac{(A) a_{\text{f.d.}}}{(B) a_{\text{f.d.}}} \frac{(B) M_z^{(1,\text{spec})} / (B) I}{(A) M_z^{(1,\text{spec})} / (A) I} = \frac{(A) a_{\text{n.p.}}}{(B) a_{\text{n.p.}}} \frac{(B) M_z^{(1,\text{spec})} / (B) I}{(A) M_z^{(1,\text{spec})} / (A) I} \frac{(1 - \epsilon_{\text{BR}}^{(A)})(1 - \epsilon_{\text{BW}}^{(A)})}{(1 - \epsilon_{\text{BR}}^{(B)})(1 - \epsilon_{\text{BW}}^{(B)})} \quad (7.59)$$

$$\stackrel{(7.50)}{=} \frac{(1 - \epsilon_{\text{BR}}^{(A)})(1 - \epsilon_{\text{BW}}^{(A)})}{(1 - \epsilon_{\text{BR}}^{(B)})(1 - \epsilon_{\text{BW}}^{(B)})}$$

Therefore, the hyperfine anomaly can be computed via

$$\Delta_B^A = \frac{(1 - \epsilon_{\text{BR}}^{(A)})(1 - \epsilon_{\text{BW}}^{(A)})}{(1 - \epsilon_{\text{BR}}^{(B)})(1 - \epsilon_{\text{BW}}^{(B)})} - 1. \quad (7.60)$$

If we assume that the Breit-Rosenthal and Bohr-Weisskopf effects are small, one can write, to first order

$$\Delta_B^A \approx \epsilon_{\text{BR}}^{(B)} + \epsilon_{\text{BW}}^{(B)} - \epsilon_{\text{BR}}^{(A)} - \epsilon_{\text{BW}}^{(A)}. \quad (7.61)$$

The order sequence of the corrections to the hyperfine constants and their origin are summarized in Tab. 7.1.

$\vec{j}(\vec{R}) \backslash \rho(\vec{R})$	Point charge	Charge distribution model
Point dipole	1	$(1 - \epsilon_{\text{BR}}^{\text{model}})$
Current distribution model	N/A	$(1 - \epsilon_{\text{BR}}^{\text{model}})(1 - \epsilon_{\text{BW}})$

Table 7.1: Summary of the corrections to the hyperfine constants by progressively including the finite charge distribution of the nucleus and the finite current distribution of the nucleus.

7.3.4 Quadrupole hyperfine anomaly

The quadrupole hyperfine anomaly is defined in the same way as the magnetic dipole hyperfine anomaly, but with the quadrupole hyperfine constants:

Definition: (*Quadrupole hyperfine anomaly*)

$${}_Q \Delta_B^A = \frac{b^{(A)}}{b^{(B)}} \frac{(B) Q_0^{(2,\text{spec})}}{(A) Q_0^{(2,\text{spec})}} - 1. \quad (7.62)$$

There is no two sets of corrections, one due to the finite charge distribution of the nucleus and the other due to the finite current distribution of the nucleus, as for the magnetic dipole hyperfine anomaly. The quadrupole constant is only affected by the finite charge distribution of the nucleus, since this effects both ρ and the wavefunctions P, Q in the definition of b in (7.42), recalled here, for the multi-electronic case

$$b = \frac{2eQ_0^{(2,\text{spec})}}{4\pi\epsilon_0} \sqrt{\frac{2J(2J-1)}{[J](2J+2)(2J+3)}} \langle \mathcal{K}_a || C^{(2)}(\theta, \phi) || \mathcal{K}_a \rangle \int_{r=0}^{+\infty} \frac{1}{r^3} (P_{n_a\kappa_a}^2(r) + Q_{n_a\kappa_a}^2(r)) dr. \quad (7.42)$$

One can then define the quadrupole correction due to the finite charge distribution of the nucleus as

Definition: (*Quadrupole Shift*)

$$\begin{aligned} \Delta B &= 1 - \frac{b_{\text{f.d.}}}{b_{\text{p.q.}}} \\ &= 1 - \frac{\int_{r=0}^{+\infty} \left(\frac{1}{r^3} \int_{R=0}^r \rho(\vec{R}) R^2 C_0^{(2)}(\Theta, \Phi) d^3\vec{R} + r^2 \int_{R=r}^{+\infty} \frac{\rho(\vec{R}) C_0^{(2)}(\Theta, \Phi)}{R^3} d^3\vec{R} \right) \left(\times P_{n\kappa}^{(\text{f.c.})^2}(r) + Q_{n\kappa}^{(\text{f.c.})^2}(r) \right) dr}{Q_0^{(2,\text{int})} \int_{r=0}^{+\infty} \frac{1}{r^3} (P_{n\kappa}^{(\text{pt})^2}(r) + Q_{n\kappa}^{(\text{pt})^2}(r)) dr}, \end{aligned} \quad (7.63)$$

with $b_{\text{f.d.}}$ the quadrupole hyperfine constant for the chosen model of finite charge distribution of the nucleus, and $b_{\text{p.q.}}$ the quadrupole hyperfine constant for a point charge nucleus and a point quadrupole, where the superscripts f.c. and pt refer to the electronic wavefunctions for a nucleus with a finite charge distribution and a point nucleus, respectively.

And once this is defined, similarly to the magnetic dipole hyperfine anomaly, one can write

$$Q\Delta_B^A = \frac{1 - \Delta B^{(A)}}{1 - \Delta B^{(B)}} - 1. \quad (7.64)$$

7.4 The non-relativistic limit and the Fermi Contact term

7.4.1 The Pauli approximation

We recall that the solution of the radial Dirac equation for the electron in a central potential are given by (5.24)

$$\psi_{n\kappa}(r) = \frac{1}{r} \begin{pmatrix} iP_{n\kappa}(r)\chi_{\kappa,m_j}(\theta, \phi) \\ Q_{n-\kappa}(r)\chi_{-\kappa,m_j}(\theta, \phi) \end{pmatrix} \quad (5.24)$$

where $P_{n\kappa}(r)$ and $Q_{n\kappa}(r)$ are the large and small components of the radial wavefunction, respectively, and $\xi_{\kappa}(\theta, \phi)$ are the spin-angular functions.

The radial Dirac equation is given by (5.27)

$$\begin{aligned} -\left(\frac{d}{dr} + \frac{\kappa}{r}\right) P_{n\kappa}(r) + \left(\frac{Z\alpha}{r} - \frac{mc^2}{\hbar c}\right) Q_{n\kappa} &= \frac{E_{n\kappa}}{\hbar c} Q_{n\kappa}(r), \\ \left(\frac{d}{dr} - \frac{\kappa}{r}\right) Q_{n\kappa}(r) + \left(\frac{Z\alpha}{r} + \frac{mc^2}{\hbar c}\right) P_{n\kappa} &= \frac{E_{n\kappa}}{\hbar c} P_{n\kappa}(r), \end{aligned} \quad (7.65)$$

Separating $P_{n\kappa}(r)$ and $Q_{n\kappa}(r)$ on either side of the equality one can write

$$\begin{aligned}\left(\frac{Z\alpha}{r} - \frac{mc^2}{\hbar c} - \frac{E_{n\kappa}}{\hbar c}\right) Q_{n\kappa} &= \left(\frac{d}{dr} + \frac{\kappa}{r}\right) P_{n\kappa}(r), \\ \left(\frac{Z\alpha}{r} + \frac{mc^2}{\hbar c} - \frac{E_{n\kappa}}{\hbar c}\right) P_{n\kappa} &= \left(\frac{d}{dr} - \frac{\kappa}{r}\right) Q_{n\kappa}(r).\end{aligned}\quad (7.66)$$

By defining $\epsilon_\kappa = E_\kappa - mc^2$, the energy of the electron without the rest mass energy, this reads

$$\begin{aligned}\left(\frac{Z\alpha\hbar c}{r} - \epsilon_{n\kappa} - 2mc^2\right) Q_{n\kappa} &= \hbar c \left(\frac{d}{dr} + \frac{\kappa}{r}\right) P_{n\kappa}(r), \\ \left(\frac{Z\alpha\hbar c}{r} - \epsilon_{n\kappa}\right) P_{n\kappa} &= \hbar c \left(\frac{d}{dr} - \frac{\kappa}{r}\right) Q_{n\kappa}(r).\end{aligned}\quad (7.67)$$

If we consider typical atomic lengthscales, $\frac{Z\alpha\hbar c}{r}$ is of the order of $\sim 14Z^2$ eV, and $\epsilon_{n\kappa}$ is of the order of $\sim 14Z/n^2$ eV, on the other side $2mc^2$ is of the order of ~ 1 MeV. Therefore, the assumption that $\frac{Z\alpha\hbar c}{r} - \epsilon_{n\kappa} \ll 2mc^2$ is reasonable, especially for low Z . This is known as the **Pauli approximation**. In this case, one can write

$$\begin{aligned}-2mc^2 Q_{n\kappa} &= \hbar c \left(\frac{d}{dr} + \frac{\kappa}{r}\right) P_{n\kappa}(r), \\ \left(\frac{Z\alpha\hbar c}{r} - \epsilon_{n\kappa}\right) P_{n\kappa} &= \hbar c \left(\frac{d}{dr} - \frac{\kappa}{r}\right) Q_{n\kappa}(r).\end{aligned}\quad (7.68)$$

The Pauli approximation allows to write the radial Dirac equation as a Schrödinger-like equation, since the first equality allows one to write

Definition: (*Pauli approximation*)

$$Q_{n\kappa} = -\frac{\hbar}{2mc} \left(\frac{d}{dr} + \frac{\kappa}{r}\right) P_{n\kappa}(r). \quad (7.69)$$

Substituting this into the second equality of (7.68) one can write

$$\begin{aligned}\left(\frac{Z\alpha\hbar c}{r} - \epsilon_{n\kappa}\right) P_{n\kappa} &= \hbar c \left(\frac{d}{dr} - \frac{\kappa}{r}\right) \left(-\frac{\hbar}{2mc} \left(\frac{d}{dr} + \frac{\kappa}{r}\right) P_{n\kappa}(r)\right) \\ &= -\frac{\hbar^2}{2m} \left(\frac{d^2}{dr^2} - \frac{\kappa(\kappa+1)}{r^2}\right) P_{n\kappa}(r),\end{aligned}\quad (7.70)$$

which, by rearranging terms, and noticing that $\kappa(\kappa+1) = \ell(\ell+1)$, yields the Schrödinger-like equation for the radial wavefunction $P_{n\kappa}(r)$

$$-\frac{\hbar^2}{2m} \left(\frac{d^2}{dr^2} - \frac{\ell(\ell+1)}{r^2}\right) P_{n\ell}(r) + \frac{Z\alpha\hbar c}{r} P_{n\ell} = \epsilon_{n\kappa} P_{n\ell}. \quad (7.71)$$

Note: In summary, the Pauli approximation allows one to write that in the non-relativistic limit one has:

$$\begin{aligned}
\kappa(\kappa + 1) &= \ell(\ell + 1), \\
P_{n\kappa}(r) &\rightarrow R_{n\ell}(r), \\
Q_{n\kappa}(r) &\rightarrow \frac{\hbar}{2mc} \frac{dR_{n\ell}(r)}{dr} + \frac{\hbar\kappa}{2mcr} R_{n\ell}(r),
\end{aligned} \tag{7.72}$$

where $R_{n\ell}(r)$ is the radial wavefunction of the non-relativistic Schrödinger equation and $\ell(\ell + 1)$ is the eigenvalue of the angular momentum operator \vec{L} .

We notice the Pauli approximation does not allow to keep the spin-orbit coupling term, and is purely a non-relativistic approximation. In order to keep the spin-orbit coupling term, one would need to consider the **Foldy-Wouthuysen transformation** [156, 157], an approximation that still retains the first non-vanishing order of the relativistic effects and that allows to write the Dirac equation in a form where the spin-orbit coupling term is kept.

7.4.2 The non-relativistic limit of the hyperfine dipole constant

The Pauli approximation will prove to be a very useful tool to obtain the non-relativistic limit of the hyperfine dipole constant a . For example one recalls that, in the one-electron case (7.24)

$$\begin{aligned}
a &= ec \frac{\mu_0}{2\pi} \frac{\kappa_a}{I j_a(j_a + 1)} \mathcal{I}_{\text{lab}}^{\text{M}} \int_{r=0}^{+\infty} \frac{1}{2} \left(\frac{1}{r^2} \int_{R=0}^r \left(\vec{R} \wedge \vec{j}(\vec{R}) \right)_z d^3\vec{R} + r \int_{R=r}^{+\infty} \frac{\left(\vec{R} \wedge \vec{j}(\vec{R}) \right)_z d^3\vec{R}}{R^3} \right) \times \\
&\quad P_{n_a\kappa_a}(r) Q_{n_a\kappa_a}(r) dr.
\end{aligned} \tag{7.24}$$

Indeed, in (7.24) as well as the other expressions of a in (7.28) and (7.31) those expressions contain integrals of the form $\int_r f(r) P_{n\kappa}(r) Q_{n\kappa}(r) dr$, and in the naive non-relativistic limit where one assumes $Q_{n\kappa}(r) = 0$, this would yield $a = 0$. However, the Pauli approximation allows to write $Q_{n\kappa}(r)$ in terms of $P_{n\kappa}(r)$. Therefore,

$$\begin{aligned}
\int_{r=0}^{+\infty} f(r) P_{n\kappa}(r) Q_{n\kappa}(r) dr &\sim \int_{r=0}^{+\infty} f(r) R_{n\ell}(r) \left(-\frac{\hbar}{2mc} \left(\frac{d}{dr} + \frac{\kappa}{r} \right) R_{n\ell}(r) \right) dr \\
&= -\frac{\hbar}{2mc} \int_{r=0}^{+\infty} f(r) R_{n\ell}(r) \left(\frac{d}{dr} + \frac{\kappa}{r} \right) R_{n\ell}(r) dr \\
&= -\frac{\hbar}{2mc} \int_{r=0}^{+\infty} f(r) R_{n\ell}(r) \frac{d}{dr} R_{n\ell}(r) dr - \frac{\hbar\kappa}{2mc} \int_{r=0}^{+\infty} \frac{f(r)}{r} R_{n\ell}^2(r) dr.
\end{aligned} \tag{7.73}$$

Integrating the first term by parts yields

$$\begin{aligned}
-\frac{\hbar}{2mc} \int_{r=0}^{+\infty} f(r) R_{n\ell}(r) \frac{d}{dr} R_{n\ell}(r) dr &= -\frac{\hbar}{4mc} \int_{r=0}^{+\infty} f(r) \frac{dR_{n\ell}^2(r)}{dr} dr \\
&= -\frac{\hbar}{4mc} [f(r) R_{n\ell}^2(r)]_{r=0}^{+\infty} + \frac{\hbar}{4mc} \int_{r=0}^{+\infty} \frac{df(r)}{dr} R_{n\ell}^2(r) dr.
\end{aligned} \tag{7.74}$$

Since $R_{n\ell}(r)$ is vanishing at $r \rightarrow +\infty$, it leads to

Definition: (Non-relativistic limit of the integral of the cross product of the relativistic wavefunc-

tions)

$$\int_{r=0}^{+\infty} f(r) P_{n\kappa}(r) Q_{n\kappa}(r) dr \sim \frac{\hbar}{4mc} \left(\int_{r=0}^{+\infty} \left[\left(\frac{d}{dr} - \frac{2\kappa}{r} \right) f(r) \right] R_{n\ell}^2(r) dr - [f(r) R_{n\ell}^2(r)]_{r=0} \right). \quad (7.75)$$

In the case of a point-dipole nucleus, the hyperfine dipole constant is given by (7.31)

$$a_{\text{n.p.}} = ec \frac{\mu_0}{2\pi} \frac{M_z^{(1)}}{I} \frac{\kappa_a}{j_a(j_a + 1)} \int_{r=0}^{+\infty} \frac{1}{r^2} P_{n_a \kappa_a}(r) Q_{n_a \kappa_a}(r) dr, \quad (7.31)$$

or (7.30) for multiple electrons, in both cases $f(r) = \frac{1}{r^2}$, and therefore

$$\begin{aligned} \int_{r=0}^{+\infty} f(r) P_{n\kappa}(r) Q_{n\kappa}(r) dr &\sim \frac{\hbar}{4mc} \left(\int_{r=0}^{+\infty} \left[\left(\frac{d}{dr} - \frac{2\kappa}{r} \right) \frac{1}{r^2} \right] R_{n\ell}^2(r) dr - \left[\frac{1}{r^2} R_{n\ell}^2(r) \right]_{r=0} \right) \\ &= -\frac{\hbar}{2mc} (\kappa + 1) \int_{r=0}^{+\infty} \frac{1}{r^3} R_{n\ell}^2(r) dr - \frac{\hbar}{4mc} \left[\frac{1}{r^2} R_{n\ell}^2(r) \right]_{r=0}, \end{aligned} \quad (7.76)$$

with $R_{n\ell}(r)$ the non-relativistic wavefunction of the electron in the $n\kappa$ state, solution to the Schrödinger equation.

Therefore, the non-relativistic limit of (7.31) i.e. the hyperfine dipole constant for a point-dipole nucleus in a single-electron ion, is given by

Definition: (*Non-relativistic hyperfine dipole constant for a point-dipole nucleus*)

If $\kappa = -1$ i.e. for s states, the hyperfine dipole constant is given by

$$a_{\text{n.p.}}^{(s)} = \frac{2e\hbar}{3m} \frac{M_z^{(1)}}{I} \frac{\mu_0}{4\pi} \left[\frac{R_{ns}^2(0)}{r^2} \right]_{r=0}. \quad (7.77)$$

If $\kappa \neq -1$ i.e. for all the states with $\ell \neq 0$, the non-relativistic wavefunction vanishes at $r = 0$, and the hyperfine dipole constant is given by ^a

$$a_{\text{n.p.}}^{(\ell)} = -\frac{e\hbar}{2m} \frac{M_z^{(1)}}{I} \frac{\mu_0}{4\pi} \frac{\ell(\ell + 1)}{J_a(J_a + 1)} \left\langle \frac{1}{r^3} \right\rangle_{n\ell}. \quad (7.78)$$

^aReminder: $\kappa(\kappa + 1) = \ell(\ell + 1)$

Traditionally, in non-relativistic atomic physics, the hyperfine dipole constant is written in terms of the Fermi contact term, that is the expectation value of the Dirac delta function at the origin, and the expectation value of the inverse of the distance cubed. This is indeed the non-relativistic limit of the hyperfine dipole constant calculated here for a point-dipole nucleus.

The Fermi contact term is then given by

Definition: (*Fermi contact term*)

$$a_{\text{n.p.}}^{\text{Fermi}} = \frac{2e\hbar}{3m} \frac{M_z^{(1)}}{I} \frac{\mu_0}{4\pi} |\psi_{ns}(0)|^2, \quad (7.79)$$

with $\psi_{ns} = \frac{1}{r} R_{ns}$ the radial wavefunction of the electron in the ns state.

For hydrogen-like ions, assuming an infinitely massive point charge nucleus, $|\psi_{ns}(0)|^2 = 4 \frac{Z^3}{n^3 a_0^3}$, and therefore the Fermi contact term is given by

$$a_{\text{n.p}}^{\text{Fermi}} = \frac{2e\hbar}{3m} \frac{M_z^{(1)}}{I} \frac{\mu_0}{4\pi} 4 \frac{Z^3}{n^3 a_0^3} = \frac{8e\hbar}{3m} \frac{M_z^{(1)}}{I} \frac{\mu_0}{4\pi} \frac{Z^3}{n^3 a_0^3}, \quad (7.80)$$

which is the expression encountered in the previous part in (2.92).

Note: One can compare this value to the experimental one for the $F = 1 \rightarrow F = 0$ hyperfine transition in the electronic ground state of hydrogen, i.e. the 21cm line of hydrogen that is very useful in different fields of astronomy [158]. It has been measured to be 1420.40575177 MHz [159], and (7.27) and (7.80) yield a value of ~ 1421.2 MHz. This value can be improved slightly by including the mass correction discussed in 6.1 via the reduced mass $\mu = \frac{m_e m_p}{m_e + m_p}$ where m_p is the mass of a proton. The constant a is then given by

$$a_{\text{n.p}}^{\text{Fermi}} = \frac{8e\hbar}{3\mu} \frac{M_z^{(1)}}{I} \frac{\mu_0}{4\pi} \frac{Z^3}{\left(a_0 \frac{m_e}{\mu}\right)^3} \sim 1419.7 \text{ MHz}, \quad (7.81)$$

however a rigorous relativistic, and even QED approach is needed to achieve higher accuracies.

7.4.3 Fermi contact term for a finite current distribution nucleus

If one were to consider the finite current distribution model for the nucleus as in (7.24), and therefore the electronic penetration inside the nucleus. The value of the non-relativistic hyperfine dipole constant can be obtained by assuming

$$f(r) = \frac{1}{2r^2} \int_{R=0}^r \left(\vec{R} \wedge \vec{j}(\vec{R}) \right)_z d^3 \vec{R} + r \int_{R=r}^{+\infty} \frac{\left(\vec{R} \wedge \vec{j}(\vec{R}) \right)_z}{2R^3} d^3 \vec{R}, \quad (7.82)$$

in (7.75). Interestingly, in that case, the term $[f(r) R_{n\ell}^2(r)]_{r=0}$ is vanishing, since $f(0) = 0$. And one is left to calculate the integral

$$\begin{aligned} & \int_{r=0}^{+\infty} \left[\left(\frac{d}{dr} - \frac{2\kappa}{r} \right) f(r) \right] R_{n\ell}^2(r) dr \\ &= \int_{r=0}^{+\infty} \left[\left(\frac{d}{dr} - \frac{2\kappa}{r} \right) \left(\frac{1}{2r^2} \int_{R=0}^r \left(\vec{R} \wedge \vec{j}(\vec{R}) \right)_z d^3 \vec{R} + r \int_{R=r}^{+\infty} \frac{\left(\vec{R} \wedge \vec{j}(\vec{R}) \right)_z}{2R^3} d^3 \vec{R} \right) \right] R_{n\ell}^2(r) dr. \\ &= \int_{r=0}^{+\infty} \left[- \left(\frac{\kappa+1}{r^3} \int_{R=0}^r \left(\vec{R} \wedge \vec{j}(\vec{R}) \right)_z d^3 \vec{R} + (2\kappa-1) \int_{R=r}^{+\infty} \frac{\left(\vec{R} \wedge \vec{j}(\vec{R}) \right)_z}{2R^3} d^3 \vec{R} \right) \right] R_{n\ell}^2(r) dr. \end{aligned} \quad (7.83)$$

Therefore, while there is still a term that vanishes for s states ($\kappa = -1$), the other term does not vanish for $\ell \neq 0$ states, as in the case of the point-dipole nucleus.

Definition: (*Non-relativistic hyperfine dipole constant for a finite current distribution nucleus*) If $\kappa = -1$ i.e. for s states, the hyperfine dipole constant is given by

$$a^{(s)} = 8 \frac{\mu_0}{4\pi} \frac{e\hbar}{2m} \int_{r=0}^{+\infty} \left(\frac{1}{I} \int_{R=r}^{+\infty} \frac{(\vec{R} \wedge \vec{j}(\vec{R}))_z}{2R^3} d^3\vec{R} \right) R_{ns}^2(r) dr. \quad (7.84)$$

If $\kappa \neq -1$ i.e. for all the states with $\ell \neq 0$, the hyperfine dipole constant is given by

$$a^{(\ell)} = \frac{\mu_0}{2\pi} \frac{\ell(\ell+1)}{IJ(J+1)} \frac{e\hbar}{2m} \times \\ \times \int_{r=0}^{+\infty} \left(\frac{1}{r^3} \int_{R=0}^r (\vec{R} \wedge \vec{j}(\vec{R}))_z d^3\vec{R} + \frac{2\kappa-1}{\ell(\ell+1)} \int_{R=r}^{+\infty} \frac{(\vec{R} \wedge \vec{j}(\vec{R}))_z}{2R^3} d^3\vec{R} \right) R_{n\ell}^2(r) dr. \quad (7.85)$$

Therefore, while it would be incorrect to say that $a^{(s)}$ is a contact term, since the same term still appears in the expression of $a^{(\ell)}$, the expression of $a^{(s)}$ can still be identified to the Fermi contact term, as it is the non-relativistic limit of the hyperfine dipole constant of s states, albeit for a finite current distribution nucleus. More importantly, given a model for the current distribution inside the nucleus, the expression of $a^{(s)}$ allows for an ab-initio, non-relativistic, calculation of the Fermi contact term. It should also converge towards the Fermi contact term in the limit of a point-dipole nucleus, although, the current distribution model of a point dipole nucleus is not trivial to define³.

Note: If one were to consider the electronic penetration inside the nucleus too hastily, without accounting for the irregular multipoles (the integrals from $R = r$ to $+\infty$) the assumption in (7.75) would be

$$f(r) = \frac{1}{2r^2} \int_{R=0}^r (\vec{R} \wedge \vec{j}(\vec{R}))_z d^3\vec{R}, \quad (7.86)$$

Thus, $f(0) = 0$, still, but the non-relativistic limit of the $\int \cdot P(r)Q(r)dr$ integral would be different

$$\int_{r=0}^{+\infty} \left[\left(\frac{d}{dr} - \frac{2\kappa}{r} \right) f(r) \right] R_{n\ell}^2(r) dr \\ = \left\langle \frac{(\vec{r} \wedge \vec{j}(\vec{r}))_z}{2r^2} \right\rangle_{n\ell} - \int_{r=0}^{+\infty} \left[\frac{\kappa+1}{r^3} \int_{R=0}^r (\vec{R} \wedge \vec{j}(\vec{R}))_z d^3\vec{R} \right] R_{n\ell}^2(r) dr. \quad (7.87)$$

Which also yields the correct limit of the hyperfine dipole constant for a point-dipole nucleus. It also provides for an approximation for the non-relativistic Fermi contact term from the current distribution model of the nucleus, which is then simply given by $\int_{r=0}^{+\infty} \left[\frac{\vec{r} \wedge \vec{j}(\vec{r})}{2r^2} \right] R_{n\ell}^2(r) dr$.

Note: The non-relativistic limit of (7.42) for the hyperfine quadrupole constant is obtained by simply assuming $Q_{n\kappa}(r) = 0$.

³under the assumption that \vec{j}_{pt} satisfies

$$r^2 \int_{R=r}^{\infty} \frac{(\vec{R} \wedge \vec{j}_{\text{pt}}(\vec{r}))_z}{2R^3} d^3\vec{R} = \frac{4}{3} M_z^{(1, \text{spec})} \delta(r).$$

7.5 Hyperfine constants in matter

The values obtained for the hyperfine constants in the previous sections are valid for free ions, where the nucleus is the only source of magnetic field. However, in matter, the hyperfine constants are modified by the presence of the environment, and the external fields. The main consequence of this is that F is not a good quantum number indexing eigenenergies of the system.

The eigenstates are then majoritarilly states in the uncoupled basis of the electron and nucleus $|JM_JIM_I\rangle$, where the electronic eigenstates are obtained from the considerations made in [Part I](#).

The effective hyperfine Hamiltonians given in (7.13) and (7.47) are then still valid for states in the same J multiplet, and the hyperfine constants are then given by the expectation values of the effective Hamiltonians in the decoupled states, which can be shown to yield the same expressions as in (7.28) and (7.42).

However, in matter, the effect of the Ligand Field mixes the states of different J multiplets, and therefore, the value of the hyperfine constant will depend on the linear combination of the states in the uncoupled basis that form the eigenstates of the system. To a first order approximation, since the hyperfine hamiltonian amplitude is small compared to the Ligand Field, if the considered state is a linear combination of the states $|JM_JIM_I\rangle$ with different J (but same M_J and M_I), the hyperfine constant is given by the same linear combination of the hyperfine constants of the states forming the eigenstate.

Moreover, if the Ligand-Field presents negligible off-diagonal elements in the J basis, the hyperfine constants of the states in the same J multiplet are not modified by the Ligand-Field, and the hyperfine constants are then given by the same expressions as in (7.28) and (7.42). However, as the eigenstates are in the decoupled basis, the hyperfine energy levels can be computed as a perturbation

$$\langle JM_JIM_I | a\vec{I} \cdot \vec{J} | JM_JIM_I \rangle = aM_IM_J. \quad (7.88)$$

This yields a constant hyperfine splitting between two states of adjacent M_J , equal to aM_I .

The same considerations can be made for the hyperfine quadrupole constant, and the hyperfine quadrupole energy contribution is given by

$$\langle JM_JIM_I | \frac{b}{2} \frac{3(\vec{I} \cdot \vec{J})^2 + \frac{3}{2}\vec{I} \cdot \vec{J} - I^2J^2}{I(2I-1)J(2J-1)} | JM_JIM_I \rangle = \frac{b}{2} \frac{(3M_I^2 - I(I+1))(3M_J^2 - I(I+1))}{I(2I-1)J(2J-1)}. \quad (7.89)$$

Note: The important take-away from this is that the hyperfine constants are modified by the presence of the environment, and an exact diagonalization of the atomic Hamiltonian including the Ligand Field and the Hyperfine Hamiltonian is needed to obtain the energy splittings of the hyperfine levels, and effective hyperfine constants can then be computed by fitting the energy levels given by first-order perturbation of the hyperfine Hamiltonian with variable hyperfine constants.

Main takeaways from Chapter 7

- **Hyperfine Interactions and Constants:**

- Hyperfine structure arises from nuclear magnetic dipole and electric quadrupole interactions with electrons.
- Hyperfine constants a and b quantify these interactions.

- **Isotope Shifts and Hyperfine Anomaly:**

- Deviations in hyperfine constants between isotopes are explained by Breit-Rosenthal and Bohr-Weisskopf corrections. These account for finite nuclear size and magnetization distributions and are sensitive to the chosen nuclear model.

- **Non-Relativistic Limit:**

- The Pauli approximation simplifies the Dirac equation to non-relativistic form.
- Leads to the Fermi contact term for s -states, involving electron density at the nucleus.

- **Hyperfine Constants in Matter:**

- Environmental effects like ligand fields modify hyperfine constants in materials by mixing states.
- Calculations must include these effects for accurate descriptions in solids.

Chapter Contents

8.1	Wavefunctions of the electron and muon in H-like ions	143
8.2	Muonic and electronic H-like energy levels .	144
8.3	Hyperfine isotope shifts of $^{161/163}\text{Dy}^{65+}$. . .	151
8.4	Additional examples of $^{159}\text{Tb}^{64+}$ and $^{165}\text{Ho}^{66+}$	163

CHAPTER 8

The electron/muon as a nuclear probe: hydrogen-like Dy ions

As previously stated, the Dirac equation for the electron and muon can be numerically solved in the presence of a nucleus, considering both a point-like dipole and a finite charge distribution. The resulting wavefunctions allow for the calculation of the energy levels, helping to assess how different corrections affect these observables. Ideally, by comparing these theoretical results with experimental data, one can validate the models used for the nucleus. Using the electron and muon as probes in this manner provides a means to evaluate the accuracy of nuclear models; improvements in the calculated observables, relative to other models, suggest a more accurate representation of the nucleus. In this section we will focus on two dysprosium isotopes that are of particular interest in lanthanide-based complexes and that have two different hyperfine structures albeit with the same electronic structure: ^{161}Dy and ^{163}Dy . As a matter of fact, they are the only two naturally abundant dysprosium isotopes with a non-vanishing nuclear spin in their nuclear ground state, see [Tab. 8.1](#)

Their nuclei differ by 2 neutrons, and we will investigate how this difference affects the hyperfine structure of the electronic (and muonic) states. Moreover, for the sake of simplicity, we will consider one-particle ions, or *hydrogen-like* ions: $^{161}\text{Dy}^{65+}$ and $^{163}\text{Dy}^{65+}$.

8.1 Wavefunctions of the electron and muon in H-like ions

[Figure 8.1](#) presents the two components of the relativistic radial wavefunctions, as defined in (5.24), for the $1s_{1/2}$ and $2p_{1/2}$ states of the electron in hydrogen-like $^{163}\text{Dy}^{65+}$. The figure includes various models for the nuclear monopole potential. The most noticeable distinction between the point-like model and the more realistic ones is the behavior of the wavefunctions within the nucleus, where the surface is marked by the vertical line. Due to the finite size of the nucleus, there is a reduction in the wavefunction amplitude at its center. As expected, the differences between the finite size models are negligible outside the nucleus, but inside, the differences are also not particularly significant.

As discussed in [Sections 6.1](#) and [6.2](#), increasing the mass of the orbiting negatively charged particle leads to a rescaling of the wavefunctions. Therefore, how do different nuclear charge models influence muonic ions, for which stronger penetration into the nucleus is expected? [Figure 8.2](#) shows the radial wavefunctions for the $1s_{1/2}$ and $2p_{1/2}$ states of the muon in hydrogen-like $^{163}\text{Dy}^{65+}(\mu^-)$, using different nuclear monopole potential models. Aside from the length rescaling, the main difference between the electronic and muonic wavefunctions is the greater penetration of the muonic wavefunctions into the

A	$T_{1/2}$	NA (%)	K^π	μ (nm)	Q (eb)
147	1.3 m	0	1/2+	-0.915(9)	0
149	4.23 m	0	7/2-	-0.119(7)	-0.62(5)
151	17 m	0	7/2-	-0.945(7)	-0.30(5)
153	6.3 h	0	7/2-	-0.782(6)	-0.02(5)
155	10.0 h	0	3/2-	-0.385(4)	+1.04(3)
156	Obs. Stable	0.056	0+	0	0
157	8.1 h	0	3/2-	-0.301(2)	+1.30(2)
158	Obs. Stable	0.095	0+	0	0
159	144 d	0	3/2-	-0.354(3)	+1.37(2)
160	Obs. Stable	2.33	0+	0	0
161	Obs. Stable	25.5	5/2+	-0.480(3)	+2.51(2)
162	Obs. Stable	18.9	0+	0	0
163	Stable	24.9	5/2-	+0.673(4)	+2.318(6)
164	Stable	28.3	0+	0	0
165	2.33 h	0	7/2+	-0.520(5)	-3.48(7)

Table 8.1: Table listing the isotopes of dysprosium (${}_{66}\text{Dy}$) with experimentally observed ground-states, only naturally abundant even-even ground state nuclei are included. The table, adapted from Stone [145], lists the isotopes, half-lives, natural abundances, spin-parities, magnetic moments (in nm) and charge quadrupole moments (in eb). Isotopes with "Obs. Stable" lifetimes are theoretically expected to be unstable, but have not been observed to decay, and are therefore assumed to have extremely long lifetimes hence being "Observationally Stable". The two isotopes of interest in this chapter are indicated in bold. The natural abundances are taken from [160].

nucleus. Although the finite size of the nucleus still results in a reduced amplitude at the center, the effect is more pronounced for muonic wavefunctions. Moreover, the distinctions between the different finite size models within the nucleus are more significant for the muon compared to the electron.

Once the wavefunctions are determined, they can be used to compute various observables, e.g. the energy levels of electrons and muons in hydrogen-like ions or hyperfine constants. These calculations can then be compared to experimental data, providing a way to validate the nuclear models used in the study.

8.2 Energy levels of the electron and muon in H-like ions

In particular, as a first step, one can consider the energy levels of the electron and muon in hydrogen-like ions. As an indication, the computed energy levels of the electron in the ${}^{163}\text{Dy}^{65+}$ for different excited states ($1s_{1/2}$ to $4f_{7/2}$) are shown in Tab. 8.2. The energy levels are given in atomic units and for different models of the monopole charge distribution of the nucleus. The first column, labeled "pt", corresponds to the point charge model, and the values obtained are in accordance with (5.28) after subtracting the electron rest mass energy. The labels "sp", "fm", and "hf" correspond to the spherical, Fermi, and HFBCS models, respectively.

Table 8.3 shows the same information for the muon in the ${}^{163}\text{Dy}^{65+}(\mu^-)$ ion. One can note the rescaling discussed in Section 6.1 for the muon binding energies for the point charge model, with a reduced muonic mass of $m_\mu \approx 206.6m_e$.

One can define the relative energy shift of the $n\ell\kappa$ state due to the finite size of the nucleus, considering a given model for the monopole charge distribution of the nucleus, as

$$\Delta E_{\text{m1}}^{\text{m2}}(n\ell\kappa) = (E^{\text{m2}}(n\ell\kappa) - E^{\text{m1}}(n\ell\kappa)) / E^{\text{m2}}(n\ell\kappa), \quad (8.1)$$

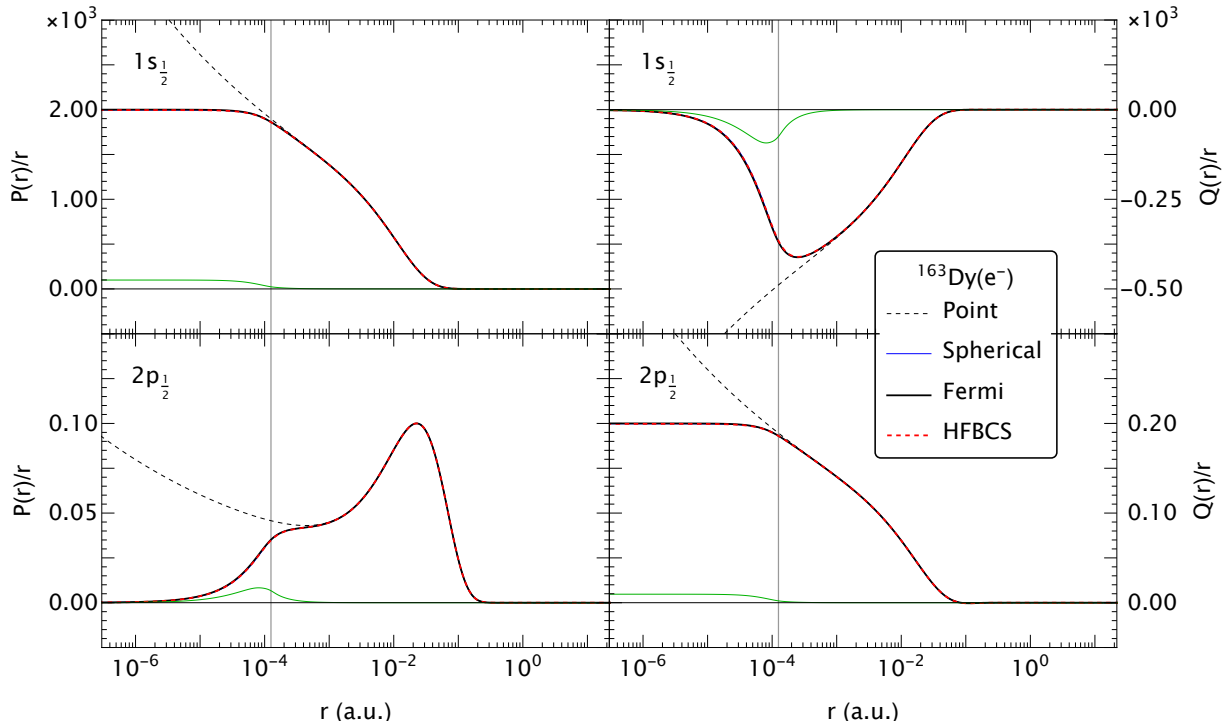


Figure 8.1: Relativistic radial wavefunctions of the $1s_{1/2}$ and $2p_{1/2}$ states of the electron in the hydrogen-like $^{163}\text{Dy}^{65+}$, accounting for different nuclear potentials. The coloured curves correspond to the different models for the monopole charge distribution of the nucleus: (dashed) a point-like ($\frac{Ze}{r}$) nuclear model, (blue) a uniformly distributed spherical model, (black) a smooth Fermi distribution, and (red) a more realistic model using the HFBCS code. The green curve represents the difference between the HFBCS models for the two isotopes. The vertical line indicates the nuclear radius R_N . The radial coordinate r is in atomic units i.e. in units of the Bohr radius a_0 .

where $E^{\text{model}}(n\ell\kappa)$ is the energy of the $n\ell\kappa$ state with a chosen monopole charge distribution model. The computed energy shifts from the point charge model for different $n\ell\kappa$ states of the electron and muon in hydrogen-like $^{163}\text{Dy}^{65+}$ are shown in the histograms in the upper parts (Fig. 8.3a) and (Fig. 8.3b), respectively. The relative energy shifts are given in percentage, and the different colors represent the different models for the monopole charge distribution of the nucleus. The energy shifts are positive for all states, indicating that the finite size of the nucleus leads to a decrease in the energy levels of the electron or muon. These shifts are more pronounced for the muon than for the electron, and the differences between the different finite size models are more pronounced for the muon than for the electron, as would have been expected from the behaviour of the wavefunctions.

Note: We also observe a degeneracy lifting between states of same j but different ℓ , that is due to the finite charge distribution of the nucleus. Therefore the finite charge distribution, on top of the Lamb shift and the vacuum polarization, also contributes to this well-known effect.

The lower parts of (Fig. 8.3a) and (Fig. 8.3b) show the relative energy shifts between the HFBCS models for the two isotopes, ^{161}Dy and ^{163}Dy as well as the shift between the Fermi distribution and the HFBCS model. The energy shifts are still given in percentage.

In more detail, the monopolar energy shifts for the electronic ion are significant only for the $j = \frac{1}{2}$ states ($s_{1/2}$ and $p_{1/2}$). These shifts are on the order of $10^{-2}\%$ for the $s_{1/2}$ state and $10^{-3}\%$ for the $p_{1/2}$ state, with a notable maximum of 0.02% for the $1s_{1/2}$ orbital. This observation (that energy shifts are

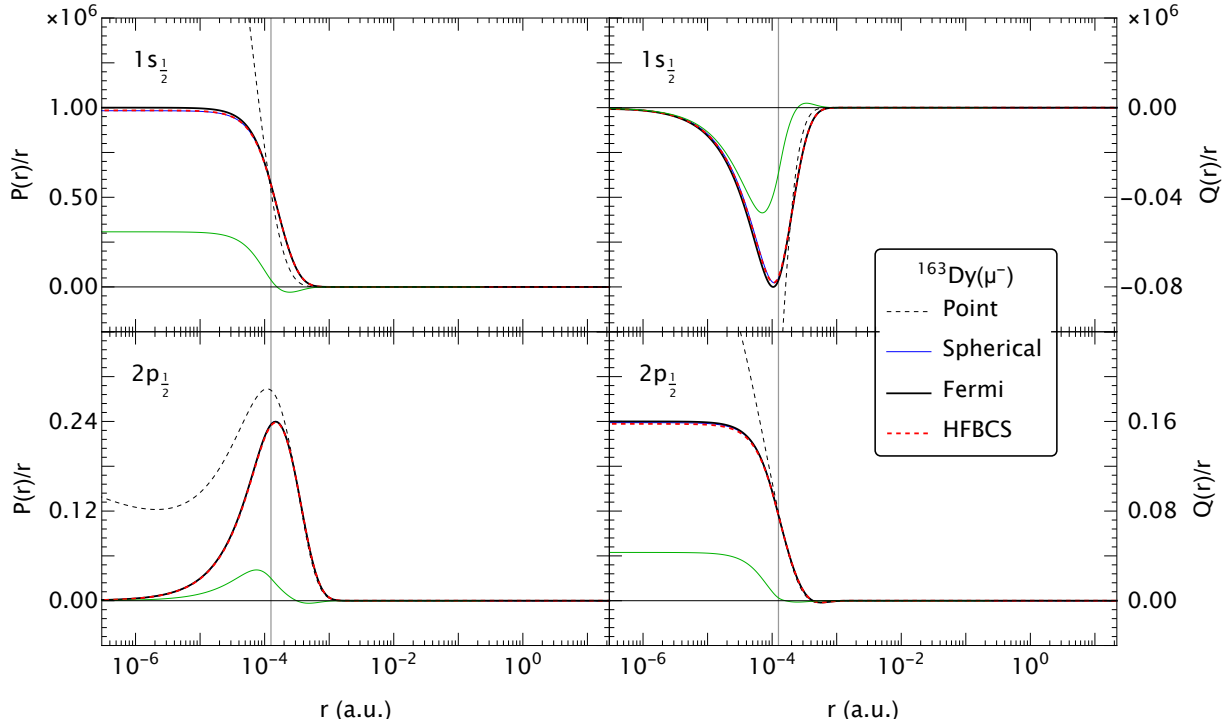


Figure 8.2: Same as Fig. 8.1 but for the muon in the hydrogen-like $^{163}\text{Dy}^{65+}(\mu^-)$.

noticeable only for $j = \frac{1}{2}$ states) is consistent with the non-relativistic limit, where only states with $j = \frac{1}{2}$ have a non-zero probability density at the nucleus, as discussed in more detail in Section 7.4.

In contrast, the energy shifts for the muonic ion are significantly more pronounced than those for the electronic ion. For the muonic ion, the maximum shift is 40% for the $1s_{1/2}$ orbital, while the shifts are on the order of 10% for the other $s_{1/2}$ states and 1% for the $p_{1/2}$ states and even the $p_{3/2}$ states. This difference can be attributed to the fact that the wavefunctions of the muon are more localized around and inside the nucleus, as discussed in Section 6.3.3.

The energy shifts between the Fermi distribution and the HFBCS model is of the order of $10^{-4}\%$ at best for the electronic ion, rendering electronic monopolar energy shifts quite ill-suited for discriminating between different nuclear models. Based on the values for the binding energy of the $s_{1/2}$ states in Tab. 8.2, this would correspond to a difference in energy of the order of tens of meV. On the other side, the energy shifts between the Fermi distribution and the HFBCS model for the muonic ion are on the order of $10^{-1}\%$, this coupled with the high bonding energies of the muon (Tab. 8.3), corresponds to a difference in energy of the order of keV. This suggests that muonic monopolar energy shifts could already be used to discriminate between different nuclear models.

Note: Interestingly, the root-mean-square radius ($R_{\text{rms}} = \sqrt{\langle R^2 \rangle}$) of both the spherical distribution (6.22) and the Fermi distribution (6.23) can be redefined to match the R_{rms} of the HFBCS model.

The renormalized distributions are displayed in the lower section of Fig. 8.4, note that $R_N = \sqrt{\frac{5}{3}R_{\text{rms}}^2}$ has changed according to the new value of R_{rms} , while the monopole potential experienced by the electron is shown in the upper section. These can be compared with that in Fig. 6.5. The recalculated binding energies for both electronic and muonic ions are summarized in Tab. 8.4 and can be compared with the results in Tab. 8.2 and Tab. 8.3.

By performing this renormalization, one observes that the energy shifts between the Fermi distribution and the HFBCS model for the electronic ion are on the order of $10^{-6}\%$, corresponding to a

$n\ell_j$	E^{pt}	E^{sp}	E^{fm}	E^{hf}
$1s_{1/2}$	-2321.4948	-2321.0385	-2321.0392	-2321.0245
$2s_{1/2}$	-589.6305	-589.5601	-589.5603	-589.5580
$2p_{1/2}$	-589.6305	-589.6269	-589.6269	-589.6268
$2p_{3/2}$	-552.6315	-552.6315	-552.6315	-552.6315
$3s_{1/2}$	-257.8394	-257.8184	-257.8184	-257.8177
$3p_{1/2}$	-257.8394	-257.8382	-257.8382	-257.8381
$3p_{3/2}$	-246.8293	-246.8293	-246.8293	-246.8293
$3d_{3/2}$	-246.8293	-246.8293	-246.8293	-246.8293
$3d_{5/2}$	-243.5797	-243.5797	-243.5797	-243.5797
$4s_{1/2}$	-143.2890	-143.2802	-143.2802	-143.2799
$4p_{1/2}$	-143.2890	-143.2884	-143.2884	-143.2884
$4p_{3/2}$	-138.6699	-138.6699	-138.6699	-138.6699
$4d_{3/2}$	-138.6699	-138.6699	-138.6699	-138.6699
$4d_{5/2}$	-137.2922	-137.2922	-137.2922	-137.2922
$4f_{5/2}$	-137.2922	-137.2922	-137.2922	-137.2922
$4f_{7/2}$	-136.6220	-136.6220	-136.6220	-136.6220

Table 8.2: Binding energies in Hartrees for $n\ell_j$ states of the $^{163}\text{Dy}^{65+}$ ion. E^{m} denotes the relativistic energy values (excluding the rest mass) calculated by solving the Dirac equation for a (m=pt) point nucleus, (m=sp) sphere model, (m=fm) Fermi model, and (m=hf) spherically averaged HFBC realistic model.

difference of hundreds of μeV . This indicates that, for electronic ions, the R_{rms} is the dominant factor in determining energy levels, as previously noted in [149]. Consequently, one can use the HFBCS model to determine the R_{rms} of the nucleus and calculate the energy levels using the Fermi distribution, renormalized with the same R_{rms} . This approach yields accurate results while reducing computational costs.

The energy shifts between the Fermi distribution and the HFBCS model for the muonic ion are on the order of $10^{-3}\%$, corresponding to a difference of hundreds of eV , which is still significant. This means that the R_{rms} is not the only factor necessary in determining the energy levels of the muonic ion, and their binding energies still represent a valuable tool for discriminating between different nuclear models.

Finally, the isotopic shift in energies between the two isotopes, ^{161}Dy and ^{163}Dy , is on the order of $10^{-5} - 10^{-4}\%$ for $s_{1/2}$ states and $10^{-6}\%$ for $p_{1/2}$ states for the electronic ion, corresponding to energy shifts of the order of the meV . For the muonic ion, the isotopic shifts are on the order of $10^{-2} - 10^{-1}\%$ corresponding to energy shifts of the order of the hundreds of eV . This suggests that muonic isotopic energy shifts could also be used to discriminate between different isotopes of the same element.

nl_j	E^{pt}	E^{sp}	E^{fm}	E^{hf}
$1s_{1/2}$	-479680.4	-285823.2	-286916.6	-284560.7
$2s_{1/2}$	-121832.8	-90810.8	-91087.4	-90671.6
$2p_{1/2}$	-121832.8	-115503.4	-115443.9	-115250.1
$2p_{3/2}$	-114187.8	-111674.2	-111596.0	-111468.7
$3s_{1/2}$	-53276.2	-43553.2	-43650.9	-43513.4
$3p_{1/2}$	-53276.2	-51122.5	-51106.6	-51042.3
$3p_{3/2}$	-51001.3	-50101.0	-50076.4	-50032.1
$3d_{3/2}$	-51001.3	-50980.2	-50978.1	-50976.4
$3d_{5/2}$	-50329.8	-50322.2	-50320.8	-50319.9
$4s_{1/2}$	-29607.2	-25412.2	-25456.7	-25395.6
$4p_{1/2}$	-29607.2	-28664.8	-28658.5	-28630.5
$4p_{3/2}$	-28652.8	-28250.6	-28240.1	-28220.4
$4d_{3/2}$	-28652.8	-28640.1	-28638.8	-28637.8
$4d_{5/2}$	-28368.1	-28363.4	-28362.6	-28362.1
$4f_{5/2}$	-28368.1	-28368.1	-28368.1	-28368.1
$4f_{7/2}$	-28229.6	-28229.6	-28229.6	-28229.6

Table 8.3: Binding energy values in Hartrees for nl_j states of the muonic $^{163}\text{Dy}^{65+}(\mu^-)$ ion. The notations are the same as in Tab. 8.2.

nl_j	E^{sp}	E^{fm}	E^{hf}
$1s_{1/2}$	-2321.0242	-2321.0249	-2321.0245
$2s_{1/2}$	-589.5579	-589.5581	-589.5580
$2p_{1/2}$	-589.6268	-589.6268	-589.6268
$2p_{3/2}$	-552.6315	-552.6315	-552.6315
$3s_{1/2}$	-257.8177	-257.8178	-257.8177
$3p_{1/2}$	-257.8381	-257.8381	-257.8381
$3p_{3/2}$	-246.8293	-246.8293	-246.8293
$3d_{3/2}$	-246.8293	-246.8293	-246.8293
$3d_{5/2}$	-243.5797	-243.5797	-243.5797
$4s_{1/2}$	-143.2799	-143.2799	-143.2799
$4p_{1/2}$	-143.2884	-143.2884	-143.2884
$4p_{3/2}$	-138.6699	-138.6699	-138.6699
$4d_{3/2}$	-138.6699	-138.6699	-138.6699
$4d_{5/2}$	-137.2922	-137.2922	-137.2922
$4f_{5/2}$	-137.2922	-137.2922	-137.2922
$4f_{7/2}$	-136.6220	-136.6220	-136.6220

(a) Binding energies for the electronic $^{163}\text{Dy}^{65+}$ ion.

nl_j	E^{sp}	E^{fm}	E^{hf}
$1s_{1/2}$	-283536.8	-284602.4	-284560.7
$2s_{1/2}$	-90405.7	-90677.2	-90671.6
$2p_{1/2}$	-115315.7	-115256.5	-115250.1
$2p_{3/2}$	-111551.3	-111473.7	-111468.7
$3s_{1/2}$	-43419.0	-43515.2	-43513.4
$3p_{1/2}$	-51060.0	-51044.4	-51042.3
$3p_{3/2}$	-50058.0	-50033.7	-50032.1
$3d_{3/2}$	-50978.7	-50976.5	-50976.4
$3d_{5/2}$	-50321.5	-50320.0	-50319.9
$4s_{1/2}$	-25352.5	-25396.3	-25395.6
$4p_{1/2}$	-28637.6	-28631.4	-28630.5
$4p_{3/2}$	-28231.5	-28221.1	-28220.4
$4d_{3/2}$	-28639.2	-28637.9	-28637.8
$4d_{5/2}$	-28363.0	-28362.1	-28362.1
$4f_{5/2}$	-28368.1	-28368.1	-28368.1
$4f_{7/2}$	-28229.6	-28229.6	-28229.6

(b) Binding energies for the muonic $^{163}\text{Dy}^{65+}(\mu^-)$ ion.

Table 8.4: Binding energies in Hartrees for different nl_j states of the $^{163}\text{Dy}^{65+}$ ion, with spherical and Fermi distributions normalized for the same R_{rms} values as the HFBCS model.

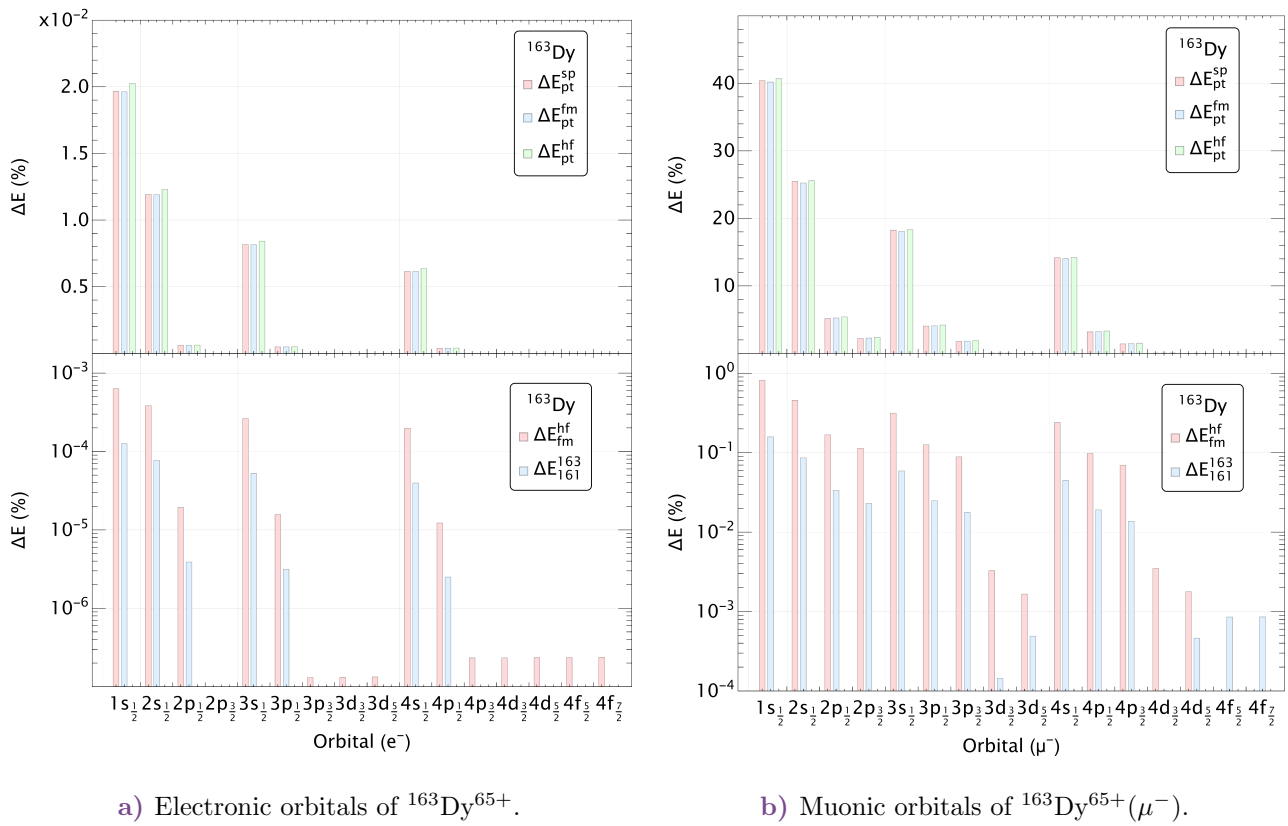


Figure 8.3: (upper panels) Monopolar shifts in the energy levels of the electronic or muonic orbitals of $^{163}\text{Dy}^{65+}$ (from $1s_{1/2}$ to $4f_{7/2}$) in different nuclear models: point (pt), spherical (sp), Fermi (fm), and HFBCS (hf). (lower panels) Relative energy shifts between the HFBCS models for the two isotopes, ^{161}Dy and ^{163}Dy ($\Delta E_{161}^{163} \equiv (E_{163}^{\text{hf}} - E_{161}^{\text{hf}}) / E_{163}^{\text{hf}}$), as well as the shift between the Fermi distribution and the HFBCS model $\Delta E_{\text{fm}}^{\text{hf}}$.

Z

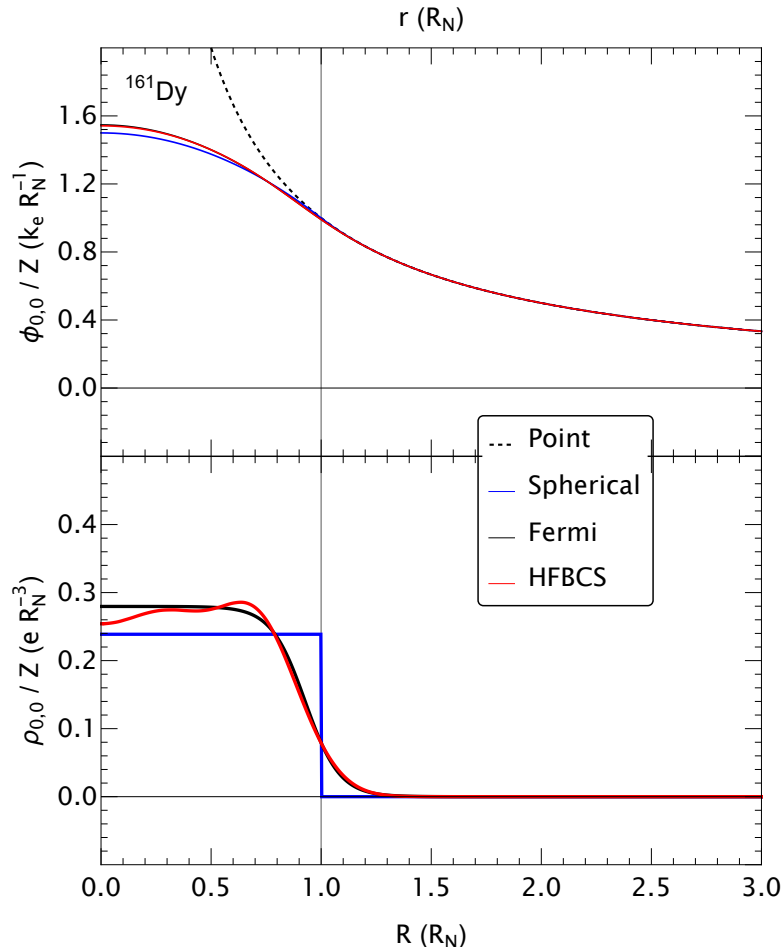


Figure 8.4: Z -normalized proton monopole density (bottom part) obtained for the ^{161}Dy nucleus from a uniform sharp-edge (blue), a Fermi-function type (black) and the distribution resulting from the HFBCS type (red) calculation, the first two have been renormalized so as to have the same value of R_{rms} as the last one. And the Z -normalized monopole potential experienced by the electron resulting from the different approaches for the density (upper part). The Coulomb potential generated by a nuclear point-charge density is shown by the dotted line. $k_e \equiv \frac{e}{4\pi\epsilon_0}$ is the Coulomb constant.

8.3 Isotope shifts in the hyperfine structures of $^{161/163}\text{Dy}^{65+}$

The next observables of interest were discussed in Section 7.3, the hyperfine structures of the electronic and muonic ions for two different isotopes of the same element and the ratio of the computed magnetic hyperfine constants. The hyperfine anomaly refers to the deviation that occurs when comparing two isotopes' magnetic properties. Specifically, it measures the difference between the ratio of the magnetic hyperfine constants and the ratio of the nuclear gyromagnetic ratios $M_z^{(1,\text{spec})}/I$ for those isotopes.

We recall the definition (7.51) of the hyperfine anomaly between isotopes A and B as

Definition: (*Hyperfine anomaly*)

$$\Delta_B^A \equiv \frac{{}^{(A)}a}{{}^{(B)}a} \frac{{}^{(B)}M_z^{(1,\text{spec})}/{}^{(B)}I}{{}^{(A)}M_z^{(1,\text{spec})}/{}^{(A)}I} - 1, \quad (7.51)$$

where ${}^{(A)}a$ and ${}^{(B)}a$ are the magnetic hyperfine constants of the electronic or muonic ion for isotopes A and B , respectively, and ${}^{(A)}M_z^{(1,\text{spec})}$ and ${}^{(B)}M_z^{(1,\text{spec})}$ are the nuclear magnetic moments of the isotopes A and B , respectively, finally ${}^{(A)}I$ and ${}^{(B)}I$ are the nuclear spins of the isotopes A and B , respectively.

We recall the different steps in calculating the hyperfine anomaly shown in Tab. 7.1 here for convenience.

$\vec{j}(\vec{R}) \backslash \rho(\vec{R})$	Point charge	Charge distribution model
Point dipole	1	$(1 - \epsilon_{\text{BR}}^{\text{model}})$
Current distribution model	N/A	$(1 - \epsilon_{\text{BR}}^{\text{model}})(1 - \epsilon_{\text{BW}})$

The first step is obtaining the Breit-Rosenthal correction (7.55) to the hyperfine constants, which is a direct consequence of the change in the radial wavefunctions due to the finite size of the nucleus. The second step is the Bohr-Weisskopf correction (7.58), which accounts for the penetration of the electronic or muonic wavefunctions into the nucleus.

8.3.1 Breit-Rosenthal corrections to the hyperfine constants

Figure 8.5 shows the Breit-Rosenthal corrections to the hyperfine constants of the electronic orbitals of $^{163}\text{Dy}^{65+}$ (from $1s_{1/2}$ to $4f_{7/2}$) in different nuclear models, as well as the relative Breit-Rosenthal corrections between the HFBCS models for the two isotopes, ^{161}Dy and ^{163}Dy , and the correction between the Fermi distribution and the HFBCS model. The electronic Breit-Rosenthal corrections seem to be noticeable for the same sets of states as the monopolar energy shifts, i.e. the $s_{1/2}$ and $p_{1/2}$ states, and are on the order of 4% for the $1s_{1/2}$ state and 1% for the $2p_{1/2}$ state.

Fig. 8.6 shows the same information for the muonic orbitals of $^{163}\text{Dy}^{65+}(\mu^-)$. The same trend as in the monopolar energy shifts is observed, with the Breit-Rosenthal corrections being more pronounced for the s and p states. The Breit-Rosenthal corrections are on the order of as much as 100% for the $s_{1/2}$ states, 50% for the $p_{1/2}$ states and 25% for the $p_{3/2}$ states. Notably, the Breit-Rosenthal corrections are still of the order of 1% for the d states.

When comparing the Breit-Rosenthal corrections between the Fermi distribution and the HFBCS model for the electronic and muonic ions, one can see that the relative difference for the predicted correction is of the order of 1% for the electronic ion. The muonic ion shows an interesting behaviour regarding that relative difference between models, as it seems to grow from less than 1% for the $s_{1/2}$ states to more than 10% for the $f_{7/2}$ states, increasing with the orbital angular momentum of the state.

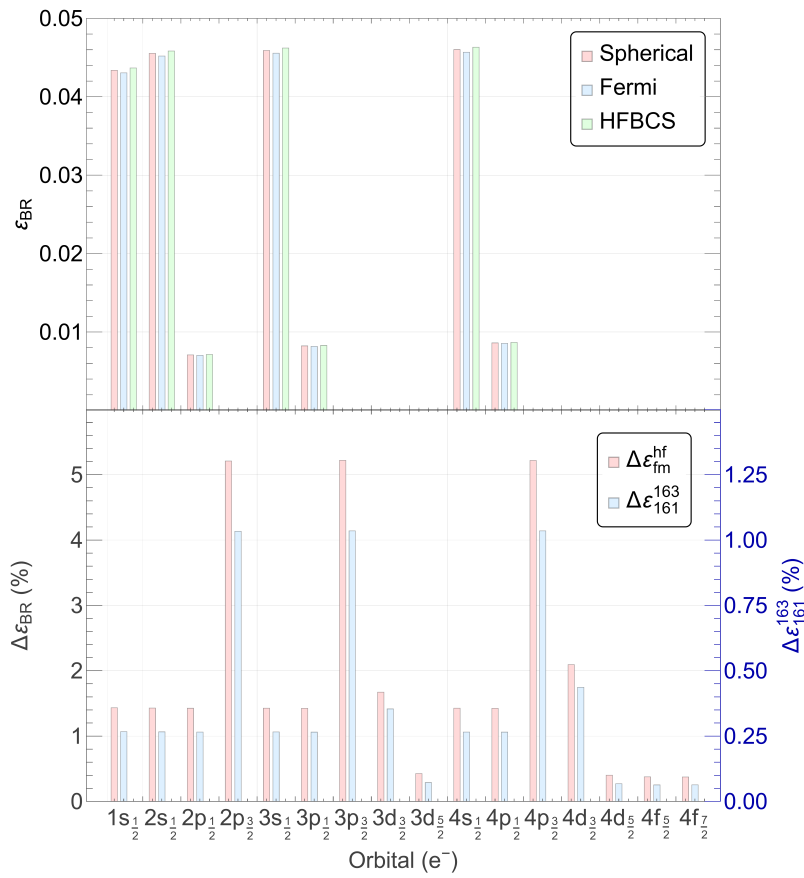


Figure 8.5: (upper pannel) Breit-Rosenthal corrections to the hyperfine constants of electronic orbitals of $^{163}\text{Dy}^{65+}$ (from $1s_{1/2}$ to $4f_{7/2}$) in different nuclear models, point (pt), spherical (sp), Fermi (fm) and HFBCS (hf). (lower pannel) Relative Breit-Rosenthal corrections between the HFBCS models for the two isotopes, ^{161}Dy and ^{163}Dy ($\Delta\epsilon_{161}^{163} \equiv (\epsilon_{163}^{hf} - \epsilon_{161}^{hf}) / \epsilon_{163}^{hf}$), as well as the correction between the Fermi distribution and the HFBCS model $\Delta\epsilon_{fm}^{hf} \equiv (\epsilon_{fm}^{hf} - \epsilon_{hf}^{hf}) / \epsilon_{fm}^{hf}$.

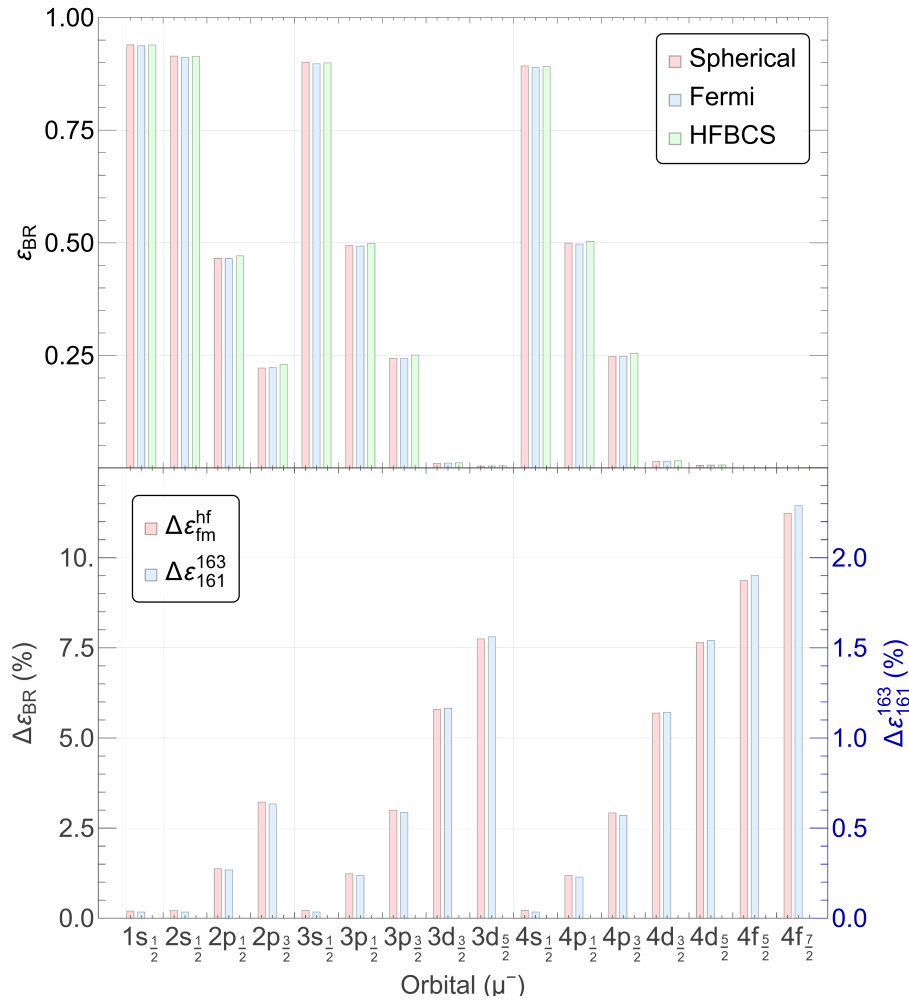


Figure 8.6: (upper panel) Breit-Rosenthal corrections to the hyperfine constants of muonic orbitals of $^{163}\text{Dy}^{65+}(\mu^-)$ (from $1s_{1/2}$ to $4f_{7/2}$) in different nuclear models, point (pt), spherical (sp), Fermi (fm) and HFBCS (hf). (lower panel) Relative Breit-Rosenthal corrections between the HFBCS models for the two isotopes, ^{161}Dy and ^{163}Dy ($\Delta\epsilon_{161}^{163} \equiv (\epsilon_{163}^{hf} - \epsilon_{161}^{hf}) / \epsilon_{163}^{hf}$), as well as the correction between the Fermi distribution and the HFBCS model $\Delta\epsilon_{fm}^{hf} \equiv (\epsilon_{fm}^{hf} - \epsilon_{hf}^{hf}) / \epsilon_{fm}^{hf}$.

8.3.2 Bohr-Weisskopf corrections to the hyperfine constants

The Bohr-Weisskopf corrections to the hyperfine constants of the electronic orbitals of $^{163}\text{Dy}^{65+}$ and $^{161}\text{Dy}^{65+}$ (from $1s_{1/2}$ to $4f_{7/2}$) as well as the relative Bohr-Weisskopf corrections between the HFBCS models for the two isotopes, ^{161}Dy and ^{163}Dy , and the correction between the Fermi distribution and the HFBCS model are shown in Fig. 8.7. Only the HFBCS model has been used to obtain a distribution of the magnetization inside the nucleus, over which to integrate according to (7.58). The Bohr-Weisskopf corrections are of the order of 10^{-2} for both isotopes, with the neutron spin current seemingly being the most significant contribution to the correction.

Fig. 8.8 shows the same information for the muonic orbitals of $^{163}\text{Dy}^{65+}(\mu^-)$ and $^{161}\text{Dy}^{65+}(\mu^-)$. The Bohr-Weisskopf corrections are of the order of 1 for the $j = \frac{1}{2}$ states, and decrease with the orbital angular momentum of the state. The neutron spin current is still the most significant contribution to the correction. This can be expected within even the single-particle model of the nucleus, as the two isotopes under consideration are even-odd, meaning they have an unpaired neutron, that is the most likely to contribute to the magnetic moment of the nucleus, the core polarization effect we discussed in Section 6.4.1 does seem to act as a screening effect, as the smaller proton contributions to the correction are opposite in sign to the neutron contributions and thus reduce the total correction by a certain amount.

As has been noted, for both types of corrections, the s and p orbitals are the most affected by the finite size of the nucleus, echoing the non-relativistic limit of the Fermi contact term. It would be interesting to observe how those corrections change with the quantum number n of the state.

Figure 8.9 shows the Breit-Rosenthal and Bohr-Weisskopf corrections for the electronic orbitals of $^{163}\text{Dy}^{65+}$ and $^{161}\text{Dy}^{65+}$ as a function of the quantum number n for the orbitals $ns_{1/2}$, $np_{1/2}$, and $np_{3/2}$. It can be observed that apart for a very slightly lower value for the $1s_{1/2}$ and $2p_{1/2}$ orbitals, the corrections are fairly constant, and their approximate values are summarized in Tab. 8.5.

Orbital	Breit-Rosenthal	Bohr-Weisskopf
$s_{1/2}$	4.7	1.6
$p_{1/2}$	0.9	0.4
$p_{3/2}$	0	0

Table 8.5: Approximate plateau values of the Breit-Rosenthal and Bohr-Weisskopf corrections (in %) for the electronic orbitals of $^{163}\text{Dy}^{65+}$ and $^{161}\text{Dy}^{65+}$.

Figure 8.10 shows the same information for the muonic orbitals of $^{163}\text{Dy}^{65+}(\mu^-)$ and $^{161}\text{Dy}^{65+}(\mu^-)$. The corrections now show a bigger variation with the quantum number n of the state, the Bohr-Weisskopf correction especially shows a significant dip for the $1s_{1/2}$ orbital. But the curves do also eventually show a plateau. The approximate values of the plateau are summarized in Tab. 8.6.

Orbital	Breit-Rosenthal	Bohr-Weisskopf
$s_{1/2}$	90	80
$p_{1/2}$	50	65
$p_{3/2}$	25	20

Table 8.6: Approximate plateau values of the Breit-Rosenthal and Bohr-Weisskopf corrections (in %) for the muonic orbitals of $^{163}\text{Dy}^{65+}(\mu^-)$ and $^{161}\text{Dy}^{65+}(\mu^-)$.

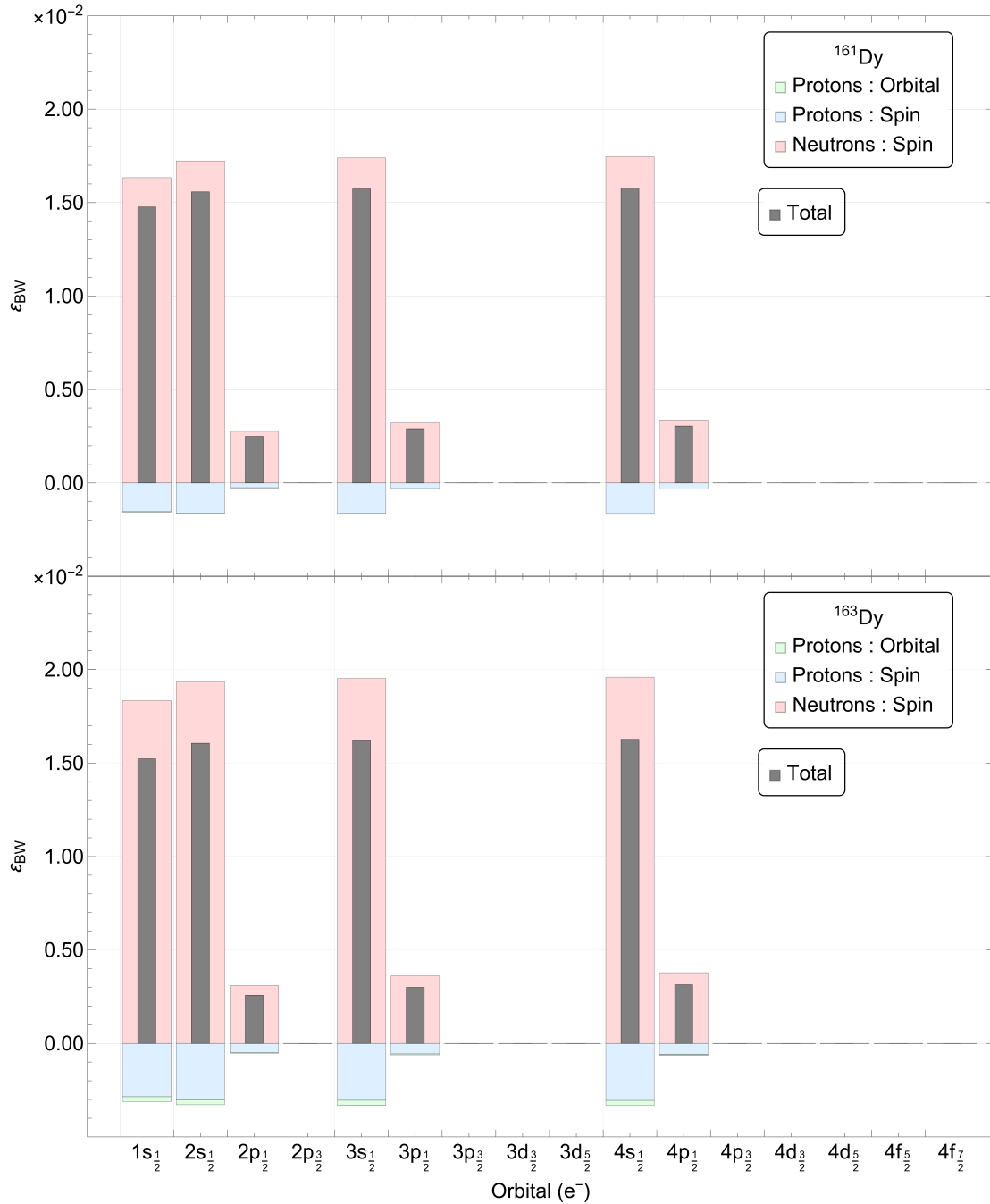


Figure 8.7: Bohr-Weisskopf correction ϵ_{BW} for $^{161}\text{Dy}^{65+}$ (top panel) and $^{163}\text{Dy}^{65+}$ (lower panel) for the orbitals from $1s_{1/2}$ to $4f_{7/2}$. Only the HFBCS model is used to obtain the current distribution. The various magnetic contributions (proton and neutron spins and proton orbital motion) are shown, together with the total correction.

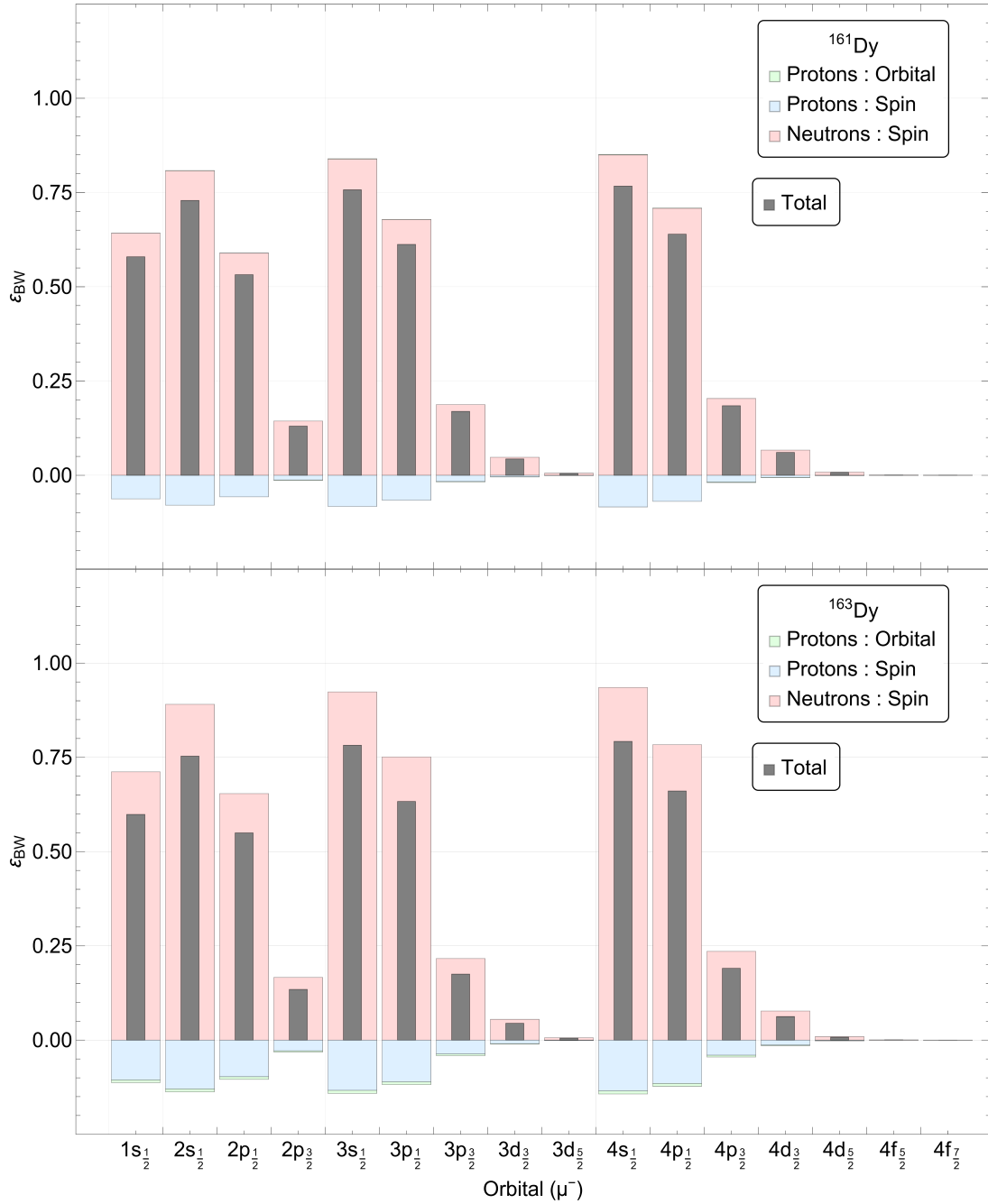


Figure 8.8: Bohr-Weisskopf correction ϵ_{BW} for $^{161}\text{Dy}^{65+}(\mu^-)$ (top panel) and $^{163}\text{Dy}^{65+}(\mu^-)$ (lower panel) for the orbitals from $1s_{1/2}$ to $4f_{7/2}$. Only the HFBCS model is used to obtain the current distribution. The various magnetic contributions (proton and neutron spins and proton orbital motion) are shown, together with the total correction.

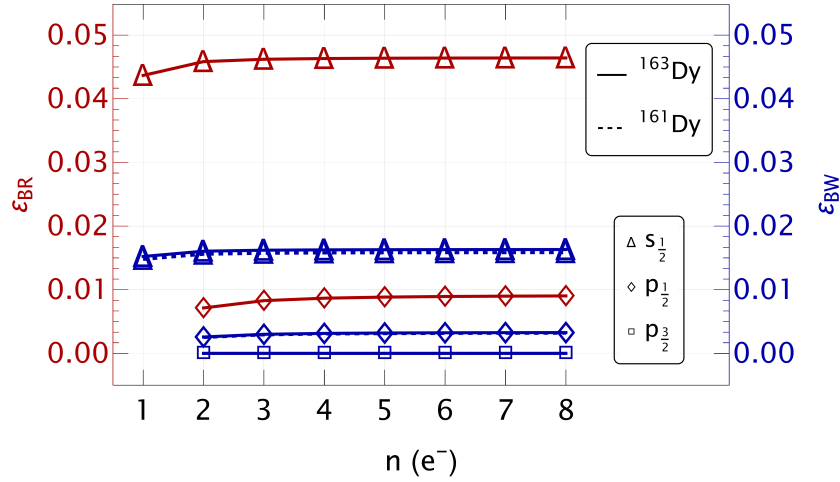


Figure 8.9: Breit-Rosenthal (in red and reading on the left axis) and Bohr-Weisskopf (in blue and reading on the left axis) corrections for $^{163}\text{Dy}^{65+}$ (solid line) and $^{161}\text{Dy}^{65+}$ (dashed line). The results are plotted as a function of quantum number n for the orbitals $ns_{1/2}$, $np_{1/2}$, and $np_{3/2}$. It is important to note that, with the exception of the Bohr-Weisskopf correction for the $s_{1/2}$ and $p_{1/2}$ orbitals, where there is a slight difference for $^{161}\text{Dy}^{65+}$ and $^{163}\text{Dy}^{65+}$, the other curves are superimposed for both isotopes. For $p_{3/2}$, as the corrections are very small, the straight line with square symbols actually corresponds to four superimposed curves including the two corrections and the two isotopes.

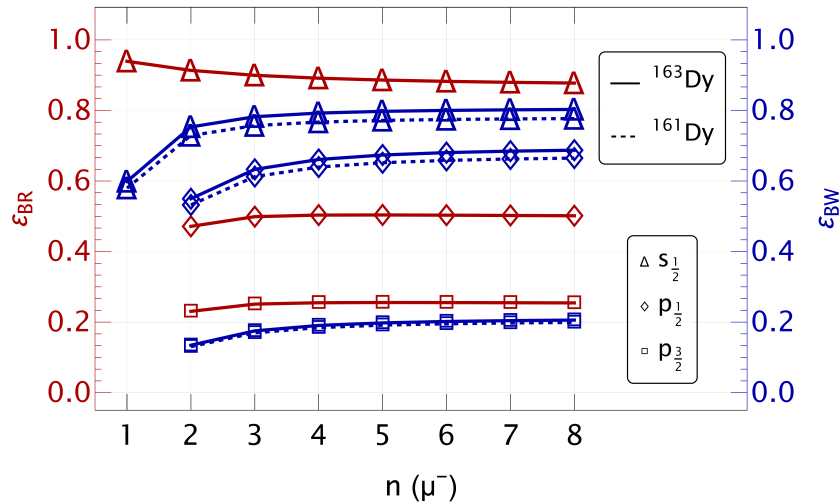


Figure 8.10: Breit-Rosenthal (in red and reading on the left axis) and Bohr-Weisskopf (in blue and reading on the left axis) corrections for $^{163}\text{Dy}^{65+} (\mu^-)$ (solid line) and $^{161}\text{Dy}^{65+} (\mu^-)$ (dashed line). The results are plotted as a function of quantum number n for the orbitals $ns_{1/2}$, $np_{1/2}$, $np_{3/2}$, and $nd_{5/2}$.

8.3.3 Hyperfine anomaly between ^{161}Dy and ^{163}Dy

Finally, since both the Breit-Rosenthal and Bohr-Weisskopf corrections could be computed, one can now calculate the hyperfine anomaly (7.60) between the isotopes ^{161}Dy and ^{163}Dy for the electronic and muonic ions. The results are shown in Fig. 8.11 for the electronic and muonic ions.

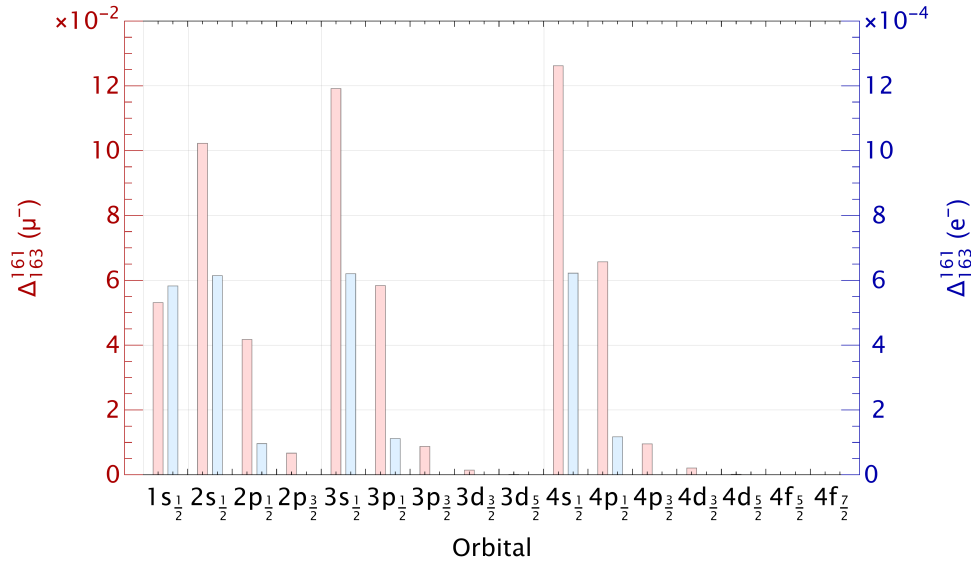


Figure 8.11: Hyperfine anomaly between ^{161}Dy and ^{163}Dy is depicted for muon (in red and reading on the left axis) and electron (in blue and reading on the right axis) for the orbitals from $1s_{1/2}$ to $4f_{7/2}$.

The orders of magnitude for the anomalies for the electronic ion is around 10^{-4} while it is of the order of 10^{-2} up to 10^{-1} for the muonic ion. Both orders of magnitude seem coherent with the litterature [155, 161].

The states with the largest anomaly are still the $j = 1/2$ and to a certain extent the $p_{3/2}$ states, therefore the same trend analysis as for ϵ_{BR} and ϵ_{BW} can be applied, and the values of the anomaly as a function of the principal quantum number n for the $s_{1/2}$, $p_{1/2}$, and $p_{3/2}$ states are plotted in ??.

Orbital	Anomaly
$s_{1/2}$	0.065
$p_{1/2}$	0.01
$p_{3/2}$	0

(a) Electronic orbitals of $^{163}\text{Dy}^{65+}$ and $^{161}\text{Dy}^{65+}$.

Orbital	Anomaly
$s_{1/2}$	13.5
$p_{1/2}$	7.5
$p_{3/2}$	1

(b) Muonic orbitals of $^{163}\text{Dy}^{65+}(\mu^-)$ and $^{161}\text{Dy}^{65+}(\mu^-)$.

Table 8.7: Approximate plateau values of the hyperfine anomaly (in %) for different orbitals.

We can see that for the electronic ion, the anomaly is fairly constant with the quantum number n of the state, with the exception of the $1s_{1/2}$ state, where the anomaly is slightly lower. The approximate values of the anomaly are summarized in Tab. 8.7a.

For the muonic ion, the anomaly is more variable with the quantum number n of the state, with the anomaly being, interstingly, the lowest for the $1s_{1/2}$ state and then growing until a plateau value, that is more than twice the value of the anomaly for the $1s_{1/2}$ state. The approximate values of the anomaly are summarized in Tab. 8.7b.

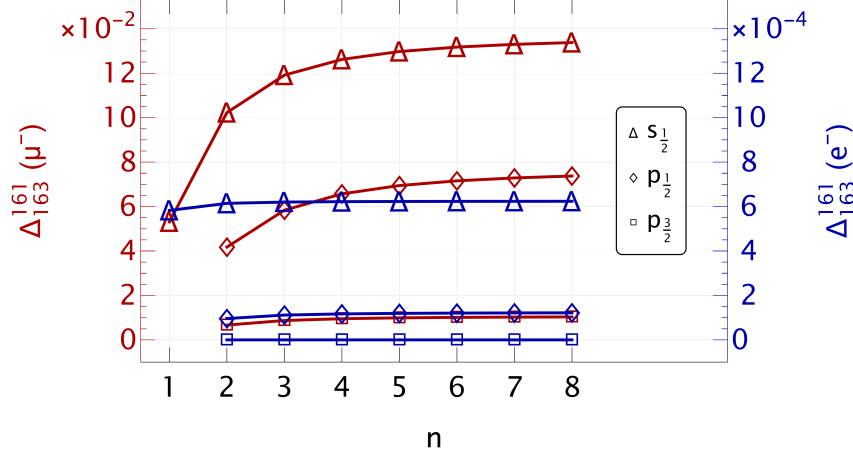


Figure 8.12: Hyperfine anomaly between ^{161}Dy and ^{163}Dy is depicted for muon (in red and reading on the left axis) and electron (in blue and reading on the right axis) for the orbitals $ns_{1/2}$, $np_{1/2}$, and $np_{3/2}$.

8.3.4 Quadrupole hyperfine anomaly

The quadrupole hyperfine anomaly refers to the deviation that arises when comparing the quadrupole properties of two isotopes. It specifically describes the difference between the ratio of the quadrupole hyperfine constants and the ratio of the nuclear quadrupole moments for those isotopes. It is defined in (7.62). Ideally, these two ratios would be equal, resulting in a value of one. However, when a discrepancy occurs between the ratios, this deviation from unity is what we call the quadrupole hyperfine anomaly.

Definition: (*Quadrupole hyperfine anomaly*)

$$Q\Delta_B^A \equiv \frac{b^{(A)} Q_0^{(2,\text{spec})}}{b^{(B)} Q_0^{(2,\text{spec})}} - 1, \quad (8.2)$$

where $b^{(A)}$ and $b^{(B)}$ are the quadrupole hyperfine constants of the electronic or muonic ion for isotopes A and B , respectively, and $Q_0^{(2,\text{spec})}$ and $Q_0^{(2,\text{spec})}$ are the nuclear quadrupole moments of the isotopes A and B , respectively.

The quadrupole hyperfine anomaly is calculated in the same way as the magnetic hyperfine anomaly. The first quantity that was calculated was the quadrupole shift defined in (7.63), that represents the change in the quadrupole moment due to the finite size of the nucleus. The quadrupole shift for the electronic orbitals of $^{163}\text{Dy}^{65+}$ is shown in the upper pannel of Fig. 8.13 for the orbitals from $2p_{3/2}$ to $4f_{7/2}$ in different nuclear models, as well as, in the lower panel, the relative quadrupole shifts between the HFBCS models for the two isotopes, ^{161}Dy and ^{163}Dy , and the shift between the Fermi distribution and the HFBCS model.

Note that the finite charge distribution used for the nuclear density ρ is the one obtained from the HFBCS model, and that the different nuclear charge models mentioned in Fig. 8.13 are the ones used to obtain the wavefunction only, and not the charge distribution itself, therefore it can be seen as more of numerical interest than physical interest. Moreover, the expression of the quadrupole hyperfine constant given in (7.42) is zero for $J = 1/2$, and therefore the quadrupole hyperfine anomaly is not defined for the $s_{1/2}$ and $p_{1/2}$ states.

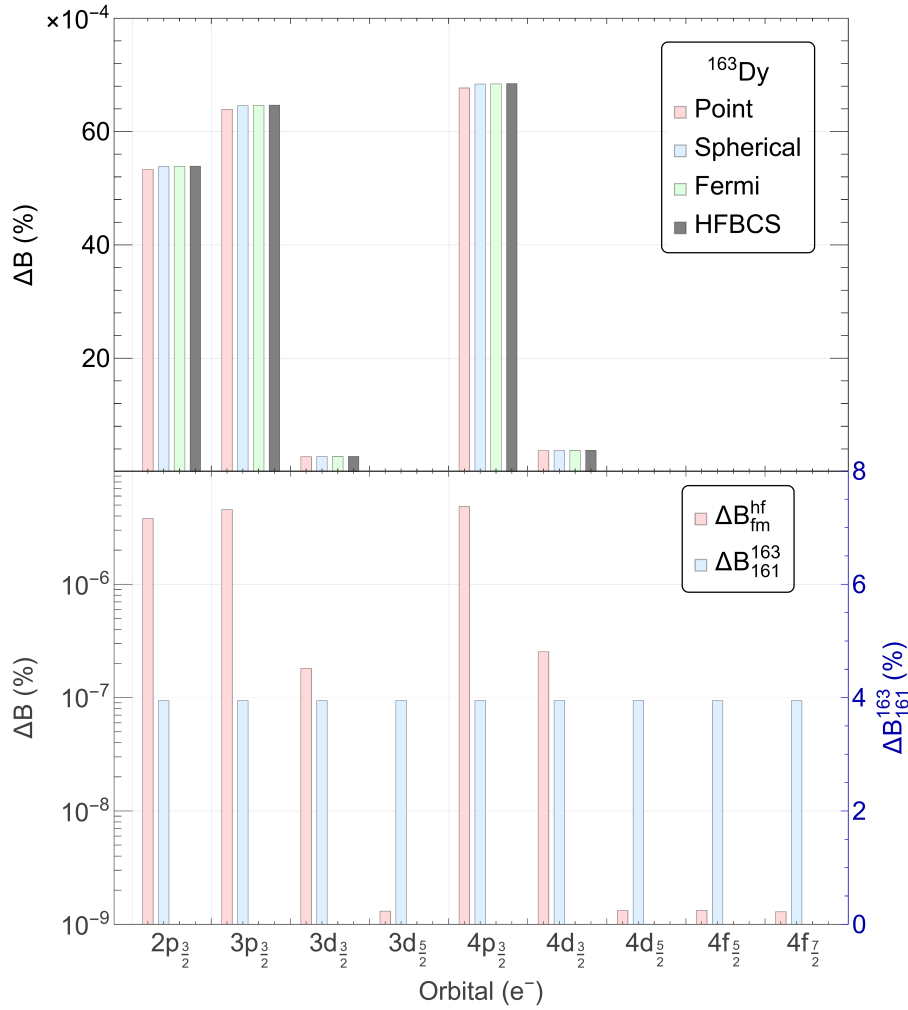


Figure 8.13: (upper) Quadrupole shifts in the hyperfine constants of electronic orbitals of $^{163}\text{Dy}^{65+}$ (from $2p_{3/2}$ to $4f_{7/2}$) in different nuclear models, point (pt), spherical (sp), Fermi (fm) and HFBCS (hf). (lower) Relative quadrupole shifts between the HFBCS models for the two isotopes, ^{161}Dy and ^{163}Dy ($\Delta B_{161}^{163} \equiv (b_{163}^{\text{hf}} - b_{161}^{\text{hf}})/b_{163}^{\text{hf}}$), as well as the shift between the Fermi distribution and the HFBCS model $\Delta B_{\text{fm}}^{\text{hf}} \equiv (b_{\text{fm}}^{\text{hf}} - b_{\text{hf}}^{\text{hf}})/b_{\text{fm}}^{\text{hf}}$.

One can see that the quadrupole shifts for the electronic ion are of the order of $10^{-3}\%$ for the $p_{3/2}$ states, this can be compared to the value of the hyperfine corrections in Fig. 8.9 and ?? for the same states, which are around $10^{-5}\%$. In terms of energy, for example, the dipole contribution to the hyperfine splitting of the $2p_{3/2}$ state for the $F = 4$ to $F = 3$ transition in the $^{163}\text{Dy}^{65+}$ ion can be calculated¹ to be around 3keV, while the quadrupole contribution² is around 24keV, this means that the quadrupole shift is almost three orders of magnitude larger than the dipole shift. However, the absolute value of the quadrupole shift is still of the order of $10^{-3}\%$ of the energy of the transition, and therefore the quadrupole hyperfine shift is not reasonably measurable for the electronic ion.

The quadrupole shift for the muonic orbitals of $^{163}\text{Dy}^{65+}(\mu^-)$ is shown in the upper panel of Fig. 8.14 for the orbitals from $2p_{3/2}$ to $4f_{7/2}$ in different nuclear models, as well as, in the lower panel, the relative quadrupole shifts between the HFBCS models for the two isotopes, ^{161}Dy and ^{163}Dy , and the shift between the Fermi distribution and the HFBCS model.

¹Using (7.24).

²Computed using (7.41)

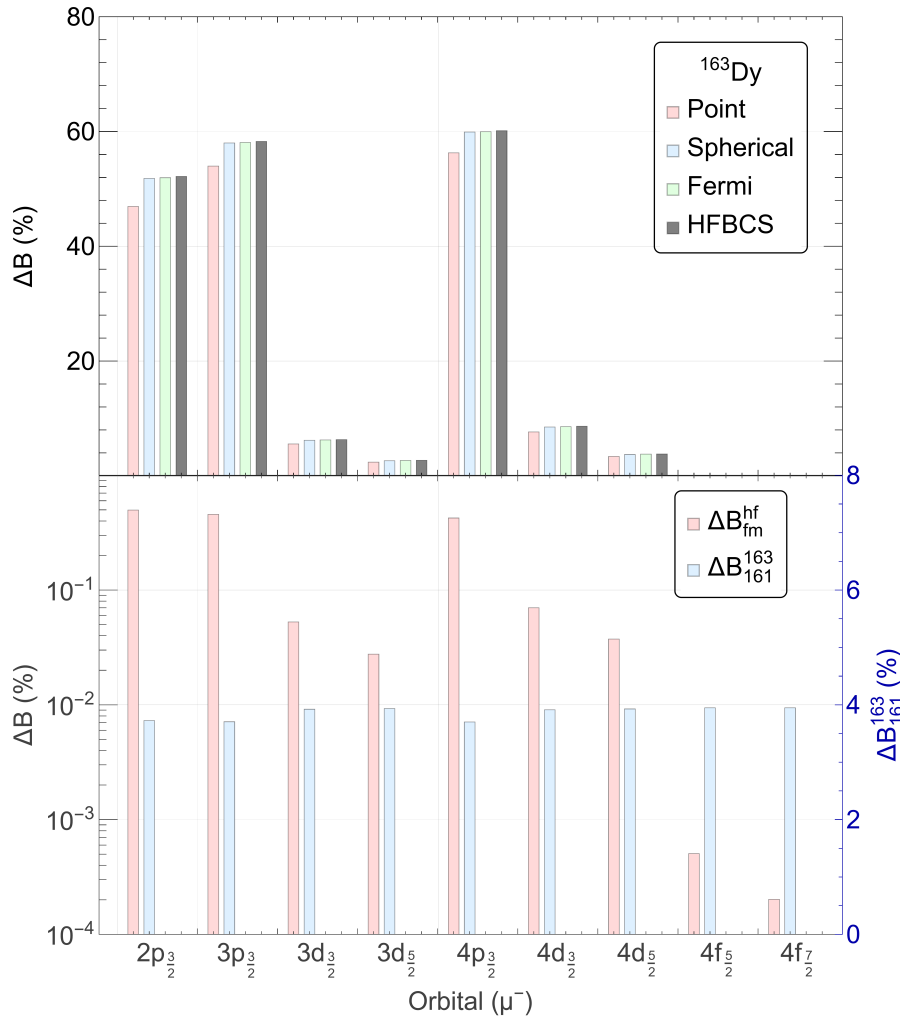


Figure 8.14: (upper) Quadrupole shifts in the hyperfine constants of muonic orbitals of $^{163}\text{Dy}^{65+}(\mu^-)$ (from $2p_{3/2}$ to $4f_{7/2}$) in different nuclear models, point (pt), spherical (sp), Fermi (fm) and HFBCS (hf). (lower) Relative quadrupole shifts between the HFBCS models for the two isotopes, ^{161}Dy and ^{163}Dy ($\Delta b_{161}^{163} \equiv (b_{163}^{\text{hf}} - b_{161}^{\text{hf}})/b_{163}^{\text{hf}}$), as well as the shift between the Fermi distribution and the HFBCS model $\Delta b_{\text{fm}}^{\text{hf}} \equiv (b_{\text{fm}}^{\text{hf}} - b_{\text{hf}}^{\text{hf}})/b_{\text{fm}}^{\text{hf}}$.

One can see that the quadrupole shifts for the muonic ion are of the order of 50% for the $p_{3/2}$ states, 5 – 10% for the $d_{3/2}$ states and 5% for the $d_{5/2}$ states. This can be compared to the value of the magnetic hyperfine corrections in Figs. 8.10 and 8.12 for the same states in muonic ions, which are around 1 – 2%. In terms of energy, for example, the quadrupole contribution to the hyperfine splitting of the $2p_{3/2}$ state for the $F = 4$ to $F = 3$ transition in the $^{163}\text{Dy}^{65+}(\mu^-)$ ion can be calculated similarly to the electronic ion to be around 100 keV, while the dipole contribution is around 100 eV. Those values are fairly consistent with the literature [161]. This means that the main contribution to the hyperfine splitting of the $2p_{3/2}$ state for the muonic ion is by far the quadrupole interaction, and therefore the quadrupole hyperfine shift is reasonably measurable for the muonic ion, as it would be a shift of energy of tens of keV. A relative difference of around 4% is consistently observed between the B of the two isotopes. This is to be expected, as the relative difference between the two nuclear quadrupole moments is of the same order, see 6.1. The hyperfine anomaly allows to eliminate this dependence on the nuclear quadrupole moment, and therefore the quadrupole hyperfine anomaly is a more relevant quantity to compare the quadrupole hyperfine constants of two isotopes.

Therefore, in the same way as for the magnetic hyperfine anomaly, the quadrupole hyperfine anomaly are calculated and shown in Fig. 8.15 for the electronic and muonic ions.

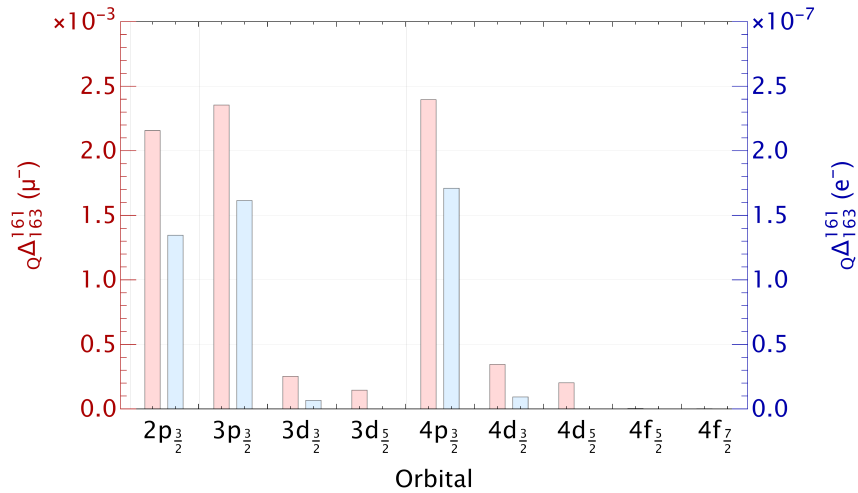


Figure 8.15: Quadrupole hyperfine anomaly between ^{161}Dy and ^{163}Dy is depicted for muon (in red and reading on the left axis) and electron (in blue and reading on the right axis) for the orbitals from $2p_{3/2}$ to $4f_{7/2}$.

Anomalies can be measured entirely experimentally and do not require a comparison with a theoretical calculation, since it is a direct measurement of two different isotopes. Therefore, our calculations predict that the quadrupole hyperfine anomaly is of the order of $10^{-7} - 10^{-8}$ for the electronic ion and $10^{-3} - 10^{-4}$ for the muonic ion, which, coupled to the much higher quadrupole hyperfine interaction amplitude for the muonic ion, reinforces the observation that the quadrupole hyperfine anomaly is reasonably measurable for the muonic ion and not for the electronic ion.

The same trend analysis as for the magnetic hyperfine anomaly can be applied, and the values of the anomaly as a function of the principal quantum number n of the state for the $p_{3/2}$ and $d_{5/2}$ states are plotted in Fig. 8.16.

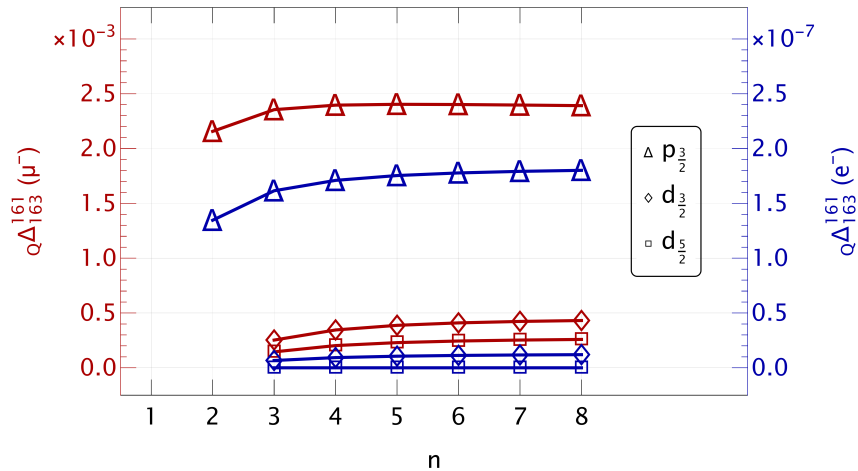


Figure 8.16: Quadrupole hyperfine anomaly between ^{161}Dy and ^{163}Dy is depicted for muon (in red and reading on the left axis) and electron (in blue and reading on the right axis) for the orbitals $2p_{3/2}$ and $d_{5/2}$.

The quadrupole hyperfine anomaly is fairly constant with the quantum number n of the state, with the exception of the $2p_{3/2}$ state, where the anomaly is slightly lower, which is fairly similar to the trend observed for the magnetic hyperfine anomaly. Contrary to the magnetic hyperfine anomaly, the quadrupole hyperfine anomaly behaves fairly similarly for the electronic and muonic ions, except for the 4 orders of magnitude difference.

8.4 Additional examples of $^{159}\text{Tb}^{64+}$ and $^{165}\text{Ho}^{66+}$

8.4.1 Nuclear charge and current densities

In this subsection, we present the results of the HFBCS calculations for the nuclear charge and current densities of the isotopes ^{159}Tb and ^{165}Ho . These isotopes are two of the candidates considered by our group for nuclear qubits in lanthanide-based materials, with Terbium Bisphthalocyanine being the most extensively studied chemical system by our team. Dysprosium proved useful in providing insights into the hyperfine anomaly and its corrections, as we were able to disregard the electronic degrees of freedom. This is because we expected them to cancel out in the calculated ratios, given that the electron cloud remains the same between isotopes.

However, Terbium and Holmium, which we focus on here, each have only one naturally abundant stable isotope. As a result, any study of their hyperfine structure must account for the electronic degrees of freedom. Fortunately, ^{165}Ho , in its simplest electronic configuration, H -like Ho^{66+} , has been investigated in the context of the hyperfine structure of the $1s_{1/2}$ state [162]. This allows us to perform a preliminary benchmarking of our model against available experimental data.

The nucleon densities for the isotopes ^{159}Tb and ^{165}Ho are shown in Fig. 8.17.

It is interesting to compare elements with different numbers of protons, including the two Dy isotopes in Fig. 6.3. The nuclear charge density spatial expansion increases with R_N and therefore with Z which is expected. There is a variation in the shapes of the nuclei, in particular their prolate deformations. Their inner structures are also different, with ^{159}Tb 's inner composition that is more similar to the ones of ^{161}Dy and ^{163}Dy , even if the first is an nucleus with an odd number of protons and the latter are even. The internal composition of ^{165}Ho is the most different from the other elements, with a more pronounced prolate deformation as can be seen in the values of the quadrupole moments in Tab. 8.8 and Tab. 6.1.

	$R_{\text{rms}}^{(\text{cal})}$	$R_{\text{rms}}^{(\text{exp})}$ [148]	$R_{\text{rms}}^{(\text{emp})}$	$Q_0^{(2,\text{spec},\text{cal})}$	$Q_0^{(2,\text{spec},\text{exp})}$ [145]
^{159}Tb	5.19	5.06	5.099	1.45	1.43
^{165}Ho	5.25	5.21	5.16	3.60	3.58

Table 8.8: Comparison with the experimental data of charge rms radii (in fm^2) and spectroscopic charge quadrupole moments (in ebarn) for ^{159}Tb and ^{165}Ho . $\langle R^2 \rangle_{\text{emp}} \equiv (0.836A^{1/3} + 0.57)$ [149].

Moreover Tab. 8.8 shows the comparison of the calculated charge rms radii and the spectroscopic charge quadrupole moments with the experimental data. The calculated values are again in good agreement with the experimental data.

Finally, one can observe the compared radial spherically averaged charge densities of the isotopes ^{161}Dy , ^{163}Dy and ^{165}Ho , relative to ^{159}Tb , in Fig. 8.18, they are shown Z -normalized and rescaled to be expressed in units of the respective nuclear radii eR_N^{-3} . One can observe that adding 2 nucleons has for effect to seemingly concentrate the charges near the surface. Since R_N increases with A , the charge distributions are also more spread out for the heavier isotopes, as expected.

The current densities are shown in Fig. 8.19 for the protons and Fig. 8.20 for the neutrons. The current distributions present the most variety across the isotopes, for the protons they can be compared with

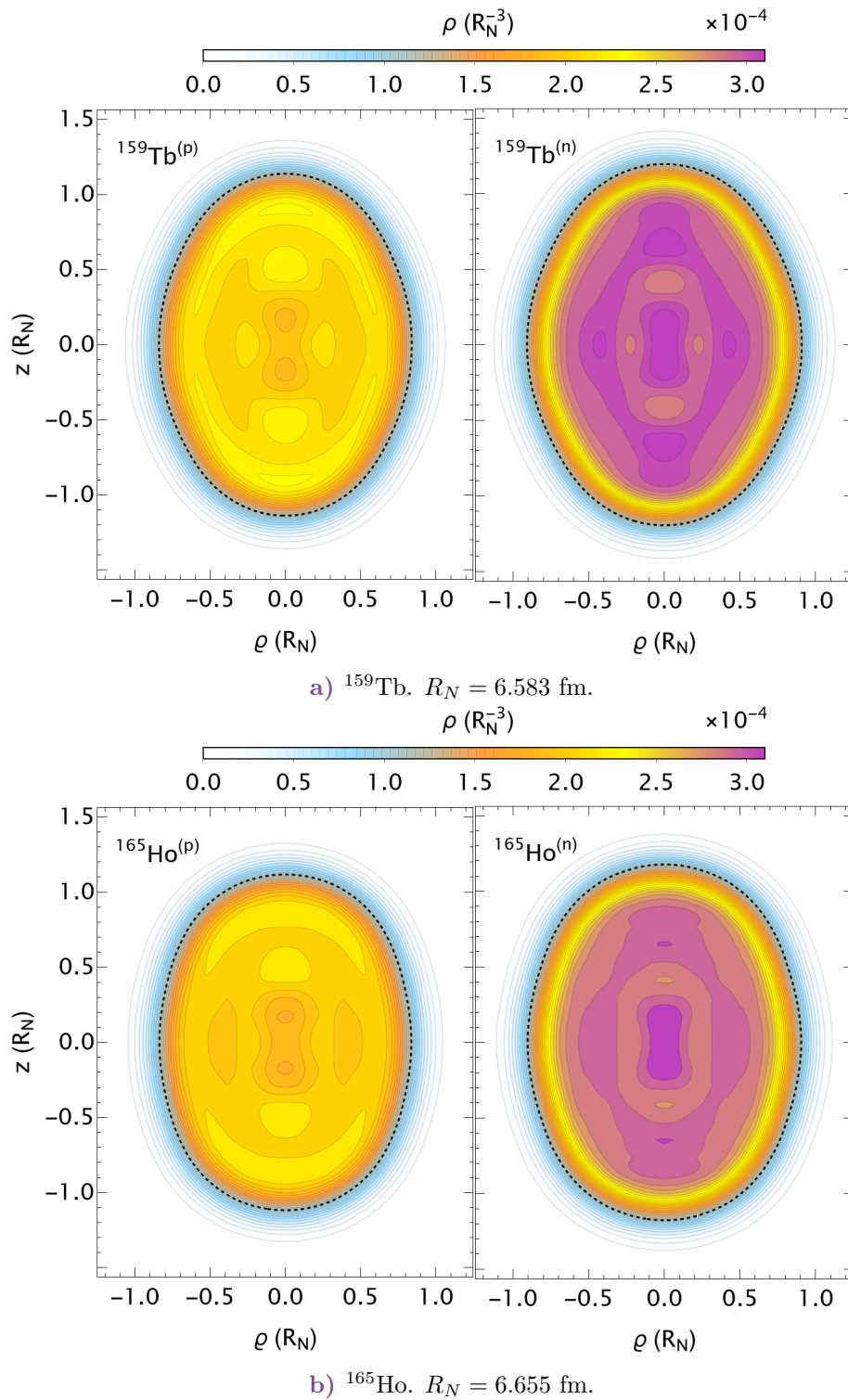


Figure 8.17: Nucleon densities distributions of ^{159}Tb and ^{165}Ho with logarithmically spaces contour curves. (p) and (n) stand for proton and neutron, respectively. The figures are plotted in cylindrical coordinates (z, ρ) on a planer slice throught the z -axis. The spacial coordinates are in units of R_N the empirical nuclear radius (see text) for each isotope, leading to a density distribution in units of eR_N^{-3} . The contours represent curves of equivalent density, with numerical values as indicated by the legend above. The dashed curve indicates the contour line of the FWHM of the isotope's proton density, representing the outer shell of the nucleus.

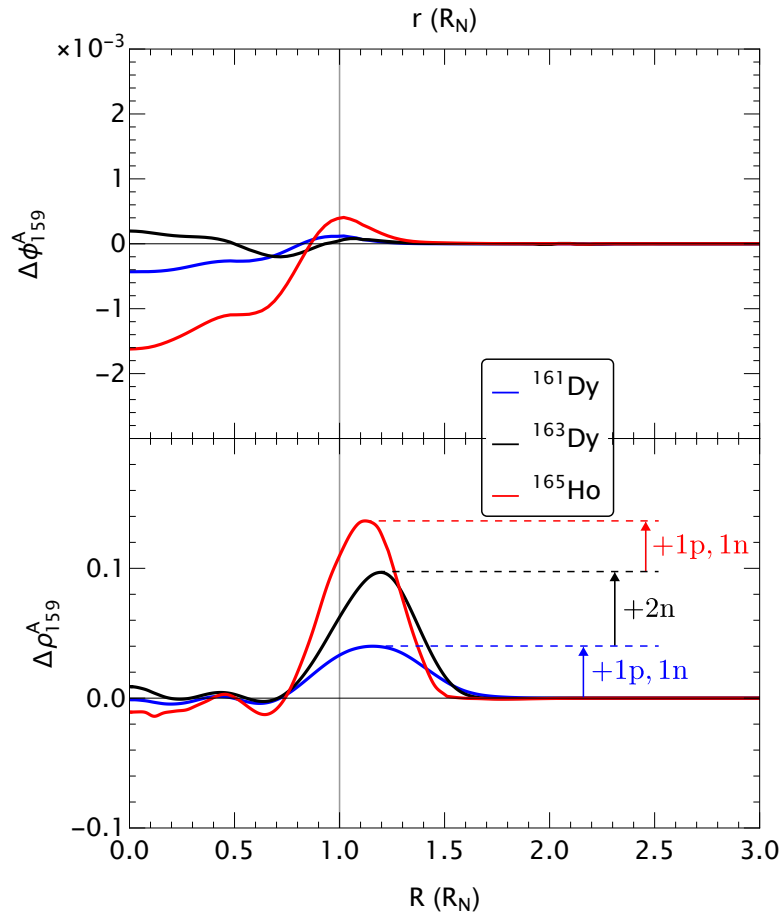


Figure 8.18: (lower panel) Radial spherically averaged charge densities of ^{161}Dy , ^{163}Dy and ^{165}Ho relative to ^{159}Tb . The densities are Z -normalized and rescaled to be expressed in units depending of the respective nuclear radii R_N of the isotope. The radial coordinate is in units of R_N and the charge distribution is in units of Z/R_N^3 . (top panel) The same relative difference in potentials stemming from the charge distributions, in units of k_e/R_N . $k_e \equiv \frac{e}{4\pi\epsilon_0}$ is the Coulomb constant.

the proton current distributions for the Dy isotopes in Fig. 6.7 and Fig. 6.8 for the neutrons. We note the node-current-loop structural pattern of the neutrons mostly matches that of the protons for each isotope. However, the proton contributions exhibit a higher amplitude than the neutron contributions. Referring to our discussion regarding Dysprosium, we observe that, since in this case, both isotopes are odd-even, in the single-particle model, they have an unpaired proton, which now polarizes the core neutrons. This represents the reverse situation compared to Dysprosium, where an unpaired neutron was seemingly polarizing the core protons. The ^{159}Tb nucleus shows the current distributions with the larger spread and inner penetration, while the other isotopes seem to have currents that are more concentrated on the surface of the nucleus. The Dysprosium isotopes seem to present the largest current localised intensities, in particular for the neutrons.

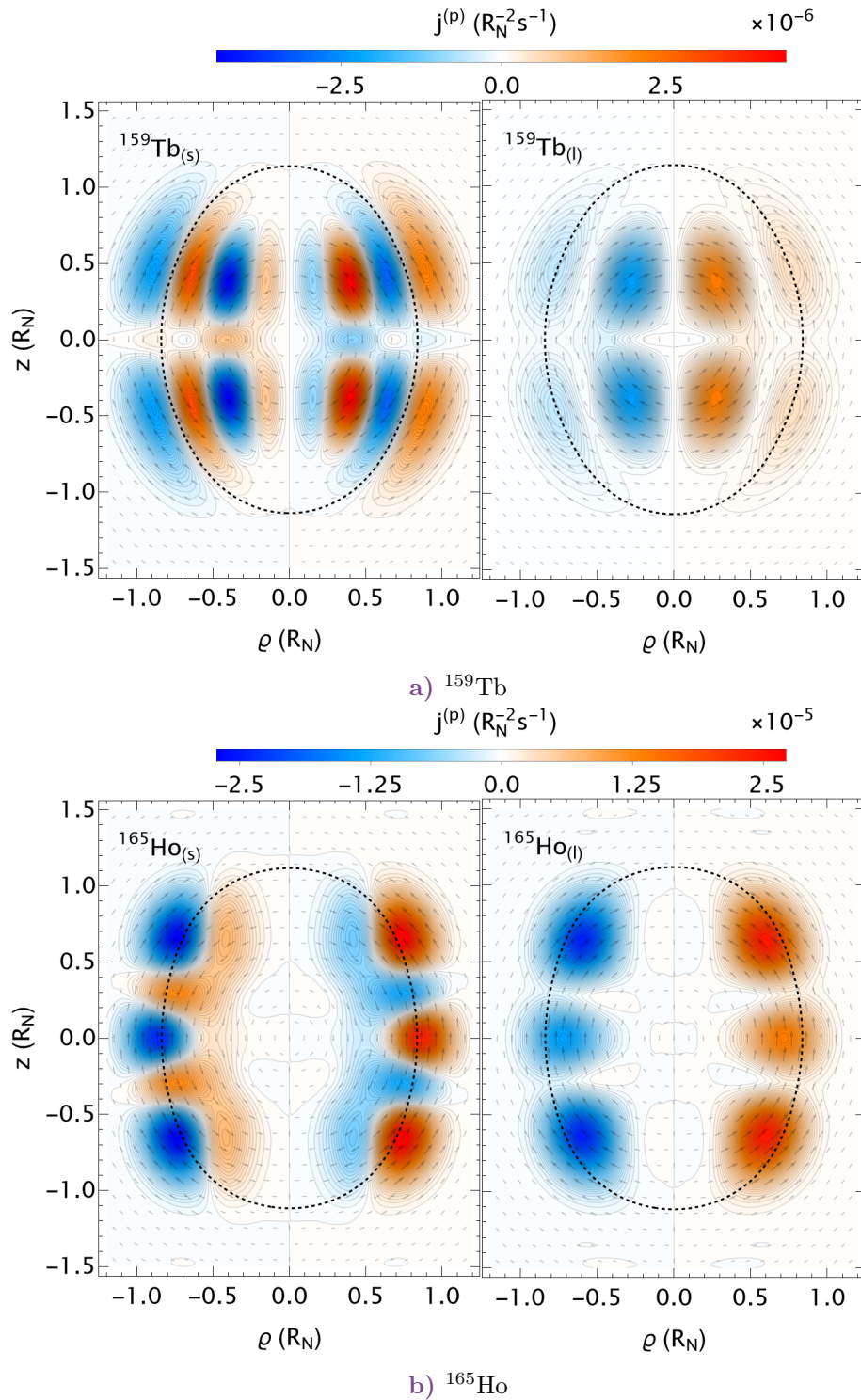


Figure 8.19: Proton current distributions, $\vec{j}^{(p)}(\vec{R})$ (upper : spin contributions, lower: orbital contributions), of ^{159}Tb and ^{165}Ho with associated magnetic dipole moments $\vec{R} \wedge \frac{1}{2} \left(\vec{j}^{(p)}(\vec{R}) \right)$ indicated by the arrow vectors. The figures are plotted in cylindrical coordinates (z, ρ) , on a planar slice through the z -axis. The contours represent curves of equivalent density, with numerical values as indicated by the legend. The dashed curve indicates the contour line of the FWHM of the isotope's proton density, representing the outer shell of the nucleus. The spatial coordinates are in units of R_N , the empirical nuclear radius, leading to a current distribution in units of $R_N^{-2} \cdot \text{s}^{-1}$.

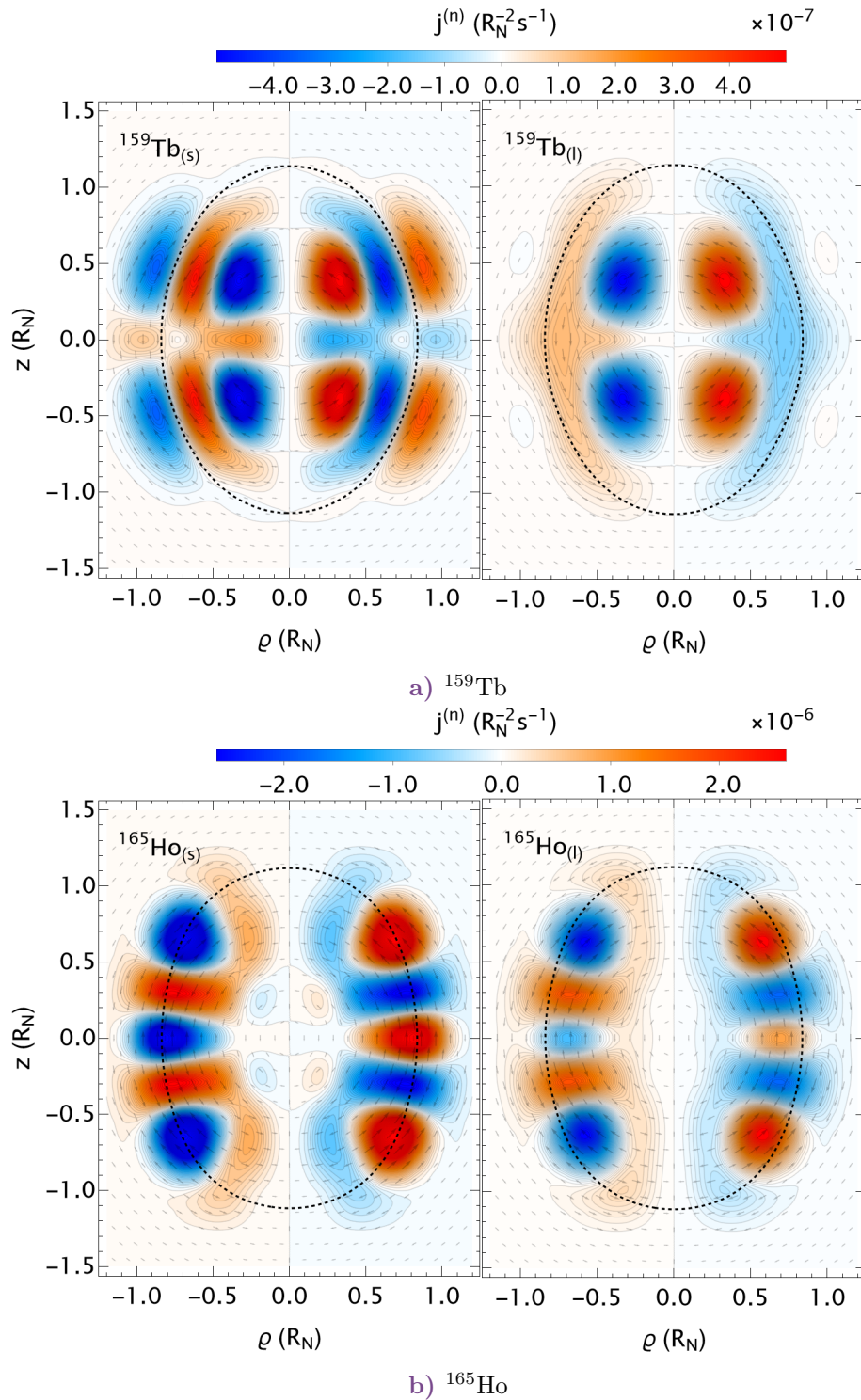


Figure 8.20: Neutron current distributions, $\vec{j}^{(n)}(\vec{R})$ (upper : spin contributions, lower: orbital contributions), of ^{159}Tb and ^{165}Ho with associated magnetic dipole moments $\vec{R} \wedge \frac{1}{2} \left(\vec{j}^{(n)}(\vec{R}) \right)$ indicated by the arrow vectors. The figures are plotted in cylindrical coordinates (z, ρ) , on a planar slice through the z -axis. The contours represent curves of equivalent density, with numerical values as indicated by the legend. The dashed curve indicates the contour line of the FWHM of the isotope's proton density, representing the outer shell of the nucleus. The spatial coordinates are in units of R_N , the empirical nuclear radius, leading to a current distribution in units of $R_N^{-2} \cdot s^{-1}$.

8.4.2 Hyperfine constants

The hyperfine constants for some electronic and muonic orbitals of $^{159}\text{Tb}^{64+}$ and $^{165}\text{Ho}^{66+}$ have been computed using (7.24) and (7.31), and are shown in Tab. 8.9.

$n\ell_j$	$a_{\text{np}}(^{159}\text{Tb}^{65+})$	$a_{\text{wp}}(^{159}\text{Tb}^{65+})$	$a_{\text{np}}(^{165}\text{Ho}^{65+})$	$a_{\text{wp}}(^{165}\text{Ho}^{65+})$
$1s_{1/2}$	520.6450	515.4131	523.8773	517.9916
$2s_{1/2}$	75.8488	75.0460	77.1217	76.2066
$2p_{1/2}$	25.1710	25.1298	25.6203	25.5699
$2p_{3/2}$	3.2432	3.2432	3.1953	3.1953
$3s_{1/2}$	22.4880	22.2477	22.8652	22.5912
$3p_{1/2}$	7.6400	7.6255	7.7891	7.7713
$3p_{3/2}$	0.9922	0.9922	0.9795	0.9795
$3d_{3/2}$	0.5912	0.5912	0.5834	0.5834
$3d_{5/2}$	0.2374	0.2374	0.2333	0.2333
$4s_{1/2}$	9.3997	9.2989	9.5509	9.4361
$4p_{1/2}$	3.2186	3.2122	3.2809	3.2730
$4p_{3/2}$	0.4215	0.4215	0.4163	0.4163
$4d_{3/2}$	0.2519	0.2519	0.2488	0.2488
$4d_{5/2}$	0.1014	0.1014	0.0997	0.0997
$4f_{5/2}$	0.0722	0.0722	0.0710	0.0710
$4f_{7/2}$	0.0392	0.0392	0.0385	0.0385

Table 8.9: Hyperfine anomalies in meV for $n\ell_j$ states of $^{159}\text{Tb}^{65+}$ and $^{165}\text{Ho}^{65+}$ ions. a_{np} and a_{wp} denote the hyperfine anomalies calculated without accounting for the penetration inside the nucleus and with the penetration inside the nucleus, respectively. The wavefunctions used for the calculation are the ones obtained with the HFBC nuclear model.

Interestingly, the $F = 4$ to $F = 3$ transition in the $1s_{1/2}$ orbital of $^{165}\text{Ho}^{66+}$ has been experimentally observed and measured [162] at $\Delta E_{\text{exp}} = 2.1651(6)$ eV. According to (7.27), the splitting should be equal to $\Delta E = a_{\text{wp}}F$. Naively, our calculation would yield a splitting of $\Delta E = 2.0720$ eV, which is 4.3% lower than the experimental value. One can account for the radiative correction to the hyperfine splitting, which is computed in [138] to be -0.0104 eV, which would bring our calculated value to $\Delta E = 2.0616$ eV, and therefore even further from the experimental value.

However, if one were to look at the obtained total magnetic dipoles for the isotopes shown in Tab. 8.10, one can see that the calculated values still have some discrepancies with the experimental values. The magnetic dipole moment of ^{159}Tb is underestimated by 6.3%, while the one of ^{165}Ho is underestimated by 6.5%.

	$\langle\mu_z\rangle$	$\mu^{(\text{spec})}$	$\mu^{(\text{exp})}$ [145]
^{159}Tb	3.145	1.887	2.014
^{165}Ho	5.071	3.944	4.17

Table 8.10: Comparison of the calculated and experimental magnetic dipole moments (in μ_N) for ^{159}Tb and ^{165}Ho .

Interestingly, rescaling the hyperfine constant of the $1s_{1/2}$ orbital of $^{165}\text{Ho}^{66+}$ by the ratio of the experimental and calculated magnetic dipole moments, one obtains a splitting of $\Delta E = 2.1635$ eV, which is only 0.1% lower than the experimental value, and the radiative correction would bring the calculated value to $\Delta E = 2.1531$ eV, which is still 0.5% lower than the experimental value. This is summarized in the following Tab. 8.11.

Point-like	HBCS without penetration	HBCS with penetration	QED corr. [138]	Exp. [162]
2.1967	2.0955	2.0720	-0.0104	2.1651(6)
After rescaling				
2.2941	2.1883	2.1633	-0.0104	
Breit-Rosenthal	Bohr-Weisskopf			
4.6081%	1.1235%			
0.1012	0.0235			

Table 8.11: Table of the calculated and experimental $F = 4 \rightarrow F = 3$ hyperfine splitting of the $1s_{1/2}$ orbital of $^{165}\text{Ho}^{66+}$. The values are in eV. The Breit-Rosenthal and Bohr-Weisskopf corrections (in %) are also shown, as well as their corresponding energy shifts.

We note that the percentage we obtained for the Bohr-Weisskopf correction is sensibly the same as the one obtained in [138], which is 1.125%.

To enhance the predictive accuracy of our model, it is important to emphasize that the QED corrections have not been computed using our specific model or wavefunctions but are instead assumed to be identical to those reported by [138]. Furthermore, one could consider the effect of a R_{rms} rescaling of the currents to have the value be equal to the experimentally obtained one, in a manner consistent with the approach applied to the magnetic dipole moment. Although the preliminary results are promising, there remains scope for refinement, and further investigation is warranted to improve the model.

Main takeaways from Chapter 8

- **Electron and Muon as Nuclear Probes:**

- Solving the Dirac equation for electrons and muons in the presence of a nucleus allows for calculating energy levels and assessing nuclear models.
- The differences in wavefunctions between electrons and muons highlight the increased nuclear penetration of muons.
- Comparing experimental spectra with model-dependent theoretical calculations can help discriminate between nuclear models.

- **Energy Levels in Hydrogen-like Ions:**

- Finite nuclear size leads to shifts in energy levels, more pronounced for muonic ions due to greater nuclear penetration.
- Monopolar energy shifts are significant for $s_{1/2}$ and $p_{1/2}$ states, especially in muonic ions.

- **Hyperfine Structure and Isotope Shifts:**

- Hyperfine anomalies arise from deviations in hyperfine constants between isotopes.
- Breit-Rosenthal and Bohr-Weisskopf corrections are significant for muonic ions and must be considered.
- Quadrupole shifts are more significant in muonic ions, making them suitable for studying quadrupole hyperfine anomalies.
- The anomalies can provide insights into nuclear charge distributions.

- **Nuclear Models and Current Densities:**

- HFBCS nuclear models provide detailed charge and current densities for isotopes like ^{159}Tb and ^{165}Ho .
- These models help in understanding nuclear deformation across lanthanides and the effects of a change of the number of nucleons on hyperfine interactions.

- **Comparison with Experimental Data:**

- Calculations for $^{165}\text{Ho}^{66+}$ show good agreement with experimental hyperfine splittings after considering corrections.
- Rescaling theoretical values using experimental magnetic moments improves accuracy.

Conclusion

In this work, we have presented a theoretical model for the calculation of hyperfine constants in highly charged ions. The model is based on the HFBCS method, that we combine with a numerical solver for the Dirac equation in order to compute different energetical shifts due to the finite size of the nucleus. We have shown it is possible to compute the Bohr-Rosenthal and Bohr-Weisskopf corrections to the magnetic hyperfine constant, allowing to obtain the hyperfine anomaly between different isotopes of dysprosium in a fully *ab-initio* manner. We have also shown that the quadrupole hyperfine anomaly can be calculated in the same way, and that it is reasonably measurable for muonic ions. The latter have been shown to be particularly useful in probing the internal structure of the nucleus and, coupled with our methodology, could allow us to benchmark different nuclear models.

Moreover, we have shown that the magnetic dipole moments of $^{165}\text{Ho}^{66+}$ can be computed quite accurately, in particular considering our approach doesn't require any fitting parameters. However, the accuracy can be further improved by allowing for such parameters to fit the experimental values of easily obtainable quantities whose calculated values in our model are not in perfect agreement with the experimental values.

This methodology has still room for improvement, in particular on the atomic side, it doesn't include the radiative corrections originating from QED, while on the nuclear side, we don't account for nuclear excitation effects. The latter could prove particularly important via the configuration mixing they induce, and could help reduce the discrepancies between the calculated and experimental values.

The model presented in this work is a first step towards a fully *ab-initio* model for the computation of hyperfine constants in highly charged ions, and could be further improved on the nuclear side to include more effects and be more accurate, like for example Higher Tamm-Dancoff Approximation (HTDA) on top of the HFBCS calculation [163]. Moreover, coupled to atomic structure calculations, especially the ones introduced in I, it could be generalized to multi-electronic systems, and could be used to compute hyperfine constants in complex systems such as atoms and molecules.

This part of the work has provided a solid insight in the nuclear effects and internal structures, that transpires through the hyperfine anomaly via the nucleus' interaction with the electrons and muons.

References of this part

- [38] De Groote, R. P.; Neyens, G. In *Handbook of Nuclear Physics*, Tanihata, I., Toki, H., Kajino, T., Eds.; Springer Nature: Singapore, 2020, pp 1–36.
- [39] Skyrme, T. “The effective nuclear potential”, *Nuclear Physics*, 1958, *9*:4, 615–634.
- [40] Vautherin, D.; Brink, D. M. “Hartree-Fock Calculations with Skyrme’s Interaction. I. Spherical Nuclei”, *Physical Review C*, 1972, *5*:3, 626–647.
- [43] Hartree-Fock-Bogoliubov results based on the Gogny force https://www-phynu.cea.fr/science_en_ligne/carte_potentiels_microscopiques/carte_potentiel_nucleaire_eng.htm (accessed 08/15/2024).
- [46] Dirac, P. A. M. “The quantum theory of the electron”, *Proceedings of the Royal Society of London. Series A, Containing Papers of a Mathematical and Physical Character*, 1928, *117*:778, 610–624.
- [131] Lämmerzahl, C. “The pseudodifferential operator square root of the Klein–Gordon equation”, *Journal of Mathematical Physics*, 1993, *34*:9, 3918–3932.
- [132] Anderson, C. D. “The Apparent Existence of Easily Deflectable Positives”, *Science*, 1932, *76*:1967, 238–239.
- [133] Gerlach, W.; Stern, O. “Der experimentelle Nachweis der Richtungsquantelung im Magnetfeld”, *Zeitschrift für Physik*, 1922, *9*:1, 349–352.
- [134] Strange, P., *Relativistic Quantum Mechanics: With Applications in Condensed Matter and Atomic Physics*; Cambridge University Press: Cambridge, 1998.
- [135] Johnson, W. R., *Atomic Structure Theory*; Springer: Berlin, Heidelberg, 2007.
- [136] Michelson, A. A.; Morley, E. W. “On a method of making the wavelength of sodium light the actual and practical standard of length”, *American Journal of Science*, 1887, *s3-34*:204, 427–430.
- [137] Bullis, R. G.; Rasor, C.; Tavis, W. L.; Johnson, S. A.; Weiss, M. R.; Yost, D. C. “Ramsey Spectroscopy of the $2S_{1/2}$ Hyperfine Interval in Atomic Hydrogen”, *Physical Review Letters*, 2023, *130*:20, 203001.
- [138] Boucard, S. Calcul de haute precision d’énergies de transitions dans les atomes exotiques et les lithiumoides : corrections relativistes, corrections radiatives, structure hyperfine et interaction avec le cortège électronique résiduel, These de doctorat, Paris 6, 1998.
- [139] Hinschberger, Y.; Dixit, A.; Manfredi, G.; Hervieux, P.-A. “Equivalence between the semirelativistic limit of the Dirac-Maxwell equations and the Breit-Pauli model in the mean-field approximation”, *Physical Review A*, 2015, *91*:1, 012101.
- [140] Borie, E.; Rinker, G. A. “The energy levels of muonic atoms”, *Reviews of Modern Physics*, 1982, *54*:1, 67–118.
- [141] Shabaev, V. In *Large Coulomb Systems: Lecture Notes on Mathematical Aspects of QED*, Dereziński, J., Siedentop, H., Eds.; Springer: Berlin, Heidelberg, 2006, pp 275–295.
- [142] Damgaard, J.; Pauli, H.; Pashkevich, V.; Strutinsky, V. “A method for solving the independent-particle Schrödinger equation with a deformed average field”, *Nuclear Physics A*, 1969, *135*:2, 432–444.

- [143] Vautherin, D. “Hartree-Fock Calculations with Skyrme’s Interaction. II. Axially Deformed Nuclei”, *Physical Review C*, 1973, 7:1, 296–316.
- [144] Flocard, H.; Quentin, P.; Kerman, A.; Vautherin, D. “Nuclear deformation energy curves with the constrained Hartree-Fock method”, *Nuclear Physics A*, 1973, 203:3, 433–472.
- [145] Stone, N. J. “Table of nuclear magnetic dipole and electric quadrupole moments”, *Atomic Data and Nuclear Data Tables*, 2005, 90:1, 75–176.
- [146] Bohr, A.; Mottelson, B. R., *Nuclear Structure*; World Scientific: 1998; 500 pp.
- [147] Rowe, D. J., *Nuclear Collective Motion: Models and Theory*; WORLD SCIENTIFIC: 2010.
- [148] *Numerical data and functional relationships in science and technology. Bd. 20: Gruppe 1: Kern- und Teilchenphysik = Group 1: @Nuclear and particle physics Nuclear charge radii / ed.: H. Schopper. Authors: G. Fricke; Fricke, G., Schopper, H., Eds.; Springer: Berlin Heidelberg, 2004; Vol. 20, 385 pp.*
- [149] Pálffy, A. “Nuclear effects in atomic transitions”, *Contemporary Physics*, 2010, 51:6, 471–496.
- [150] Negele, J. W. “The mean-field theory of nuclear structure and dynamics”, *Reviews of Modern Physics*, 1982, 54:4, 913–1015.
- [151] Bonneau, L.; Minkov, N.; Duc, D. D.; Quentin, P.; Bartel, J. “Effect of core polarization on magnetic dipole moments in deformed odd-mass nuclei”, *Physical Review C*, 2015, 91:5, 054307.
- [152] Schwartz, C. “Theory of Hyperfine Structure”, *Physical Review*, 1955, 97:2, 380–395.
- [153] Bouchiat, M. A.; Bouchiat, C. “I. Parity violation induced by weak neutral currents in atomic physics”, *Journal de Physique*, 1974, 35:12, 899–927.
- [154] Büttgenbach, S. “Magnetic hyperfine anomalies”, *Hyperfine Interactions*, 1984, 20:1, 1–64.
- [155] Persson, J. R. “Table of hyperfine anomaly in atomic systems — 2023”, *Atomic Data and Nuclear Data Tables*, 2023, 154, 101589.
- [156] Hinschberger, Y. Etude théorique des effets relativistes induits par une impulsion lumineuse ultra-rapide dans la matière, These de doctorat, Strasbourg, 2012.
- [157] Hinschberger, Y.; Hervieux, P.-A. “Foldy–Wouthuysen transformation applied to the interaction of an electron with ultrafast electromagnetic fields”, *Physics Letters A*, 2012, 376:6, 813–819.
- [158] Pritchard, J. R.; Loeb, A. “21 cm cosmology in the 21st century”, *Reports on Progress in Physics*, 2012, 75:8, 086901.
- [159] Hellwig, H.; Vessot, R. F. C.; Levine, M. W.; Zitzewitz, P. W.; Allan, D. W.; Glaze, D. J. “Measurement of the Unperturbed Hydrogen Hyperfine Transition Frequency”, *IEEE Transactions on Instrumentation and Measurement*, 1970, 19:4, 200–209.
- [160] Pointillart, F.; Bernot, K.; Guennic, B. L.; Cador, O. “Isotopic enrichment in lanthanide coordination complexes: contribution to single-molecule magnets and spin qudit insights”, *Chemical Communications*, 2023, 59:55, 8520–8531.
- [161] Persson, J. “Muonic Hyperfine Structure and the Bohr-Weisskopf Effect”, 2023.
- [162] Crespo López-Urrutia, J. R.; Beiersdorfer, P.; Savin, D. W.; Widmann, K. “Direct Observation of the Spontaneous Emission of the Hyperfine Transition $F = 4$ to $F = 3$ in Ground State Hydrogenlike $\text{H } 165 \text{ o } 6 \text{ 6}^+$ in an Electron Beam Ion Trap”, *Physical Review Letters*, 1996, 77:5, 826–829.
- [163] Bonneau, L.; Quentin, P.; Sieja, K. “Ground-state properties of even-even $N=Z$ nuclei within the Hartree-Fock-BCS and higher Tamm–Dancoff approaches”, *Physical Review C*, 2007, 76:1, 014304.

PART III

Quantum Computing with Nuclear Spins in Lanthanides

9	From bits to qubits to qudits	179
9.1	What is a qubit?	179
9.2	Quantum gates	182
9.3	Quantum algorithms	184
9.4	What is a qudit?	189
9.5	Timescales	190
10	Markovian open quantum systems	195
10.1	The Lindblad equation	195
10.2	Alternative way to model errors: Kraus operators	196
10.3	Link with T_1 and T_2 timescales	197
10.4	Issues in solving the Lindblad equation numerically	198
11	Noisy qudits vs. qubits: First-order approach	201
11.1	The AGI: Definition and First-Order Approximation	201
11.2	Numerical validation and deviation	207
11.3	Linear and exp. scalings from the perspective of the AGI	215
12	Noisy qudit: Beyond the first-order approach	221
12.1	The Lindblad equation as a superoperator	221
12.2	Perturbative expression of the AGI	224
12.3	Universal bounds on the AGI for large noise and gate times	231
13	Optimal gate generation	237
13.1	Rotating Wave Approximation and Rotating Frame	237
13.2	Quantum Speed Limits	243
13.3	An overview of gate generation methods	251
13.4	Towards optimal qudit gates	258

Quantum Computing with Nuclear Spins in Lanthanides

"Nature isn't classical, dammit, and if you want to make a simulation of nature, you'd better make it quantum mechanical, and by golly it's a wonderful problem, because it doesn't look so easy."

— **Richard Feynman**

This section builds upon the foundational concepts of quantum mechanics, and the tools from linear algebra used to describe quantum states, to introduce the principles of quantum computing. A review of these mathematical tools is provided in [Appendix A](#). Initially, the section covers the core principles of quantum computing, such as qubits, quantum gates, and quantum algorithms, before expanding to d -dimensional quantum systems, known as qudits, and their potential applications. This exploration aims to enhance understanding of the mathematical behavior of the computational space underlying lanthanide-based nuclear qudits, which are central to this work.

Since the Hilbert space of multiple qubits and qudits is mathematically equivalent when their dimensions match, we will explore the origins of their differences, focusing on the noise channels affecting these systems. Specifically, we introduce the Lindblad master equation as a general framework for describing the evolution of open quantum systems, along with the Kraus representation, which characterizes quantum channels that include these noise effects. Our analysis will emphasize how noise channels impact the coherence and computational fidelity of operations on d -dimensional quantum systems and how this differs from multi-qubit systems. We will examine how computational fidelity scales with increasing dimension, given that one of the project's long-term objectives is to leverage isotopologue degrees of freedom to increase the dimension d of qudits linearly, thereby expanding the computational space. Thus, it is crucial to understand how these noise channels influence the fidelity of quantum operations as the system's dimension grows.

Finally, we introduce the concepts of quantum optimal control and quantum speed limits as strategies for implementing quantum gates in the shortest possible time. This approach is vital for mitigating the detrimental effects of noise channels on computational fidelity, especially as higher-dimensional systems experience greater noise impacts. To ensure competitiveness with qubit platforms, faster gate implementations are necessary to offset the increased influence of noise in higher-dimensional qudit systems. By leveraging these strategies, we aim to enhance the computational capabilities of lanthanide-based nuclear qudits and enable the development of robust quantum algorithms for quantum computing applications.

Note: For the entirety of this part, we will use $\hbar = 1$ units, unless specified otherwise.

Chapter Contents

9.1	What is a qubit?	179
9.2	Quantum gates	182
9.3	Quantum algorithms	184
9.4	What is a qudit?	189
9.5	Timescales	190

CHAPTER 9

From bits to qubits to qudits

9.1 What is a qubit?

A **qubit**, or quantum bit, is the fundamental unit of quantum information. Unlike a classical bit, which can be either 0 or 1, a qubit can exist in a state that is a superposition of both 0 and 1. This property allows quantum systems to process information in ways that classical systems cannot.

9.1.1 State Representation

A qubit is mathematically represented by a vector in a two-dimensional Hilbert space. The canonical basis states of this space are denoted by $|0\rangle$ and $|1\rangle$, analogous to the classical bits 0 and 1. However, a qubit can exist in any superposition of these states:

$$|\psi\rangle = \alpha |0\rangle + \beta |1\rangle, \quad (9.1)$$

where α and β are complex numbers satisfying the normalization condition $|\alpha|^2 + |\beta|^2 = 1$.

9.1.2 Density matrix representation

The density matrix formalism (see [Appendix A.3](#)) proves useful in representing an ensemble of qubit realisations, providing an object that displays the ensemble's average dynamics, whether it is a multitude of physical qubits or a statistical ensemble of repeated single-qubit experiments/measurements, an element of the ensemble is simply called *realisation*. Given an operator A and ensemble of states $\{|\phi\rangle\}$ and a pure state $|\psi\rangle$, with ρ and σ their respective density matrices, we have

$$\mathbb{E} [\langle A \rangle_\phi] = \text{Tr}(A\rho) \quad \text{and} \quad \mathbb{E} [|\langle \psi | \phi \rangle|^2] = \langle \psi | \rho | \psi \rangle = \text{Tr}(\sigma\rho) \quad (9.2)$$

where $\mathbb{E} [\cdot]$ is the average over the realisations.

Therefore the density matrix of a qubit takes the form:

$$\rho = \begin{pmatrix} \rho_{00} & \rho_{01} \\ \rho_{10} & \rho_{11} \end{pmatrix}, \quad (9.3)$$

where $\rho_{00} + \rho_{11} = 1$ and $\rho_{01} = \rho_{10}^*$, also, by construction, the density matrix for the pure state $\alpha |0\rangle + \beta |1\rangle$ is such that $\rho_{00} = |\alpha|^2$, $\rho_{11} = |\beta|^2$ and $\rho_{01} = \alpha^* \beta$.

9.1.3 Bloch Sphere Representation

The state of a qubit can also be visualised on the Bloch sphere, where every point on the surface of a unit sphere represents a possible state of the qubit. The north and south poles of the sphere correspond to the states $|0\rangle$ and $|1\rangle$, respectively, while any other point on the sphere represents a superposition of these states. The Bloch sphere is a powerful tool for visualising the state space of a qubit and the effect of quantum gates, and quantum channels in general.

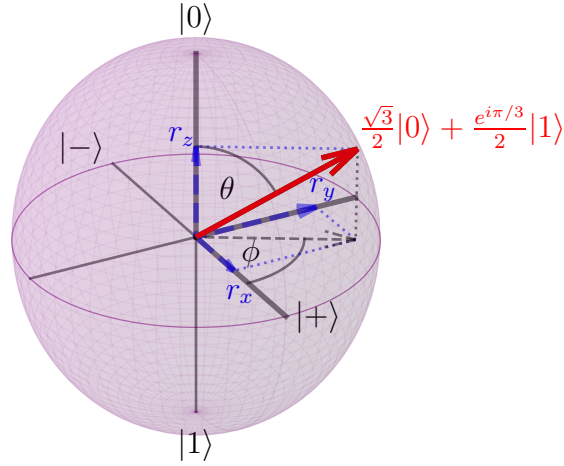


Figure 9.1: Example of a Bloch Sphere representation, for the state $\frac{\sqrt{3}}{2}|0\rangle + \frac{e^{i\pi/3}}{2}|1\rangle$ with $\theta = \phi = \pi/3$.

There are multiple ways of defining the mapping of a quantum state to the Bloch sphere.

1. **From ψ :** The quantum state $|\psi\rangle = \alpha|0\rangle + \beta|1\rangle$ can be mapped onto the Bloch sphere by expressing the state vector's coefficients in terms of spherical coordinates:

$$\alpha = \cos\left(\frac{\theta}{2}\right), \quad \beta = e^{i\phi} \sin\left(\frac{\theta}{2}\right), \quad (9.4)$$

where θ and ϕ are the polar and azimuthal angles, respectively. These angles uniquely determine the position on the Bloch sphere, with θ varying from 0 to π and ϕ from 0 to 2π .

2. **Thanks to σ_x , σ_y , and σ_z :** These Pauli matrices play a crucial role in mapping quantum states onto the Bloch sphere. They are defined as follows:

$$\sigma_x = \begin{pmatrix} 0 & 1 \\ 1 & 0 \end{pmatrix}, \quad \sigma_y = \begin{pmatrix} 0 & -i \\ i & 0 \end{pmatrix}, \quad \sigma_z = \begin{pmatrix} 1 & 0 \\ 0 & -1 \end{pmatrix}. \quad (9.5)$$

The expectation values of these matrices with respect to the state ρ determine the coordinates on the Bloch sphere, thus providing a comprehensive geometrical interpretation of the qubit's state. The components of the Bloch vector $\vec{r} = (r_x, r_y, r_z)$ are given by:

$$r_x = \text{Tr}(\rho\sigma_x) = \langle\psi|\sigma_x|\psi\rangle, \quad r_y = \text{Tr}(\rho\sigma_y) = \langle\psi|\sigma_y|\psi\rangle, \quad r_z = \text{Tr}(\rho\sigma_z) = \langle\psi|\sigma_z|\psi\rangle. \quad (9.6)$$

This vector fully characterises the state within the Bloch sphere.

3. **Link with ρ :** As consequence of the previous point, the density matrix of a state whose Bloch vector is $\vec{r} = (r_x, r_y, r_z)$ is

$$\rho = \frac{1}{2} (I + r_x\sigma_x + r_y\sigma_y + r_z\sigma_z) \quad (9.7)$$

Note: One can see that a pure state is necessarily on the surface of the Bloch sphere, while a density matrix can also represent states inside the Bloch ball, i.e. mixed states, see [Appendix A.3](#).

9.1.4 Entanglement

One of the most powerful features of qubits is their ability to become entangled with each other. Entanglement is a quantum phenomenon in which the states of two or more qubits become interdependent enough that the state of each qubit cannot be described independently of the state of the others. This property is the basis for many quantum algorithms and protocols, including quantum teleportation and quantum cryptography [164].

The phenomenon of interest related to quantum entanglement in this context is the exponential expansion of the Hilbert space. Analogous to how classical bits exist in one of two states —either 0 or 1— a qubit can be in a complex superposition, representing a combination of both $|0\rangle$ and $|1\rangle$. For a system of N classical bits, the total number of possible configurations is 2^N , and a system of N qubits can exist in a superposition encompassing all 2^N potential states simultaneously, illustrating the profound scaling advantage of quantum systems over classical systems, as shown in [Tab. 9.1](#).

Number of bits	Possible classical states	Possible quantum states
1	0 or 1	$\alpha 0\rangle + \beta 1\rangle$ $\forall \alpha, \beta \in \mathbb{C} \text{ s.t. } \alpha ^2 + \beta ^2 = 1$
2	00, 01, 10, 11	$\alpha_{00} 00\rangle + \alpha_{01} 01\rangle + \alpha_{10} 10\rangle + \alpha_{11} 11\rangle$ $\forall \alpha_{ij} \in \mathbb{C} \text{ s.t. } \sum_{ij} \alpha_{ij} ^2 = 1$
3	000, 001, 010, 011, 100, 101, 110, 111	$\sum_{ijk} \alpha_{ijk} ijk\rangle$ $\forall \alpha_{ijk} \in \mathbb{C} \text{ s.t. } \sum_{ijk} \alpha_{ijk} ^2 = 1$
\vdots		
N	one of 2^N states	$\sum_{i_1 i_2 \dots i_N} \alpha_{i_1 i_2 \dots i_N} i_1 i_2 \dots i_N\rangle$ $\forall \alpha_{i_1 i_2 \dots i_N} \in \mathbb{C} \text{ s.t. } \sum_{i_1 i_2 \dots i_N} \alpha_{i_1 i_2 \dots i_N} ^2 = 1$

Table 9.1: Comparison of classical and quantum states for different numbers of bits.

One can discriminate between separable and non-separable (or entangled) states. If a N -qubits state $|\psi_N\rangle$ can be represented as

$$|\psi_N\rangle = \bigotimes_{k=0}^{N-1} |\psi^{(k)}\rangle, \quad (9.8)$$

with $\psi^{(k)}$ being a pure state of qubit k , it is said to be **separable**. Any state that cannot be put in

this form is said to be **non-separable**.

Note: For example, $\frac{1}{2}(|000\rangle - |001\rangle + |100\rangle - |101\rangle) = \sqrt{\frac{1}{2}}(|0\rangle + |1\rangle) \otimes |0\rangle \otimes \sqrt{\frac{1}{2}}(|0\rangle - |1\rangle)$ is a separable state. While $\frac{1}{2}(|000\rangle + |001\rangle + |100\rangle - |101\rangle)$ is not.

A noteworthy example is the non-separable **GHZ state**:

Definition: (*GHZ state*)

$$|\text{GHZ}\rangle = \sqrt{\frac{1}{2}} \left(\bigotimes_{k=0}^{N-1} |0\rangle + \bigotimes_{k=0}^{N-1} |1\rangle \right), \quad (9.9)$$

the GHZ state is sometimes referred to as the maximally entangled state.

9.2 Quantum gates

Quantum gates are essential tools in quantum information processing, functioning as quantum analogues of classical logic gates. They perform operations on qubits and qudits, enabling the manipulation of quantum states, which is foundational for quantum computing and related technologies.

9.2.1 Characteristics of Quantum Gates

Quantum gates are represented by unitary operators, ensuring that all operations are reversible and preserve the normalisation of quantum states, as discussed in previous sections. These operators conform to the unitarity condition $UU^\dagger = U^\dagger U = I$, where I is the identity matrix.

Table 9.2 lists some common quantum gates and their matrix representations.

9.2.2 Types of Quantum Gates

Quantum gates can be broadly categorized based on their operation either on single qubits or on multiple qubits:

- **Single-Qubit Gates** These gates operate on individual qubits and include the already mentioned Pauli gates (X, Y, Z), and the Hadamard gate for example. These gates typically act as rotations on the Bloch sphere, transforming the state of a single qubit.
- **Multi-Qubit Gates** These gates operate across multiple qubits, creating entanglements and enabling more complex operations. The most notable among these is the Controlled NOT (CNOT) gate, which was previously discussed. Other examples include the SWAP gate, which exchanges the states of two qubits, and the Toffoli gate, an extension of the CNOT gate that operates on three qubits.

9.2.3 Implementing Quantum Gates

To implement a quantum gate, we apply the corresponding unitary matrix to the state vector or density matrix of the qubits. For example, if a quantum gate represented by the unitary operator U acts on a qubit initially in the state $|\psi\rangle$, the new state of the qubit is given by $U|\psi\rangle$. In terms of density matrices, the transformation is represented as $U\rho U^\dagger$, where ρ is the density matrix of the qubit state.

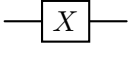
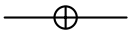
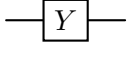
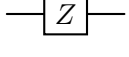
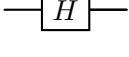
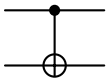
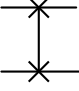
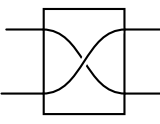
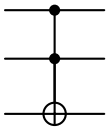
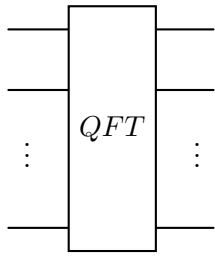
Gate	Circuit Symbol	Matrix Representation	Operation
Pauli-X	 or 	$\begin{pmatrix} 0 & 1 \\ 1 & 0 \end{pmatrix}$	Bit-flip
Pauli-Y		$\begin{pmatrix} 0 & -i \\ i & 0 \end{pmatrix}$	Bit and phase flip
Pauli-Z		$\begin{pmatrix} 1 & 0 \\ 0 & -1 \end{pmatrix}$	Phase flip
Hadamard		$\frac{1}{\sqrt{2}} \begin{pmatrix} 1 & 1 \\ 1 & -1 \end{pmatrix}$	Superposition
CNOT		$\begin{pmatrix} 1 & 0 & 0 & 0 \\ 0 & 1 & 0 & 0 \\ 0 & 0 & 0 & 1 \\ 0 & 0 & 1 & 0 \end{pmatrix}$	Entanglement of two qubits
SWAP	 or 	$\begin{pmatrix} 1 & 0 & 0 & 0 \\ 0 & 0 & 1 & 0 \\ 0 & 1 & 0 & 0 \\ 0 & 0 & 0 & 1 \end{pmatrix}$	Exchange of two qubits
Toffoli		$\begin{pmatrix} 1 & 0 & 0 & 0 & 0 & 0 & 0 & 0 \\ 0 & 1 & 0 & 0 & 0 & 0 & 0 & 0 \\ 0 & 0 & 1 & 0 & 0 & 0 & 0 & 0 \\ 0 & 0 & 0 & 1 & 0 & 0 & 0 & 0 \\ 0 & 0 & 0 & 0 & 1 & 0 & 0 & 0 \\ 0 & 0 & 0 & 0 & 0 & 1 & 0 & 0 \\ 0 & 0 & 0 & 0 & 0 & 0 & 0 & 1 \\ 0 & 0 & 0 & 0 & 0 & 0 & 1 & 0 \end{pmatrix}$	Controlled-controlled-NOT on three qubits
QFT		$(e^{2ijk\pi/2^N})_{j,k}$	N -qubits Quantum Fourier Transform

Table 9.2: Common quantum gates and their matrix representations.

A quantum gate U is only really the time-evolution operator of that qubit during a certain gate time T . If the gate starts acting on the qubit at time t_0 , we have:

$$U = \mathcal{T} \exp \left(-i \int_{t_0}^{t_0+T} H(\tau) d\tau \right), \quad (9.10)$$

at least up to a root-of-unity prefactor, a.k.a. a global phase, where H is the Hamiltonian acting on the system.

Note: Two quantum states $|\psi\rangle$ and $e^{i\phi}|\psi\rangle$, with $\phi \in \mathbb{R}$, are indistinguishable with respect to any physical measurement.

This is because an overall phase factor $e^{i\phi}$ does not affect the observable properties of a quantum state. When we compute measurable quantities such as expectation values or probabilities, the phase factor cancels out. The inner product, which relates to probabilities in quantum mechanics, remains unchanged:

$$\langle e^{i\phi}\psi | e^{i\phi}\psi \rangle = \langle \psi | e^{-i\phi} e^{i\phi} | \psi \rangle = \langle \psi | \psi \rangle.$$

Thus, global phases do not affect the outcomes of any physical experiment, meaning that $|\psi\rangle$ and $e^{i\phi}|\psi\rangle$ are physically indistinguishable.

For the same reason, the difference between two gates U and $e^{i\phi}U$ being to apply a global phase to the state, we can consider them indistinguishable too.

9.2.4 Physical Realisation

Implementing quantum gates in physical systems requires precise control over quantum interactions and the environment. Technologies such as superconducting qubits, trapped ions, and photonic systems are commonly used. Each technology offers different advantages and challenges, particularly in relation to gate fidelity, coherence times, and operational speeds.

Mathematically, a physical qubit realization is characterized by its Hamiltonian, more specifically, we generally assume it is composed of: H_0 the free evolution, or **drift Hamiltonian**, and $\{H_k\}_k$ an ensemble of **control Hamiltonian**, characterized by the selection rules inside the system, the total Hamiltonian that is plugged in (9.10), is then:

$$H(\tau) = H_0 + \sum_k u_k(\tau) H_k, \quad (9.11)$$

with $u_k(\tau)$ being the control amplitudes of the Hamiltonian H_k .

To physically apply a certain gate on qubits, it is therefore a matter of finding the good control amplitudes given the physical constraints of the particular realisation, in particular H_0 and $\{H\}$, but also the possible constraints on $\{u\}$, like the maximal amplitude, or the noise.

9.3 Quantum algorithms

A quantum algorithm is a step-by-step procedure in which each step is implemented using a quantum gate, as previously discussed. These algorithms are designed to operate within the quantum circuit model and exploit the unique properties of quantum states to perform computations.

9.3.1 Quantum Circuit

A quantum circuit is a graphical representation of a quantum algorithm, illustrating the sequence of quantum gates applied to qubits. The circuit consists of qubits represented by lines and quantum

gates represented by boxes that act on these qubits. The circuit model provides a visual framework for understanding the flow of information and operations in a quantum algorithm. See Tab. 9.2 for a list of common quantum gates and their circuit notation. An example of a quantum circuit is shown in Fig. 9.2.

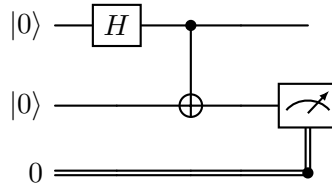


Figure 9.2: Example of a quantum circuit with two qubits, the first qubit undergoes a Hadamard gate and then both qubits undergo a CNOT gate, finally a measurement of the second qubit is performed, whose result is stored in the classical bit at the bottom of the circuit.

A useful feature of quantum circuits is the ability to represent controlled gates, that generally entangle 2 qubits, where the application of a gate on one qubit is contingent on the state of another qubit. If the control qubit is in the state $|1\rangle$, the gate is applied; otherwise, it is not. Moreover if the control qubit is in a superposition of $|0\rangle$ and $|1\rangle$, the gate output state of the second qubit will be in the same superposition of the gate being applied or not. To represent that a qubit controls the application of a gate on another qubit in a quantum circuit, we use the notation shown in Fig. 9.3.

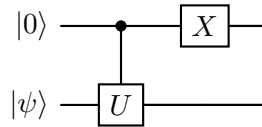


Figure 9.3: Example of a controlled gate, where the first qubit controls the application of the gate U on the second qubit.

Note: The controlled gate in Fig. 9.3 can be written as

$$C(U) = \begin{pmatrix} I & 0 \\ 0 & U \end{pmatrix} \quad (9.12)$$

in matrix form, in the computational basis.

9.3.2 Prominent Quantum Algorithms

Shor's Algorithm One of the most famous quantum algorithms, Shor's algorithm, factors large integers exponentially faster than the best known classical algorithms. This capability has significant implications for cryptography, particularly for systems that rely on the difficulty of factoring large numbers as a security measure [7].

Grover's Algorithm Grover's algorithm provides a quadratic speed-up for unstructured search problems compared to their classical counterparts. This algorithm is particularly useful for searching databases and solving optimisation problems where no specific structure is exploitable by classical algorithms. A general example of Grover's algorithm is shown in Fig. 9.4 and more concrete ones in Fig. 9.5 with 3 qubits, while Fig. 9.6 shows a less trivial example with an additional ancilla qubit.

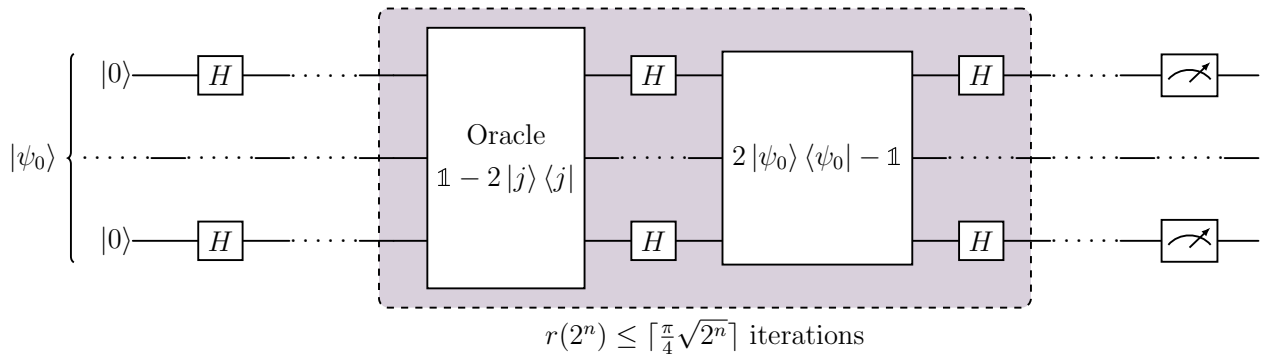


Figure 9.4: Example of Grover's algorithm with n qubits, where the Oracle marks the solution state $|j\rangle$, and the diffusion operator amplifies the probability of that state. The algorithm is composed of (i) the Hadamard gate H , (ii) the oracle gate $\mathbb{1} - 2|j\rangle\langle j|$, and (iii) the diffusion operator $2|\psi_0\rangle\langle\psi_0| - \mathbb{1}$, arranged as shown. The first set of Hadamard gates prepare the uniform superposition states from the initial states $|0\rangle$. The Grover iteration, framed in color, is the composition of the oracle and diffusion operators, and is repeated $\lceil \frac{\pi}{4} \sqrt{2^n} \rceil$ times to find the target state with maximum probability.

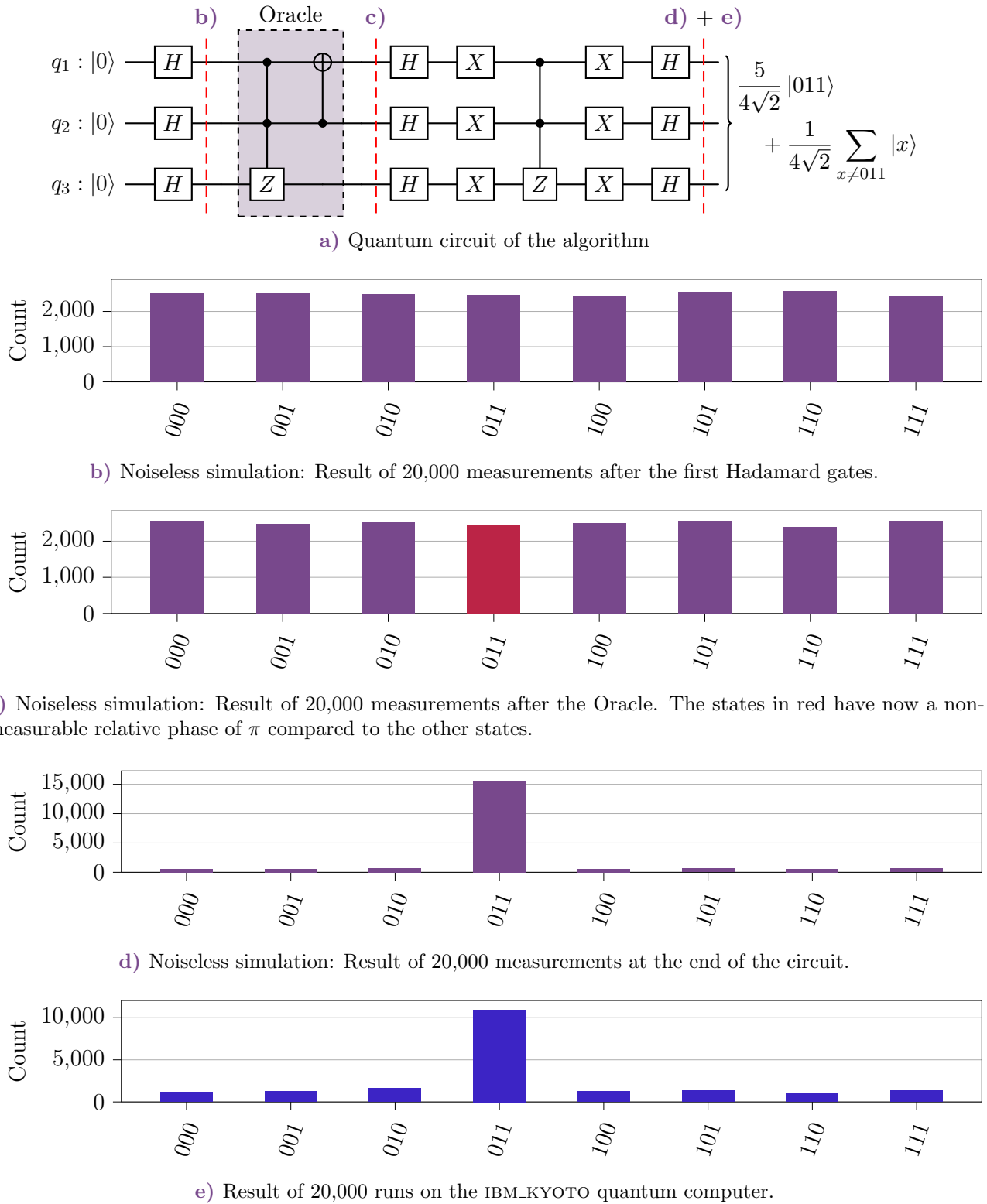
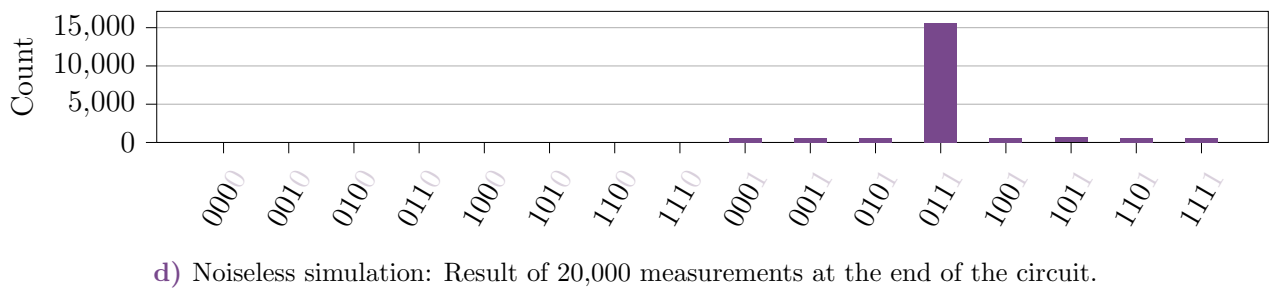
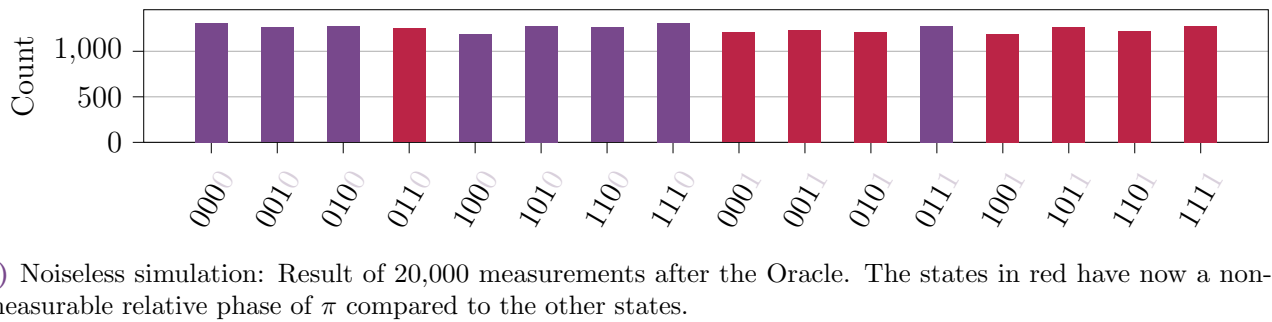
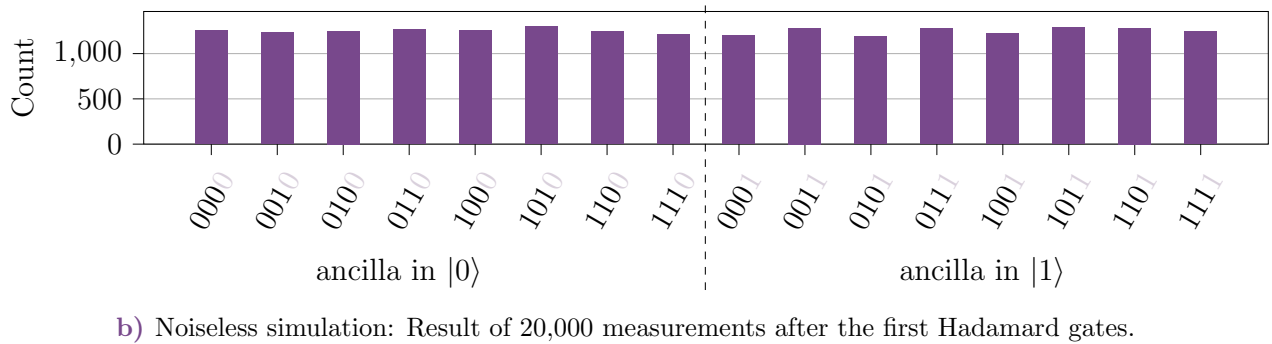
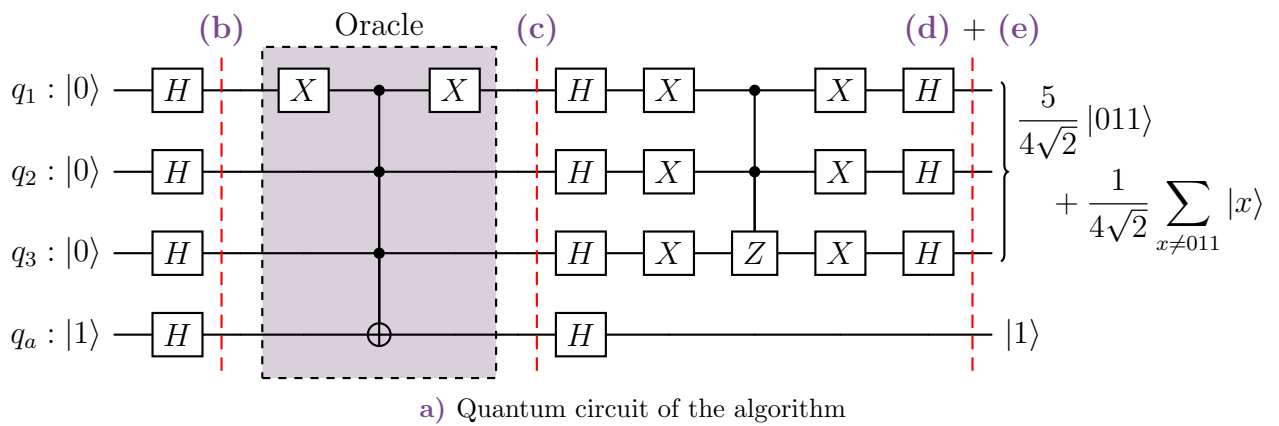
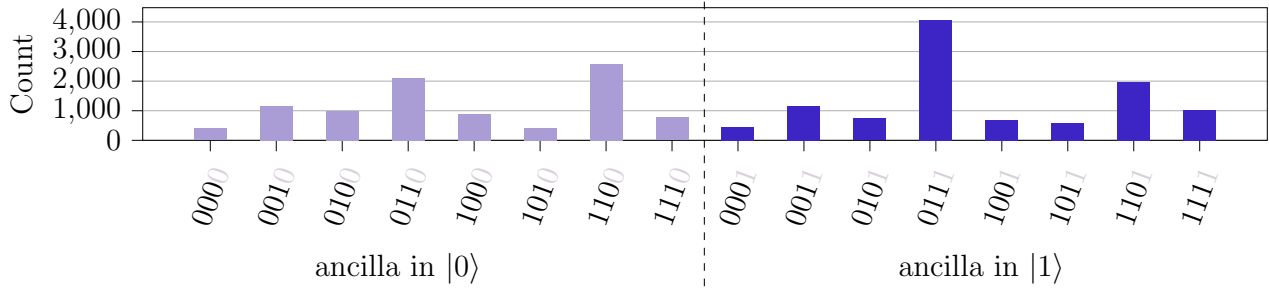


Figure 9.5: Example of Grover's Algorithm with 3 qubits, where the Oracle marks the solution state $|011\rangle$, and the diffusion operator amplifies the probability of that state. Each histogram b)-d) represents the results of potential measurements at different points in the circuit. e) represents real measurements on multiple runs on the IBM_KYOTO quantum computer.





e) Result of 20,000 runs on the IBM_KYOTO quantum computer.

Figure 9.6: Example of Grover's Algorithm with 3 qubits and an ancilla qubit, where the Oracle marks the solution state $|011(1)_a\rangle$, and the diffusion operator amplifies the probability of that state. The aim is to first measure the ancilla qubit and if it is in the state $|0\rangle$, the run can be discarded since an error has occurred before or during the oracle, otherwise, the yet unperturbed state of the 3 qubits is measured. Re-adapted from [165]. Each histogram b)-d) represents the results of potential measurements at different points in the circuit. e) represents real measurements on multiple runs on the IBM_KYOTO quantum computer.

9.4 What is a qudit?

A **qudit** generalises the concept of a qubit to higher dimensions. While a qubit represents quantum information using two levels (typically denoted $|0\rangle$ and $|1\rangle$), a qudit extends this idea to d levels, where d can be any integer greater than 2. These levels are represented by the states $|0\rangle, |1\rangle, |2\rangle, \dots, |d-1\rangle$ in the computational basis.

9.4.1 State Representation

The state of a qudit is described in a d -dimensional Hilbert space. A general state of a qudit can be represented as:

$$|\psi\rangle = \sum_{j=0}^{d-1} \alpha_j |j\rangle, \quad (9.13)$$

where $\{\alpha_j\}$ are complex coefficients satisfying the normalization condition $\sum_{j=0}^{d-1} |\alpha_j|^2 = 1$.

9.4.2 Density Matrix Representation

Similar to qubits, the density matrix formalism can be employed to describe the state of a qudit. The density matrix for a qudit is a $d \times d$ matrix defined as:

$$\rho = \sum_{i,j=0}^{d-1} \rho_{ij} |i\rangle \langle j|, \quad (9.14)$$

with the conditions that ρ is Hermitian ($\rho^\dagger = \rho$), trace-one ($\text{Tr}(\rho) = 1$), and positive semi-definite.

9.4.3 Generalized Bloch Representation

For qubits, the Bloch sphere provides a convenient visualisation of the state space. In the case of qudits, the concept of the Bloch sphere generalises to higher dimensions, often visualised through the use of

generalised Gell-Mann matrices, which are the $SU(d)$ analogues to the Pauli matrices of $SU(2)$. These matrices help in describing the state as a point in a higher-dimensional space, providing a geometric interpretation of qudit states, but a graphical representation is unfortunately hard to come by, as pure states of a qudit lie on a subset of dimension $d^2 - d$ on the hypersurface of a (d^2) -dimensional ball [166].

9.4.4 Quantum Gates for Qudits

Quantum gates for qudits extend the unitary operations applicable to qubits. A quantum gate that acts on a qudit is a $d \times d$ unitary matrix, the relationship of qubit gates to time evolution and physical realisations still applies to qudit quantum gates. These gates, however, allow for a richer set of transformations due to the higher dimensionality, and, for example, a higher number of linearly-independent control Hamiltonians per qudit.

9.4.5 Advantages of Qudits

The use of qudits in quantum computing offers several advantages. Primarily, they provide a more compact representation of quantum information, as a single qudit can encode more information than a qubit. This compactness can lead to reductions in the number of quantum gates and the overall complexity of quantum circuits. In short, the principal motivations of qudit platforms over qubits include: (i) the underlying physical systems having lower decoherence rates [23], (ii) using the redundancy in additional levels for quantum error correction [167, 168], (iii) the higher density of information per physical system (site) [100], (iv) the reduced number of nonlocal, hence more decoherence-sensitive, operations [169] or (v) more robust flying quantum memories [170, 171]. Furthermore, qudits present fundamental theoretical advantages, enabling QIP capabilities offered by $\otimes SU(d)$ vs. $\otimes SU(2)$ of qubits [172] such as simplifying some quantum algorithms [173]. Hence, qudits provide an alternative scaling solution by linearly increasing d , instead of scaling up n , the number of sites, as well as increasing efficiency through single qudit gates operating on larger computational subspaces

9.5 Timescales

In quantum computing, the coherence of qubits—how long they maintain their quantum states—is fundamental for performing quantum operations. The timescales T_1 , T_2 , and T_2^* represent different aspects of how qubit states decay and dephase over time, directly influencing the performance and feasibility of quantum computations.

9.5.1 T_1 : Longitudinal Relaxation Time

The T_1 time, often referred to as the **longitudinal relaxation time**, measures the time it takes for a qubit to return to its thermal equilibrium state along the Z-axis of the Bloch sphere. This process is also known as *energy relaxation* or *spin-lattice relaxation*, where an ensemble of qubits in an excited state $|1\rangle$ relaxes to the ground state $|0\rangle$ on its own in the interaction picture¹:

$$\mathbb{E} [|\langle \psi(0) | \psi(t) \rangle|^2] = |\langle 1 | \psi(0) \rangle|^2 e^{-t/T_1}. \quad (9.15)$$

Here $\mathbb{E}[\cdot]$ is the average of the realisations. This time is critical for quantum systems, as it sets an upper limit on how long computations can run before the qubits lose their energy state. Figures 9.7 and 9.8 illustrate the time evolution of a qubit under pure longitudinal relaxation.

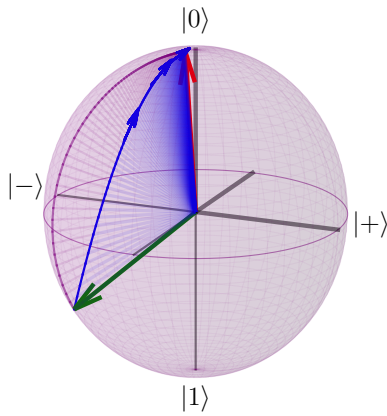


Figure 9.7: Time evolution under pure longitudinal relaxation of an arbitrary state (green), for a time $t = 5T_1$, leading to the final state (red). The trajectory (resp. its projection on the surface of the sphere) are represented in blue (resp. purple).

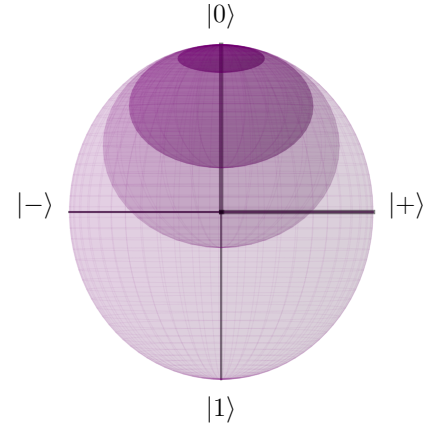


Figure 9.8: Illustrative transformation of the Bloch Sphere's surface under pure longitudinal relaxation, with opacity increasing with time.

9.5.2 T_2 : Decoherence Time

T_2 , or the **transverse relaxation time/decoherence time**, is another crucial metric that describes how quickly the off-diagonal elements of a qubit's pure state density matrix decay. T_2 reflects the loss of quantum coherence due to the dephasing between the states of a qubit in the Heisenberg picture.

$$|\rho_{01}(t)| = |\rho_{01}(0)|e^{-t/T_2}. \quad (9.16)$$

T_2 is generally shorter than T_1 and determines the time window within which the quantum gates can operate effectively before coherence is lost. Figures 9.9 and 9.10 illustrate the time evolution of a qubit under pure dephasing.

Note: There exists cases with $T_2 > T_1$, but $T_2 \leq 2T_1$ (*Proof in appendix*).

A system where $T_2 = 2T_1$ is said to be " T_1 -limited". And sometimes one can define $\frac{1}{T_\phi} = \frac{1}{T_2} - \frac{1}{2T_1}$, the **pure dephasing time**, that is, the supplementary dephasing time that is not due to the longitudinal relaxation.

Note: Fig. 9.10 shows that pure dephasing can be interpreted as a form of transition to classicality, since at $t \rightarrow \infty$, the Bloch sphere becomes a simple line joining the two poles. Which means, the final state is indiscernible from an ensemble of classical bits that are either in $|0\rangle$ or $|1\rangle$.

9.5.3 T_2^* : Dephasing time

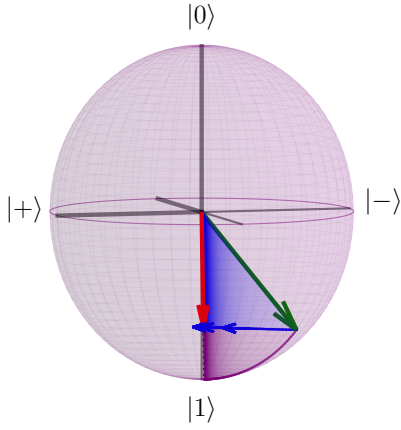


Figure 9.9: Time evolution under pure dephasing of an arbitrary state (green), for a time $t = 2T_2$, leading to the final state (red). The trajectory (resp. its projection on the surface of the sphere) are represented in blue (resp. purple).

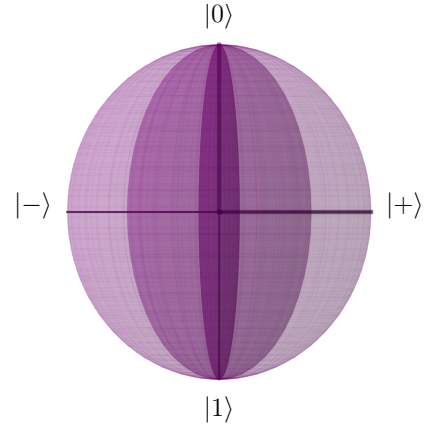


Figure 9.10: Illustrative transformation of the Bloch Sphere's surface under pure dephasing, with opacity increasing with time.

T_2^* (T_2 star) represents the **total dephasing time**, including all sources of noise, not just those intrinsic to the qubit system. It is often shorter than T_2 due to additional dephasing effects from environmental instabilities. By changing the reference frame to the interaction picture and defining $|\pm\rangle := \frac{1}{\sqrt{2}}(|0\rangle \pm |1\rangle)$, and initializing the system in the state $|+\rangle$ and letting it evolve, we define

$$\mathbb{E} [|\langle\psi(0)|\psi(t)\rangle|^2] = \mathbb{E} [|\langle+\psi(t)\rangle|^2] = \frac{1}{2} \left(1 + e^{-t/T_2^*}\right) \quad (9.17)$$

This metric is essential for understanding the overall stability and reliability of qubit systems in real-world environments.

Note: The difference between T_2 and T_2^* might not seem very obvious at first glance, and those two are oftentimes used interchangeably. It becomes even more confusing when one considers that, if $\rho(0) = |+\rangle\langle+|$

$$|\langle+\psi(t)\rangle|^2 \stackrel{(9.15)}{=} \langle+\rho|+\rangle = \frac{1}{2}(\rho_{00} + \rho_{11} + \rho_{10} + \rho_{11}) = \frac{1}{2} \left(1 + e^{-t/T_2}\right) \quad (9.18)$$

This makes it seem that $T_2 = T_2^*$. However, let us consider, that in the interaction picture of a unitary evolution, there is a non-characterised interaction term $H_I(t) = \delta(t)|1\rangle\langle 1|$ — it can be an external field noise, uncalibrated controls, etc.— that varies from one realisation to another, but can be represented by a Gaussian noise of variance $2/\tau$. Initialising the state in $|+\rangle$ at time 0, and letting it evolve for a time t according to the Schrodinger equation, produces a system in the state $\frac{1}{\sqrt{2}} \left(|0\rangle + \exp\left(-i \int_0^t \delta(t')dt'\right)|1\rangle\right)$. This means that averaging over all the different realisations:

$$\mathbb{E} [|\langle+\psi(t)\rangle|^2] = \frac{1}{2} \left(1 + \mathbb{E} \left[\cos \left(\int_0^t \delta(t')dt' \right) \right] \right) = \frac{1}{2} \left(1 + e^{-t/\tau}\right).$$

(Proof in appendix)

This is then a similar expression as before.

In reality, T_2 represents a type of decoherence that occurs because of non-unitary evolution. This means that it arises from interactions not described by the standard quantum mechanical framework

of Hamiltonians within the system's Hilbert Space. On the other hand, T_2^* includes everything that T_2 covers, plus an additional dephasing term. This extra term comes from averaging the effects across a group of systems. These systems undergo unitary evolution, meaning that they evolve in a predictable quantum manner, but they experience variations due to Gaussian noise or a normally distributed variation in their base Hamiltonian settings.

For instance, consider a qubit with two energy levels that are initially degenerate but are split due to a longitudinal field that has some noise in its control. Alternatively, imagine a group of qubits that are in slightly different environments. In such cases, the dephasing included in T_2^* would account for these variations.

Finally, one could say that the total dephasing time T_2^* includes: the inhomogeneous dephasing time τ , the pure dephasing time T_ϕ (see definition of T_2), and the longitudinal relaxation time T_1 , as follows:

$$\frac{1}{T_2^*} = \frac{1}{\tau} + \frac{1}{T_\phi} + \frac{1}{2T_1} \quad (9.19)$$

These timescales — T_1 , T_2 , and T_2^* — are essential for designing and evaluating quantum circuits, as they directly impact the error rates and practicality of implementing quantum algorithms. T_2^* , as the limiting parameter, is crucial for any qubit system. It sets the operational timescale, beyond which quantum computing is unfeasible due to decoherence. Moreover, each one corresponds to a particular type of qubit error, and each of those can be modelled by a specific quantum channel, in an open quantum system approach, that will be seen in the next part.

Note: It is also possible to define T_2^* as the decoherence time, i.e. the time it takes for the off-diagonal elements of the density matrix to decay to $1/e$ of their initial value. This is a more general definition that can be applied to any system, not just qubits. Therefore, in d -dimensional systems, T_2^* would be the time it takes for the off-diagonal elements between two adjacent levels to decay to $1/e$ of their initial value. This could imply $d - 1$ different T_2^* timescales, for each pair of adjacent levels, as, depending on the system, the dephasing between different levels might not be the same. A similar definition can be applied to T_1 , as the time it takes a level to decay to $1/e$ of its initial value to other levels.

Main takeaways from Chapter 9

- **Qubits:**
 - Qubits are quantum information units, existing in superpositions of $|0\rangle$ and $|1\rangle$. They are visualized on the Bloch sphere.
- **Entanglement:**
 - Qubits can be entangled, leading to non-separable states essential for quantum algorithms and exponential scaling of information.
- **Quantum Gates:**
 - Quantum gates manipulate qubits using unitary operations, with common gates like Pauli-X,Y,Z, Hadamard, and CNOT.
- **Qudits:**
 - Qudits generalize qubits to d levels, offering higher information density and potential advantages in error correction and complexity reduction.
- **Key Timescales:**
 - T_1 : Energy relaxation Time
 - T_2 : Decoherence time,
 - T_2^* : Total dephasing time, all critical for quantum computation stability.

Chapter Contents

10.1 The Lindblad equation	195
10.2 Alternative way to model errors: Kraus operators	196
10.3 Link with T_1 and T_2 timescales	197
10.4 Issues in solving the Lindblad equation numerically	198

CHAPTER 10

Open quantum systems with Markovian noise

"Oh no!"

** in the form of Quantum "*

— **Jean-Gabriel Hartmann**, *my colleague, before being hit by a quantum error*

10.1 The Lindblad equation

The time dynamics of a finite-dimensional quantum system that interacts with an environment can be modeled in various different ways. However, if we assume that the dynamics are Markovian, this imposes some conditions on the form of the equation governing the evolution of the system. Since our goal is to model a noisy quantum systems, it will be interesting to work with the density matrix formalism¹. The state of our quantum system will indeed, by definition, not be pure anymore, since it will be interacting with (and losing information to) an environment.

It is then a matter of finding a time-independent generator \mathcal{L} such that:

$$\frac{d\rho}{dt} = \mathcal{L}[\rho]. \quad (10.1)$$

It follows that:

$$\rho(t) = e^{\mathcal{L}t}[\rho(0)] \quad (10.2)$$

\mathcal{L} needs to respect the following properties imposed by physical constraints:

1. In the absence of noise, \mathcal{L} needs to reduce to $-i[H, \cdot]$, yielding the traditional closed-system Von-Neumann equation.
2. $e^{\mathcal{L}t}$ must be trace-preserving, since $\text{Tr}(\rho) = 1$ always. Hence, \mathcal{L} must be traceless.
3. $e^{\mathcal{L}t}$ needs to be positive, i.e. if $\rho \geq 0$, then $e^{\mathcal{L}t}[\rho] \geq 0$.

¹See [Appendix A.3](#).

4. This last property is actually not sufficient, $e^{\mathcal{L}t}$ needs to be completely positive². This is crucial to avoid any inconsistencies with composite systems, and therefore also entanglement dynamics.

A quantum channel that is Completely Positive and Trace-preserving is generally referred to as a **CPT map**. It can be shown [174] that the only \mathcal{L} that complies with these properties; and describes a Markovian evolution, takes the form

Definition: (*Lindblad – or GKSL – equation*)

$$\frac{d\rho}{dt} = -i[H, \rho] + \sum_{k=1}^K \gamma_k \left(L_k \rho L_k^\dagger - \frac{1}{2} \{L_k^\dagger L_k, \rho\} \right), \quad (10.3)$$

Here ρ represents the density evolution of the system, H is the Hamiltonian of the said system, and $\{L_k\}$ are a set of *collapse* operators, representing dissipation channels, with the dissipation strength given by their associated γ_k .

The Gorini-Kossakowski-Sudarshan-Lindblad (GKSL) equation is named this way because it was independently discovered by Gorini, Kossakowski, and Sudarshan in 1976 [175], and by Lindblad in 1976 [176]. It is the most general form of a Markovian master equation, and it is the most general form of a quantum dynamical semigroup. It is also the most general form of a quantum channel that is both trace-preserving and completely positive.

10.2 Alternative way to model errors: Kraus operators

The Lindblad equation is a general way to model noise in quantum systems, but it is not the only one. Another way to model noise is through the use of Kraus operators, named after Karl Kraus, who introduced them in 1983 [177]. The Kraus representation of a quantum channel is given by:

Definition: (*Kraus representation of a quantum channel*)

$$\rho \rightarrow \sum_{k=1}^K E_k \rho E_k^\dagger. \quad (10.4)$$

While the Lindblad equation models noise as a continuous process, the Kraus representation models noise as a discrete process, as it assumes that the system interacts with the environment in a series of discrete steps or events, corresponding to the application of the Kraus operators. The two representations are however equivalent, and one can be transformed into the other through the consideration of the problem in superoperator form (Appendix A.5) [178, 179].

Example: Let's consider the pure spin dephasing channel in Lindblad form [180].

$$\frac{d\rho}{dt} = -i[H, \rho] + \gamma \left(J_z \rho J_z - \frac{1}{2} \{J_z^2, \rho\} \right) \quad (10.5)$$

It can be shown [181] that this can be rewritten in Kraus form as:

²A map \mathcal{V} is completely positive iff $\forall n, \mathcal{V} \otimes \mathbb{1}_n$ is positive. See [174] for an in-depth discussion for the Lindblad equation, generators of CPT maps and how the Lindblad equation can also be obtained by tracing out an environment bath.

$$\rho \rightarrow \sum_{k=0}^{\infty} E_k \rho E_k^\dagger \quad (10.6)$$

with the Kraus operators, $\forall k \in \mathbb{N}$:

$$E_k = \sqrt{\frac{(\gamma t)^k}{k!}} e^{-\gamma t J_z^2/2} J_z^k. \quad (10.7)$$

10.3 Link with T_1 and T_2 timescales

Each of the error channels presented in Section 9.5 can be modelled by a specific set of Lindblad (or Kraus) operators.

10.3.1 Pure dephasing

The pure dephasing channel, characterised by the T_2 timescale, can be modelled by the following Lindblad operator:

$$L_1 = \sqrt{\frac{2}{T_2}} \sigma_z \quad (10.8)$$

leading to the following evolution equation:

$$\frac{d\rho}{dt} = -i[H, \rho] + \frac{2}{T_2} \left(\sigma_z \rho \sigma_z - \frac{1}{2} \{ \sigma_z^2, \rho \} \right) \quad (10.9)$$

Figures 9.9 and 9.10 were generated using this evolution equation for the pure dephasing channel.

Moreover, as shown in [181], the pure dephasing channel can be modelled by the following Kraus operators, $\forall k \in \mathbb{N}$:

$$E_k = \sqrt{\frac{(2t/T_2)^k}{k!}} e^{-t/T_2} \sigma_z^k. \quad (10.10)$$

Note: We have the correspondance $\gamma = 2/T_2$ for pure dephasing.

10.3.2 Longitudinal relaxation

The longitudinal relaxation channel, characterised by the T_1 timescale, can be modelled by the following Kraus operator:

$$E_0 = \begin{pmatrix} 1 & 0 \\ 0 & e^{-t/2T_1} \end{pmatrix}, \quad E_1 = \sqrt{1 - e^{-t/2T_1}} |0\rangle \langle 1| \quad (10.11)$$

10.3.3 Dephasing in qudits

In the case of qudits, the dephasing channel can be modelled by

$$\frac{d\rho}{dt} = -i[H, \rho] + \gamma \left(J_z \rho J_z - \frac{1}{2} \{J_z^2, \rho\} \right) \quad (10.12)$$

If we assume that the system is initialised in the state $\rho = \frac{1}{d} \sum_{i,j=0}^{d-1} |i\rangle \langle j|$, and $H = \mathbb{0}_d$, then the evolution of the density can be written:

$$\rho_{ij}(t) = \rho_{ij}(0) e^{-\frac{\gamma}{2}(i-j)^2 t}, \quad (10.13)$$

By defining a generalisation of the T_2^* timescale to qudits, as the time it takes for the off-diagonal elements between two adjacent levels to decay to $1/e$ of their initial value, we can see by identifying

$$\rho_{i(i+1)}(t) = \rho_{ij}(0) e^{-\frac{t}{T_2^*}}, \quad (10.14)$$

with (10.13), that $T_2^* = \frac{2}{\gamma}$.

10.4 Issues in solving the Lindblad equation numerically

This discussion is directly adapted from our collaborative paper with mathematicians Hao Chen from Chongqing Normal University and Alfio Borzi from the University of Würzburg, **Full- and low- rank exponential Euler integrators for the Lindblad equation** submitted for publication in SIAM Journal on Scientific Computing and uploaded as a preprint manuscript to arXiv. The bibliographical citation of the preprint can be found in [182].

Solving the Schrödinger equation for N qudits requires the manipulation of d^N complex numbers for each component of the pure state under consideration. However, the Lindblad equation requires the manipulation of d^{2N} complex numbers for each component of the density matrix, as it cannot be expressed in a form acting on the state vector. These computational costs can become even more prohibitive when one wants to obtain the time evolution operator and not just the final state, as it requires the manipulation of d^{2N} complex numbers in the unitary case, in the form of a time-evolution operator, and d^{4N} complex numbers in the case of the Lindblad equation, in the form of a superoperator (see Appendix A.4).

Numerical approaches to solving the Lindblad equation must also ensure that key properties such as positivity and trace preservation are maintained throughout the evolution. However, many standard numerical techniques, including explicit Runge-Kutta methods [183] and even more advanced techniques like Crank-Nicolson methods [184, 185], fail to preserve these properties in practice, particularly in long-time simulations. This is a critical issue because the physical validity of the simulations relies on the positivity of the density matrix, as it represents probabilities that must be non-negative.

To address these computational challenges, we collaborated with mathematicians to develop new numerical methods for the Lindblad equation. Specifically, we designed novel full- and low-rank exponential Euler integrators that are capable of approximating the Lindblad equation while preserving positivity and trace unconditionally, as discussed in Chen *et al.* [182]. These methods provide sharp error estimates and exhibit improved computational efficiency over conventional approaches. The low-rank variant, in particular, drastically reduces computational costs by approximating the solution with reduced-rank representations, making it feasible for simulations with high-dimensional systems.

Our work introduces two classes of exponential integrators—namely, the full-rank exponential Euler integrator (FREE) and the low-rank exponential Euler integrator (LREE). Both methods focus on the Gorini-Kossakowski-Sudarshan-Lindblad (GKSL) form of the Lindblad equation, which ensures positivity and trace preservation for density matrices. The FREE integrator is a straightforward

approach that directly computes the matrix exponentials and ensures both positivity and unit trace without normalization procedures. It is highly accurate, albeit computationally intensive, due to the manipulation of large-scale algebraic Lyapunov equations.

In contrast, the LREE approach significantly reduces computational complexity by utilizing a low-rank approximation to the density matrix. By working with an approximation of rank $r \ll d^N$, the LREE integrates the Lindblad equation in a more efficient manner. Specifically, instead of computing full matrix exponentials, the LREE relies on a more manageable number of matrix-vector products and a truncated Singular Value Decomposition (SVD), allowing for reduced storage and faster computations. The low-rank approach comes at the cost of introducing an additional approximation error, which is bounded and analyzed [182], Theorem 5.3.

Moreover, the numerical experiments reported in the article demonstrate the efficacy of both methods. The experiments compare the new schemes with standard solvers in the well-known QuTip library for quantum simulations. The results show that while the QuTip solvers may achieve higher accuracy, they struggle to maintain positivity, particularly in the presence of dissipation, which the new exponential Euler integrators handle well. Furthermore, the LREE scheme is shown to be computationally superior as the system size increases, especially for problems involving sparse Hamiltonians and dense jump operators.

Overall, if one were to consider the simulation of quantum systems under markovian noise with a large Hilbert Space, of which only certain subspaces are of interest, such as the d hyperfine levels of the electronic ground state of the lanthanide-based complexes we study, the LREE method would be a valuable tool to consider.

Main takeaways from Chapter 10

- **Lindblad Equation:**

- Serves as the most general form for Markovian quantum master equations in open quantum systems.
- Ensures complete positivity and trace preservation of the density matrix, crucial for physical validity.

- **Kraus Operators:**

- Provide an alternative, equivalent representation to the Lindblad equation for modeling quantum noise.
- Model noise as discrete processes through a set of operators, facilitating different analytical and numerical approaches.

- **Modeling Error Channels:**

- **Pure Dephasing (T_2):** Modeled using Lindblad operators like $L = \sqrt{\frac{2}{T_2}} \sigma_z$, representing dephasing without energy exchange.
- **Longitudinal Relaxation (T_1):** Modeled using Kraus operators that describe energy relaxation processes.
- **Qudit Dephasing:** Generalization of dephasing to higher-dimensional systems, with off-diagonal elements decaying according to their level differences s.t.

$$\rho_{ij}(t) = \rho_{ij}(0)e^{-\frac{\gamma}{2}(i-j)^2t}$$

- **Numerical Challenges in Solving the Lindblad Equation:**

- Computational complexity increases exponentially with system size due to the density matrix's dimensionality.
- Standard numerical methods may fail to preserve key physical properties like positivity and trace, leading to unphysical results.
- **Low-Rank Exponential Euler Integrators (LREE):** Advanced numerical methods that efficiently solve the Lindblad equation while maintaining positivity and trace preservation, reducing computational costs significantly.

Chapter Contents

11.1 The AGI: Definition and First-Order Approximation	201
11.2 Numerical validation and deviation	207
11.3 Linear and exp. scalings from the perspective of the AGI	215

CHAPTER 11

Noisy qudits vs. qubits: First-order approach

This chapter was written in conjunction with the writing of our article **Noisy Qudit vs Multiple Qubits: Conditions on Gate Efficiency for Enhancing Fidelity** that was published in npj Quantum Information. The bibliographical citation of the publication can be found in [186], and the code and data used in the study have been made publicly available at [187].

As we have seen in the previous chapter, the dynamics of a quantum system can be modelled by the Lindblad equation, which describes the evolution of the system's density matrix under the influence of noise. In this chapter, we will focus on the case of a qudit, a d -level quantum system, and study the effect of noise on the system's computational performance. In particular, we will consider how it scales with the dimension of the system in the case of pure dephasing, and how it compares to the case of multiple qubits with an equivalent number of levels.

11.1 The Average Gate Infidelity: Definition and First-Order Approximation

11.1.1 Fluctuation-dissipation relation for a perturbed pure state

Consider a qudit, a d -level quantum system whose dynamics are governed by the Lindblad master equation:

$$\frac{d\rho}{dt} = -i[H, \rho] + \sum_{k=1}^K \gamma_k \left(L_k \rho L_k^\dagger - \frac{1}{2} \{L_k^\dagger L_k, \rho\} \right), \quad (11.1)$$

where $\rho(t)$ is the density matrix of the system at time t , H the Hamiltonian of the system, L_k the so-called collapse operators characterizing the Markovian noise, and γ_k the decay parameters for each of the K noise processes. $H = H_0 + H_c(t)$ where H_0 models the free evolution of the physical system and encompassing its internal interactions, and $H_c(t)$ is a time-dependent pulse Hamiltonian implementing the controlled evolution. Moreover, the interactions of H with the collapse operators determine relevant timescales such as the gate-time t and the decoherence time T_2 that are thus inherent to the physical realization under consideration.

The aim is to study the effect of a single collapse operator $\sqrt{\gamma_1} L_1 = \sqrt{\gamma} L$ on short timescales and under small-amplitude noise, i.e., $\gamma t \ll 1$. Under these assumptions, one can consider an *ansatz* of the

form:

$$\rho(t) = \rho^* - \gamma t M + \mathcal{O}((\gamma t)^2), \quad (11.2)$$

with ρ^* the noiseless target state, which is the solution of $\dot{\rho}^* = -i[H, \rho^*]$ after time t , and M the perturbation matrix resulting from the presence of a small-amplitude noise. Terms in $\mathcal{O}((\gamma t)^2)$ include terms whose prefactor is of the form $(\gamma^l t^k)_{l+k \geq 3}$, a more in-depth discussion is done later in this chapter.

One can easily see that the use of (11.2) in (11.1) leads to

$$M = \frac{1}{2} \left\{ L^\dagger L, \rho^* \right\} - L \rho^* L^\dagger. \quad (11.3)$$

Consider now a quantum operation bringing the initial state ρ_0 to a final state $\rho(t)$ at time t . One defines the fidelity \mathcal{F} of this final state relative to some target state ρ^* [188] as

$$\mathcal{F}(\rho(t), \rho^*) \equiv \left[\text{Tr} \left(\sqrt{\sqrt{\rho(t)} \rho^* \sqrt{\rho(t)}} \right) \right]^2. \quad (11.4)$$

Subsequently, the infidelity, is then defined as

$$\mathcal{E} \equiv 1 - \mathcal{F}. \quad (11.5)$$

Since ρ^* is a pure state ($\rho^* = |\varphi^*\rangle \langle \varphi^*|$) (11.4) simplifies to [188]

$$\mathcal{F}(\rho(t), \rho^*) = \text{Tr}(\rho(t) \rho^*). \quad (11.6)$$

Finally, substituting (11.2) into (11.6) leads to

Definition: (*Fluctuation-Dissipation Relation for the Infidelity of a perturbed pure state*)

$$\mathcal{E}(\rho^*) = \gamma t \Delta_* L + \mathcal{O}((\gamma t)^2). \quad (11.7)$$

where $\Delta_* L = \langle L^\dagger L \rangle_* - \langle L^\dagger \rangle_* \langle L \rangle_*$ with $\langle L^\dagger L \rangle_* \equiv \text{Tr}(\rho^* L^\dagger L)$. (*Proof in appendix*)

11.1.2 Average Gate Fidelity of a single qudit

Only $\mathcal{E}(\rho^*)$ for a specific ρ^* was obtained in the previous subsection. However, is there a state-independent approach to obtaining the infidelity of a quantum gate under small-amplitude noise? One defines the quantum gate U applied during a time duration t , whose resulting operation brings all initial states ρ_0 to all corresponding $\rho^* = U \rho_0 U^\dagger$. There is then a definition of the average gate fidelity of a quantum channel \mathcal{E} , attempting to carry the unitary operation U despite a noisy environment, which reads as follows [189]

Definition: (*Average Gate Fidelity*)

$$\begin{aligned} \bar{\mathcal{F}}(\mathcal{E}, U) &= \int d\rho_0 \mathcal{F}(\rho(t), \rho^*) \\ &= \int d\rho_0 \left\langle U^\dagger \mathcal{E}[\rho_0] U \right\rangle_0 = \int d\rho_0 \left\langle \left(\mathcal{U}^\dagger \circ \mathcal{E} \right) [\rho_0] \right\rangle_0, \end{aligned} \quad (11.8)$$

where the normalized integral is over the Fubini-Study measure on pure states (sometimes called the Haar measure) [190], $\mathcal{U}^\dagger[\rho] \equiv U^\dagger \rho U$ and $\mathcal{E}[\rho_0] = \rho(t)$.

Introducing $\tilde{E}_k = E_k U$ the Kraus operators such that

$$\rho(t) = (\mathcal{U}^\dagger \circ \mathcal{E})[\rho_0] = \sum_k \tilde{E}_k \rho_0 \tilde{E}_k^\dagger = \sum_k E_k \rho^* E_k^\dagger, \quad (11.9)$$

the Average Gate Fidelity $\bar{\mathcal{F}}$ given in (11.8) can be rewritten as [191]

$$\bar{\mathcal{F}}(\mathcal{E}, U) = \frac{d + \sum_k |\text{Tr}(\tilde{E}_k U^\dagger)|^2}{d(d+1)} = \frac{d + \sum_k |\text{Tr}(E_k)|^2}{d(d+1)}. \quad (11.10)$$

Using (11.3), one seeks the sets of Kraus operators $\{\tilde{E}_k\}$ or $\{E_k\}$ such that, to $\mathcal{O}((\gamma t)^2)$, $\forall \rho_0, \rho^*$,

$$\begin{aligned} \sum_k \tilde{E}_k \rho_0 \tilde{E}_k^\dagger &= U \rho_0 U^\dagger - \gamma t \frac{1}{2} \left\{ L^\dagger L, U \rho_0 U^\dagger \right\} + \gamma t L U \rho_0 U^\dagger L^\dagger \\ \sum_k E_k \rho^* E_k^\dagger &= \rho^* - \gamma t \frac{1}{2} \left\{ L^\dagger L, \rho^* \right\} + \gamma t L \rho^* L^\dagger. \end{aligned} \quad (11.11)$$

One can see that the following two sets would work up to the first order in γt

$$\begin{aligned} \tilde{E}_0 &= \left(\mathbb{1}_d - \frac{\gamma t}{2} L^\dagger L \right) U, & \tilde{E}_1 &= \sqrt{\gamma t} L U, \\ E_0 &= \mathbb{1}_d - \frac{\gamma t}{2} L^\dagger L, & E_1 &= \sqrt{\gamma t} L. \end{aligned} \quad (11.12)$$

In order to use (11.12) in (11.8), it is necessary to calculate the traces of the operators. Let us consider a pure dephasing channel of a qudit coupled to a thermal environment through the operator J_z (In general the coupling of a qudit, or qubit, to a thermal environment can be represented by a linear combination, or mixture, of collapse operators, though a pure dephasing channel will typically be present and can be represented by the operator J_z . As a toy model, let us consider a coupling term dominated by a pure dephasing channel.) i.e. \mathcal{E}_z with $L = J_z$ [180].

11.1.3 Average Gate Infidelity for the Pure Dephasing Channel of one qudit

In a trivial way we have $\text{Tr}(E_1) \propto \text{Tr}(J_z) = 0$, and

$$\begin{aligned} \text{Tr}(E_0) &= d - \frac{\gamma t}{2} \text{Tr}(J_z^2) \\ &= d - \frac{\gamma t}{2} \sum_{k=0}^{d-1} \left(\frac{d-1-2k}{2} \right)^2 \\ &= d - \frac{\gamma t}{8} \left[d(d-1)^2 - 4(d-1) \sum_{k=0}^{d-1} k + 4 \sum_{k=0}^{d-1} k^2 \right] \\ &= d - \frac{\gamma t}{8} \left[d(d-1)^2 - 2d(d-1)^2 + 4 \frac{d(d-1)(2d-1)}{6} \right] \\ &= d - \frac{\gamma t}{24} d(d^2 - 1), \end{aligned}$$

which results in

$$|\text{Tr}(E_0)|^2 = d^2 - \frac{\gamma t}{12} d^2 (d^2 - 1) + \mathcal{O}((\gamma t)^2). \quad (11.13)$$

Therefore

$$\overline{\mathcal{F}}(\mathcal{E}_z) = \frac{d + d^2 - \frac{\gamma t}{12} d^2 (d^2 - 1)}{d(d+1)} + \mathcal{O}((\gamma t)^2) = 1 - \frac{\gamma t}{12} d(d-1) + \mathcal{O}((\gamma t)^2), \quad (11.14)$$

which leads to the simplified expression (11.15).¹

One obtains a *gate*- (and Hamiltonian-) independent result for the Average Gate Fidelity which reads as

$$\overline{\mathcal{F}}(\mathcal{E}_z) = 1 - \frac{\gamma t}{12} d(d-1) + \mathcal{O}((\gamma t)^2). \quad (11.15)$$

In other words the Average Gate Infidelity (AGI) is given by

Definition: (*First-order approximation of the Average Gate Infidelity for a single qudit under pure dephasing*)

$$\overline{\mathcal{E}}(\mathcal{E}_z) = \frac{\gamma t}{12} d(d-1) + \mathcal{O}((\gamma t)^2), \quad (11.16)$$

or more generally for an arbitrary quantum channel \mathcal{X} with collapse operator L

$$\overline{\mathcal{E}}(\mathcal{X}) = \frac{\gamma t}{d+1} \left(\text{Tr}(L^\dagger L) - \frac{1}{d} |\text{Tr}(L)|^2 \right) + \mathcal{O}((\gamma t)^2). \quad (11.17)$$

Note that it is always possible to find a traceless collapse operator L emulating \mathcal{X} [174], so the previous expression can be, in this case, simplified as follows

Definition: (*First-order approximation of the Average Gate Infidelity for a single qudit under a general quantum channel \mathcal{X}*)

$$\overline{\mathcal{E}}(\mathcal{X}) = \frac{\gamma t}{d+1} \text{Tr}(L^\dagger L) + \mathcal{O}((\gamma t)^2). \quad (11.18)$$

It follows from (11.18) that, if L were independent of d , increasing the dimension d of the Hilbert space would also increase the *robustness* of qudit gates to a dimension-independent quantum channel.

11.1.4 One dephasing qudit vs. multiple qubits: Different AGI scalings

Now let us apply the same technique as described above to another system: an ensemble of n identical dephasing qubits (Hilbert space of dimension $d = 2^n$). In order to compare it with the qudit analysis in the previous subsection, each individual qubit decoheres with the same rate (has the same type, and strength, of environmental coupling) through its spin operator S_z in the same way as the individual qudit (with $d = 2$). Considering any additional coupling mechanism to the environment arising from inter-qubit interactions would only further disadvantage the multi-qubit implementation. Our considerations then provide a best-case scenario for comparable qubits. This yields the master equation

$$\frac{d\rho}{dt} = -i[H, \rho] + \sum_{k=1}^n L_k \rho L_k^\dagger - \frac{1}{2} \sum_{k=1}^n \{L_k^\dagger L_k, \rho\}, \quad (11.19)$$

with

$$L_k = \underbrace{\mathbb{1}_2^{(1)} \otimes \dots \otimes \mathbb{1}_2^{(k-1)}}_{k-1} \otimes S_z^{(k)} \otimes \underbrace{\mathbb{1}_2^{(k+1)} \otimes \dots \otimes \mathbb{1}_2^{(n)}}_{n-k} \quad (11.20)$$

¹Moreover, this is the origin of the factor $\frac{1}{12}$ in (11.16) whose ratio with the $\frac{1}{4}$ obtained in (11.24) and (11.23) leads to the non-trivial factor $\frac{1}{3}$ in (11.26).

for $k \in \llbracket 1, n \rrbracket$.

Using the same reasoning as for dephasing qudits one obtains $n + 1$ Kraus operators to first order in γt

$$E_0 = \mathbb{1}_{2^n} - \sum_{k=1}^n \frac{\gamma t}{2} L_k^\dagger L_k, \quad E_k = \sqrt{\gamma t} L_k. \quad (11.21)$$

In this case, since $\text{Tr}(E_k) = 0 \ \forall k \neq 0$, only $\text{Tr}(E_0)$ is left and is given by

$$\begin{aligned} \text{Tr}(E_0) &= 2^n - \frac{\gamma t}{2} \sum_{k=1}^n \left[\text{Tr} \left(S_z^{2^{(k)}} \right) \prod_{j \neq k} \text{Tr} \left(\mathbb{1}_2^{(j)} \right) \right] \\ &= 2^n - n \frac{\gamma t}{8} 2^n, \end{aligned} \quad (11.22)$$

leading to

$$|\text{Tr}(E_0)|^2 = 2^{2n} - \frac{\gamma t}{4} n 2^{2n} + \mathcal{O}((\gamma t)^2), \quad (11.23)$$

which allows to obtain, using (11.10),

Definition: (*First-order approximation of the Average Gate Infidelity for an ensemble of n qubits under pure dephasing*)

$$\overline{\mathcal{E}}(\mathcal{E}_z) = \frac{\gamma t}{4} \frac{n 2^n}{2^n + 1} + \mathcal{O}((\gamma t)^2) = \frac{\gamma t \log_2(d) d}{4(d+1)} + \mathcal{O}((\gamma t)^2). \quad (11.24)$$

Let us stress that (11.24) yields the same result as Abad *et al.*[192] in the case of identically dephasing qubits with no energy relaxation.

The analytical expressions (11.18) and (11.24) are one of the main results of this work.

Following those last two results, two expressions for the AGI have been found: for a single qudit, one finds an infidelity that scales as d^2 : $\overline{\mathcal{E}}_d(\mathcal{E}_z) = c_d \gamma t$ in (11.16) and for an ensemble of n qubits one finds an infidelity that scales as $\log_2(d)$: $\overline{\mathcal{E}}_{b,n}(\mathcal{E}_z) = c_{b,n} \gamma t$ in (11.24). Moreover, in the case of pure dephasing, one can define the $T_{2,d}$ dephasing time between two energy-adjacent levels for a qudit. It then shares the same expression (in terms of γ) as the typical $T_{2,b}$ dephasing time of a single qubit, namely $\frac{1}{T_2} = \frac{\gamma}{2}$.

The ratio between two average gate infidelities, of duration t_d and $t_{b,n}$ for qudit and n qubits, respectively, becomes

$$\frac{\overline{\mathcal{E}}_d(\mathcal{E}_z)}{\overline{\mathcal{E}}_{b,n}(\mathcal{E}_z)} = \frac{c_d t_d / T_{2,d}}{c_{b,n} t_{b,n} / T_{2,b}}. \quad (11.25)$$

Therefore, in order for a *single* qudit ($d = 2^n$) to outperform *an ensemble* of n qubits in noise-robustness, i.e., to have a smaller AGI, the following inequality must hold true

Definition: (*Condition for a single qudit to outperform an ensemble of n qubits in noise-robustness*)

$$\frac{t_{b,n} / T_{2,b}}{t_d / T_{2,d}} > \frac{c_d}{c_{b,n}} = \frac{d^2 - 1}{3 \log_2(d)} = \frac{4^n - 1}{3n}. \quad (11.26)$$

This expression quantifies the requirements on the figure of merit which is the gate time in units of decoherence time $\tau_d = t_d / T_{2,d}$ relative to $\tau_{b,n} = t_{b,n} / T_{2,b}$ in order for the qudit to yield higher-fidelity

gates. Moreover, it confirms that the infidelity of an ensemble of n identical qubits and the infidelity of a single qudit will generally not have the same linear behaviour in γt even if they have the same T_2 , thus simply having $\tau_d < \tau_{b,n}$ is not sufficient to guarantee a more noise-resilient qudit. Moreover, (11.26) provides a more precise condition on the ratio of figure of merits than a simple qualitative result such as $\frac{d^2}{\log_2(d)}$, while maintaining the expected $O(d^2/\log_2(d))$ behaviour as $d \rightarrow \infty$. In particular, see Section 11.1.3 for the full analytical calculations, including the derivation of the non-trivial factor $\frac{1}{3}$. On a side note, the previous calculations could also be applied to an ensemble of N qudits under identical pure dephasing, in which case we have

$$\overline{\mathcal{E}_{d,N}}(\mathcal{E}_z) = \frac{\gamma t}{12} \frac{Nd^N}{d^N + 1} (d^2 - 1) + \mathcal{O}((\gamma t)^2), \quad (11.27)$$

and for $2^n = d^N$ one obtains

$$\frac{t_{b,n}/T_{2,b}}{t_{d,N}/T_{2,d}} > \frac{c_{d,N}}{c_{b,n}} = \frac{d^2 - 1}{3 \log_2(d)}. \quad (11.28)$$

Let us also note that for L arbitrary (11.27) yields

Definition: (General expression for the Average Gate Infidelity for an ensemble of N qudits under a general quantum channel \mathcal{X})

$$\overline{\mathcal{E}_{d,N}}(\mathcal{X}) = \gamma t N \frac{d^{N-1}}{d^N + 1} \left(\text{Tr}(L^\dagger L) - \frac{1}{d} |\text{Tr}(L)|^2 \right) + \mathcal{O}((\gamma t)^2). \quad (11.29)$$

This equation encompasses both scenarios under investigation in this section until this point. We recall that we construct two systems of equivalent Hilbert Space dimension: a single qudit of dimension d and a system of N qubits. (11.29) reflects two different scalings of the AGI in N and d respectively. In N , it is linear, and, in d , it scales as $\left(\text{Tr}(L^\dagger L) - \frac{1}{d} |\text{Tr}(L)|^2 \right)$ since the dimension affects the definition of L . In Section 11.1.3 we computed that spin-based L lead to a quadratic scaling in d . Therefore, in the qudit subsection, for a single qudit, we study this quantity for fixed $N = 1$ and varying d , while in the multiqubits subsection, it is for fixed $d = 2$, but varying N . The subtlety in the latter case being that, by construction $N := \log_2(d)$, with d being that of the single qudit, hence the different scalings in d in (11.16) and (11.24). See Fig. Fig. 11.1 for a visual summary of the results.

And if each qudit k has a different set of noise parameters (γ_k, L_k) , an even more general formula arises :

$$\overline{\mathcal{E}_{d,N}}(\mathcal{X}) = \frac{d^{N-1}}{d^N + 1} \sum_{k=1}^N \gamma_k t \left(\text{Tr}(L_k^\dagger L_k) - \frac{1}{d} |\text{Tr}(L_k)|^2 \right) + \mathcal{O}((\gamma_k t)^2). \quad (11.30)$$

This formula through its general form, can be applied to any qudits whose physical implementation implies different collapse operators from the ones considered in this work.

11.1.5 Process fidelity & averaged fluctuation-dissipation relation

One may link the fluctuation-dissipation relation obtained in (11.7) with the results regarding average gate infidelities from (11.17),

$$\overline{\mathcal{E}}(\mathcal{X}) = \gamma t \int d\rho^* \mathcal{E}(\rho^*) = \gamma t \int d\rho^* \Delta_* L + \mathcal{O}((\gamma t)^2). \quad (11.31)$$

This integral over the Fubini-Study measure can formally be computed using Weingarten calculus

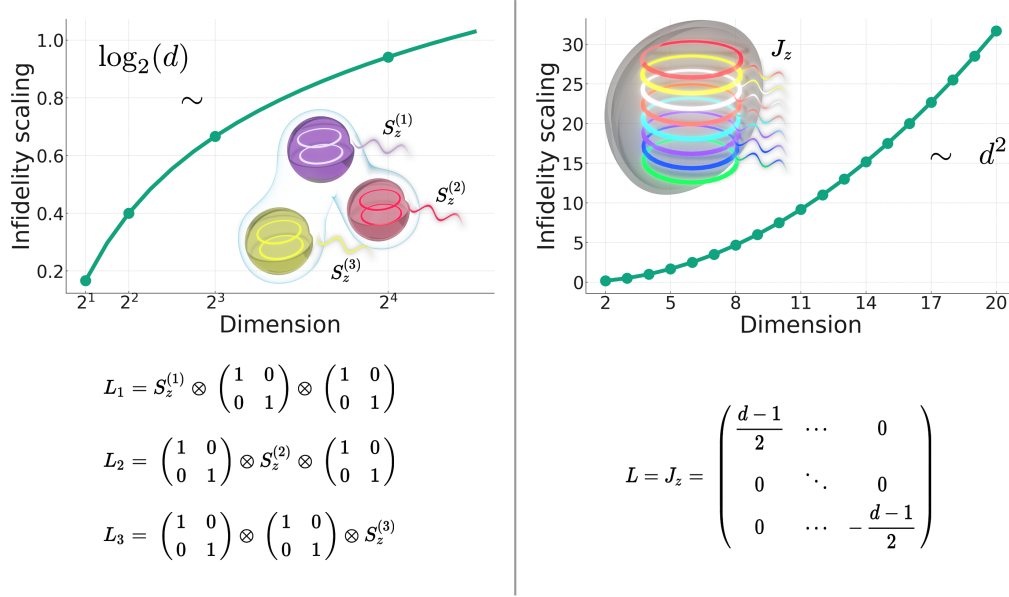


Figure 11.1: Summary diagram illustrating the selected collapse operators and the associated analytically derived expected infidelity scalings as functions of the Hilbert Space dimension, as derived from (11.24) and (11.16). This is depicted for two distinct systems: multiple qubits (left) and a single qudit (right). The term infidelity scaling here refers to the slopes of the first-order-in- γt AGIs, denoted as c in (11.25).

methods [193] which can be expressed as

$$\int d\rho \Delta L = \frac{1}{d+1} \text{Tr}(L^\dagger L) - \frac{1}{d(d+1)} |\text{Tr}(L)|^2, \quad (11.32)$$

leading to (11.17). (*Proof in appendix*)²

In contrast to this formal approach that will prove useful later on, a more physically-informed approach to obtain the same result was proposed in the previous subsections.

Furthermore, it is possible to express all the computed average gate infidelities as process/entanglement infidelities $\mathcal{E}^{(p)}$ making use of the relation $D\mathcal{E}^{(p)} = (D+1)\overline{\mathcal{E}}$, with $D = d, 2^n$ or d^N the dimension of the Hilbert space [194]. This yields the expression

$$\mathcal{E}_{d,n}^{(p)}(\mathcal{X}) = \gamma t \frac{n}{d} \left(\text{Tr}(L^\dagger L) - \frac{1}{d} |\text{Tr}(L)|^2 \right) + \mathcal{O}((\gamma t)^2), \quad (11.33)$$

which is linear in the number of subsystems n . Likewise we have

$$\mathcal{E}_d^{(p)}(\mathcal{E}_z) = \frac{\gamma t}{12} (d^2 - 1) + \mathcal{O}((\gamma t)^2), \quad (11.34)$$

$$\mathcal{E}_{b,n}^{(p)}(\mathcal{E}_z) = \frac{\gamma t}{4} n + \mathcal{O}((\gamma t)^2). \quad (11.35)$$

Note that (11.35) has been verified experimentally, for example by Ozaeta *et al.* [195].

11.2 Numerical validation and deviation

²This methodology will be used again in Chapter 12.

"13, 14, 15... Enfin tous les chiffres impairs jusqu'à 22.
13, 14, 15... In fact all the odd numbers up to 22."

– Perceval, Kaamelott

11.2.1 Fit and deviation from the linear behaviour

Using the procedures described in the [Methods section](#) ([Appendix B](#)), we simulated single qudits of dimension d under pure dephasing, with $H = \mathbb{0}_d$ and small $\gamma t \in [0, 10^{-4}]$ ($\gamma \sim 10^{-4}$ in some nuclear spins in molecular magnets such as in the experiments of Godfrin *et al.* [99]). For example, the simulations were performed for even dimensions $d \in \llbracket 2, 22 \rrbracket$. Fitting the AGIs $\overline{\mathcal{E}}_d(\mathcal{E}_z) = c_d \gamma t$ as a function of γt yielded the slopes c_d that are shown in [Fig. 11.2](#), along with their analytical expression as a function of d predicted in [\(11.16\)](#).

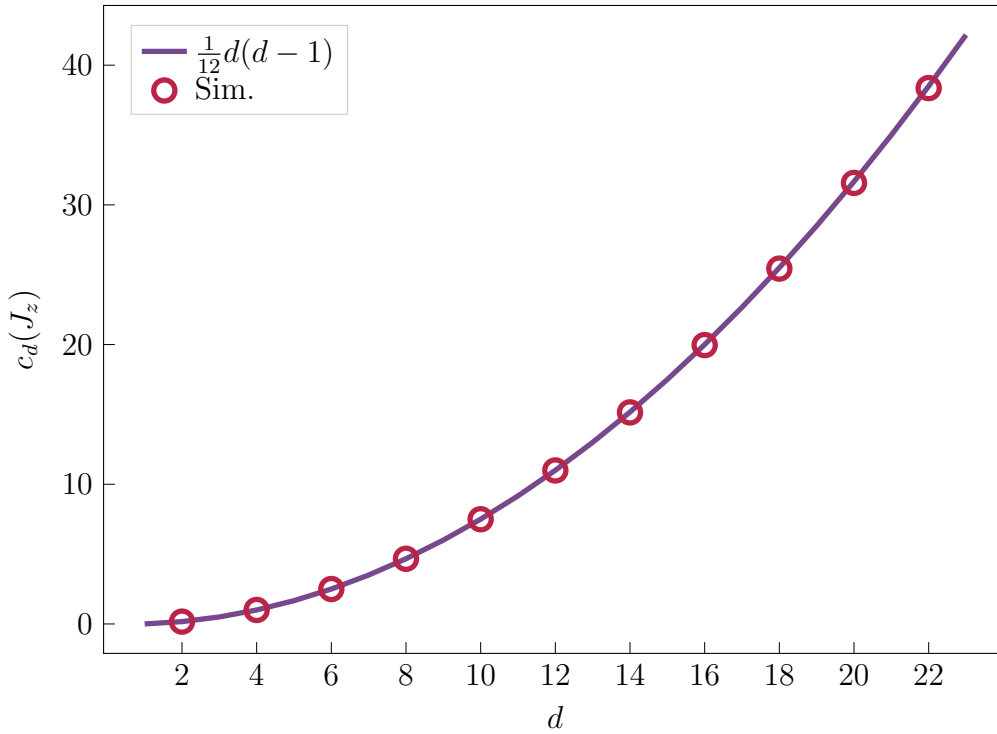


Figure 11.2: Rate of increase of $\overline{\mathcal{E}}_d(\mathcal{E}_z) = c_d(J_z)\gamma t$ as a function of qudit dimension for $H = \mathbb{0}_d$ and $\gamma t \in [0, 10^{-4}]$. The circled dots show the numerical results. The solid curve presents the expected analytical result given by [\(11.16\)](#).

The same simulations were repeated for larger values of $\gamma t \in [5 \times 10^{-4}, 1 \times 10^{-2}]$ and $H = \mathbb{0}_d$. The AGIs were then computed and are shown in [Fig. 11.3](#) alongside the linear infidelity predicted in [\(11.16\)](#). For more insight, [Fig. 11.4](#) shows the relative deviation of the computed infidelities from the expected first-order linear behaviour for a broader range of γt up to 5×10^{-2} .

11.2.2 Gate dependence

While the linearity of the AGI does not scale well with d , [\(11.16\)](#) has another important characteristic that deserves to be studied: the gate independence of the AGI. This was investigated over a large number of random gates for a given dimension d . Random unitary quantum gates in $U(d)$ were sampled from the circular unitary ensemble, which represents a uniform distribution over the unitary square matrices of dimension d , also known as the Haar measure on the unitary group $U(d)$, and implemented

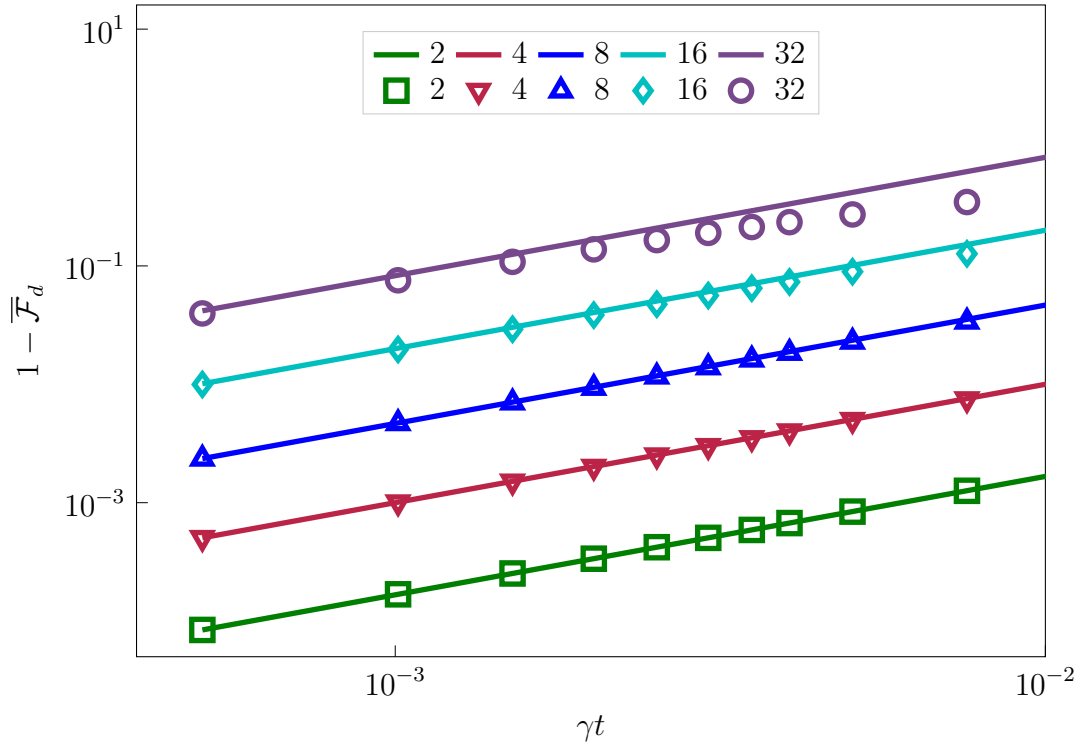


Figure 11.3: Average gate infidelities as a function of γt . The data points show the computed values. The solid lines represent the linear theoretical behaviour from (11.15). Each colour/marker pair corresponds to a different value of d .

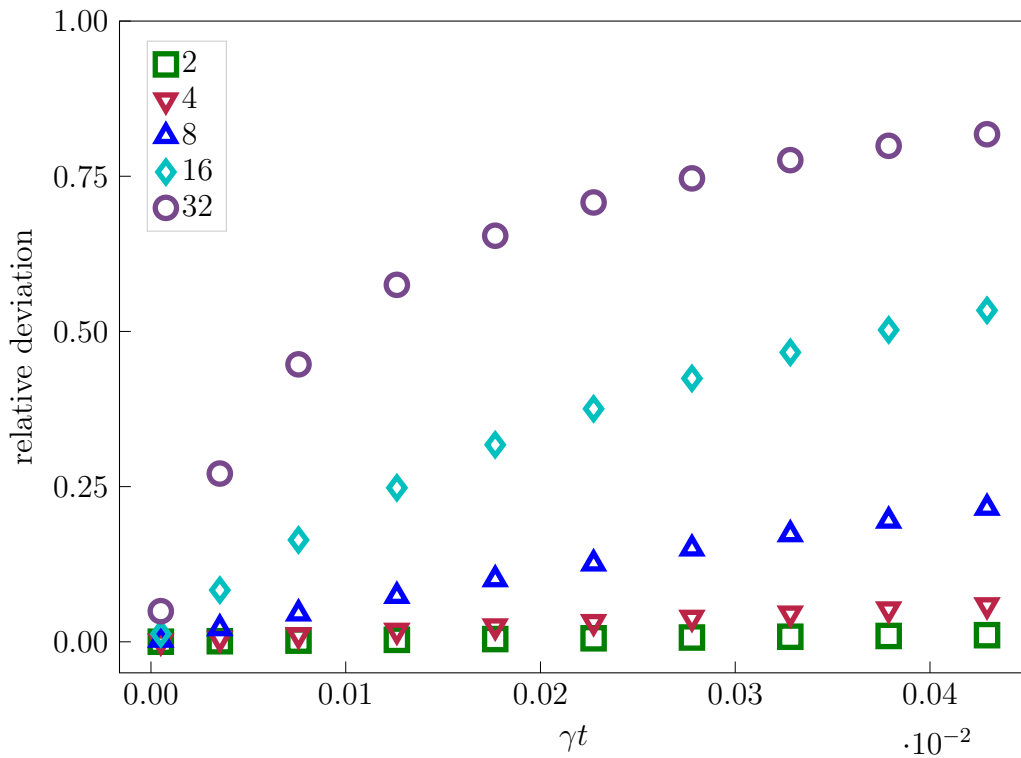


Figure 11.4: Relative deviation $1 - \frac{\overline{\mathcal{E}}_d^{\text{sim}}}{\overline{\mathcal{E}}_d^{\text{th}}}$ as a function of γt for $H = \mathbb{0}_d$. $\overline{\mathcal{E}}_d^{\text{sim}}$ and $\overline{\mathcal{E}}_d^{\text{th}}$ were obtained from numerical computations and (11.16) respectively. Each marker corresponds to a different value of d .

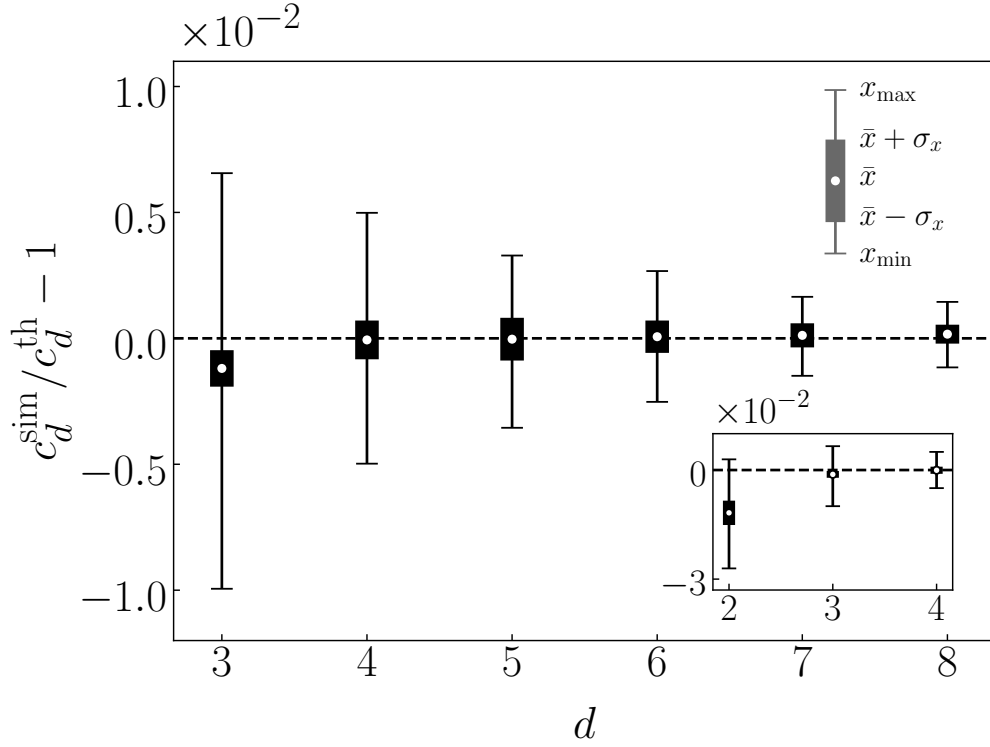


Figure 11.5: Statistical distributions of the relative deviation from the linear behaviour in (11.16) of the numerically obtained infidelity gradients c_d for $N_g = 5000$ gates for $\gamma t \in [10^{-5}, 10^{-3}]$, as a function of the dimension $d \in \llbracket 3, 8 \rrbracket$. The candlestick bar chart should be interpreted as indicated in the upper right, with σ denoting the standard deviation. The lower right inset shows the same results for $d \in \llbracket 2, 4 \rrbracket$.

on a qudit through a Hamiltonian obtained by gradient-ascent methods. We decided to model qudits as ladder systems, with one pulse per transition between adjacent levels as considered for example in the experiments of Godfrin *et al.* [99], for a single-molecule magnet (TbPc₂, qudit with $d = 4$), the $d - 1$ pulses are then each represented by a control Hamiltonian in the interaction picture. More details are discussed in the [methods section](#). There are a large number of parameters that can influence the results under consideration, such as the free-evolution Hamiltonian or the matrix form of the control pulses, both of which are inherent to the physical realization. Therefore other physical implementations and reference frames for the pulses can be considered, and the deviation from linearity they cause needs to be studied in more detail. The AGIs were then computed for $\gamma t \in [10^{-5}, 10^{-3}]$, which lie in the typical ranges observed in current platforms as seen in [Tab. 11.2](#), and their rate of increase as a function of γt was fitted. [Fig. 11.5](#) shows the statistical distributions of the relative deviations from the linear behaviour of the obtained rates.

11.2.3 Other cases than pure dephasing

[Fig. 11.6](#) shows AGI rates of increase for channels different from pure dephasing namely: $\overline{\mathcal{E}}_d(\mathcal{E}_x)$, $\overline{\mathcal{E}}_d(\mathcal{E}_+)$, and $\overline{\mathcal{E}}_d(\mathcal{E}_{x,y,z})$ corresponding to bit-flip, amplitude damping and depolarizing channels respectively. The simulations were performed again with $H = \mathbb{0}_d$, small $\gamma t \in [0, 10^{-4}]$ and for even dimensions $d \in \llbracket 2, 22 \rrbracket$.

Consider \mathcal{R} , the unitary transformation representing a change of basis, such as a 3D real-space rotation. The average gate fidelity defined in (11.8) is invariant under the transformation $\rho \rightarrow \mathcal{R}^\dagger \rho \mathcal{R}$. This is supported by a comparison of the results for $L = J_z$ and $L = J_x$ in [Fig. 11.2](#) and [Fig. 11.6](#),

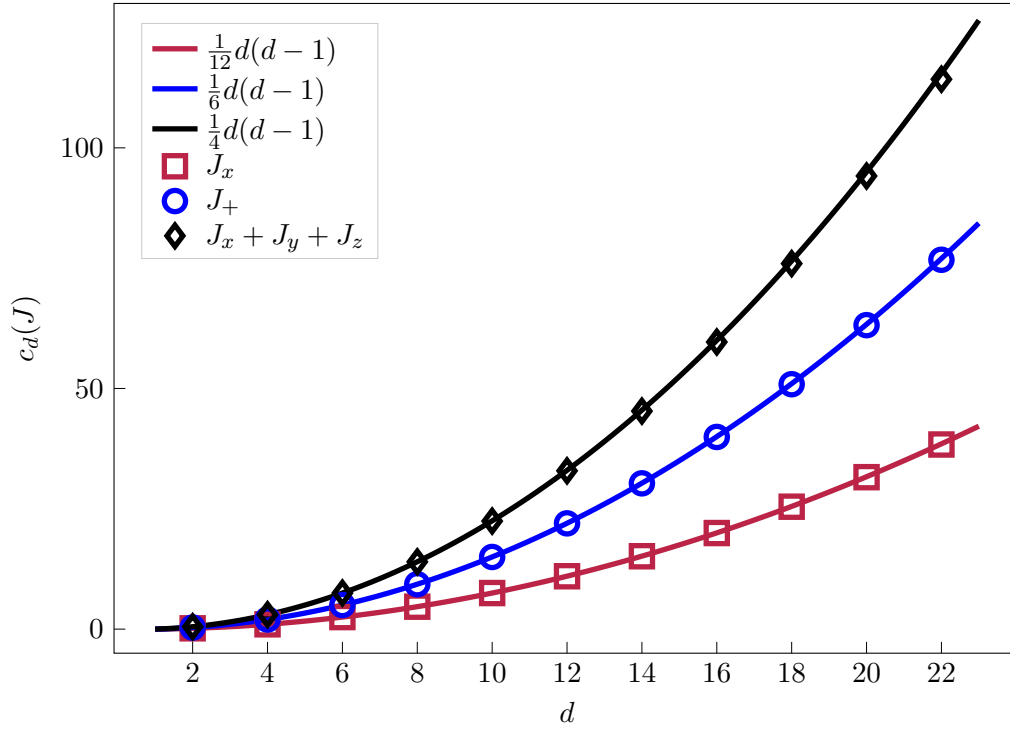


Figure 11.6: Rate of increase of $\overline{\mathcal{E}}_d(\mathcal{X}) = c_d(J)\gamma t$ as a function of the qudit dimension with $H = \mathbb{0}_d$ and $\gamma t \in [0, 10^{-4}]$. The markers show the numerical results. The solid curves represent the expected linear responses according to (11.18). Each marker/colour pair corresponds to a different error channel \mathcal{X} , with collapse operators J specified in the legend.

respectively, since the two gradients appear to share the same dependency in d . Moreover, let $\{l_k\}$ be an ensemble of traceless collapse operators with corresponding error channels $\{e_k\}$, then define $L = \sum_k l_k$ and associated error channel \mathcal{E} . From (11.10) and (11.12), as long as $\text{Tr}(l_k^\dagger l_j) = 0, \forall j \neq k$ then $\overline{\mathcal{E}}(\mathcal{E}) = \sum_k \overline{\mathcal{E}}(e_k)$. Fig. 11.6 again supports such behaviour since simulations with the collapse operator $L = J_+ \equiv J_x + iJ_y$ yield gradients twice as large as, and $L = J_x + J_y + J_z$ yield gradients three times as large as, the $L = J_z$ case.

11.2.4 A single qudit vs an ensemble of qubits

An ensemble of n qubits were simulated under identical pure dephasing, with $H = \mathbb{0}_{2^n}$ and small $\gamma t \in [0, 10^{-4}]$. The simulations were performed for $n \in [1, 7]$. Fitting the AGI $\overline{\mathcal{E}}_{b,n}(\mathcal{E}_z) = c_{b,n}\gamma t$ as a function of γt yielded the slopes $c_{b,n}$ that are shown in Fig. 11.7, along with their analytical expression as a function of d given in (11.24).

The same simulations were performed on a single qudit with dimension $d = 2^n$ and Fig. 11.8 shows the ratios $\frac{c_d}{c_{b,n}}$ for $n \in [1, 6]$ as well as the theoretical curve provided by (11.26) on which the points should be falling. According to the same (11.26), this curve also highlights the critical values of τ_b/τ_d , denoting the figure of merit $\tau_k = t_k/T_{2,k} = \gamma_k t_k/2$, with respect to qudit/qubits advantage in terms of the rate of increase of the AGI.

The AGI gradients obtained for an ensemble of n qubits under identical pure dephasing were expected to follow a $\frac{d \log_2(d)}{4(d+1)}$ relationship as a function of d (11.24). Fig. 11.7 justifies this for small values of γt with the least-square fit now yielding $1 - R^2 < 10^{-7}$. Finally, Fig. 11.8 provides quantitative data for the ratio of the decoherence times of a single qudit vs an ensemble of qubits. Some values of interest are summarised in Tab. 11.1. For example, in order for a qu-8-it (qudit with $d = 8$) to present

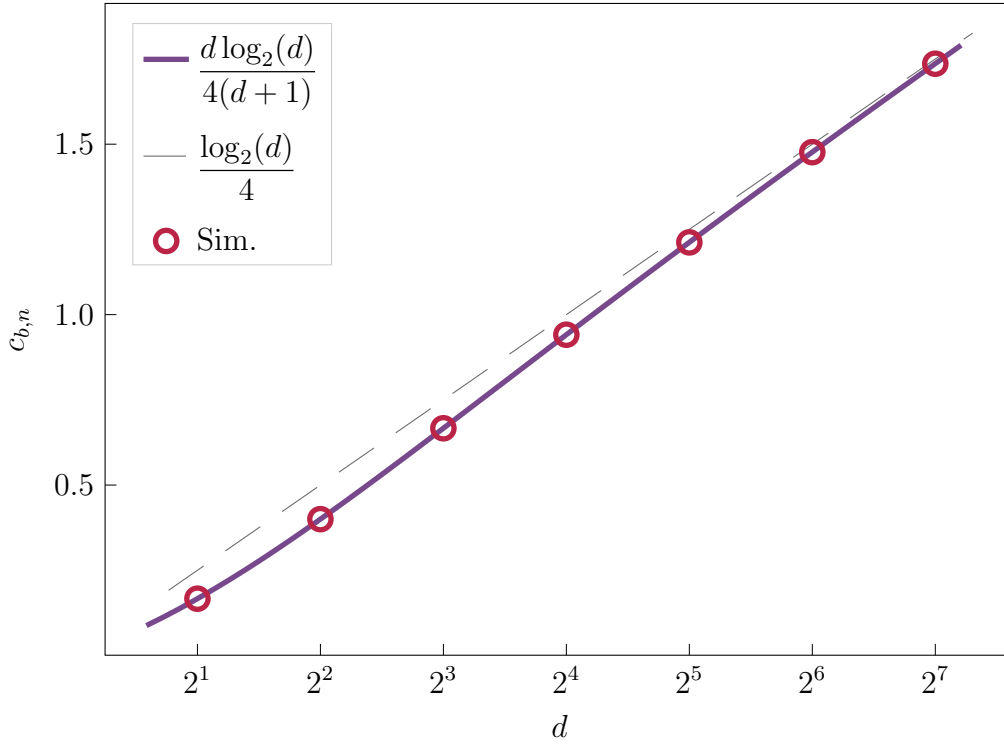


Figure 11.7: Rate of increase of $\overline{\mathcal{E}_{b,n}}(\mathcal{E}_z) = c_{b,n}(\{L_k\})\gamma t$ as a function of qudit dimension $d = 2^n$ with $H = 0_{2^n}$ and $\gamma t \in [0, 10^{-4}]$. The $\{L_k\}$ collapse operators are the ones defined in (11.20). The circled dots show the numerical results. The solid curve presents the expected theoretical result according to (11.24). The dashed line shows $\mathcal{E}_{b,n}^{(p)}(\mathcal{E}_z)$ given in (11.35) which is linear in $n = \log_2(d)$.

a computational fidelity advantage over 3 qubits for a fixed gate time, the qudit platform needs a coherence time at least 7 times longer than the multiqubit platform. Note that an intuitive scaling such as $\frac{d^2}{\log_2(d)}$ would indicate a much more demanding constraint of 21.5.

Number n of qubits	1	2	3	6
Dimension d of the qudit	2	4	8	64
Critical τ_b/τ_d	1	2.5	7	227.5

Table 11.1: Ratios of gate times in units of decoherence times between qubits and qudits for specific values of n and d . τ_b/τ_d needs to be larger than the critical values in order for a single qudit to be advantageous vs an equivalent ensemble of n qubits.

From Tab. 11.2, state-of-the-art single qudit platforms, such as trapped ions [59], present coherence times of the order of 100ms for a single qu-7-it, orders of magnitude longer than superconducting qubits [195, 196, 197, 198]. Trapped ions present $\gamma t \approx 10^{-3}$, while $\gamma t \approx 10^{-2}$ for superconducting qubits; this ratio of 10 would allow qudits with $d \lesssim 10$ to still be advantageous i.e., according to (11.26), the single qu-7-it would still maintain a higher average gate fidelity over one gate acting on the whole Hilbert Space than the multiqubit platform. Another comparison with superconducting qubits could be molecular nuclear spin qudits, where some proposals put $\gamma t \approx 10^{-4}$ (see Moreno-Pineda *et al.* [102]), and whose coherence times are $\sim 6 - 7$ times larger than the superconducting qubit case. With figure of merits $\tau \sim 100$ larger than superconduction platforms, single molecular nuclear spin qudits with

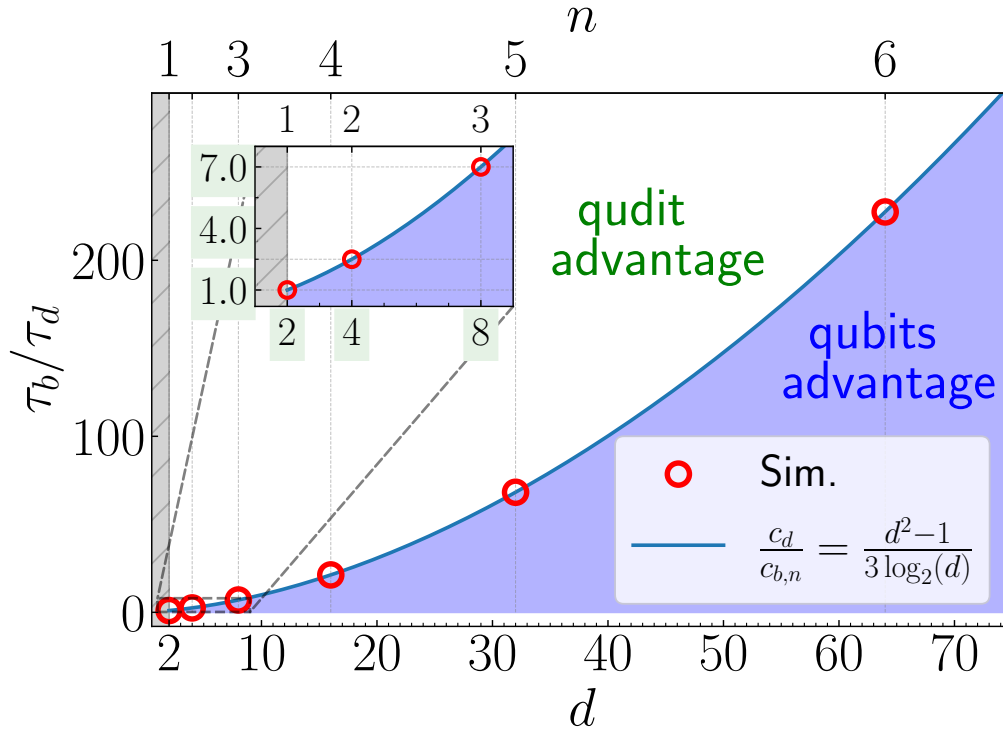


Figure 11.8: Potential range for τ_b/τ_d . The rounded circles show the numerical values obtained for $c_d/c_{b,n}$. The solid curve comes from (11.26) and highlights the theoretical critical values of $T_{2,d}/T_{2,b}$.

$d \lesssim 40$ are still advantageous over equivalent superconducting qubits, i.e. $n \sim 5$. Such high- d qudit platforms can still be conceivable, given that some specific quantum operations on $d = 52$ have already successfully been implemented on, for example, Rydberg atoms [199]. However, it remains to be seen if universal quantum gate generation will become easily achievable in practice with such high d .

Finally, one can compare (11.26) and (11.28) to discuss conditions on N qudits outperforming $N \log_2(d)$ qubits. From this, if a single qudit outperforms $\log_2(d)$ qubits, the advantage remains conserved as long as the multiqubit gate time scales slower from 1 qudit to N qudits than the multiqubit from $\log_2(d)$ to $N \log_2(d)$ qubits.

11.2.5 Summary

Given the rapid development of quantum computing platforms with very different physical properties, such as decoherence time or Hilbert space dimension (see Table II), there is a growing need for detailed elaboration of the tradeoffs between their information density and noise error rates. By combining analytical results and numerical simulations, we have performed a comparative study of gate efficiency for systems composed of sets of qubits or qudits. A fluctuation-dissipation-like relation for the gate infidelity of an operation on a pure state was derived. We then put forward a physically-informed method to obtain the first-order effect of Markovian noise on the *average gate infidelity* (AGI). A connection was made between the latter and the first gate-independent result. The rate of increase of the AGI of a single qudit vs equivalent multiple qubits under pure dephasing was compared. This yielded a critical curve of the ratio of their respective gate times in units of decoherence time, a quantity indicating how time-efficient operations on a particular system are. Values on either side of the curve specify which of the two systems had a higher rate of increase of the AGI. To compete in terms of gate fidelity, as the dimension increases, the efficiency of qudit gates must not simply always be larger than the multiqubit one by a factor $O(d^2/\log_2(d))$, but precisely by a factor $\frac{d^2-1}{3\log_2(d)}$, which

	d	n	T_2	t_n	τ_n	ref.
qubits	2	2	$\sim 10 \mu\text{s}$	60 ns	$\sim 10^{-2}$	[10] (2020)
	2	2	$\sim 2 \mu\text{s}$	51 ns	$\sim 10^{-2}$	[16] (2020)
	2	17	$\sim 30 \mu\text{s}$	$\sim 100 \text{ ns}$	$\sim 10^{-3}$	[200] (2022)
	2	24	$\sim 100 \text{ ms}$	$\sim 200 \mu\text{s}$	$\sim 10^{-3}$	[12] (2021)
	2	1	$\sim 1 \text{ ms}$	$\sim 1 \mu\text{s}$	$\sim 10^{-3}$	[201] (2023)
qudits	4	1	0.32 ms	$\sim 100 \text{ ns}$	$\sim 10^{-4}$	[102] (2018)
	4	1	$\sim 100 \mu\text{s}$	$\sim 150 \text{ ns}$	$\sim 10^{-3}$	[202, 203] ('20,'23)
	3	2	$\sim 100 \text{ ms}$	$\sim 100 \mu\text{s}$	$\sim 10^{-3}$	[59] (2022)
	4	2	∞^3	–	0	[14] (2022)
	52	1	–	$\sim 100 \text{ ns}^4$	–	[199] (2020)

Rydberg atoms , trapped ions , electronic spins in molecular magnets
superconducting qubits , nuclear spins in molecular magnets , photonic qudits

Table 11.2: Decoherence times (T_2) and gate times (t_n) of different qubit/qudit platforms. d and n are the maximum dimension and number of qudits an operation was applied to, while $\tau_n = t_n/T_2$ is the figure of merit.

makes a significant difference for lower values of d for which it provides less demanding constraints. Additionally, analytical expressions of linear response for arbitrary collapse operators and a general multiqutrit system were presented (see (11.18) and (11.29)). They may be useful to those working in the field of quantum computing e.g. to benchmark qudit platforms either in terms of maximal practical d or in terms of conditions on the figure of merit to compensate for the greater noise scaling, in comparison with current state-of-the-art multiqubit platforms.

Numerical simulations contributed to the discussion on the validity and limits of the linear response assumption. This further restricted the ranges of possible $\gamma t \ll 1$ accounting for qudit dimension, gate, and noise type. For example, the larger the dimension, the lower the relative gate-dependent response. Finally, after simulations supported the analytical critical curve, different current platforms were studied with respect to this condition on gate time efficiency. Given equivalent Hilbert space dimensions, viable qudit platforms (leveraging advantageous decoherence times and gate speeds to compensate for the higher rate of increase in AGI) capable of outperforming equivalent state-of-the-art multiqubit ones in gate fidelity have been found for pure dephasing. Moreover, this performance could be extended to qudits with d as large as ~ 40 in the case of nuclear spins in molecular magnets, for example. Some multiqubit platforms still outperform any existing qudit platform regarding scalability in the number of subsystems. However, it is conceivable that some scalable qudit platforms continue to outperform equivalent multiqubit systems in terms of attainable fidelity. Further study of how multiqutrit and multiqubit gate times scale with the number of subsystems is needed. Moreover, this study was limited to first-order noise responses. However, using the notation qu- j -it for a qudit of dimension $d = j$, through carefully chosen quantum error correction schemes, it was recently demonstrated it is possible

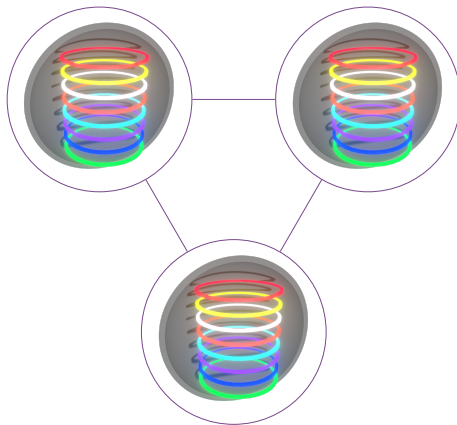
to entirely remove the first-order response of logical qu- k -its embedded in physical qu- d -its ($k < d$) through carefully chosen encodings [167, 168]. In the next chapter (Chapter 12), we will study the gate-dependent response of the AGI, and do a more general higher-order expansion of the AGI.

11.3 Linear and exponential scalings from the perspective of the AGI

The main takeaway from the study done in the previous subsection is that, *in fine*, as qubit technology improves, the advantage of single qudit in terms of gate fidelity will eventually always be surpassed, as the noise of an equivalent single qudit scales exponentially with the number of qubits. However, the study of the AGI has been only limited to a single qudit. However, as the number of qudits is allowed to increase, there will be a new, non-trivial scaling of the AGI with the number of qudits. In particular, the AGI to first order has been shown to be proportional to the gate time, and the latter for a network of N qudits might scale advantageously in N compared to a network of qubits. The same remark can be made for γ , the strength of the noise, which might scale differently in N for qudits compared to qubits.

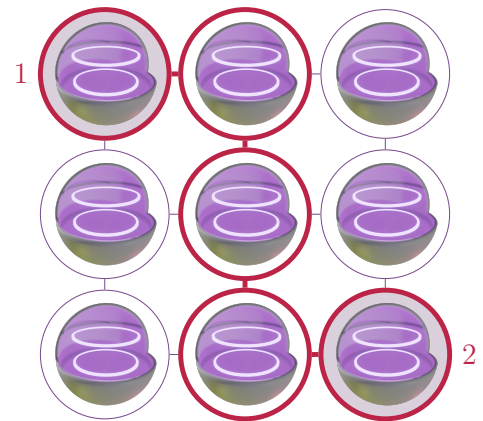
11.3.1 Scaling of the gate durations with the number of qudits

Let us consider a network of N qudits, it can be represented by a graph G with N vertices, each vertex representing a qudit. The edges of the graph represent the interactions between the qudits. For example, Fig. 11.9 shows two different networks of qudits and qubits with a Hilbert Space dimension of $d = 8^3 = 2^9 = 512$. One can see any two-qu-8-it gate can be implemented by a single edge, while an entangling two-qubit gate between the qubits 1 and 2 would require, at minimum, 4 edges and therefore 3 intermediate qubits, to be implemented.



a) A simple complete^a 2D graph representing a network of 3 qu-8-its.

^aFeaturing all-to-all connectivity/Where every qu-8-it is connected to every other.



b) A simple 2D lattice graph representing a network of 9 qubits with a possible marked path to implement a two-qubit gate between qubits 1 and 2.

Figure 11.9: Graphs representing two different networks of qudits and qubits with a Hilbert Space dimension of $d = 8^3 = 2^9 = 512$.

This can be formalized by defining the diameter of a graph.

Definition: (*Diameter of a graph*) The diameter of a graph G is the maximum eccentricity of any vertex in the graph. The eccentricity of a vertex v is the greatest distance between v and any other

vertex. Or, more formally

$$\text{diam}(G) = \max_{u,v \in V(G)} d(u,v), \quad (11.36)$$

where $d(u,v)$ is the distance/minimum number of edges between u and v .

Note: For example, the graph in Fig. 11.9a) has a diameter of 1, while the graph in Fig. 11.9b) has a diameter of 4.

Assuming reasonably that the gate time of an ensemble of N qudits scales linearly with the diameter of the graph, it becomes clear the question of the scaling of the gate time with the number of qudits is a question about the physical constraints on the connectivity between the qudits. In some platforms such as trapped ions, all-to-all connectivity is achievable, and qudits do not present a scaling advantage over qubits since the diameter will always be 1. However, in other platforms, such as superconducting qubits, the connectivity is limited to nearest neighbours and the 2D plane, and qudits would allow for networks with a smaller diameter to be implemented while maintaining the same Hilbert Space dimension, as seen in the examples of Fig. 11.9.

If we consider 2D square lattices with k vertices, the number of edges is $2(\sqrt{k} - 1)$ and the diameter of the graph is $2\sqrt{k}(\sqrt{k} - 1)$. This means that for equivalent Hilbert Space dimension $D = d^N = 2^n$, the gate time will approximately grow as the diameter +1, a.k.a. $2(\sqrt{\log_2(D)} - 1) + 1$ for qubits and $2(\sqrt{\log_d(D)} - 1) + 1$ for qudits.

If one includes this in (11.28), one obtains

$$\frac{t_{b,\log_2(d)}/T_{2,b}}{t_d/T_{2,d}} \frac{2\sqrt{\log_2(D)} + 1}{2\sqrt{\log_d(D)} + 1} \geq \frac{d^2 - 1}{3\log_2(d)}, \quad (11.37)$$

where t_d is the gate time for a single qudit, and $t_{b,\log_2(d)}$ is the gate time for a network of qubits with the same Hilbert Space dimension as the single qudit. Recall that $\tau = t/T_2$, is the figure of merit. This inequality can then be simplified to

$$\frac{\tau_{b,\log_2(d)}}{\tau_d} \underset{N \gg 1}{\gtrsim} \frac{d^2 - 1}{3\log_2(d)} \frac{\sqrt{\log_d(D)}}{\sqrt{\log_2(D)}} = \frac{d^2 - 1}{3(\log_2(d))^{3/2}}. \quad (11.38)$$

See Fig. 11.10 for a visual representation of this inequality, where a new zone is highlighted, where the single qudit is not advantageous, but a sizeable multiqubit 2D-lattice implementation will be advantageous. Referring to (11.37), a large number of N qudits of dimension $d = 64$ would be advantageous over a network of $6N$ qubits for a critical value of $\tau_{b,6N}/\tau_{d,N} \approx 93$, corresponding to a more than factor 2 improvement compared to the single qudit case in Tab. 11.1 ($\tau_b/\tau_d \approx 228$).

The same reasoning can be applied to 3D lattices, where the diameter of the graph is $3\sqrt[3]{k}(\sqrt[3]{k} - 1)$. And (11.38) can be modified to

$$\frac{t_{b,\log_2(d)}}{t_d} \underset{N \gg 1}{\gtrsim} \frac{d^2 - 1}{3\log_2(d)} \frac{\sqrt[3]{\log_d(D)}}{\sqrt[3]{\log_2(D)}} = \frac{d^2 - 1}{3(\log_2(d))^{4/3}}. \quad (11.39)$$

This condition is still eased compared to the single qudit case (11.26), but provides less of an advantage compared to the 2D lattice case.

One can also mention 1D linear chains, where the diameter of the graph is always equal to the number of edges: $k - 1$. The gate time will grow as k , and the condition (11.38) will be

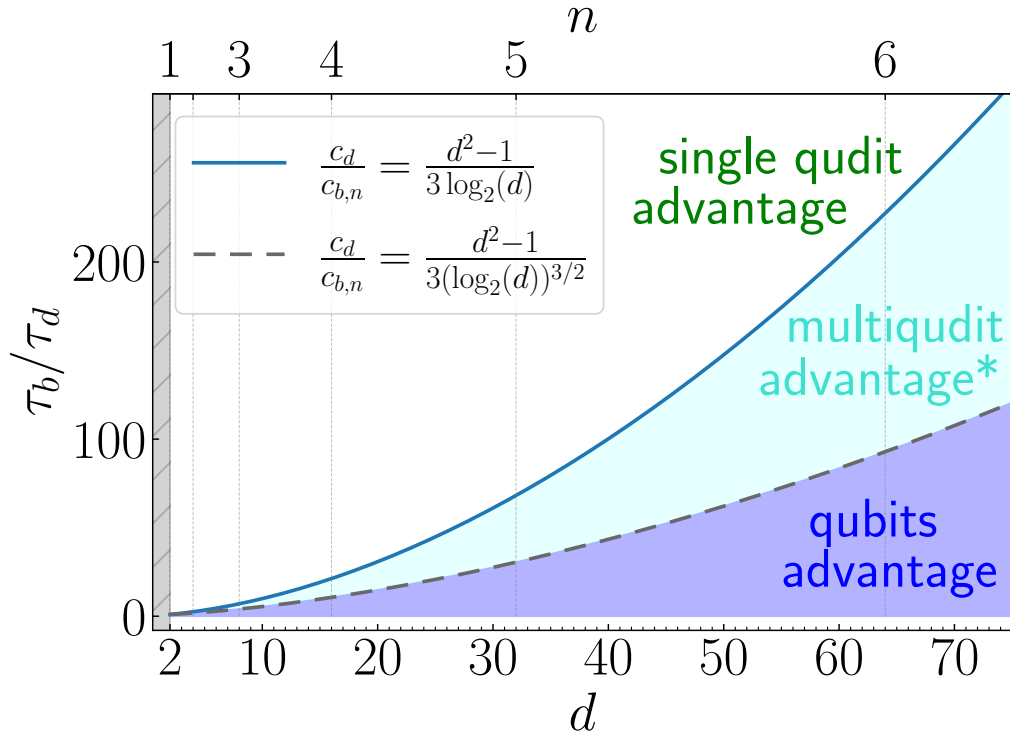


Figure 11.10: Potential range for τ_b/τ_d . In addition to Fig. 11.8, a new zone is highlighted, where the single qudit is not advantageous, but a sizeable multiqudit *2D-lattice implementation will be advantageous.

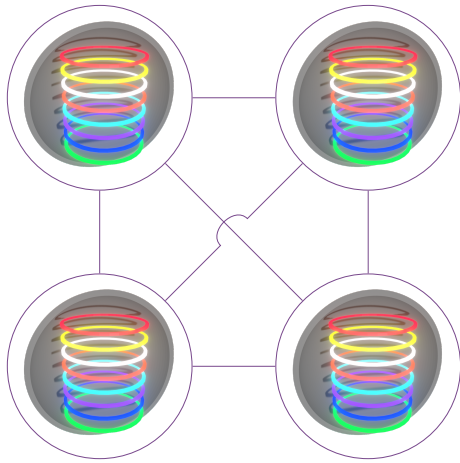
$$\frac{t_{b, \log_2(d)}}{t_d} \underset{N \gg 1}{\gtrsim} \frac{d^2 - 1}{3 \log_d(d) \log_2(D)} = \frac{d^2 - 1}{3 \log_2(d)^2}. \quad (11.40)$$

This condition is the least demanding, and the single qudit will be advantageous for the largest range of τ_b/τ_d values. For example, once again, for $d = 64$, the single qudit will be advantageous over a network of 6 qubits for a critical value of $\tau_{b,6}/\tau_d \approx 13$, corresponding to an almost factor 20 improvement compared to the single qudit case ($\tau_b/\tau_d \approx 228$). As a matter of fact, one of the upscaling proposal for the phthalocyanine SMM nuclear qudit platform of our group is a 1D chain, of $\text{Ln}_x\text{Pc}_{x+1}$ molecules [100, 102] as depicted in Fig. 1.8. This would be a good example of a platform where one gets the most out of the multiqudit advantage in terms of gate fidelity.

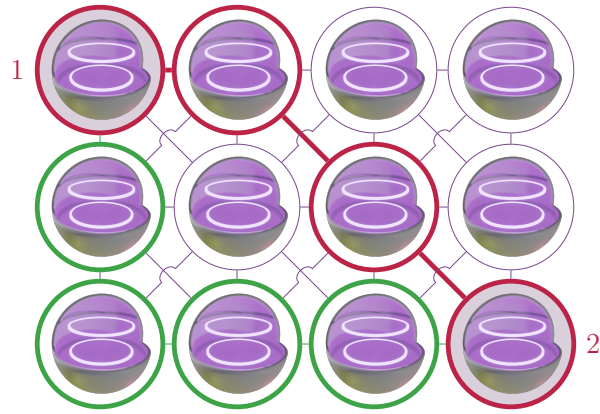
These discussions provide approximate conditions for the figure-of-merit ratios in the large N, n limit, and are not meant to be exact. They provide a qualitative understanding of the scaling of the AGI with the number of qudits, and the potential additional advantages of qudits over qubits in terms of gate fidelity depending on the physical constraints of the platform on connectivity. In order to obtain more precise results, a more detailed study of the noise acting on a network of qudits would be required, and the results would be platform- and setup-specific. For example Fig. 11.11 shows a network that is a bit more complicated than simple 2D square graphs that are physically realizable, and the scaling of the diameter of the graph and consequently the scaling of the gate time with the Hilbert space dimension would be different than previously discussed.

11.3.2 Scaling of the noise strength with the number of qudits

A less trivial reasoning can be applied to the scaling of the noise strength with the number of qudits. In this work, until now, The Lindblad approach with collapse operators was used to model the noise



a) A less trivial 2D graph representing a network of 4 qu-8-its, the bend in the edge between two qubits represents that the connection goes over the other one.



b) A less trivial 2D lattice graph representing a network of 12 qubits with a possible shortest marked path to implement a two-qubit gate between qubits 1 and 2. We see that thanks to the diagonal connections, the diameter of the graph is 3, whereas it would be 5 without them (path in green).

Figure 11.11: Graphs representing two different networks of qudits and qubits with a Hilbert Space dimension of $d = 8^4 = 2^{12} = 1024$.

acting on each single qudit. It may be possible to extend this approach to a network of qudits, by envisioning collapse operators arising from the interactions between the qudits and in particular the interaction between the environment and the physical subsystem mediating the interaction. The physical mechanism underlying such error channels would then become primordial. This is a more complex problem, and the scaling of the noise strength with the number of qudits will depend on the physical constraints. Hence this is a question that will require a more detailed study, and the results are hard to predict in a platform-agnostic way.

Main takeaways from Chapter 11

- **Average Gate Infidelity (AGI):**

- A metric for quantifying the error introduced by noise in quantum gates regardless of the state the gate is applied to.
- Derived a first-order approximation for AGI under small-amplitude noise conditions.

- **Fluctuation-Dissipation Relation:**

- Established a relation linking the infidelity of a perturbed pure state to the fluctuations of the noise operator.
- The infidelity is independent of the Hamiltonian in first order of noise strength.
- Shows that infidelity is proportional to the variance of the noise operator applied to the target state.

- **Qudits vs. Qubits Under Pure Dephasing:**

- For a single qudit, AGI scales as $\overline{\mathcal{E}} \propto \gamma t d(d-1)$.
- For n qubits, AGI scales as $\overline{\mathcal{E}} \propto \gamma t n 2^n$.
- Derived conditions under which a qudit outperforms multiple qubits in terms of gate fidelity, depending on gate times and decoherence rates. A critical value of τ_b/τ_d , where $\tau = t/T_2$, was found for a given Hilbert space dimension

$$\frac{d^2 - 1}{3 \log_2(d)} = \frac{4^n - 1}{3n},$$

which gives the requirements for the qudit to outperform the qubits – if this quantity is larger than the critical value, the qudit is advantageous.

- **Scaling of Gate Durations and Noise:**

- Discussed how gate durations scale with the number of qudits, influenced by system connectivity.
- Considered the impact of connectivity graph diameter on the previously obtained critical value for. Qudit networks seem to be the most advantageous vs qubit networks in 1D chains, followed by 2D lattices.

Chapter Contents

12.1 The Lindblad equation as a superoperator	221
12.2 Perturbative expression of the AGI	224
12.3 Universal bounds on the AGI for large noise and gate times	231

CHAPTER 12

Noisy qudit: Beyond the first-order approach

This chapter presents a summary of our article **Nonlinearity of the Fidelity in Open Qudit Systems: Gate and Noise Dependence in High-dimensional Quantum Computing** submitted for publication in Quantum and uploaded as a preprint manuscript to arXiv. The bibliographical citation of the preprint can be found in [204], and all code and data used to generate the results presented in this study have been made publicly available on Zenodo [205]. The preprint is also included in [Appendix E](#) of this manuscript.

The numerical simulations presented in [Section 11.2](#) have shown that the AGI of a single qudit under pure dephasing scales linearly with the noise strength γt for small values of γt . However, for larger values of γt , the AGI deviates from this linear behaviour. This deviation is due to higher-order terms in the AGI series expansion, which are not accounted for in the first-order approach. In this section, through a perturbative approach, we will investigate the scaling of the AGI with the noise strength for different types of noise channels and discuss the implications of these results for the design of quantum gates.

12.1 The Lindblad equation as a superoperator

Definition: (*Lindblad equation in superoperator form*) The Lindblad equation (11.1) can be written in terms of a superoperator acting on the density matrix ρ as

$$\frac{d\rho}{dt} = \mathcal{S}[\rho] + \mathcal{D}[\rho], \quad (12.1)$$

where $\mathcal{S}[\rho]$ is the unitary evolution of the system and $\mathcal{D}[\rho]$ is the dissipative part of the evolution due to the noise. The superoperator \mathcal{S} is given by

$$\mathcal{S}(t)[\rho] = -i[H(t), \rho], \quad (12.2)$$

while the dissipative superoperator \mathcal{D} is given by

$$\mathcal{D}[\rho] = \gamma_k \sum_k \left(L_k \rho L_k^\dagger - \frac{1}{2} \{L_k^\dagger L_k, \rho\} \right). \quad (12.3)$$

H is the time-dependent Hamiltonian of the system, and L_k are the Lindblad operators corresponding to the noise channels acting on the system.

The solution of the Lindblad equation can also be written as a superoperator acting on the initial density matrix $\rho(0)$ as

$$\begin{aligned}\rho(t) &= \mathcal{E}(t)[\rho(0)], \\ &= \mathcal{T} \exp \left(\int_0^t (\mathcal{S}(t') + \mathcal{D}) dt' \right) [\rho(0)],\end{aligned}\quad (12.4)$$

where \mathcal{T} is the time-ordering operator. The superoperator $\mathcal{E}(t)$ is the quantum channel describing the evolution of the system under the action of the noise.

Moreover, one can define \mathcal{U} as the superoperator describing the ideal unitary evolution of the system with no dissipation, i.e.,

$$\mathcal{U}(t)[\rho] = \mathcal{T} \exp \left(\int_0^t \mathcal{S}(t') dt' \right) [\rho]. \quad (12.5)$$

Looking back at the definition of the AGF (11.8), one can see that it is particularly compatible with this superoperator form of the Lindblad equation since the AGF can in this form be written as

$$\overline{\mathcal{F}}(\mathcal{E}, \mathcal{U}) = \int d\rho_0 \operatorname{Tr} \left(\mathcal{U}^\dagger \circ \mathcal{E}[\rho_0] \rho_0 \right) = \int d\rho_0 \operatorname{Tr} \left(\mathcal{E}[\rho_0] \mathcal{U}[\rho_0] \right), \quad (12.6)$$

the second term is fairly reminiscent of the form of the fidelity between two pure states given in (11.6)

$$\mathcal{F}(\rho(t), \rho^*) = \operatorname{Tr} (\rho(t) \rho^*). \quad (11.6)$$

The **average gate fidelity (AGF)** is then easily interpreted as a normalized integral over all possible initial states. Looking at the AGF from a superoperatorial point of view will prove quite useful as it allows for a more general approach to the problem, and in particular, the study of higher-order terms in the AGF series expansion.

The main advantage of this approach is that it allows to eliminate the need to integrate over the Haar measure, whose evaluation was done exclusively numerically in the previous section. Since, given an arbitrary superoperator M acting on the density matrix, we propose to calculate the integral

$$\int_{\mathcal{H}} \operatorname{Tr}(M[\rho] \rho) d\rho \quad (12.7)$$

using methods from [193] relating to Weingarten calculus. Specifically, we make use of the following result,

$$\begin{aligned}& \int_{\mathcal{H}} U_{ka} U_{ic} \bar{U}_{jb} \bar{U}_{rd} dU \\ &= \frac{1}{(d^2 - 1)} [(\delta_{kj} \delta_{ab} \delta_{ir} \delta_{cd} + \delta_{kr} \delta_{ad} \delta_{ij} \delta_{cb})] - \\ & \quad - \frac{1}{d(d^2 - 1)} [(\delta_{kj} \delta_{ad} \delta_{ir} \delta_{cb} + \delta_{kr} \delta_{ab} \delta_{ij} \delta_{cd})],\end{aligned}\quad (12.8)$$

where, and for the remainder of this section, the indices represent the matrix elements using Einstein sum notation and d is the dimension of the Hilbert space of the system.

Now, beginning with the element-wise definition of the superoperator term,

$$(M[\rho])_{pi} = M_{pi}^{kj} \rho_{kj}, \quad (12.9)$$

where we identify ρ and ρ_0 for convenient usage of the element-wise sum notation, this extends to

$$\begin{aligned} (M[\rho]\rho)_{pq} &= (M[\rho])_{pi} \rho_{iq} \\ &= M_{pi}^{kj} \rho_{kj} \rho_{iq}. \end{aligned} \quad (12.10)$$

Taking the trace of this term corresponds to

$$\begin{aligned} \text{Tr}(M[\rho]\rho) &= \delta_{pq} (M[\rho]\rho)_{pq} \\ &= M_{ri}^{kj} \rho_{kj} \rho_{ir}, \end{aligned} \quad (12.11)$$

where we define $r := p = q$. Rewriting the integral of this expression in terms of the associated unitary operator U leads to

$$\begin{aligned} &\int_{\mathcal{H}} \text{Tr} \left(M \left[U \rho U^\dagger \right] U \rho U^\dagger \right) dU \\ &= \int_{\mathcal{H}} M_{ri}^{kj} (U_{ka} \rho_{ab} \bar{U}_{jb}) (U_{ic} \rho_{cd} \bar{U}_{rd}) dU \\ &= \rho_{ab} M_{ri}^{kj} \rho_{cd} \int_{\mathcal{H}} (U_{ka} \bar{U}_{jb} U_{ic} \bar{U}_{rd}) dU. \end{aligned} \quad (12.12)$$

If we now substitute the result of this integral from (12.8), and evaluate all of the delta function terms, we arrive at

$$\begin{aligned} &\int_{\mathcal{H}} \text{Tr}(M[\rho]\rho) d\rho \\ &= \frac{1}{(d^2 - 1)} \left[\rho_{aa} \rho_{cc} M_{ii}^{jj} + \rho_{ac} \rho_{ac} M_{ki}^{ki} \right] \\ &\quad - \frac{1}{d(d^2 - 1)} \left[\rho_{ac} \rho_{ac} M_{ii}^{jj} + \rho_{aa} \rho_{cc} M_{ki}^{ki} \right] \\ &= \frac{1}{(d^2 - 1)} \left[(\text{Tr}(\rho))^2 \text{Tr}(M[\mathbb{1}_d]) + \text{Tr}(\rho^2) \text{Tr}(M) \right] \\ &\quad - \frac{1}{d(d^2 - 1)} \left[\text{Tr}(\rho^2) \text{Tr}(M[\mathbb{1}_d]) + (\text{Tr}(\rho))^2 \text{Tr}(M) \right]. \end{aligned} \quad (12.13)$$

Returning to the matrix forms from the Einstein sum notation, it can be seen that:

$$\rho_{aa} \rho_{cc} = (\text{Tr}(\rho))^2, \quad (12.14)$$

$$\rho_{ac} \rho_{ac} = \text{Tr}(\rho^2), \quad (12.15)$$

$$M_{ii}^{jj} = \text{Tr}(M[\mathbb{1}_d]), \quad (12.16)$$

$$M_{ki}^{ki} = \text{Tr}(M), \quad (12.17)$$

which results in

$$\begin{aligned} &\int_{\mathcal{H}} \text{Tr}(M[\rho]\rho) d\rho \\ &= \frac{1}{(d^2 - 1)} \left[(\text{Tr}(\rho))^2 \text{Tr}(M[\mathbb{1}_d]) + \text{Tr}(\rho^2) \text{Tr}(M) \right] - \\ &\quad - \frac{1}{d(d^2 - 1)} \left[\text{Tr}(\rho^2) \text{Tr}(M[\mathbb{1}_d]) + (\text{Tr}(\rho))^2 \text{Tr}(M) \right]. \end{aligned} \quad (12.18)$$

Finally, noting that $\text{Tr}(\rho) = 1$, $\text{Tr}(\rho^2) = 1$ and $\rho^2 = \rho$, we arrive at

$$\int_{\mathcal{H}} \text{Tr}(M[\rho]\rho) d\rho = \frac{\text{Tr}(M) + \text{Tr}(M[\mathbb{1}_d])}{d(d+1)}. \quad (12.19)$$

This general result can then be applied to the AGF

$$\bar{\mathcal{F}}(\mathcal{E}, \mathcal{U}) = \int d\rho_0 \text{Tr}(\mathcal{U}^\dagger \circ \mathcal{E}[\rho_0]\rho_0) = \frac{\text{Tr}(\mathcal{U}^\dagger \circ \mathcal{E}) + \text{Tr}((\mathcal{U}^\dagger \circ \mathcal{E})[\mathbb{1}_d])}{d(d+1)} \quad (12.20)$$

Note: The first trace $\text{Tr}(\mathcal{U}^\dagger \circ \mathcal{E})$ is over the $\mathcal{U}^\dagger \circ \mathcal{E}$ superoperator, while the second trace $\text{Tr}((\mathcal{U}^\dagger \circ \mathcal{E})[\mathbb{1}_d])$ is over the $(\mathcal{U}^\dagger \circ \mathcal{E})[\mathbb{1}_d]$ density matrix.

Considering \mathcal{U} and \mathcal{E} are trace-preserving, the AGF can be simplified to

Definition: (*Non-integral form of the AGF*) The average gate fidelity can be written as

$$\bar{\mathcal{F}}(\mathcal{E}, \mathcal{U}) = \frac{\text{Tr}(\mathcal{U}^\dagger \circ \mathcal{E}) + d}{d(d+1)} = \frac{1}{d+1} + \frac{\text{Tr}(\mathcal{U}^\dagger \circ \mathcal{E})}{d(d+1)}. \quad (12.21)$$

Note: Recalling the relation of the AGF to the process fidelity $\mathcal{F}^{(p)}$ [189]

$$\mathcal{F} = \frac{d\mathcal{F}^{(p)} + 1}{d+1}, \quad (12.22)$$

yields the process fidelity as

$$\bar{\mathcal{F}}^{(p)} = \frac{\text{Tr}(\mathcal{U}^\dagger \circ \mathcal{E})}{d^2}. \quad (12.23)$$

One can also express the AGI in terms of the superoperators \mathcal{U} and \mathcal{E} as

Definition: (*Non-integral form of the AGI*) The average gate infidelity can be written as

$$\bar{\mathcal{E}}(\mathcal{E}, \mathcal{U}) = 1 - \bar{\mathcal{F}}(\mathcal{E}, \mathcal{U}) = \frac{d}{d+1} - \frac{\text{Tr}(\mathcal{U}^\dagger \circ \mathcal{E})}{d(d+1)}. \quad (12.24)$$

While the expression (12.24) is more practical to work with than the integral one, it is still not useable without a closed form for \mathcal{E} , which is generally not available.

12.2 Perturbative expression of the AGI

Let's consider the simplest case of a time-independent Hamiltonian H and a time-independent dissipative superoperator \mathcal{D} , and a single dissipative channel of strength γ such that $\mathcal{D} = \gamma\mathcal{L}$, thus the superoperator \mathcal{E} can be written as

$$\mathcal{E} = \exp \left(\int_0^t (\mathcal{S} + \gamma \mathcal{L}) dt' \right) = \exp (\mathcal{S}t + \gamma \mathcal{L}t). \quad (12.25)$$

Note: The exponential can only be naively factored in the case of commuting superoperators, which is not the case in general.

In the special cases where the superoperators commute, the superoperator \mathcal{E} can be written as

$$\mathcal{E} = \exp (\mathcal{S}t) \exp (\gamma \mathcal{L}t) = \mathcal{U} \exp (\gamma \mathcal{L}t), \quad (12.26)$$

such that the AGF simplifies to

$$\overline{\mathcal{F}}(\mathcal{E}, \mathcal{U}) = \frac{1}{d+1} + \frac{\text{Tr}(\exp(\gamma \mathcal{L}t))}{d(d+1)} = \frac{1}{d+1} + \frac{e^{\text{Tr}(\mathcal{L})\gamma t}}{d(d+1)}. \quad (12.27)$$

In order to obtain a perturbative expression for the AGI, one can expand the superoperator \mathcal{E} in powers of γ as [206]

$$\mathcal{E} = e^{\mathcal{S}t} + e^{\mathcal{S}t} \sum_{m=1}^{\infty} \gamma^m \left(\int_0^t \int_0^{t_1} \cdots \int_0^{t_{m-1}} \left(\prod_{i=1}^m e^{-\mathcal{S}t_i} \mathcal{L} e^{\mathcal{S}t_i} \right) dt_m \cdots dt_2 dt_1 \right). \quad (12.28)$$

We recall $\mathcal{U} = e^{\mathcal{S}t}$ and, consequently, $\mathcal{U}^\dagger = e^{-\mathcal{S}t}$. The AGI can then be written as

$$\begin{aligned} \overline{\mathcal{E}}(\mathcal{E}, \mathcal{U}) &= \frac{d}{d+1} - \frac{\text{Tr}(\mathcal{U}^\dagger \circ \mathcal{E})}{d(d+1)} \\ &= -\frac{1}{d(d+1)} \sum_{m=1}^{\infty} \gamma^m \text{Tr} \left(\int_0^t \int_0^{t_1} \cdots \int_0^{t_{m-1}} \left(\prod_{i=1}^m e^{-\mathcal{S}t_i} \mathcal{L} e^{\mathcal{S}t_i} \right) dt_m \cdots dt_2 dt_1 \right). \end{aligned} \quad (12.29)$$

Now, in order to render the term in the trace into a more computationally tractable form, we make use of the eponymous lemma of Campbell resulting from the Baker-Campbell-Hausdorff (BCH) Formula [207, 208],

$$e^X Y e^{-X} = \sum_{n=0}^{\infty} \frac{[(X)^n, Y]}{n!}, \quad (12.30)$$

utilising the iterated commutator defined by the recursion relation

$$[(X)^n, Y] = [X, [(X)^{n-1}, Y]] \quad (12.31)$$

with the halting condition $[(X)^0, Y] = Y$. With \mathcal{S} and \mathcal{L} time-independent, the trace in (12.29) simplifies to (*Proof in appendix*)

$$\gamma^m \text{Tr} \left(\int_0^t \int_0^{t_1} \cdots \int_0^{t_{m-1}} \left(\prod_{i=1}^m e^{-\mathcal{S}t_i} \mathcal{L} e^{\mathcal{S}t_i} \right) dt_m \cdots dt_2 dt_1 \right) \quad (12.32)$$

$$= (\gamma t)^m \sum_{n_1=0}^{\infty} \sum_{n_2=0}^{\infty} \cdots \sum_{n_m=0}^{\infty} \text{Tr} \left(\prod_{i=1}^m \frac{(-t)^{n_i} [(\mathcal{S})^{n_i}, \mathcal{L}]}{n_i! \sum_{j=i}^m (n_j + 1)} \right) \quad (12.33)$$

$$= (\gamma t)^m \left[\frac{\text{Tr}(\mathcal{L}^m)}{m!} + \sum_{n_1=1}^{\infty} \sum_{n_2=1}^{\infty} \cdots \sum_{n_m=1}^{\infty} \text{Tr} \left(\prod_{i=1}^m \frac{(-t)^{n_i} [(\mathcal{S})^{n_i}, \mathcal{L}]}{n_i! \sum_{j=i}^m (n_j + 1)} \right) \right]. \quad (12.34)$$

Therefore, the AGI can be expressed as

Definition: (*Perturbative expression of the AGI*) The average gate infidelity can be expanded in powers of the noise strength γ as

$$\bar{\mathcal{E}}(\mathcal{E}, \mathcal{U}) = -\frac{1}{d(d+1)} \sum_{m=1}^{\infty} (\gamma t)^m \left[\frac{\text{Tr}(\mathcal{L}^m)}{m!} + \sum_{n_1=1}^{\infty} \sum_{n_2=1}^{\infty} \cdots \sum_{n_m=1}^{\infty} \text{Tr} \left(\prod_{i=1}^m \frac{(-t)^{n_i} [(\mathcal{S})^{n_i}, \mathcal{L}]}{n_i! \sum_{j=i}^m (n_j + 1)} \right) \right]. \quad (12.35)$$

The inner sum over the n 's in (12.35) is split into the first Hamiltonian-/gate-independent term and the remaining terms, which are gate-dependent.

Figure 12.1 shows the cumulative correction terms up to fourth order in γt for the QFT gate QFT_4 (see Tab. 9.2) acting on a qudit of $d = 4$. With $t = 1$ normalised by the amplitude of the control Hamiltonian $H_c = -i \log(\text{QFT}_4)$, the pure dephasing operator $L = J_z$ was applied over the couplings $\gamma t \in [0, 0.5]$. While the first-order approximation shows good agreement with the simulated AGI for small $\gamma t \ll 1$, as seen in the previous chapter, the deviation becomes significant as the coupling grows large, necessitating the addition of the higher-order corrections.

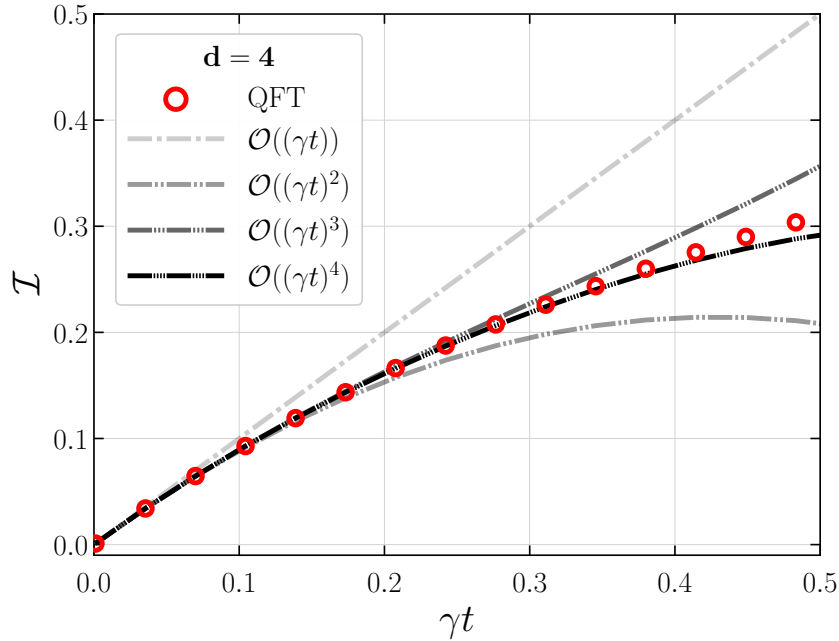


Figure 12.1: Comparison of the first four correction terms of the AGI to numerical simulations. AGIs for the QFT gate applied to a $d = 4$ qudit undergoing pure dephasing ($L = J_z$) at couplings $\gamma t \in [0, 0.5]$. The discrete points (red) represent the simulated AGI values, while the successive dashed-dotted lines represent the correction terms from first to fourth order.

12.2.1 First-order AGI

To check the validity of the perturbative expansion, we first consider the first-order-in- γt term in the AGI expansion, that should be equal to the AGI obtained in the previous chapter (11.17) for the quantum channel \mathcal{X} acting on a single qudit via the collapse operator L .

$$\bar{\mathcal{E}}(\mathcal{X}) = \frac{\gamma t}{d+1} \left(\text{Tr}(L^\dagger L) - \frac{1}{d} |\text{Tr}(L)|^2 \right) + \mathcal{O}((\gamma t)^2). \quad (11.17)$$

The first order term in the AGI expansion is given by

$$\overline{\mathcal{E}}^{(1)}(\mathcal{E}, \mathcal{U}) = -\frac{1}{d(d+1)} \gamma t \left[\text{Tr}(\mathcal{L}) + \sum_{n_1=1}^{\infty} \text{Tr} \left(\frac{(-t)^{n_1} [(\mathcal{S})^{n_1}, \mathcal{L}]}{n_1! (n_1 + 1)} \right) \right]. \quad (12.36)$$

Using (A.33), the trace of the superoperator $\mathcal{L} = L \boxtimes L^\dagger - \frac{1}{2} LL^\dagger \boxtimes \mathbb{1}_d - \frac{1}{2} \mathbb{1}_d \boxtimes LL^\dagger$ can be expressed as

$$\begin{aligned} \text{Tr}(\mathcal{L}) &= \text{Tr}(L) \text{Tr}(L^\dagger) - \frac{1}{2} \text{Tr}(LL^\dagger) \text{Tr}(\mathbb{1}_d) - \frac{1}{2} \text{Tr}(\mathbb{1}_d) \text{Tr}(LL^\dagger) \\ &= |\text{Tr}(L)|^2 - d \text{Tr}(LL^\dagger) \end{aligned} \quad (12.37)$$

and the second term in the sum actually vanishes, since the trace of a commutator is zero and $\forall, n_1 > 0$

$$\text{Tr} \left(\frac{(-t)^{n_1} [(\mathcal{S})^{n_1}, \mathcal{L}]}{n_1! (n_1 + 1)} \right) = \frac{(-t)^{n_1} \text{Tr}([(\mathcal{S})^{n_1}, \mathcal{L}])}{n_1! (n_1 + 1)} = 0 \quad (12.38)$$

Equation (12.36) then simplifies to (11.17), as expected.

Note: Note that (12.38) also confirms that to first order in γ , the AGI expansion to first order in t is exact, and there is no need to consider terms of the form γt^k with $k > 1$ in the AGI expansion. Moreover, since the effect of the gate is included in \mathcal{S} , there is no gate-dependent term to first order in γ .

12.2.2 Second-order AGI

The second-order term in the AGI expansion is given by

$$\overline{\mathcal{E}}^{(2)}(\mathcal{E}, \mathcal{U}) = -\frac{(\gamma t)^2}{d(d+1)} \left[\frac{\text{Tr}(\mathcal{L}^2)}{2} + \sum_{n_1=1}^{\infty} \sum_{n_2=1}^{\infty} \frac{(-t)^{n_1+n_2} \text{Tr}([(\mathcal{S})^{n_1}, \mathcal{L}] [(\mathcal{S})^{n_2}, \mathcal{L}])}{n_1! (n_2 + 1)! (n_1 + n_2 + 2)} \right]. \quad (12.39)$$

Interestingly, it can be simplified (*Proof in appendix*), using the definition $s \equiv n_1 + n_2 + 2$, to

Definition: (*Second-order-in-noise AGI*) The second-order term in the AGI expansion is given by

$$\overline{\mathcal{E}}^{(2)}(\mathcal{E}, \mathcal{U}) = -\frac{(\gamma t)^2}{d(d+1)} \left[\frac{\text{Tr}(\mathcal{L}^2)}{2} + \sum_{\substack{s=2 \\ s \text{ even}}}^{\infty} \text{Tr}(\mathcal{L} [(\mathcal{S})^s, \mathcal{L}]) \frac{(-t)^s}{(s+2)!} \right]. \quad (12.40)$$

Computationally, this simplification is very useful, as it reduces the complexity quite significantly, the double sum over n_1 and n_2 becomes a single sum over s , with only one iterated commutator to compute per term instead of two, and finally, the sum is only necessary over even values of s , since it vanishes for odd values of s .

The second-order-in- γ term in the AGI expansion is also the first one to depend on the gate \mathcal{U} via its dependence on the superoperator \mathcal{S} . Note the first gate-dependent term in the AGI expansion is of order $\gamma^2 t^4$, since it corresponds to the $s = 2$ first term in the sum.

Definition: (*Lowest order gate-dependent AGI term*) The lowest order gate-dependent term in the AGI expansion is given by

$$-\frac{\gamma^2 t^4}{24d(d+1)} \text{Tr}(\mathcal{L}[\mathcal{S}, [\mathcal{S}, \mathcal{L}]]) = -\frac{(\gamma t^2)^2}{12d(d+1)} [\text{Tr}(\mathcal{S}^2 \mathcal{L}^2) - \text{Tr}((\mathcal{S}\mathcal{L})^2)]. \quad (12.41)$$

Equation (12.41) is then the proeminent term responsible for the gate-dependent deviations observed in Fig. 11.5 in the previous chapter.

Explicit operator form

The two terms in (12.40), the Hamiltonian-independent term $\text{Tr}(\mathcal{L}^2)$ and the Hamiltonian-dependent term, can be expressed, not in terms of the superoperators, but in terms of the operators L and H .

The Hamiltonian-independent term is a simple matter of expressing the square of the superoperator \mathcal{L} in terms of the operators L , the vectorized form of the superoperator defined in (A.8) and (A.31) proves quite useful here, as it allows us to write the square of the superoperator as

$$\begin{aligned} \text{vec}(\mathcal{L}^2) &= \left(L^* \otimes L - \frac{1}{2} \left(L^\dagger L^* \otimes \mathbb{1}_d + \mathbb{1}_d \otimes L^\dagger L \right) \right)^2 \\ &= (L^*)^2 \otimes L^2 - \frac{1}{2} L^* L^\dagger L^* \otimes L - \frac{1}{2} L^* \otimes L^\dagger L^2 + \dots \end{aligned} \quad (12.42)$$

And by use of (A.33), the cyclic property of the trace, and some fortuitous cancellations, we find that

$$\text{Tr}(\mathcal{L}^2) = |\text{Tr}(L^2)|^2 + \frac{1}{2} \text{Tr}(L^\dagger L)^2 + \frac{d}{2} \text{Tr}((L^\dagger L)^2). \quad (12.43)$$

Similarly, the Hamiltonian-dependent term can be expressed in terms of the operators L and H as (*Proof in appendix*)

$$\begin{aligned} &\text{Tr}(\mathcal{L}[(\mathcal{S})^s, \mathcal{L}]) \\ &= \sum_{k=0}^s \sum_{j=0}^k \sum_{l=0}^{s-k} \binom{s}{k} \binom{k}{j} \binom{s-k}{l} (-1)^{s+k-j-l} \times \\ &\times \text{Re} \left[\text{Tr}(LH^{k-j} LH^{s-k-l})^* \text{Tr}(LH^j LH^l) \right. \\ &+ \frac{1}{2} \text{Tr}(L^T L^* H^{s-j-l})^* \text{Tr}(L^T L^* H^{j+l}) \\ &+ \frac{1}{2} \text{Tr}(L^T L^* H^{k-j} L^T L^* H^{s-k-l})^* \text{Tr}(H^{j+l}) \\ &- \text{Tr}(LH^{k-j} L^T L^* H^{s-k-l})^* \text{Tr}(LH^{j+l}) \\ &\left. - \text{Tr}(L^T L^* H^{k-j} LH^{s-k-l})^* \text{Tr}(LH^{j+l}) \right] \end{aligned} \quad (12.44)$$

These expressions are quite complex, and might not be of significant analytical use, but they are of great computational value, as they allow for the direct computation of the AGI expansion terms without resorting to computing the superoperators \mathcal{L} and \mathcal{S} . The latter are $(d \times d) \times (d \times d)$ matrices,

while the operators L and H are only $d \times d$ matrices, and therefore the computational cost of the former is significantly higher than the latter. However, this is to be compared with the increased number of summing terms, as the superoperator form is only a sum over s from 2 to the chosen cutoff s_{\max} , while the operator form requires additional sums over k, j , and l for each s .

The complexity of the superoperator form is therefore $O(s_{\max}^2 d^6)$ while the operator form is $O(s_{\max}^3 d^3)$, and the choice of which form to use will depend on the specific problem at hand. For example for s_{\max} fixed a system of small dimension d will benefit from the superoperator form, while a system of large dimension will benefit from the operator form. Reciprocally for fixed d , a system with a large characteristic time t would require a larger s_{\max} and therefore benefit from the superoperator form, while a system with a small characteristic time would benefit from the operator form.

12.2.3 Pure dephasing example and error correction considerations

Second-order for $L = J_z$

If the collapse operator is $L = J_z$ as in the pure dephasing case, we can define $\mathcal{L} = \mathcal{J}_z$, just as it was calculated for the first order in (11.16), one can calculate the second-order gate-independent term in the AGI expansion in (12.40) as

$$\text{Tr}(\mathcal{J}_z^2) = \frac{d^2(3 - 5d^2 + 2d^4)}{120}, \quad (12.45)$$

this allows us express the $\gamma^2 t^2$ correction in terms of the first-order correction term from (11.17), as

$$\overline{\mathcal{E}}^{(2)} = -\frac{(\gamma t)^2}{d(d+1)} \frac{\text{Tr}(\mathcal{J}_z^2)}{2} = -(\gamma t) \frac{2d^2 - 3}{20} \overline{\mathcal{E}}^{(1)}. \quad (12.46)$$

However, it is not necessarily the case that any m -th order expression can be written recursively in terms of the previous order. Equation (12.46) for the second-order appears to be a special case.

The expression in (12.46) allows one to quantify the deviation observed in Fig. 11.3 in the previous chapter.

Gate-independent term

One can study the evolution of the AGI when no gates are applied and the system is left to evolve under the sole action of the collapse operators. The AGI expansion is then given by (12.35) with $\mathcal{S} = \mathbb{0}_{d \times d}$ and hence $\mathcal{U} = \exp(\mathcal{S}t) = \mathbb{1}_{d \times d}$.

Definition: (AGI for $\mathcal{S} = \mathbb{0}_{d \times d}$)

$$\overline{\mathcal{E}}(\mathcal{E}, \mathbb{1}_{d \times d}) = -\frac{1}{d(d+1)} \sum_{m=1}^{\infty} \frac{\text{Tr}((\gamma t \mathcal{L})^m)}{m!} = \frac{1}{d(d+1)} \text{Tr}(\mathbb{1}_{d \times d} - e^{-\gamma t \mathcal{L}}). \quad (12.47)$$

It would also be useful to express the term $\text{Tr}(\mathcal{L}^m)$ in terms of the operator L , here we assume $L = L^\dagger = L^*$, and thus

$$\text{Tr}(\mathcal{L}^m) = \text{Tr}\left(\left(L^* \otimes L - \frac{1}{2}L^\dagger L \otimes \mathbb{1} - \frac{1}{2}\mathbb{1} \otimes L^\dagger L\right)^m\right) \quad (12.48)$$

$$= m! \sum_{k_1+k_2+k_3=m} \frac{\text{Tr}(L^{k_1+2k_2}) \text{Tr}(L^{k_1+2k_3})}{k_1!k_2!k_3!(-2)^{k_2+k_3}}. \quad (12.49)$$

Therefore in the case of pure dephasing with $L = J_z$, we have that the m -th order trace $\text{Tr}(\mathcal{L}^m)$ scales as $O(d^{2(m+1)})$.

This qualitative scaling study can be used to analyze the work of Chiesa *et al.* [181]. In their approach, a logical qubit is implemented within a qudit system using a proposed binomial encoding. This encoding facilitates a quantum error correction protocol that renders the logical qubit robust to pure dephasing up to order $(\gamma t)^{m-1}$, where $d = 2(m+1)$ is the dimension of the physical qudit. As the order of error correction increases, so does the required dimension of the physical qudit. Based on the discussion so far regarding the AGI's scaling with the dimension, one can then assess how this increased dimension affects the error correction capabilities of the system.

The average gate infidelity (AGI) of such a system, denoted as $\overline{\mathcal{E}}^{(m)}$, to first non-vanishing order, scales as follows:

$$\overline{\mathcal{E}}^{(m)} = \frac{(\gamma t)^m |\text{Tr}(\mathcal{L}^m)|}{d(d+1)m!}.$$

Given the expression for d as a function of m , this becomes approximately:

$$\overline{\mathcal{E}}^{(m)} \sim O\left((\gamma t)^m \frac{m^{2m}}{m!}\right).$$

It is important to note that while $(\gamma t)^m$ decreases with increasing m (or equivalently, d) — as expected for a dephasing process — the term $m^{2m}/m!$ increases with m . Therefore, given a fixed (small) value of $\gamma t \ll 1$, set by the physical constraints of the system, maintaining the infidelity at an acceptable level $\ll 1$ imposes an upper bound on the corrected order m , and consequently, on the dimension d of the physical qudit.

The condition for this bound can be expressed as:

$$\begin{aligned} \frac{(\gamma t)^m m^{2m}}{m!} &\ll 1, \\ m \ln(\gamma t) + 2m \ln(m) - \ln(m!) &\ll 0, \\ m \ln(\gamma t) + 2m \ln(m) - m \ln(m) + m &\ll 0, \\ \ln(m) &< \ln\left(\frac{1}{\gamma t}\right) - 1, \\ \log_{10}(d) &\lesssim \log_{10}\left(\frac{1}{\gamma t}\right). \end{aligned} \quad (12.50)$$

This implies that for a system where γt is known, the dimension of the qudit is approximately bounded by the order of magnitude of $\frac{1}{\gamma t}$. If the time t also scales with the dimension d , as indicated in the work of Chiesa *et al.* [181], where the encoding time scales with d , then the dimension is ultimately bounded by the order of magnitude of $\frac{1}{\sqrt{\gamma t}}$, where t is the gate time of the physical qudit.

An exact value of this bound can be determined by computing $\text{Tr}(\mathcal{L}^m)$ in (12.49) for a given m and solving for m such that:

$$\overline{\mathcal{E}}^{(m)} > \frac{\gamma t}{12} d(d-1), \quad (12.51)$$

which would indicate that the impact of the additional noise channels, arising from the increased dimension of the qudit, has exceeded the error correction capabilities of the system. At this point, the system's performance with error correction is worse than that of the logical qudit of dimension d without error correction. Note that in (12.51), the value of t may depend on the dimension of the qudit (or m), and it can differ on both sides of the inequality; specifically, the encoding and decoding operations may require different times in the error-corrected and uncorrected cases.

Furthermore, finding the dimension d such that:

$$\frac{\partial}{\partial d} \left(\frac{\overline{\mathcal{E}}^{(m)}}{\frac{\gamma t}{12} d(d-1)} \right) = 0 \quad (12.52)$$

yields the optimal dimension of the qudit for a given γ . This is the point where the error is corrected to the highest possible order before the noise channels introduced by each additional dimension begin to degrade the system's performance.

Let us define by

$$\mathcal{R} \equiv \frac{\frac{\gamma t}{12} d(d-1)}{\overline{\mathcal{E}}^{(m)}}, \quad (12.53)$$

the approximate gain in error correction due to the encoding compared to the unencoded case. Figure 12.2 shows the behaviour of \mathcal{R} as a function of γt for different spin qudits of spin $S = (d-1)/2$. Moreover, the colored regions indicate the range of γt for which the error correction capabilities of the qudit of dimension $d = 2S + 1$ are surpassing the ones for higher d . Figure 12.3 represents the same study, assuming however that the gate time of the error corrected logical qubit scales linearly with the dimension of the qudit, where we observe γt thresholds one order of magnitude lower than in Fig. 12.2. It is to be noted that this is only a qualitative approximate result, and the exact values of $\overline{\mathcal{E}}^{(m)}$ and $\overline{\mathcal{E}}^{(1)}$ that aren't truncated at the first non-vanishing order would yield a more accurate result, that would probably correspond to γt thresholds one additional order of magnitude lower. However, this approximation is sufficient to illustrate the behaviour of the error correction capabilities of the system as a function of the noise level and the dimension of the qudit.

12.3 Universal bounds on the AGI for large noise and gate times

Throughout the numerous numerical simulations of a large set of random gates and their corresponding AGI computations conducted in this work, we consistently observed that the AGIs plateaus, that they reach at high noise level and/or long gate times, exhibit upper and lower bounds, as well as means, that only depend on the dimension. This is for example shown in Fig. 12.4, that shows the said behaviour for qubit gates under pure dephasing. Denoting them as \mathcal{I}_{\max}^* , \mathcal{I}_{\min}^* , and $\mathcal{I}_{\text{mean}}^*$, respectively, they are given precisely by

$$\mathcal{I}_{\max}^* = 1 - \frac{1}{d+1}, \quad (12.54)$$

$$\mathcal{I}_{\min}^* = 1 - \frac{1}{d}, \quad (12.55)$$

$$\mathcal{I}_{\text{mean}}^* = 1 - \frac{2}{d+1}. \quad (12.56)$$

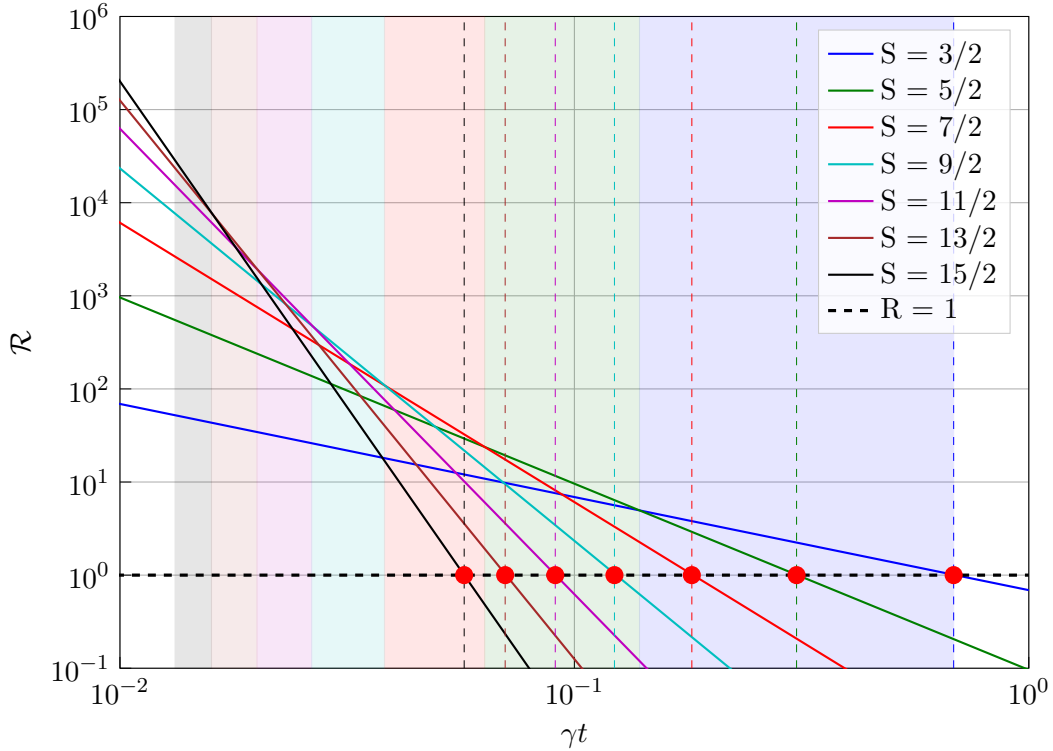


Figure 12.2: Approximate gain in error correction \mathcal{R} as a function of γt for different values of S . Each curve represents a system with a logical qubit encoded in a spin S system that is a physical qudit of dimension $d = 2(m + 1)$. Each colored region indicates the range of γt for which the error correction capabilities of the qudit of dimension $d = 2S + 1$, for the corresponding S , are optimal. The red points indicate the crossing points of the curves with the line $\mathcal{R} = 1$, which correspond to the non-error corrected physical qudit.

Referring to (12.24)

$$\overline{\mathcal{E}}(\mathcal{E}, \mathcal{U}) = 1 - \frac{1}{d+1} - \frac{\text{Tr}(\mathcal{U}^\dagger \circ \mathcal{E})}{d(d+1)}, \quad (12.24)$$

we can rewrite these values as consequences of the behaviour of the superoperator $\mathcal{U}^\dagger \circ \mathcal{E}$ as $t \rightarrow \infty$ and/or $\gamma \rightarrow \infty$.

$$\mathcal{I}_{\max}^* = 1 - \frac{1}{d+1} \implies \text{Tr}(\mathcal{U}^\dagger \circ \mathcal{E}) = 0, \quad (12.57)$$

$$\mathcal{I}_{\min}^* = 1 - \frac{1}{d} \implies \text{Tr}(\mathcal{U}^\dagger \circ \mathcal{E}) = d, \quad (12.58)$$

$$\mathcal{I}_{\text{mean}}^* = 1 - \frac{2}{d+1} \implies \text{Tr}(\mathcal{U}^\dagger \circ \mathcal{E}) = 1. \quad (12.59)$$

Considering the Kraus decomposition of the superoperator $\text{vec}(\mathcal{U}^\dagger \circ \mathcal{E}) = \sum_{k=1}^K E_k^* \otimes E_k$ as defined in (A.35)¹, we can write the trace as

$$\text{Tr}(\mathcal{U}^\dagger \circ \mathcal{E}) = \sum_{k=1}^K |\text{Tr}(E_k)|^2. \quad (12.60)$$

¹With the Kraus operators $U^\dagger E_k \rightarrow E_k$.

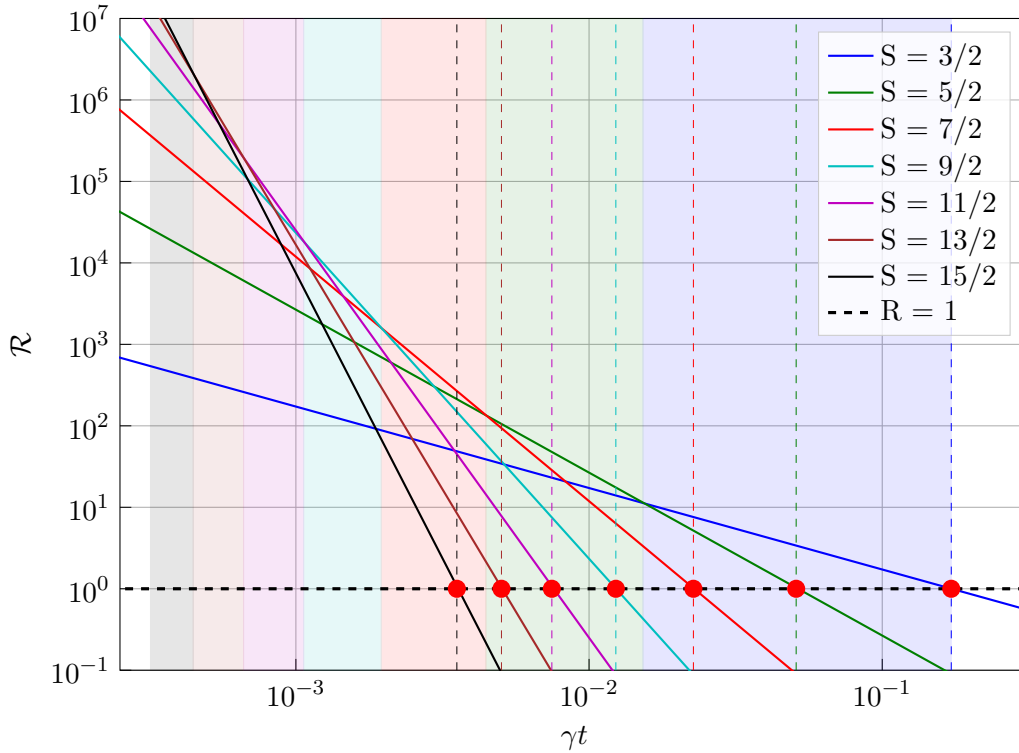


Figure 12.3: Approximate gain in error correction \mathcal{R} as a function of γt for different values of S , assuming the gate time of the error corrected qubit scales linearly with m , and t is then the gate time of the physical qudit. Each curve represents a system with a logical qubit encoded in a spin S system that is a physical qudit of dimension $d = 2(m + 1)$. Each colored region indicates the range of γt for which the error correction capabilities of the qudit of dimension $d = 2S + 1$, for the corresponding S , are optimal. The red points indicate the crossing points of the curves with the line $\mathcal{R} = 1$, which correspond to the non-error corrected physical qudit.

Therefore, proving that the AGI is bounded by \mathcal{I}_{\min}^* and \mathcal{I}_{\max}^* is equivalent to proving that the sum of the squares of the traces of the Kraus operators is bounded by d and 0 , respectively. (*Proof in appendix*)

This confirms the observation that there is a universal bound on the AGI for large dephasing noise and gate times, and that this bound values only depends on the dimension of the system.

Moreover, the gates that reach these bounds possess a specific structure relative to the noise channel, or vice-versa:

- **Maximum AGI** (\mathcal{I}_{\max}^*):
 - Occurs when $\text{Tr}(\mathcal{U}^\dagger \circ \mathcal{E}) = 0$.
 - The quantum channel is completely uncorrelated with the target unitary operation.
 - Represents a completely noisy channel relative to the gate.
 - For example, for pure dephasing, $L = J_z$, this is the case if the unitary is a SHIFT gate which cyclically flips the states downwards ($|k \bmod d\rangle \rightarrow |(k - 1) \bmod d\rangle$) and is a qudit generalization of the X gate.
- **Minimum AGI** (\mathcal{I}_{\min}^*):
 - Occurs when $\text{Tr}(\mathcal{U}^\dagger \circ \mathcal{E}) = d$.
 - One can show that this is the case if \mathcal{S} and \mathcal{L} commute and \mathcal{L} has d steady states, then \mathcal{E} is

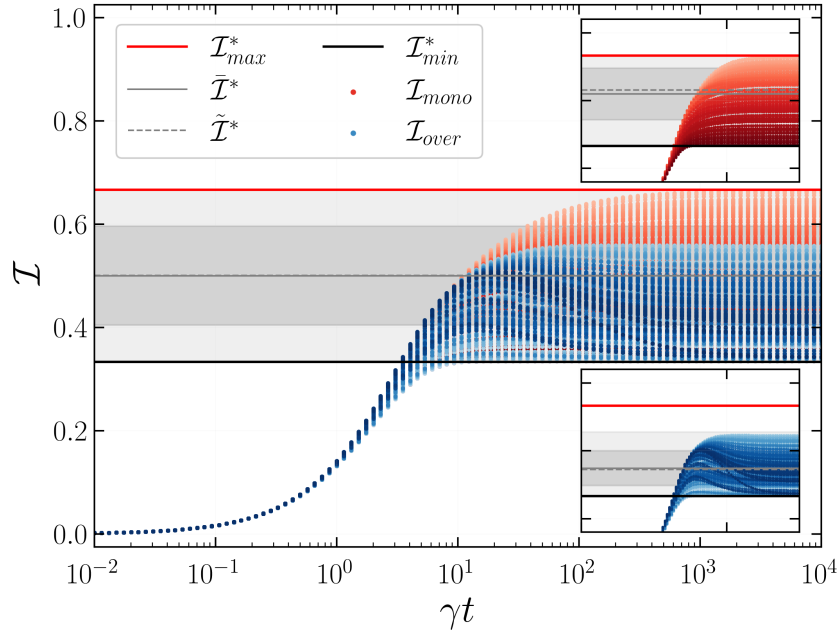


Figure 12.4: Large- γt behaviour of the AGIs for Haar-random qubit gates under pure dephasing. Simulations of the AGI were performed for a sample of one million (300 displayed) Haar-random qubit ($d = 2$) gates under pure dephasing ($L = J_z$) for $\gamma t \in [10^{-2}, 10^4]$. For each gate, the AGI curves fall into one of two groups, exhibiting different behaviour near their respective saturation points $((\gamma t)^*)$. The curves in red (\mathcal{I}_{mono}) approach their plateau values monotonically from below. The blue curves (\mathcal{I}_{over}) rapidly approach their plateau values, before overshooting once with a single turning point, and then converging monotonically from above. The degree of blue shading for each curve indicates the degree of overshoot above the plateau value. All sampled gates converged to their \mathcal{I}^* plateau values within the range $[\mathcal{I}_{min}^*, \mathcal{I}_{max}^*]$ indicated by the black and red horizontal lines.

simply² $\mathcal{U} \exp(\gamma t \mathcal{L})$, thus $\text{Tr}(\mathcal{U}^\dagger \circ \mathcal{E}) = \text{Tr}(e^{\gamma t \mathcal{L}}) \xrightarrow{\gamma t \rightarrow +\infty} d$.

– This is in particular the case if \mathcal{U} is the identity superoperator since then $\mathcal{S} = \mathbb{0}_{d \times d}$.

• **Mean AGI** ($\mathcal{I}_{\text{mean}}^*$):

– Occurs when $\text{Tr}(\mathcal{U}^\dagger \circ \mathcal{E}) = 1$.

– The channel has an average level of correlation with the target unitary.

– This is interestingly the case for the QFT gate $U = (QFT_d)_{ij} = \frac{1}{\sqrt{d}} e^{2\pi i \frac{ij}{d}}$ and the pure dephasing channel $L = J_z$.

An in-depth study of the computational costs, convergence properties in both γ and t of the perturbative series, as well as a more detailed analysis of the bounds and their implications, is presented in our paper **Nonlinearity of the Fidelity in Open Qudit Systems: Gate and Noise dependence in High-dimensional Quantum Computing** [204].

²see (12.26). Moreover $\text{Tr}(e^{\gamma t \mathcal{L}}) \xrightarrow{\gamma t \rightarrow +\infty} d$ since \mathcal{L} has d eigenvalues.

Main takeaways from Chapter 12

- **Lindblad Equation in Superoperator Form:**
 - Reformulated the Lindblad equation using superoperators, facilitating the analysis of open quantum systems.
 - Enabled the expression of the average gate fidelity (AGF) in terms of superoperators, simplifying the integration over the Haar measure.
- **Perturbative Expansion of the Average Gate Infidelity (AGI):**
 - Developed a series expansion of the AGI that includes higher-order terms, capturing nonlinearity in the fidelity.
- **First-Order AGI:**
 - Demonstrated that higher-order commutator terms vanish at first order, simplifying the expression.
- **Second-Order AGI:**
 - Derived the second-order term, revealing first non-vanishing gate-dependent contributions to the AGI in the perturbative expansion.
 - Provided explicit operator forms for computational convenience.
- **Examples and Error Correction Implications:**
 - Applied the expansion to the pure dephasing case with $L = J_z$, illustrating the calculation of higher-order terms.
 - Discussed how the increased dimension d of a qudit impacts error correction capabilities, highlighting a trade-off between noise suppression with supplementary levels and increased number of noise channels.
- **Universal Bounds on AGI:**
 - Identified upper and lower bounds on the AGI at high noise levels, dependent only on the system dimension d .

Chapter Contents

13.1 Rotating Wave Approximation and Rotating Frame	237
13.2 Quantum Speed Limits	243
13.3 An overview of gate generation methods	251
13.4 Towards optimal qudit gates	258

CHAPTER 13

Optimal gate generation

The main takeaway from the previous chapters is that as the dimension increases, the computational fidelity of the operations decreases and an important quantity, the figure of merit γt has been identified, which is the product of the noise strength and the gate time. This quantity is crucial in determining the optimal dimension of the system for a given noise strength and gate time. In order to improve the performance of a qudit system, whether to increase the dimension d , or to simply improve the fidelity of the gates, it is necessary to improve this figure of merit to counteract the pure dephasing. One way is to mitigate the noise by engineering the system to reduce the noise strength γ , or to reduce the gate time t . In this chapter, we will explore the latter option, by optimizing the gate generation process to reduce the gate time.

13.1 Rotating Wave Approximation and Rotating Frame

13.1.1 Laboratory frame to rotating frame

Let's consider a d -level system in the laboratory frame that evolves with the hamiltonian

$$H_{\text{lab}} = H_0 + \sum_{k=1}^d u_k(t) H_k \quad (13.1)$$

where H_0 is the free, so-called "drift", Hamiltonian, if we define the computational basis as the eigenbasis of H_0 with eigenvalues $\{\omega\}$, then H_0 is diagonal. The H_k are the control Hamiltonians, and $u_k(t)$ are the control fields. We can further simplify the problem by considering a single control field $u(t)$ and a single control Hamiltonian H_c , as this methodology can be generalized to multiple control fields and Hamiltonians [209]. In this case we have

$$H_{\text{lab}} = H_0 + u(t) H_c. \quad (13.2)$$

Let's consider a control H_c of the following form

$$H_c = \sum_{n' > n} g_{n,n'} \sigma_{n,n'}^x, \quad (13.3)$$

where $\sigma_{n,n'}^x$ is the flip operator between states $|n\rangle$ and $|n'\rangle$, and $g_{n,n'}$ is the coupling strength between these states, the summation is over all $d(d-1)$ possible transitions. Typically, only a few of these transitions are driven by the control field, so only a few $g_{n,n'}$ are non-zero.

Assuming $u(t)$ can be decomposed into a Fourier series,

$$u(t) = \sum_{k=-\infty}^{\infty} u_k \cos(\omega_k t + \phi_k), \quad (13.4)$$

it can be shown that only the ω_k close to the resonance frequencies $\omega_{n,n'} = \omega_{n'} - \omega_n$ with corresponding non-vanishing $g_{n,n'}$ will have a significant effect on the system, and the other terms can be neglected, rewriting $u(t)$ as

$$u(t) = \sum_{n'>n} u_{n,n'} \cos(\omega_{n,n'} t + \phi_{n,n'}). \quad (13.5)$$

To move from the laboratory frame to the rotating frame and eliminate the high-frequency oscillations of the control fields, allowing us to go to the rotating wave approximation picture, we use a unitary transformation defined by a time-dependent operator $R(t)$ [209]. This transformation simplifies the analysis.

Note: In order for the computational states $|0\rangle$ and $|1\rangle$ (and $\dots |d-1\rangle$ for qudits), to stay the same between different reference frames, $R(t)$ needs to be diagonal.

The transformation to the rotating frame is given by:

$$|\psi\rangle_{\text{rot}} = e^{-iR(t)} |\psi\rangle_{\text{lab}}, \quad (13.6)$$

$$H_{\text{rot}}(t) = e^{-iR(t)} H_{\text{lab}}(t) e^{iR(t)} - \frac{dR(t)}{dt}. \quad (13.7)$$

Interaction Picture Hamiltonian

We define $R(t)$ as a linear combination of the diagonal operators corresponding to the energies of the states involved in the transitions. Specifically, we set:

$$R(t) = \sum_n \omega_n t |n\rangle \langle n| = H_0 t \quad (13.8)$$

where ω_n are the eigenvalues of the free Hamiltonian H_0 , corresponding to the energy levels of the system. This operator $R(t)$ captures the free evolution of each energy level and allows us to move into a frame where this evolution is effectively "rotated away."

Substituting $H_{\text{lab}}(t) = H_0 + u(t)H_c$ into (13.7), we obtain:

$$H_{\text{rot}}(t) = e^{-iR(t)} (H_0 + u(t)H_c) e^{iR(t)} - \frac{dR(t)}{dt} \quad (13.9)$$

$$= e^{-iR(t)} H_0 e^{iR(t)} + e^{-iR(t)} u(t) H_c e^{iR(t)} - \frac{dR(t)}{dt}. \quad (13.10)$$

Since H_0 commutes with $R(t)$ (both are diagonal in the computational basis), the first term simplifies:

$$e^{-iR(t)} H_0 e^{iR(t)} = H_0. \quad (13.11)$$

Since $R(t)$ is defined as in (13.8), its derivative is:

$$\frac{dR(t)}{dt} = \sum_n \omega_n |n\rangle \langle n| = H_0. \quad (13.12)$$

Substituting back into (13.10), we find that the terms involving H_0 cancel out:

$$H_{\text{rot}}(t) = H_0 + e^{-iR(t)} u(t) H_c e^{iR(t)} - H_0 \quad (13.13)$$

$$= e^{-iR(t)} u(t) H_c e^{iR(t)}. \quad (13.14)$$

Thus, the new Hamiltonian depends only on the transformed control Hamiltonian. We proceed to compute $e^{-iR(t)} H_c e^{iR(t)}$.

Note: We realize this is then simply the interaction picture Hamiltonian with no controls (see Appendix A.2.5) and we can write it as $H_{\text{rot}}(t) = H_{\text{int}}(t)$.

Recall that the control Hamiltonian is given by:

$$H_c = \sum_{n' > n} g_{n,n'} \sigma_{n,n'}^x, \quad (13.15)$$

where $\sigma_{n,n'}^x = |n\rangle \langle n'| + |n'\rangle \langle n|$ is the flip operator between states $|n\rangle$ and $|n'\rangle$, and $g_{n,n'}$ is the coupling strength.

Since $R(t)$ is diagonal, its action on $\sigma_{n,n'}^x$ is straightforward:

$$e^{-iR(t)} \sigma_{n,n'}^x e^{iR(t)} = e^{-i(\omega_n - \omega_{n'})t} |n\rangle \langle n'| + e^{i(\omega_n - \omega_{n'})t} |n'\rangle \langle n| \quad (13.16)$$

where we have used the property:

$$e^{-iR(t)} |n\rangle \langle n'| e^{iR(t)} = e^{-i(\omega_n - \omega_{n'})t} |n\rangle \langle n'|. \quad (13.17)$$

Substituting (13.16) back into (13.14), we get:

$$H_{\text{int}}(t) = u(t) \sum_{n' > n} g_{n,n'} e^{-i(\omega_n - \omega_{n'})t} |n\rangle \langle n'| + \text{h.c.} \quad (13.18)$$

This is the Hamiltonian in the interaction picture, assuming that $u(t)$ consists of oscillating terms at frequencies close to the transition frequencies $\omega_{n,n'} = \omega_{n'} - \omega_n$ as mentioned previously, we can write:

$$u(t) = \sum_{n' > n} u_{n,n'}(t) \cos((\omega_{n,n'} - \delta_{n,n'})t + \phi_{n,n'}), \quad (13.19)$$

where $\delta_{n,n'} \ll \omega_{n,n'}$ is the detuning from the resonance frequency, and $\phi_{n,n'}$ is the phase of the control field for the transition between states $|n\rangle$ and $|n'\rangle$.

Using the identity $\cos(a) = \frac{1}{2} (e^{ia} + e^{-ia})$, we can rewrite (13.19) as:

$$u(t) = \sum_{n' > n} \frac{u_{n,n'}(t)}{2} \left[e^{i((\omega_{n,n'} - \delta_{n,n'})t + \phi_{n,n'})} + e^{-i((\omega_{n,n'} - \delta_{n,n'})t + \phi_{n,n'})} \right]. \quad (13.20)$$

Substituting (13.20) into (13.18), we obtain:

$$H_{\text{int}}(t) = \sum_{n' > n} \frac{u_{n,n'}(t)g_{n,n'}}{2} \left[e^{i((\omega_{n,n'} - \delta_{n,n'})t + \phi_{n,n'})} + e^{-i((\omega_{n,n'} - \delta_{n,n'})t + \phi_{n,n'})} \right] e^{-i\omega_{n,n'}t} |n\rangle \langle n'| + \text{h.c.} \quad (13.21)$$

$$= \sum_{n' > n} \frac{u_{n,n'}(t)g_{n,n'}}{2} \left[e^{-i(\delta_{n,n'}t - \phi_{n,n'})} + e^{-i(2\omega_{n,n'}t - \delta_{n,n'}t - \phi_{n,n'})} \right] |n\rangle \langle n'| + \text{h.c.} \quad (13.22)$$

Under the Rotating Wave Approximation (RWA), we neglect the rapidly oscillating terms at frequency $2\omega_{n,n'}$ because their average effect over time is negligible. This leaves us with:

$$H_{\text{int}}(t) = \sum_{n' > n} \frac{u_{n,n'}(t)g_{n,n'}}{2} e^{-i(\delta_{n,n'}t - \phi_{n,n'})} |n\rangle \langle n'| + \text{h.c.} \quad (13.23)$$

Substituting back into (13.23), we have:

Definition: (*Interaction Picture Hamiltonian*)

$$\begin{aligned} H_{\text{int}}(t) &= \sum_{n' > n} \Omega_{n,n'}(t) \left[e^{i\phi_{n,n'}(t)} |n\rangle \langle n'| + e^{-i\phi_{n,n'}(t)} |n'\rangle \langle n| \right], \\ &= \sum_{n' > n} \left[\Omega_{n,n'}(t) \cos(\phi_{n,n'}(t)) \sigma_{n,n'}^x + \Omega_{n,n'}(t) \sin(\phi_{n,n'}(t)) \sigma_{n,n'}^y \right], \end{aligned} \quad (13.24)$$

where we have defined:

$$\Omega_{n,n'}(t) \equiv \frac{u_{n,n'}(t)g_{n,n'}}{2}, \quad (13.25)$$

$$\phi_{n,n'}(t) \equiv \delta_{n,n'}t - \phi_{n,n'}. \quad (13.26)$$

and where $\sigma_{n,n'}^y = -i(|n\rangle \langle n'| - |n'\rangle \langle n|)$ is the generalized Pauli-Y operator for the transition between $|n\rangle$ and $|n'\rangle$.

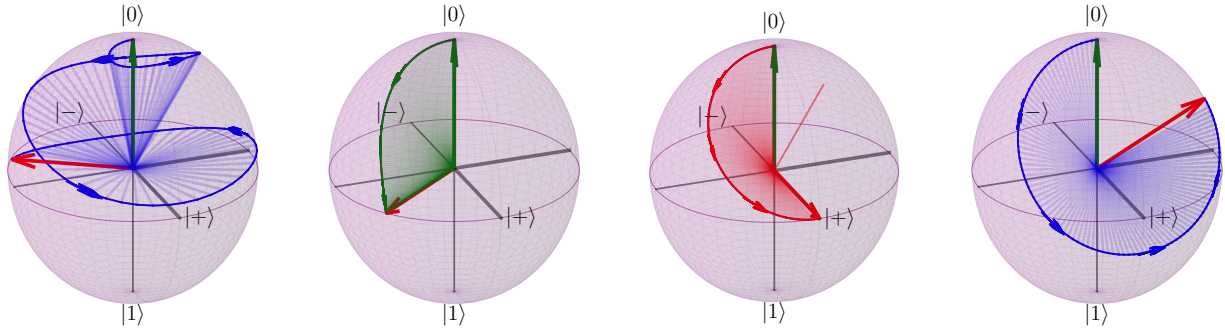
Rotating Frame Hamiltonian

It is however possible to show that, given some additional conditions on the resonance frequencies of the allowed transitions, but still close to resonance with $\delta_{n,n'} \ll \omega_{n,n'}$ [209], one can find $R(t)$ such that the term $H_0 - \frac{dR(t)}{dt}$ that vanished in (13.9) in the case of the interaction picture frame transformation can be chosen so that (i) $\phi_{n,n'}(t) = \phi_{n,n'}$ and (ii) the detuning term appears with $\omega_{n,n'}$ in the diagonal hamiltonian $H_0 - \frac{dR(t)}{dt}$ that now takes the form $H_\delta(t) = \sum_n f(\{\omega_{n,n'}\}, \{\delta_{n,n'}\}, t) |n\rangle \langle n|$.

In which case the rotating frame Hamiltonian becomes

Definition: (*Rotating frame Hamiltonian*)

$$H_{\text{rot}}(t) = \sum_{n' > n} \Omega_{n,n'}^x(t) \sigma_{n,n'}^x + \Omega_{n,n'}^y(t) \sigma_{n,n'}^y + H_\delta(t) \quad (13.27)$$



a) Laboratory frame b) Interaction frame c) Rotating frame d) Lab. frame for $\omega \sim \delta$

Figure 13.1: a-c) Bloch sphere representation of the qubit states in the laboratory frame, interaction picture, and rotating frame. The control Hamiltonian is applied for a time $t = 1$ and is given in the laboratory frame is given by $H_c = \Omega \cos((\omega + \delta)t) \sigma_x$, where $\Omega = \pi/2\sqrt{2}$ is the control amplitude, $\omega = 6\pi$ is the drift frequency and $\delta = \pi/\sqrt{2}$. d) shows the laboratory frame for a detuning term close to the drift frequency $\omega = \pi$, we observe that while the rotating frame still presents the desired transformation to the equator, the laboratory final state is not on the equator anymore.

Note: This form, compared to the interaction picture one, presents the advantage of having constant controls and a detuning term that can be used to implement a phase gate since it is diagonal.

Note: In the case of a qubit with the drift hamiltonian

$$H_0 = \frac{\omega}{2} \sigma_z, \quad (13.28)$$

and the lab frame controls

$$H_c = 2\Omega \cos((\omega - \delta)t + \phi) \sigma_x \quad (13.29)$$

the rotating frame Hamiltonian under the RWA becomes

$$H_{\text{rot}}(t) = \frac{\delta}{2} \sigma_z + \Omega(\cos(\phi) \sigma_x + \sin(\phi) \sigma_y) \quad (13.30)$$

while the interaction frame Hamiltonian is

$$H_{\text{int}}(t) = \Omega(\cos(\delta t - \phi) \sigma_x + \sin(\delta t - \phi) \sigma_y) \quad (13.31)$$

Figure 13.1 shows the Bloch sphere representation of the qubit states in the laboratory frame, interaction frame, and rotating frame. It also shows the laboratory frame for a detuning term close to the drift frequency $\omega \sim \delta$, we observe that while the rotating frame does not represent the true dynamics of the system anymore, since the final states in the rotating frame and the laboratory frame do not have the same latitude on the Bloch sphere and since R only generates rotations around the z axes, it is not due to the change of reference frame. This is a consequence of the RWA, which is only valid when the **detuning is much smaller than the transition frequencies**.

Equations (13.24) and (13.27) represent the control Hamiltonians in the interaction and rotating frames with the RWA, showing that each transition between states $|n\rangle$ and $|n'\rangle$ can be effectively treated as a

two-level system with a Hamiltonian similar to that of a qubit. This parameterization is advantageous because it allows the control fields to be viewed as rotations within the two-level subspaces spanned by $\{|n\rangle, |n'\rangle\}$. Consequently, the control problem reduces to finding the optimal sequences of amplitudes $\Omega_{n,n'}(t)$, phases $\phi_{n,n'}(t)$ and, in the case of the rotating frame, detunings $\delta_{n,n'}$ to implement the desired quantum operations.

Each rotation can be represented as a planar rotation of the form:

$$R_{n,n'}(\Omega_{n,n'}, \phi_{n,n'}) = \exp \left(-i\Omega_{n,n'}(t) \left(\cos(\phi_{n,n'}(t)) \sigma_{n,n'}^x + \sin(\phi_{n,n'}(t)) \sigma_{n,n'}^y \right) \right), \quad (13.32)$$

This representation allows us to visualize the control fields as rotations about axes in the (x, y) -plane of the Bloch sphere corresponding to each two-level subspace. The goal is to find the optimal control parameters $\Omega_{n,n'}(t)$ and $\phi_{n,n'}(t)$ that generate the desired unitary transformation in the qudit system.

In summary, by defining the transformation operator $R(t)$ and applying it to move into the rotating frame, we simplify the Hamiltonian to a form where each transition can be treated independently under the RWA. This greatly facilitates the design and analysis of control pulses for implementing quantum gates in a multi-level quantum system.

Note: For the rest of this chapter, we will assume, unless specified otherwise that the Hamiltonian is given in the rotating picture, or the interaction picture, depending on the presence of a diagonal term $H_\delta(t)$ or not.

Energy cost of the rotating frame

An important property of the rotating reference frame is that, oftentimes, the amplitude of H_{rot} is proportional to the amplitude and dephasing of the control fields. This simplifies the control problem by allowing us to focus on the control fields that generate the desired quantum operations. In particular, in the interaction picture, by defining the amplitude of the control fields $\Omega_{n,n'}(t) = \Omega_{n,n'}^x(t) + i\Omega_{n,n'}^y(t)$, and the norm of the control Hamiltonian as $\|H_{\text{rot}}(t)\| = \sqrt{\sum_{n'>n} (|\Omega_{n,n'}|^2(t))}$, we can analyze the control problem in terms of

$$\int_0^T \|H_{\text{rot}}(t)\| dt, \quad (13.33)$$

the total energy cost required to implement the desired quantum operation in time T . This energy is a key metric for evaluating the efficiency of the control fields and optimizing the gate generation process.

Definition: (*Gate duration under constant amplitude controls*) A last property of interest is that when the duration of the pulses is $T = 1$,

$$\Theta = \int_0^1 \|H_{\text{rot}}(t)\| dt \quad (13.34)$$

represents the duration of the quantum operation in units of $1/\Omega_{\text{max}}$ when the Hamiltonian $H_{\text{rot}}(t)$ is normalized to $\tilde{H}(t)$ such that $\|\tilde{H}_{\text{rot}}(t)\| = \Omega_{\text{max}}$ for all t .

Note: The integral $\int_0^1 \|H_{\text{rot}}(t)\| dt = \int_0^{\Theta/\Omega_{\text{max}}} \|\tilde{H}_{\text{rot}}(t)\| dt$ represents the accumulated "action" or

”path length” of the Hamiltonian over time.

To prove that Θ/Ω_{\max} is indeed the time required to implement the gate, we can consider the rescaled Hamiltonian

$$\tilde{H}_{\text{rot}}(s) = \Omega_{\max} \frac{H_{\text{rot}}(\frac{\Omega_{\max}}{\Theta}s)}{\|H_{\text{rot}}(\frac{\Omega_{\max}}{\Theta}s)\|}. \quad (13.35)$$

can trivially be shown to have a norm of Ω_{\max} for all s and

$$\int_0^{\frac{\Theta}{\Omega_{\max}}} \|\tilde{H}_{\text{rot}}(s)\| ds = \int_0^1 \|H_{\text{rot}}(t')\| dt' = \Theta, \quad (13.36)$$

but, more generally, $\forall t \in [0, 1]$,

$$\int_0^{\frac{\Theta}{\Omega_{\max}}t} \tilde{H}_{\text{rot}}(s) ds = \int_0^t H_{\text{rot}}(t') dt', \quad (13.37)$$

therefore, let \tilde{U} be the evolution operator generated by \tilde{H} , and U the evolution operator generated by H_{rot} , then

$$\tilde{U}\left(\frac{\Theta}{\Omega_{\max}}t\right) = U(t). \quad (13.38)$$

Confirming that the system evolving under the rescaled Hamiltonian \tilde{H}_{rot} for a time $\frac{\Theta}{\Omega_{\max}}t$ will undergo the same quantum operation as the system evolving under the original Hamiltonian H_{rot} for a time t , and in particular in the case of $t = 1$.

Note: This means that if Ω_{\max} is the maximum possible control amplitude at any time t , the time $\tau \equiv \Theta/\Omega_{\max}$ is the fastest possible time to implement the gate, as the controls are maximally driven.

13.2 Quantum Speed Limits

”And it’s a dead heat... they’re checking the electron microscope... and the winner is... Number 3! In a quantum finish!

-No fair! You changed the outcome by measuring it!”

– **Professor Farnsworth at a horse race, Futurama**

13.2.1 Example for a qubit

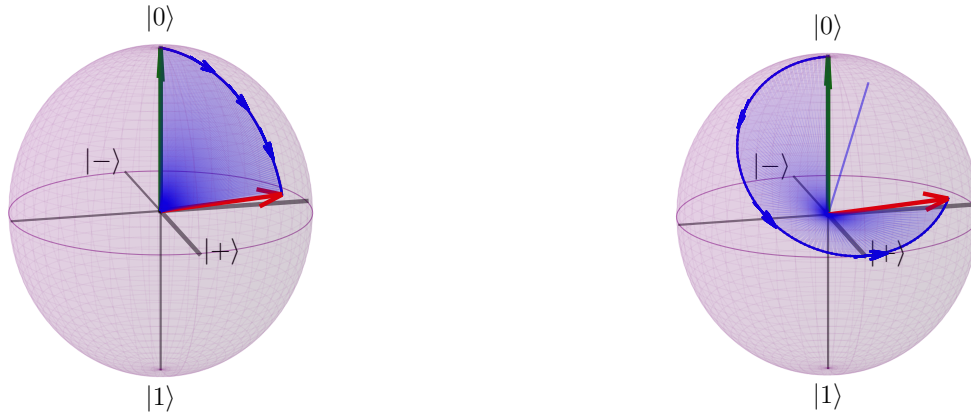
Optimal state-to-state transfer

Let us consider a single-qubit system undergoing a unitary evolution given by $U(T) = e^{-iHT}$, where H is the Hamiltonian of the system applied for time T . We can express the Hamiltonian as $H = H_0\mathbb{1}_2 + H_x\sigma_x + H_y\sigma_y + H_z\sigma_z$. On the Bloch sphere, the state evolution is represented as a rotation around the axis $\vec{H} = (H_x, H_y, H_z)$ with a rotation angle $\theta = T\sqrt{H_x^2 + H_y^2 + H_z^2}$. The angular speed of the evolution corresponds to the norm of the Hamiltonian, $\|H\| = |H_0| + \sqrt{H_x^2 + H_y^2 + H_z^2}$.

Therefore, to minimize the time T required for a state-to-state transfer, the optimal protocol involves evolving the system along a geodesic path on the Bloch sphere from the initial to the final state, as

illustrated in Fig. 13.2a). The optimal Hamiltonian H generating this rotation is characterized by a vector \vec{H} originating at the origin and normal to the plane whose intersection with the Bloch sphere traces out the geodesic. The norm of the optimal Hamiltonian is the minimum norm required to achieve the state-to-state transfer in time T , and is given by $\|H\| = \theta/T$.¹

In contrast, Fig. 13.2b) depicts the same state-to-state transfer using a non-optimal Hamiltonian. To achieve the transfer in the same duration t as the optimal case, the non-optimal Hamiltonian requires a higher norm, and consequently, a greater energy input to the system. Conversely, if the energy input is fixed for both scenarios, the non-optimal state-to-state transfer will take longer to complete compared to the optimal transfer. Figure 13.2b) also depicts the axis of rotation \vec{H} for $H \propto (\sigma_z + \sigma_x)$, which is applied for a duration of T . The observed rotation angle θ is given by $\theta = \sqrt{H_x^2 + H_z^2}T = \frac{2\pi}{3}$.



a) Geodesic path on the Bloch sphere between two states. The initial state is denoted in green and the final state in red.

b) Unitary evolution on the Bloch sphere between the same initial and final states, with a non-optimal Hamiltonian. The initial state is denoted in green and the final state in red. The axis represent \vec{H} for $H = \frac{2\pi}{3\sqrt{2}}(\sigma_z + \sigma_x)$ where H is applied for 1 unit of time.

Figure 13.2: Comparison of the geodesic path on the Bloch sphere between two states and a non-optimal unitary gate between the same initial and final states.

Definition: (*State-to-state transfer Quantum Speed Limit (QSL)*) The *Quantum Speed Limit* (QSL) τ_{QSL} for a state-to-state transfer is the minimum time required to evolve a quantum system from a chosen initial state to a final state. It is determined by the norm of the Hamiltonian, $\|H\|$, and the angle of rotation, θ , between the initial and final states.

$$\tau_{\text{QSL}}^{\text{state}} = \frac{\theta}{\|H\|} \quad (13.39)$$

The QSL can be generalized to d level systems, where the norm of the Hamiltonian is defined according to the physical constraints of the control, for example the energy input or the maximum amplitude of the control field. Moreover, the angle of rotation is defined as the angle between the initial and final states on the $(d^2 - d)$ -dimensional hypersurface of $d \times d$ density matrices for pure states.

¹Since $\|H\| = |H_0| + \sqrt{H_x^2 + H_y^2 + H_z^2}$ and the effect of H_0 is only to add a global phase, an optimal Hamiltonian will have $|H_0| = 0$.

Note: The QSL is related to the Heisenberg Uncertainty Principle, as it sets a lower bound on the product of the time and the energy required to perform a state-to-state transfer.*

For any transfer of length τ via the Hamiltonian H between two states separated by an arc of angle θ on the Bloch sphere, the following condition holds true

$$\|H\|\tau \geq \theta \quad (13.40)$$

Note: θ for a qudit is not necessarily the angle defined by the geodesic on the surface of $(d^2 - 1)$ -dimensional ball of norm 1, as $SU(d)$ is not isomorphic to $SO(d^2 - 1)$ but instead the angle between the initial and final states on the $(d^2 - d)$ -dimensional hypersurface contained in the larger hyperspherical surface.[166, 210, 211]

Optimal gates

In the previous example, we explored what an optimal state-to-state transfer looks like. In quantum computing, however, the goal is often to implement a specific unitary gate G that transforms any initial state $|\psi_i\rangle$ to its corresponding final state $|\psi_f\rangle = G|\psi_i\rangle$. The optimal control problem now involves finding a Hamiltonian H that minimizes the product $\|H\|t$, ensuring that within time t , all states are transformed to their desired final states.

This problem differs from single state-to-state transfer because we seek an optimal Hamiltonian that minimizes the time required to perform a state-to-state transfer for *all* possible initial states simultaneously. Essentially, we are considering a transformation of the entire Bloch sphere onto itself via the unitary gate U . The optimal Hamiltonian is then the one that minimizes the time required for this global transformation. For qubits, and the familiar 3D Bloch sphere, any such unitary transformation can be represented as a rotation around a specific axis.

One might consider the QSL for a gate to be the minimal maximum state-to-state transfer time. For a qubit, this would correspond to the time required to transfer between two antipodal points on the Bloch sphere—a rotation by an angle π —yielding a potential quantum speed limit of

$$\tau = \frac{\pi}{\|H\|}.$$

However, this is not always the case. For example, the identity gate has a QSL of zero, as it requires no time to implement. Intuitively, unitary transformations close to the identity should have a smaller QSL than a π rotation, since the required state-to-state transfers involve shorter paths on the Bloch sphere. Nevertheless, the π rotation provides an upper bound on the QSL of any gate, as any gate should be capable of transferring between any two states in a time less than or equal to that required for the antipodal operation.

To account for the specific characteristics of the gate under study, one can identify the pair of initial and final states whose geodesic distance is the longest among all possible pairs transformed by the gate. The quantum speed limit of the gate could then be defined as the maximum state-to-state QSL over all these pairs. Since the unitary transformation is a rotation around a certain axis, this corresponds to the distance between two states on the equatorial plane of the Bloch sphere, relative to the rotation axis as depicted in Fig. 13.3. The angle θ_G between these two states defines the QSL of the gate. The optimal Hamiltonian H is then one whose vector \vec{H} aligns with the axis of rotation of the gate, and is given by solving for H in the equation $G = e^{-iHT}$, which yields

$$H = i \frac{\log(G)}{T}.$$

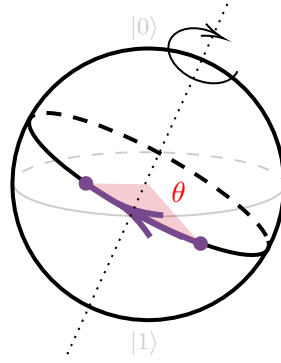


Figure 13.3: Illustration of the longest possible state-to-state transfer on a qubit's Bloch sphere during a rotation corresponding to a certain gate.

Choosing τ to be the QSL of the gate, the angle of rotation θ_G is given

$$\theta_G = \|H\|\tau = \|\log(G)\|. \quad (13.41)$$

The Quantum Speed Limit for a gate is then given by

Definition: (*Qubit gate Quantum Speed Limit (QSL)*) The *Quantum Speed Limit* (QSL) τ_{QSL} for a unitary gate G is the minimum time required to evolve a quantum system from any initial state to its corresponding final state. It is determined by the norm of the Hamiltonian, $\|H\|$, and the angle of rotation, θ_G , between the initial and final states that are the farthest apart on the Bloch sphere under the action of the gate U .

$$\tau_{\text{QSL}}^{\text{gate}}(G) = \frac{\theta_G}{\|H\|} = \frac{\|\log(G)\|}{\|H\|} \quad (13.42)$$

Note: The matrix logarithm is itself not unique, and the choice of the principal branch of the logarithm is made to ensure that the norm of the logarithm is minimal. Moreover, since $\forall \phi \in \mathbb{R}$ the difference between $e^{i\phi}U$ and U on their action on a state $|\psi\rangle$ is a global phase, they are equivalent. However $\|\log(e^{i\phi}U)\| = \|\log(U) + i\phi\mathbb{1}\| = \|\log(U)\| + |\phi|$ is not the same as $\|\log(U)\|$. It can be proven that $\|\log(U)\|$ is minimal up to a factor 2π for $U \in SU(d)$ (*Proof in appendix*). The factor of 2π can then be absorbed in the global phase of the gate. The optimal protocol is then given by looking at $U \in SU(d)$, and finding the principal branch of the logarithm that minimizes the norm of the logarithm.

Constrained controls

In practice, it is not uncommon to have a set of control Hamiltonians that do not span the whole space of $d \times d$ Hermitian matrices. This can be due to physical constraints on the control fields, for example, the electric field on the system can only be applied orthogonally to the quantization axis, or the selection rules of the system only allow a certain set of transitions. This can also be due to the chosen reference frame, for example in the interaction picture with the rotating wave approximation, one is left with generalised σ_x and σ_y terms only.

For example, let's consider the Hadamard gate

$$U = \frac{1}{\sqrt{2}} \begin{pmatrix} 1 & 1 \\ 1 & -1 \end{pmatrix}, \quad (13.43)$$

the optimal Hamiltonian generating this gate in time T is given by [212]

$$H = -i \log(U) = \frac{\pi}{2\sqrt{2}T} (\sigma_z + \sigma_x). \quad (13.44)$$

However, in the chosen reference frame (laboratory, interaction picture or rotating frame) if the control Hamiltonians are constrained to the form $H(t) = f_x(t)\sigma_x + f_y(t)\sigma_y$, the optimal Hamiltonian is not achievable, as no linear combination of σ_x and σ_y can produce a matrix logarithm of U . In this case, the gate can still be implemented, but the Hamiltonian will be time-dependent and the gate will take longer to implement than the QSL.

Figure 13.4 illustrates the evolution of the initial state $|0\rangle$ under the action of the Hadamard gate with the optimal Hamiltonian and a Hamiltonian that is constrained to the form $H(t) = f_x(t)\sigma_x + f_y(t)\sigma_y$. The optimal Hamiltonian stops evolving the state after it reaches the desired final state at the optimal time τ_{QSL} , while the constrained Hamiltonian continues evolving the state for a longer time to attain the same final state at $t_{\text{tot}} \sim 1.332\tau_{\text{QSL}}$. It is an open question now to determine the optimal Hamiltonian for a gate when the control Hamiltonians are constrained, but it is clear that this new optimal time will depend on the set of control Hamiltonians available. [213]

13.2.2 General case

The definition of a QSL of a state-to-state transfer can easily be generalized to the QSL of a gate for a d -level system as already discussed² But the definition of the QSL for a gate is not as straightforward, as the reasoning done for qubits does not hold for qudits, whose Hilbert Space is not isomorphic to a simple hypersphere [166, 210, 211] and the analogies of geodesics and axes of rotations fall short of a direct naive generalization. *A priori*, it is actually not even clear if the optimal Hamiltonian for a qudit gate is constant in time, or if, a time-dependent Hamiltonian is required to achieve the optimal gate in the shortest time possible on a qudit.

Let's formally define the energetic cost of a gate U as

$$C[H] = \int_0^\tau \|H(t)\| dt, \quad (13.45)$$

where $H(t)$ is the time-dependent Hamiltonian generating the gate U in a time τ . The QSL of a gate U is then defined as the minimum time τ required to implement the gate with a fixed energetic cost $C[H]$.

$$\tau_{\text{QSL}}^{\text{gate}} = \min_{\tau} \left\{ \tau \mid \int_0^\tau \|H(t)\| dt = C[H] \right\} \quad (13.46)$$

In their work, Aïfer *et al.* [212] derive that the definition for a gate QSL we obtained for a qubit can be generalized to a qudit, and that the optimal Hamiltonian for a gate is constant in time. They also show that the optimal Hamiltonian generating the gate is given by the logarithm of the gate

$$H = i \frac{\log(G)}{T}. \quad (13.47)$$

They note however that the optimal Hamiltonian is not unique either.

Note: This ideal implementation still assumes that the control Hamiltonians are not constrained, and therefore that the control Hamiltonians span the whole space of $d \times d$ Hermitian matrices.

²with still some non-trivial considerations in the complex representation of a qudit's Hilbert Space about the geodesics and direction vectors of the rotation to find the optimal Hamiltonian if the latter is not known in advance [212].

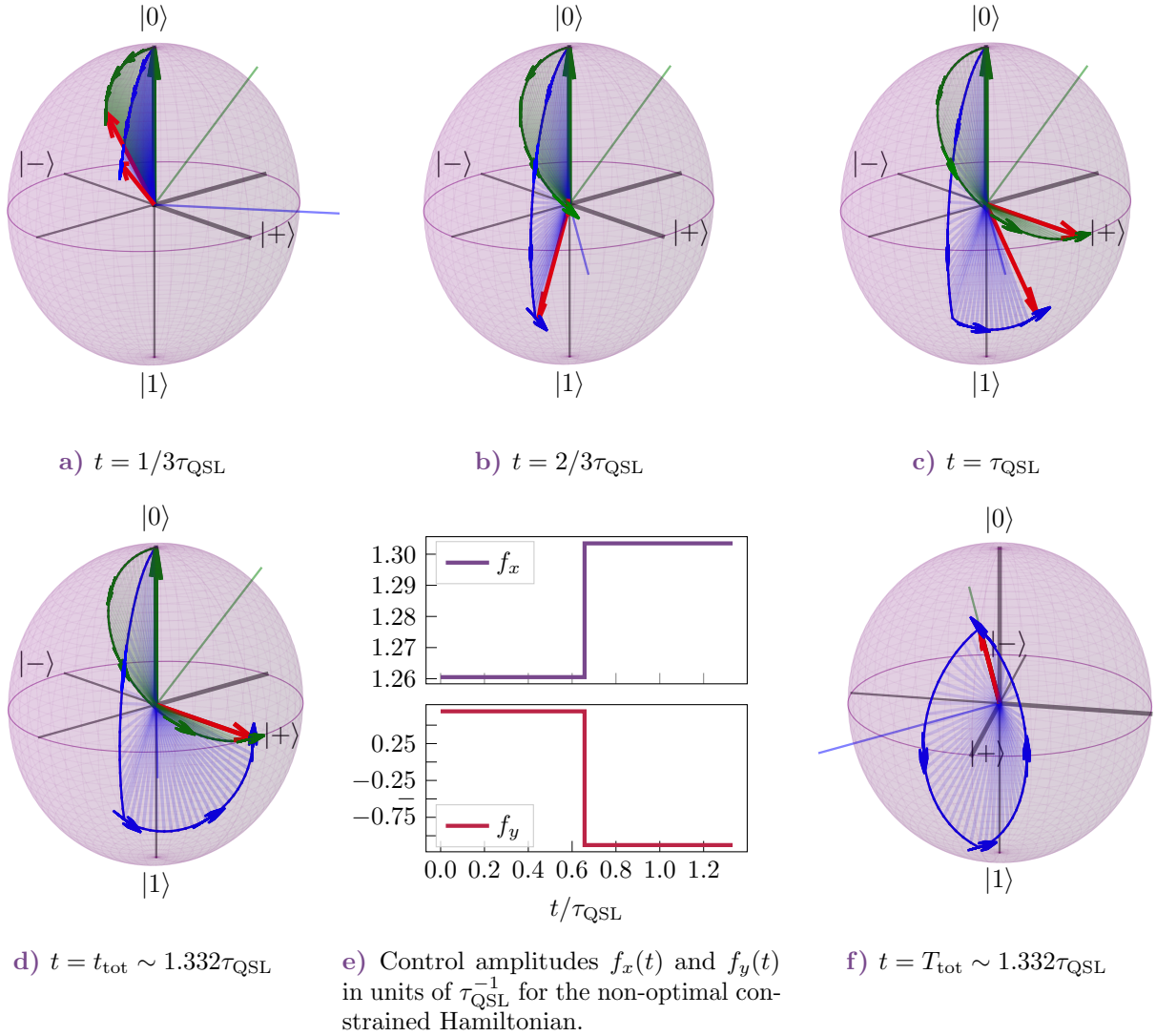


Figure 13.4: a) to d) show the evolution of the initial state $|0\rangle$ (green vector) for different times t under the action of the Hadamard gate with (green) the optimal Hamiltonian and (blue) a Hamiltonian that is not optimal but is constrained to the form $H(t) = f_x(t)\sigma_x + f_y(t)\sigma_y$. The optimal Hamiltonian stops evolving the state after it reached the desired final state at the optimal time $\tau_{\text{QSL}} = \tau_{\text{QSL}}^{\text{gate}}(U)$ (c), while the constrained Hamiltonian continues evolving the state for a longer time to attain the same final state at $t_{\text{tot}} \sim 1.332\tau_{\text{QSL}}$ (d). Both Hamiltonian have a norm of $\frac{\pi}{2\tau_{\text{QSL}}}$. e) shows the control amplitudes $f_x(t)$ and $f_y(t)$ for the constrained Hamiltonian. f) Shows the time evolution of the steady-state of the optimal Hamiltonian, whose Bloch vector is aligned with the axis of rotation of the Hadamard gate. The red vector represents the state at time t .

Aifer *et al.* define an important quantity, $L[G]$ the *shortest covering arc length* of the gate G , which is the shortest arc on the unit circle which includes all the eigenvalues of G . This quantity provides a tight lower bound on the cost of implementing the gate in time T as the authors show that

$$C[H] = \int_0^T \|H(t)\| dt \geq \frac{L[G]}{2}. \quad (13.48)$$

Effectively, $L[G]$ provides a qudit generalisation of the considered θ_G for qubits.

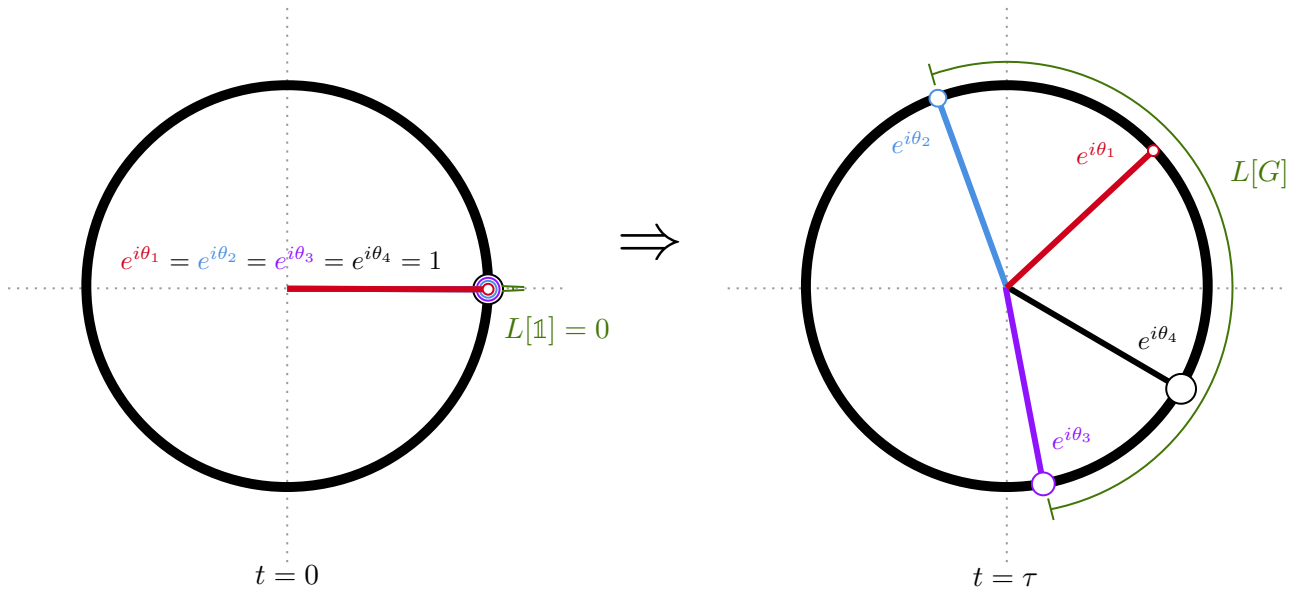


Figure 13.5: Illustration of the shortest covering arc length $L[G]$ of a qu4it gate G on the unit circle. The covering arc length is the shortest arc on the unit circle which includes all the eigenvalues of G . $L[G]$ quantifies the spread of the eigenvalues during the duration τ of the gate. Re-Adapted from [212].

If one therefore applies the constant optimal Hamiltonian defined in (13.47), (13.48) gives a closed form definition of the gate Quantum Speed Limit for qudits in units of $\|H\|^{-1}$, where $\|H\|$ will now be the energy input for the control of the system.

Definition: (*Quantum Speed Limit for qudits*) The Quantum Speed Limit for a qudit gate U is given by the shortest covering arc length of the gate $L[G]$ on the unit circle, and is defined as the minimum time τ_{QSL} required to implement the gate with a fixed energetic cost $C[H] = \frac{L[G]}{2}$, which in the rotating wave reference frame is given by

$$\tau_{\text{QSL}}^{\text{gate}}(G) = \frac{L[G]}{2\|H\|}. \quad (13.49)$$

Note: Finding the $\tau_{\text{QSL}}^{\text{gate}}$ for a gate G in a given system, while in the rotating frame, might not return the optimal time to implement the gate in the lab frame. As cross-talks and off-resonance, that are not accounted for in the rotating frame, might be used to implement the gate in an even shorter time.

Figure 13.5 shows an illustrative example of the shortest covering arc length of a gate G on the unit circle, for a qu4it gate.

Therefore, a corollary of this result is that any gate G can be implemented with an energetic cost smaller than π , since the maximum length of the unit circle is 2π .

Note: Given a dimension d and a gate G , the longest possible covering arc length corresponds to the case where all the eigenvalues of G are equally spaced on the unit circle. In this case, the shortest covering arc length is given by $L[G] = \frac{2\pi}{d}(d-1)$, meaning that the maximum possible

optimal energetic cost of implementing a gate for a qudit is $\frac{\pi}{\tau}(1 - \frac{1}{d})$. Assuming, again, that the control Hamiltonians are not constrained and span the whole space of $d \times d$ traceless Hermitian matrices.^a

^aThe dimension of the space of $d \times d$ Hermitian matrices is d^2 , however the Hamiltonian can always be chosen as traceless, and the dimension of the space of linear combinations of the generators of $SU(d)$ is $d^2 - 1$. Therefore if the control Hamiltonians are constrained to the set of linear combinations of the generators of $SU(d)$, the control Hamiltonian is unconstrained and an optimal constant Hamiltonian can be implemented.

It becomes however once again of interest to determine the optimal Hamiltonian for a gate when the control Hamiltonians are constrained, and to determine the optimal time to implement the gate.

Lie Algebra Rank Condition (LARC)

While it is possible to still implement a gate with a constrained set of Hamiltonians, albeit not the optimal one, e.g. Fig. 13.4, it is not always the case. Before addressing this scenario, it is essential to first determine the conditions that the control Hamiltonians must meet to implement any gate, whether optimal or not. This concept is known in the literature as complete controllability.

Since any gate G is equivalent to any other gate of the form $e^{i\phi}G$ with ϕ a real number, it is sufficient to consider the ensemble of $SU(d)$ gates instead of the ensemble of $U(d)$ gates. The set of $SU(d)$ gates is a Lie group of dimension $d^2 - 1$, and the set of $d \times d$ traceless Hermitian matrices is a Lie algebra of dimension $d^2 - 1$. If the set of control Hamiltonians contains $d^2 - 1$ linearly independent traceless elements, one can immediately implement any gate in the $SU(d)$ group, including the optimal one obtained by the logarithm of the gate.

However, the set of control Hamiltonians does not need to be of dimension $d^2 - 1$ to implement any gate. Let's consider a set of traceless control Hamiltonians:

$$\mathcal{H}_c = \{H_1, H_2, \dots, H_n\}, \quad \text{with } n < d^2 - 1. \quad (13.50)$$

We can generate new elements by taking commutators of these Hamiltonians. The Lie algebra generated by \mathcal{H}_c , denoted \mathfrak{g} , is the smallest Lie algebra containing \mathcal{H}_c . It includes all finite linear combinations of the control Hamiltonians and their iterated commutators:

$$\mathfrak{g} = \text{span} \left\{ H_i, [H_i, H_j], [[H_i, H_j], H_k], \dots \mid H_i, H_j, H_k, \dots \in \mathcal{H}_c \right\}. \quad (13.51)$$

The **Lie Algebra Rank Condition (LARC)** states that if the Lie algebra \mathfrak{g} generated by \mathcal{H}_c spans the entire space of $d \times d$ traceless Hermitian matrices (the Lie algebra of $SU(d)$), then \mathcal{H}_c is sufficient to implement any gate in the $SU(d)$ group. In other words, even with a set of control Hamiltonians where $n < d^2 - 1$, if their generated Lie algebra is full rank, they are complete for universal control [214].

One way to understand it is to consider a set of consecutive gates $G_1(t), G_2(t), \dots, G_n(t)$ generated by the control Hamiltonians in \mathcal{H}_c as a function of the applied time t . An arbitrary succession of N of these gates can be represented by the product of the corresponding unitary matrices:

$$U(T) = \prod_{k \in \llbracket 1, n \rrbracket} G_k(t_k), \quad (13.52)$$

with $\sum_k t_k = T$.

Using the Baker-Campbell-Hausdorff (BCH) formula³ iteratively, we can write the product of the gates as a single gate $U(T)$ generated by a new Hamiltonian $H(T)$:

³ $e^A e^B = e^{A+B+\frac{1}{2}[A,B]+\frac{1}{12}[A,[A,B]]-\frac{1}{12}[B,[A,B]]+\dots}$

$$U(T) = \mathcal{T} e^{i \int_0^T H(t) dt} \quad (13.53)$$

where $H(t)$ is a linear combination⁴ of the control Hamiltonians in \mathfrak{g} , and therefore, if the set of control Hamiltonians \mathcal{H}_c is complete for universal control, the generated Lie algebra \mathfrak{g} is full rank, and the gate $U(T)$ can be any gate in the $SU(d)$ group.

This observation underscores the complexity of solving the reverse problem: determining the optimal sequence of control Hamiltonians required to implement a specific gate G in the shortest possible time. Any adjustment in the duration t_k of a control Hamiltonian influences the infinite series of nested commutators in the Baker-Campbell-Hausdorff (BCH) expansion. This, in turn, alters the effective Hamiltonian $H(t)$ and subsequently the final gate $U(T)$ in a highly non-linear manner. Additionally, this analysis does not consider the continuous limit as $t_k \rightarrow 0$. These factors collectively pose a significant challenge in quantum control, and highlight why the optimal control problem remains unresolved analytically when constraints are placed on the set of possible control Hamiltonians. In the next subsection, we will explore some existing methods that aim to address this problem.

13.3 An overview of gate generation methods

"Capital letters were always the best way of dealing with things you didn't have a good answer to."
— Douglas Adams, *Dirk Gently's Holistic Detective Agency*

13.3.1 (GRD) Givens Rotation Decomposition

The Givens Rotation Decomposition (GRD) is a method to generate quantum gates by breaking down a target unitary operator into a sequence of simpler, elementary rotations known as Givens rotations, as defined in (13.54).

Definition: (*Givens Rotation*) A Givens rotation in the 2-dimensional subspace spanned by $\{|j\rangle, |k\rangle\}$ is a (unitary) planar rotation matrix

$$U(\theta, \phi) = \begin{pmatrix} \cos \theta & -ie^{-i\phi} \sin \theta \\ -ie^{i\phi} \sin \theta & \cos \theta \end{pmatrix}, \quad (13.54)$$

which, when written in the full $d \times d$ matrix representation as $G_{j,k}(\theta, \phi)$, is a block-diagonal matrix with matrix elements $|j\rangle\langle j| = |k\rangle\langle k| = \cos \theta$, and $|j\rangle\langle k| = |k\rangle\langle j|^* = -ie^{-i\phi} \sin \theta$ at the intersections of the j -th and k -th rows and columns in the (j, k) block and the identity elsewhere.

Refereing to (13.32), the Givens rotation $G_{j,k}(\theta, \phi)$ is a unitary operator that rotates the j -th and k -th states in a d -dimensional quantum system by an angle θ in the complex plane, with an additional phase ϕ . It would correspond to the application, for a duration Δt , in the interaction frame, of a control Hamiltonian

$$H_{j,k}(t) = \Omega_{j,k}(t) \cos(\phi(t)) \sigma_x + \Omega_{j,k}(t) \sin(\phi(t)) \sigma_y, \text{ s.t. } \begin{cases} \int_t^{t+\Delta t} \Omega_{j,k}(t) dt = \theta \\ \text{and } \frac{1}{\Delta t} \int_t^{t+\Delta t} \phi(t) dt = \phi. \end{cases} \quad (13.55)$$

i.e.

⁴The BCH formula would yield $H(t)$ as a possibly infinite series of nested commutators of the control Hamiltonians

$$G_{j,k}(\theta, \phi) = \mathcal{T} \exp \left(-i \int_0^\tau H_{j,k}(t) dt \right). \quad (13.56)$$

In particular, choosing $\Omega_{j,k}$ to be a square pulse of duration Δt and amplitude $\theta/\Delta t$, and ϕ to be constant and equal to ϕ , we have a simple implementation scheme for the Givens rotation $G_{j,k}(\theta, \phi)$, and this method proves then quite adapted when working in the interaction picture.

In the absence of control and environmental errors, this decomposition provides an exact solution to the control problem by directly constructing the desired unitary operator.

Givens rotations were originally introduced by Givens in 1958 [215] for solving systems of linear equations using the GRD, which decomposes a matrix into an orthogonal matrix Q and an upper triangular matrix R . Later, Murnaghan applied this concept to the decomposition of unitary groups into elementary planar rotations [216, 217]. Building upon foundational work in the 1990s on circuit-based quantum computation with finite gate sets [164, 218, 219], Cybenko demonstrated how Givens rotations can be used to implement single-qubit gates [220]. This idea was further generalized to qudits by Brennen, Bullock, and O’Leary [221], who showed that the GRD is exactly universal for single-qudit systems. Additionally, they proved that when combined with a properly designed two-qudit gate, it is universal for multi-qudit systems [222].

To achieve universal implementation of this decomposition, Brennen *et al.* established a key condition:

For a d -node coupling graph \mathcal{G} representing the allowed Givens rotations, any unitary $U \in SU(d)$ can be diagonalized using $d(d-1)/2$ Givens rotations if and only if \mathcal{G} is connected.

To clarify this condition, we define a **coupling graph** $\mathcal{G}(V, E)$, which represents a d -dimensional quantum system. Here, the vertex set $V = \{v_0, v_1, \dots, v_{d-1}\}$ corresponds to the states of the system, and the edge set $E \subseteq V \times V$ consists of unordered pairs (v_i, v_j) representing allowed transitions between states. A graph is **connected** if there is a path between any pair of vertices, where a path is a sequence of edges connecting those vertices.

For our purposes, we consider a minimally connected ladder system with d vertices and $d-1$ edges, where each vertex is only connected to its nearest neighbors. This configuration satisfies the universality condition while minimizing the number of allowed transitions, thus reducing issues like frequency crowding and cross-talk. Moreover, this ladder structure naturally models molecular nuclear spin qudit systems, as demonstrated in experimental works by Thiele *et al.* [26] and Godfrin *et al.* [99].

We can now outline the constructive procedure to decompose any unitary operator $U \in SU(d)$ using Givens rotations. The decomposition expresses U as a product of Givens rotations and a diagonal phase matrix R :

$$\begin{aligned} U &= G_{d,d-1}^{(1)}(\theta_1, \phi_1) G_{d-1,d-2}^{(1)}(\theta_2, \phi_2) \cdots G_{2,1}^{(1)}(\theta_{d-1}, \phi_{d-1}) \\ &\quad \times G_{d,d-1}^{(2)}(\theta_d, \phi_d) \cdots G_{3,2}^{(2)}(\theta_{d+(d-2)-1}, \phi_{d+(d-2)-1}) \\ &\quad \vdots \\ &\quad \times G_{d,d-1}^{(d-1)}(\theta_{\frac{d(d-1)}{2}}, \phi_{\frac{d(d-1)}{2}}) \times R(\alpha_1, \dots, \alpha_{d-1}), \end{aligned} \quad (13.57)$$

where each $G_{i,i-1}^{(k)}(\theta, \phi)$ is a Givens rotation acting on the $(i-1)$ -th and i -th states, and the diagonal matrix R contains the phase adjustments:

$$R(\alpha_1, \dots, \alpha_{d-1}) = \text{diag} \left(e^{i\alpha_1}, e^{i\alpha_2}, \dots, e^{i\alpha_{d-1}}, e^{-i \sum_{j=1}^{d-1} \alpha_j} \right). \quad (13.58)$$

This method is constructive because each Givens rotation is sequentially applied to eliminate specific

off-diagonal elements, bringing U into upper triangular form. At each step, the parameters θ_i and ϕ_i are chosen to zero out the (j, k) -th element of the matrix. Specifically, for the i -th rotation:

$$\theta_i = \arctan \left(\left| \frac{U_{j,k}^{(i-1)}}{U_{j-1,k}^{(i-1)}} \right| \right), \quad (13.59)$$

$$\phi_i = \arg \left(U_{j,k}^{(i-1)} \right) - \arg \left(U_{j-1,k}^{(i-1)} \right) + \frac{\pi}{2}, \quad (13.60)$$

where $U^{(i-1)}$ is the matrix after the first $(i - 1)$ rotations.

Once all Givens rotations are applied, the resulting matrix becomes diagonal, but its phases may still need adjustment. This is achieved using the diagonal matrix R , implemented as a sequence of z -rotations:

$$R = \prod_{j=1}^{d-1} \exp \left(-i\theta_j^z H_{j,j+1}^z \right), \quad (13.61)$$

where $H_{j,j+1}^z$ are operators corresponding to z -rotations between states j and $j + 1$. Since direct z -rotations may not be feasible in a ladder system, each z -rotation is decomposed into a sequence of three Givens rotations (Euler decomposition):

$$\exp \left(-i\theta_j^z H_{j,j+1}^z \right) = G_{j,j+1} \left(-\frac{\pi}{4}, \frac{\pi}{2} \right) G_{j,j+1} \left(-\theta_j^z, 0 \right) G_{j,j+1} \left(\frac{\pi}{4}, \frac{\pi}{2} \right). \quad (13.62)$$

In total, the number of elementary rotations required to implement any unitary $U \in SU(d)$ scales quadratically with the system dimension d :

$$N = \frac{d(d-1)}{2} + 3(d-1). \quad (13.63)$$

This constructive method provides an exact implementation of any desired unitary operator, though it may not always be optimal in terms of gate time or resilience to errors.

13.3.2 GRAPE Algorithm

Defining the fidelity of the obtained gate as the overlap between the target unitary operator and the implemented one,

$$\mathcal{F} = \left| \text{Tr} \left(U_{\text{target}}^\dagger U(T) \right) \right|^2, \quad (13.64)$$

we observe that by definition, the GRD yields a fidelity of exactly 1 in the absence of control or environmental errors. However, it does not generalize to include other considerations of the physical system. For example, the GRD does not account for the duration of the gate, and one can observe the GRD is quite inefficient with that regard, simply since it is not possible to address two adjacent transitions at the same time, or to address all transitions at the same time, which can provide a significant speedup in the implementation of the gate.

To tackle this more general and physically realistic problem, we turn to the Gradient Ascent Pulse Engineering (GRAPE) algorithm. Introduced by Khaneja *et al.* [32] in their seminal work on optimal control in nuclear magnetic resonance, the GRAPE algorithm has since been widely adopted in the field of quantum control [31, 223, 224, 225].

The GRAPE algorithm is a gradient-based numerical optimization method that seeks to maximize the fidelity of the target unitary operator by adjusting the control fields. It iteratively updates the control fields in the direction of the gradient of the fidelity with respect to the control parameters, following the gradient ascent method.

The algorithm relies on a discretization of the control pulses into N time steps, with the control fields $u_k^{(n)}$ defined at each time step n and for each control Hamiltonian H_k . The aim is to then minimize the cost functional $\mathcal{J}[u]$ in the parameter landscape of the $\{u_k^{(n)}\}_{k,n}$ as scalar parameters.

The total unitary propagator over the entire time interval $[0, T]$ is given by the product of the individual propagators:

$$H^{(n)} = \sum_{k=1}^d u_k^{(n)} H_k, \quad (13.65)$$

$$U^{(n)} = \exp \left(-i\Delta t \sum_{k=1}^d u_k^{(n)} H_k \right). \quad (13.66)$$

Therefore, the total unitary propagator over the entire time interval $[0, T]$ is given by the product of the individual propagators:

$$U(T) = \prod_{n=N}^1 U^{(n)}. \quad (13.67)$$

If we consider a small perturbation to the k -th control amplitude at step n , $u_k^{(n)} \rightarrow u_k^{(n)} + \delta u_k^{(n)}$, the change in the propagator is given by

$$U^{(n)} = \exp \left(-i\Delta t \sum_{l=1}^d u_l^{(n)} H_l - i\Delta t \delta u_k^{(n)} H_k \right). \quad (13.68)$$

Using the property [32, 209]

$$\left. \frac{d}{dx} e^{A+xB} \right|_{x=0} = e^A \int_0^{\Delta t} e^{A\tau} B e^{-A\tau} d\tau, \quad (13.69)$$

the sensitivity of the propagator to the control perturbation is

$$\frac{\partial U^{(n)}}{\partial u_k^{(n)}} = -i \left(\int_0^{\Delta t} U^{(n)}(\tau) H_k U^{(n)}(-\tau) d\tau \right) U^{(n)}, \quad (13.70)$$

where

$$U^{(n)}(\tau) = \exp \left(-i\tau \sum_{l=1}^d u_l^{(n)} H_l \right). \quad (13.71)$$

In the limit of small time steps,

$$\Delta t \ll \left\| \sum_{k=1}^d u_k^{(n)} H_k \right\|^{-1}, \quad (13.72)$$

the integral in (13.70) can be approximated using a Taylor series expansion. To first order in Δt , we have

$$\frac{\partial U^{(n)}}{\partial u_k^{(n)}} \approx -i\Delta t H_k U^{(n)}, \quad (13.73)$$

$$\Rightarrow \frac{\partial U(T)}{\partial u_k^{(n)}} \approx U^{(N)} \dots U^{(n+1)} \left(-i\Delta t H_k U^{(n)} \right) U^{(n-1)} \dots U^{(1)}. \quad (13.74)$$

Finally, we compute the gradient of the fidelity with respect to the control field:

$$\frac{\partial \mathcal{F}}{\partial u_k^{(n)}} = \frac{1}{d} \frac{\partial}{\partial u_k^{(n)}} \left| \text{Tr} \left(U_{\text{target}}^\dagger U(T) \right) \right|^2 \quad (13.75)$$

$$= \frac{2}{d} \text{Re} \left\{ \text{Tr} \left(U_{\text{target}}^\dagger U(T) \right) \text{Tr} \left(\frac{\partial U^\dagger(T)}{\partial u_k^{(n)}} U_{\text{target}} \right) \right\}, \quad (13.76)$$

where U_{target} is the target unitary operator. The first trace term represents the unperturbed propagator, and the second term involves the derivative with respect to the control.

Therefore, we update the control fields using:

$$u_k^{(n)} \rightarrow u_k^{(n)} + \epsilon \frac{\partial \mathcal{F}}{\partial u_k^{(n)}}, \quad (13.77)$$

where ϵ is a small step size chosen to ensure that the fidelity increases.

Repeating this process over all control fields and time steps leads to the following procedure:

1. Initialize the control amplitudes $u_k^{(n)}$ with an initial guess.
2. Calculate the unperturbed propagator $U(T)$.
3. For each control amplitude $u_k^{(n)}$, compute $\frac{\partial U(T)}{\partial u_k^{(n)}}$.
4. Compute the gradient $\frac{\partial \mathcal{F}}{\partial u_k^{(n)}}$ and update the control fields.
5. Repeat steps 2–4 until the fidelity converges or the maximum number of iterations is reached.

Steps 2–4 are represented in Fig. 13.6, for an arbitrary control pulse, for illustrative purposes.

The GRAPE algorithm is a powerful tool for solving the optimal control problem and generating high-fidelity quantum gates. It has been successfully applied to a wide range of quantum systems, including nuclear magnetic resonance, trapped ions, and superconducting qubits. By combining numerical optimization with the physical constraints of the system, the GRAPE algorithm efficiently searches the control landscape to find control fields that (at least locally) maximize the fidelity of the target unitary operator.

It can be noted, that compared with the GRD, the GRAPE algorithm is a numerical optimization algorithm that requires an initial guess. It is not guaranteed to find the global optimum, and the quality of the solution as well as the possible convergence towards a local minimum depends on the choice of the initial guess and the optimization parameters.

To discuss this a bit more in detail and illustrate the matter, in Fig. 13.7b), we compare the gate times for the GRAPE algorithm and the GRD when implementing Haar random unitary gates specifically

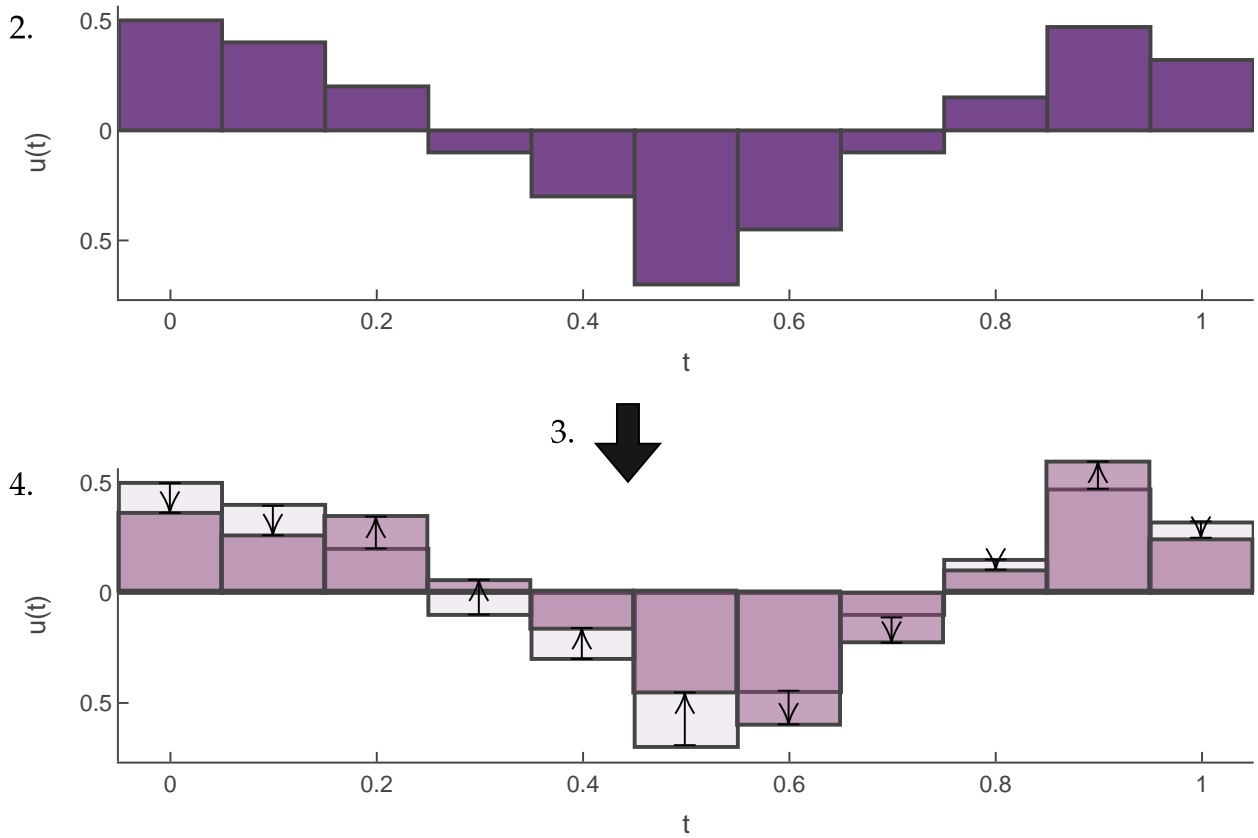


Figure 13.6: Schematic representation of the steps 2. to 4. of the GRAPE algorithm for $N = 11$ time steps between time $t = 0$ to $t = 1$ for an arbitrary control function.

for qudits with $d = 4$. For each configuration, the pulse amplitudes were normalized by Ω_{max} , as previously discussed, and the results are presented as probability densities over the range of recorded total gate times.

In Fig. 13.7a), we examine the impact of various initial pulse guesses on the gate times produced by the GRAPE algorithm, as a preliminary step towards understanding the sensitivity of the optimization algorithm to its hyperparameters. Here, 1000 Haar random gates were generated and repeatedly simulated using the GRAPE algorithm with four different initial pulse guesses: a sinusoidal pulse (red), zero amplitude (yellow), zero-mean random (green), and a square pulse (blue). The findings indicate that the choice of initial guess significantly influences the gate time, with the zero amplitude (empty, null) pulse guesses generally yielding the fastest gates and exhibiting the smallest variance, whereas the square pulse guesses result in the slowest gates with the largest variance.

In Fig. 13.7, a comparison is made between the GRAPE algorithm and the GRD across a set of 50,000 Haar random gates. The results demonstrate that the GRAPE algorithm typically produces gates with a mean time of $T \sim 7$, while the GRD yields gates with a mean time of $T \sim 13.5$. Thus, as shown in Fig. 13.7b), GRAPE pulses are generally faster than Givens pulses for $d = 4$, with a smaller variance. However, it is important to note that, due to the numerical nature of the optimization process, the GRAPE algorithm may generate suboptimal solutions for certain gates, as suggested by the longer tail in the distribution of gate times. In contrast, the Givens method guarantees gates below a threshold time of $T_{max} = 2\pi N_{pulses}$ within the amplitude normalization scheme, due to the 2π rotational symmetry inherent to the Givens rotations.

In the third panel, Fig. 13.7c), a Gaussian distribution is fitted to the distribution of gate times produced by the GRD, revealing a clear asymmetry. The origin of this asymmetry is not immediately

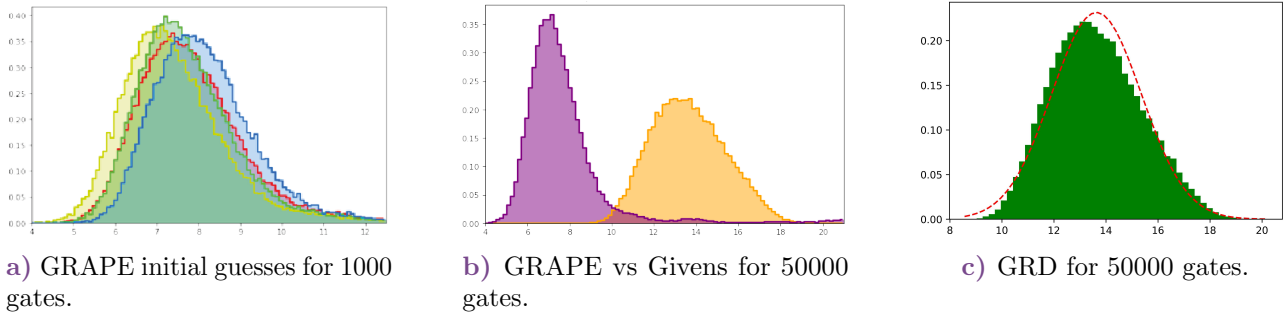


Figure 13.7: The GRAPE algorithm was compared to the GRD for implementing Haar random unitary gates for single qudits with dimension $d = 4$. In each configuration, the pulse amplitudes were normalised by Ω_{max} and the results displayed as probability densities over the range of recorded total gate times. In (a), 1000 Haar random gates were generated and simulated by the GRAPE algorithm, repeated for 4 different initial pulse guesses: a sinusoidal pulse (red), zero amplitude (yellow), zero-mean random (green) and a square pulse (blue). In (b), the GRAPE algorithm (purple) was compared to the GRD (orange) over a set of 50000 Haar random gates. In (c), the asymmetry in the distribution of the total gate times for the GRD algorithm (green) is shown by fitting a Gaussian distribution (red).

apparent, but it does indicate a potential bias in the GRD towards generating slower gates, as the distribution skews towards longer gate times. However, this characteristic may not be unique to the GRD, as the GRAPE distributions also exhibit a degree of asymmetry.

Note: Comparatively to GRD, where the control Hamiltonians are constrained to ones generating Givens rotations, and in particular for control Hamiltonians in the interaction picture, the GRAPE algorithm is more general and can be applied to any set of control Hamiltonians, and also include a drift Hamiltonian, so it can be applied in the laboratory frame as well as any other frame of reference.

The GRAPE algorithm however still is designed to only solve the problem of minimizing the cost in (13.64), however, it can be extended to include additional constraints on the control fields such as bounds on the amplitude or duration of the pulses, the latter will however affect the expression of (13.76). This allows for the generation of robust and experimentally feasible control pulses. In the context of qudit gates, the GRAPE algorithm can be used to optimize the control fields for the ladder operators of the system.

Fig. 13.8 presents an example of the application of the GRAPE algorithm to implement a Grover's algorithm (see Fig. 9.4) in a qudit system of dimension $d = 4$. The GRAPE algorithm was used to generate the QFT and diffusion gates, while the Oracle phase inversion was implemented by Givens rotations. The qudit was initialized in the ground state $\rho(0) = |0\rangle\langle 0|$, and the state $|2\rangle\langle 2|$ was marked as the search state. The states $\rho_{i,i}$ were evolved by the normalized complex pulse sequences, resulting in the final state after one Grover iteration. The set of control Hamiltonians were the generalized $\sigma_{j,j+1}^x$ and $\sigma_{j,j+1}^y$ operators in the interaction picture. It was straightforward to run the individual algorithms separately on their respective gates, and then concatenate the resulting pulse sequences as shown in Fig. 13.8b), provided that the final pulses were normalised by the maximum amplitude as before. The populations shown in Fig. 13.8a) demonstrate the evolution of the state density matrix, successfully producing the marked search state $|2\rangle\langle 2|$ after one Grover iteration.

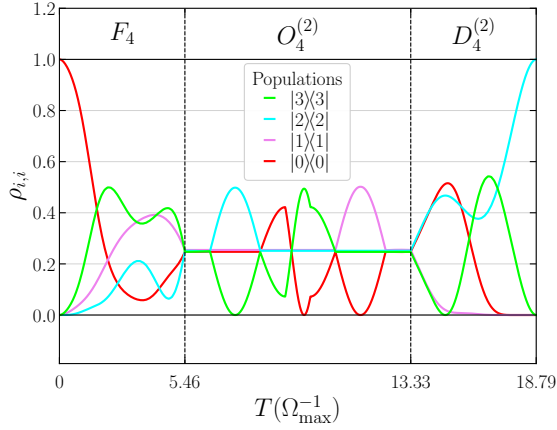
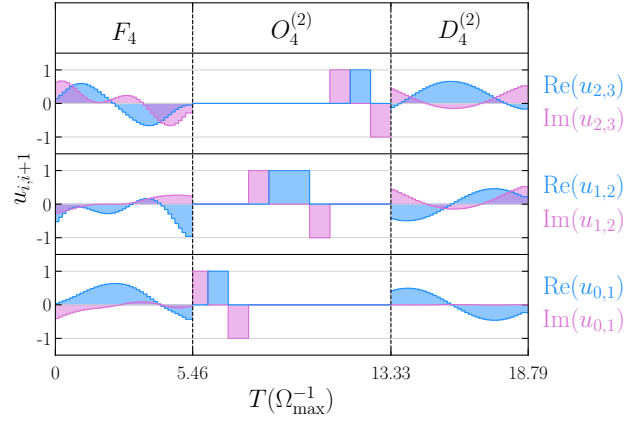
a) Populations $\rho_{i,i}$.b) Pulses $u_{i,i+1}(t)$.

Figure 13.8: Hybrid GRD-GRAPE algorithm implementation of the Grover's Algorithm. The GRAPE algorithm was applied to a qudit system of dimension $d = 4$ to generate the QFT and diffusion gates, while the Oracle phase inversion was implemented by Givens rotations. The qudit was initialised in the ground state $\rho(0) = |0\rangle\langle 0|$ and the state $|2\rangle\langle 2|$ marked as the search state. The states $\rho_{i,i}$ shown in (a) were evolved by the normalised complex pulse sequences as shown in (b), resulting in the final state after one Grover iteration.

13.4 Towards optimal qudit gates

13.4.1 Optimal Control and Cost Functions

The GRD method didn't consider the time required to implement a gate, nor the energetic cost of the control Hamiltonians, as its only aim was to provide an exact solution for a decomposition of the gate into elementary rotations.

In practice, the time required to implement a gate is a crucial factor, as seen in the previous chapter, it impacts the coherence time of the system, and the energetic cost of the control Hamiltonians is also an important factor to consider, as it impacts the energy dissipated in the system. Moreover, in the presence of control and environmental errors, the robustness of the gate to these errors is also a key factor to consider. To address these issues, we turn to the field of optimal control theory, which aims to find the control fields that minimize a certain cost functional that can take into account one or multiple of these factors.

In the context of this work we consider two general types of objective or cost functionals [214, 226], known as problems of

(i) **Mayer type:**

$$\mathcal{J}[u] = \phi(\rho(T), T), \quad (13.78)$$

and (ii) **Lagrange type:**

$$\mathcal{J}[u] = \int_0^T \mathcal{L}[\rho(t), u(t), t] dt. \quad (13.79)$$

As shown in (13.78), Mayer problems focus on quantities dependent solely on the final state at time T , such as maximizing the fidelity between the evolved state $\rho(T)$ and a desired target state. Lagrange problems, represented in (13.79), account for costs accumulated over the entire time interval $[0, T]$,

including factors like the total energy used by control fields $u(t)$ or penalties for deviations during the system's evolution. This is for example the case for $C[H]$ defined in (13.48).

One often considers hybrid cost functionals that combine both Mayer and Lagrange terms, known as problems of **Bolza type**:

$$\mathcal{J}[u] = \alpha \phi(\rho(T), T) + (1 - \alpha) \int_0^T \mathcal{L}[\rho(t), u(t), t] dt, \quad (13.80)$$

where $\alpha \in [0, 1]$ is a weighting parameter that balances the optimization priorities. By varying α , one can smoothly transition between focusing on the final-state fidelity and minimizing resource costs. For instance, starting with $\alpha = 1$ emphasizes reaching the target state with maximum fidelity. Gradually decreasing α introduces considerations like energy efficiency, allowing the optimization to find control fields that are both effective and resource-conscious [227].

The choice of a good cost functional is crucial for the success of the optimization process, in particular if implemented numerically and it is not a global optimization, the wrong choice of cost functional can lead to suboptimal solutions due to the optimization algorithm getting stuck in local minima.

13.4.2 Pontryagin's Maximum Principle

There are numerous numerical optimization algorithms that can be used to solve the optimal control problem, such as the GRAPE algorithm that we saw, the Krotov method, or the CRAB algorithm, among others[30, 31]. However, these algorithms are often computationally expensive and can be sensitive to the choice of initial conditions and parameters. Moreover, they may not always provide the global optimum of the cost functional, and they may not be able to handle constraints on the control fields.

The cost problem can also be tackled analytically, and, while it is probably not solvable analytically, it can give us insights that could then be used to design better numerical optimization algorithms, with less free parameters for example.

The optimal control problem is a well-studied field in control theory, and one of the most powerful tools to solve it is **Pontryagin's Maximum Principle (PMP)**. The PMP is a necessary condition for optimality in optimal control problems, and it provides a set of differential equations, known as the Pontryagin equations, that the optimal control fields must satisfy. The PMP is a generalization of the Euler-Lagrange equations in classical mechanics, and it is a cornerstone of optimal control theory.

Let us consider a general optimal control problem, where we aim to minimize a cost functional of the form (13.79):

$$\mathcal{J}[x, \vec{u}] = \int_0^T \mathcal{L}[x(t), \vec{u}(t), t] dt, \quad (13.81)$$

where $x(t)$ is the state of the system at time t , $\vec{u}(t)$ are the control fields, and $\mathcal{L}[x(t), \vec{u}(t), t]$ is then the Lagrangian of the system.

Assuming the system is governed by a set of differential equations, known as the state equations, that describe the evolution of the system in the absence of control fields:

$$\dot{x}(t) = f[x(t), t], \quad (13.82)$$

Definition: (*Pontryagin's Maximum Principle (PMP)*) The PMP states that if $\vec{u}^*(t)$ is the optimal control field that minimizes the cost functional, then there exists a set of adjoint variables $\vec{\lambda}(t)$ and a pseudo-Hamiltonian $\mathcal{H}[x(t), \vec{\lambda}(t), \vec{u}(t), t]$ such that the optimal control field $\vec{u}^*(t)$ and

the optimal state $x^*(t)$ satisfy the following set of equations:

$$\mathcal{H}[x, \vec{\lambda}, \vec{u}, t] = \vec{\lambda}^\dagger \cdot f[x, t] + \mathcal{L}(x, \vec{u}, t) \quad (13.83)$$

$$\dot{x} = \frac{\partial \mathcal{H}}{\partial \vec{\lambda}}, \quad (13.84)$$

$$\dot{\vec{\lambda}}^\dagger = -\frac{\partial \mathcal{H}}{\partial x} = -\vec{\lambda}^\dagger \frac{\partial f}{\partial x} - \frac{\partial \mathcal{L}}{\partial x}, \quad (13.85)$$

$$\vec{0} = \left. \frac{\partial \mathcal{H}}{\partial \vec{u}} \right|_{\vec{u}=\vec{u}^*}. \quad (13.86)$$

The optimal control field $\vec{u}^*(t)$ is then given by the solution of the third equation, and the optimal state $x^*(t)$ is given by the solution of the first equation evaluated at the optimal control field.

Note: When one applies the PMP where x are the center of mass coordinates of an object in classical mechanics and the Lagrangian is the traditional kinetic energy minus the potential energy, the PMP gives the equations of motion of the object, with λ being the momentum p of the object, and the pseudo-Hamiltonian is then the real Hamiltonian, i.e. total energy of the object. Therefore, the PMP is a generalization of the Hamilton equations in classical mechanics.

In our particular case, the state is not the density matrix (i.e. the litteral state of the system), but the unitary operator $U(t)$, and the control fields are $u_k(t)$ in the control Hamiltonian

$$H_c(t) = \sum_k u_k(t) H_k(t). \quad (13.87)$$

The previous set of equations can be written as:

$$f[U] = \dot{U} = -iHU, \quad (13.88)$$

$$\mathcal{H}[U, \vec{\lambda}, \vec{u}, t] = \vec{\lambda}^\dagger(t) \cdot f[U] + \mathcal{L}[U, \vec{u}, t], \quad (13.89)$$

$$\dot{\vec{\lambda}} = -iH\vec{\lambda} - \left(\frac{\partial \mathcal{L}}{\partial U} \right)^\dagger, \quad (13.90)$$

$$\vec{0} = \left. \frac{\partial \mathcal{H}}{\partial \vec{u}} \right|_{u=u^*}. \quad (13.91)$$

where λ is the adjoint matrix, and \mathcal{L} is the Lagrangian to be determined. The scalar product for two matrices A and B is defined as $A \cdot B = \text{ReTr}(A^\dagger B)$.

Let us apply the PMP to the problem of finding the optimal control fields to implement a qudit gate. We consider a qudit system with d levels, and we aim to implement a target unitary operator U_{target} at time 1. The PMP now allows to account for the time required to implement the gate in the interaction picture, which is given, in inverse units of the maximal possible driving amplitude (Ω_{max}^{-1}) (see (13.34)):

$$T = \int_0^1 \sqrt{\sum_k u_k^2(t)} dt, \quad (13.92)$$

where Ω_{max} is the maximal possible driving amplitude $\Omega(t) = \sqrt{\sum_k u_k^2(t)}$ of the control fields at any time t .

If our goal is to minimize the time required to implement the gate, i.e. $\mathcal{J}[U, \vec{u}] = T$, then the Lagrangian \mathcal{L} is given by

$$\mathcal{L}[U, \vec{u}, t] = \mathcal{L}[U, \vec{u}] = \sqrt{\sum_k u_k^2(t)}, \quad (13.93)$$

The fidelity of the final obtained gate $U(1)$ with the target gate U_{targ}

$$\mathcal{F}(U(1), 1) = \left| \text{Tr} \left(U_{\text{targ}}^\dagger U(1) \right) \right|^2, \quad (13.94)$$

is however not accounted for in this cost functional, and we could consider a hybrid cost functional of the form (13.80) to account for both the time required to implement the gate and the fidelity of the obtained gate with the target gate. The PMP can be applied in this case too [228], but, in this work, we will focus on the insight that the PMP can provide on the control pulses minimizing the time required to implement the gate.

Inserting the Lagrangian (13.93) into the equations of the PMP (13.89) to (13.91), we obtain

$$\mathcal{H}[U(t), \vec{\lambda}(t), \vec{u}(t)] = \text{ImTr} \left(\lambda^\dagger(t) H(t) U(t) \right) + \sqrt{\sum_k u_k^2(t)}, \quad (13.95)$$

$$\dot{\lambda}(t) = -iH(t)\lambda(t) - \left(\frac{\partial \mathcal{L}}{\partial U} \right)^\dagger = -iH(t)\lambda(t), \quad (13.96)$$

$$\vec{0} = \text{ImTr} \left(\lambda^\dagger(t) \frac{\partial H(t)}{\partial \vec{u}^*} U(t) \right) + 2 \vec{u}^*(t) / \sqrt{\sum_k u_k^2(t)}. \quad (13.97)$$

Note: If the cost function to minimize is different than the one defined here, due to a different choice of norm for H [212], the last term in the last equation will be different. For example, if the norm the cost function is such that

$$\mathcal{J} = \int_0^T \sum_k u_k^2(t) dt. \quad (13.98)$$

Then one would have

$$\mathcal{H}[U(t), \vec{\lambda}(t), \vec{u}(t)] = \text{ImTr} \left(\lambda^\dagger(t) H(t) U(t) \right) + \sum_k u_k^2(t), \quad (13.99)$$

$$\dot{\lambda}(t) = -iH(t)\lambda(t) - \left(\frac{\partial \mathcal{L}}{\partial U} \right)^\dagger = -iH(t)\lambda(t), \quad (13.100)$$

$$\vec{0} = \text{ImTr} \left(\lambda^\dagger(t) \frac{\partial H(t)}{\partial \vec{u}^*} U(t) \right) + 2 \vec{u}^*(t). \quad (13.101)$$

The last equation is notably easier to solve, as it is a linear equation in the control fields.

Let's focus on (13.96), the adjoint equation. Since $U \in SU(d)$, then λ is an element of the tangent space of $SU(d)$ at U , given by the Lie algebra $\mathfrak{su}(d)$, left multiplied by U

$$\lambda(t) = U(t)\lambda_0(t), \quad (13.102)$$

with $\lambda_0(t)$ an element of the Lie algebra $\mathfrak{su}(d)$, a skew-hermitian $d \times d$ matrix. The adjoint equation then becomes

$$\begin{aligned} \dot{\lambda}_0(t) &= -iH(t)U(t)\lambda_0(t) \\ \dot{U}(t)\lambda_0(t) + U(t)\dot{\lambda}_0(t) &= -iH(t)U(t)\lambda_0(t) \\ U\dot{\lambda}_0(t) &= \mathbb{0}_d, \end{aligned} \quad (13.103)$$

meaning that $\lambda_0(t)$ is a constant matrix, and since $U(0) = \mathbb{1}_d$, then $\lambda(0) = \lambda_0$. The adjoint matrix $\lambda(t)$ is then uniquely determined by the initial condition λ_0

$$\lambda(t) = U(t)\lambda_0. \quad (13.104)$$

Inserting this result into (13.97), and considering $\frac{\partial H}{\partial u_k} = H_k$, we obtain $\forall k$,

$$\text{ImTr} \left(\lambda_0 U^\dagger(t) H_k U(t) \right) = \text{ImTr} \left(U(t) \lambda_0 U^\dagger(t) H_k \right) = -2 \frac{u_k^*(t)}{\sqrt{\sum_j (u_j^*)^2(t)}} \quad (13.105)$$

By simply defining $g = -i\lambda_0$, we get that g is a traceless $d \times d$ hermitian matrix and that the optimal control fields are given by, $\forall k$,

$$\frac{u_k^*(t)}{\sqrt{\sum_j (u_j^*)^2(t)}} = \frac{1}{2} \text{ReTr} \left(U(t) g U^\dagger(t) H_k \right) = \frac{1}{2} g(t) \cdot H_k = \frac{1}{2} g \cdot H_k(-t) \quad (13.106)$$

with $g(t) = U(t)gU^\dagger(t)$, the time-evolved adjoint matrix or $H_k(-t) = U^\dagger(t)H_kU(t)$, the reverse time-evolved control Hamiltonian.

Any control fields satisfying this for any time $t \in [0, 1]$ are then optimal in the sense that they minimize the time required to implement the gate on a maximally driven system with the constraint that $u_k^*(0) = \sqrt{\frac{1}{2} \sum_j (u_j^*)^2(0) \text{ReTr}(gH_k)}$. The trivial solution is $u_k(t) = 0$, for $g = \mathbb{1}_d$, we recall that the H_k are traceless, this solution corresponds to the identity gate.

Equation (13.106) provides then a look into the mathematical structure of an optimal control field, however, it does not provide (i) a direct way to compute the optimal control fields, and (ii) a way to account for the fidelity of the obtained gate with the target gate. These are the topics that we will address in the following.

By defining the $c(t) = \sqrt{\sum_k u_k^2(t)}$, the normalization envelope of the control fields, (13.106) provides an test of optimality for the control fields.

Definition: (*Optimal control field*) The control fields $u_k(t)$ implementing U in time $t = 1$ minimize the duration of applying the same gate in a maximally-driven qudit if there exists a constant, traceless, hermitian matrix g such that $\forall k, \forall t$,

$$\frac{u_k(t)}{c(t)} = \frac{1}{2} \text{ReTr} \left(U(t) g U^\dagger(t) H_k \right), \quad (13.107)$$

where $c(t) = \sqrt{\sum_k u_k^2(t)}$ is the normalization envelope of the control fields.

Note: As a consequence, if the system is already maximally driven, i.e. $\forall t, c(t) = \Omega_{\max}$, then the set of pulses implementing a gate G in time $t = T$ are optimal in time if there exists a g such that $\forall k, \forall t$

$$u_k(t) = \frac{\Omega_{\max}}{2} \text{ReTr} \left(U(t) g U^\dagger(t) H_k \right). \quad (13.108)$$

13.4.3 PMP-informed discrete gradient ascent: MAGICARP

One can develop a numerical optimization algorithm that uses the insights from the PMP to guide the optimization process. This algorithm can be seen as a hybrid between the GRAPE algorithm and the PMP, where the solution provided by the PMP is used to construct the optimal control fields at each time step through a self-iterative method, and a gradient-ascent method algorithm is used to adjust the control fields by updating the initial value for the adjoint, g , in the direction of the gradient of the cost functional.

We will refer to this algorithm as the **Method for Adjoint- and Gradient-based self-Iterative Construction And Refinement of Pulses (MAGICARP)**. The algorithm is outlined as follows:

1. Start with an initial guess for the adjoint g matrix.
2. This will define the control fields at $t = 0$ through

$$\frac{u_k(0)}{\sqrt{\sum_j (u_j(0))^2}} = \frac{1}{2} \text{ReTr}(g H_k), \quad \text{if the cost function is simply } \sqrt{\sum_k u_k^2}. \quad (13.109)$$

$$u_k(0) = \frac{1}{2} \text{ReTr}(g H_k), \quad \text{if } T \text{ is arbitrary and the cost function is } \sum_k u_k^2. \quad (13.110)$$

we recall (13.109) with $T = 1$ is the optimal control problem to find the minimal duration for a maximally driven system (see (13.34)), and (13.110) is the optimal control problem minimizing the energy cost in time T discussed around (13.98).

We now define $\tilde{u}_k(t) \equiv \begin{cases} \frac{u_k(t)}{\sqrt{\sum_j (u_j(t))^2}} \\ u_k(t) \end{cases}$, depending on the chosen cost function.

3. Compute the unitary operator $U(\delta t)$ at the next time step δt using the control fields $u_k(0)$.

$$U(\delta t) = \exp \left(-i \delta t \sum_k u_k(0) H_k \right). \quad (13.111)$$

This steps assumes that the control fields are constant over the time step δt , providing some sort of discretization of the control fields similar in idea to the GRAPE algorithm.

4. Compute the control fields at the same time step δt using the adjoint g matrix and the newly obtained unitary operator $U(\delta t)$.

$$\tilde{u}_k(\delta t) = \frac{1}{2} \text{ReTr} \left(U(\delta t) g U^\dagger(\delta t) H_k \right). \quad (13.112)$$

5. Repeat steps 3 and 4 until the final time T is reached.
6. Compute the fidelity \mathcal{F} of the obtained gate with the target gate defined in (13.94), and update the adjoint g matrix in the direction of the gradient of the cost functional $\frac{\partial \mathcal{F}}{\partial g}$. Similarly to GRAPE where the derivative is taken with respect to the pulses' amplitudes.

7. Repeat steps 2 to 6 until the cost functional converges or the maximum number of iterations is reached.

Figure 13.9 shows the flowchart of the MAGICARP algorithm.

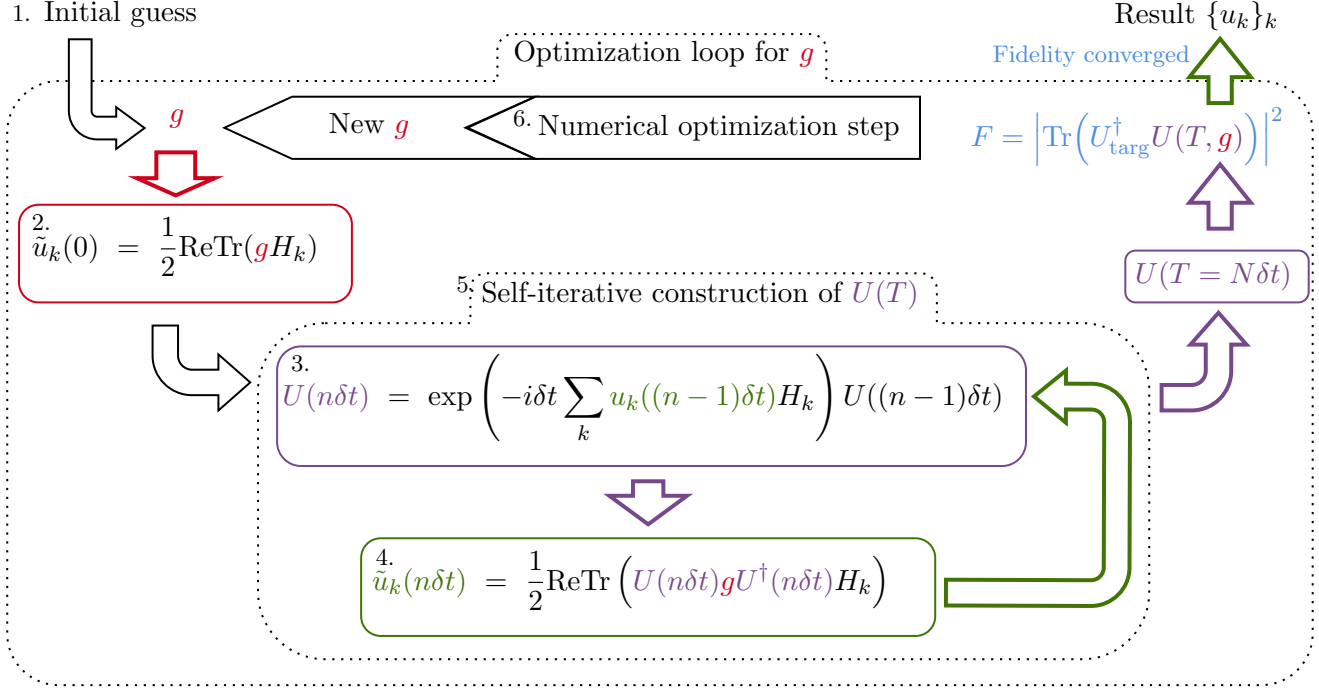


Figure 13.9: Flowchart of the MAGICARP algorithm.

Let us compare the numerical requirements and advantages of MAGICARP and GRAPE, the two algorithms that we have discussed in this chapter.

Number of optimization parameters GRAPE requires $N_{\text{steps}} \times N_{\text{controls}}$ real optimization parameters, where N_{steps} is the number of time steps for the discretization of the evolution and N_{controls} is the number of control fields. MAGICARP on the other hand requires $d^2 - 1$ real optimization parameters, where d is the dimension of the system. This is because MAGICARP optimizes the adjoint matrix g , which is a $d \times d$ traceless hermitian matrix, and the control fields are then computed from g through the self-iterative method. The dimension of the optimization space can then be very different for the two methods, and is summarised in Tab. 13.1.

Algorithm	# of optimization parameters
GRAPE	$N_{\text{steps}} \times N_{\text{controls}}$
MAGICARP	$d^2 - 1$

Table 13.1: Comparison of the number of optimization parameters required by GRAPE and MAGICARP.

MAGICARP can be very useful for systems with a large number of control fields, and/or a large number of time steps, which means more continuous-looking pulses. However, MAGICARP scales poorly with the dimension of the system, as the number of optimization parameters grows quadratically with the dimension of the system, on the other hand GRAPE scales linearly with the number of control fields and time steps, which, for systems with a small number of control fields relatively to the dimension of the system, can yield a smaller number of optimization parameters than MAGICARP, in particular as the number of time steps can always be adjusted and therefore allows for a trade-off between the number of optimization parameters and the accuracy of the optimization for example.

Note: The number of optimization parameters for MAGICARP is $d^2 - 1$ in order to find the optimal control fields $\tilde{u}_k(t)$, which are equal to $u_k(t)$ in the case of the cost function $\sum_k u_k^2$, but equal to $u_k(t)/c(t)$ in the case of the cost function $\sqrt{\sum_k u_k^2}$. Since $u_k(t)$ and not $u_k(t)/c(t)$ are necessary to compute the unitary operator at the next time step, it is important to keep track of the normalization envelope $c(t)$ in the optimization process. This introduces an additional optimization parameter, per time step, and is a difficulty that we still need to address, therefore in the rest of this chapter, we will only consider the cost function $\sum_k u_k^2$ for simplicity.

Numerical complexity and stability The numerical complexity of the two algorithms is also different. GRAPE relies on analytically computed gradients of the cost functional with respect to the control fields, which can be evaluated efficiently. MAGICARP on the other hand relies on the numerical computation of the gradients of the cost functional with respect to the adjoint matrix g , which can be computationally expensive.

An interesting point can be made about the numerical stability of the MAGICARP method, as the adjoint matrix g is a traceless hermitian matrix, it is possible to use the Lie algebra $\mathfrak{su}(d)$ to represent g as a linear combination of the generators (up to a global prefactor i) of $SU(d)$, which could maybe be used to compute the gradients of the cost functional with respect to g efficiently.

Moreover, the dependence of the final evolution operator $U(N\delta)$ with N the number of time steps, on the initial guess for the adjoint matrix g can be a source of numerical instability. $U(N\delta) \in SU(d)$, therefore it has $d^2 - 1$ real degrees of freedom, and the adjoint matrix g has also $d^2 - 1$ real degrees of freedom, which means that the optimization space is the same for the two matrices. However, the mapping between the two spaces is not straightforward and highly non-linear, and an in-depth study of the stability of $U(N\delta t)$ or at least $\text{Tr}(U_{\text{targ}}^\dagger U(N\delta t))$ with respect to small variations in g is necessary. For example, can two different adjoint matrices g_1 and g_2 that are very close in the optimization space lead to two very different final evolution operators $U(N\delta)$?

Finally a crucial point is the stability and convergence of the solution with respect to δt , the time step for the discretization of the evolution. Does the solution converge to the optimal continuous solution for $\delta t \rightarrow 0$? A possible improvement to the algorithm could be to use a variable time step, where the time step is decreased as the optimization progresses, in order to refine the solution for example. Otherwise, the discretization of the evolution can be accounted for in the PMP in the first place for example, as in the work of Dionis *et al.* [213].

Optimality of the solution A straightforward advantage of MAGICARP is that it combines the insights from the PMP to restrict the mathematical structure of the optimal control fields with respect to a Lagrange type cost functional. The gradient-ascent is then used to adjust this mathematical form in order to minimize the Mayer-type cost functional that is the fidelity of the obtained gate. Therefore, MAGICARP aims for an optimal solution, while basic GRAPE only aims for a solution that minimizes the fidelity, moreover if one includes other costs in GRAPE, the gradient of the new cost functional with respect to the control fields amplitude at each time step is not straightforward to compute, and the optimization process can be very slow.

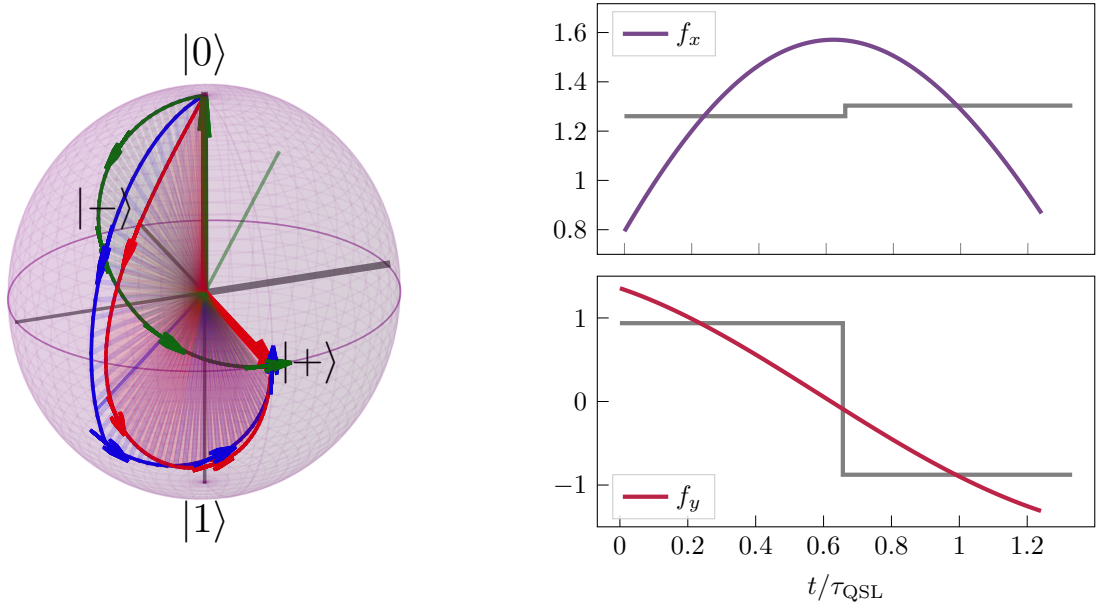
Example of results

As an example, consider the two-qubit system and the Hadamard gate $H = \frac{1}{\sqrt{2}} \begin{pmatrix} 1 & 1 \\ 1 & -1 \end{pmatrix}$ as the target gate, the control Hamiltonians are chosen to be σ_x and σ_y . The results of the optimization process for the Hadamard gate using MAGICARP are shown in Fig. 13.10 where it is compared with the constrained control field from Fig. 13.4. The MAGICARP constrained control field is more continuous

and has a duration of $\sim 1.25\tau_{QSL}$ compared to the constrained control field from Fig. 13.4 that has a duration of $\sim 1.33\tau_{QSL}$. The latter was actually calculated using an augmented GRAPE algorithm with 2 time-steps, with the term

$$\left(1 - \int_0^T \left(\sum_k u_k^2\right) dt \tau_{QSL}^{-1}\right)$$

added to the cost functional $1 - \text{Tr}(U_{\text{targ}}^\dagger U(T))$ to ensure that the duration of the gate is minimized.



a) Bloch sphere evolution of the two-qubit system under (green) the optimal control field, (blue) the constrained control field and (red) the MAGICARP constrained control field. The initial state is $|0\rangle$ and represented by a green vector, the target state is $|+\rangle$ and represented by a red vector.

b) Control amplitudes $f_x(t)$ and $f_y(t)$ in units of τ_{QSL}^{-1} for (gray) the non-optimal constrained Hamiltonian and (color) the MAGICARP constrained control field.

Figure 13.10: Comparison of the MAGICARP constrained control field with the constrained one from Fig. 13.4 for the Hadamard gate. a) represents the evolution on the Bloch sphere of the state $|0\rangle$ under (green) the optimal control field $H = \frac{\pi}{2\sqrt{\pi}}(\sigma_x + \sigma_y)$, (blue) the constrained control field from Fig. 13.4 and (red) the MAGICARP constrained control field $H(t) = f_x(t)\sigma_x + f_y(t)\sigma_y$. b) represents the control amplitudes $f_x(t)$ and $f_y(t)$ in units of τ_{QSL}^{-1} for the constrained control field (gray) and the MAGICARP constrained control field (color). One notices that the MAGICARP constrained control field is more continuous and has a duration of $\sim 1.25\tau_{QSL}$ compared to the constrained control field from Fig. 13.4 that has a duration of $\sim 1.33\tau_{QSL}$.

As an example, let us consider the optimization of the Hadamard gate for systems of dimension $d = 2, 3, 4, 5, 6$. For each dimension, the control Hamiltonians in the interaction picture are chosen to be the $2(d-1)$ generalized Pauli matrices $\sigma_{k,k+1}^x$ and $\sigma_{k,k+1}^y$ ⁵. The adjoint matrix g is initialized randomly, and the optimization process is repeated 300 times for each dimension.

The results of this optimization process for the QFT gate using MAGICARP are shown in Fig. 13.11, where the cost functional $1 - \frac{1}{d} \text{Tr}(U_{\text{targ}}^\dagger U(T))$ is plotted as a function of the gate duration T in units

⁵We recall that $\sigma_{k,k+1}^x = |k\rangle\langle k+1| + |k+1\rangle\langle k|$ and $\sigma_{k,k+1}^y = -i|k\rangle\langle k+1| + i|k+1\rangle\langle k|$, where $|k\rangle$ is the k -th computational basis state.

of Ω_{\max}^{-1} , where Ω_{\max} represents the maximum Rabi field driving the system. The results are also presented in Fig. 13.12, where the durations are given in units of $\tau_{QSL} = \pi/\Omega_{\max} (1 - \frac{1}{d})$, the quantum speed limit time for the QFT(d) gate.

The results indicate that as the dimension increases, the fidelity of achieving the target gate decreases, and the required duration increases. This is expected because the optimization space grows quadratically with the system's dimension. Consequently, the numerical optimization is more likely to converge to local minima, rather than the global minimum, as the dimension increases. This also explains why, at higher dimensions, the optimization results are more scattered and the process becomes less stable.

It is noteworthy however that, for every dimension, there appears to be a minimal achievable duration for the gate. The dashed lines in Figs. 13.11 and 13.12 indicate, for each dimension, the minimal duration at which a cost functional of $1 - \frac{1}{d} \text{Tr}(U_{\text{targ}}^\dagger U(T))$ of 10^{-7} or lower is reached. A significant fraction of the runs achieve durations close to this minimal duration, particularly for lower dimensions. This suggests that the optimization process is often able to find solutions that are near-optimal and possibly close to the quantum speed limit time with the chosen constrained set of control fields. The latter is different than the previously discussed τ_{QSL} , the quantum speed limit with unconstrained set of controls.

If verified, it would be interesting to analyze how this minimal duration evolves with the system's dimension, especially in comparison to the quantum speed limit time with unconstrained control fields. As it stands, the minimal duration appears to deviate further from the quantum speed limit time with unconstrained control fields as the system's dimension increases. This can be expected since, while the set of control Hamiltonians satisfies the Lie Algebra Rank Condition (LARC), the ratio of these control Hamiltonians to the total number of $SU(d)$ generators decreases as the system's dimension increases. Specifically, this ratio is $2(d-1)/(d^2-1) = 2/(d+1)$.

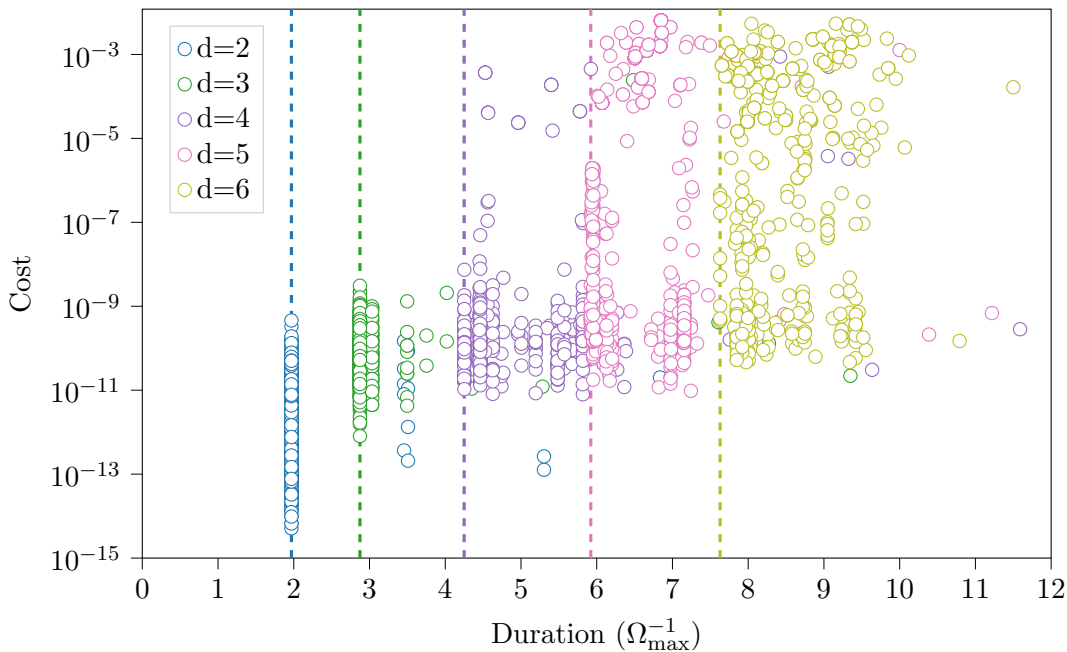


Figure 13.11: Results of 600 runs of the MAGICARP algorithm with the Hadamard gate as a target with random initial guesses for the adjoint matrix g . Each color represents a different dimension d of the system $d = 2, 3, 4, 5, 6$, there is then 3000 runs in total. The cost functional $1 - \frac{1}{d} \text{Tr}(U_{\text{targ}}^\dagger U(T))$ is plotted as a function of the duration of the gate (T) in units of Ω_{\max}^{-1} , where Ω_{\max} is the Rabi fields maximally driving the system.

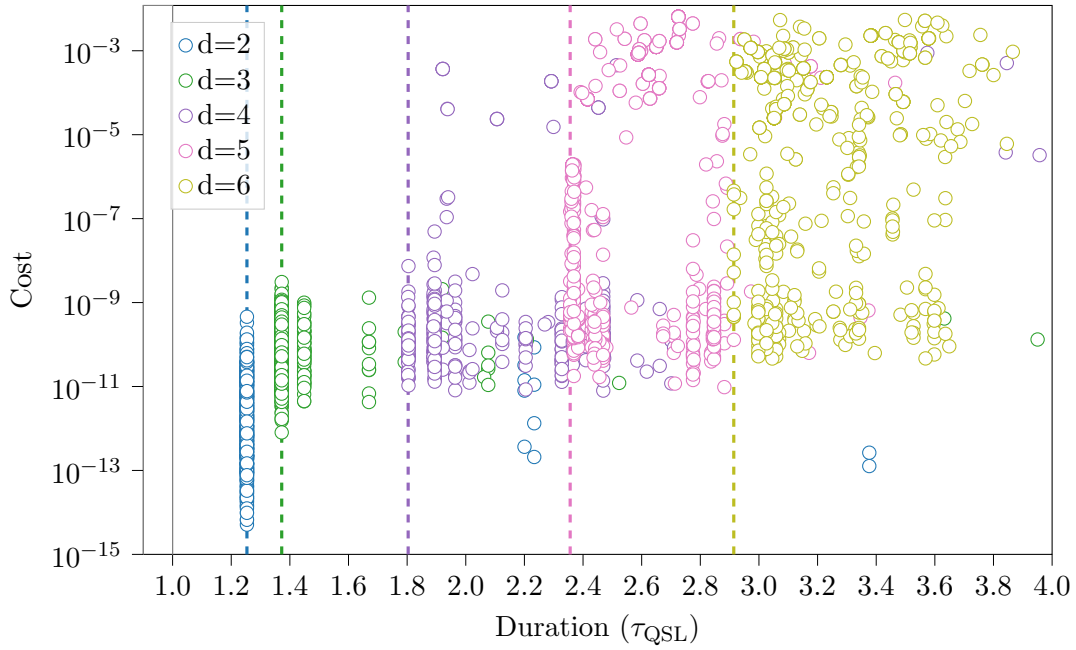


Figure 13.12: Same as Fig. 13.11 but the durations are given in units of τ_{QSL} , the quantum speed limit time. The dashed lines represent, for each dimension, the minimal duration reached with a cost functional $1 - \frac{1}{d} \text{Tr}(U_{\text{targ}}^\dagger U(T))$ of 10^{-7} or lower.

Conclusive remarks

The MAGICARP algorithm seems to provide some insights on the quantum speed limit with a constrained set of control pulses. In particular, in a system where the control hamiltonians are the $2(d-1)$ generalized Pauli-X and Pauli-Y matrices between two adjacent levels of the system, the minimal achievable durations seem to increase with the dimension, and to stray from optimality relative to an unconstrained set of linearly independent $d^2 - 1$ control Hamiltonians as the dimension increases. This would imply that in order to minimize the duration of a gate with increased dimension, a higher connectivity is required, i.e. more allowed and controllable transitions.

The results also suggest that the optimization process is often able to find solutions that are near-optimal and possibly close to the quantum speed limit time with the chosen constrained set of control fields however. The MAGICARP algorithm proves quite promising, and, provided the necessary improvements and studies of the numerical stability and convergence are made, it could be a valuable tool for the optimization of quantum gates in the future.

Main takeaways from Chapter 13

- **Reducing Gate Time to Improve Performance:**
 - Reducing the gate time t can improve the figure of merit γt and counteract pure dephasing.
- **Rotating Wave Approximation and Rotating Frame:**
 - Transitioned from the laboratory frame to the rotating frame to simplify the analysis of quantum control, thus derived the rotating frame Hamiltonian, facilitating effective control of multi-level quantum systems.
- **Quantum Speed Limits (QSL):**
 - Defined QSLs for state-to-state transfers and gate implementations.
 - Showed that the minimal time to implement a gate is related to the norm of the Hamiltonian.
- **Constraints on Control Hamiltonians:**
 - Discussed the impact of constrained number of controls on the ability to implement arbitrary gates and introduced the Lie Algebra Rank Condition (LARC) for controllability.
- **Gate Generation Methods:**
 - Explored the Givens Rotation Decomposition (GRD) method, which is exact but not time-optimal.
 - Discussed the GRAPE algorithm, which numerically optimizes control fields to maximize gate fidelity, it provides shorter gates but is still built for time-optimality.
- **Pontryagin's Maximum Principle (PMP):**
 - Applied PMP to derive necessary conditions for optimal control fields and derived expressions for optimal control fields that minimize gate time or energy cost.
- **MAGICARP Algorithm:**
 - Proposed the Method for Adjoint- and Gradient-based self-Iterative Construction And Refinement of Pulses (MAGICARP) that combines PMP insights with gradient ascent to find near-optimal control fields.
 - Number of optimization parameters $d^2 - 1$ only depend on the system's dimension d .

Conclusion

In this comprehensive study, we explored the performance and optimization of qudit-based quantum systems under noisy conditions, providing a detailed framework for understanding and improving gate fidelity in higher-dimensional quantum computing. Our work is structured around three key areas: the first-order analysis of noise scaling, the inclusion of higher-order noise effects, and the optimization of gate operations to mitigate noise.

Firstly, we conducted a first-order analysis of noisy qudit systems in comparison with multiple qubits, focusing on how noise scales with system size and dimension. By modeling Markovian noise using the Lindblad equation, we derived analytical expressions for the **average gate infidelity (AGI)** under pure dephasing for both qudits and qubit ensembles. Our findings revealed significant differences in noise scaling: qudits suffer from noise that scales quadratically with their dimension (d), whereas qubit ensembles scale logarithmically. This initially suggests that qubits are more noise-resilient. However, we established a precise condition— $\frac{d^2-1}{3\log_2(d)}$ —under which qudits can outperform qubit ensembles by optimizing the ratio of their gate times to decoherence times. This condition refines the understanding of noise resilience as a function of system dimension and highlights the potential advantages of qudits when properly optimized.

Building upon this, we delved beyond the first-order approximation to account for higher-order terms in the AGI expansion, which become significant at larger noise strengths (γt). By reformulating the Lindblad equation in superoperator form and employing a perturbative approach, we captured the nonlinear scaling of AGI with noise strength. Our analysis showed that while the first-order term is gate-independent and scales linearly with noise strength, the second-order term introduces gate-dependent corrections due to the non-commutativity between the system's Hamiltonian and noise operators. We derived explicit expressions for these higher-order terms and identified universal bounds on the AGI for large noise strengths and gate durations, which depend solely on the system's dimension. These bounds manifest as plateaus in the AGI, representing intrinsic limits to the fidelity achievable under strong noise conditions. Understanding these limits is crucial for setting realistic expectations for quantum gate performance and for guiding the development of effective noise mitigation strategies.

In the final part of our study, we focused on optimizing gate generation for qudit systems to reduce gate times and counteract the detrimental effects of pure dephasing noise. We explored both theoretical and practical methodologies to accelerate quantum gate operations without compromising fidelity. By transitioning to the rotating frame using the Rotating Wave Approximation (RWA), we simplified the time-dependent Hamiltonians and derived the rotating frame Hamiltonian, facilitating easier control of multi-level qudit systems. We introduced the concept of **Quantum Speed Limits (QSL)** to determine the minimum time required for gate implementations and discussed the challenges posed by the complex geometry of higher-dimensional Hilbert spaces.

Recognizing that practical quantum systems often have constraints on control Hamiltonians, we examined the Lie Algebra Rank Condition (LARC) to ensure **complete controllability**. However, achieving the theoretical speed limits under practical constraints remains challenging. To address this, we reviewed optimization methods like the **Givens Rotation Decomposition (GRD)** and the

Gradient Ascent Pulse Engineering (GRAPE) algorithm. While GRD provides a constructive approach to gate decomposition, it often results in longer gate times. GRAPE, though effective, can be computationally intensive and sensitive to initial conditions.

To overcome these limitations, we proposed the **Method for Adjoint- and Gradient-based self-Iterative Construction and Refinement of Pulses (MAGICARP)**. This algorithm integrates the analytical strengths of **Pontryagin's Maximum Principle (PMP)** with the adaptability of gradient-based optimization. MAGICARP aims to find time-optimal control pulses that achieve high-fidelity gate operations while reducing the number of optimization parameters and enhancing convergence efficiency. Through numerical simulations, we demonstrated that MAGICARP effectively optimizes quantum gates for qudit systems across various dimensions, often finding near-optimal solutions that approach the constrained quantum speed limits.

In summary, our work provides a detailed quantitative framework for comparing qudits and qubits in terms of gate fidelity under noisy conditions, accounting for both first-order and higher-order noise effects. We offer practical guidelines for optimizing qudit-based platforms by reducing gate times and employing advanced control optimization techniques like MAGICARP. These findings contribute to a deeper understanding of the interplay between noise, system dimension, and gate optimization. They also pave the way for future research into more complex noise models, scalable qudit networks, and the implementation of optimized control strategies in real quantum hardware. As quantum technology evolves, leveraging the higher information density of qudits while minimizing the impact of noise could unlock new pathways for more efficient and robust quantum computation.

References of this part

- [7] Shor, P. W. “Polynomial-Time Algorithms for Prime Factorization and Discrete Logarithms on a Quantum Computer”, *SIAM Journal on Computing*, 1997, 26:5, 1484–1509.
- [10] Kjaergaard, M.; Schwartz, M. E.; Greene, A.; Samach, G. O.; Bengtsson, A.; O’Keeffe, M.; McNally, C. M.; Braumüller, J.; Kim, D. K.; Krantz, P., et al. “Programming a quantum computer with quantum instructions”, 2020.
- [12] Pogorelov, I. et al. “Compact Ion-Trap Quantum Computing Demonstrator”, *PRX Quantum*, 2021, 2:2, 020343.
- [14] Chi, Y.; Huang, J.; Zhang, Z.; Mao, J.; Zhou, Z.; Chen, X.; Zhai, C.; Bao, J.; Dai, T.; Yuan, H., et al. “A programmable qudit-based quantum processor”, *Nature Communications*, 2022, 13:1, 1166.
- [16] Madjarov, I. S.; Covey, J. P.; Shaw, A. L.; Choi, J.; Kale, A.; Cooper, A.; Pichler, H.; Schkolnik, V.; Williams, J. R.; Endres, M. “High-fidelity entanglement and detection of alkaline-earth Rydberg atoms”, *Nature Physics*, 2020, 16:8, 857–861.
- [23] Wang, Y.; Hu, Z.; Sanders, B. C.; Kais, S. “Qudits and High-Dimensional Quantum Computing”, *Frontiers in Physics*, 2020, 8.
- [26] Thiele, S.; Balestro, F.; Ballou, R.; Klyatskaya, S.; Ruben, M.; Wernsdorfer, W. “Electrically driven nuclear spin resonance in single-molecule magnets”, *Science (New York, N.Y.)*, 2014, 344:6188, 1135–1138.
- [30] Glaser, S. J.; Boscain, U.; Calarco, T.; Koch, C. P.; Köckenberger, W.; Kosloff, R.; Kuprov, I.; Luy, B.; Schirmer, S.; Schulte-Herbrüggen, T.; Sugny, D.; Wilhelm, F. K. “Training Schrödinger’s cat: quantum optimal control: Strategic report on current status, visions and goals for research in Europe”, *The European Physical Journal D*, 2015, 69:12, 279.
- [31] Koch, C. P.; Boscain, U.; Calarco, T.; Dirr, G.; Filipp, S.; Glaser, S. J.; Kosloff, R.; Montangero, S.; Schulte-Herbrüggen, T.; Sugny, D.; Wilhelm, F. K. “Quantum optimal control in quantum technologies. Strategic report on current status, visions and goals for research in Europe”, *EPJ Quantum Technology*, 2022, 9:1, 19.
- [32] Khaneja, N.; Reiss, T.; Kehlet, C.; Schulte-Herbrüggen, T.; Glaser, S. J. “Optimal control of coupled spin dynamics: design of NMR pulse sequences by gradient ascent algorithms”, *Journal of Magnetic Resonance*, 2005, 172:2, 296–305.
- [59] Ringbauer, M.; Meth, M.; Postler, L.; Stricker, R.; Blatt, R.; Schindler, P.; Monz, T. “A universal qudit quantum processor with trapped ions”, *Nature Physics*, 2022, 18:9, 1053–1057.
- [99] Godfrin, C.; Ferhat, A.; Ballou, R.; Klyatskaya, S.; Ruben, M.; Wernsdorfer, W.; Balestro, F. “Operating Quantum States in Single Magnetic Molecules: Implementation of Grover’s Quantum Algorithm”, *Physical Review Letters*, 2017, 119:18, 187702.
- [100] Wernsdorfer, W.; Ruben, M. “Synthetic Hilbert Space Engineering of Molecular Qudits: Isotopologue Chemistry”, *Advanced Materials*, 2019, 31:26, 1806687.
- [102] Moreno-Pineda, E.; Godfrin, C.; Balestro, F.; Wernsdorfer, W.; Ruben, M. “Molecular Spin Qudits for Quantum Algorithms”, *Chemical Society Reviews*, 2018, 47:2, 501–513.

- [164] Nielsen, M. A.; Chuang, I. L., *Quantum Computation and Quantum Information: 10th Anniversary Edition*; Cambridge University Press: Cambridge, 2010.
- [165] Figgatt, C.; Maslov, D.; Landsman, K. A.; Linke, N. M.; Debnath, S.; Monroe, C. “Complete 3-Qubit Grover search on a programmable quantum computer”, *Nature Communications*, 2017, 8:1, 1918.
- [166] Mandilara, A.; Dellen, B.; Jaekel, U.; Valtinos, T.; Syvridis, D. “Classification of data with a qudit, a geometric approach”, *Quantum Machine Intelligence*, 2024, 6:1, 17.
- [167] Chiesa, A.; Petiziol, F.; Macaluso, E.; Wimberger, S.; Santini, P.; Carretta, S. “Embedded quantum-error correction and controlled-phase gate for molecular spin qubits”, *AIP Advances*, 2021, 11:2, 025134.
- [168] Petiziol, F.; Chiesa, A.; Wimberger, S.; Santini, P.; Carretta, S. “Counteracting dephasing in Molecular Nanomagnets by optimized qudit encodings”, *npj Quantum Information*, 2021, 7:1, 1–10.
- [169] Luis, F. et al. “A dissymmetric [Gd₂] coordination molecular dimer hosting six addressable spin qubits”, *Communications Chemistry*, 2020, 3:1.
- [170] Zheng, Y.; Sharma, H.; Borregaard, J. “Entanglement Distribution with Minimal Memory Requirements Using Time-Bin Photonic Qudits”, *PRX Quantum*, 2022, 3:4, 040319.
- [171] Bouchard, F.; Fickler, R.; Boyd, R. W.; Karimi, E. “High-dimensional quantum cloning and applications to quantum hacking”, *Science Advances*, 2017, 3:2, e1601915.
- [172] Campbell, E. T.; Anwar, H.; Browne, D. E. “Magic-State Distillation in All Prime Dimensions Using Quantum Reed-Muller Codes”, *Physical Review X*, 2012, 2:4, 041021.
- [173] Lanyon, B. P. et al. “Simplifying quantum logic using higher-dimensional Hilbert spaces”, *Nature Physics*, 2008, 5:2, 134–140.
- [174] Manzano, D. “A short introduction to the Lindblad master equation”, *AIP Advances*, 2020, 10:2, 025106.
- [175] Gorini, V.; Kossakowski, A.; Sudarshan, E. C. G. “Completely positive dynamical semigroups of N -level systems”, *Journal of Mathematical Physics*, 1976, 17:5, 821–825.
- [176] Lindblad, G. “On the generators of quantum dynamical semigroups”, *Communications in Mathematical Physics*, 1976, 48:2, 119–130.
- [177] Kraus, K., *States, Effects, and Operations: Fundamental Notions of Quantum Theory*; Springer Berlin Heidelberg: 1983; 176 pp.
- [178] Havel, T. F. “Procedures for Converting among Lindblad, Kraus and Matrix Representations of Quantum Dynamical Semigroups”, *Journal of Mathematical Physics*, 2003, 44:2, 534.
- [179] Andersson, E.; Cresser, J. D.; Hall, M. J. W. “Finding the Kraus decomposition from a master equation and vice versa”, *Journal of Modern Optics*, 2007.
- [180] Zhong, W.; Sun, Z.; Ma, J.; Wang, X.; Nori, F. “Fisher information under decoherence in Bloch representation”, *Physical Review A*, 2013, 87:2, 022337.
- [181] Chiesa, A.; Macaluso, E.; Petiziol, F.; Wimberger, S.; Santini, P.; Carretta, S. “Molecular Nanomagnets as Qubits with Embedded Quantum-Error Correction”, *The Journal of Physical Chemistry Letters*, 2020, 11:20, 8610–8615.
- [182] Chen, H.; Borzì, A.; Janković, D.; Hartmann, J.-G.; Hervieux, P.-A. Full- and low-rank exponential Euler integrators for the Lindblad equation, 2024.
- [183] Riesch, M.; Jirauschek, C. “Analyzing the positivity preservation of numerical methods for the Liouville-von Neumann equation”, *Journal of Computational Physics*, 2019, 390, 290–296.
- [184] Ziolkowski, R. W.; Arnold, J. M.; Gogny, D. M. “Ultrafast pulse interactions with two-level atoms”, *Physical Review A*, 1995, 52:4, 3082–3094.
- [185] Bidégaray, B.; Bourgeade, A.; Reignier, D. “Introducing Physical Relaxation Terms in Bloch Equations”, *Journal of Computational Physics*, 2001, 170:2, 603–613.
- [186] Janković, D.; Hartmann, J.-G.; Ruben, M.; Hervieux, P.-A. “Noisy qudit vs multiple qubits: conditions on gate efficiency for enhancing fidelity”, *npj Quantum Information*, 2024, 10:1, 59.

- [187] Jankovic, D. Source Code for data generation and pulses data for Noisy Qudit vs Multiple Qubits, 2024.
- [188] Jozsa, R. “Fidelity for Mixed Quantum States”, *Journal of Modern Optics*, 1994, 41:12, 2315–2323.
- [189] Nielsen, M. A. “A simple formula for the average gate fidelity of a quantum dynamical operation”, *Physics Letters A*, 2002, 303:4, 249–252.
- [190] Qi, J.; Ng, H. K. “Comparing the randomized benchmarking figure with the average infidelity of a quantum gate-set”, *International Journal of Quantum Information*, 2019, 17:4, 1950031.
- [191] Johnston, N.; Kribs, D. W. “Quantum gate fidelity in terms of Choi matrices”, *Journal of Physics A: Mathematical and Theoretical*, 2011, 44:49, 495303.
- [192] Abad, T.; Fernández-Pendás, J.; Frisk Kockum, A.; Johansson, G. “Universal Fidelity Reduction of Quantum Operations from Weak Dissipation”, *Physical Review Letters*, 2022, 129:15, 150504.
- [193] Collins, B.; Matsumoto, S.; Novak, J. “The Weingarten Calculus”, 2021.
- [194] Horodecki, M.; Horodecki, P.; Horodecki, R. “General teleportation channel, singlet fraction, and quasidistillation”, *Physical Review A*, 1999, 60:3, 1888–1898.
- [195] Ozaeta, A.; McMahon, P. L. “Decoherence of up to 8-qubit entangled states in a 16-qubit superconducting quantum processor”, *Quantum Science and Technology*, 2019, 4:2, 025015.
- [196] Chen, Y.; Neill, C.; Roushan, P.; Leung, N.; Fang, M.; Barends, R.; Kelly, J.; Campbell, B.; Chen, Z.; Chiaro, B., et al. “Qubit Architecture with High Coherence and Fast Tunable Coupling”, *Physical Review Letters*, 2014, 113:22, 220502.
- [197] Kjaergaard, M.; Schwartz, M. E.; Braumüller, J.; Krantz, P.; Wang, J. I.-J.; Gustavsson, S.; Oliver, W. D. “Superconducting Qubits: Current State of Play”, *Annual Review of Condensed Matter Physics*, 2020, 11:1, 369–395.
- [198] Rosenblum, S.; Gao, Y. Y.; Reinhold, P.; Wang, C.; Axline, C. J.; Frunzio, L.; Girvin, S. M.; Jiang, L.; Mirrahimi, M.; Devoret, M. H.; Schoelkopf, R. J. “A CNOT gate between multiphoton qubits encoded in two cavities”, *Nature Communications*, 2018, 9:1, 652.
- [199] Larrouy, A.; Patsch, S.; Richaud, R.; Raimond, J.-M.; Brune, M.; Koch, C. P.; Gleyzes, S. “Fast Navigation in a Large Hilbert Space Using Quantum Optimal Control”, *Physical Review X*, 2020, 10:2, 021058.
- [200] Krinner, S. et al. “Realizing repeated quantum error correction in a distance-three surface code”, *Nature*, 2022, 605:7911, 669–674.
- [201] Chiesa, A.; Roca, S.; Chicco, S.; de Ory, M.; Gómez-León, A.; Gomez, A.; Zueco, D.; Luis, F.; Carretta, S. “Blueprint for a Molecular-Spin Quantum Processor”, *Phys. Rev. Appl.*, 2023, 19:6, 064060.
- [202] Wu, X.; Tomarken, S. L.; Petersson, N. A.; Martinez, L. A.; Rosen, Y. J.; DuBois, J. L. “High-Fidelity Software-Defined Quantum Logic on a Superconducting Qudit”, *Phys. Rev. Lett.*, 2020, 125:17, 170502.
- [203] Cao, S.; Bakr, M.; Campanaro, G.; Fasciati, S. D.; Wills, J.; Lall, D.; Shteynas, B.; Chidambaram, V.; Rungger, I.; Leek, P. Emulating two qubits with a four-level transmon qudit for variational quantum algorithms, 2023.
- [204] Hartmann, J.-G.; Janković, D.; Pasquier, R.; Ruben, M.; Hervieux, P.-A. Nonlinearity of the Fidelity in Open Qudit Systems: Gate and Noise Dependence in High-dimensional Quantum Computing, 2024.
- [205] Hartmann, J.-G.; Jankovic, D.; Pasquier, R.; Ruben, M.; Hervieux, P.-A. Code and Data for “Nonlinearity of the Fidelity in Open Qudit Systems: Gate and Noise Dependence in High-dimensional Quantum Computing”, version 1.0.0, 2024.
- [206] Villegas-Martínez, B. M.; Soto-Eguibar, F.; Moya-Cessa, H. M. “Application of Perturbation Theory to a Master Equation”, *Advances in Mathematical Physics*, 2016, 2016:1, 9265039.
- [207] Campbell, J. E. “On a Law of Combination of Operators bearing on the Theory of Continuous Transformation Groups”, *Proceedings of the London Mathematical Society*, 1896, s1-28:1, 381–390.

- [208] Hall, B. C., *Lie groups, Lie algebras, and representations: an elementary introduction*, Second edition; Graduate texts in mathematics 222; Springer: Cham ; New York, 2015; 449 pp.
- [209] Fisher, R. M. Optimal Control of Multi-Level Quantum Systems, Ph.D. Thesis, echnische Univ. Muenchen (Germany). Fakultaet fuer Chemie.
- [210] Bengtsson, I.; Życzkowski, K., *Geometry of Quantum States: An Introduction to Quantum Entanglement*; Cambridge University Press: Cambridge, 2006.
- [211] Eltschka, C.; Huber, M.; Morelli, S.; Siewert, J. “The shape of higher-dimensional state space: Bloch-ball analog for a qutrit”, *Quantum*, 2021, 5, 485.
- [212] Aïfer, M.; Deffner, S. “From quantum speed limits to energy-efficient quantum gates”, *New Journal of Physics*, 2022, 24:5, 055002.
- [213] Dionis, E.; Sugny, D. “Time-optimal control of two-level quantum systems by piecewise constant pulses”, *Physical Review A*, 2023, 107:3, 032613.
- [214] D’Alessandro, D., *Introduction to quantum control and dynamics*, 2nd edition; Advances in mathematics series; CRC Press: Boca Raton, 2021.
- [215] Givens, W. “Computation of Plain Unitary Rotations Transforming a General Matrix to Triangular Form”, *Journal of the Society for Industrial and Applied Mathematics*, 1958, 6:1, 26–50.
- [216] Murnaghan, F. D. “The orthogonal and symplectic groups”, *Commun. Dublin Inst. Adv. Stud.*, 1958, 13, 156.
- [217] Murnaghan, F. D., *The Unitary and Rotation Groups*; Lecture Notes in Applied Mathematics, Vol. 3; Spartan Books, [Washington, D.C., 1962.
- [218] Barenco, A.; Bennett, C. H.; Cleve, R.; DiVincenzo, D. P.; Margolus, N.; Shor, P.; Sleator, T.; Smolin, J. A.; Weinfurter, H. “Elementary gates for quantum computation”, *Physical Review A*, 1995, 52:5, 3457–3467.
- [219] DiVincenzo, D. P. “Two-bit gates are universal for quantum computation”, *Physical Review A*, 1995, 51:2, 1015–1022.
- [220] Cybenko, G. “Reducing quantum computations to elementary unitary operations”, *Computing in Science and Engg.*, 1996, 3:2, 27–32.
- [221] O’Leary, D. P.; Bullock, S. S. “QR factorizations using a restricted set of rotations”, *Electronic Transactions on Numerical Analysis*, 2005, 21, 20–27.
- [222] Brennen, G.; O’Leary, D.; Bullock, S. “Criteria for exact qudit universality”, *Physical Review A*, 2005, 71:5, 052318.
- [223] Rong, X.; Geng, J.; Shi, F.; Liu, Y.; Xu, K.; Ma, W.; Kong, F.; Jiang, Z.; Wu, Y.; Du, J. “Experimental fault-tolerant universal quantum gates with solid-state spins under ambient conditions”, *Nature Communications*, 2015, 6:1, 8748.
- [224] Devra, A.; Prabhu, P.; Singh, H.; Arvind; Dorai, K. “Efficient experimental design of high-fidelity three-qubit quantum gates via genetic programming”, *Quantum Information Processing*, 2018, 17:3, 67.
- [225] Rowland, B.; Jones, J. A. “Implementing quantum logic gates with gradient ascent pulse engineering: principles and practicalities”, *Philosophical Transactions of the Royal Society A: Mathematical, Physical and Engineering Sciences*, 2012, 370:1976, 4636–4650.
- [226] Shapiro, S. “Lagrange and Mayer problems in optimal control”, *Automatica*, 1966, 3:3, 219–230.
- [227] Lutz, K.; Privat, Y. Decoherence control for quantum information, Master Thesis, Université de Strasbourg, 2023.
- [228] Bergounioux, M.; Bourdin, L. “Pontryagin maximum principle for general Caputo fractional optimal control problems with Bolza cost and terminal constraints”, *ESAIM: Control, Optimisation and Calculus of Variations*, 2020, 26, 35.

———— PART IV ————

The Ubiquitous Prouhet-Thue-Morse Sequence

————

14 The Ubiquitous Prouhet-Thue-Morse Sequence	279
14.1 The multiple defintions of the Prouhet-Thue-Morse sequence	279
14.2 The T-M sequence in Quantum Computing	281
14.3 Link to quantum chaos	288
14.4 Link with number theory	289
14.5 Conclusion	291

Chapter Contents

14.1 The multiple definitions of the Prouhet-Thue-Morse sequence	279
14.2 The T-M sequence in Quantum Computing	281
14.3 Link to quantum chaos	288
14.4 Link with number theory	289
14.5 Conclusion	291

CHAPTER 14

The Ubiquitous Prouhet-Thue-Morse Sequence

This chapter was written in conjunction with the writing of our article **Elucidating the Physical and Mathematical Properties of the Prouhet-Thue-Morse Sequence in Quantum Computing**, that is ready to be submitted to the *Journal of Physics A: Mathematical and Theoretical*.

This chapter explores the applications of the Prouhet-Thue-Morse (PTM) sequence in quantum computing, highlighting its mathematical elegance and practical relevance. We demonstrate the PTM sequence's critical role in quantum error correction, noise-resistant quantum memories, and providing insights into quantum chaos. Notably, we show how the PTM sequence naturally appears in Ising X-X interacting systems, leading to proposed robust encoding of quantum memories in such systems. Furthermore, connections to number theory, including the Riemann zeta function, bridge quantum computing with pure mathematics. Our findings emphasize the PTM sequence's importance in understanding the mathematical structure of quantum computing systems and the development of the full potential of quantum technologies and invite further interdisciplinary research.

The intersection of quantum computing and mathematical sequences opens a fascinating frontier for research, with potential implications for both theoretical advancements and practical applications. Among these mathematical constructs, the Prouhet-Thue-Morse (PTM) sequence stands out due to its rich structure and multifaceted utility. Originally discovered in the 19th century and renowned for its unique properties and recursive definition, the PTM sequence has garnered attention across various scientific disciplines [229].

14.1 The multiple definitions of the Prouhet-Thue-Morse sequence

The Prouhet-Thue-Morse (PTM) sequence is a binary sequence with a rich mathematical structure and wide-ranging applications in physics, from quasicrystals to quantum mechanics [229, 230].

Definition: (*Explicit definition of the PTM sequence*) Mathematically, the sequence is defined by its n -th term t_n , which is the sum of the binary digits of $n \pmod{2}$, formally given by:

$$t_n = \left(\sum_{k=0}^{\infty} \left\lfloor \frac{n}{2^k} \right\rfloor \right) \pmod{2}. \quad (14.1)$$

Historically, the sequence was first discovered by Prouhet in 1851 [231], later independently rediscovered by Axel Thue in 1906 [232], and again by Marston Morse in the 1920s [233]. Its discovery and subsequent investigations have revealed deep connections to various fields of mathematics and physics, illustrating the sequence's profound universality and versatility.

Beyond this initial, explicit, definition, the PTM sequence can also be constructed through iterative or recursive methods.

Definition: (*Iterative definition of the PTM sequence*) The iterative approach involves starting with the initial term 0 and then repeatedly appending the binary complement of the sequence so far. Formally, if T_i represents the sequence at the i -th iteration (with 2^i elements), then:

$$T_0 = \{0\}, \quad T_{i+1} = T_i \parallel \overline{T_i}, \quad (14.2)$$

where $\overline{T_i}$ denotes the binary complement of T_i , and \parallel denotes concatenation.

Definition: (*Recursive definition of the PTM sequence*) Another method is through recursion, where the n -th term can be defined in relation to its predecessors, given by:

$$t_n = (t_{\lfloor n/2 \rfloor} + n) \pmod{2}, \quad t_0 = 0. \quad (14.3)$$

This recursive formula reflects the *self-similarity* and *fractal* nature of the Prouhet-Thue-Morse sequence, emphasizing its deep mathematical properties and relevance to the study of non-periodic structures in physics [229, 230, 234, 235, 236, 237].

Definition: (*Another recursive definition of the PTM sequence*) Another similar recursive formula is:

$$t_0 = 0, \quad t_{2n} = t_n, \quad t_{2n+1} = 1 - t_n \equiv \overline{t_n}. \quad (14.4)$$

Finally, an interesting property of the PTM sequence can be described as follows:

Definition: (*The sets of Evil and Odious numbers*) We define two sets based on the value of t_n within the first 2^N terms of the sequence:

- $E(N)$, the set of indices n for which $t_n = 0$, for all n in the range $0 \leq n \leq 2^N - 1$.
- $O(N)$, the set of indices n for which $t_n = 1$, for all n in the same range.

For any natural number N and for all integers k such that $0 \leq k < N$:

$$\sum_{e \in E(N)} e^k = \sum_{o \in O(N)} o^k. \quad (14.5)$$

i.e. the sum of the k -th powers of the elements in $E(N)$ equals the sum of the k -th powers of the elements in $O(N)$.

This relation demonstrates that the Thue-Morse sequence provides a solution to the Prouhet-Tarry-Escott problem (or multigrades problem) for the given k [238].

14.2 The T-M sequence in Quantum Computing

14.2.1 Definition of PTM (logical) states

First, we define the notation $|(k)_2\rangle$, representing the N qubits state indexed by the base 2 notation of k with N digits, such that, for example, $|(0)_2\rangle = \underbrace{|00\dots 0\rangle}_{N \text{ times}}$ or $|(2^N - 1)_2\rangle = \underbrace{|11\dots 1\rangle}_{N \text{ times}}$.

Definition: (*PTM logical quantum states*) We define the *PTM (logical) states* on a N qubits system, in the uncoupled basis, as:

$$|1_{\text{TM}}^{(N)}\rangle = \frac{1}{\sqrt{2^{N-1}}} \sum_{k=0}^{2^N-1} t_k |(k)_2\rangle = \frac{1}{\sqrt{2^{N-1}}} \sum_{o \in O(N)} |(o)_2\rangle, \quad (14.6)$$

and its complementary (using again $\bar{t} \equiv 1 - t$):

$$|0_{\text{TM}}^{(N)}\rangle = \frac{1}{\sqrt{2^{N-1}}} \sum_{k=0}^{2^N-1} \bar{t}_k |(k)_2\rangle = \frac{1}{\sqrt{2^{N-1}}} \sum_{e \in E(N)} |(e)_2\rangle. \quad (14.7)$$

Note the $1/\sqrt{2^{N-1}}$ prefactor, it arises simply because, by construction, in the first 2^N elements of the PTM sequence, exactly half are 1's.

If one notes that the PTM sequence is equal to 1 if and only if the binary representation has an odd amount of 1's, we get trivially the following property: $\forall N \in \mathbb{N}^*$,

$$|0_{\text{TM}}^{(N+1)}\rangle = \frac{1}{\sqrt{2}} \left(|0\rangle \otimes |0_{\text{TM}}^{(N)}\rangle + |1\rangle \otimes |1_{\text{TM}}^{(N)}\rangle \right)$$

and

$$|1_{\text{TM}}^{(N+1)}\rangle = \frac{1}{\sqrt{2}} \left(|0\rangle \otimes |1_{\text{TM}}^{(N)}\rangle + |1\rangle \otimes |0_{\text{TM}}^{(N)}\rangle \right)$$

Here is an example of construction, the states contributing to $|0_{\text{TM}}^{(2)}\rangle$ (blue) and $|1_{\text{TM}}^{(2)}\rangle$ (red) are highlighted.

$$\boxed{N=2} \quad T_2 = \{ \underset{0}{0} \quad \underset{1}{1} \quad \underset{2}{1} \quad \underset{3}{0} \}$$

$$\begin{aligned} E(2) &= \{ \underset{0}{0} \quad \underset{3}{3} \} \implies |0_{\text{TM}}^{(2)}\rangle = \frac{1}{\sqrt{2}} (|00\rangle + |11\rangle) \\ (E(2))_2 &= \{ \underset{00}{00} \quad \underset{11}{11} \} \end{aligned}$$

$$\begin{aligned} O(2) &= \{ \quad \underset{1}{1} \quad \underset{2}{2} \quad \} \implies |1_{\text{TM}}^{(2)}\rangle = \frac{1}{\sqrt{2}} (|01\rangle + |10\rangle) \\ (O(2))_2 &= \{ \quad \underset{01}{01} \quad \underset{10}{10} \quad \} \end{aligned}$$

Moreover, by adding one more qubit, one can iterate the construction of, this time, $|0_{\text{TM}}^{(3)}\rangle$ and $|1_{\text{TM}}^{(3)}\rangle$. The components of the $|0_{\text{TM}}^{(2)}\rangle$ (resp. $|1_{\text{TM}}^{(2)}\rangle$) PTM state of the two qubit subsystem are underlined in blue (resp. red).

$$\boxed{N=3} \quad T_3 = \{ \underset{0}{0} \quad \underset{1}{1} \quad \underset{2}{1} \quad \underset{3}{0} \quad \underset{4}{1} \quad \underset{5}{0} \quad \underset{6}{0} \quad \underset{7}{1} \}$$

$$\begin{aligned} E(3) &= \{ \underset{0}{0} \quad \quad \underset{3}{3} \quad \quad \underset{5}{5} \quad \underset{6}{6} \quad \} \\ (E(3))_2 &= \{ \underset{000}{000} \quad \underset{011}{011} \quad \underset{101}{101} \quad \underset{110}{110} \quad \} \\ \implies |0_{\text{TM}}^{(3)}\rangle &= \frac{1}{2} (| \underline{000} \rangle + | \underline{011} \rangle + | \underline{101} \rangle + | \underline{110} \rangle) = \frac{1}{\sqrt{2}} (|0\rangle \otimes | \underline{0_{\text{TM}}^{(2)}} \rangle + |1\rangle \otimes | \underline{1_{\text{TM}}^{(2)}} \rangle) \end{aligned}$$

$$\begin{aligned} O(3) &= \{ \quad \underset{1}{1} \quad \underset{2}{2} \quad \quad \underset{4}{4} \quad \quad \underset{7}{7} \quad \} \\ (O(3))_2 &= \{ \quad \underset{001}{001} \quad \underset{010}{010} \quad \underset{100}{100} \quad \underset{111}{111} \quad \} \\ \implies |1_{\text{TM}}^{(3)}\rangle &= \frac{1}{2} (| \underline{001} \rangle + | \underline{010} \rangle + | \underline{100} \rangle + | \underline{111} \rangle) = \frac{1}{\sqrt{2}} (|0\rangle \otimes | \underline{1_{\text{TM}}^{(2)}} \rangle + |1\rangle \otimes | \underline{0_{\text{TM}}^{(2)}} \rangle) \end{aligned}$$

Definition: (Reminder: qubit spin operators) We define the qubit spin operators:

$$\sigma_x = \begin{pmatrix} 0 & 1 \\ 1 & 0 \end{pmatrix}, \quad \sigma_y = \begin{pmatrix} 0 & -i \\ i & 0 \end{pmatrix}, \quad \sigma_z = \begin{pmatrix} 1 & 0 \\ 0 & -1 \end{pmatrix}. \quad (14.8)$$

We will use $\sigma_i^{(k)}$ to indicate that the operator σ_i acts on qubit k among N , i.e. $\sigma_i^{(k)} = \underbrace{\mathbb{1}_2 \otimes \cdots \otimes \mathbb{1}_2}_{k-1 \text{ times}} \otimes \sigma_i \otimes \underbrace{\mathbb{1}_2 \otimes \cdots \otimes \mathbb{1}_2}_{n-k \text{ times}}.$

The PTM states present a certain number of interesting properties regarding spin operators $\sigma_{x,y,z}$:

Property 14.2.1.1 $\forall N > 1, \langle 0_{\text{TM}}^{(N)} | \sum_{k=1}^N \sigma_{x,y,z}^{(k)} | 0_{\text{TM}}^{(N)} \rangle = 0$ and $\langle 1_{\text{TM}}^{(N)} | \sum_{k=1}^N \sigma_{x,y,z}^{(k)} | 1_{\text{TM}}^{(N)} \rangle = 0$. (Proof in appendix)

Property 14.2.1.2 Let Z be an ensemble of $\sigma_z^{(k)}$ acting on M qubits ($M < N$)

$$\begin{aligned} \left\langle 0_{\text{TM}}^{(N)} \left| \prod_{k \in Z} \sigma_z^{(k)} \right| 0_{\text{TM}}^{(N)} \right\rangle &= \left\langle 1_{\text{TM}}^{(N)} \left| \prod_{k \in Z} \sigma_z^{(k)} \right| 1_{\text{TM}}^{(N)} \right\rangle, \\ \text{and } \left\langle 1_{\text{TM}}^{(N)} \left| \prod_{k \in Z} \sigma_z^{(k)} \right| 0_{\text{TM}}^{(N)} \right\rangle &= 0. \end{aligned}$$

(Proof in appendix)

Property 14.2.1.3 Moreover $\forall j < N, i \in \{y, z\}$

$$\left\langle 0_{\text{TM}}^{(N)} \left| \left(\sum_{k=1}^N \sigma_i^{(k)} \right)^j \right| 0_{\text{TM}}^{(N)} \right\rangle = \left\langle 1_{\text{TM}}^{(N)} \left| \left(\sum_{k=1}^N \sigma_i^{(k)} \right)^j \right| 1_{\text{TM}}^{(N)} \right\rangle,$$

$$\text{and } \left\langle 1_{\text{TM}}^{(N)} \left| \left(\sum_{k=1}^N \sigma_i^{(k)} \right)^j \right| 0_{\text{TM}}^{(N)} \right\rangle = 0.$$

(Proof in appendix)

Property 14.2.1.4 $\forall k, j < N, \quad \sigma_x^{(k)} \sigma_x^{(j)} |0_{\text{TM}}^{(N)}\rangle = |0_{\text{TM}}^{(N)}\rangle$ and $\sigma_x^{(k)} \sigma_x^{(j)} |1_{\text{TM}}^{(N)}\rangle = |1_{\text{TM}}^{(N)}\rangle$. (Proof in appendix)

14.2.2 Relations between the PTM states and the Hadamard gate

Definition: (Reminder: Hadamard Gate) We define the single qubit Hadamard gate, acting on qubit k among N qubits:

$$H^{(k)} = \underbrace{\mathbb{1}_2 \otimes \cdots \otimes \mathbb{1}_2}_{k-1 \text{ times}} \otimes \frac{1}{\sqrt{2}} \begin{pmatrix} 1 & 1 \\ 1 & -1 \end{pmatrix} \otimes \underbrace{\mathbb{1}_2 \otimes \cdots \otimes \mathbb{1}_2}_{n-k \text{ times}} \quad (14.9)$$

The first interesting property of the Hadamard gate relating to these newly defined PTM states is that

$$\bigotimes_{k=1}^N H^{(k)} |(0)_2\rangle = \frac{1}{\sqrt{2}} \left(|0_{\text{TM}}^{(N)}\rangle + |1_{\text{TM}}^{(N)}\rangle \right) \quad (14.10)$$

$$\bigotimes_{k=1}^N H^{(k)} |(2^N - 1)_2\rangle = \frac{1}{\sqrt{2}} \left(|0_{\text{TM}}^{(N)}\rangle - |1_{\text{TM}}^{(N)}\rangle \right),$$

allowing for a simple and natural passage from the PTM states to the uncoupled basis, namely

$$\bigotimes_{k=1}^N H^{(k)} |0_{\text{TM}}^{(N)}\rangle = \frac{1}{\sqrt{2}} (|(0)_2\rangle + |(2^N - 1)_2\rangle) \quad (14.11)$$

$$\bigotimes_{k=1}^N H^{(k)} |1_{\text{TM}}^{(N)}\rangle = \frac{1}{\sqrt{2}} (|(0)_2\rangle - |(2^N - 1)_2\rangle).$$

An example of a circuit for encoding a state $|\psi\rangle = \alpha |0\rangle + \beta |1\rangle$ into $|\psi_{\text{TM}}\rangle = \alpha |0_{\text{TM}}^{(N)}\rangle + \beta |1_{\text{TM}}^{(N)}\rangle$ is given in Fig.14.1.

14.2.3 X-X Spin chain and the PTM states

Property 1.3.1.4 can be generalized to verify that the PTM states are among the eigenstates of X - X rotations, and share the same eigenvalue:

$$\forall k, j < N, \quad e^{i\theta \sigma_x^{(k)} \sigma_x^{(j)}} |0_{\text{TM}}^{(N)}\rangle = e^{i\theta} |0_{\text{TM}}^{(N)}\rangle \quad \text{and} \quad e^{i\theta \sigma_x^{(k)} \sigma_x^{(j)}} |1_{\text{TM}}^{(N)}\rangle = e^{i\theta} |1_{\text{TM}}^{(N)}\rangle$$

This means that X - X interactions only add a global phase in the Thue-Morse basis, making the encoding particularly useful to store memory qubits in X - X PTM spin lattices or chains.

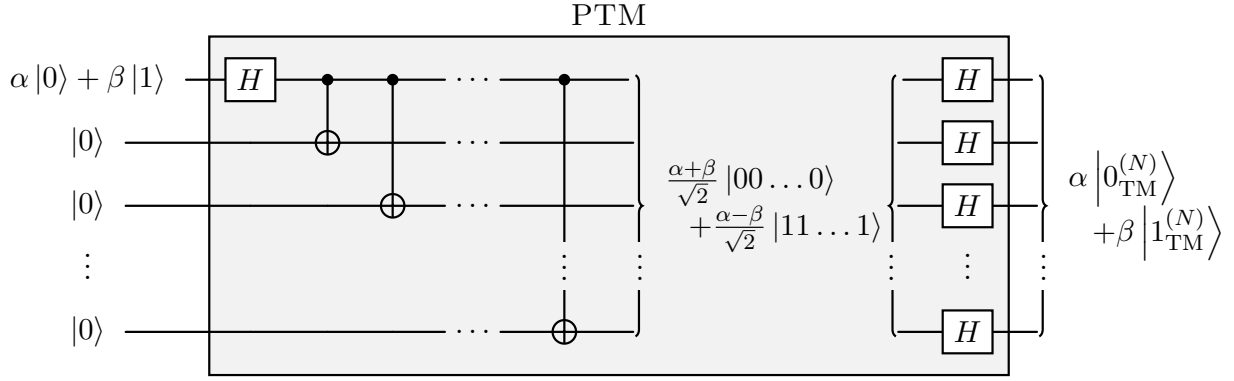


Figure 14.1: Definition of the PTM Gate acting on N qubits.

14.2.4 PTM states as eigenvalues of S_x

By defining $S_{x,z} = \sum_{k=1}^N \sigma_{x,z}^{(k)}$, we have that

$$S_z |(0)_2\rangle = -N |(0)_2\rangle \quad \text{and} \quad S_z |(2^N - 1)_2\rangle = N |(2^N - 1)_2\rangle. \quad (14.12)$$

Using (14.10), the relation $H^{(k)} \sigma_z^{(k)} H^{(k)} = \sigma_x^{(k)}$ and consequently $\left(\bigotimes_{k=1}^N H^{(k)}\right) S_z \left(\bigotimes_{k=1}^N H^{(k)}\right) = S_x$, it is easy to see that

$$S_x |0_{\text{TM}}^{(N)}\rangle = N |1_{\text{TM}}^{(N)}\rangle \quad \text{and} \quad S_x |1_{\text{TM}}^{(N)}\rangle = N |0_{\text{TM}}^{(N)}\rangle. \quad (14.13)$$

The states $\frac{1}{\sqrt{2}} \left(|0_{\text{TM}}^{(N)}\rangle \pm |1_{\text{TM}}^{(N)}\rangle \right)$ are therefore eigenstates of S_x with eigenvalues $\pm N$.

14.2.5 The PTM sequence as the indicator function of the purely dephased X - X Ising chain

Definition: (X - X Ising chain) We define an X - X Ising chain of decohering qubits as a system of N qubits evolving according to the equation:

$$\forall k \in [1, N], \quad L_k = \underbrace{\mathbb{1}_2^{(1)} \otimes \dots \otimes \mathbb{1}_2^{(k-1)}}_{k-1} \otimes S_z^{(k)} \otimes \underbrace{\mathbb{1}_2^{(k+1)} \otimes \dots \otimes \mathbb{1}_2^{(N)}}_{N-k}, \quad (14.14)$$

$$\partial_t \rho(t) = -\frac{i}{\hbar} [H(t), \rho(t)] + \gamma \sum_{k=1}^N L_k \rho(t) L_k^\dagger - \frac{1}{2} \left\{ L_k^\dagger L_k, \rho(t) \right\}.$$

With $H(t) = g \sum_{k=1}^{N-1} S_x^{(k)} \otimes S_x^{(k+1)}$

If the system is initialized in the pure eigenstate $\rho(0) = |i_0\rangle \langle i_0|$, where i_0 belongs to either the set $E(N)$ or $O(N)$, then the final state will be a statistical mixture of states within the same set as the initial state. This implies that the PTM sequence acts as an indicator function, determining whether a state is present in the statistical mixture at the end of the evolution. In other words, $\forall t', \rho_{i,k}(t') \neq 0$ if $t_i = t_k = t_{i_0}$.

The linearity of time evolution allows us to extend this concept: if the initial state is a linear combination of eigenstates, all of which are elements of $E(N)$ (or $O(N)$), then the final state will also be a statistical mixture of states in $E(N)$ (or $O(N)$). Furthermore, if the initial state includes eigenstates from both sets, the final state will be a mixture of all eigenstates.

A special consideration applies to initial states of the form $|\text{GHZ}\rangle = \frac{1}{\sqrt{2}} (|0\rangle_2 + |2^N - 1\rangle_2)$. By definition, $0 \in E(N)$, but $2^N - 1 \in E(N)$ if and only if N is even; otherwise, $2^N \in O(N)$. Therefore, an odd number of qubits initialized in a GHZ state will decohere into a statistical mixture of all eigenstates, whereas an even number of qubits will decohere into a statistical mixture of eigenstates only in E . See Fig. 14.2.

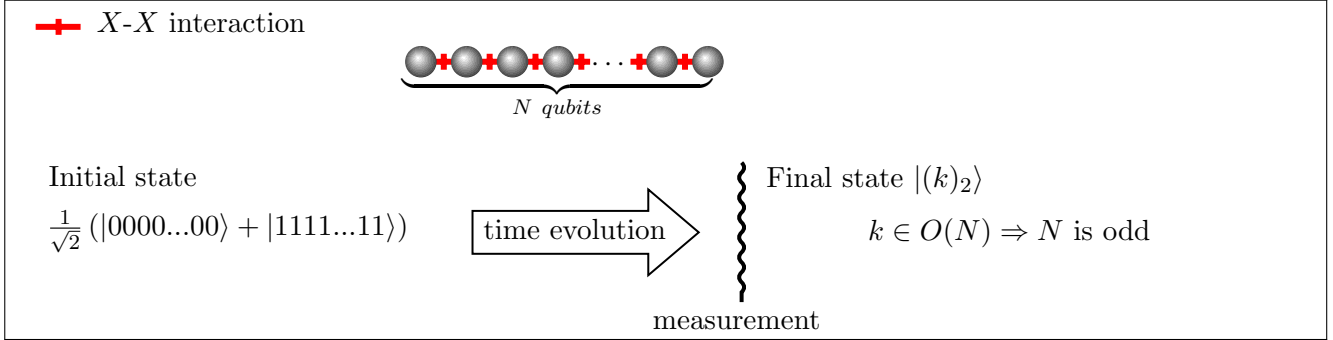


Figure 14.2: Schematic representation of the interplay between the decoherence behavior of a X - X Ising chain initialized in the GHZ state, and the PTM sequence.

14.2.6 Initializing a spin system in a Thue-Morse state

As has been seen in subsection 14.2.4, the Thue-Morse states are mutually reciprocal under S_x , playing a role similar to $\frac{1}{\sqrt{2}} (|0\rangle_2 \pm |2^N - 1\rangle_2)$ for S_z , as hinted at by (14.10).

By using the property that, for a single qubit, $\frac{\pi}{2T\sqrt{2}} (\sigma_z + \sigma_x)$ is the Hamiltonian that optimally generates the Hadamard gate in a time T up to a global phase [212], we get that $H^{(k)} \equiv \exp\left(\frac{-i\pi}{2\sqrt{2}} (\sigma_z^{(k)} + \sigma_x^{(k)})\right)$.

It is therefore clear that implementing the Hamiltonian $\frac{\pi}{2\sqrt{2}} (S_z + S_x)$ on a chain of spins in the $\frac{1}{\sqrt{2}} (|0\rangle_2 \pm |2^N - 1\rangle_2)$ state would allow to initialize a state in either $|0_{\text{TM}}^{(N)}\rangle$ or $|1_{\text{TM}}^{(N)}\rangle$, since, from (14.10) we have that

$$\frac{1}{\sqrt{2}} \bigotimes_{k=1}^N H^{(k)} (|0\rangle_2 \pm |2^N - 1\rangle_2) = |0, 1_{\text{TM}}^{(N)}\rangle. \quad (14.15)$$

Examples of implementations for different N are shown on Fig.14.3.

14.2.7 Quantum Error Correction (QEC)

Property 1.3.1.2 shows that the PTM states satisfy the Knill-Laflamme conditions [239], meaning up to $\frac{N-1}{2}$ single-qubit phase flip errors are detectable, and provided additional ancilla qubits, correctable.

Let us consider the traditional 3 qubit phase-flip error detection circuit depicted in Fig.14.4.

We notice, from (14.10), that in essence by applying the Hadamard gates at the beginning, the state was mapped to the PTM basis as $|\phi_{\text{TM}}\rangle = \frac{\alpha+\beta}{\sqrt{2}} |0_{\text{TM}}^{(3)}\rangle + \frac{\alpha-\beta}{\sqrt{2}} |1_{\text{TM}}^{(3)}\rangle$ just before the error step. Therefore to adapt this error correction code to the PTM basis, it is only necessary to map $|\phi\rangle$ to $|\phi_{\text{TM}}\rangle$ by applying Hadamard gates at the end, see Fig.14.5. This provides an error-correcting gate that is applied after the error has occurred, without the need for any state preparation prior to errors happening.

The same argument about error detection and correction can be applied to Property 1.3.1.3 for errors due to a global magnetic field along the z or y direction.

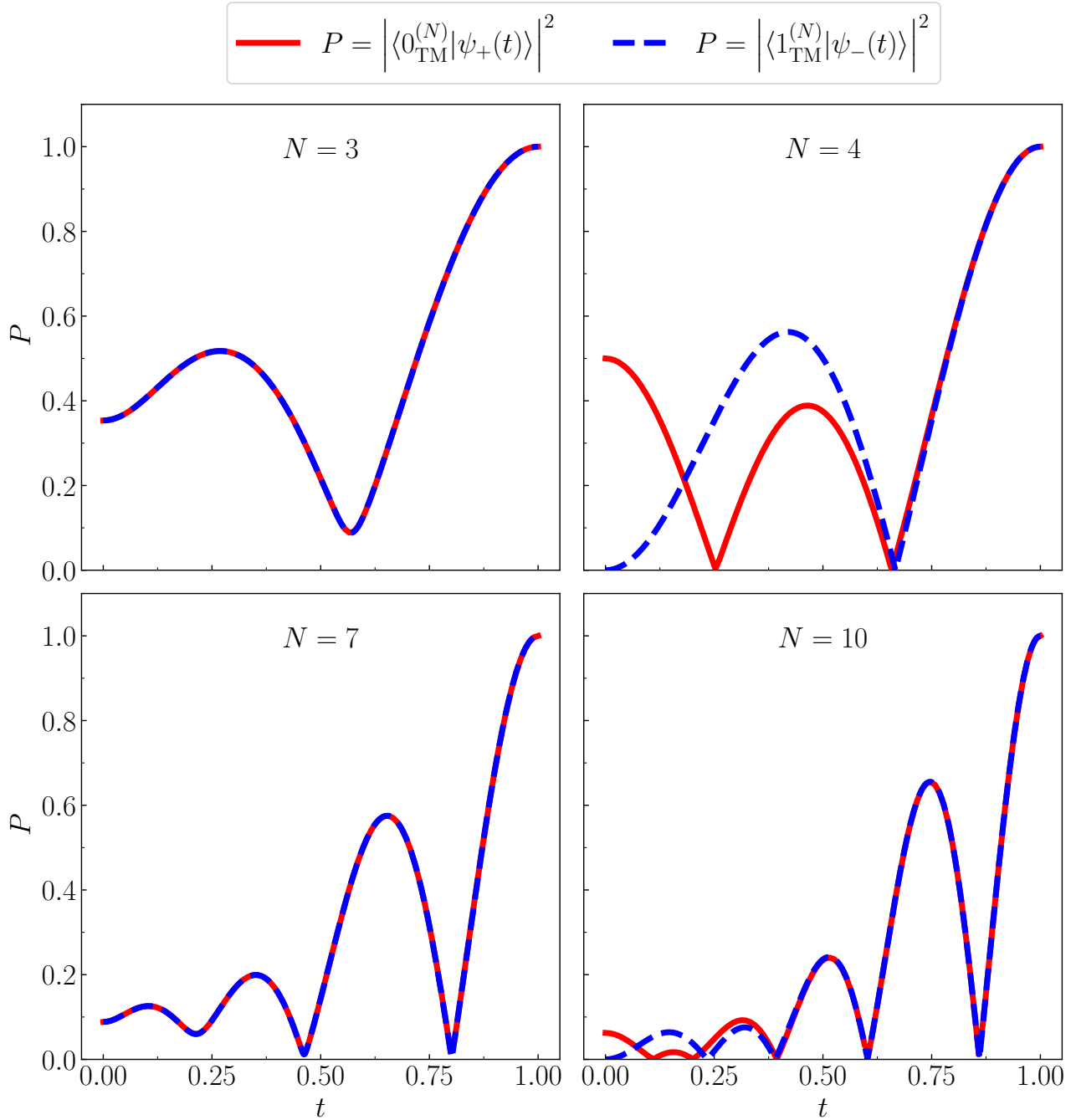


Figure 14.3: Time-evolution of the populations P of different states initialized in $|\psi_{0,+}\rangle = \frac{1}{\sqrt{2}}(|(0)_2\rangle + |(N)_2\rangle)$ (red) or $|\psi_{0,-}\rangle = \frac{1}{\sqrt{2}}(|(0)_2\rangle - |(N)_2\rangle)$ (blue). With $|\psi_{\pm}(t)\rangle = \exp\left(\frac{-i\pi}{2\sqrt{2}}(S_z + S_x)t\right)|\psi_{0,\pm}\rangle$. The final state corresponds to $|\psi_{\pm}(1)\rangle = \bigotimes_{k=1}^N H^{(k)}|\psi_{0,\pm}\rangle$.

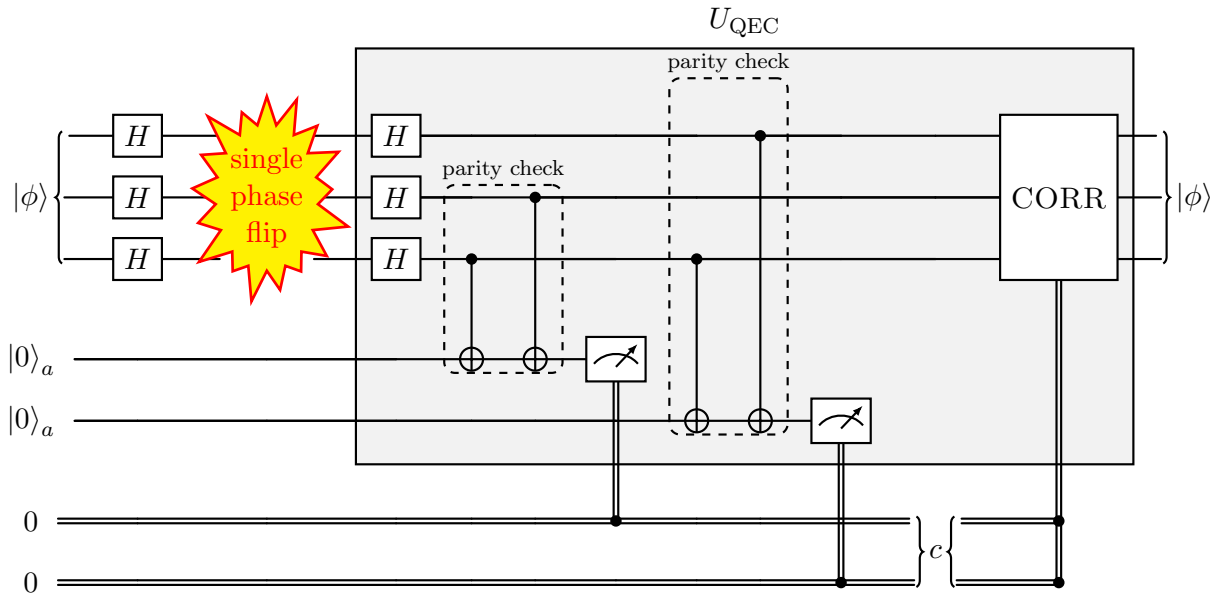


Figure 14.4: Traditional (Shor's) 3-qubit phase-flip error correction code. One can detect and correct 1 phase flip error using 2 ancilla qubits for parity checks, and with initial state $|\phi\rangle = \alpha|000\rangle + \beta|111\rangle$. CORR takes as an input the classical two-bits registry $c = (i)_2$, does nothing if $i = 0$, and flips qubit i otherwise, counting from top to bottom.

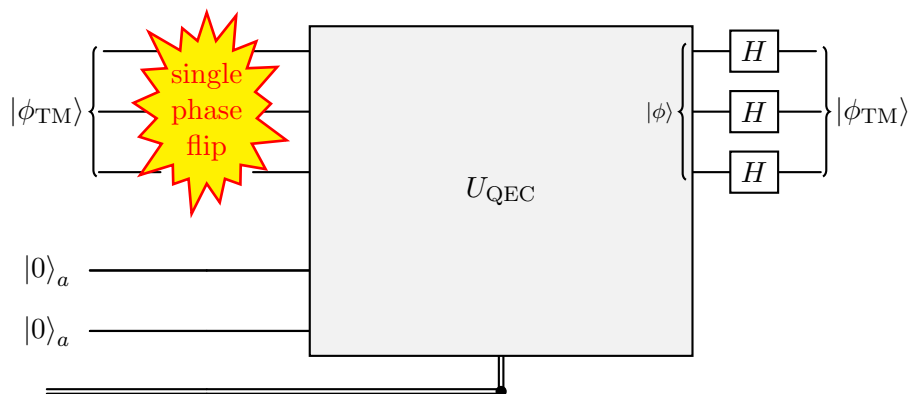


Figure 14.5: 3-qubit single phase-flip error correction code for one logical PTM state.

Property 1.3.1.3 can be generalized for d -level quantum bases of information, or qudits (*Proof in appendix*), if one defines the Thue-Morse states as:

$$\left|1_{\text{TM}}^{(N)}\right\rangle = \sqrt{\frac{2}{d}} \sum_{k=0}^{d-1} t_k |k\rangle, \quad \left|0_{\text{TM}}^{(N)}\right\rangle = \sqrt{\frac{2}{d}} \sum_{k=0}^{d-1} \bar{t}_k |k\rangle. \quad (14.16)$$

Qudits may present certain advantages over qubits, providing a higher density of information, and a reduced number of non-local gates. Moreover their higher error rates, due to the increased number of excited states, can be compensated in certain platforms with fast gate times and slow decoherence times [186, 204].

In this case, it can be proven that PTM states provide noise detection for J_z (spin- $\frac{d-1}{2}$ operator) up to order $\frac{1}{2}(\log_2(d) - 1)$, providing an encoding of error robust states conceptually similar to Chiesa *et al.* (2020) [181].

14.2.8 Noise-resistant quantum memories

Property 1.3.1.1. implies that the PTM states are robust to external magnetic fields along any spatial direction to first order.

Moreover, in the PTM logical basis, the different total spin operators take the following matrix forms:

$$\left\langle 0, 1_{\text{TM}}^{(N)} \left| S_x \right| 0, 1_{\text{TM}}^{(N)} \right\rangle = \begin{pmatrix} 0 & 1 \\ 1 & 0 \end{pmatrix}, \quad S_y = \begin{pmatrix} 0 & 0 \\ 0 & 0 \end{pmatrix}, \quad S_z = \begin{pmatrix} 0 & 0 \\ 0 & 0 \end{pmatrix}. \quad (14.17)$$

This makes the PTM states particularly useful for storing a logical qubit in an environment with strong magnetic noise along the y or z -direction. This is not applicable in the x -direction, as only the states $\left|0_{\text{TM}}^{(N)}\right\rangle$ and $\left|1_{\text{TM}}^{(N)}\right\rangle$ are robust, but not superposition states.

14.3 Link to quantum chaos

From the analysis presented in (14.10), it becomes evident that the last row of the Walsh-Hadamard matrix corresponds to a modified PTM sequence, specifically represented as $(-1)^{t_n}$. This particular element and its connection to quantum chaos has been explored in depth in [240, 241], where the interplay between the PTM sequence and the quantum Fourier transform is investigated. This synergy is central to the construction of an approximate multifractal eigenstate of the quantum baker's map, providing a novel approach to unraveling the complexity of quantum chaotic systems. Such findings not only highlight the multifaceted role of the PTM sequence within quantum chaos but also contribute significantly to our broader understanding of the dynamical properties of quantum systems.

Definition: ((Reminder) Quantum Fourier Transform) An example of these interesting properties can be observed by defining the N -qubits Quantum Fourier Transform $QFT(N)$ gate, elementwise ($0 \leq j, k < N$)

$$(QFT(N))_{jk} = \frac{1}{\sqrt{2^N}} e^{i \frac{2\pi}{2^N} jk}. \quad (14.18)$$

This gate, that applies the discrete Fourier transform over the Hilbert Space of the qubits, is essential for some quantum algorithms such as Shor's factorization algorithm [7].

Applying the QFT gate to a state in the PTM basis proves interesting, since

$$QFT(N) \left(\alpha \left| 0_{\text{TM}}^{(N)} \right\rangle + \beta \left| 1_{\text{TM}}^{(N)} \right\rangle \right) = \frac{\sqrt{2}}{2^N} \sum_{j=0}^{2^N-1} \sum_{k=0}^{2^N-1} \frac{1}{2} (\alpha + \beta + (-1)^{t_k} (\alpha - \beta)) e^{i \frac{2\pi}{2^N} jk} |(j)_2\rangle \quad (14.19)$$

Therefore, by defining $F_j^{TM} \equiv \langle j | QFT(N) (\alpha \left| 0_{\text{TM}}^{(N)} \right\rangle + \beta \left| 1_{\text{TM}}^{(N)} \right\rangle) \rangle$ and since $\forall j \in \mathbb{N}^*$, $\sum_{k=0}^{2^N-1} e^{i \frac{2\pi}{2^N} jk} = 0$, we have

$$F_{j \neq 0}^{TM} = \frac{\alpha - \beta}{2^N \sqrt{2}} \sum_{k=0}^{2^N-1} (-1)^{t_k} e^{i \frac{2\pi}{2^N} jk}. \quad (14.20)$$

Moreover [238],

$$\forall x \in \mathbb{R}, \quad \prod_{k=0}^{N-1} (1 - x^{2^k}) = \sum_{k=0}^{2^N-1} (-1)^{t_k} x^k, \quad (14.21)$$

hence,

$$F_{j \neq 0}^{TM} = \frac{\alpha - \beta}{2^N \sqrt{2}} \prod_{k=0}^{N-1} (1 - e^{i \frac{2\pi j}{2^{N-k}}}). \quad (14.22)$$

The specific case of $j = 0$, is given by

$$F_0^{TM} = \frac{\alpha + \beta}{\sqrt{2}}. \quad (14.23)$$

Further simplifying, we obtain, for $j \neq 0$

$$|F_j^{TM}|^2 = \frac{(\alpha - \beta)^2}{2} \prod_{k=0}^{N-1} \sin^2(\pi j 2^{k-N}). \quad (14.24)$$

For the case $\alpha = -\beta = \frac{1}{\sqrt{2}}$, $|F_j^{TM}|^2 = \langle j | QFT(N) \otimes_{k=1}^N H^{(k)} | (2^N - 1)_2 \rangle$ are shown in Fig.14.6 for $N = 20$. One can notice self-similarity and infer the multifractal nature of the state in the Hilbert Space.

It is these multifractal properties [242] and the recursive definition of the Thue-Morse states that have been used in to construct, for example, approximate eigenstates of the quantum baker map $B(N)$ [240].

$$B(N) = QFT(N)^{-1} \begin{pmatrix} QFT(N-1) & 0 \\ 0 & QFT(N-1) \end{pmatrix}. \quad (14.25)$$

Moreover, considering the use of both the Hadamard gate $\otimes_{k=1}^N H^{(k)}$ and QFT gate $QFT(N)$ in Shor's factorization algorithm, it would be interesting to study further the appearance of quantum chaos that we showed arising from their interactions in such a well-known quantum algorithm [241].

14.4 Link with number theory

There are several interesting formulae that use the PTM sequence [229, 243], including:

- The product generating function formula for the PTM sequence

$$\forall x \in \mathbb{R}, \quad \prod_{i=0}^N (1 - x^{2^i}) = \sum_{j=0}^{2^{N+1}-1} (-1)^{t_j} x^j, \quad (14.26)$$

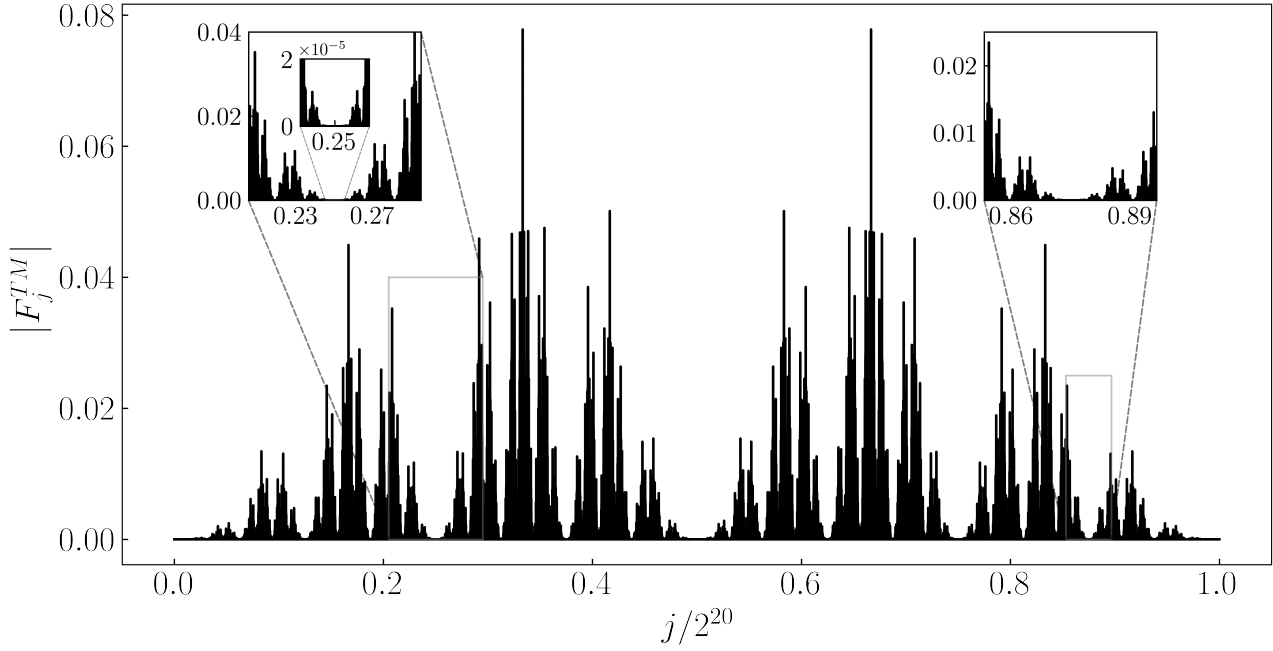


Figure 14.6: Amplitudes of $F_j^{TM} = \frac{1}{\sqrt{2}} \langle j | (20) \left(|0_{TM}^{(20)}\rangle - |1_{TM}^{(20)}\rangle \right) = \langle j | QFT(20) \otimes_{k=1}^{20} H^{(k)} | (2^N - 1)_2 \rangle$ for $j = 0$ to $2^N - 1$. Two zooms, around 0.2 and 0.88 show the self-similarity of the curve. An additional zoom around 0.25 further shows the self similar behaviour.

it can also be generalized for $N \rightarrow \infty$,

$$\forall x \in \mathbb{R}, \quad \prod_{i=0}^{\infty} (1 - x^{2^i}) = \sum_{j=0}^{\infty} (-1)^{t_j} x^j \quad (14.27)$$

- $\prod_{n=0}^{\infty} \left(\frac{2n+1}{2n+2} \right)^{2(1-t_n)} \left(\frac{2n+3}{2n+2} \right) = \frac{\sqrt{2}}{\pi}$
- $\prod_{n=0}^{\infty} \left(\frac{2n+1}{2n+2} \right)^{2t_n} \left(\frac{2n+3}{2n+2} \right) = \frac{2\sqrt{2}}{\pi}$
- $\prod_{n=0}^{\infty} \left(\frac{2n+1}{2n+2} \right)^{(-1)^{t_n}} = \frac{\sqrt{2}}{2}$
- $\prod_{n=1}^{\infty} \left(\frac{2n}{2n+1} \right)^{(-1)^{t_n}} = 1.6281\dots$ converges towards a number whose algebraic nature remains unknown [229].
- $\tau = \sum_{i=0}^{\infty} \frac{t_i}{2^{i+1}} = 0.41245\dots$ is known as the PTM constant and has been proved to be a transcendental number.
- $\forall s \in \mathbb{C}$ s.t. $\text{Re}(s) > 1$, $\zeta(s) = (1 + \frac{1}{2^s}) \sum_{n \geq 1} \frac{t_{n-1}}{n^s} + (1 - \frac{1}{2^s}) \sum_{n \geq 1} \frac{t_n}{n^s}$, where ζ is the Riemann Zeta function.

In particular, the last formula presents an interesting linear combination of Dirichlet series. When linked to the work of Feiler and Schleich [244], it becomes of particular interest as it provides a link

between quantum computing and number theory. Just as in the cited work, one can obtain the result of this sum of Dirichlet series using the interference of two initial quantum states in a non-linear interaction with logarithmic energy spectrum. Let us assume a given system evolves under a non-linear oscillator Hamiltonian with a logarithmic energy spectrum: $H = \hbar\omega \ln(n+1) |n\rangle$ [245]. Given a certain $s = \sigma + i\tau$ complex argument, one can consider two non-normalized states:

$$\begin{aligned}
|\psi_1\rangle &= \sum_{n \geq 0} t_n \cdot (n+1)^{-\sigma/2} |n\rangle \\
|\psi_2\rangle &= \sum_{n \geq 0} t_{n+1} \cdot (n+1)^{-\sigma/2} |n\rangle.
\end{aligned} \tag{14.28}$$

If one measures the conjugate auto-correlation probability amplitude $\langle \psi^* | \psi(t) \rangle$ for any of those states, evolved for time $t = \tau/\omega$, the result will be the first (resp. second) Dirichlet series in $\zeta(s) = (1 + \frac{1}{2^s}) \sum_{n \geq 1} \frac{t_{n-1}}{n^s} + (1 - \frac{1}{2^s}) \sum_{n \geq 1} \frac{t_n}{n^s}$.

Following the arguments of *Feiler et al.* [244], we remark that by evolving the initial state

$$|\psi_0\rangle = \mathcal{N} \left(\left(1 + \frac{1}{2^s}\right) |\psi_1\rangle + \left(1 - \frac{1}{2^s}\right) |\psi_2\rangle \right), \tag{14.29}$$

for a time $t = \tau/g$ under an interaction with a logarithmic energy spectrum in the interaction picture [246] ($H_I = \hbar g \ln(\hat{n} + 1) \hat{\sigma}_z$), the measurement of the conjugate auto-correlation probability amplitude $\langle \psi_0^* | \psi_0(t) \rangle$ is expected to yield the exact value of $\zeta(s) = \mathcal{N}^2 \left[\left(1 + \frac{1}{2^s}\right) \sum_{n \geq 1} \frac{t_{n-1}}{n^s} + \left(1 - \frac{1}{2^s}\right) \sum_{n \geq 1} \frac{t_n}{n^s} \right]$.

This provides a method to determine the value of the Riemann ζ function through quantum measurements.

14.5 Conclusion

In this chapter, we have explored the many manifestations and uses of the Prouhet-Thue-Morse (PTM) sequence in quantum computing, highlighting its intrinsic mathematical beauty and practical significance. Through rigorous analysis, we have shown that the PTM sequence, beyond its mathematical appeal, plays a central role in quantum error correction, the design of noise-resistant quantum memories. We also elucidated its links with quantum chaos and number theory.

Our investigations have shown how logical states whose encoding is based on the PTM sequence exhibit remarkable properties, such as resilience to spin flip errors and low sensitivity to external magnetic fields, thus providing valuable insights for the design of fault-tolerant quantum computing architectures. Furthermore, the integration of the sequence into the Hilbert space of quantum computing platforms, particularly in the context of the X-X Ising chain and spin systems, demonstrates its potential to increase the efficiency and reliability of quantum information processing.

The connection between the PTM sequence and quantum chaos, through the Walsh-Hadamard transform and the quantum baker's map, enriches our understanding of the dynamical behaviors of quantum systems and provides a novel lens through which to view quantum chaos. Moreover, the intriguing links between the PTM sequence and number theory, exemplified by its relation to the Riemann zeta function and Dirichlet series, open new avenues for interdisciplinary research, bridging quantum computing and mathematical number theory.

While the novelty of our results is tempered by the fundamental nature of the PTM sequence in both mathematics and physics, the implications of our findings for quantum computing are profound. The insights gained from this study not only contribute to the ongoing development of quantum computing technologies but also stimulate further research into the underlying mathematical structures that govern quantum mechanics.

As we continue to unravel the complexities of quantum systems and their computing capabilities, the PTM sequence stands as a testament to the deep connections between abstract mathematical concepts and practical quantum technologies. Our exploration of these links also highlights the importance of interdisciplinary research, in this case, physics and mathematics, in order to reveal the full potential of quantum computing.

References of this part

- [7] Shor, P. W. “Polynomial-Time Algorithms for Prime Factorization and Discrete Logarithms on a Quantum Computer”, *SIAM Journal on Computing*, 1997, 26:5, 1484–1509.
- [181] Chiesa, A.; Macaluso, E.; Petiziol, F.; Wimberger, S.; Santini, P.; Carretta, S. “Molecular Nanomagnets as Qubits with Embedded Quantum-Error Correction”, *The Journal of Physical Chemistry Letters*, 2020, 11:20, 8610–8615.
- [186] Janković, D.; Hartmann, J.-G.; Ruben, M.; Hervieux, P.-A. “Noisy qudit vs multiple qubits: conditions on gate efficiency for enhancing fidelity”, *npj Quantum Information*, 2024, 10:1, 59.
- [204] Hartmann, J.-G.; Janković, D.; Pasquier, R.; Ruben, M.; Hervieux, P.-A. Nonlinearity of the Fidelity in Open Qudit Systems: Gate and Noise Dependence in High-dimensional Quantum Computing, 2024.
- [212] Aifer, M.; Deffner, S. “From quantum speed limits to energy-efficient quantum gates”, *New Journal of Physics*, 2022, 24:5, 055002.
- [229] Allouche, J.-P.; Shallit, J. In *Sequences and their Applications*, ed. by Ding, C.; Helleseth, T.; Niederreiter, H., Springer London: London, 1999, pp 1–16.
- [230] Kolářík, M.; Ali, M. K.; Nori, F. “Generalized Thue-Morse chains and their physical properties”, *Phys. Rev. B*, 1991, 43:1, 1034–1047.
- [231] Prouhet, E. “Memoire sur quelques relations entre les puissances des nombres”, *C. R. Acad. Sci. Paris Ser. I*, 1851, 33, 225.
- [232] Thue, A. “Über unendliche Zeichenreihen”, *Kra. Vidensk. Selsk. Skrifter. I. Mat.-Nat. Kl.*, 1906:7.
- [233] Morse, H. M. “Recurrent geodesics on a surface of negative curvature”, *Transactions of the American Mathematical Society*, 22, 84–100.
- [234] Xiong, L.; Zhang, Y.; Liu, Y.; Zheng, Y.; Jiang, X. “Higher-order topological states in photonic Thue-Morse quasicrystals: Quadrupole insulator and the origin of corner states”, *Physical Review Applied*, 2022, 18:6, 064089.
- [235] Deng, X.-H.; Yuan, R.; Hong, W.-Q.; Ouyang, H. “Tunable filters based on Thue-Morse quasicrystals composed of single-negative materials”, *Physics Procedia*, 2011, 22, 360–365.
- [236] Matarazzo, V.; De Nicola, S.; Zito, G.; Mormile, P.; Rippa, M.; Abbate, G.; Zhou, J.; Petti, L. “Spectral characterization of two-dimensional Thue–Morse quasicrystals realized with high resolution lithography”, *Journal of Optics*, 2010, 13:1, 015602.
- [237] Yang, J.-K.; Noh, H.; Boriskina, S. V.; Rooks, M. J.; Solomon, G. S.; Dal Negro, L.; Cao, H. In *2012 Conference on Lasers and Electro-Optics (CLEO)*, 2012, pp 1–2.
- [238] Nguyen, H. D. A New Proof of the Prouhet-Tarry-Escott Problem, 2014.
- [239] Knill, E.; Laflamme, R. “Theory of quantum error-correcting codes”, *Phys. Rev. A*, 1997, 55:2, 900–911.
- [240] Meenakshisundaram, N.; Lakshminarayan, A. “Multifractal eigenstates of quantum chaos and the Thue-Morse sequence”, *Phys. Rev. E*, 2005, 71:6, 065303.

- [241] Maity, K.; Lakshminarayan, A. “Quantum chaos in the spectrum of operators used in Shor’s algorithm”, *Phys. Rev. E*, 2006, *74*:3, 035203.
- [242] Fan, A.; Schmeling, J.; Shen, W. Multifractal Analysis of generalized Thue-Morse trigonometric polynomials, 2022.
- [243] Tóth, L. “Linear Combinations of Dirichlet Series Associated with the Thue-Morse Sequence”, 2022.
- [244] Feiler, C.; Schleich, W. P. “Dirichlet series as interfering probability amplitudes for quantum measurements”, *New Journal of Physics*, 2015, *17*:6, 063040.
- [245] Gleisberg, F.; Mack, R.; Vogel, K.; Schleich, W. P. “Factorization with a logarithmic energy spectrum”, *New Journal of Physics*, 2013, *15*:2, 023037.
- [246] Feiler, C.; Schleich, W. P. “Entanglement and analytical continuation: an intimate relation told by the Riemann zeta function”, *New Journal of Physics*, 2013, *15*:6, 063009.

PART V

Conclusion

15 Overview and Perspectives	297
15.1 Current state of the art	297
15.2 Areas left to explore	299

Chapter Contents

15.1 Current state of the art	297
15.2 Areas left to explore	299

CHAPTER 15

Overview and Perspectives

"I may not have gone where I intended to go, but I think I have ended up where I needed to be."

— **Douglas Adams**, *The Long Dark Tea-Time of the Soul*

15.1 Current state of the art

15.1.1 A theoretical toolbox for lanthanide-based qudit engineering

Throughout this work, we have developed a comprehensive theoretical toolbox aimed at the non-empirical engineering of lanthanide-based molecular qudits. One of our primary achievements was demonstrating that the atomic theoretical framework—which is particularly well-suited for lanthanides in materials—can be effectively applied to predict the electronic structures of lanthanide complexes. Specifically, we have proposed that the Ligand Field Density Functional Theory (LFDFT) method proves to be exceptionally useful for performing rapid quantitative benchmarking of various molecular environments. By combining swift DFT calculations with wavefunction-based full Hamiltonian matrix computations, this method would allow us to accurately obtain the hyperfine energy levels of the lanthanide ions under consideration across different ligand environments and orientations of external fields. This powerful computational approach would serve as a robust tool for predicting the specific symmetries, ligand compositions, and metal-ligand combinations that will lead to the desired hyperfine energy levels. It also enables us to identify important properties necessary for or improving response to electric or light fields, which are crucial for applications in quantum information processing.

By systematically exploring the parameter space of molecular designs without resorting to empirical and oftentimes costly trial-and-error methods in the lab, we can tailor the properties of lanthanide-based qudits to meet specific requirements, doing *in-silico* experiments instead. This capability would significantly accelerate the development of advanced lanthanide-based materials for quantum information processing. Overall, our work lays a solid theoretical foundation that supports the rational and efficient design of lanthanide-based molecular systems for use in quantum information processing.

15.1.2 A how-to guide for Ln-molecular QIP implementations

This work also lays the groundwork for the practical implementation of universal single-qudit quantum gates, a significant challenge that our group faced in previous experiments. We have explored various methods for devising pulses that can implement the desired quantum gates in a controlled and precise manner. By employing optimal control theory, we have demonstrated that it is possible to find optimal

pulse sequences that achieve high-fidelity implementation of these gates.

Furthermore, we have shown that the computational performance of qudits is extremely sensitive to increases in the system's dimensionality, and we have quantified this scaling behavior. This sensitivity makes it crucial to decrease the duration of the pulses to prevent the accumulation of errors over time, which can severely impact performance. To address this issue, we introduced the Method for Adjoint- and Gradient-based self-Iterative Construction and Refinement of Pulses (MAGICARP). This hybrid method builds upon the Pontryagin Maximum Principle to determine the mathematical form of the time-optimal pulse and utilizes the gradient-ascent techniques to find the optimal parameters for the pulse to implement the desired gate. An important advantage of the MAGICARP method is that the number of optimization parameters depends only on the dimension of the system, not on the number of control pulses or the number of discretization time steps.

Overall, our contributions provide a practical pathway toward realizing universal single-qudit quantum gates, addressing key challenges related to pulse design and optimization in high-dimensional quantum systems. This advancement not only benefits our group's experimental efforts but also has broader implications for the field of quantum information processing. Efficient control of qudit systems is essential for developing scalable quantum technologies, and our work significantly contributes to this goal by offering innovative solutions to previously intractable problems.

By systematically applying these methods, we can accelerate the development of quantum devices that leverage the higher-dimensional state spaces of qudits. This opens up new avenues for more complex quantum computations and simulations, potentially leading to breakthroughs in areas such as quantum cryptography, quantum error correction, and quantum algorithms. Our research thus serves as a critical stepping stone toward the next generation of quantum technologies, where control precision and system dimensionality play pivotal roles in performance and capability.

15.1.3 Nuclear and hyperfine structure of lanthanides

Our exploration into low-energy nuclear physics has highlighted the potential of using highly charged muonic lanthanide ions to benchmark nuclear models of highly deformed nuclei. Specifically, we have computed the Bohr-Weisskopf and Breit-Rosenthal corrections for various lanthanide isotopes, including ^{159}Tb , ^{161}Dy , ^{163}Dy , and ^{165}Ho . The latter results were compared to experimental ones to assess the model. These computations have provided valuable insights into both even-odd and odd-even nuclei, revealing the complex and diverse nuclear properties exhibited by lanthanides despite minimal changes in their nucleon compositions.

The observed complexity and variation in nuclear properties make lanthanides particularly intriguing candidates for isotopic exploration within this family of elements. By manipulating their nuclear and electrical properties through isotopic variation, we can optimize the Hilbert space of qudits for quantum information processing applications. This ability to fine-tune properties at the nuclear level offers a promising avenue for enhancing the performance and scalability of qudit-based quantum systems.

Furthermore, our findings suggest that leveraging the unique characteristics of lanthanide isotopes could lead to improved nuclear models, especially for highly deformed nuclei as it is the case for lanthanides. By bridging the gap between nuclear physics and atomic physics and quantum chemistry, we open up new possibilities for the design and control of quantum systems at the intersection of these disciplines.

Overall, our detour into low-energy nuclear physics has enriched our understanding of the intricate interplay between nuclear structure and quantum information processing. It underscores the importance of interdisciplinary approaches in tackling complex scientific challenges and paves the way for future research that could further optimize the properties of qudits. By exploring the isotopic variations of lanthanides, we can continue to refine our models and techniques, ultimately contributing to the advancement of both nuclear physics and quantum computing.

15.2 Areas left to explore

15.2.1 Ab-initio study of the decoherence

In our current model, the incorporation of ligands and external fields is purely static, which limits our ability to fully understand the dynamical properties of lanthanide ions within a matrix. Introducing time-dependent elements into the model would provide additional insights into these dynamics. This enhancement can be achieved by extending the perturbative approaches utilized in this work to include time-dependent perturbation theory. Such an extension would allow us to capture the evolution of the system over time, offering a more comprehensive understanding of the interactions at play.

Moreover, the dynamics of the ligand field can be incorporated by advancing Ligand Field Theory beyond its static framework. By including spin-phonon coupling through a first-order expansion of the ligand field parameters with respect to the nuclear motion of the ligands [247, 248, 249], we can account for the interactions between the electronic spins and lattice vibrations. This method should be considered a priority for future research, as it would provide valuable insights into the T_1 (spin-lattice relaxation) and T_2 (spin-spin relaxation) timescales of nuclear qubits. Understanding these relaxation processes is crucial for quantum information applications, where decoherence can significantly impact performance.

Additionally, incorporating time-dependent dynamics into our model would prove highly beneficial in studying the optical properties of lanthanides. Beyond the static model's capability to calculate transition amplitudes, a dynamic approach could enable us to predict the linewidths of the forbidden f - f transitions. These transitions are of particular interest due to their sharp spectral features and potential applications in optical devices and quantum technologies. A better understanding of the linewidths would enhance our ability to design lanthanide-based materials with specific optical properties.

By extending our theoretical framework to include time-dependent effects and dynamic ligand fields, we pave the way for a deeper understanding of lanthanide-based systems. This advancement not only contributes to the fundamental science of these complex materials but also facilitates the design of new compounds with tailored properties for specific applications in quantum computing, photonics, and materials science. Such a comprehensive model would allow us to manipulate nuclear and electrical properties more effectively, optimizing the Hilbert space of qubits and potentially leading to breakthroughs in experimentally-realizations of high-dimensional quantum information processing.

In summary, moving beyond static models to incorporate time-dependent dynamics and spin-phonon interactions holds significant promise for advancing both our theoretical understanding and practical capabilities. It opens up new avenues for exploring the intricate behaviors of lanthanide ions and designing materials that can meet the demanding requirements of next-generation quantum technologies. This approach aligns with the broader goals of our research, aiming to bridge gaps between theoretical predictions and experimental realizations, ultimately contributing to the development of more efficient and scalable quantum systems.

15.2.2 In-depth study of the effect of ligand composition and geometry

In our research, the effective operator formalism developed for the hyperfine Stark effect and hyperfine-induced optical transitions has provided valuable insights into the conditions imposed on ligand field parameters within the analytical expressions of the effective operators. Previously, we only briefly discussed these conditions in terms of straightforward selection rules derived from Racah algebra. However, conducting an in-depth study of these selection rules, along with a more quantitative evaluation of the various terms in the effective Hamiltonian, could yield particularly useful insights into the specific requirements for the ligand field. Such an analysis could also elucidate the relative importance of certain odd-rank contributions compared to others.

Delving deeper into the selection rules of the effective operators would allow us to understand better how different ligand field parameters influence the hyperfine interactions and optical transitions in lanthanide complexes. By quantitatively assessing the contributions of each term in the effective Hamiltonian, we can identify which parameters are most critical for achieving desired properties in the system. This approach is akin to the insights provided by the Judd-Ofelt theory when it was first introduced, which significantly advanced our understanding of electric-dipole transitions in rare-earth ions by systematically accounting for the contributions of different tensor operator ranks.

Such a comprehensive study would not only refine our theoretical models but also guide the practical design of new materials with tailored properties for quantum information processing and other advanced applications. By understanding the specific roles of various ligand field parameters and the significance of odd-rank tensor operators, we can optimize the ligand field environment to enhance certain hyperfine electrical field responses or optical transitions. This optimization is crucial for improving the performance and scalability of molecular qubits in quantum computing.

Moreover, this deeper analysis could reveal subtle effects that are not apparent from a cursory examination of selection rules. It might uncover, for instance, how small changes in ligand geometry or composition can have significant impacts on the hyperfine interactions due to the sensitive dependence on certain ligand field parameters. Such insights would be invaluable for experimentalists seeking to synthesize new compounds with precisely controlled properties.

Extending our investigation to include a detailed examination of the selection rules and a quantitative evaluation of the effective Hamiltonian terms holds significant promise. It would enhance our understanding of the interplay between ligand fields and hyperfine interactions, similar to the way Judd-Ofelt theory enriched our knowledge of optical transitions in rare-earth elements. This advancement would ultimately contribute to the development of more effective strategies for engineering lanthanide-based quantum systems, pushing the boundaries of what is achievable in high-dimensional quantum information processing.

15.2.3 Calculating the hyperfine structure of multielectronic ions in molecules/crystals

Our methodology for computing Fermi contact terms and hyperfine constants in lanthanide complexes has thus far primarily focused on single-electron (or single-muon) systems, where electronic correlation effects are relatively straightforward to manage. However, extending this methodology to multielectronic systems presents a significant challenge due to the increased complexity arising from electron-electron interactions. Despite these challenges, developing accurate methods for calculating hyperfine constants in multielectronic systems is crucial for a comprehensive understanding of hyperfine interactions in lanthanide complexes, which typically involve multiple electrons in the $4f$ and sometimes $6s$ orbitals.

Incorporating the exact hyperfine Hamiltonians—beyond their traditional effective form within a given J -multiplet—into the atomistic Hamiltonian of the lanthanide ion in the ligand field would be particularly advantageous and allow to account for multiplet and even configuration mixing. This approach would enable us to calculate the hyperfine Stark effect and hyperfine-induced optical transitions with greater accuracy through exact diagonalization of the full Hamiltonian. However, exact diagonalization of such large Hamiltonians can be computationally demanding and may not be feasible for systems with a high number of electrons.

To overcome this computational hurdle, we can employ faster and less resource-intensive partial diagonalization methods [250]. These techniques allow us to obtain only the energies of the ground hyperfine doublets and possibly the corresponding eigenvectors without the need to compute the entire spectrum of the Hamiltonian. For instance, iterative algorithms like the Lanczos method or the Davidson algorithm can efficiently find a few extremal eigenvalues and eigenvectors of large sparse matrices, making them well-suited for our purposes.

Applying these partial diagonalization methods would be particularly useful for studying the hyperfine

Stark effect in the presence of external electric fields. By performing successive diagonalizations of the Hamiltonian for different values of electric field strength and orientations, we can quantitatively assess how the hyperfine energy levels shift in response to the field. Additionally, analyzing the composition of the eigenvectors provides valuable information on the expected Stark shifts, enhancing our understanding of the system's response to external perturbations.

Advancing our computational methods to handle multielectronic systems and incorporating exact hyperfine Hamiltonians will deepen our understanding of hyperfine interactions in lanthanide complexes. This progress will significantly enhance our ability to predict and control the properties of these complexes for applications in quantum information processing and other advanced technologies. Furthermore, these improved methods could facilitate the design of new lanthanide-based materials with optimized properties for specific applications, ultimately contributing to the advancement of quantum technologies.

15.2.4 A methodology for exploring the isotopologue quantum chemical space

Although we have proposed a model for exploring the chemical space of ligand compositions and geometries—with the aim of tailoring the electrical and hyperfine properties of nuclear spin qubits in lanthanide organic complexes—we have not yet had the opportunity to conduct such an extensive study. Exploring this chemical space is crucial because variations in ligand composition and geometry can significantly influence the electronic structure of lanthanide complexes, thereby affecting the performance and coherence properties of the qubits. Understanding these influences is essential for optimizing the design of qubit systems for quantum information applications.

The next logical step is to utilize the developed methodology to perform an in-depth study of different ligands, considering various types of structural deformations. For example, in the case of TbPc_2 , we could investigate how changing the twist angles between the phthalocyanine planes, introducing deviations from coplanarity of the two phthalocyanines, altering bond lengths, and implementing other structural modifications affect the qubit properties. Additionally, exploring different ligand compositions would allow us to assess how chemical variations impact the electronic structure and hyperfine interactions. Such a comprehensive study would provide valuable insights into how specific ligand modifications can be employed to fine-tune the properties of lanthanide qubits.

The computational efficiency of the LFDFT method makes this extensive exploration feasible. This method can rapidly provide ligand field parameters for a given geometry and composition, enabling us to survey a wide range of ligand configurations in a relatively short time. Coupled with our ability to obtain an atomistic Hamiltonian for the complex under study—which can also incorporate external fields—we can perform detailed simulations of the electronic and hyperfine structures. The combination of these capabilities allows us to systematically investigate the effects of various ligand modifications on the qubit properties, accelerating the discovery of optimal ligand designs.

Moreover, conducting a combined study that leverages both the results from exact diagonalization and the effective operator approach—now accessible due to our knowledge of the off-diagonal ligand field parameters—would offer multiple benefits. First, it would serve as a consistency check for the effective operator method, ensuring that it yields results in agreement with the more computationally intensive exact diagonalization. Second, it would enable us to empirically understand the interplay between the different terms in the effective Hamiltonian and the role of specific ligand field parameters. By quantitatively evaluating the contributions of various Hamiltonian terms, we can identify which interactions are most significant and how they are affected by ligand modifications. This deeper understanding would guide the rational design of new lanthanide complexes with optimized qubit properties.

In summary, while we have laid the theoretical groundwork for exploring the chemical space of ligand compositions and geometries, the practical application of this methodology to a comprehensive study

remains an important future direction. By leveraging the computational efficiency of the LFDFT method and combining it with detailed Hamiltonian analyses, we can systematically investigate how ligand modifications affect the properties of lanthanide qudits. This approach holds the promise of uncovering new insights into the design principles of qudit systems.

15.2.5 Computational performance scalings with increased number of qudits

Our research has compared the computational performance—in terms of Average Gate Infidelity (AGI)—of a single qudit system with that of a multi-qubit system of the same Hilbert space dimension. We observed that under pure dephasing, the AGI of single qudit systems scales quadratically with the number of levels d , whereas the AGI of multi-qubit systems scales linearly with the number of qubits, i.e., logarithmically with the Hilbert space dimension. To first order, this scaling of the AGI is proportional to the ratio of gate time to decoherence time—the figure of merit. This fundamental difference in scaling highlights how dephasing affects single qudit systems more severely than multi-qubit systems as the Hilbert space dimension increases.

Furthermore, we briefly discussed the case of multi-qudit systems, where qudits can offer advantages in terms of connectivity and a reduced number of nonlocal gates compared to qubit systems. This reduction in the need for nonlocal gates can relax the requirements on gate times, allowing qudit systems to potentially compete with multi-qubit systems in terms of AGI. The ability to perform fewer nonlocal gates reduces the impact of decoherence, which could offset the disadvantages of the quadratic scaling of AGI in qudit systems.

However, a more detailed study of how computational performance scales with the number of qudits is needed to better understand the potential advantages and limitations of qudit systems compared to qubit systems. Such an analysis would involve examining factors such as the connectivity graph between qudits and the number of local and nonlocal control Hamiltonians available for gate implementation. These additional factors, and the scalings of both the error rate, and the gate implementation durations with those factors, are essential for gaining a nuanced understanding of the trade-offs involved in scaling up qudit systems for quantum computing applications.

By conducting a thorough investigation into these factors, we can determine the conditions under which multi-qudit systems may outperform multi-qubit systems, particularly in terms of AGI and gate efficiency. This analysis would provide valuable insights into the scalability of qudit-based quantum computing and help identify the most promising approaches for implementing high-performance quantum gates in practical systems.

In summary, while our initial comparison has revealed important differences in AGI scaling between qudit and qubit systems, further research is needed to fully explore the potential of qudits. By studying the effects of system connectivity, the number of control Hamiltonians, and other practical constraints, we can develop a more comprehensive understanding of the trade-offs involved in scaling up qudit systems and identify optimal strategies for their implementation in quantum computing applications.

15.2.6 Quantifying the optimality of a qudit gate implementation

In our research, we have developed a comprehensive methodology for designing optimal pulse sequences to implement universal single-qudit quantum gates. By leveraging optimal control theory and utilizing the Method for Adjoint- and Gradient-based self-Iterative Construction and Refinement of Pulses (MAGICARP), we have demonstrated that it is possible to find high-fidelity pulse sequences that achieve the desired gate operations with minimal errors.

However, quantifying the optimality of these pulse sequences remains an open question. While we can use the optimal cost—specifically, the minimal duration for a given maximally driven system—for an unconstrained set of control Hamiltonians as a benchmark to measure the optimality of a gate implemented using a constrained number of control Hamiltonians (less than $d^2 - 1$), this approach

does not provide a definitive value for the optimal cost when implementing the gate with a smaller number of control Hamiltonians.

As discussed, in quantum systems of dimension d , the number of independent generators of the unitary group $SU(d)$ is $d^2 - 1$. Therefore, having access to all $d^2 - 1$ control Hamiltonians corresponds to full controllability without constraints. However, in practical implementations, it is often challenging to have such a large number of control Hamiltonians due to physical limitations. Consequently, understanding how to optimally implement quantum gates with a reduced set of control Hamiltonians is of great importance.

From the results of our simulations, we have observed behaviors that are consistent with the existence of a minimal possible duration for the implementation of the Quantum Fourier Transform (QFT) gate when using a number of control Hamiltonians less than $d^2 - 1$. Specifically, as the number of available control Hamiltonians decreases relative to the total possible number $d^2 - 1$, the minimal duration required to implement the gate with high fidelity tends to increase. This behavior suggests that the optimality of the pulse sequences is closely related to the number of control Hamiltonians available for the implementation.

An in-depth study of this minimal duration as a function of both the number of control Hamiltonians and the connectivity graph of the qudit levels implied by the controls would provide valuable insights into the optimality of our pulse sequences. The connectivity graph represents the allowed transitions between the qudit levels facilitated by the control Hamiltonians. By analyzing how different connectivity configurations affect the minimal achievable gate durations, we can identify the most efficient control schemes.

Such a study would need to be conducted in tandem with a detailed analysis of the numerical stability and convergence properties of the MAGICARP method, as these factors can significantly impact the optimality and practicality of the pulse sequences obtained. Moreover this could provide a deeper understanding of the optimization landscape and its potential pitfalls, which would be invaluable for designing more robust and efficient pulse sequences.

By understanding the relationship between the number of control Hamiltonians, the connectivity graph, and the minimal achievable duration, we can gain a better understanding of the trade-offs involved in implementing fast universal single-qudit gates. This knowledge would enable us to design more efficient pulse sequences that optimize resource utilization without compromising gate fidelity.

Ultimately, this deeper insight would allow us to optimize the design of pulse sequences not only for fidelity but also for efficiency and practicality, which are critical factors in the realization of quantum computing technologies. By addressing the challenges associated with constrained control Hamiltonians and understanding the limitations imposed by physical systems, we can move closer to implementing fast and reliable quantum gates in experimental settings.

15.2.7 Towards noise-robust and error-corrected qudit quantum computing

In our research, we have focused on developing optimal pulse sequences for implementing universal time-optimal single-qudit quantum gates. While these gates are crucial for performing quantum computations, they are inherently vulnerable to various sources of noise, including decoherence, control imperfections, and environmental fluctuations. Of these, Markovian decoherence is effectively minimized through time-optimal control, as discussed in this work. However, the other sources of noise, such as control imperfections and environmental fluctuations, can still introduce significant errors that degrade the fidelity of gate operations. Additionally, one could argue that time-optimal control, by design, lacks redundancy and may therefore be more sensitive to control errors and environmental noise compared to other control strategies.

To address these challenges, techniques from quantum optimal control can be employed to design pulse sequences that are inherently robust to noise, improving the reliability and performance of qudit-based

quantum computing systems. One common approach to achieving noise resilience is incorporating noise robustness directly into the cost function to be optimized. For instance, robustness to control errors or fluctuations in the system parameters can be encoded in the optimization problem, allowing the resulting pulse sequence to tolerate deviations from ideal conditions without significantly impacting gate fidelity. This can be done by using a robust cost function that takes into account variations in the system parameters during the optimization process [251, 252, 253].

In the doctoral work of my colleague Jean-Gabriel Hartmann, a detailed investigation into the noise robustness of pulse sequences generated through Givens Rotations Decomposition (GRD) and Gradient Ascent Pulse Engineering (GRAPE) was conducted. The quantification of their natural robustness, i.e. without robustness optimization, to both control errors and Markovian noise [254].

Beyond simply incorporating noise robustness into the cost function, there are other strategies for enhancing the noise resilience of quantum gates. For example, dynamical decoupling techniques, which involve the application of carefully timed pulses to average out the effects of environmental noise, can be used to mitigate the impact of slow fluctuations and low-frequency noise [255]. Another approach is using error-robust control techniques, such as "shortcuts to adiabaticity," which can achieve fast, high-fidelity quantum operations while being less sensitive to noise [256].

Additionally, composite pulse sequences, which combine multiple imperfect pulses in such a way that their errors cancel each other out, can be employed to improve robustness to control imperfections [257]. These methods are particularly effective for reducing systematic errors in control fields, making them useful in systems where such imperfections are a dominant source of noise.

In summary, while our current focus has been on minimizing decoherence through time-optimal control, there is a need to explore additional strategies for enhancing the robustness of qudit gates against other sources of noise. Incorporating noise-resilience into the cost function, and leveraging other error-mitigation strategies such as dynamical decoupling and composite pulses, are promising avenues for improving the fidelity and reliability of qudit-based quantum computing systems.

Moreover, we have also explored proposals for error-corrected logical qubits implemented in physical qudits [167, 258], and conducted a qualitative study of the optimal dimensionality for a given noise rate. However, our investigation focused on binomial codes as a method for embedding qubits in qudits for error correction. While this approach has promising advantages, it is not the only technique available for implementing error-corrected qudits [168].

One promising avenue for further research is conducting a detailed study to determine the exact optimal dimensionality of qudits for a given noise rate. Such a study would provide valuable insights into the trade-offs between adding redundancy via the extra levels of the qudit and the associated increase in error rates. For instance, while larger qudits offer more degrees of freedom for encoding logical qubits and implementing error correction, they are also more susceptible to noise, as it has been discussed multiple times in this thesis. Identifying the dimensional "sweet spot" where the qudit can offer the best balance between redundancy and noise resilience is critical for realizing practical error-corrected qudit-based quantum computing.

Let us also note that the use of decoherence-free subspaces in qudit systems have the potential to protect logical information from certain types of noise, offering an alternative to traditional quantum error correction [259]. These techniques could exploit the symmetries of the system to encode logical qubits in a way that naturally suppresses specific error channels. Investigating the feasibility and performance of decoherence-free subspaces in qudit systems would be an exciting direction for future research.

To fully realize these advantages, a comprehensive analysis of the performance of different error correction schemes for qudits under realistic noise models is necessary. This analysis would involve not only studying the error-correcting capacity of various codes but also examining how different noise rates and types (such as depolarizing, dephasing, or amplitude damping) affect the performance of

qudit-based quantum error correction. By optimizing the dimensionality of qudits and the choice of error-correcting code, we can identify the most efficient configurations for implementing fault-tolerant quantum computing with qudits.

References of this part

- [1] Veldhorst, M.; Eenink, H. G. J.; Yang, C. H.; Dzurak, A. S. “Silicon CMOS architecture for a spin-based quantum computer”, *Nature Communications*, 2017, 8:1, 1766.
- [2] Gonzalez-Zalba, M. F.; De Franceschi, S.; Charbon, E.; Meunier, T.; Vinet, M.; Dzurak, A. S. “Scaling silicon-based quantum computing using CMOS technology”, *Nature Electronics*, 2021, 4:12, 872–884.
- [3] Manin, J. I. “Mathematics as Metaphor: Selected Essays of Yuri I. Manin”, *Philosophia Mathematica*, 2008, 17:1, 122–123.
- [4] Benioff, P. “The computer as a physical system: A microscopic quantum mechanical Hamiltonian model of computers as represented by Turing machines”, *Journal of Statistical Physics*, 1980, 22:5, 563–591.
- [5] Feynman, R. P. “Simulating physics with computers”, *International Journal of Theoretical Physics*, 1982, 21:6, 467–488.
- [6] Deutsch, D. “Quantum theory, the Church–Turing principle and the universal quantum computer”, *Proceedings of the Royal Society of London. A. Mathematical and Physical Sciences*, 1985, 400:1818, 97–117.
- [7] Shor, P. W. “Polynomial-Time Algorithms for Prime Factorization and Discrete Logarithms on a Quantum Computer”, *SIAM Journal on Computing*, 1997, 26:5, 1484–1509.
- [8] Grover, L. K. In *Proceedings of the twenty-eighth annual ACM symposium on Theory of computing - STOC '96*, ACM Press: 1996, pp 212–219.
- [9] Lloyd, S. “Universal Quantum Simulators”, *Science*, 1996, 273:5278, 1073–1078.
- [10] Kjaergaard, M.; Schwartz, M. E.; Greene, A.; Samach, G. O.; Bengtsson, A.; O’Keeffe, M.; McNally, C. M.; Braumüller, J.; Kim, D. K.; Krantz, P., et al. “Programming a quantum computer with quantum instructions”, 2020.
- [11] Bruzewicz, C. D.; Chiaverini, J.; McConnell, R.; Sage, J. M. “Trapped-ion quantum computing: Progress and challenges”, *Applied Physics Reviews*, 2019, 6:2, 021314.
- [12] Pogorelov, I. et al. “Compact Ion-Trap Quantum Computing Demonstrator”, *PRX Quantum*, 2021, 2:2, 020343.
- [13] Slussarenko, S.; Pryde, G. J. “Photonic quantum information processing: A concise review”, *Applied Physics Reviews*, 2019, 6:4, 041303.
- [14] Chi, Y.; Huang, J.; Zhang, Z.; Mao, J.; Zhou, Z.; Chen, X.; Zhai, C.; Bao, J.; Dai, T.; Yuan, H., et al. “A programmable qudit-based quantum processor”, *Nature Communications*, 2022, 13:1, 1166.
- [15] Morgado, M.; Whitlock, S. “Quantum simulation and computing with Rydberg-interacting qubits”, *AVS Quantum Science*, 2021, 3:2, 023501.
- [16] Madjarov, I. S.; Covey, J. P.; Shaw, A. L.; Choi, J.; Kale, A.; Cooper, A.; Pichler, H.; Schkolnik, V.; Williams, J. R.; Endres, M. “High-fidelity entanglement and detection of alkaline-earth Rydberg atoms”, *Nature Physics*, 2020, 16:8, 857–861.
- [17] Burkard, G.; Ladd, T. D.; Pan, A.; Nichol, J. M.; Petta, J. R. “Semiconductor spin qubits”, *Reviews of Modern Physics*, 2023, 95:2, 025003.

- [18] Zhang, X.; Li, H.-O.; Cao, G.; Xiao, M.; Guo, G.-C.; Guo, G.-P. “Semiconductor quantum computation”, *National Science Review*, 2019, 6:1, 32–54.
- [19] Arute, F.; Arya, K.; Babbush, R.; Bacon, D.; Bardin, J. C.; Barends, R.; Biswas, R.; Boixo, S.; Brandao, F. G. S. L.; Buell, D. A., et al. “Quantum supremacy using a programmable superconducting processor”, *Nature*, 2019, 574:7779, 505–510.
- [20] First IBM Quantum Data Center in Europe Opens; Will Include IBM’s Most Performant Quantum Systems <https://newsroom.ibm.com/2024-10-01-first-ibm-quantum-data-center-in-europe-opens-will-include-ibms-most-performant-quantum-systems> (accessed 10/02/2024).
- [21] Ezratty, O. “Perspective on superconducting qubit quantum computing”, *The European Physical Journal A*, 2023, 59:5, 94.
- [22] DiVincenzo, D. P. “The Physical Implementation of Quantum Computation”, *Fortschritte der Physik*, 2000, 48:9, 771–783.
- [23] Wang, Y.; Hu, Z.; Sanders, B. C.; Kais, S. “Qudits and High-Dimensional Quantum Computing”, *Frontiers in Physics*, 2020, 8.
- [24] Brusentsov, N. P.; Ramil Alvarez, J. In *Perspectives on Soviet and Russian Computing*, Impagliazzo, J., Proydakov, E., Eds.; Springer Berlin Heidelberg: Berlin, Heidelberg, 2011; Vol. 357, pp 74–80.
- [25] Moreno-Pineda, E.; Wernsdorfer, W. “Measuring molecular magnets for quantum technologies”, *Nature Reviews Physics*, 2021, 3:9, 645–659.
- [26] Thiele, S.; Balestro, F.; Ballou, R.; Klyatskaya, S.; Ruben, M.; Wernsdorfer, W. “Electrically driven nuclear spin resonance in single-molecule magnets”, *Science (New York, N. Y.)*, 2014, 344:6188, 1135–1138.
- [27] Boltyanski, V.; Martini, H.; Soltan, V., *Geometric Methods and Optimization Problems*; Springer Science & Business Media: 2013; 438 pp.
- [28] Pontryagin, L. S., *Mathematical Theory of Optimal Processes*; Routledge: London, 2017; 360 pp.
- [29] Bellman, R.; Bellman, R. E., *Dynamic Programming*; Princeton University Press: 1957; 339 pp.
- [30] Glaser, S. J.; Boscain, U.; Calarco, T.; Koch, C. P.; Köckenberger, W.; Kosloff, R.; Kuprov, I.; Luy, B.; Schirmer, S.; Schulte-Herbrüggen, T.; Sugny, D.; Wilhelm, F. K. “Training Schrödinger’s cat: quantum optimal control: Strategic report on current status, visions and goals for research in Europe”, *The European Physical Journal D*, 2015, 69:12, 279.
- [31] Koch, C. P.; Boscain, U.; Calarco, T.; Dirr, G.; Filipp, S.; Glaser, S. J.; Kosloff, R.; Montangero, S.; Schulte-Herbrüggen, T.; Sugny, D.; Wilhelm, F. K. “Quantum optimal control in quantum technologies. Strategic report on current status, visions and goals for research in Europe”, *EPJ Quantum Technology*, 2022, 9:1, 19.
- [32] Khaneja, N.; Reiss, T.; Kehlet, C.; Schulte-Herbrüggen, T.; Glaser, S. J. “Optimal control of coupled spin dynamics: design of NMR pulse sequences by gradient ascent algorithms”, *Journal of Magnetic Resonance*, 2005, 172:2, 296–305.
- [33] Rutherford, E. “The scattering of alpha and beta particles by matter and the structure of the atom”, *The London, Edinburgh, and Dublin Philosophical Magazine and Journal of Science*, 1911, 21:125, 669–688.
- [34] Gamow, G.; Rutherford, E. “Mass defect curve and nuclear constitution”, *Proceedings of the Royal Society of London. Series A, Containing Papers of a Mathematical and Physical Character*, 1930, 126:803, 632–644.
- [35] Bohr, N.; Wheeler, J. A. “The Mechanism of Nuclear Fission”, *Physical Review*, 1939, 56:5, 426–450.
- [36] Mayer, M. G. “On Closed Shells in Nuclei. II”, *Physical Review*, 1949, 75:12, 1969–1970.
- [37] Haxel, O.; Jensen, J. H. D.; Suess, H. E. “On the ”Magic Numbers” in Nuclear Structure”, *Physical Review*, 1949, 75:11, 1766–1766.
- [38] De Groote, R. P.; Neyens, G. In *Handbook of Nuclear Physics*, Tanihata, I., Toki, H., Kajino, T., Eds.; Springer Nature: Singapore, 2020, pp 1–36.

- [39] Skyrme, T. “The effective nuclear potential”, *Nuclear Physics*, 1958, 9:4, 615–634.
- [40] Vautherin, D.; Brink, D. M. “Hartree-Fock Calculations with Skyrme’s Interaction. I. Spherical Nuclei”, *Physical Review C*, 1972, 5:3, 626–647.
- [41] Ring, P.; Schuck, P., *The nuclear many body problem*, 1. ed., 3. print., study ed; Texts and monographs in physics; Springer: Berlin Heidelberg, 2004; 716 pp.
- [42] Casten, R., *Nuclear Structure from a Simple Perspective*; Oxford University Press: 2000; 484 pp.
- [43] Hartree-Fock-Bogoliubov results based on the Gogny force https://www-phynu.cea.fr/science_en_ligne/carte_potentiels_microscopiques/carte_potentiel_nucleaire_eng.htm (accessed 08/15/2024).
- [44] Gerginov, V.; Calkins, K.; Tanner, C.; McFerran, J.; Diddams, S.; Bartels, A.; Hollberg, L. “Optical frequency measurements of 6s 2S_{1/2}-6p 2P_{1/2} (D1) transitions in Cs133 and their impact on the fine-structure constant”, *Physical Review A*, 2006, 73, 32504.
- [45] Goudsmit, S. “La découverte du spin de l’électron”, *Journal de Physique*, 1967, 28:1, 123–128.
- [46] Dirac, P. A. M. “The quantum theory of the electron”, *Proceedings of the Royal Society of London. Series A, Containing Papers of a Mathematical and Physical Character*, 1928, 117:778, 610–624.
- [47] Casimir, H. B. G. In *On the Interaction between Atomic Nuclei and Electrons*, Casimir, H. B. G., Ed.; Springer Netherlands: Dordrecht, 1936, pp 201–283.
- [48] Christy, R. F.; Kusaka, S. “Electric Quadrupole Moment of the Deuteron”, *Physical Review*, 1939, 55:7, 665–665.
- [49] Ramsey, N. F. “Theory of Molecular Hydrogen and Deuterium in Magnetic Fields”, *Physical Review*, 1952, 85:1, 60–65.
- [50] Bohr, A.; Weisskopf, V. F. “The Influence of Nuclear Structure on the Hyperfine Structure of Heavy Elements”, *Physical Review*, 1950, 77:1, 94–98.
- [51] Rosenthal, J. E.; Breit, G. “The Isotope Shift in Hyperfine Structure”, *Physical Review*, 1932, 41:4, 459–470.
- [52] Engfer, R.; Schneuwly, H.; Vuilleumier, J. L.; Walter, H. K.; Zehnder, A. “Charge-distribution parameters, isotope shifts, isomer shifts, and magnetic hyperfine constants from muonic atoms”, *Atomic Data and Nuclear Data Tables*, 1974, 14:5, 509–597.
- [53] Daum, C., *Muonic atoms and nuclear charge distributions*, 1967.
- [54] The SI, BIPM <https://www.bipm.org/en/measurement-units> (accessed 10/13/2024).
- [55] Wynands, R.; Weyers, S. “Atomic fountain clocks”, *Metrologia*, 2005, 42:3, S64.
- [56] Pla, J. J.; Tan, K. Y.; Dehollain, J. P.; Lim, W. H.; Morton, J. J. L.; Zwanenburg, F. A.; Jamieson, D. N.; Dzurak, A. S.; Morello, A. “High-fidelity readout and control of a nuclear spin qubit in silicon”, *Nature*, 2013, 496:7445, 334–338.
- [57] Harty, T. P.; Allcock, D. T. C.; Ballance, C. J.; Guidoni, L.; Janacek, H. A.; Linke, N. M.; Stacey, D. N.; Lucas, D. M. “High-Fidelity Preparation, Gates, Memory, and Readout of a Trapped-Ion Quantum Bit”, *Physical Review Letters*, 2014, 113:22, 220501.
- [58] Ballance, C. J.; Harty, T. P.; Linke, N. M.; Sepiol, M. A.; Lucas, D. M. “High-Fidelity Quantum Logic Gates Using Trapped-Ion Hyperfine Qubits”, *Physical Review Letters*, 2016, 117:6, 060504.
- [59] Ringbauer, M.; Meth, M.; Postler, L.; Stricker, R.; Blatt, R.; Schindler, P.; Monz, T. “A universal qudit quantum processor with trapped ions”, *Nature Physics*, 2022, 18:9, 1053–1057.
- [60] Butler, P. A.; Nazarewicz, W. “Intrinsic reflection asymmetry in atomic nuclei”, *Reviews of Modern Physics*, 1996, 68:2, 349–421.
- [61] Sajid, M. A. Blocks of the Periodic Table — s-p-d-f Blocks, PSIBERG <https://psiberg.com/blocks-of-the-periodic-table/> (accessed 10/14/2024).
- [62] Greenwood, N. N.; Earnshaw, A., *Chemistry of the elements*, 2nd ed; Butterworth-Heinemann: Oxford ; Boston, 1997; 1341 pp.
- [63] *The rare earth elements: fundamentals and applications*; Atwood, D. A., Ed.; EIC Bks; John Wiley & Sons, Inc: Chichester, West Sussex, United Kingdom Hoboken, 2012, 606 pp.
- [64] SEABORG, G. T. In *Modern Alchemy*, 1951, pp 256–279.

- [65] Gutfleisch, O.; Willard, M. A.; Brück, E.; Chen, C. H.; Sankar, S. G.; Liu, J. P. “Magnetic Materials and Devices for the 21st Century: Stronger, Lighter, and More Energy Efficient”, *Advanced Materials*, 2011, *23*:7, 821–842.
- [66] Ramanantoanina, H.; Urland, W.; García-Fuente, A.; Cimpoesu, F.; Daul, C. “Ligand field density functional theory for the prediction of future domestic lighting”, *Physical Chemistry Chemical Physics*, 2014, *16*:28, 14625–14634.
- [67] Liu, G., *Spectroscopic Properties of Rare Earths in Optical Materials*, 1st ed; Springer Series in Materials Science Ser v.83; Springer Berlin / Heidelberg: Berlin, Heidelberg, 2005; 1 p.
- [68] Eliseeva, S. V.; Bünzli, J.-C. G. “Lanthanide luminescence for functional materials and bio-sciences”, *Chemical Society Reviews*, 2009, *39*:1, 189–227.
- [69] Jordens, A.; Cheng, Y. P.; Waters, K. E. “A review of the beneficiation of rare earth element bearing minerals”, *Minerals Engineering*, 2013, *41*, 97–114.
- [70] Atwood, D. A., *Sustainable Inorganic Chemistry*, 1. Aufl; EIC Books; Wiley: s.l., 2016; 1 p.
- [71] Binnemans, K.; Jones, P. T.; Blanpain, B.; Van Gerven, T.; Yang, Y.; Walton, A.; Buchert, M. “Recycling of rare earths: a critical review”, *Journal of Cleaner Production*, 2013, *51*, 1–22.
- [72] Bethe, H. “Termaufspaltung in kristallen”, *Annalen der Physik*, 1929, *395*:2, 133–208.
- [73] Bethe, H. “Zur Theorie des Zeemaneffektes an den Salzen der seltenen Erden”, *Zeitschrift für Physik*, 1930, *60*:3, 218–233.
- [74] Van Vleck, J. “Valence strength and the magnetism of complex salts”, *The Journal of Chemical Physics*, 1935, *3*:12, 807–813.
- [75] *Advanced inorganic chemistry*, 6th ed; Cotton, F. A., Cotton, F. A., Eds.; Wiley: New York, 1999, 1355 pp.
- [76] Crystal Field Theory, Chemistry LibreTexts [https://chem.libretexts.org/Bookshelves/Inorganic_Chemistry/Supplemental_Modules_and_Websites_\(Inorganic_Chemistry\)/Crystal_Field_Theory/Crystal_Field_Theory](https://chem.libretexts.org/Bookshelves/Inorganic_Chemistry/Supplemental_Modules_and_Websites_(Inorganic_Chemistry)/Crystal_Field_Theory/Crystal_Field_Theory) (accessed 10/14/2024).
- [77] Alessandri, R.; Zulfikri, H.; Autschbach, J.; Bolvin, H. “Crystal Field in Rare-Earth Complexes: From Electrostatics to Bonding”, *Chemistry (Weinheim an Der Bergstrasse, Germany)*, 2018, *24*:21, 5538–5550.
- [78] Jung, J.; Islam, M. A.; Pecoraro, V. L.; Mallah, T.; Berthon, C.; Bolvin, H. “Derivation of Lanthanide Series Crystal Field Parameters From First Principles”, *Chemistry – A European Journal*, 2019, *25*:66, 15112–15122.
- [79] Sessoli, R.; Gatteschi, D.; Caneschi, A.; Novak, M. A. “Magnetic bistability in a metal-ion cluster”, *Nature*, 1993, *365*:6442, 141–143.
- [80] Woodruff, D. N.; Winpenny, R. E. P.; Layfield, R. A. “Lanthanide Single-Molecule Magnets”, *Chemical Reviews*, 2013, *113*:7, 5110–5148.
- [81] Cap, G.; F, O.; D, R.; Nf, C.; Dp, M. “Molecular magnetic hysteresis at 60 kelvin in dysprosocene”, *Nature*, 2017, *548*:7668.
- [82] Hauser, A.; Münzfeld, L.; Uhlmann, C.; Lebedkin, S.; Schlittenhardt, S.; Ruan, T.-T.; Kappes, M. M.; Ruben, M.; Roesky, P. W. “It’s not just the size that matters: crystal engineering of lanthanide-based coordination polymers”, *Chemical Science*, 2024, *15*:4, 1338–1347.
- [83] Curie, P., *Propriétés magnétiques des corps à diverses températures*; Gauthier-Villars et fils: 1895; 148 pp.
- [84] Langevin, P., *Magnétisme et Théorie Des électrons*; Independently Published: 1905; 44 pp.
- [85] Pauling, L. “Nature of the Iron–Oxygen Bond in Oxyhaemoglobin”, *Nature*, 1964, *203*:4941, 182–183.
- [86] Stranski, I. N. “Zur Theorie des Kristallwachstums”, *Zeitschrift für Physikalische Chemie*, 1928, *136U*:1, 259–278.
- [87] Van Vleck, J. H. “Theory of the Variations in Paramagnetic Anisotropy Among Different Salts of the Iron Group”, *Physical Review*, 1932, *41*:2, 208–215.
- [88] Stumpf, H. O.; Pei, Y.; Kahn, O.; Ouahab, L.; Grandjean, D. “A Molecular-Based Magnet with a Fully Interlocked Three-Dimensional Structure”, *Science*, 1993, *261*:5120, 447–449.

- [89] Gatteschi, D.; Sessoli, R.; Villain, J., *Molecular Nanomagnets*; OUP Oxford: 2006; 408 pp.
- [90] Thomas, L.; Lionti, F.; Ballou, R.; Gatteschi, D.; Sessoli, R.; Barbara, B. “Macroscopic quantum tunnelling of magnetization in a single crystal of nanomagnets”, *Nature*, 1996, *383*:6596, 145–147.
- [91] Naoto Ishikawa; Miki Sugita; Tadahiko Ishikawa; T. Ishikawa; Shin-ya Koshihara; Youkoh Kaizu; Youkoh Kaizu “Lanthanide Double-Decker Complexes Functioning as Magnets at the Single-Molecular Level”, *Journal of the American Chemical Society*, 2003, *125*:29, 8694–8695.
- [92] Ishikawa, N.; Sugita, M.; Wernsdorfer, W. “Quantum Tunneling of Magnetization in Lanthanide Single-Molecule Magnets”, *Angewandte Chemie International Edition*, 2005, *44*:19, 2931–2935.
- [93] Bogani, L.; Wernsdorfer, W. “Molecular spintronics using single-molecule magnets”, *Nature Materials*, 2008, *7*:3, 179–186.
- [94] Leuenberger, M. N.; Loss, D. “Quantum computing in molecular magnets”, *Nature*, 2001, *410*:6830, 789–793.
- [95] Ardavan, A.; Rival, O.; Morton, J. J. L.; Blundell, S. J.; Tyryshkin, A. M.; Timco, G. A.; Winpenny, R. E. P. “Will Spin-Relaxation Times in Molecular Magnets Permit Quantum Information Processing?”, *Physical Review Letters*, 2007, *98*:5, 057201.
- [96] Zadrozny, J. M.; Freedman, D. E. “Qubit Control Limited by Spin–Lattice Relaxation in a Nuclear Spin-Free Iron(III) Complex”, *Inorganic Chemistry*, 2015, *54*:24, 12027–12031.
- [97] Wernsdorfer, W. “From micro- to nano-SQUIDS: applications to nanomagnetism”, *Superconductor Science and Technology*, 2009, *22*:6, 064013.
- [98] Romain Vincent; Svetlana Klyatskaya; Mario Ruben; Wolfgang Wernsdorfer; Franck Balestro “Electronic read-out of a single nuclear spin using a molecular spin transistor”, *Nature*, 2012, *488*:7411, 357–360.
- [99] Godfrin, C.; Ferhat, A.; Ballou, R.; Klyatskaya, S.; Ruben, M.; Wernsdorfer, W.; Balestro, F. “Operating Quantum States in Single Magnetic Molecules: Implementation of Grover’s Quantum Algorithm”, *Physical Review Letters*, 2017, *119*:18, 187702.
- [100] Wernsdorfer, W.; Ruben, M. “Synthetic Hilbert Space Engineering of Molecular Qudits: Isotopologue Chemistry”, *Advanced Materials*, 2019, *31*:26, 1806687.
- [101] Kumar, K. S.; Serrano, D.; Nonat, A. M.; Heinrich, B.; Karmazin, L.; Charbonnière, L. J.; Goldner, P.; Ruben, M. “Optical spin-state polarization in a binuclear europium complex towards molecule-based coherent light-spin interfaces”, *Nature Communications*, 2021, *12*:1, 2152.
- [102] Moreno-Pineda, E.; Godfrin, C.; Balestro, F.; Wernsdorfer, W.; Ruben, M. “Molecular Spin Qudits for Quantum Algorithms”, *Chemical Society Reviews*, 2018, *47*:2, 501–513.
- [103] Thiele, S. Read-out and coherent manipulation of an isolated nuclear spin using a single molecule magnet spin transistor, Ph.D. Thesis, Université de Grenoble, 2014.
- [104] Godfrin, C. Quantum information processing using a molecular magnet single nuclear spin qudit, These de doctorat, Université Grenoble Alpes (ComUE), 2017.
- [105] Leuenberger, M. N.; Loss, D.; Poggio, M.; Awschalom, D. D. “Quantum Information Processing with Large Nuclear Spins in GaAs Semiconductors”, *Physical Review Letters*, 2002, *89*:20, 207601.
- [106] Leuenberger, M. N.; Loss, D. “Grover algorithm for large nuclear spins in semiconductors”, *Physical Review B*, 2003, *68*:16, 165317.
- [109] Tuszynski, J. A., *Spherical tensor operators: tables of matrix elements and symmetries*; World Scientific: 1990.
- [124] DLMF: Chapter 34 3j,6j,9j Symbols <https://dlmf.nist.gov/34> (accessed 08/11/2024).
- [132] Anderson, C. D. “The Apparent Existence of Easily Deflectable Positives”, *Science*, 1932, *76*:1967, 238–239.
- [133] Gerlach, W.; Stern, O. “Der experimentelle Nachweis der Richtungsquantelung im Magnetfeld”, *Zeitschrift für Physik*, 1922, *9*:1, 349–352.

- [138] Boucard, S. Calcul de haute precision d'énergies de transitions dans les atomes exotiques et les lithumoides : corrections relativistes, corrections radiatives, structure hyperfine et interaction avec le cortege electronique residuel, These de doctorat, Paris 6, 1998.
- [140] Borie, E.; Rinker, G. A. "The energy levels of muonic atoms", *Reviews of Modern Physics*, 1982, 54:1, 67–118.
- [141] Shabaev, V. In *Large Coulomb Systems: Lecture Notes on Mathematical Aspects of QED*, Dereziński, J., Siedentop, H., Eds.; Springer: Berlin, Heidelberg, 2006, pp 275–295.
- [167] Chiesa, A.; Petiziol, F.; Macaluso, E.; Wimberger, S.; Santini, P.; Carretta, S. "Embedded quantum-error correction and controlled-phase gate for molecular spin qubits", *AIP Advances*, 2021, 11:2, 025134.
- [168] Petiziol, F.; Chiesa, A.; Wimberger, S.; Santini, P.; Carretta, S. "Counteracting dephasing in Molecular Nanomagnets by optimized qudit encodings", *npj Quantum Information*, 2021, 7:1, 1–10.
- [182] Chen, H.; Borzì, A.; Janković, D.; Hartmann, J.-G.; Hervieux, P.-A. Full- and low-rank exponential Euler integrators for the Lindblad equation, 2024.
- [186] Janković, D.; Hartmann, J.-G.; Ruben, M.; Hervieux, P.-A. "Noisy qudit vs multiple qubits: conditions on gate efficiency for enhancing fidelity", *npj Quantum Information*, 2024, 10:1, 59.
- [187] Jankovic, D. Source Code for data generation and pulses data for Noisy Qudit vs Multiple Qubits, 2024.
- [193] Collins, B.; Matsumoto, S.; Novak, J. "The Weingarten Calculus", 2021.
- [204] Hartmann, J.-G.; Janković, D.; Pasquier, R.; Ruben, M.; Hervieux, P.-A. Nonlinearity of the Fidelity in Open Qudit Systems: Gate and Noise Dependence in High-dimensional Quantum Computing, 2024.
- [205] Hartmann, J.-G.; Jankovic, D.; Pasquier, R.; Ruben, M.; Hervieux, P.-A. Code and Data for "Nonlinearity of the Fidelity in Open Qudit Systems: Gate and Noise Dependence in High-dimensional Quantum Computing", version 1.0.0, 2024.
- [207] Campbell, J. E. "On a Law of Combination of Operators bearing on the Theory of Continuous Transformation Groups", *Proceedings of the London Mathematical Society*, 1896, s1-28:1, 381–390.
- [208] Hall, B. C., *Lie groups, Lie algebras, and representations: an elementary introduction*, Second edition; Graduate texts in mathematics 222; Springer: Cham ; New York, 2015; 449 pp.
- [247] Mirzoyan, R.; Kazmierczak, N. P.; Hadt, R. G. "Deconvolving Contributions to Decoherence in Molecular Electron Spin Qubits: A Dynamic Ligand Field Approach", *Chemistry – A European Journal*, 2021, chem.202100845.
- [248] Mirzoyan, R.; Hadt, R. G. "The dynamic ligand field of a molecular qubit: decoherence through spin–phonon coupling", *Physical Chemistry Chemical Physics*, 2020, 22:20, 11249–11265.
- [249] C. Kragssow, J. G.; Mattioni, A.; K. Staab, J.; Reta, D.; M. Skelton, J.; F. Chilton, N. "Spin–phonon coupling and magnetic relaxation in single-molecule magnets", *Chemical Society Reviews*, 2023, 52:14, 4567–4585.
- [250] Mandelshtam, V. A.; Taylor, H. S. "A low-storage filter diagonalization method for quantum eigenenergy calculation or for spectral analysis of time signals", *The Journal of Chemical Physics*, 1997, 106:12, 5085–5090.
- [251] Green, T. J.; Sastrawan, J.; Uys, H.; Biercuk, M. J. "Arbitrary quantum control of qubits in the presence of universal noise", *New Journal of Physics*, 2013, 15:9, 095004.
- [252] Koch, C. P. "Controlling open quantum systems: tools, achievements, and limitations", *Journal of Physics: Condensed Matter*, 2016, 28:21, 213001.
- [253] Jandura, S.; Pupillo, G. "Time-Optimal Two- and Three-Qubit Gates for Rydberg Atoms", *Quantum*, 2022, 6, 712.
- [254] Hartmann, J.-G. Hilbert space engineering and optimal control for quantum computing with applications for rare-earth single molecule magnets, Ph.D. Thesis, Université de Strasbourg, 2024.

- [255] Viola, L.; Lloyd, S. “Dynamical suppression of decoherence in two-state quantum systems”, *Physical Review A*, 1998, *58*:4, 2733–2744.
- [256] Guéry-Odelin, D.; Ruschhaupt, A.; Kiely, A.; Torrontegui, E.; Martínez-Garaot, S.; Muga, J. G. “Shortcuts to adiabaticity: Concepts, methods, and applications”, *Reviews of Modern Physics*, 2019, *91*:4, 045001.
- [257] Wimperis, S. “Broadband, Narrowband, and Passband Composite Pulses for Use in Advanced NMR Experiments”, *Journal of Magnetic Resonance, Series A*, 1994, *109*:2, 221–231.
- [258] Chizzini, M.; Crippa, L.; Chiesa, A.; Tacchino, F.; Petiziol, F.; Tavernelli, I.; Santini, P.; Carretta, S. “Molecular nanomagnets with competing interactions as optimal units for qudit-based quantum computation”, *Physical Review Research*, 2022, *4*:4, 043135.
- [259] Lidar, D. A.; Chuang, I. L.; Whaley, K. B. “Decoherence-Free Subspaces for Quantum Computation”, *Physical Review Letters*, 1998, *81*:12, 2594–2597.
- [260] Johansson, J.; Nation, P.; Nori, F. “QuTiP: An open-source Python framework for the dynamics of open quantum systems”, *Computer Physics Communications*, 2012, *183*:8, 1760–1772.
- [261] Suez, M. Bristol: A Python Package for Random Matrix Ensembles, 2017.
- [262] Srinivasa Rao, K.; Rajeswari, V.; Srinavasa Rao, K., *Quantum theory of angular momentum: selected topics*; Springer [u.a.]: Berlin Heidelberg, 1993; 315 pp.
- [263] Volkin, H.; Aeronautics, U. S. N.; Administration, S.; Center, L. R., *Iterated commutators and functions of operators*; NASA technical note; National Aeronautics and Space Administration: 1968.

PART VI

Appendix

A	Mathematical Prelude to Quantum Information Processing	317
A.1	Hilbert Spaces and States	317
A.2	Schrödinger Equation and Evolution Operator	319
A.3	Density matrices	322
A.4	Superoperators and vectorisation	323
A.5	Quantum channels and Kraus operators	324
B	Methods for the numerical simulations	327
B.1	Numerical noisy qudit/multiqubit simulation	327
B.2	Random gate and pulse Hamiltonian generation	328
C	Symmetries I: Spherical Harmonics and Multipoles	329
C.1	Spherical Harmonics	329
C.2	Multipolar expansion	331
D	Symmetries II: Tensor Operators and Racah-Wigner coefficients	335
D.1	Coordinate systems	335
D.2	Irreducible Tensor Operators	335
D.3	nj symbols	337
E	Preprint summarized in the main text	343
E.1	Nonlinearity of the Fidelity in Open Qudit Systems	344
F	Proofs of the statements in the main text	373
.1	Proofs for Section 9.5 (Timescales)	374
.2	Proofs for Section 11.1 (The Average Gate Infidelity: Definition and First-Order Approximation)	375
.3	Proofs for Section 12.2 (Perturbative expression of the AGI)	376
.4	Proofs for Section 12.3 (Universal bounds on the AGI for large noise and gate times) . . .	382
.5	Proofs for Section 13.2 (Quantum Speed Limits)	383
.6	Proofs for Section 14.2 (The T-M sequence in Quantum Computing)	384
.7	Proofs for Section 15.2 (Areas left to explore)	388

Chapter Contents

A.1 Hilbert Spaces and States	317
A.2 Schrödinger Equation and Evolution Operator	319
A.3 Density matrices	322
A.4 Superoperators and vectorisation	323
A.5 Quantum channels and Kraus operators . .	324

CHAPTER A

Mathematical Prelude to Quantum Information Processing

Quantum Information Processing (QIP) harnesses the principles of quantum mechanics to develop new ways of computing, communicating, and even measuring. The mathematical formulation of QIP is rooted in linear algebra, complex numbers, and the theory of Hilbert spaces, which describe the state space for quantum systems.

A.1 Hilbert Spaces and States

A **Hilbert space** is a complete vector space equipped with an inner product, which allows measurement of the length and angle between vectors. In the context of quantum computing, these vectors (states) are typically represented in the Dirac notation as $|\psi\rangle$, $|\phi\rangle$, etc. These are called **kets**.

An important operation is conjugate transposition or Hermitian transposition, \dagger :

$$\langle\psi| = |\psi\rangle^\dagger = (|\psi\rangle)^*, \quad (\text{A.1})$$

$\langle\psi|$, the conjugate transpose of a ket is called a **bra**.

A key property of quantum states is that they must be normalised, that is, $\langle\psi|\psi\rangle = 1$.

A.1.1 Operators on Hilbert Spaces

Operators in quantum mechanics represent observable quantities and transformations. They act on elements of Hilbert spaces, changing one state to another. An operator A is **linear** if $A(\alpha|\psi\rangle + \beta|\phi\rangle) = \alpha A|\psi\rangle + \beta A|\phi\rangle$ for any state $|\psi\rangle$, $|\phi\rangle$, and scalars α , β . Key types of operators include:

- **Hermitian operators (Observables):** These operators are equal to their own adjoint $A = A^\dagger$, and have real eigenvalues. They represent measurable properties of the system.
- **Unitary operators:** Satisfying $U^\dagger U = U U^\dagger = I$ (where I is the identity operator), unitary operators describe the evolution of closed quantum systems and are fundamental in constructing quantum gates.
- **Projection operators:** These are Hermitian ($P = P^\dagger$) and idempotent ($P^2 = P$), used to represent measurements corresponding to specific quantum states.

A.1.2 Quantum Postulates

The framework of quantum mechanics is built upon several foundational postulates:

1. **State Space Postulate:** The state of a quantum system is represented by a vector in a Hilbert space.
2. **Evolution Postulate:** The evolution of a closed quantum system is described by a unitary operator.
3. **Quantum Measurement Postulate:** Measurements are described by a collection of projection operators $\{P_i\}$, where P_i projects onto the eigenspace associated with the eigenvalue i . Moreover the probability of a state $|\psi\rangle$ to be measured in the state $|\phi\rangle$, is given by $|\langle\phi|\psi\rangle|^2$.
4. **State Collapse Postulate:** On measuring a state $|\psi\rangle$, the system collapses to one of the eigenstates of the measurement operator, and the probability of collapsing to a particular state is given by the square of the projection's amplitude.

A.1.3 Finite Dimensional Hilbert Spaces and Basis Representation

In quantum computing, we often deal with finite-dimensional Hilbert spaces, particularly when discussing qubits. For such spaces, it is convenient to represent states and operators in terms of matrices and vectors by selecting a basis of orthonormal states. By choosing an orthonormal basis $\{|e_i\rangle\}$ for our Hilbert space, any ket $|\psi\rangle$ can be expressed as a linear combination of these basis kets:

$$|\psi\rangle = \sum_i \psi_i |e_i\rangle, \quad (\text{A.2})$$

where ψ_i are complex coefficients. In this representation, the ket $|\psi\rangle$ can be written as a column vector whose elements are the coefficients ψ_i . Correspondingly, the bra $\langle\psi|$, which is the conjugate transpose of the ket, is represented as a row vector:

$$\langle\psi| = |\psi\rangle^\dagger = \sum_i \psi_i^* \langle e_i|, \quad (\text{A.3})$$

where ψ_i^* denotes the complex conjugate of ψ_i .

Operators that act on these states can also be represented as matrices. For example, an operator A acting on the state $|\psi\rangle$ can be represented by a matrix whose elements are given by $A_{ij} = \langle e_i| A |e_j\rangle$.

$$A = \sum_i \sum_j A_{ij} |e_i\rangle \langle e_j| \quad (\text{A.4})$$

This matrix form enables easy manipulation and calculation of quantum states, especially when quantum gates are applied or quantum systems are measured. The matrix representation is particularly powerful because it allows the application of linear algebra techniques to solve quantum mechanics problems, simplifying the computation and visualisation of quantum operations and their effects on the states of quantum systems.

A.1.4 Composite Systems and Tensor Products

When dealing with quantum systems that consist of multiple parts, such as multiple qubits in quantum computing, the Hilbert space for the composite system is constructed as the tensor product of the Hilbert spaces of the individual components. This mathematical construction allows us to describe the state of the entire system in a way that accounts for the states of its constituent parts.

Suppose we have two quantum systems, each described by Hilbert spaces \mathcal{H}_A and \mathcal{H}_B . The Hilbert space of the composite system, \mathcal{H}_{AB} , is the tensor product of these spaces, denoted as $\mathcal{H}_{AB} = \mathcal{H}_A \otimes \mathcal{H}_B$.

If $|\psi\rangle$ is a state in \mathcal{H}_A and $|\phi\rangle$ is a state in \mathcal{H}_B , the state of the composite system can be represented as $|\psi\rangle \otimes |\phi\rangle$, often simplified to $|\psi\rangle |\phi\rangle$ or $|\psi, \phi\rangle$.

$$|\psi\rangle \otimes |\phi\rangle = |\psi\rangle |\phi\rangle = |\psi, \phi\rangle, \quad (\text{A.5})$$

This formalism extends to any number of subsystems, each contributing to the larger Hilbert space through their own tensor products. For a system of n parts, where each part is described by a state $|\psi_i\rangle$ in a Hilbert space \mathcal{H}_i , the state of the entire system is given by:

$$|\Psi\rangle = |\psi_1\rangle \otimes |\psi_2\rangle \otimes \cdots \otimes |\psi_n\rangle. \quad (\text{A.6})$$

In the case of finite-dimensional Hilbert spaces, such as those used for qubits, tensor product spaces can be visually represented in terms of matrices and vectors. If $|\psi\rangle$ and $|\phi\rangle$ are represented by column vectors, their tensor product is the Kronecker product of these vectors, resulting in a new column vector that combines every element of $|\psi\rangle$ with every element of $|\phi\rangle$.

For operators, the extension to composite systems follows similarly. If A and B are operators acting on \mathcal{H}_A and \mathcal{H}_B respectively, the operator on \mathcal{H}_{AB} representing independent actions on each subsystem is given by $A \otimes B$. This operator acts on state vectors in \mathcal{H}_{AB} according to the rule:

$$(A \otimes B)(|\psi\rangle \otimes |\phi\rangle) = A|\psi\rangle \otimes B|\phi\rangle. \quad (\text{A.7})$$

Note: We note the following property, since A, B, C, D are square matrices:

$$(A \otimes B)(C \otimes D) = AC \otimes BD. \quad (\text{A.8})$$

A.2 Schrödinger Equation and Evolution Operator

The Schrödinger equation is central to the description of quantum systems, providing a mathematical formulation for the time evolution of the quantum state. It can be expressed in both time-dependent and time-independent forms depending on the nature of the Hamiltonian of the system.

A.2.1 Time-Dependent Schrödinger Equation

The time-dependent Schrödinger equation describes the evolution of a quantum system when the Hamiltonian H is a function of time, and at any time t is a Hermitian operator. It is given by:

$$i\hbar \frac{\partial}{\partial t} |\psi(t)\rangle = H(t) |\psi(t)\rangle, \quad (\text{A.9})$$

where \hbar is the reduced Planck constant, and $|\psi(t)\rangle$ represents the state of the system at time t . This formulation allows us to understand how quantum states evolve in response to changing external conditions, such as varying electromagnetic fields.

A.2.2 Time-Independent Schrödinger Equation

When the Hamiltonian H does not depend on time, the Schrödinger equation simplifies to its time-independent form, which is particularly useful for studying stationary states:

$$H |\psi_E\rangle = E |\psi_E\rangle, \quad (\text{A.10})$$

since the Hamiltonian is the observable representing the energy of the system, E represents the energy eigenvalues associated with the energy eigenstates $|\psi_E\rangle$, called stationary states. This equation is fundamental in quantum mechanics, as it facilitates the analysis of systems at equilibrium and is the basis for much of quantum theory, including quantum chemistry and condensed matter physics.

It is possible to demonstrate that there always exists a set of n eigenstates of a Hermitian operator which constitute an orthonormal basis of an n dimensional Hilbert space. As a result, the stationary states are typically selected as the foundation for the system's Hilbert space. This is under the assumption that the system can be represented by a time-independent Hamiltonian, at least as a preliminary approximation.

A.2.3 Evolution Operator

For quantum systems described by a time-independent Hamiltonian, the evolution of the state can be expressed succinctly using the evolution operator $U(t)$, defined as:

$$U(t) = e^{-iHt/\hbar}, \quad (\text{A.11})$$

where the exponential of an operator is defined through its Taylor series expansion. This operator is unitary, ensuring the conservation of probability. It directly links the state at any time t to the state at time zero:

$$|\psi(t)\rangle = U(t) |\psi(0)\rangle. \quad (\text{A.12})$$

The evolution operator simplifies the computation of the state at any future time given its initial state and is integral to the operation of quantum gates in quantum computing.

The expression of the time-evolution operator is useful in showing why the eigenstates of H are stationary, such as $U(t) |\psi_E(t)\rangle = e^{-iEt/\hbar} \psi_E(t)$. Since a global phase is physically insignificant, this is virtually the same state no matter t .

A.2.4 Time-Dependent Evolution Operator

For systems with a Hamiltonian H that varies with time, the evolution of quantum states is governed by a more complex form of the evolution operator, which takes into account the non-commutativity of the Hamiltonian at different times. The time-dependent evolution operator $U(t, t_0)$, where t_0 is the initial time, is defined as:

$$U(t, t_0) = \mathcal{T} \exp \left(-\frac{i}{\hbar} \int_{t_0}^t H(\tau) d\tau \right), \quad (\text{A.13})$$

where \mathcal{T} denotes the time-ordering operator which is necessary due to the potential non-commutativity of the Hamiltonian at different times ($[H(t_1), H(t_2)] \neq 0$ for $t_1 \neq t_2$). The time-ordering operator \mathcal{T} arranges the Hamiltonians so that times increase from right to left within the exponential.

The time-ordered exponential is formally defined as a series expansion:

$$\mathcal{T} \exp \left(-\frac{i}{\hbar} \int_{t_0}^t H(\tau) d\tau \right) = \mathbb{1} + \sum_{n=1}^{\infty} \left(-\frac{i}{\hbar} \right)^n \int_{t_0}^t d\tau_1 \int_{t_0}^{\tau_1} d\tau_2 \cdots \int_{t_0}^{\tau_{n-1}} d\tau_n H(\tau_1) H(\tau_2) \cdots H(\tau_n), \quad (\text{A.14})$$

where $\mathbb{1}$ is the identity operator. This expansion ensures that the effect of the Hamiltonian at each moment is applied in the correct sequence, preserving the causal structure of the quantum dynamics.

This time-dependent evolution operator is crucial for accurately describing the dynamics of quantum systems under time-varying external influences, such as changing magnetic fields or oscillating electric fields, and is fundamental for the implementation of certain quantum control and computation techniques as we will see later. It provides the mathematical tool needed to predict how quantum

states evolve in real-world quantum devices, where the Hamiltonian is often engineered or subjected to external control during computation or other quantum processes.

A.2.5 Interaction picture

In the case of a system's Hamiltonian being decomposable into a time-independent and a time-dependent part:

$$H(t) = H_0 + H_t(t), \quad (\text{A.15})$$

In general, H_0 is called the free evolution Hamiltonian and is characteristic of the internal dynamics of the system, and H_t is characteristic of some outside controls/fields being applied on the system.

We define the interaction picture as the change of the reference frame from the original Schrödinger picture to one where the free evolution Hamiltonian H_0 is treated as the base part. The transformation between the pictures is mediated by the time evolution operator $U_0(t)$ generated by H_0 . In mathematical terms, the interaction picture is defined by the transformation

$$U_0(t) = e^{-iH_0t/\hbar}, \quad (\text{A.16})$$

where \hbar is the reduced Planck constant and i is the imaginary unit. This operator acts on the state vectors and operators to shift the perspective from the Schrödinger to the interaction picture.

In the interaction picture, the state of the system at time t , denoted as $|\psi_I(t)\rangle$, is related to the Schrödinger picture state $|\psi_S(t)\rangle$ by

$$|\psi_I(t)\rangle = U_0^\dagger(t)|\psi_S(t)\rangle. \quad (\text{A.17})$$

Similarly, any operator A_S in the Schrödinger picture is transformed to the interaction picture as

$$A_I(t) = U_0^\dagger(t)A_S U_0(t). \quad (\text{A.18})$$

This transformation leads to a new effective Hamiltonian in the interaction picture, which accounts for the dynamics induced by the external controls or fields. This effective Hamiltonian, denoted $H_I(t)$, is given by the transformation

$$H_I(t) = U_0^\dagger(t)H_t(t)U_0(t), \quad (\text{A.19})$$

and it governs the evolution of the system in the interaction picture according to the modified Schrödinger equation:

$$i\hbar \frac{d}{dt}|\psi_I(t)\rangle = H_I(t)|\psi_I(t)\rangle. \quad (\text{A.20})$$

This representation simplifies the problem of dealing with time-dependent Hamiltonians by isolating the time-dependent effects into the interaction term.

A.2.6 The Heisenberg Picture

An alternative formulation to the Schrödinger picture is the Heisenberg picture, which provides a different perspective on the dynamics of quantum systems. Unlike the Schrödinger picture, where the state vectors evolve over time and the operators are constant, in the Heisenberg picture, the state vectors are fixed and the operators evolve with time.

Time Evolution of Operators

In the Heisenberg picture, the time evolution of an operator A is given by the equation:

$$A_H(t) = U^\dagger(t) A_S U(t), \quad (\text{A.21})$$

where $U(t)$ is the unitary evolution operator from the Schrödinger picture, A_S is the operator in the Schrödinger picture, and $A_H(t)$ is the corresponding operator in the Heisenberg picture. The adjoint $U^\dagger(t)$ reverses the time evolution, effectively keeping the quantum state fixed.

Heisenberg Equation of Motion

The dynamics of operators in the Heisenberg picture are described by the Heisenberg equation of motion, which is analogous to the classical equations of motion. This equation is derived using the time derivative of the operator:

$$\frac{d}{dt} A_H(t) = \frac{i}{\hbar} [H, A_H(t)] + \left(\frac{\partial A}{\partial t} \right)_H, \quad (\text{A.22})$$

where $[H, A_H(t)]$ denotes the commutator of the Hamiltonian H with the operator $A_H(t)$, and $\left(\frac{\partial A}{\partial t} \right)_H$ represents any explicit time dependence of the operator. This formulation highlights the correspondence principle linking quantum mechanics with classical mechanics through the operator formalism.

Advantages of the Heisenberg Picture

The Heisenberg picture is particularly useful in problems where the observables' time evolution is more relevant than the state's time evolution. It is commonly used in quantum field theory and certain problems in quantum optics and quantum electrodynamics where dealing with changing observables rather than states simplifies the calculations and conceptual understanding.

Comparison with Other Pictures

While the Schrödinger picture is usually clearer for problems where you're looking at how quantum states change over time, the Heisenberg and interaction pictures are also very useful for understanding the dynamics of quantum systems from different angles. Although all these perspectives are fundamentally the same in terms of mathematics, they each provide unique advantages depending on the situation.

The key distinction between the interaction and Heisenberg pictures is that the interaction picture simplifies the Schrödinger approach by removing the part of the Hamiltonian that describes the system's inherent (free) evolution. This makes it easier to focus on how external influences change the state, the focus still being on state dynamics. On the other hand, the Heisenberg picture considers all parts of the Hamiltonian together and shifts the focus away from how states change. Instead, it looks at how the measurable properties of the system evolve. In this picture, the state of the system is constant, and the dynamics are all about the observables.

A.3 Density matrices

Let us consider a physical system in the pure state $|\psi\rangle$, its **density matrix** is defined as the following operator:

$$\rho = |\psi\rangle \langle \psi|, \quad (\text{A.23})$$

and its time dynamics are obtained via the **Von Neumann equation**:

$$\frac{\partial \rho(t)}{\partial t} = -i[H(t), \rho(t)] \quad (\text{A.24})$$

The advantage of the density matrix formalism over the simple ket-state formalism is that it can describe mixed states, not just pure states. It is therefore more general as it can describe both classical and quantum statistical mixtures.

For example, let us consider the statistical mixture of n pure states $|\psi_i\rangle$, each with a probability p_i :

$$\rho = \sum_{i=1}^n p_i |\psi_i\rangle \langle \psi_i| \quad (\text{A.25})$$

will represent that statistical mixture and provide a more comprehensive representation of the system's state. This is because the density matrix ρ includes not only the probabilities p_i of each state, but also the phase information between different states, which is crucial for quantum systems.

(A.23) defines a pure state, while the more general (A.25) defines a mixed state.

With both of those definitions, one can obtain the mean value of a given operator A via:

$$\langle A \rangle = \sum_{i=1}^n p_i \langle \psi_i | A | \psi_i \rangle = \text{Tr}(A\rho) \quad (\text{A.26})$$

Every density matrix exhibits the subsequent characteristics:

1. Hermitian nature: $\rho = \rho^\dagger$
2. Trace is unity: $\text{Tr}(\rho) = 1$, and $\text{Tr}(\rho^2) \leq 1$, the latter being equal in the case of a pure state.
3. Eigenvalues are nonnegative: All eigenvalues of ρ are zero or positive.
4. Positive semi-definiteness: For any given state $|\psi\rangle$, the expression $\langle \psi | \rho | \psi \rangle$ is always nonnegative.

Note: For a pure state, we also have that $\rho^2 = \rho$, therefore the density matrix of a pure state is then simply the projection operator on that state.

A.4 Superoperators and vectorisation

In the same way that an operator A interacts with a pure state $|\psi_0\rangle$ to change it to $|\psi_1\rangle = A|\psi_0\rangle$, it also modifies ρ_0 into

$$\rho_1 = |\psi_1\rangle \langle \psi_1| = A|\psi_0\rangle \langle \psi_0| A^\dagger = A\rho_0 A^\dagger. \quad (\text{A.27})$$

Consequently, any arbitrary linear operation on a density matrix can be characterized as a **superoperator**. For instance, considering two operators A and B , we can establish the superoperator $A \boxtimes B$ such that $(A \boxtimes B)[\rho] = A\rho B$, or the superoperator $\mathcal{A} = A \boxtimes A^\dagger$ where $\mathcal{A}[\rho] = A\rho A^\dagger$, or even a superoperator \mathcal{X} that satisfies $\mathcal{X} = \mathcal{A} + \mathcal{B} + AB \boxtimes 1$, and so on. We call those superoperators mapping one density matrix to another: **quantum channels**.

The **vectorisation** of a matrix ρ is denoted as $\text{vec}(\rho)$ and is obtained by stacking the d columns of ρ into a single column vector of size d^2 :

$$\text{vec}(\rho) = \sum_{ij} \rho_{ij} |j\rangle \otimes |i\rangle, \quad (\text{A.28})$$

where \otimes symbolises the Kronecker product.

With this in mind, similar to how an operator acting on a qudit of dimension d can be represented as a $d \times d$ matrix, a superoperator \mathcal{E} can be represented as a $d^2 \times d^2$ matrix acting on ρ_0 to yield ρ_1 .

$$(\rho_1)_{il} = \mathcal{E}_{il}^{jk} (\rho_0)_{jk} \quad (\text{A.29})$$

Moreover, assuming $\mathcal{E} = A \boxtimes B$,

$$(\text{vec}(\mathcal{E}[\rho]))_{il} = \text{vec}(A\rho B) = A_{ij}\rho_{jk}B_{kl} = (B^T \otimes A)_{il}^{jk} \rho_{jk} = ((B^T \otimes A)\text{vec}(\rho))_{il}. \quad (\text{A.30})$$

Therefore, the simple rule of vectorisation of a superoperator to its matrix form ends up being:

$$\text{vec}(A \boxtimes B) = B^T \otimes A. \quad (\text{A.31})$$

Noting that the vectorisation process is linear, this allows one to vectorise any superoperator.

For the remaining of this work, for any superoperator E we will use the shortcut

$$\text{Tr}(\mathcal{E}) := \text{Tr}(\text{vec}(\mathcal{E})). \quad (\text{A.32})$$

Note: This definition gives rise to a useful property:

$$\text{Tr}(A \boxtimes B) = \text{Tr}(A) \text{Tr}(B). \quad (\text{A.33})$$

Note: Moreover, using vectorization, we can also define the trace on an operator A as:

$$\text{Tr}(A) = \text{vec}(\mathbb{1})^T \text{vec}(A) \quad (\text{A.34})$$

A.5 Quantum channels and Kraus operators

While the vectorisation process allows for a matrix representation of superoperators, another one can be the Kraus representation, stating that, there exists, for any completely quantum channel \mathcal{E} , a non-unique and not necessarily finite set of operators E_k such that $\forall \rho$:

$$\mathcal{E}[\rho] = \sum_k E_k \rho E_k^\dagger, \quad (\text{A.35})$$

moreover, if the channel is trace preserving, $\sum_k E_k E_k^\dagger = \mathbb{1}$.

Note: For example, for $\mathcal{U}(t_0, t_f)$, the quantum channel mapping the density matrix evolving according to the Von Neumann equation at t_0 to the density matrix at time t_f . A possible set of Kraus operators is $\{U(t, t_0)\}$, the evolution operator, since $\rho(t_f) = U(t, t_0)\rho(t_0)U^\dagger(t, t_0)$.

Note: Using the Kraus representation of \mathcal{E} we can also reformulate the trace of a superoperator as

$$\text{Tr}(\mathcal{E}) = \sum_k |\text{Tr}(E_k)|^2, \quad (\text{A.36})$$

and more generally,

$$(\text{vec}(\mathcal{E}[\rho]))_{nm}^{ij} = \sum_k E_{k,jm}^* E_{k,in}. \quad (\text{A.37})$$

Chapter Contents

B.1 Numerical noisy qudit/multiqubit simulation	327
B.2 Random gate and pulse Hamiltonian generation	328

CHAPTER B

Methods for the numerical simulations

B.1 Numerical noisy qudit/multiqubit simulation

All simulations were done using the Python package QuTiP [260] version 4.7, SciPy version 1.7.3, and NumPy version 1.21.5. This subsection aims to present the *modus operandi* for obtaining the numerical results referenced in the different figures: the AGIs (\mathcal{E}) for Fig.11.3 and Fig.11.4 and the slope of the AGIs (c) in the other figures.

Standard packages: Essential functions for simulating quantum dynamics and fitting curves to data are provided by the QuTiP library, including functions for propagator calculation in superoperator form (`qt.propagator`) and gate fidelity evaluation (`average_gate_fidelity` from `qutip.metrics`), along with the `curve_fit` function from `scipy.optimize`.

Parameters: We define the system's dimension d , the decay parameter γ , and the collapse operators $\{L_k\}$ under consideration. The collapse operators are `QObj` instances characterized by their matrix form in the canonical basis. Additionally, we generate a list of time points for simulating the system's evolution. Considering the quantity of interest in this study is γt , γ is chosen as fixed, and the range of γt is then given by the range of the time points.

Time evolution: The simulation of the quantum system's time evolution is facilitated by computing the propagator using the system's Hamiltonian, the list of time points, and the collapse operators multiplied by $\sqrt{\gamma}$. This generates a time-dependent propagator in the form of a list of `QObj` superoperators for different values of γt . The system's Hamiltonian will be discussed in further detail in the following subsection. However, apart from Fig.11.5 studying the gate/Hamiltonian-dependence, the other figures report simulations done with a vanishing Hamiltonian $H = 0_d$ since the quantities under consideration are considered Hamiltonian-independent.

Fidelity Calculation: At each γt the average gate fidelity is computed relative to a target gate, in the case of $H = 0_d$: the identity matrix. This is the quantity displayed in Fig.11.3 and Fig.11.4.

Curve Fitting: A curve is fitted to the calculated fidelities over the range of γt using the `curve_fit` function. This process involves fitting the function $1 - c\gamma t$ for the parameter c . The obtained slopes $c(\{L_k\})$ are then the ones displayed in the figures 11.2, 11.5, 11.6, 11.7 and 11.8. Moreover the least-square fit parameter R given by the fitting functions is the one reported in this study.

B.2 Random gate and pulse Hamiltonian generation

Gate generation: In the study of the gate-dependent deviation from the analytical results of this manuscript, for each dimension d under consideration, a set of $N_g = 5000$ gates have been randomly generated with the `Bristol`[261] package in `Python`. The gates have been drawn from the circular unitary ensemble, and are thus considered to be uniformly distributed over the Haar measure. Subsequently, to generate an associated set of pulses for each gate, we have used the `optimize_pulse_unitary` function from the pulse optimization module (`control.pulse_optim`) of `QuTiP`.

Pulse generation: The pulse generation is done through gradient-ascent methods using the `GRAPE` algorithm [32] and was run in parallel for each gate using a high-performance cluster. The numerical optimizer used by default is the L-BFGS-B method. Assuming the control hamiltonian, as discussed after (11.1), takes the form

$$H_c(t) = \sum_{k=0}^N u_k(t) H_k, \quad (\text{B.1})$$

with H_k being a basis set of controls and $u_k(t)$ representing the time-dependent control amplitudes, the optimization process involves finding the set of $u_k(t)$ that best approximates the target gate.

Choice of Hamiltonian: For the simulations reported in this paper, we decided to model qudits as ladder systems, with one pulse per transition between adjacent levels as considered for example in the experiments of Godfrin *et al.*[99], for a single-molecule magnet (TbPc_2 , qudit with $d = 4$), the $d - 1$ pulses are then each represented by two control Hamiltonians in the interaction picture. More explicitly, the basis set of controls is chosen to be the ensemble of pairs $|k\rangle \langle k+1| + |k+1\rangle \langle k|$ and $i(|k\rangle \langle k+1| - |k+1\rangle \langle k|)$, with k running from 1 to $d - 1$. Moreover, H_0 , the free-evolution, is chosen to be vanishing since we consider the interaction reference frame.

Chapter Contents

C.1 Spherical Harmonics	329
C.2 Multipolar expansion	331

CHAPTER C

Symmetries I: Spherical Harmonics and Multipoles

C.1 Spherical Harmonics

Spherical harmonics are special functions defined on the surface of a sphere. They are often used in solving partial differential equations in spherical coordinates. The spherical harmonics $Y_m^{(\ell)}(\theta, \phi)$ are defined as:

$$Y_m^{(\ell)}(\theta, \phi) = \sqrt{\frac{2\ell+1}{4\pi}} \sqrt{\frac{(\ell-m)!}{(\ell+m)!}} P^{(\ell)}(\cos \theta) e^{im\phi}$$

where:

- ℓ is a non-negative integer called the degree,
- m is an integer such that $-\ell \leq m \leq \ell$,
- θ is the polar angle,
- ϕ is the azimuthal angle,
- $P^{(\ell)}$ are the associated Legendre polynomials.

One can also define the normalized spherical harmonics as:

Definition: (*Normalized spherical harmonics*)

$$C_m^{(\ell)}(\theta, \phi) = \sqrt{\frac{4\pi}{2\ell+1}} Y_m^{(\ell)}(\theta, \phi). \quad (\text{C.1})$$

Spherical harmonics form a complete set of orthonormal functions on the sphere, meaning any square-integrable function defined on the sphere can be expanded in terms of spherical harmonics.

The orthogonality relation for spherical harmonics is given by:

$$\int_{\Omega} C_m^{(\ell)}(\theta, \phi) C_{m'}^{(\ell')*}(\theta, \phi) d^2\Omega = \int_0^{2\pi} \int_0^{\pi} C_m^{(\ell)}(\theta, \phi) C_{m'}^{(\ell')*}(\theta, \phi) \sin \theta d\theta d\phi = \frac{4\pi}{2\ell+1} \delta_{\ell\ell'} \delta_{mm'}. \quad (\text{C.2})$$

Note: The spherical harmonics obey the following relation:

$$C_m^{(\ell)*}(\theta, \phi) = (-1)^m C_{-m}^{(\ell)}(\theta, \phi). \quad (\text{C.3})$$

Let's assume that we have a function $f(\vec{r})$ that is defined in all space. We can expand this function in terms of spherical harmonics as follows:

$$f(\vec{r}) = \sum_{\ell=0}^{\infty} \sum_{m=-\ell}^{\ell} f_m^{(\ell)}(r) C_m^{(\ell)}(\theta, \phi), \quad (\text{C.4})$$

where $f_m^{(\ell)}(r)$ are the expansion coefficients. The expansion coefficients can be found by projecting the function $f(\vec{r})$ onto the spherical harmonics and making use of the orthogonality relation (C.2):

$$f_m^{(\ell)}(r) = \int_{\Omega} f(\vec{r}) C_m^{(\ell)*}(\theta, \phi) d^2\Omega. \quad (\text{C.5})$$

The spherical harmonics are also eigenfunctions of the angular part of the Laplace operator:

$$\nabla^2 C_m^{(\ell)}(\theta, \phi) = -\ell(\ell+1) C_m^{(\ell)}(\theta, \phi). \quad (\text{C.6})$$

This becomes quite useful when solving partial differential equations in spherical coordinates, especially with a central potential. The Laplacian of $f(\vec{r})$ can be written as:

$$\nabla^2 f(\vec{r}) = \frac{1}{r^2} \frac{\partial}{\partial r} \left(r^2 \frac{\partial f(\vec{r})}{\partial r} \right) + \frac{1}{r^2 \sin \theta} \frac{\partial}{\partial \theta} \left(\sin \theta \frac{\partial f(\vec{r})}{\partial \theta} \right) + \frac{1}{r^2 \sin^2 \theta} \frac{\partial^2 f(\vec{r})}{\partial \phi^2}. \quad (\text{C.7})$$

Therefore, let's consider the differential equation:

$$\nabla^2 f(\vec{r}) = -V(r) f(\vec{r}), \quad (\text{C.8})$$

where $V(r)$ is a central potential. We can expand the function $f(\vec{r})$ in terms of spherical harmonics as:

$$f(\vec{r}) = \sum_{\ell=0}^{\infty} \sum_{m=-\ell}^{\ell} f_m^{(\ell)}(r) C_m^{(\ell)}(\theta, \phi). \quad (\text{C.9})$$

Substituting (C.9) into (C.8) and projecting onto the spherical harmonics, we obtain:

$$\sum_{\ell=0}^{\infty} \sum_{m=-\ell}^{\ell} \left[\frac{1}{r^2} \frac{d}{dr} \left(r^2 \frac{df_m^{(\ell)}(r)}{dr} \right) - \frac{\ell(\ell+1)}{r^2} f_m^{(\ell)}(r) \right] C_m^{(\ell)}(\theta, \phi) = -V(r) \sum_{\ell=0}^{\infty} \sum_{m=-\ell}^{\ell} f_m^{(\ell)}(r) C_m^{(\ell)}(\theta, \phi). \quad (\text{C.10})$$

Multiplying both sides of (C.10) by $C_{m'}^{(\ell')*}(\theta, \phi)$ and integrating over the sphere, we obtain:

$$\begin{aligned}
& \sum_{\ell=0}^{\infty} \sum_{m=-\ell}^{\ell} \left[\frac{1}{r^2} \frac{d}{dr} \left(r^2 \frac{df_m^{(\ell)}(r)}{dr} \right) - \frac{\ell(\ell+1)}{r^2} f_m^{(\ell)}(r) \right] \int_{\Omega} C_m^{(\ell)}(\theta, \phi) C_{m'}^{(\ell)'}(\theta, \phi) d^2\Omega \\
& = -V(r) \sum_{\ell=0}^{\infty} \sum_{m=-\ell}^{\ell} f_m^{(\ell)}(r) \int_{\Omega} C_m^{(\ell)}(\theta, \phi) C_{m'}^{(\ell)'}(\theta, \phi) d^2\Omega.
\end{aligned} \tag{C.11}$$

Using the orthogonality relation (C.2), we can simplify (C.11) to:

$$\sum_{\ell=0}^{\infty} \sum_{m=-\ell}^{\ell} \left[\frac{1}{r^2} \frac{d}{dr} \left(r^2 \frac{df_m^{(\ell)}(r)}{dr} \right) - \frac{\ell(\ell+1)}{r^2} f_m^{(\ell)}(r) \right] \delta_{\ell\ell'} \delta_{mm'} = -V(r) \sum_{\ell=0}^{\infty} \sum_{m=-\ell}^{\ell} f_m^{(\ell)}(r) \delta_{\ell\ell'} \delta_{mm'}. \tag{C.12}$$

Therefore, (C.12) can be simplified to:

$$\frac{1}{r^2} \frac{d}{dr} \left(r^2 \frac{df_{m'}^{(\ell)'}(r)}{dr} \right) - \ell'(\ell'+1) f_{m'}^{(\ell)'}(r) = -V(r) f_{m'}^{(\ell)'}(r). \tag{C.13}$$

Therefore, the radial part of the differential equation (C.8) can be solved by solving (C.13) for each ℓ and m . The solution of the radial part can then be multiplied by the spherical harmonics to obtain the full solution of the differential equation.

C.2 Multipolar expansion

Let's consider the two variable function $f(\vec{r}_1, \vec{r}_2)$ that is defined in all space and is given by

$$f(\vec{r}_1, \vec{r}_2) = \frac{1}{|\vec{r}_1 - \vec{r}_2|}. \tag{C.14}$$

It can be proven this function is solution to the local Poisson equation

$$\nabla_1^2 f(\vec{r}_1, \vec{r}_2) = -4\pi\delta(\vec{r}_1 - \vec{r}_2). \tag{C.15}$$

This means, using the Green function formalism, that the potential $\phi(\vec{r})$ that satisfies the Poisson equation

$$\nabla^2 \phi(\vec{r}) = -4\pi\rho(\vec{r}), \tag{C.16}$$

is given by

$$\phi(\vec{r}) = \int d^3r' \frac{\rho(\vec{r}')}{|\vec{r} - \vec{r}'|}. \tag{C.17}$$

The function $f(\vec{r}_1, \vec{r}_2)$ can be expanded in terms of spherical harmonics, to see it, we can write the distance between \vec{r}_1 and \vec{r}_2 as

$$|\vec{r}_1 - \vec{r}_2| = \sqrt{r_1^2 + r_2^2 - 2r_1r_2 \cos \gamma}, \tag{C.18}$$

where γ is the angle between \vec{r}_1 and \vec{r}_2 . If we define $r_> = \max(r_1, r_2)$ and $r_< = \min(r_1, r_2)$, we can write

$$|\vec{r}_1 - \vec{r}_2| = r_{>} \sqrt{1 + \left(\frac{r_{\leq}}{r_{>}}\right)^2 - 2\frac{r_{\leq}}{r_{>}} \cos \gamma}, \quad (\text{C.19})$$

where, by definition $\left(\frac{r_{\leq}}{r_{>}}\right) < 1$. We can then expand the square root in terms of Legendre polynomials

$$\frac{1}{r_{>} \sqrt{1 + \left(\frac{r_{\leq}}{r_{>}}\right)^2 - 2\frac{r_{\leq}}{r_{>}} \cos \gamma}} = \sum_{\ell=0}^{\infty} \frac{r_{\leq}^{\ell}}{r_{>}^{\ell+1}} P^{(\ell)}(\cos \gamma). \quad (\text{C.20})$$

Writing $\cos \gamma$ in terms of the spherical coordinates of \vec{r}_1 and \vec{r}_2 , we have

$$\cos \gamma = \cos \theta_1 \cos \theta_2 + \sin \theta_1 \sin \theta_2 \cos(\phi_1 - \phi_2), \quad (\text{C.21})$$

where θ_1 and ϕ_1 are the polar and azimuthal angles of \vec{r}_1 , and θ_2 and ϕ_2 are the polar and azimuthal angles of \vec{r}_2 . Substituting this in the Legendre polynomials, and remembering that $\cos(\phi_1 - \phi_2) = \cos \phi_1 \cos \phi_2 + \sin \phi_1 \sin \phi_2$, we have

$$P^{(\ell)}(\cos \gamma) = P^{(\ell)}(\cos \theta_1 \cos \theta_2 + \sin \theta_1 \sin \theta_2 \cos(\phi_1 - \phi_2)) = P^{(\ell)}(\hat{r}_1 \cdot \hat{r}_2), \quad (\text{C.22})$$

where $\hat{r}_1 = (\sin \theta_1 \cos \phi_1, \sin \theta_1 \sin \phi_1, \cos \theta_1)$ and $\hat{r}_2 = (\sin \theta_2 \cos \phi_2, \sin \theta_2 \sin \phi_2, \cos \theta_2)$, or in spherical coordinates $\hat{r}_1 = (\theta_1, \phi_1)$ and $\hat{r}_2 = (\theta_2, \phi_2)$.

The addition theorem for spherical harmonics states that

$$P^{(\ell)}(\hat{r}_1 \cdot \hat{r}_2) = \sum_{m=-\ell}^{\ell} C_m^{(\ell)}(\theta_1, \phi_1) C_m^{\ell*}(\theta_2, \phi_2). \quad (\text{C.23})$$

Therefore, reintroducing the normalized spherical harmonics defined in (C.1), we can write the expansion of $f(\vec{r}_1, \vec{r}_2)$ in terms of spherical harmonics as

Definition: (Expansion of $\frac{1}{|\vec{r}_1 - \vec{r}_2|}$ in terms of spherical harmonics)

$$\frac{1}{|\vec{r}_1 - \vec{r}_2|} = \sum_{\ell=0}^{\infty} \sum_{m=-\ell}^{\ell} \frac{r_{\leq}^{\ell}}{r_{>}^{\ell+1}} C_m^{(\ell)}(\theta_1, \phi_1) C_m^{(\ell)*}(\theta_2, \phi_2). \quad (\text{C.24})$$

Note: Equation (C.24) can be used to prove that $f(\vec{r}_1, \vec{r}_2)$ is a solution to the Poisson equation (C.15). By comparing with (C.4), the expansion coefficients of $f(\vec{r}_1, \vec{r}_2)$ are given by

$$f_m^{(\ell)}(r, \vec{r}') = \frac{r_{\leq}^{\ell}}{r_{>}^{\ell+1}} C_m^{(\ell)}(\theta', \phi'). \quad (\text{C.25})$$

Using the expression of the Laplacian in spherical coordinates (C.6), and following the same steps as those used to derive (C.13), one can obtain the desired result.

Substituting (C.24) into the potential $\phi(\vec{r})$ defined in (C.17), we obtain

Definition: (Multipole expansion a potential satisfying the Poisson equation (C.17))

$$\phi(\vec{r}) = \sum_{\ell=0}^{\infty} \sum_{m=-\ell}^{\ell} (-1)^m C_m^{(\ell)}(\theta, \phi) \int_{r'} \frac{r_{\leq}^{\ell}}{r_{>}^{\ell+1}} C_{-m}^{(\ell)}(\theta', \phi') \rho(\vec{r}') d^3 r'. \quad (\text{C.26})$$

The expansion coefficients of the potential $\phi(\vec{r})$ are given by

$$\phi_m^{(\ell)}(r) = \int_{r'} \frac{r_{\leq}^{\ell}}{r_{>}^{\ell+1}} C_{-m}^{(\ell)}(\theta', \phi') \rho(\vec{r}') d^3 r', \quad (\text{C.27})$$

and are called the **multipole moments** of the potential $\phi(\vec{r})$.

Chapter Contents

D.1	Coordinate systems	335
D.2	Irreducible Tensor Operators	335
D.3	nj symbols	337

CHAPTER D

Symmetries II: Tensor Operators and Racah-Wigner coefficients

D.1 Coordinate systems

D.1.1 Polar Coordinates

We define polar coordinates (r, ϑ, φ) through their relation to the cartesian coordinates (x, y, z) through the relations:

$$\begin{aligned}
 x &= r \sin \vartheta \cos \varphi & r &= \sqrt{x^2 + y^2 + z^2} & 0 \leq r < \infty \\
 y &= r \sin \vartheta \sin \varphi & \vartheta &= \arccos \frac{z}{\sqrt{x^2 + y^2 + z^2}} & 0 \leq \vartheta \leq \pi \\
 z &= r \cos \vartheta & \varphi &= \arccos \frac{x}{\sqrt{x^2 + y^2}} \left(\tan \varphi = \frac{y}{x} \right) & 0 \leq \varphi < 2\pi
 \end{aligned} \tag{D.1}$$

D.1.2 Spherical Coordinates (or circular polarization basis)

We can also define a different set of basis vectors from the cartesian basis vectors :

$$\begin{aligned}
 \mathbf{e}_{+1} &= -\frac{1}{\sqrt{2}} (\mathbf{e}_x + i\mathbf{e}_y) \\
 \mathbf{e}_0 &= \mathbf{e}_z \\
 \mathbf{e}_{-1} &= \frac{1}{\sqrt{2}} (\mathbf{e}_x - i\mathbf{e}_y)
 \end{aligned} \tag{D.2}$$

D.2 Irreducible Tensor Operators

D.2.1 Angular Momentum Operators

A physical system's angular momentum is quantum mechanically characterised by an operator \mathbf{J} whose components satisfy the following commutation relations :

$$[J_x, J_y] = iJ_z, \quad [J_y, J_z] = iJ_x, \quad [J_z, J_x] = iJ_y, \quad [\mathbf{J}^2, J_{x,y,z}] = 0, \tag{D.3}$$

and, physically, represents an observable quantity that is conserved in a closed system or in a system with rotational symmetry. The eigenvalues of \mathbf{J}^2 and J_z are denoted $J(J+1)\hbar^2$ and $M_J\hbar$ respectively. This operator, then, also spans a basis of eigenstates, in Dirac notation :

$$J_z |J, M_J\rangle = \hbar M_J |J, M_J\rangle, \quad \mathbf{J}^2 |J, M_J\rangle = \hbar^2 J(J+1) |J, M_J\rangle. \quad (\text{D.4})$$

Finally, we can define the two ladder operators, using Condon and Shortley convention :

$$J_{\pm} |J, M_J\rangle = (J_x \pm iJ_y) |J, M_J\rangle = \hbar \sqrt{J(J+1) - M_J(M_J \pm 1)} |J, M_J \pm 1\rangle. \quad (\text{D.5})$$

Let $\mathbf{j}_{1,2}$ be two angular momenta such as

$$\mathbf{J} = \mathbf{j}_1 + \mathbf{j}_2. \quad (\text{D.6})$$

And :

$$j_{1,2} |j_1 m_1, j_2 m_2\rangle = \hbar m_{1,2} |j_1 m_1, j_2 m_2\rangle, \quad \mathbf{j}_{1,2}^2 |j_1 m_1, j_2 m_2\rangle = \hbar^2 j_{1,2}(j_{1,2} + 1) |j_1 m_1, j_2 m_2\rangle \quad (\text{D.7})$$

The eigenstates of \mathbf{J} , if it is a composed angular momentum (Eq.D.6), are also denoted : $|(j_1, j_2)JM_J\rangle$. We then say that \mathbf{j}_1 and \mathbf{j}_2 couple to \mathbf{J} . And we call $|j_1 m_1, j_2 m_2\rangle$ the uncoupled basis, as opposed to $|(j_1, j_2)JM_J\rangle$ the coupled basis.

Definition: (*Clebsh-Gordon coefficients*) We then define Clebsh-Gordon coefficients as $\langle j_1 m_1, j_2 m_2 | JM_J \rangle$:

$$|(j_1 j_2)JM_J\rangle = \sum_{m'_s} \langle j_1 m_1, j_2 m_2 | JM_J \rangle |j_1 m_1, j_2 m_2\rangle. \quad (\text{D.8})$$

We imposed Condon and Shortley constraints i.e. $\langle j_1 j_1, j_2(J - j_1) | JJ \rangle > 0$.

Clebsh-Gordon coefficients facilitate the connection between the coupled and uncoupled bases.

D.2.2 Definition

Definition: (*Irreducible Tensor Operators*) An ensemble of $2k+1$ operators $\{T_q^{(k)}\}_{q \in [-k, k]}$ that satisfy :

$$\begin{aligned} [J_z, T_q^{(k)}] &= \hbar q T_q^{(k)} \\ [J_{\pm}, T_q^{(k)}] &= \hbar \sqrt{k(k+1) - q(q \pm 1)} T_{q \pm 1}^{(k)} \end{aligned} \quad (\text{D.9})$$

Where \mathbf{J} is an angular momentum operator, form a $(2k+1)$ -component **irreducible tensor operator** (ITO) of rank k : $\mathbf{T}^{(k)}$.

Examples of irreducible tensor operators of rank 1 are any vector operator whose components are expressed in the spherical basis (cf. Eq. D.1).

In particular the orbital angular momentum operator \mathbf{L} :

$$L_{-1}^{(1)} = \frac{1}{\sqrt{2}} L_-, \quad L_0^{(1)} = L_z, \quad L_{+1}^{(1)} = -\frac{1}{\sqrt{2}} L_+ \quad (\text{D.10})$$

The same goes for any angular momentum operator \mathbf{J} .

Spherical harmonics (see C.1) can be used to define a rank l irreducible tensor operator : $Y_m^{(l)}(\vartheta, \varphi) = Y_l^m(\vartheta, \varphi)\mathbb{1}$. As well as the normalized spherical harmonics: $\mathbf{C}^{(l)} = \sqrt{\frac{4\pi}{2l+1}}\mathbf{Y}^{(l)}$.

Irreducible Tensor Operators have the following properties:

- They form a basis for the $(2k+1)$ -dimensional irreducible representation of $SO(3)$.
- They are generators of the $U(2k+1)$ group.
- They behave as the $|k, q\rangle$ states of the angular momentum operator.
- $\forall k \in \mathbb{N}, \forall q \in [-k, k], [J^2, T_q^{(k)}] = \hbar^2 k(k+1)T_q^{(k)}$

Note: The ITOs defined in this work are defined over the position space. One can also define ITOs over the momentum space, as polynomials of \mathbf{J} . The latter set still satisfies the commutation relations in (D.9), but, notably $[J^2, T_q^{(k)}(\mathbf{J})] = 0$ is not satisfied. See [109] for more details.

D.3 n_j symbols

Note: We define across this document :

$$[k] := 2k + 1.$$

D.3.1 $3j$ symbols

Wigner n_j -symbols are a system of notations allowing one to deal with coupling of angular momenta in a more symmetric way than Clebsh-Gordon coefficients.

Definition: ($3j$ -symbol) We define :

$$\begin{pmatrix} j_2 & J & j_1 \\ m_2 & M_J & m_1 \end{pmatrix} = \frac{(-1)^{j_1-j_2-M_J}}{[J]^{\frac{1}{2}}} \langle j_1 m_1, j_2 m_2 | J - M_J \rangle. \quad (\text{D.11})$$

Symmetries of the $3j$ symbols

The $3j$ -symbols have the following symmetries :

- Symmetry with respect to an even permutation of the columns :

$$\begin{pmatrix} j_1 & J & j_2 \\ m_1 & M_J & m_2 \end{pmatrix} = \begin{pmatrix} J & j_2 & j_1 \\ M_J & m_2 & m_1 \end{pmatrix} = \begin{pmatrix} j_2 & j_1 & J \\ m_2 & m_1 & M_J \end{pmatrix}. \quad (\text{D.12})$$

- Symmetry with respect to an odd permutation of the columns :

$$\begin{pmatrix} j_1 & J & j_2 \\ m_1 & M_J & m_2 \end{pmatrix} = (-1)^{j_1+j_2+J} \begin{pmatrix} j_2 & J & j_1 \\ m_2 & M_J & m_1 \end{pmatrix} = (-1)^{j_1+j_2+J} \begin{pmatrix} j_1 & j_2 & J \\ m_1 & m_2 & M_J \end{pmatrix}. \quad (\text{D.13})$$

- Symmetry with respect to a change of sign in the bottom row :

$$\begin{pmatrix} j_1 & J & j_2 \\ m_1 & M_J & m_2 \end{pmatrix} = (-1)^{j_1+j_2+J} \begin{pmatrix} j_1 & J & j_2 \\ -m_1 & -M_J & -m_2 \end{pmatrix}. \quad (\text{D.14})$$

Properties of the $3j$ symbols

We define $\{x \ y \ z\} \equiv \begin{cases} 1 & \text{if } |x - y| \leq z \leq x + y \\ 0 & \text{otherwise} \end{cases}$.

The $3j$ -symbols have the following properties :

- Orthogonality :

$$\sum_{m_1, m_2} \begin{pmatrix} j_1 & J & j_2 \\ m_1 & M_J & m_2 \end{pmatrix} \begin{pmatrix} j_1 & J' & j_2 \\ m_1 & M'_J & m_2 \end{pmatrix} = \frac{\delta_{J, J'} \delta_{M_J, M'_J}}{2J + 1} \quad (\text{D.15})$$

$$\sum_{J, M_J} \begin{pmatrix} j_1 & J & j_2 \\ m_1 & M_J & m_2 \end{pmatrix} \begin{pmatrix} j_1 & J & j_2 \\ m'_1 & M_J & m'_2 \end{pmatrix} = \frac{\delta_{m_1, m'_1} \delta_{m_2, m'_2}}{2J + 1} \quad (\text{D.16})$$

$$\sum_{m_1, m_2, M_J} \begin{pmatrix} j_1 & J & j_2 \\ m_1 & M_J & m_2 \end{pmatrix} \begin{pmatrix} j_1 & J & j_2 \\ m_1 & M_J & m_2 \end{pmatrix} = 1 \quad (\text{D.17})$$

- Selection rules :

$$\begin{pmatrix} j_1 & J & j_2 \\ m_1 & M_J & m_2 \end{pmatrix} = 0 \text{ if } \begin{cases} m_1 + m_2 \neq M_J \\ j_1 + j_2 + J \notin \mathbb{N} \\ \{j_1 \ j_2 \ J\} = 0 \\ |m_1| \geq j_1 \\ |m_2| \geq j_2 \\ |M_J| \geq J \end{cases} \quad (\text{D.18})$$

- Special case for $J = 0$:

$$\begin{pmatrix} j & 0 & j' \\ m & M & m' \end{pmatrix} = \frac{(-1)^{j-m}}{\sqrt{2j+1}} \delta_{m, -m'} \delta_{j, j'} \delta_{M, 0} \quad (\text{D.19})$$

Other properties can be found in [262].

D.3.2 $6j$ and $9j$ symbols

If one has three angular momenta $\mathbf{j}_1, \mathbf{j}_2, \mathbf{j}_3$ that couple all to give rise to \mathbf{J} , it is not possible to express the coupled states $|JM_J\rangle$ unambiguously as linear combinations of the uncoupled $|j_1 m_1, j_2 m_2, j_3 m_3\rangle$ s. But this ambiguity can be lifted by choosing one of the following schemes :

- \mathbf{j}_1 and \mathbf{j}_2 couple to \mathbf{j}_{12} , that then couples with \mathbf{j}_3 to \mathbf{J} : $((j_1 j_2) j_{12} j_3) J$,
- \mathbf{j}_{23} results from the coupling of \mathbf{j}_2 with \mathbf{j}_3 . \mathbf{j}_1 then couples with \mathbf{j}_{23} to \mathbf{J} : $(j_1 (j_2 j_3) j_{23}) J$.

One can then express $|JM_J\rangle$ s as linear combinations of $|((j_1 j_2) j_{12} m_{12} j_3 m_3)\rangle$ s or linear combinations of $|j_1 m_1 (j_2 j_3) j_{23} m_{23}\rangle$ s. (Eq.D.8).

Moreover, one can link the two expressions of $|JM_J\rangle$ together :

$$|(j_1 (j_2 j_3) j_{23}) JM_J\rangle = \sum_{j_{12} s} \langle ((j_1 j_2) j_{12} j_3) JM_J | (j_1 (j_2 j_3) j_{23}) JM_J \rangle | ((j_1 j_2) j_{12} j_3) JM_J \rangle.$$

By applying J_{\pm} on this expression, we see that the $\langle ((j_1 j_2) j_{12} j_3) JM_J | (j_1 (j_2 j_3) j_{23}) JM_J \rangle$ s are independent of M_J , therefore :

Definition: ($6j$ -symbol) We define :

$$\left\{ \begin{matrix} j_1 & j_2 & j_{12} \\ j_3 & J & j_{23} \end{matrix} \right\} = \frac{(-1)^{j_1+j_2+j_3+J}}{([j_{12}][j_{23}])^{\frac{1}{2}}} \langle ((j_1 j_2) j_{12} j_3) J | (j_1 (j_2 j_3) j_{23}) J \rangle. \quad (\text{D.20})$$

This whole discussion can be analogously done for the coupling of 4 angular momenta, and we then would have :

Definition: ($9j$ -symbol) We define :

$$\left\{ \begin{matrix} j_1 & j_2 & j_{12} \\ j_3 & j_4 & j_{34} \\ j_{13} & j_{24} & J \end{matrix} \right\} = \frac{1}{([j_{12}][j_{34}][j_{13}][j_{24}])^{\frac{1}{2}}} \langle ((j_1 j_2) j_{12} (j_3 j_4) j_{34}) J | ((j_1 j_3) j_{13} (j_2 j_4) j_{24}) J \rangle. \quad (\text{D.21})$$

This can then be generalized to define many more Wigner $3nj$ -symbols.

Symmetries of the $6j$

The $6j$ -symbols have the following symmetries :

- Symmetry with respect to any permutation of the columns :

$$\left\{ \begin{matrix} j_1 & j_2 & j_{12} \\ j_3 & J & j_{23} \end{matrix} \right\} = \left\{ \begin{matrix} j_2 & j_1 & j_{12} \\ J & j_3 & j_{23} \end{matrix} \right\} = \left\{ \begin{matrix} j_{12} & j_1 & j_2 \\ j_{23} & j_3 & J \end{matrix} \right\} = \left\{ \begin{matrix} j_1 & j_{12} & j_2 \\ j_3 & j_{23} & J \end{matrix} \right\} = \dots \quad (\text{D.22})$$

- Symmetry if any two elements in two columns are exchanged :

$$\left\{ \begin{matrix} j_1 & j_2 & j_{12} \\ j_3 & J & j_{23} \end{matrix} \right\} = \left\{ \begin{matrix} j_3 & j_2 & j_{23} \\ j_1 & J & j_{12} \end{matrix} \right\} = \left\{ \begin{matrix} j_1 & J & j_{23} \\ j_3 & j_2 & j_{12} \end{matrix} \right\} = \left\{ \begin{matrix} j_3 & J & j_{12} \\ j_1 & j_2 & j_{23} \end{matrix} \right\} \quad (\text{D.23})$$

Properties of the $6j$ symbols

The $6j$ -symbols have the following properties :

- Orthogonality :

$$\sum_{j_{12}} (2j_{12} + 1) \left\{ \begin{matrix} j_1 & j_2 & j_{12} \\ j_3 & J & j_{23} \end{matrix} \right\} \left\{ \begin{matrix} j_1 & j_2 & j_{12} \\ j_3 & J & j'_{23} \end{matrix} \right\} = \frac{\delta_{j_{23}, j'_{23}}}{2j_{23} + 1} \quad (\text{D.24})$$

- Integer selection rules :

$$\left\{ \begin{matrix} j_1 & j_2 & j_{12} \\ j_3 & J & j_{23} \end{matrix} \right\} = 0 \text{ if } \begin{cases} j_1 + j_2 + j_3 \notin \mathbb{N} \\ j_1 + j_{12} + J \notin \mathbb{N} \\ j_2 + j_3 + j_{23} \notin \mathbb{N} \\ j_3 + j_{12} + J \notin \mathbb{N} \end{cases} \quad (\text{D.25})$$

- Triangular selection rules :

$$\left\{ \begin{matrix} j_1 & j_2 & j_{12} \\ j_3 & J & j_{23} \end{matrix} \right\} = 0 \text{ if } \begin{cases} \{j_1 \ j_2 \ j_3\} = 0 \\ \{j_1 \ j_{12} \ J\} = 0 \\ \{j_2 \ j_3 \ j_{23}\} = 0 \\ \{j_3 \ j_{12} \ J\} = 0 \end{cases} \quad (\text{D.26})$$

- Special case for $J = 0$:

$$\left\{ \begin{matrix} j_1 & j_2 & j_{12} \\ j_3 & 0 & j_{23} \end{matrix} \right\} = \frac{(-1)^{j_1+j_2+j_3}}{\sqrt{(2j_1+1)(2j_3+1)}} \delta_{j_1,j_{23}} \delta_{j_3,j_{12}} \quad (\text{D.27})$$

- Relation with $3j$ -symbols :

$$\left\{ \begin{matrix} j_1 & j_2 & j_3 \\ j_4 & j_5 & j_6 \end{matrix} \right\} = \sum_{m_1, \dots, m_6} (-1)^{\sum_{k=1}^6 (j_k - m_k)} \begin{pmatrix} j_1 & j_2 & j_3 \\ -m_1 & -m_2 & -m_3 \end{pmatrix} \begin{pmatrix} j_1 & j_5 & j_6 \\ m_1 & -m_5 & m_6 \end{pmatrix} \times \\ \times \begin{pmatrix} j_4 & j_2 & j_6 \\ m_4 & m_2 & -m_6 \end{pmatrix} \begin{pmatrix} j_4 & j_5 & j_3 \\ -m_4 & m_5 & m_3 \end{pmatrix} \quad (\text{D.28})$$

Other relations and properties can be found in [124], including similar properties for the $9j$ -symbols. The main advantage to using Wigner nj -symbols are their symmetry with respect to some argument permutations and row/column permutations, their relations with each other and more importantly their selection rules making them equal to 0 if certain conditions on their argument are not respected. Finally, these symbols appear extensively in, and simplify a lot of, expressions involving irreducible tensor operators as can be seen in the following sections.

D.3.3 Wigner-Eckart theorem

The Wigner-Eckart theorem is a theorem that allows one to express the matrix elements of an irreducible tensor operator in terms of Clebsch-Gordon coefficients and Wigner $3j$ -symbols, it also allows to decouple the matrix elements of any tensor operator in two parts, one that depends on the angular momentum quantum number m and one that depends on the other quantum numbers.

Definition: (*Wigner-Eckart theorem*) Let $\mathbf{T}^{(k)}$ be a tensor operator of rank k and $|jm\rangle$ and $|j'm'\rangle$ two states of angular momentum j and j' respectively. We also denote all quantum numbers other than the angular momentum quantum numbers by α . We then have :

$$\langle \alpha j m | \mathbf{T}^{(k)} | \alpha j' m' \rangle = (-1)^{j-m} \begin{pmatrix} j & k & j' \\ -m & 0 & m' \end{pmatrix} \langle \alpha j || \mathbf{T}^{(k)} || \alpha j' \rangle. \quad (\text{D.29})$$

One can apply the Wigner-Eckart theorem to the matrix elements of the angular momentum operators:

$$\langle JM | J_q | J' M' \rangle = (-1)^{J-M} \begin{pmatrix} J & 1 & J' \\ -M & q & M' \end{pmatrix} \langle J || \mathbf{J} || J' \rangle, \quad (\text{D.30})$$

noting that

$$\langle JM | J_q | J' M' \rangle = \delta_{M,M'} \delta_{J,J'} \delta_{q,M}, \quad (\text{D.31})$$

one can deduce that

$$\langle \alpha J || \mathbf{J} || \alpha' J' \rangle = \delta_{\alpha, \alpha'} \delta_{J,J'} \delta_{q,m} \sqrt{J(J+1)(2J+1)}. \quad (\text{D.32})$$

It is also possible to show that the reduce matrix element of the normalized spherical harmonics is

$$\langle \alpha \ell \| \mathbf{C}^{(l)} \| \alpha' \ell' \rangle = \delta_{\alpha, \alpha'} (-1)^l ([l][l'])^{\frac{1}{2}} \begin{pmatrix} \ell & l & \ell' \\ 0 & 0 & 0 \end{pmatrix}. \quad (\text{D.33})$$

Finally, it is noteworthy that the reduced matrix element of the identity operator is not unity but rather

$$\langle \alpha l \| \mathbb{1} \| \alpha' l' \rangle = \delta_{\alpha, \alpha'} \delta_{l, l'} \sqrt{2l+1}. \quad (\text{D.34})$$

Note: A quite useful consequence of the Wigner-Eckart theorem is that the diagonal matrix elements of any vector operator (tensor operator of rank 1) are proportional to the expectation value of the angular momentum operator with the proportionality factor being the ratio of the reduced matrix element of the vector operator to the reduced matrix element of the angular momentum operator.

D.3.4 Coupled tensor operators

Definition: (*Coupled Tensor Operator*) Let $\mathbf{T}^{(k_1)}$ and $\mathbf{U}^{(k_2)}$ be two tensor operators of rank k_1 and k_2 respectively. We define the coupled tensor operator $\mathbf{X}^{(k_1, k_2)K}$ as :

$$\begin{aligned} X_q^{(k_1, k_2)K} &= \sum_{q_1, q_2} \langle k_1 q_1, k_2 q_2 | K q \rangle T_{q_1}^{(k_1)} U_{q_2}^{(k_2)}. \\ &= [K]^{\frac{1}{2}} \sum_{q_1, q_2} (-1)^{k_1 - k_2 - q} \begin{pmatrix} k_1 & k_2 & K \\ q_1 & q_2 & -q \end{pmatrix} T_{q_1}^{(k_1)} U_{q_2}^{(k_2)}. \end{aligned} \quad (\text{D.35})$$

This definition has a similar structure to (D.8) that allows to go from the coupled to the uncoupled basis and also provides a definition for the **Tensor Product of rank K of two irreducible tensor operators**. The latter, depending on the conventions, can be missing the factor $[K]^{1/2}$.

In this work we will write

$$\mathbf{X}^{(k_1, k_2)K} = [\mathbf{T}^{(k_1)} \times \mathbf{U}^{(k_2)}]^{(K)}. \quad (\text{D.36})$$

Equation (D.35) can also be simplified to the 0-rank tensor operator, by setting $K = 0$, that similarly defines the scalar product of two tensor operators.

Definition: (*Scalar Product*) The scalar product of two tensor operators $\mathbf{T}^{(k_1)}$ and $\mathbf{U}^{(k_2)}$ is given by:

$$(\mathbf{T}^{(k)} \cdot \mathbf{U}^{(k)}) = \sum_q (-1)^q T_q^{(k_1)} U_{-q}^{(k_2)}. \quad (\text{D.37})$$

As a reminder

$$\begin{pmatrix} k_1 & k_2 & 0 \\ q_1 & q_2 & 0 \end{pmatrix} = (-1)^{k_1} [k]^{-\frac{1}{2}} \delta_{k_1, k_2} \delta_{q_1, -q_2}, \quad (\text{D.38})$$

hence

$$[T^{(k)} \times U^{(k)}]_0^{(0)} = \frac{(-1)^k}{2k+1} (T^{(k_1)} U^{(k_2)})_0 \quad (\text{D.39})$$

Reduced Matrix Elements of Coupled Tensor Operators

The reduced matrix elements of a tensor product of two tensor operators can be expressed in terms of the reduced matrix elements of the individual tensor operators and $9j$ -symbols.

$$\begin{aligned} \langle \alpha J \| [\mathbf{T}^{(k_1)} \times \mathbf{U}^{(k_2)}]^{(K)} \| \alpha' J' \rangle &= \sum_{\alpha''} \langle \alpha j_1 \| \mathbf{T}^{(k_1)} \| \alpha'' j_1' \rangle \langle \alpha'' j_2 \| \mathbf{U}^{(k_2)} \| \alpha' j_2' \rangle \times \\ &\times \sqrt{[J][J'][K]} \begin{Bmatrix} k_1 & k_2 & K \\ j_1 & j_2 & J \\ j_1' & j_2' & J' \end{Bmatrix}. \end{aligned} \quad (\text{D.40})$$

The following relation holds true

$$\begin{Bmatrix} k & k_2 & 0 \\ j_1 & j_2 & J \\ j_1' & j_2' & J' \end{Bmatrix} = \delta_{k_1, k_2} \delta_{J, J'} \frac{(-1)^{j_1+k_1+j_2'+J}}{\sqrt{[J][K]}} \begin{Bmatrix} j_1' & j_2' & J \\ j_2 & j_1 & k \end{Bmatrix}, \quad (\text{D.41})$$

hence, combining this with the Wigner-Eckart theorem, we can express the reduced matrix elements of a coupled tensor operator in terms of the reduced matrix elements of the individual tensor operators and $6j$ -symbols

$$\begin{aligned} \langle \alpha j_1 j_2 J M | (\mathbf{T}^{(k)} \cdot \mathbf{U}^{(k)}) | \alpha' j_1' j_2' J' M' \rangle &= \delta_{J, J'} \delta_{M, M'} (-1)^{j_1'+j_2+J} \begin{Bmatrix} j_1' & j_2' & J \\ j_2 & j_1 & k \end{Bmatrix} \times \\ &\times \sum_{\alpha''} \langle \alpha j_1 \| \mathbf{T}^{(k)} \| \alpha'' j_1' \rangle \langle \alpha'' j_2 \| \mathbf{U}^{(k)} \| \alpha' j_2' \rangle. \end{aligned} \quad (\text{D.42})$$

Equation (D.40) can be simplified in another way to obtain the matrix element of an operator $\mathbf{T}^{(k)}$ that acts only on part 1 of the coupled state $|\alpha j_1 j_2 J M\rangle$. Since such an operator is simply $[\mathbf{T}^{(k)} \times \mathbb{1}]^{(k)}$, therefore $k_2 = 0$ and by using (D.41) and the invariance under permutation of the $9j$ -symbols, we obtain :

$$\begin{aligned} \langle \alpha j_1 j_2 J \| \mathbf{T}^{(k)} \| \alpha' j_1' j_2' J' \rangle &= \delta_{j_2, j_2'} (-1)^{j_1+j_2'+J+k} ([J][J'])^{\frac{1}{2}} \begin{Bmatrix} J & k & J' \\ j_1' & j_2 & j_1 \end{Bmatrix} \\ &\times \langle \alpha j_1 \| \mathbf{T}^{(k)} \| \alpha' j_1' \rangle. \end{aligned} \quad (\text{D.43})$$

Similarly, an operator $\mathbf{U}^{(k)}$ that acts only on part 2 of the coupled state $|\alpha j_1 j_2 J M\rangle$ can be expressed as :

$$\begin{aligned} \langle \alpha j_1 j_2 J \| \mathbf{U}^{(k)} \| \alpha' j_1' j_2' J' \rangle &= \delta_{j_1, j_1'} (-1)^{j_1+j_2'+J+k} ([J][J'])^{\frac{1}{2}} \begin{Bmatrix} J & k & J' \\ j_2' & j_1 & j_2 \end{Bmatrix} \\ &\times \langle \alpha j_2 \| \mathbf{U}^{(k)} \| \alpha' j_2' \rangle. \end{aligned} \quad (\text{D.44})$$

Chapter Contents

E.1 Nonlinearity of the Fidelity in Open Qudit Systems	344
--	-----

CHAPTER E

Preprint summarized in the main text

E.1 Nonlinearity of the Fidelity in Open Qudit Systems

Jean-Gabriel Hartmann,^{1,*} Denis Janković,^{1,2,†} Rémi Pasquier,^{1,‡} Mario Ruben,^{2,3,4,§} and Paul-Antoine Hervieux^{1,¶}

¹*Institut de Physique et Chimie des Matériaux de Strasbourg (IPCMS), UMR 7504 CNRS, Université de Strasbourg, 67000 Strasbourg, France*

²*Institute of Nanotechnology (INT), Karlsruhe Institute of Technology, P.O. Box 3640, 76021 Karlsruhe, Germany*

³*Institute for Quantum Materials and Technologies (IQMT), Karlsruhe Institute of Technology, P.O. Box 3640, 76021 Karlsruhe, Germany*

⁴*Centre Européen de Science Quantique (CESQ), Institut de Science et d'Ingénierie Supramoléculaires (ISIS), UMR 7006 CNRS, Université de Strasbourg, 67000 Strasbourg, France*

(Dated: September 5, 2024)

High-dimensional quantum computing has generated significant interest due to its potential to address scalability and error correction challenges faced by traditional qubit-based systems. This paper investigates the Average Gate Fidelity (AGF) of single qudit systems under Markovian noise in the Lindblad formalism, extending previous work by developing a comprehensive theoretical framework for the calculation of higher-order correction terms. We derive general expressions for the perturbative expansion of the Average Gate Infidelity (AGI) in terms of the environmental coupling coefficient and validate these with extensive numerical simulations, emphasizing the transition from linear to nonlinear behaviour in the strong coupling regime. Our findings highlight the dependence of AGI on qudit dimensionality, quantum gate choice, and noise strength, providing critical insights for optimising quantum gate design and error correction protocols. Additionally, we utilise our framework to identify universal bounds for the AGI in the strong coupling regime and explore the practical implications for enhancing the performance of near-term qudit architectures. This study offers a robust foundation for future research and development in high-dimensional quantum computing, contributing to the advancement of robust, high-fidelity quantum operations.

I. INTRODUCTION

High-dimensional quantum computing (QC) has generated remarkable scientific interest of late, introducing a shift from traditional computing paradigms. While qubit-based quantum information processing (QIP) platforms, particularly superconducting qubits, have the highest technological maturity, they are faced with near-term technical challenges of scalability and error correction [1, 2]. On the other hand, recent advancements have highlighted the potential of qudits — quantum systems with d levels — as powerful alternatives for novel QC architectures [3–6].

Indeed, qudits offer several advantages, including (i) lower decoherence rates in certain physical systems [7], (ii) enhanced quantum error correction through additional levels [8–10] and stabiliser codes [11], as well as (iii) higher information density for reducing circuit complexity and enabling novel algorithm design [12]. They also promise more robust flying quantum memories [13, 14].

While classical computing ultimately settled on bits once sufficient scalability and fault-tolerance were

achieved, early platforms did experiment with multi-level systems [15]. Analogously, it can be argued that quantum computing's infancy stage could benefit from exploring higher-dimensional bases to address these current issues. In the push towards universal QC, increasing the total Hilbert space dimension of quantum systems is critical [16]. This dimension is determined by d^n , where d is the dimensionality and n the number of qudits. Despite impressive advancements in superconducting platforms [17], scaling the number of qubits continues to pose significant challenges. Thus, qudit-based approaches may provide an avenue for increasing the Hilbert space with fewer physical units [6, 17–19].

On the other hand, with the increased number of excited states utilised to implement higher-dimensional states in physical systems, qudits may introduce a greater number of error channels compared to qubits. This could lead to increased sensitivity to environmental noise, affecting coherence times and complicating error correction processes [20]. In a previous paper [21], we studied this scenario in detail by comparing the effects of Markovian noise on multi-qubit and single-qudit systems of equal Hilbert space dimension. We developed a theoretical model of the first-order effects of the noise in the Lindblad formalism, demonstrating how the noise impacts the performance of quantum gates in these different systems, and supported these results with numerical simulations.

The fundamental quantities investigated were the average gate fidelity (AGF, \bar{F}) - equivalently infidelity (AGI,

* jeangabriel.hartmann@ipcms.unistra.fr

† denis.jankovic@ipcms.unistra.fr

‡ rpradeep@outlook.fr

§ mario.ruben@kit.edu

¶ hervieux@unistra.fr

\bar{I}) - and the figure-of-merit ($\tau = t_{\text{gate}}/T_2$). As the name suggests, the AGF is useful in that it integrates out any specific features due to a particular choice of initial state. Therefore, unlike the state fidelity or process fidelity, which compute the target-to-output overlaps of quantum state transfers and unitary gates, respectively, the AGF is fundamental as a platform-agnostic measure of the quality of a system's interaction with its environment [22, 23]. Similarly, the figure-of-merit is important for quantifying realistically the circuit depth that can be achieved in a system, based on the gate time, t_{gate} , and decoherence time, T_2 .

Those results showed that in the quasi-error-free - weak coupling - regime, the first-order response of the AGI (a linear function of the dimensionless coupling strength γt_{gate}) was sufficient to characterise the behaviour of the qudit or multi-qubit system. However, first-order approximations are insufficient for fully understanding the behavior of qudits under realistic, near-term, conditions where higher-order noise effects are expected to become significant, either through stronger coupling or longer gate times (or circuit depths) approaching the decoherence limit.

Thus, this paper aims to extend the understanding of the AGF of single qudit systems under Markovian noise conditions through a general perturbative expansion. Specifically, we focus on higher-order correction terms and their implications on quantum gate performance in the strong coupling regime. Building upon our previous work, we develop a comprehensive theoretical framework that includes these nonlinear effects, with a constructive method generalising the AGF to arbitrary order in γt . This is supported by detailed numerical simulations, with an emphasis on the differences between the first and second order terms in the case of pure dephasing. By doing so, we aim to capture the nuanced impact of noise on the fidelity of quantum gates more precisely.

The key research question addressed in our study is: How do higher-order correction terms and noise coupling strength influence the AGI of single qudit systems, and what implications do these have for the selection and design of quantum gates? Our findings provide important insights on: (i) setting benchmarks, as well as limits, for the performance of noisy quantum systems of arbitrary dimension by identifying gate-dependent effects, (ii) methodologies for improving performance through optimising basis gates that have favourable decoherence characteristics, and (iii) advancing error correction protocols by enabling the cancellation of higher-order noise effects.

The paper is structured as follows: We begin in Sec. II A with a review of the relevant theoretical background concerning the Lindblad formalism for qudit open quantum systems and the superoperator representation of noisy quantum channels, as well as generalised quantum gates on qudits. In Sec. II B, we present our general result for the perturbative expansion of the AGI in noise strength, deriving the general expressions to arbitrary

order in γt and discussing the implications of its structure. Section II C examines the nonlinearity of the AGI in the strong coupling regime of pure dephasing through numerical simulations that elucidate key characteristics of this behaviour and motivate the proceeding investigations that make the link with the theoretical results. Subsequently, in Sec. II D we explore the gate- and noise-dependence of the AGI, with particular emphasis on how the choice of quantum gate can influence the performance of the quantum channel. Finally, Sec. II E presents a detailed analytical and numerical study of the first- and second-order correction terms to the AGI, extending the results of the previous paper and placing them on a more rigorous theoretical foundation that serves future investigations.

II. RESULTS AND DISCUSSION

A. Mathematical Foundations of the Average Gate Fidelity

We begin with the study of a single qudit, of arbitrary dimension d , whose state is represented by a $d \times d$ density matrix $\rho(t)$, and evolves according to the Gorini-Kossakowski-Sudarshan-Lindblad (GKSL) master equation [24, 25], which may be expressed in superoperator form as [26]

$$\partial_t \rho = \mathcal{S}[\rho] + \mathcal{D}[\rho]. \quad (1)$$

Here, setting $\hbar = 1$, the Liouvillian superoperator \mathcal{S} represents the unitary evolution operator of the von Neumann equation, and \mathcal{D} the dissipation superoperator coupling the qudit to the environment,

$$\mathcal{S}[\rho] = -i[H, \rho], \quad (2)$$

$$\mathcal{D}[\rho] = \sum_{k=1}^K \gamma_k \mathcal{L}_k[\rho] \quad (3)$$

$$= \sum_{k=1}^K \gamma_k \left(L_k \rho L_k^\dagger - \frac{1}{2} \{L_k^\dagger L_k, \rho\} \right), \quad (4)$$

where H is the time-independent interaction Hamiltonian, and L_k one of K possible collapse operators characterising the Markovian noise with coupling coefficient γ_k and \mathcal{L}_k the matrix superoperator form [27].

The solution to the master equation for $\rho(0) = \rho_0$ is therefore given by the completely-positive and trace-preserving (CPTP) quantum channel \mathcal{E} as [28]

$$\rho(t) = \mathcal{E}[\rho_0] \quad (5)$$

$$= e^{(\mathcal{S} + \mathcal{D})t} \rho_0. \quad (6)$$

Considering the application of a quantum gate $\mathcal{U}[\rho] = U\rho U^\dagger$ to the system then corresponds to a composition

operation, that in the matrix superoperator representation reduces to the matrix product, from which we may express the AGF, $\bar{\mathcal{F}}(\mathcal{E}, \mathcal{U})$, of implementing a unitary operator over the quantum channel in the presence of a noisy environment [23]:

$$\bar{\mathcal{F}}(\mathcal{E}, \mathcal{U}) = \int_{\mathcal{H}} \langle U^\dagger \mathcal{E}[\rho_0] U \rangle_0 d\rho_0, \quad (7)$$

$$1 - \bar{\mathcal{I}}(\mathcal{E}, \mathcal{U}) = \int_{\mathcal{H}} \langle (\mathcal{U}^\dagger \circ \mathcal{E})[\rho_0] \rangle_0 d\rho_0. \quad (8)$$

The integral is taken uniformly over the Haar measure \mathcal{H} of the state space, with the expectation value $\langle \mathcal{A} \rangle_0 = \text{Tr}\{\mathcal{A}\rho_0\}$ representing the average over all initial states. For convenience, we shall use $\bar{\mathcal{F}}$ and \mathcal{F} interchangeably for the AGF, and likewise for the AGI.

In this study we shall consider pure initial states, $\text{Tr}\{\rho_0^2\} = 1$. Then the state space is reduced to the complex-projective space \mathbb{CP}^{d-1} such that the Haar measure (over all ρ_0) then induces the Fubini-Study measure, the integral of which is normalised, $\int_{\mathcal{H}} d\rho_0 = 1$, [29] and may be calculated analytically (see Appendix A3). Furthermore, unless specified, we shall also assume that: (i) the dissipator term is dominated by a single noise channel, such that $\mathcal{D} = \gamma\mathcal{L}$, (ii) the associated superoperators \mathcal{S} and \mathcal{L} are time-independent and (iii) we are working in the interaction picture, such that the free evolution Hamiltonian $H_0 = \mathbb{0}_d$, and therefore $\mathcal{S}_0 = \mathbb{0}_{d \times d}$ such that the unitary evolution simplifies to $\mathcal{U} = e^{(\mathcal{S}_0 + \mathcal{S}_c)t} = e^{\mathcal{S}t}$ with $\mathcal{S} = \mathcal{S}_c$ corresponding to only the control (driving) Hamiltonian $H = H_c$ implementing the quantum gate. This allows us to rewrite Eqs. (5) and (6) as

$$\mathcal{E}[\rho_0] = e^{(\mathcal{S} + \gamma\mathcal{L})t} \rho_0. \quad (9)$$

We note that the $(d \times d) \times (d \times d)$ superoperators acting on the $\mathcal{H} \otimes \mathcal{H}$ Hilbert space of the quantum dynamical semigroup (QDS) may be written explicitly in Liouville matrix form in terms of the standard operator form as [30]:

$$\mathcal{U}[\cdot] = (U^* \otimes U) \text{vec}(\cdot), \quad (10)$$

$$\mathcal{S}[\cdot] = -i(\mathbb{1}_d \otimes H - H^T \otimes \mathbb{1}_d) \text{vec}(\cdot), \quad (11)$$

$$\mathcal{L}[\cdot] = \left(L^* \otimes L - \frac{1}{2} \left(L^\dagger L \otimes \mathbb{1}_d + (\mathbb{1}_d \otimes L^\dagger L)^T \right) \right) \text{vec}(\cdot), \quad (12)$$

where we identify the adjoint (\dagger), complex-conjugate ($*$) and transpose (T) operations, $\mathbb{1}_d$ the $d \times d$ identity matrix, \otimes the tensor, or equivalently here for linear maps, the Kronecker product, and $\text{vec}(\cdot)$ the vectorisation operation that, when applied to a $d \times d$ density matrix ρ , produces a $1 \times d^2$ column vector by stacking vertically each column of the matrix from left to right. This corresponds to the explicit mapping

$$\text{vec}(\rho) : \sum_{i,j} \rho_{ij} |i\rangle\langle j| \rightarrow \sum_{i,j} \rho_{ij} |j\rangle \otimes |i\rangle, \quad (13)$$

of the quantum state from the Hilbert to the Fock-Liouville space [27]. Furthermore, the quantum gate U_g and associated control Hamiltonian H_c (and their respective superoperator representations \mathcal{U} and \mathcal{S}) are related by the matrix exponent (and, inversely) logarithm operations. Therefore, given some quantum gate, it may be implemented by the control term,

$$H_c t_g = i \log U_g, \quad (14)$$

where the now time-independent H_c represents a single, ideal control pulse that implements the gate in time t_g , which can be modulated by the absolute amplitude of the pulse $\|H_c\|$. Existence and uniqueness of the matrix logarithm map are well established under the conditions that U_g is unitary and $-\pi < H_c t_g \leq \pi$ [31]. This is an idealisation that necessitates simultaneous control over all pulse amplitudes, phases and detunings on each possible transition between all d states. Platform-dependent physical constraints on the control pulses may preclude experimental realisation of such a control term. Nevertheless it allows for a time-optimal multi-chromatic pulse for studying the robustness of quantum gates that is independent of constraints imposed by the physical platform or pulse control technique [32].

We now precisely define the gate and collapse operators that will be of interest in this study. We begin with the following set of single-qudit quantum gates $U_g \in \{\mathbb{1}, X, Z, F\}$ that generalise the single-qubit identity, Pauli- x , Pauli- z and Hadamard gates to d dimensions, and generate the d -dimensional generalised Clifford algebra (GCA) [33]

$$\mathbb{1}_d = \sum_{j=0}^{d-1} |j\rangle\langle j|, \quad (15)$$

$$X_d = \sum_{j=0}^{d-1} |(j+1) \bmod d\rangle\langle j|, \quad (16)$$

$$Z_d = \sum_{j=0}^{d-1} \omega^j |j\rangle\langle j|, \quad (17)$$

$$F_d = \frac{1}{\sqrt{d}} \sum_{j=0}^{d-1} \sum_{k=0}^{d-1} \omega^{jk} |j\rangle\langle k|, \quad (18)$$

where $\omega = e^{\frac{2\pi i}{d}}$ is the d -th root of unity. The subscript d is used to specify the dimension of the operator, and may be omitted in cases where it is clear from context or when referring to the general operator. The X , Z and F gates retain unitarity (and tracelessness for X and Z) as well as the relations $X^d = Z^d = \mathbb{1}_d$ and $X = FZF^\dagger$ of involution and change-of-basis, respectively. However, it is worth noting that they are no longer Hermitian for $d > 2$. Furthermore, in the generalised forms, it can be observed that (i) X is extended from a bit-flip (NOT) gate to a cyclic permutation (INC/SHIFT) gate that increments the qudit state, (ii) Z is extended from a phase-flip to a phase-shift (CLOCK) gate of each state over the d roots

of unity, and (iii) the Walsh-Hadamard gate is extended to the matrix form of the Quantum Fourier Transform (QFT) (equivalently referred to as the Discrete Fourier Transform, Sylvester or Chrestenson matrix).

Regarding the choice of collapse operators $L \in \{J_z, J_x\}$ representing the coupling of the qudit to the environment in the master equation, we shall primarily consider the effect of pure dephasing by the operator J_z , and of secondary consideration is the bit-flip error effected by the operator J_x . These higher-order spin operators from $\text{spin-}\frac{1}{2}$ to $\text{spin-}\frac{d-1}{2}$ can be obtained through the generalised Gell-Mann matrices, and written as

$$J_z = \sum_{j=1}^d \frac{1}{2}(d+1-2j) |j\rangle\langle j| \quad (19)$$

$$J_x = \sum_{j=1}^{d-1} \frac{1}{2} \sqrt{j(d-j)} (|j+1\rangle\langle j| + |j\rangle\langle j+1|) \quad (20)$$

B. Perturbative Expansion of the AGI

Given the simplified expression for the time-evolution of the quantum channel \mathcal{E} in (9), we want to study the

effects on the AGF, not only from the choice of \mathcal{S} or \mathcal{L} , but also from the coupling strength γ . Therefore, performing a Taylor series expansion of the AGF in powers of γ ,

$$\bar{\mathcal{F}}(\mathcal{E}, \mathcal{U}) = 1 - \sum_{m=1}^{\infty} \gamma^m F^{(m)}(t). \quad (21)$$

To calculate explicitly the correction terms $F^{(m)}$, we begin by expanding the solution to the master equation,

$$\rho(t) = \rho^{(0)} + \sum_{m=1}^{\infty} \gamma^m \rho^{(m)}, \quad (22)$$

where the m -th order correction to the non-perturbed solution of the master equation can be written as [34, 35]

$$\rho^{(m)} = e^{\mathcal{S}t} \left(\int_0^t \int_0^{t_1} \cdots \int_0^{t_{m-1}} \left(\prod_{i=1}^m e^{-\mathcal{S}t_i} \mathcal{L} e^{\mathcal{S}t_i} \right) dt_m \cdots dt_2 dt_1 \right) \rho_0, \quad (23)$$

and we separate the zero order term $\rho^{(0)}$ from the summation, since it corresponds to only unitary evolution through the von Neumann equation in the absence of environmental coupling.

We may then define a new quantity $\tilde{M}^{(m)}(t)$ containing the integral terms, such that $\rho^{(m)} := e^{\mathcal{S}t} (\tilde{M}^{(m)}(t)) \rho_0$, and therefore the m -th order of the solution to the master equation in terms of the quantum channel reduces to $\mathcal{E}^{(m)} = \mathcal{U} \circ M^{(m)}(t)$. Now, in order to render this term $\tilde{M}^{(m)}(t)$ into a more computationally tractable form, we make use of the eponymous lemma of Campbell result-

ing from the Baker-Campbell-Hausdorff (BCH) Formula [36, 37],

$$e^X Y e^{-X} = \sum_{n=0}^{\infty} \frac{[(X)^n, Y]}{n!}, \quad (24)$$

utilising the iterated commutator defined by the recursion relation $[(X)^n, Y] = [X, [(X)^{n-1}, Y]]$ with the halting condition $[(X)^0, Y] = Y$. With \mathcal{S} and \mathcal{L} time-independent, $\tilde{M}^{(m)}(t)$ simplifies to

$$\tilde{M}^{(m)}(t) = t^m \sum_{n_1=0}^{\infty} \sum_{n_2=0}^{\infty} \cdots \sum_{n_m=0}^{\infty} \left(\prod_{i=1}^m \frac{(-t)^{n_i} [(\mathcal{S})^{n_i}, \mathcal{L}]}{n_i! \sum_{j=i}^m (n_j + 1)} \right) \quad (25)$$

$$= t^m \frac{\mathcal{L}^m}{m!} + t^m \sum_{n_1=1}^{\infty} \sum_{n_2=1}^{\infty} \cdots \sum_{n_m=1}^{\infty} \left(\prod_{i=1}^m \frac{(-t)^{n_i} [(\mathcal{S})^{n_i}, \mathcal{L}]}{n_i! \sum_{j=i}^m (n_j + 1)} \right). \quad (26)$$

For the sake of future convenience, we define the new

quantity $\tilde{M}^{(m)}(t) := t^m M^{(m)}(t)$, from which we obtain

the following general form for the correction terms of the AGF in Eq. (21) in terms of Eq. (9):

$$\begin{aligned} F^{(m)}(t) &= - \int_{\mathcal{H}} \langle \mathcal{U}^\dagger \circ \mathcal{U} \circ (t^m M^{(m)}(t)) [\rho_0] \rangle_0 d\rho_0 \quad (27) \\ &= -t^m \int_{\mathcal{H}} \text{Tr} \{ M^{(m)} [\rho_0] \rho_0 \} d\rho_0. \quad (28) \end{aligned}$$

This integral over the Fubini-Study measure of pure initial states may now be evaluated using results from Wein-garten calculus [38] (see Appendix A 3). From here we obtain our main result for the general perturbative expansion of the AGI, $\mathcal{I} = 1 - \mathcal{F} = \sum_{m=1}^{\infty} \mathcal{I}^{(m)}$:

$$\mathcal{I} = \frac{-1}{d(d+1)} \sum_{m=1}^{\infty} (\gamma t)^m \text{Tr} \{ M^{(m)}(t) \}, \quad (29)$$

where d is the dimensionality of the qudit system, and the powers of (γt) have been grouped to form a single, dimensionless quantity.

As an illustrative example of the utility of this expression, in Fig. 1 we present the cumulative correction terms up to fourth order in γt for the QFT gate F_4 acting on a qudit of $d = 4$. With $t = 1$ normalised by the amplitude of the control Hamiltonian H_c , the pure dephasing operator $L = J_z$ was applied over the couplings $\gamma t \in [0, 0.5]$. While the first-order approximation shows good agreement with the simulated AGI for small $\gamma t \ll 1$, the deviation becomes significant as the coupling grows large, necessitating the addition of the higher-order corrections.

Looking closer at this general result for \mathcal{I} , let us consider the case of no coherent driving. This is implemented through a zero control Hamiltonian, $H = 0_d$, giving $\mathcal{S} = 0_{d \times d}$ and corresponding to evolution by the identity gate $U_g = \mathbb{1}_d$. Then, the system evolves only through decay due to the collapse operator \mathcal{L} , since only the iterated commutator terms $[(\mathcal{S})^{n_i}, \mathcal{L}]$ for $n_i = 0$ in $M^{(m)}(t)$ survive, resulting in

$$\mathcal{I}_0^{(m)} = \frac{-(\gamma t)^m}{d(d+1)} \frac{\text{Tr} \{ \mathcal{L}^m \}}{m!}, \quad (30)$$

which is precisely the first term in Eq. (26), with the subscript 0 used to refer to the gate-independent correction term. Therefore, generalising to nonzero \mathcal{S} , it is clear that the m -th order correction can always be separated into the sum of two parts as in Eq. (26): These gate-independent terms $\mathcal{O}((\gamma t)^m)$ (when all $n_i = 0$) and the product of the gate-dependent iterated commutators $\mathcal{O}((\gamma t)^m \prod_{i=1}^m t^{n_i})$.

Combining the summation over m in Eq. (29) and the m -th order expression in Eq. (30) allows us to rewrite the gate-independent part as a Taylor expansion,

$$\mathcal{I}_0 = \frac{\text{Tr} \{ \mathbb{1}_{d \times d} - e^{\gamma t \mathcal{L}} \}}{d(d+1)}. \quad (31)$$

Furthermore, as long as the collapse operator is real and symmetric, obeying $L = L^* = L^T = L^\dagger$, (as for

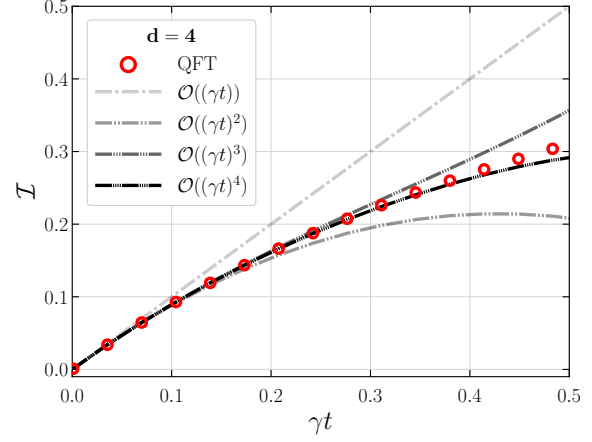


Figure 1: Comparison of the first four correction terms of the AGI to numerical simulations. AGIs for the QFT gate applied to a $d = 4$ qudit undergoing pure dephasing ($L = J_z$) at couplings $\gamma t \in [0, 0.5]$. The discrete points (red) represent the simulated AGI values, while the successive dashed-dotted lines represent the correction terms from first to fourth order.

J_z , for example), it is possible to use a multinomial expansion on the operator form of \mathcal{L} in Eq. (12) to obtain explicit expressions to arbitrary order $(\gamma t)^m$ for the gate-independent correction in Eq. (30):

$$\begin{aligned} \text{Tr} \{ \mathcal{L}^m \} &= \text{Tr} \left\{ \left(L^* \otimes L - \frac{1}{2} L^\dagger L \otimes \mathbb{1} - \frac{1}{2} \mathbb{1} \otimes L^\dagger L \right)^m \right\} \quad (32) \\ &= m! \sum_{k_1 + k_2 + k_3 = m} \frac{\text{Tr} \{ L^{k_1 + 2k_2} \} \text{Tr} \{ L^{k_1 + 2k_3} \}}{k_1! k_2! k_3! (-2)^{k_2 + k_3}}. \quad (33) \end{aligned}$$

In the case of a pure (spin) dephasing channel $L = J_z$, considering that $\text{Tr} \{ J_z^m \} \sim d^{m+1}$, it can be easily seen that this expression for the m -th-order correction scales as

$$\mathcal{O}(\text{Tr} \{ \mathcal{L}^m \}) \sim d^{2(m+1)} \quad (34)$$

$$\Rightarrow \mathcal{O}(\mathcal{I}_0^{(m)}) \sim (\gamma t)^m d^{2m}. \quad (35)$$

Now, given this scaling of the gate-independent AGI, let us refer to the work of Chiesa *et al.* [39], where the authors proposed the use of a physical qudit to encode a logical qubit. Using their binomial encoding and error-correction protocol would result in a logical qubit robust to pure dephasing up to order $(\gamma t)^m$ where $2m + 1 = d$. Effectively, the AGI of such a logical qubit would be of the same order as $\mathcal{I}_0^{(m)}$. In turn, to maintain $\mathcal{I}_0 \ll 1$, this sets a limit on the maximum dimension (equivalently, order m of noise correction), such that $d < \frac{1}{\sqrt{\gamma t}}$. Such

investigations for protecting against decoherence have already been studied with alternative logical qubit encodings and a discrete error evolution protocol in the work of Miyahara *et al.* [10].

In what follows in the remainder of this study, we shall focus on the first- and second-order correction terms to the AGF. We note that the preceding analytical approach provides a framework for computing any correction term to arbitrary order. However, explicit calculations up to second-order serve as an extension of our prior work [21], in which the first-order correction to the AGF was investigated. Thus, we study in detail the effects due to the second-order correction terms as they relate to our particular system of interest, particularly with regard to the choice of quantum gate and collapse operator.

C. Nonlinearity of the AGI in the Strong Coupling Regime

Let us now motivate our investigation into the AGI in the regime of strong coupling between the qudit and the environment. As identified in Fig. 1, the linear first-order approximation may be sufficient in the weak coupling regime, but nonlinear effects become significant above $\gamma t \sim 10^{-1}$. It is therefore necessary to identify a clear transition or separation between these two regimes, and how the AGI behaves in the limit of strong coupling.

To investigate, we perform calculations of the AGI over a large range of scales for γt . Therefore, in Fig. 2, we show numerical simulations of the AGIs for qudits under pure dephasing ($L = J_z$) where the coupling strengths varied logarithmically in $\gamma t \in [10^{-5}, 10^3]$. Evolutions were repeated on qudits with dimensions $d \in \{2, 4, 8, 16\}$ for 100 Haar-random quantum gates (see Appendix C 1 for a discussion on methods for generating random quantum gates), with the inset showing the linear regime for small $\gamma t \in [10^{-5}, 10^{-2}]$ and the main figure showing the transition region and strong-coupling regime. The dashed-dotted straight lines give the first-order correction terms at each qudit dimension, defined by the linear function [21]

$$\mathcal{I}^{(1)} = \frac{d(d-1)}{12} \gamma t, \quad (36)$$

showing the d -dependence in the weak coupling regime.

Further effects of the system dimension on the AGI are notable for larger couplings: The start of deviation from linearity, the plateau values \mathcal{I}^* that the AGI curves converge to in the large γt limit, and the associated saturation points $(\gamma t)^*$ (both denoted by the superscript $*$) at which the curves reach their respective plateau values. Each of these effects confirms an overall decrease in robustness as the system dimension increases: Compared to the behaviour for qubits, the AGIs (for arbitrary gates) of higher-dimensional qudits begin to deviate from the linear regime, and reach the higher plateau limits, at

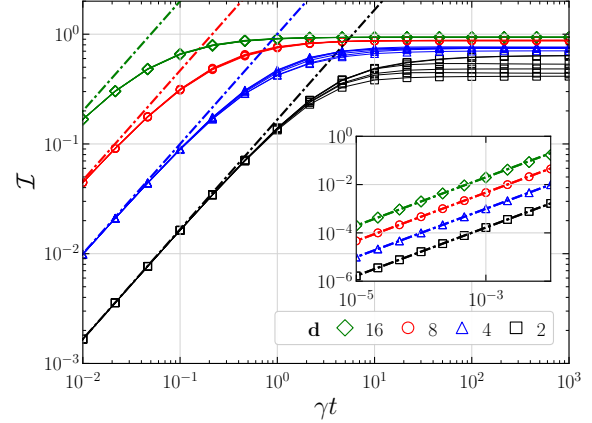


Figure 2: Deviation from linearity of the AGIs for qudits under strong dephasing. Simulations of the AGI against the strength of pure dephasing ($L = J_z$) are plotted on log-log axes over $\gamma t \in [10^{-2}, 10^3]$. The simulations were performed on a set of qudit dimensions, $d \in \{2, 4, 8, 16\}$ each for 100 Haar-random quantum gates. The dashed lines represent the linear regime given by the first-order correction to the AGI at each dimension. The inset shows the linear regime for smaller values of $\gamma t \in [10^{-5}, 10^{-2}]$. For stronger noise the AGIs exhibit a transition from the linear to nonlinear regime that then saturates at a stable plateau value. These plateau values vary for qudit dimension and also for different quantum gates, highlighting the gate-dependence. The saturation points $(\gamma t)^*$ of the stable regime are also dependent on both the qudit dimension and gate type, with higher-dimensional qudits deviating from linearity and saturating earlier.

lower noise thresholds. These quantities shall be studied in more detail in Sec. II D.

Finally, it is interesting to note the gate dependence of the \mathcal{I}^* and $(\gamma t)^*$, which is more pronounced for smaller d . Given the sample size of 100 gates, it is apparent that, at each dimension, there exists an upper and lower bound to the AGI plateau values, with all the sampled gates converging within this range. It is also noticeable (particularly so for $d = 2$) that the $(\gamma t)^*$ and \mathcal{I}^* are positively correlated, as curves with lower plateau infidelity appear to reach their plateau values at lower $(\gamma t)^*$ than those with higher plateau infidelities.

Studying these effects of the large- γt behaviour in more detail, in Fig. 3 we present simulations of a sample of 1 million Haar-random qubit ($d = 2$) gates over $\gamma t \in [10^{-2}, 10^4]$. This larger sample size provides stronger evidence that the \mathcal{I}^* are indeed bounded above and below, as shown by the red and black horizontal lines, respectively. It was observed that the randomly generated quantum gates fall into one of two groups, indicated by the red and blue shaded curves. The red shaded curves (\mathcal{I}_{mono}) approach their plateau values monotonically from below. The blue shaded curves (\mathcal{I}_{over}) all experience an overshoot above their plateau value, with a single turning point, before settling to \mathcal{I}^* monotonically.

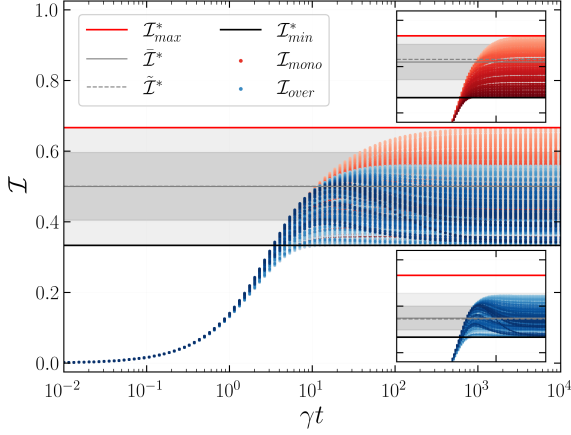


Figure 3: Large- γt behaviour of the AGIs for Haar-random qubit gates under pure dephasing. Simulations of the AGI were performed for a sample of one million (300 displayed) Haar-random qubit ($d = 2$) gates under pure dephasing ($L = J_z$) for $\gamma t \in [10^{-2}, 10^4]$. For each gate, the AGI curves fall into one of two groups, exhibiting different behaviour near their respective saturation points $((\gamma t)^*)$. The curves in red (\mathcal{I}_{mono}) approach their plateau values monotonically from below. The blue curves (\mathcal{I}_{over}) rapidly approach their plateau values, before overshooting once with a single turning point, and then converging monotonically from above. The degree of blue shading for each curve indicates the degree of overshoot above the plateau value. All sampled gates converged to their \mathcal{I}^* plateau values within the range $[\mathcal{I}_{min}^*, \mathcal{I}_{max}^*]$ indicated by the black and red horizontal lines. In the figure and insets, the lighter and darker shaded regions indicate the vertical extent of the sampled gates and their standard deviations, with the solid and dashed lines indicating the mean ($\bar{\mathcal{I}}^*$) and median ($\tilde{\mathcal{I}}^*$) AGI values, respectively. The inset figures show each group of gates in isolation. The red group span the full bounding range, but are weighted upwards by outliers near the upper limit. The blue group do not span the full range, but are weighted towards the lower limit. Only the average AGI taken over both groups converges towards the expected mean value of 0.5.

cally from above. From the full sample, approximately 73% of all gates fell in the red, monotonic group, and the remaining 27% in the blue, overshoot group. The degree of blue shading represents the amount of overshoot, defined by the difference $\mathcal{I}_{max} - \mathcal{I}^*$ between the height of the peak and the plateau value. Furthermore, there appears to be some correlation between this quantity and the saturation point; the larger the overshoot the longer the curve takes to settle. Gates that experience this overshoot may therefore perform worse at intermediate noise strengths over the strong coupling limit.

The insets show each category plotted separately, from which it may be seen that, unlike the blue curves, the red curves span the range between the upper and lower bounds, indicated by the lightly-shaded regions. The darker shaded regions, show the standard deviation about the mean, $\bar{\mathcal{I}}^*$, with the dashed line being the median value, $\tilde{\mathcal{I}}^*$. We can see from these quantities that, despite spanning the range, the red curves are not distributed uniformly, but instead weighted upwards towards the upper bound, while the blue curves are weighted towards the lower bound. Both groups have significant numbers of outliers at either extreme, shifting the medians away from the means. In fact, it is only when averaging over the combined samples that the distribution becomes centered about the mean of $\bar{\mathcal{I}}^* = 0.5$ (see Appendix C 2 for further investigations on the distributions of these groups of curves within the bounding region).

tion about the mean, $\bar{\mathcal{I}}^*$, with the dashed line being the median value, $\tilde{\mathcal{I}}^*$. We can see from these quantities that, despite spanning the range, the red curves are not distributed uniformly, but instead weighted upwards towards the upper bound, while the blue curves are weighted towards the lower bound. Both groups have significant numbers of outliers at either extreme, shifting the medians away from the means. In fact, it is only when averaging over the combined samples that the distribution becomes centered about the mean of $\bar{\mathcal{I}}^* = 0.5$ (see Appendix C 2 for further investigations on the distributions of these groups of curves within the bounding region).

D. Gate- and Noise-Dependence of the Fidelity

Having identified particular aspects of interest in the AGI behaviour in the strong coupling regime, let us investigate these characteristics in further detail.

Repeating the simulations presented in Fig. 3 for larger dimensions, we observed that the lower and upper bounds, \mathcal{I}_{min}^* and \mathcal{I}_{max}^* respectively, and the mean value, $\bar{\mathcal{I}}^*$, depend only on the dimension d of the system, and are given precisely by the following expressions, for any d :

$$\mathcal{I}_{max}^* = 1 - \frac{1}{d+1}, \quad (37)$$

$$\bar{\mathcal{I}}^* = 1 - \frac{1}{d}, \quad (38)$$

$$\mathcal{I}_{min}^* = 1 - \frac{2}{d+1}. \quad (39)$$

In Appendix C 2, we present these further examples of the distributions of \mathcal{I}^* for ensembles of Haar random gates with dimensions $d = 2, 4, 8, 16$, which follow these expressions. It has previously been shown [40] that, for the case of a qudit in the singlet state evolving in a noisy quantum channel, the infidelity is bounded by $1 - \frac{2}{d+1} \leq \mathcal{I}^* \leq 1 - \frac{1}{d}$. This result matches with our case of a single qudit in the large- d limit due to convergence of the mean and upper bound. However, for our single qudit system we shall use our existing framework to prove these limits for arbitrary d .

Writing the quantum channel as $\mathcal{E} = \mathcal{U} \circ M$, and substituting into the expression for the AGF in Eq. (8),

$$\mathcal{F} = \int_{\mathcal{H}} \text{Tr}\{M[\rho_0] \rho_0\} d\rho_0 \quad (40)$$

$$= \frac{\text{Tr}\{M\} + \text{Tr}\{M[\mathbb{1}]\}}{d(d+1)}. \quad (41)$$

Given that the quantum channel is CPTP, and that \mathcal{U} is a unitary operator, we know that the superoperator M must also be trace-preserving and thus $\text{Tr}\{M[\mathbb{1}]\} = d$. Furthermore, in the strong coupling limit where the collapse operator $L = J_z$ describes pure dephasing, it is clear that the action of M on a state ρ is to transform it

to a diagonal density matrix where the coherences (off-diagonal elements) have all decayed to zero. Expressing $M = \sum_{k=1}^K E_k^* \otimes E_k$ in the Kraus representation, the trace can be written as

$$\text{Tr}\{M\} = \sum_{k=1}^K \sum_{i=0}^{d-1} |E_{k,ii}|^2. \quad (42)$$

Furthermore, it can be shown that (see Appendix A 4 for a detailed derivation) each of the d squared-elements are bounded by $0 \leq |E_{k,ii}|^2 \leq 1$ and hence in the large noise regime the AGI is bounded by

$$1 - \frac{2}{d+1} \leq \mathcal{I}^* \leq 1 - \frac{1}{d+1}. \quad (43)$$

Given the significance of this result, it is now of interest to consider how the behaviour is affected by the choice of quantum gate. In other words, we want to identify any particular unitary operators U_g , or properties thereof, whose AGIs $\mathcal{I}(\mathcal{E}, U_g)$ when $(\gamma t) \gg 1$ are precisely the \mathcal{I}_{min}^* , \mathcal{I}_{max}^* or $\bar{\mathcal{I}}^*$.

In Fig. 4, we present simulations of the AGI, as a function of γt , on a $d = 4$ qudit for a set of gates that do indeed reflect this behaviour when undergoing pure dephasing. The AGI values (discrete data points) are accompanied by dashed and dotted curves representing the state purity and mean coherences, while the horizontal lines show the \mathcal{I}^* values of the associated gates. The purities and coherences were calculated over a set of $n = 2400$ randomly generated pure Hermitian density matrices. The purity $\text{Tr}\{\rho^2\}$ decays from 1 to a constant $\frac{1}{d-1}$, while the averages of the $\frac{d(d-1)}{2}$ coherences decay to zero, confirming the dephasing action of the J_z collapse operator.

Regarding the set of gates, in addition to the QFT gate, we introduce the interpolated- X gate (see Appendix B), X^η , where the matrix is raised to the η -th power for $\eta \in [0, 1]$. Clearly, $\eta = 1$ or 0 produces the X or $\mathbb{1}_d$ gate, respectively, while for $0 < \eta < 1$ the action interpolates between these two extremes.

We find that

$$\mathcal{I}^*(\mathcal{E}, \mathbb{1}_d) = \mathcal{I}_{min}^*, \quad (44)$$

$$\mathcal{I}^*(\mathcal{E}, F_d) = \bar{\mathcal{I}}^*, \quad (45)$$

$$\mathcal{I}^*(\mathcal{E}, X_d) = \mathcal{I}_{max}^*. \quad (46)$$

Specifically, the \mathcal{I}^* are extremised above and below by the X and identity gates, respectively, while the mean value $\bar{\mathcal{I}}^*$ indeed corresponds to the action of the QFT gate that creates a superposition state. Furthermore, by careful choice of the values of η , we can obtain intermediate values of \mathcal{I}^* . For example, the η values chosen and shown in Fig. 4 lead to curves with plateau values that are equally spaced within the bounding region. We observed that for the value $\eta = \frac{3d-2}{4d}$, the \mathcal{I}^* matches that of the QFT gate, also converging to the mean.

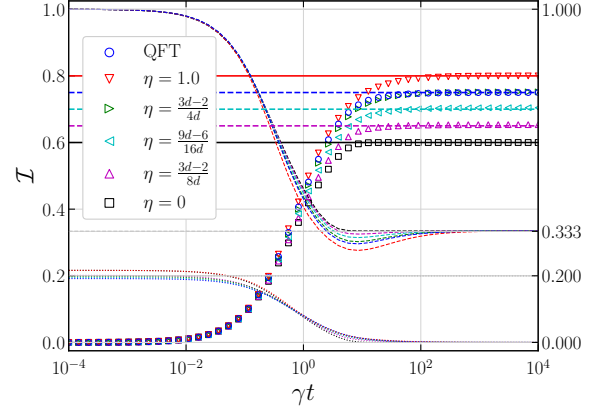


Figure 4: Gate-dependence of the AGIs and qudit state evolution as functions of noise strength. Simulations of a $d = 4$ qudit under pure dephasing were time-evolved according to one in the set of 6 listed quantum gates. The blue circular points show the AGI for the QFT gate. The other points represent the interpolated X^η gate taken to the power of a d -dependent scaling factor, $\eta \in [0, 1]$. These values produce evenly spaced plateau AGI values between the upper (X , $\eta = 1$) and lower ($\mathbb{1}$, $\eta = 0$) bounds. For $\eta = \frac{3d-2}{4d}$, the interpolating X gate (for any d) converges to the same value as the QFT gate, $\mathcal{I}^* = 1 - \frac{1}{d}$. The dashed-dotted horizontal lines show the plateaus. 2400 Randomly generated pure Hermitian states were time-evolved, and the averaged final states per gate showed: (i) The purity ($\text{Tr}(\rho^2)$) (dashed) decaying from 1 to $\frac{1}{d-1}$, and (ii) the mean coherences $\left(2 \frac{\sum_{i>j} |\rho_{i,j}|}{d(d-1)}\right)$ decaying towards zero due to dephasing. For small γt the coherences vary based on gate type. The initial stability, decay and subsequent plateau behaviour of these quantities for small-to-large γt follows the gate-dependence and trends of the respective AGI values.

The effect of these gates on the AGI can be understood by following the arguments in Appendix A 4 regarding the operator M and its form based on the choice of quantum gate. It is clear that for the identity gate, or more generally any diagonal unitary matrix, $\text{Tr}\{M\} = d$ which minimises $\mathcal{I}^* = 1 - \frac{2}{d+1}$. Similarly, the QFT gate produces a superposition state with each of the d basis elements of ρ being $\frac{1}{d}$, thus $\text{Tr}\{M\} = 1$ and $\mathcal{I}^* = 1 - \frac{1}{d}$. Finally the X gate increments all states circularly, and, having no diagonal elements, results in traceless $\text{Tr}\{M\} = 0$ and thus $\mathcal{I}^* = 1 - \frac{1}{d+1}$.

Let us now consider how the choice of quantum gate affects the saturation point $(\gamma t)^*$ at which the AGI attains the plateau value \mathcal{I}^* . Figure 5 presents simulations of the plateau saturation points as a function of the qudit dimension for set of X^η gates over a range of η values from 0 to 1. In addition, the calculations were repeated over a set of $n = 4800$ Haar random gates at each dimension from $d = 2$ to 12. The grey curve represents the mean value of the saturation point at each dimension, while

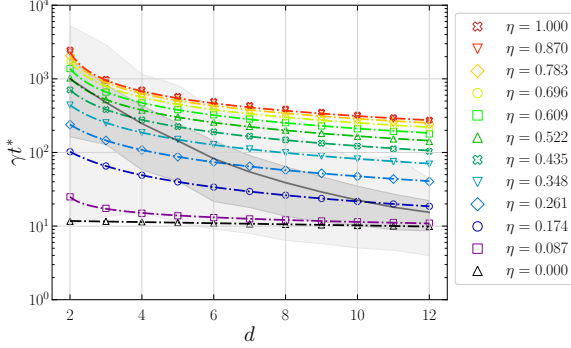


Figure 5: Saturation points $((\gamma t)^*)$ of the AGIs for interpolated X^η gates as functions of qudit dimension. AGIs were calculated for a set of 12 interpolated X^η gates for $0 \leq \eta \leq 1$, at dimensions $d \in [2, 12]$. For each dimension and gate, the AGI curve over γt was interpolated by a cubic spline. The saturation points $(\gamma t)^*$ were identified by root-finding algorithm of the points at which they converged (within $\varepsilon < 10^{-8}$) to their AGI plateau values. The plotted data points, on log-linear axes, indicate these root values as functions of d for each gate, and the dashed lines represent their associated power-law fits. This analysis was repeated for a set of $n = 4800$ Haar-random gates at each dimension. The light shaded areas are bounded by the maximum and minimum saturation points found at each dimension. The darker shaded areas represent a 1σ deviation about the mean (solid gray line).

the dark grey and light gray shaded regions indicate the standard deviations and max-min values, respectively.

For each of the simulated X^η gates, the dashed-dotted lines represent power-law fits to the discrete data points at each dimension. The power-law model is given by

$$(\gamma t)^* = \alpha(d - \beta)^\delta, \quad (47)$$

and, fitted by nonlinear least-squares regression, resulted in $R^2 > 0.999$ for each fit. It is interesting to note that for the case of the identity gate, the saturation point remains constant independent of dimension.

Continuing the investigation, we performed regression analysis of the fitted model parameters α , β and δ across the set of η values. The fits are presented in Appendix C3. Parameter α was best described by a sigmoid model while β and δ by exponential models,

$$\alpha(\eta) = \frac{\alpha_0}{(1 + e^{\alpha_1(\eta - \alpha_2)})} + \alpha_3, \quad (48)$$

$$\beta(\eta) = \beta_0 e^{\beta_1(\eta - \beta_2)} + \beta_3, \quad (49)$$

$$\delta(\eta) = \delta_0 e^{\delta_1(\eta - \delta_2)} + \delta_3. \quad (50)$$

Thus far in our investigation, we have restricted analysis to the effect of pure dephasing by the operator J_z on a qudit. Let us conclude this section by studying the effects of the $L = J_x$ operator, corresponding to bit-flip errors. In Fig. 6, we present simulations of 4 gates: the QFT gate F and 3 X^η gates for $\eta = 0, \frac{3d-2}{4d}, 1$, for qubits

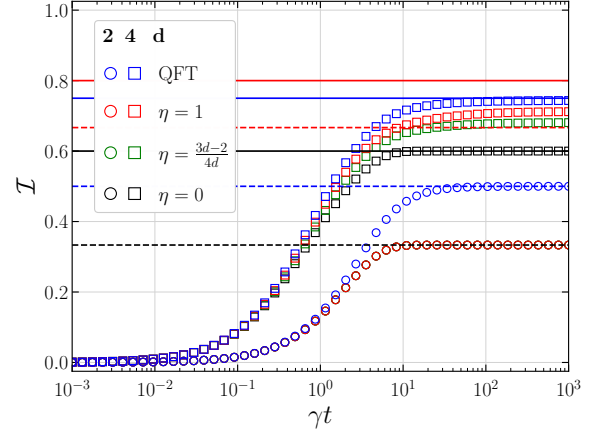


Figure 6: Effect of bit-flip errors on the AGI. X^η and QFT gate simulations were repeated on qudits for $d \in \{2, 4\}$ undergoing bit-flip ($L = J_x$) errors, rather than pure dephasing noise. For $d = 2$ (circles) and $d = 4$ (squares) the following gates were simulated: $\mathbb{1} = X^0$ (black, $\eta = 0$), X^η (green, $\eta = \frac{3d-2}{4d}$), X (red, $\eta = 1$) and QFT (blue). The dashed ($d = 2$) and solid ($d = 4$) horizontal lines show the upper ($1 - \frac{1}{d+1}$, red) and lower ($1 - \frac{2}{d+1}$, black) bounds of the AGIs, as well as the mean ($1 - \frac{1}{d}$, blue). For qubits, the AGIs for all matrix powers of the X^η gate behaved exactly as the $\mathbb{1}$ gate, while for $d = 4$ the plateau AGI values for the non-zero matrix powers were observed to deviate upwards from the identity gate, but not to the same extent as for the case of pure dephasing. On the other hand, the QFT gate response was the same for both types of noise.

(circles) and $d = 4$ qudits (squares). The qubit case for the X^η gates is pathological, since for $d = 2$ the J_x operator commutes with the X^η gates and thus the AGIs plateau at the level of the identity gate. This changes for $d = 4$ where they no longer commute. However, it is interesting to observe that the behaviour is different from the J_z case, and the X^η gates plateau below the QFT gate.

E. First- and Second-Order Correction Terms to the AGI

Section IIB presented our general result for the perturbative expansion of the AGI to arbitrary order m in Eq. (29). Now, let us investigate in further detail the first and second-order correction terms.

Beginning with the first-order correction, at $m = 1$, it can be seen that (see Appendix A5) the trace over $M^{(1)}$ simplifies to

$$\mathcal{I}^{(1)} = -\frac{(\gamma t)}{d(d+1)} \text{Tr}\{\mathcal{L}\}, \quad (51)$$

which confirms the gate-independent nature of the first-order term as the AGI depends only on the noise super-

operator \mathcal{L} . Additionally, this trace can be expressed in terms of the regular operator L as

$$\text{Tr}\{\mathcal{L}\} = |\text{Tr}\{L\}|^2 - d \text{Tr}\{L^\dagger L\}, \quad (52)$$

reproducing the results of [21]. For the case of pure dephasing, we obtain the familiar result in Eq. (36)

$$\mathcal{I}^{(1)} = \frac{\gamma t}{12} d(d-1), \quad (53)$$

using the element-wise definition of the dephasing operator in Eq. (19)

$$(J_z)_{ii} = \frac{d - (2i - 1)}{2}. \quad (54)$$

Now, if we compare this analytical result with numerical simulations, we observe in Fig. 7 the relative error of the first-order correction to the AGI for dimensions $d = 2, 4$ over $\gamma t \in [0, 0.1]$. This relative error is expressed by

$$\varepsilon_{\mathcal{I}}^{(1)} = \frac{\mathcal{I} - \mathcal{I}^{(1)}}{\mathcal{I}}. \quad (55)$$

The simulations were performed for the QFT, identity, X and X^η gates for $\eta = \frac{3d-2}{4d}$. The dashed lines show the expected analytic results for each dimension. The dark and light shaded regions represent the standard deviations and max-min values taken over a sample of Haar random gates

Clearly, the gate independence of the first-order correction term matches precisely the identity gate. The remaining gates show the expected deviation from linearity, with the analytic value underestimating the AGI values. We observe that the relative error for $d = 2$ is approximately one order of magnitude smaller than for $d = 4$.

Moving on to the second-order correction term, we have from Eq. (29)

$$\mathcal{I}^{(2)} = \sum_{n_1, n_2=0}^{\infty} \frac{-(\gamma t)^2 (-t)^{n_1+n_2} \text{Tr}\{[(S)^{n_1}, \mathcal{L}][(S)^{n_2}, \mathcal{L}]\}}{d(d+1)n_1!(n_2+1)!(n_1+n_2+2)}, \quad (56)$$

which we reduce (see Appendix A6) to a single iterated commutator using the relation $n_1 + n_2 + 2 = s$,

$$\mathcal{I}^{(2)} = -\frac{(\gamma t)^2}{d(d+1)} \sum_{s=0}^{\infty} \text{Tr}\{\mathcal{L}[(S)^s, \mathcal{L}]\} \frac{(-t)^s}{(s+2)!}. \quad (57)$$

For $s = 0$, the trace term reduces further to $\text{Tr}\{\mathcal{L}^2\}$ by definition of the iterated commutator. Additionally, we show (see Appendix A7) that, using the property [41],

$$[(A)^s, B] = \sum_{k=0}^s (-1)^k \binom{s}{k} A^{s-k} B A^k, \quad (58)$$

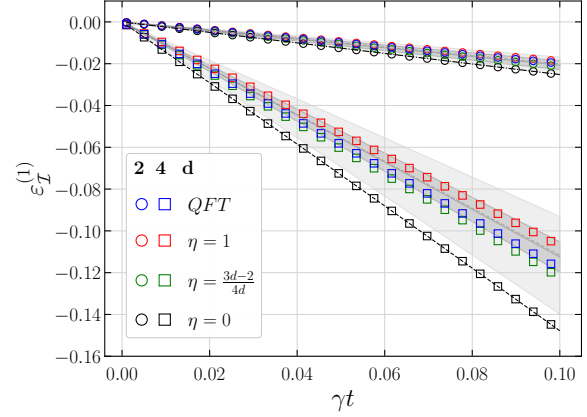


Figure 7: Relative error of the first-order correction to the AGI, and gate-dependent deviation from linearity. AGIs were simulated for 4 gates acting on qubits (circles) and $d = 4$ qudits (squares) undergoing $L = J_z$ pure dephasing. The relative error $\varepsilon_{\mathcal{I}}^{(1)} = \frac{\mathcal{I} - \mathcal{I}^{(1)}}{\mathcal{I}}$ was calculated for the first-order analytical correction. The dashed-dotted and dashed lines represent the first-order term of the perturbative expansion of the AGI, for $d = 2$ and $d = 4$, respectively. These gate-independent terms correspond to the behaviour of the identity gate, $\mathbb{1} = X^0$ (black, $\eta = 0$). The X^η (green, $\eta = \frac{3d-2}{4d}$), X^1 (red, $\eta = 1$) and F (blue, QFT) gates show significant deviation from the gate-independent term, and for $d = 4$ are roughly 10 times larger than for $d = 2$. The solid and dashed grey lines represent the mean and median relative errors over a sample of $n = 4800$ Haar-random gates, with the light and dark shaded areas indicating the min-max bounds and standard deviations.

the trace over the iterated commutator is zero for all odd values of s . Therefore,

$$\mathcal{I}^{(2)} = -\frac{(\gamma t)^2}{d(d+1)} \left(\frac{\text{Tr}\{\mathcal{L}^2\}}{2} + \sum_{s=2}^{\infty} \frac{\text{Tr}\{\mathcal{L}[(S)^s, \mathcal{L}]\} (-t)^s}{(s+2)!} \right). \quad (59)$$

This shows us that the AGI remains gate-independent at order $\gamma^2 t^2$. Indeed the first appearance of gate-dependence through the \mathcal{S} operator occurs at order $\gamma^2 t^4$, when $s = 2$ and the iterated commutator term contains \mathcal{S} and is non-zero.

Since the summation of s is over all even integers, we can introduce a maximum cutoff value to render this calculation computationally tractable. Indeed, for the correction term to not be unbound, we must have that the sum is convergent, allowing us to identify such a value. We can understand this computationally by identifying the s -th order of the summation,

$$f(s) = \text{Tr}\{\mathcal{L}[(S)^s, \mathcal{L}]\} \frac{(-t)^s}{(s+2)!}. \quad (60)$$

Then, for a given error threshold ε , the cutoff order s_ε is simply the s at which the absolute difference from the

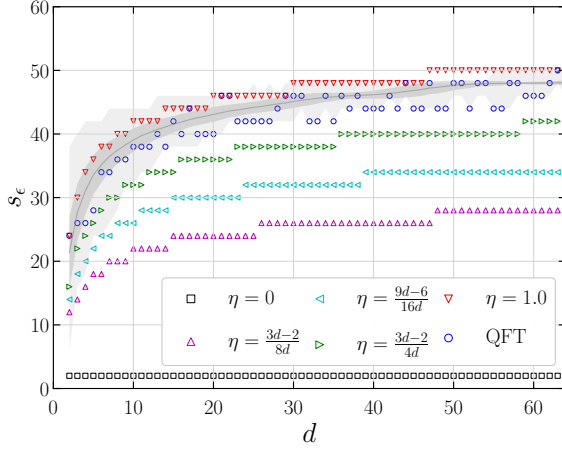


Figure 8: Iteration-dependent convergence of the second-order AGI correction against qudit dimension. The critical order s_ε was calculated as the number of iterations over the summation term in the second-order AGI correction such that the absolute difference $|f_2(s_\varepsilon) - f_2(s_\varepsilon - 1)| < \varepsilon$ is less than the error threshold $\varepsilon = 1 \times 10^{-8}$. Calculations were performed for a set of interpolated X^η gates and the QFT gate, as well as $n = 2500$ Haar-random gates, over dimensions $d \in [2, 64]$. The identity gate ($\eta = 0$) only required the minimal $s = 2$ iterations, independent of dimension, since the identity commutes with the collapse operator. Of the interpolated gates, the number of iterations required scales with the interpolation parameter η , while the QFT gate shows marked variation over d , without exceeding the critical order for $\eta = 1$. The mean of the Haar-random gates (dark grey) also lies below the $\eta = 1$ curve, while the min-max interval, (light grey), shows gates at lower dimension requiring a larger number of iterations to converge.

preceding order $s_\varepsilon - 2$ is below this threshold,

$$|f(s_\varepsilon) - f(s_\varepsilon - 2)| < \varepsilon. \quad (61)$$

In Fig. 8 we present this iteration-dependent convergence of the second-order AGI correction term. Our set of interpolated X^η gates and the QFT gate were simulated over dimensions $d \in [2, 64]$ for a uniform gate time of $t = 1$. We calculated for each of them the cutoff order s_ε within an error threshold $\varepsilon = 1 \times 10^{-8}$. This analysis was repeated for a set of $n = 2500$ Haar random gates, and shown by the grey curve (mean value) and shaded region (bounds). It is useful to note that the number of iterations required grows approximately logarithmically with d . Furthermore we have a fairly clear range of validity on s_ε for the gates, although the X gate does not give a consistent upper bound here for smaller dimensions. On the other hand, the identity gate $\mathbb{1} = X^0$ always gives the lower bound of $s_\varepsilon = 2$, since then $[\mathbb{1}, \mathcal{L}] = 0$.

Next, we need to investigate the effect of the gate time parameter t on the second-order correction term, since in the summation it is raised to the power of s . We choose our set of quantum gates, $U_g \in \{X^\eta, F\}$ with

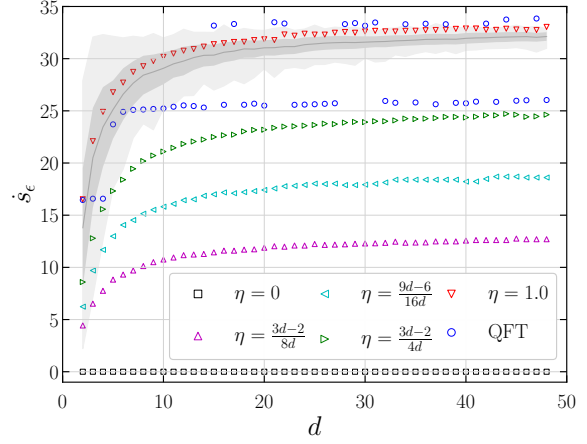


Figure 9: Time derivative of the convergence of the second-order AGI correction over qudit dimension. Linear gradients of the critical order s_ε as a function of t were fitted by linear regression for each of a set of gates at each dimension $d \in [2, 48]$. The gate set included the QFT, identity (X^0), X , and uniformly interpolated X^η gates and $n = 200$ Haar-random gates. For the identity gate this is constant at zero-gradient, while the gradients for the interpolated gates show rapid initial growth that levels off as d increases. The gradients of the QFT gates for $d > 10$ appear to populate two distinct regimes around 25 and 33. The sampled Haar-random gates exhibit behaviour similar to that of the X gate within one standard deviation of the mean, and the large variation at lower dimensions stabilises as d increases.

$\eta \in \{0, \frac{3d-2}{8d}, \frac{9d-6}{16d}, \frac{3d-2}{4d}, 1\}$, and simulate them on qudits of dimension $d \in [2, 48]$. Instead of varying the noise parameter γ with constant gate time $t = 1$, we fix $\gamma = 1$ and then vary the gate time $t \in [0, 5]$. Note that, in order to implement the full quantum gate during this modified gate time, the amplitude of the control-pulse Hamiltonian matrix must be modulated by the inverse of the gate time, $H_c \rightarrow \frac{1}{t}H_c$. We observed (see Appendix C4 for an example of s_ε against t for the X gate) that for each gate at each dimension, the number of iterations required to reach convergence was roughly linear in time: $s_\varepsilon \propto t$. Hence to each such set of data we fitted using linear regression the model

$$s_\varepsilon = mt + c, \quad (62)$$

where $m = \frac{ds_\varepsilon}{dt}$. Figure 9 shows this curve of fitted gradients for each gate as a function of the qudit dimension. This analysis is also extended to a set of $n = 200$ Haar random gates at each dimension, indicated by the grey curve and shaded regions. The interpolated gates all appear to evolve smoothly to a nearly constant value at large d . On the other hand, the QFT gate for $d > 6$ appears to oscillate randomly between two constant regimes near $\frac{ds_\varepsilon}{dt} \simeq 25$ and $\frac{ds_\varepsilon}{dt} \simeq 33$.

Based on these two analyses, we can identify a safe bound on s_ε for precise calculation of the second-order

correction. Recall our standard approach of normalising the Hamiltonian such that the gate time $t = 1$, varying γ only, and generally considering $d < 64$. Then, we observe that approximately 50 iterations are sufficient to calculate the second-order correction to a precision of $\varepsilon < 1 \times 10^{-8}$.

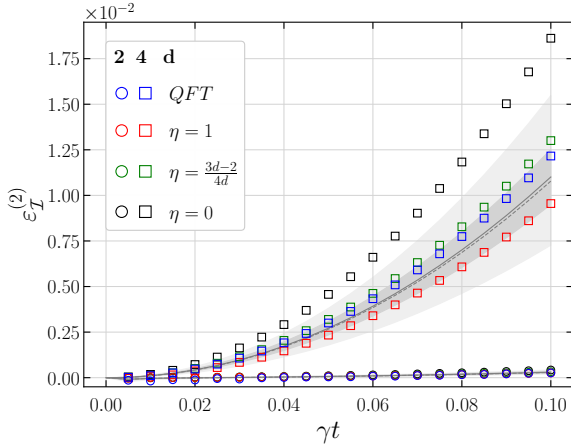


Figure 10: Relative error of the AGI up to second-order. AGIs were simulated for 4 fixed gates and $n = 1000$ Haar-random gates acting on qubits (circles) and $d = 4$ qudits (squares) undergoing $L = J_z$ pure dephasing. The relative error $\varepsilon_I^{(2)} = \frac{\mathcal{I} - \mathcal{I}^{(1)} - \mathcal{I}^{(2)}}{\mathcal{I}}$ was calculated for the second-order perturbative correction. The error for $d = 4$ is roughly 1% while for qubits this is reduced to 0.01%, two orders of magnitude lower than the relative error at first-order.

We now present in Fig. 10 our results for the relative error of the AGI up to second-order. The results presented follow the same approach as for those up to first-order shown in Fig. 7. Choosing the same set of gates, $\{X^0, X^\eta, X^1, F\}$ with $\eta = \frac{3d-2}{4d}$ and evolving over $\gamma t \in [0, 0.1]$, we show the scaling of the relative error for $d = 2, 4$,

$$\varepsilon_I^{(2)} = \frac{\mathcal{I} - \mathcal{I}^{(1)} - \mathcal{I}^{(2)}}{\mathcal{I}}. \quad (63)$$

Comparing these results with those of just the first-order in Fig. 7, we see that the error for $d = 4$ is reduced by one order of magnitude to $\sim 1\%$, while for $d = 2$ the error of $\sim 0.01\%$ is lower by two orders of magnitude. Additionally, the sign of the relative error has changed from negative to positive, indicating that despite the increased precision, the correction up to second order will tend to understate the actual AGI value, with this error growing quadratically in γt .

Finally, as for the first-order case, it is interesting to express the trace of the repeated commutator of superoperators \mathcal{S} and \mathcal{L} in terms of regular operators H and L . This will give a clear representation of the effect of the control Hamiltonian on the AGI, as well as its interaction with the collapse operator. Let us consider sep-

arately the two trace terms of $\mathcal{I}^{(2)}$ in Eq. (59): $\text{Tr}\{\mathcal{L}^2\}$ and $\text{Tr}\{\mathcal{L}[(\mathcal{S})^s, \mathcal{L}]\}$. We find (see Appendix A 5) that the gate-independent expression can be written as

$$\text{Tr}\{\mathcal{L}^2\} = |\text{Tr}\{L^2\}|^2 + \frac{1}{2} \text{Tr}\{L^\dagger L\}^2 + \frac{d}{2} \text{Tr}\{(L^\dagger L)^2\}, \quad (64)$$

which, in the case of pure dephasing, $L = J_z$, reduces to

$$\text{Tr}\{J_z^2\} = \frac{d^2(3 - 5d^2 + 2d^4)}{120}, \quad (65)$$

using the element-wise definition in Eq. (54). This allows us express the $\gamma^2 t^2$ correction in terms of the first-order correction term from Eq. (53),

$$-\frac{(\gamma t)^2}{d(d+1)} \frac{\text{Tr}\{J_z^2\}}{2} = -(\gamma t) \frac{2d^2 - 3}{20} \mathcal{I}^{(1)}. \quad (66)$$

However, it is not necessarily the case that any m -th order expression can be written recursively in terms of lower orders. Equation (66) for the second-order appears to be a special case.

For the iterated commutator, we find that (see Appendix A 6)

$$\begin{aligned} & \text{Tr}\{\mathcal{L}[(\mathcal{S})^s, \mathcal{L}]\} \\ &= \sum_{k=0}^s \sum_{j=0}^k \sum_{l=0}^{s-k} \binom{s}{k} \binom{k}{j} \binom{s-k}{l} (-1)^{s+k-j-l} \times \\ & \times \text{Re} \left[\text{Tr}\{LH^{k-j}LH^{s-k-l}\}^* \text{Tr}\{LH^jLH^l\} \right. \\ & + \frac{1}{2} \text{Tr}\{L^T L^* H^{s-j-l}\}^* \text{Tr}\{L^T L^* H^{j+l}\} \\ & + \frac{1}{2} \text{Tr}\{L^T L^* H^{k-j}L^T L^* H^{s-k-l}\}^* \text{Tr}\{H^{j+l}\} \\ & - \text{Tr}\{LH^{k-j}L^T L^* H^{s-k-l}\}^* \text{Tr}\{LH^{j+l}\} \\ & \left. - \text{Tr}\{L^T L^* H^{k-j}LH^{s-k-l}\}^* \text{Tr}\{LH^{j+l}\} \right] \end{aligned} \quad (67)$$

This gives a complete description of the second-order gate-dependence in terms of the explicit Hamiltonian terms, without resorting to the superoperator representation. The superoperator and operator expressions have complexity $\mathcal{O}(sd^6)$ and $\mathcal{O}((sd)^3)$, respectively. Since we observed in Fig. 8 that the maximal s_z needed to reach convergence is roughly logarithmic in d , the complexities can then be reduced to $\mathcal{O}(d^6 \log d)$ and $\mathcal{O}((d \log d)^3)$. Therefore, for $d \gg 2$, it is computationally preferred to use the operator-based expression, while for smaller qudits with $d \sim 2$, the superoperator representation is generally preferable for numerical simulations.

III. CONCLUSIONS AND OUTLOOK

In this work, we have performed a comprehensive analysis of the AGF for single qudit open quantum systems

coupled to Markovian noise environments in the Lindblad superoperator formalism. Our primary contributions and findings are as follows:

We have expanded the AGF perturbatively in powers of the dimensionless coupling constant γt . From this we derived our main result in Eq. (29) for the general expressions of the correction terms to arbitrary order. The result was expressed in terms of the iterated commutators of the gate and noise superoperators, \mathcal{S} and \mathcal{L} , respectively, based on the expansion obtained in Eq. (26). It is particularly significant that these corrections were expressed in a form that may be directly implemented in numerical calculations. We found that, at each order above the first, the correction term could be separated into a gate-independent term $\mathcal{O}((\gamma t)^m)$ depending only on \mathcal{L} , and gate-dependent terms containing \mathcal{S} and higher powers of t . The first-order correction term, $\mathcal{I}^{(1)}$, is gate-independent and depends solely on the noise superoperator \mathcal{L} . The gate-dependence appears for the first time at $\gamma^2 t^4$, in the second-order correction term $\mathcal{I}^{(2)}$, highlighting the significant role of the interaction between the control Hamiltonian \mathcal{S} and the noise operator \mathcal{L} . Explicit expressions for the first- and second-order correction terms in the operator representation were also derived.

Our numerical simulations under pure dephasing noise revealed a clear transition from linear to nonlinear behaviour in the AGI as the noise coupling strength γt increases. For $\gamma t \sim 1$, the AGI deviates significantly from the linear approximation and eventually reaches a plateau at a stable value. The plateau values, \mathcal{I}^* , as well as their corresponding saturation points, $(\gamma t)^*$, were found to be dependent not only on the qudit dimension d but also on the specific quantum gate implemented.

Indeed, utilising our theoretical framework we were able to derive in Eq. (43) a significant result for universal upper and lower bounds of the AGI plateau values in the strong coupling regime, depending only on the dimensionality of the system. Furthermore we were able to identify specific gates that saturate these bounds: The identity gate ($\mathbb{1}_d$) and the generalised-NOT (X) achieve the lower and upper limits, respectively, while the QFT gate (F_d) was found to plateau at the mean AGI value of the Haar measure. Additionally, we introduced the interpolated X^η gates to demonstrate the range of AGI values between these bounds. The saturation points of these interpolated gates were studied numerically, and were well-described by a power-law model of $(\gamma t)^*$ vs d .

We analyzed the convergence behavior of the second-order correction term, identifying that approximately 50 iterations are sufficient for precise calculation up to a qudit dimension of $d < 64$ within an absolute tolerance of $\varepsilon < 1 \times 10^{-8}$. The number of iterations to convergence was found to scale logarithmically with the system dimension d , and linearly with the gate time t .

Numerical simulations confirmed the analytical predictions, demonstrating that the relative error of the AGI is significantly reduced when including the second-order

correction term. For $d = 4$, the error is reduced to the order of 1%, and for $d = 2$, it is reduced to 0.01%, indicating the necessity of higher-order corrections for accurate fidelity modeling, particularly as the dimension of the system increases.

The detailed insights gained from this study have several important applications and implications for the field of quantum computing, particularly given the growing interest in qudits. Understanding the behavior of the AGI and its dependence on the type of quantum gate and environmental noise facilitates the optimization of quantum gate design. Our approach provides a methodology for identifying quantum gates that have favourable fidelity characteristics. Thus, through appropriate choice or design of basis gates it may be possible to enhance the performance of quantum circuits. This could lead to significant improvements for optimising the robustness of quantum algorithms on near-term noisy platforms.

The results underscore the importance of incorporating higher-order corrections into error correction protocols. This is particularly relevant for qudits of higher dimensions, where noise effects are more pronounced. We envisage that the detailed perturbative expansions provided in this work could be leveraged to develop advanced error correction techniques, for example by incorporating the higher-order correction terms into the cost function of optimal control methods. In particular, our correction terms can be used to quantify and mitigate the error in logical qubit embedding protocols up to arbitrary order. Future research is needed to show how this could result in protection against such errors above first-order, and how this might incorporate the gate-dependencies identified.

The derived bounds and behaviours of AGI for different gates and dimensions also serve as benchmarks for assessing the performance of quantum systems. These benchmarks can guide experimentalists in evaluating and improving their quantum hardware and gate implementations. Indeed further study is needed to extend these results from the idealised single-pulse (time-independent) Hamiltonian to realistic pulse-based optimal control techniques for gate generation.

While this study focused primarily on pure dephasing and bit-flip errors, future research should explore further the impact of other noise models, such as amplitude damping and depolarizing noise. Understanding how different types of noise affect the AGI will provide a more comprehensive framework for designing noise-resilient quantum systems.

Extending the framework to multi-qudit systems is a necessity. These introduce additional complexity due to inter-qudit interactions and correlated noise effects. Investigating these factors will be crucial for the scalability of qudit-based architectures, but could prove fruitful in reducing the circuit complexity of long range entangling operations.

Finally, it would be beneficial to have experimental verification of these predictions. Testing the derived correction terms and transition points in real quantum systems

will help to validate and refine the models presented.

In conclusion, this study provides a detailed theoretical foundation for understanding the fidelity of quantum gates in noisy environments. The findings contribute to the ongoing efforts to develop robust, high-fidelity quantum operations, paving the way for practical and scalable quantum computing.

ACKNOWLEDGMENTS

This work was funded by the French National Research Agency (ANR) through the Programme d'Investissement d'Avenir under contract ANR-11-LABX-0058_NIE and ANR-17-EURE-0024 within the Investissement d'Avenir program ANR-10-IDEX-0002-02. D.J. and M.R. gratefully acknowledge financial support from the Deutsche Forschungsgemeinschaft (DFG, German Research Foundation) through the Collaborative Research Centre "4f for Future" (CRC 1573, project number 471424360) project B3. J.-G.H. also acknowledges QUSTEC funding from the European Union's Horizon 2020 research and innovation program under the Marie Skłodowska-Curie Grant Agreement No. 847471. The authors would like to acknowledge the High Performance Computing Center of the University of Strasbourg for supporting this work by providing scientific support and access to computing resources. Part of the computing resources were funded by the Equipex Equip@Meso project (Programme Investissements d'Avenir) and the CPER Alsacalcul/Big Data.

CODE AND DATA AVAILABILITY

All code and data utilised in the simulations, analyses, and generation of the results presented in this study are publicly available via Zenodo [42] under a Creative Commons Attribution (CC BY) license.

Appendix A: Complementary Derivations

Here, we present the detailed derivations of the analytical results in the main text.

1. Integration of the m -th Order Solution to the Master Equation

Theorem A.1. Consider an open quantum system of a single qudit of dimension d , initiated in a pure state

$\text{Tr}\{\rho_0^2\} = 1$, under the influence of a time-independent noise superoperator \mathcal{L} with coupling constant γ , and evolving via a time-independent unitary superoperator \mathcal{S} over time t . The solution to the master equation in Eq. (1) is given by the quantum channel in Eq. (9), and can be expressed in a perturbative expansion in γ by Eq. (22), where the m -th order correction term is given by Eq. (23). Then, the nested integral can be evaluated, by induction, and results in Eq. (25):

$$\tilde{M}^{(m)}(t) = \int_0^t \cdots \int_0^{t_{m-1}} \left(\prod_{i=1}^m e^{-S t_i} \mathcal{L} e^{S t_i} \right) dt_m \cdots dt_1 \quad (\text{A1})$$

$$= t^m \sum_{n_1, \dots, n_m=0}^{\infty} \left(\prod_{i=1}^m \frac{(-t)^{n_i} [(\mathcal{S})^{n_i}, \mathcal{L}]}{n_i! \sum_{j=i}^m (n_j + 1)} \right). \quad (\text{A2})$$

Proof. In the calculations that follow, we make use of Campbell's lemma, based on the Baker-Campbell-Hausdorff Formula [36, 37], as stated in Eq. (24),

$$e^X Y e^{-X} = \sum_{n=0}^{\infty} \frac{[(X)^n, Y]}{n!}, \quad (\text{A3})$$

with $[(X)^n, Y] = [X, [(X)^{n-1}, Y]]$ and $[(X)^0, Y] = Y$, and proceed with proof by induction. *Base Case:* To first-order, $m = 1$,

$$\begin{aligned} \int_0^t e^{-S t_1} \mathcal{L} e^{S t_1} dt_1 &= \int_0^t \sum_{n_1=0}^{\infty} \frac{[(-S t_1)^{n_1}, \mathcal{L}]}{n_1!} dt_1 \\ &= \sum_{n_1=0}^{\infty} \frac{(-1)^{n_1}}{n_1!} [(\mathcal{S})^{n_1}, \mathcal{L}] \int_0^t t_1^{n_1} dt_1 \\ &= t \sum_{n_1=0}^{\infty} \frac{(-t)^{n_1} [(\mathcal{S})^{n_1}, \mathcal{L}]}{n_1! (n_1 + 1)} \\ &= \tilde{M}^{(1)}(t). \end{aligned}$$

Induction Step: Assume that the result in Eq. (A2) holds at m -th order, and relabel indices $t, t_1, \dots, t_{m-1} \rightarrow t_1, t_2, \dots, t_m$ and $t \rightarrow t_1$:

$$\begin{aligned} \tilde{M}^{(m)}(t_1) &= \int_0^{t_1} \cdots \int_0^{t_m} \left(\prod_{i=2}^{m+1} e^{-S t_i} \mathcal{L} e^{S t_i} \right) dt_{m+1} \cdots dt_2 \\ &= t_1^m \sum_{n_2=0}^{\infty} \cdots \sum_{n_{m+1}=0}^{\infty} \left(\prod_{i=2}^{m+1} \frac{(-t_1)^{n_i} [(\mathcal{S})^{n_i}, \mathcal{L}]}{n_i! \sum_{j=i}^{m+1} (n_j + 1)} \right). \end{aligned}$$

Then, to order $m + 1$:

$$\begin{aligned}
& \int_0^t \tilde{M}^{(m)}(t_1) (e^{-S t_1} \mathcal{L} e^{S t_1}) dt_1 \\
&= \int_0^t \left(t_1^m \sum_{n_2=0}^{\infty} \cdots \sum_{n_{m+1}=0}^{\infty} \prod_{i=2}^{m+1} \frac{(-t_1)^{n_i} [(S)^{n_i}, \mathcal{L}]}{n_i! \sum_{j=i}^{m+1} (n_j + 1)} \right) \left(\sum_{n_1=0}^{\infty} \frac{(-t_1)^{n_1} [(S)^{n_1}, \mathcal{L}]}{n_1!} \right) dt_1 \\
&= \sum_{n_2=0}^{\infty} \cdots \sum_{n_{m+1}=0}^{\infty} \frac{(-1)^{n_1} [(S)^{n_1}, \mathcal{L}]}{n_1!} \prod_{i=2}^{m+1} \left(\frac{(-1)^{n_i} [(S)^{n_i}, \mathcal{L}]}{n_i! \sum_{j=i}^{m+1} (n_j + 1)} \right) \int_0^t t_1^m t_1^{n_1} \prod_{i=2}^{m+1} t_1^{n_i} dt_1 \\
&= \sum_{n_2=0}^{\infty} \cdots \sum_{n_{m+1}=0}^{\infty} \frac{(-1)^{n_1} [(S)^{n_1}, \mathcal{L}]}{n_1!} \prod_{i=2}^{m+1} \left(\frac{(-1)^{n_i} [(S)^{n_i}, \mathcal{L}]}{n_i! \sum_{j=i}^{m+1} (n_j + 1)} \right) \frac{t^{m+1 + \sum_{i=1}^{m+1} n_i}}{m+1 + \sum_{j=1}^{m+1} n_j} \\
&= t^{m+1} \sum_{n_2=0}^{\infty} \cdots \sum_{n_{m+1}=0}^{\infty} \frac{(-t)^{n_1} [(S)^{n_1}, \mathcal{L}]}{n_1! \sum_{j=1}^{m+1} (n_j + 1)} \prod_{i=2}^{m+1} \frac{(-t)^{n_i} [(S)^{n_i}, \mathcal{L}]}{n_i! \sum_{j=i}^{m+1} (n_j + 1)} \\
&= t^{m+1} \sum_{n_2=0}^{\infty} \cdots \sum_{n_{m+1}=0}^{\infty} \prod_{i=1}^{m+1} \frac{(-t)^{n_i} [(S)^{n_i}, \mathcal{L}]}{n_i! \sum_{j=i}^{m+1} (n_j + 1)} \\
&= \tilde{M}^{(m+1)}(t).
\end{aligned}$$

□ and evaluating the expectation value over ρ_0 of initial states with $\langle \mathcal{A} \rangle_0 = \text{Tr}\{\mathcal{A}\rho_0\}$,

2. Perturbative Expansion of the AGI

We define the Average Gate Infidelity as

$$\mathcal{I}(\mathcal{E}, \mathcal{U}) = 1 - \mathcal{F}(\mathcal{E}, \mathcal{U}) \quad (\text{A4})$$

$$= 1 - \left(1 - \sum_{m=1}^{\infty} \gamma^m F^{(m)} \right), \quad (\text{A5})$$

where the quantum channel is given by

$$\mathcal{E} = \mathcal{U} + \sum_{m=1}^{\infty} \gamma^m \mathcal{E}^{(m)} \quad (\text{A6})$$

$$= \mathcal{U} + \sum_{m=1}^{\infty} \gamma^m \mathcal{U} \tilde{M}^{(m)}. \quad (\text{A7})$$

Then, from Eq. (8),

$$\begin{aligned}
\mathcal{F}(\mathcal{E}, \mathcal{U}) &= \int_{\mathcal{H}} \langle (\mathcal{U}^\dagger \circ \mathcal{E})[\rho_0] \rangle_0 d\rho_0 \\
&= \int_{\mathcal{H}} \left\langle \left(\mathcal{U}^\dagger \circ \left(\mathcal{U} + \sum_{m=1}^{\infty} \gamma^m \mathcal{U} \tilde{M}^{(m)} \right) \right) [\rho_0] \right\rangle_0 d\rho_0 \\
&= \int_{\mathcal{H}} \left\langle \rho_0 + \sum_{m=1}^{\infty} \gamma^m \tilde{M}^{(m)}[\rho_0] \right\rangle_0 d\rho_0,
\end{aligned}$$

$$\begin{aligned}
1 - \sum_{m=1}^{\infty} \gamma^m F^{(m)} &= \int_{\mathcal{H}} \text{Tr} \left\{ \rho_0^2 + \sum_{m=1}^{\infty} \gamma^m \tilde{M}^{(m)}[\rho_0] \rho_0 \right\} d\rho_0 \\
&= 1 + \sum_{m=1}^{\infty} \gamma^m \int_{\mathcal{H}} \text{Tr} \left\{ \tilde{M}^{(m)}[\rho_0] \rho_0 \right\} d\rho_0,
\end{aligned}$$

since $\text{Tr}\{\rho_0^2\} = 1$ and $\int_{\mathcal{H}} d\rho_0 = 1$, and using Eq. (21). The m -th order term of the AGF is therefore

$$F^{(m)} = - \int_{\mathcal{H}} \text{Tr} \left\{ \tilde{M}^{(m)}[\rho_0] \rho_0 \right\} d\rho_0, \quad (\text{A8})$$

and we may write the AGI in terms of $t^m M^{(m)} = \tilde{M}^{(m)}$,

$$\mathcal{I}(\mathcal{E}, \mathcal{U}) = - \sum_{m=1}^{\infty} (\gamma t)^m \int_{\mathcal{H}} \text{Tr} \left\{ M^{(m)}[\rho_0] \rho_0 \right\} d\rho_0. \quad (\text{A9})$$

3. Integral over the Fubini-Study Measure

We can evaluate Eq. (A9) to arrive at the result in Eq. (29). The integral over the Fubini-Study measure is calculated using methods from [38] relating to Weingarten calculus. Specifically, we make use of the following result,

$$\begin{aligned}
& \int_{\mathcal{H}} U_{ka} U_{ic} \bar{U}_{jb} \bar{U}_{rd} dU \\
&= \frac{1}{(d^2 - 1)} [(\delta_{kj} \delta_{ab} \delta_{ir} \delta_{cd} + \delta_{kr} \delta_{ad} \delta_{ij} \delta_{cb})] - \\
&- \frac{1}{d(d^2 - 1)} [(\delta_{kj} \delta_{ad} \delta_{ir} \delta_{cb} + \delta_{kr} \delta_{ab} \delta_{ij} \delta_{cd})], \quad (\text{A10})
\end{aligned}$$

where, and for the remainder of this section, the indices represent the matrix elements using Einstein sum notation.

Now, beginning with the element-wise definition of the superoperator term,

$$(M[\rho])_{pi} = M_{kj,pi} \rho_{kj}, \quad (\text{A11})$$

where we identify ρ and ρ_0 for convenient usage of the element-wise sum notation, this extends to

$$\begin{aligned} (M[\rho])_{pq} &= (M[\rho])_{pi} \rho_{iq} \\ &= M_{kj,pi} \rho_{kj} \rho_{iq}. \end{aligned} \quad (\text{A12})$$

Taking the trace of this term corresponds to

$$\begin{aligned} \text{Tr}\{M[\rho]\rho\} &= \delta_{pq} (M[\rho])_{pq} \\ &= M_{kj,ri} \rho_{kj} \rho_{ir}, \end{aligned} \quad (\text{A13})$$

where we define $r := p = q$. Rewriting the integral of this expression in terms of the associated unitary operator U leads to

$$\begin{aligned} &\int_{\mathcal{H}} \text{Tr}\{M[U\rho U^\dagger] U\rho U^\dagger\} dU \\ &= \int_{\mathcal{H}} M_{kj,ri} (U_{ka} \rho_{ab} \bar{U}_{jb}) (U_{ic} \rho_{cd} \bar{U}_{rd}) dU \\ &= \rho_{ab} M_{kj,ri} \rho_{cd} \int_{\mathcal{H}} (U_{ka} \bar{U}_{jb} U_{ic} \bar{U}_{rd}) dU. \end{aligned} \quad (\text{A14})$$

If we now substitute the result of this integral from Eq. (A10), and evaluate all of the delta function terms, we arrive at

$$\begin{aligned} &\int_{\mathcal{H}} \text{Tr}\{M[\rho]\rho\} d\rho \\ &= \frac{1}{(d^2 - 1)} [\rho_{aa} \rho_{cc} M_{jj,ii} + \rho_{ac} \rho_{ac} M_{ki,ki}] - \\ &\quad - \frac{1}{d(d^2 - 1)} [\rho_{ac} \rho_{ac} M_{jj,ii} + \rho_{aa} \rho_{cc} M_{ki,ki}] \\ &= \frac{1}{(d^2 - 1)} [(\text{Tr}\{\rho\})^2 \text{Tr}\{M[\mathbb{1}]\} + \text{Tr}\{\rho^2\} \text{Tr}\{M\}] - \\ &\quad - \frac{1}{d(d^2 - 1)} [\text{Tr}\{\rho^2\} \text{Tr}\{M[\mathbb{1}]\} + (\text{Tr}\{\rho\})^2 \text{Tr}\{M\}]. \end{aligned} \quad (\text{A15})$$

Returning to the matrix forms from the Einstein sum notation, it can be seen that:

$$\rho_{aa} \rho_{cc} = (\text{Tr}\{\rho\})^2, \quad (\text{A16})$$

$$\rho_{ac} \rho_{ac} = \text{Tr}\{\rho^2\}, \quad (\text{A17})$$

$$M_{jj,ii} = \text{Tr}\{M[\mathbb{1}]\}, \quad (\text{A18})$$

$$M_{ki,ki} = \text{Tr}\{M\}, \quad (\text{A19})$$

which results in

$$\begin{aligned} &\int_{\mathcal{H}} \text{Tr}\{M[\rho]\rho\} d\rho \\ &= \frac{1}{(d^2 - 1)} [(\text{Tr}\{\rho\})^2 \text{Tr}\{M[\mathbb{1}]\} + \text{Tr}\{\rho^2\} \text{Tr}\{M\}] - \\ &\quad - \frac{1}{d(d^2 - 1)} [\text{Tr}\{\rho^2\} \text{Tr}\{M[\mathbb{1}]\} + (\text{Tr}\{\rho\})^2 \text{Tr}\{M\}]. \end{aligned} \quad (\text{A20})$$

Finally, noting that $\text{Tr}\{\rho\} = 1$, $\text{Tr}\{\rho^2\} = 1$ and $\rho^2 = \rho$, we arrive at

$$\int_{\mathcal{H}} \text{Tr}\{M[\rho]\rho\} d\rho = \frac{\text{Tr}\{M\} + \text{Tr}\{M[\mathbb{1}]\}}{d(d+1)} \quad (\text{A21})$$

$$= \frac{\text{Tr}\{M\}}{d(d+1)}, \quad (\text{A22})$$

since for the cases where M is composed of a traceless lindbladian operator \mathcal{L} , $\text{Tr}\{M[\mathbb{1}]\} = 0$, and we arrive at Eq. (29).

4. Boundedness of the AGI

We make use of the relation in Eq. (A21) to prove that, in the limit of strong dephasing, the AGI of a single qudit is bounded above and below, with the bounds depending only on the dimension of the system.

Theorem A.2. *Consider an open quantum system of a single qudit of dimension d , initiated in a pure state $\text{Tr}\{\rho_0^2\} = 1$, under the influence of a time-independent noise superoperator \mathcal{L} with coupling constant γ and pure dephasing collapse operator $L = J_z$, and evolving via an arbitrary time-independent unitary superoperator \mathcal{S} over time t . Then, in the limit of strong coupling where $(\gamma t) \gg 1$, the AGI \mathcal{I} is bounded in the region*

$$1 - \frac{2}{d+1} \leq \mathcal{I} \leq 1 - \frac{1}{d+1}. \quad (\text{A23})$$

Proof. In superoperator form, the quantum channel can be written as $\mathcal{E} = \mathcal{U} \circ M$. Now, since the channel is completely positive and trace-preserving (CPTP) and \mathcal{U} is a unitary operator, M must also be CPTP. Substituting this into the integral equation for the AGF in Eq. (8) and using Eq. (A21), we have

$$\mathcal{F} = \frac{\text{Tr}\{M\} + \text{Tr}\{M[\mathbb{1}]\}}{d(d+1)}. \quad (\text{A24})$$

Therefore, proving the bound on \mathcal{I} is equivalent to proving that

$$1 \leq (d+1)\mathcal{F} \leq 2, \quad (\text{A25})$$

$$d \leq \text{Tr}\{M\} + \text{Tr}\{M[\mathbb{1}]\} \leq 2d, \quad (\text{A26})$$

$$0 \leq \text{Tr}\{M\} \leq d, \quad (\text{A27})$$

since $\text{Tr}\{M[\mathbb{1}]\} = \text{Tr}\{\mathbb{1}\} = d$ due to the trace-preservation of M .

Now, to show this, consider the action of M on the state ρ . The collapse operator $L = J_z$ of pure dephasing is a diagonal matrix which preserves the populations of ρ while causing the coherences to decay to zero. Thus,

$$M : \rho \rightarrow \sum_{i=0}^{d-1} \rho'_{ii} |i\rangle\langle i| \quad (\text{A28})$$

$$\forall \rho, M_{ij}^{kl} \rho_{kl} \propto \delta_{ij} \quad (\text{A29})$$

$$M_{ij}^{kl} = \lambda_i^{kl} \delta_{ij}. \quad (\text{A30})$$

In the Kraus representation, using $M = \sum_{k=1}^K E_k^* \otimes E_k$, the matrix elements are given, trivially, by

$$M_{ij}^{nm} = \sum_{k=1}^K E_{k,jm}^* E_{k,in}, \quad (\text{A31})$$

and, since M is trace-preserving,

$$\forall n, m, \sum_{i=0}^{d-1} M_{ii}^{nm} = \sum_{k=1}^K \sum_{i=0}^{d-1} E_{k,im}^* E_{k,in} \quad (\text{A32})$$

$$= \delta_{nm}. \quad (\text{A33})$$

Furthermore,

$$\text{Tr}\{M\rho\} = \text{Tr}\{\rho\} \quad (\text{A34})$$

$$\text{vec}(\mathbb{1})^T \cdot M \cdot \text{vec}(\rho) = \text{vec}(\mathbb{1})^T \cdot \text{vec}(\rho) \quad (\text{A35})$$

$$\therefore \sum_{n=0}^{d-1} M_{ij}^{nn} = \delta_{ij}. \quad (\text{A36})$$

Thus, in particular, if $n = m$:

$$\sum_{k=1}^K \sum_{i=0}^{d-1} |E_{k,in}|^2 = 1 \quad (\text{A37})$$

$$\iff \sum_{k,i=n} |E_{k,in}|^2 + \sum_{k,i \neq n} |E_{k,in}|^2 = 1 \quad (\text{A38})$$

$$\therefore \forall n, 0 \leq \sum_{k=1}^K |E_{k,nn}|^2 \leq 1 \quad (\text{A39})$$

Moreover, since

$$\text{Tr}\{M\} = \sum_{k,ij} E_{k,jj}^* E_{k,ii} \quad (\text{A40})$$

$$= \sum_k |\text{Tr}\{E_k\}|^2, \quad (\text{A41})$$

the trace of M can be equivalently expressed by

$$\text{Tr}\{M\} = \sum_{i=0}^{d-1} \sum_{j=0}^{d-1} M_{ij}^{ij} \quad (\text{A42})$$

$$= \sum_{i=0}^{d-1} M_{ii}^{ii} \quad (\text{A43})$$

$$= \sum_{k=1}^K \sum_{i=0}^{d-1} |E_{k,ii}|^2. \quad (\text{A44})$$

Therefore, combining this last expression with Eq. (A39) where each of the d elements $|E_{k,ii}|^2$ are bounded above by 1, it is clear that the sum of all d of them, and thus $\text{Tr}\{M\}$, must be bounded by d ,

$$0 \leq \sum_k \sum_{i=0}^{d-1} |E_{k,ii}|^2 \leq d, \quad (\text{A45})$$

proving the boundedness of \mathcal{F} and \mathcal{I} . \square

5. Gate-Independent Correction Terms

In Sec. II B, we found in Eq. (30) that the m -th order AGI correction always contains a gate-independent term proportional to the trace of the m -th power of the collapse operator \mathcal{L} in superoperator form. Specifically, in Sec. II E Eqs. (51) and (59), we presented the first- and second-order gate-independent AGI correction terms.

Since we have in Eq. (12) an expression for \mathcal{L} in terms of the (regular) collapse operators L , we can use this to express the correction terms in terms of L instead. To first-order,

$$\begin{aligned} \text{Tr}\{\mathcal{L}\} &= \text{Tr}\left\{L^* \otimes L - \frac{1}{2} \left(L^\dagger L \otimes \mathbb{1}_d + (\mathbb{1}_d \otimes L^\dagger L)^T\right)\right\} \\ &= \text{Tr}\{L^* \otimes L\} - \frac{1}{2} \text{Tr}\left\{L^\dagger L \otimes \mathbb{1}_d + \mathbb{1}_d \otimes (L^\dagger L)^T\right\} \\ &= \text{Tr}\{L^*\} \text{Tr}\{L\} - \frac{d}{2} \left(\text{Tr}\{L^\dagger L\} + \text{Tr}\{(L^\dagger L)^T\}\right) \\ &= |\text{Tr}\{L\}|^2 - d \text{Tr}\{L^\dagger L\}, \end{aligned} \quad (\text{A46})$$

giving the result of Eq. (52).

By the same procedure, it is trivial to see that the second-order term in Eq. (64) is given by,

$$\text{Tr}\{\mathcal{L}^2\} = |\text{Tr}\{L^2\}|^2 + \frac{1}{2} |\text{Tr}\{L^\dagger L\}|^2 + \frac{d}{2} \text{Tr}\{(L^\dagger L)^2\}. \quad (\text{A47})$$

Furthermore, it is possible to make use of the multinomial expansion to find the m -th power trace to arbitrary order. In general this produces a non-trivial sum over all L -words of length m . In the specific case of real and symmetric collapse operators $L = L^* = L^T = L^\dagger$, these

words can be factorised, resulting in the triangular sum

$$\begin{aligned}
& \text{Tr}\{\mathcal{L}^m\} \\
&= \text{Tr}\left\{\left(L^* \otimes L - \frac{1}{2}\left(L^\dagger L \otimes \mathbb{1}_d + (\mathbb{1}_d \otimes L^\dagger L)^T\right)\right)^m\right\} \\
&= \sum_{k_1+k_2+k_3=m} \frac{m! \text{Tr}\{(L^*)^{k_1} (L^\dagger L)^{k_2} \otimes L^{k_1} ((L^\dagger L)^T)^{k_3}\}}{(-2)^{k_2+k_3} k_1! k_2! k_3!} \\
&= m! \sum_{k_1+k_2+k_3=m} \frac{\text{Tr}\{L^{k_1+2k_2}\} \text{Tr}\{L^{k_1+2k_3}\}}{(-2)^{k_2+k_3} k_1! k_2! k_3!} \\
&= m! \sum_{k_1=0}^m \sum_{k_2=0}^{m-k_1} \frac{\text{Tr}\{L^{k_1+2k_2}\} \text{Tr}\{L^{2m-k_1-2k_2}\}}{(-2)^{m-k_1-1} k_1! k_2! (m-k_1-k_2)!}. \tag{A48}
\end{aligned}$$

6. Second-order Gate-Dependent Correction Term

Beginning with the general expression for the second-order term in the AGI expansion in Eq. (29), and combining with the $m = 2$ term $M^{(2)}(t)$ in Eq. (26), we obtain Eq. (56)

$$\mathcal{I}^{(2)} = \frac{-(\gamma t)^2}{d(d+1)} \text{Tr}\{M^{(2)}(t)\} \tag{A49}$$

$$= \frac{-(\gamma t)^2}{d(d+1)} \text{Tr}\left\{\frac{\mathcal{L}^2}{2!} + \sum_{n_1=1}^{\infty} \sum_{n_2=1}^{\infty} \left(\prod_{i=1}^2 \frac{(-t)^{n_i} [(\mathcal{S})^{n_i}, \mathcal{L}]}{n_i! \sum_{j=i}^2 (n_j+1)}\right)\right\} \tag{A50}$$

$$= \frac{-(\gamma t)^2}{d(d+1)} \left(\text{Tr}\left\{\frac{\mathcal{L}^2}{2!}\right\} + \sum_{n_1=1}^{\infty} \sum_{n_2=1}^{\infty} \frac{(-t)^{n_1+n_2} \text{Tr}\{[(\mathcal{S})^{n_1}, \mathcal{L}][(\mathcal{S})^{n_2}, \mathcal{L}]\}}{n_1! n_2! (n_1+n_2+2)(n_2+1)}\right). \tag{A51}$$

Focusing now on the gate-dependent terms only, we can express the double summation of the trace term using the relation $n_1 + n_2 + 2 = s$

$$\sum_{n_1=1}^{\infty} \sum_{n_2=1}^{\infty} \frac{(-t)^{n_1+n_2} \text{Tr}\{[(\mathcal{S})^{n_1}, \mathcal{L}][(\mathcal{S})^{n_2}, \mathcal{L}]\}}{n_1! n_2! (n_1+n_2+2)(n_2+1)} \tag{A52}$$

$$= \sum_{s=0}^{\infty} \sum_{n=0}^{s-2} \frac{(-t)^{s-2} \text{Tr}\{[(\mathcal{S})^n, \mathcal{L}][(\mathcal{S})^{s-2-n}, \mathcal{L}]\}}{n! s(s-1-n)!} \tag{A53}$$

$$= \sum_{s=0}^{\infty} \frac{(-t)^{s-2}}{s(s-1)!} \sum_{n=0}^{s-2} \binom{s-1}{n} \text{Tr}\{[(\mathcal{S})^n, \mathcal{L}][(\mathcal{S})^{s-2-n}, \mathcal{L}]\}. \tag{A54}$$

Lemma A.1. Given operators A and B the following binomial sum of the product of iterated commutators at order n and $j-n$ is traceless,

$$\sum_{n=1}^j \binom{j+1}{n} \text{Tr}\{[(A)^n, B][(A)^{j-n}, B]\} = 0. \tag{A55}$$

Proof. Using $\binom{j+1}{n} = \binom{j+1-1}{n-1} + \binom{j+1-1}{n}$, we have

$$\begin{aligned}
& \sum_{n=1}^j \binom{j+1}{n} \text{Tr}\{[(A)^n, B][(A)^{j-n}, B]\} \\
&= \sum_{n=1}^j \binom{j}{n-1} \text{Tr}\{[(A)^n, B][(A)^{j-n}, B]\} + \\
&+ \sum_{n=1}^j \binom{j}{n} \text{Tr}\{[(A)^n, B][(A)^{j-n}, B]\}. \tag{A56}
\end{aligned}$$

Now, for the first term with binomial $\binom{j+1-1}{n-1}$ and using the change of index $n = n+1$,

$$\begin{aligned}
& \sum_{n=1}^j \binom{j}{n-1} \text{Tr}\{[(A)^n, B][(A)^{j-n}, B]\} \\
&= \sum_{n=0}^{j-1} \binom{j}{n} \text{Tr}\{[(A)^{n+1}, B][(A)^{j-n-1}, B]\} \\
&= \sum_{n=0}^{j-1} \binom{j}{n} \text{Tr}\{[A, [(A)^n, B]][(A)^{j-n-1}, B]\} \\
&= - \sum_{n=0}^{j-1} \binom{j}{n} \text{Tr}\{[(A)^n, B][(A)^{j-n}, B]\}, \tag{A57}
\end{aligned}$$

by cyclic permutation of the trace. This summation is the negation of the second binomial term $\binom{j+1-1}{n}$ for all

terms $1 \leq n \leq j-1$. Therefore only the $n=0$ and $n=j$ terms remain. Moreover since $\binom{j}{j} = \binom{j}{0} = 1$, we have that

$$\begin{aligned} & \sum_{n=1}^j \binom{j+1}{n} \text{Tr}\{[(A)^n, B][(A)^{j-n}, B]\} \\ &= \text{Tr}\{[(A)^j, B]B\} - \text{Tr}\{B[(A)^j, B]\} \\ &= 0. \end{aligned} \quad (\text{A58})$$

□

Now, applying this result to the summation in Eq. (A54), where we identify $j = s-2$, we have that all terms for $n \geq 1$ are zero, and therefore only the $n=0$ term survives giving the following relation

$$\sum_{n=0}^{s-2} \binom{s-1}{n} \text{Tr}\{[(S)^n, \mathcal{L}][(S)^{s-2-n}, \mathcal{L}]\} = \text{Tr}\{\mathcal{L}[(S)^{s-2}, \mathcal{L}]\}. \quad (\text{A59})$$

From this, with a change of index $s-2 = s$, we can rewrite the full second-order correction as

$$\mathcal{I}^{(2)} = \frac{-(\gamma t)^2}{d(d+1)} \left(\frac{\text{Tr}\{\mathcal{L}^2\}}{2} + \sum_{s=2}^{\infty} \frac{(-t)^s \text{Tr}\{\mathcal{L}[(S)^s, \mathcal{L}]\}}{(s+2)!} \right), \quad (\text{A60})$$

giving the result in Eq. (59).

Now, as for the gate-independent terms, we wish to express this gate-dependent trace of superoperators explicitly in terms of the operators H and L .

Beginning with the binomial expansion of the trace of the iterated commutator [41],

$$\begin{aligned} & \text{Tr}\{\mathcal{L}[(S)^s, \mathcal{L}]\} \\ &= \sum_{k=0}^s (-1)^k \binom{s}{k} \text{Tr}\{\mathcal{L} S^k \mathcal{L} S^{s-k}\} \\ &= i^s \sum_{k=0}^s \sum_{j=0}^k \sum_{l=0}^{s-k} \binom{s}{k} \binom{k}{j} \binom{s-k}{l} (-1)^{s+k-j-l} \times \\ & \quad \times \text{Tr}\{\mathcal{L}((H^*)^{k-j} \otimes H^j) \mathcal{L}((H^*)^{s-k-l} \otimes H^l)\}, \end{aligned} \quad (\text{A61})$$

where we used the binomial expansion of the expression for \mathcal{S} in terms of H in Eq. (11),

$$S^k = i^k \sum_{j=0}^k (-1)^{k-j} \binom{k}{j} (H^*)^{k-j} \otimes H^j. \quad (\text{A62})$$

Substituting now the expression for \mathcal{L} in terms of L in Eq. (12), and expanding algebraically the products of the

operator terms in the trace, we obtain the following nine expressions, the sum of which is equivalent to the superoperator trace (omitting the prefactors and summations for convenience):

$$\text{Tr}\{LH^{k-j}LH^{s-k-l}\}^* \text{Tr}\{LH^jLH^l\}, \quad (\text{A63})$$

$$-\frac{1}{2} \text{Tr}\{LH^{k-j}L^TL^*H^{s-k-l}\}^* \text{Tr}\{LH^{j+l}\}, \quad (\text{A64})$$

$$-\frac{1}{2} \text{Tr}\{LH^{s-j-l}\}^* \text{Tr}\{LH^jL^TL^*H^l\}, \quad (\text{A65})$$

$$-\frac{1}{2} \text{Tr}\{L^TL^*H^{k-j}LH^{s-k-l}\}^* \text{Tr}\{LH^{j+l}\}, \quad (\text{A66})$$

$$\frac{1}{4} \text{Tr}\{L^TL^*H^{k-j}L^TL^*H^{s-k-l}\}^* \text{Tr}\{H^{j+l}\}, \quad (\text{A67})$$

$$\frac{1}{4} \text{Tr}\{L^TL^*H^{s-j-l}\}^* \text{Tr}\{L^TL^*H^{j+l}\}, \quad (\text{A68})$$

$$-\frac{1}{2} \text{Tr}\{LH^{s-j-l}\}^* \text{Tr}\{L^\dagger LH^jLH^l\}, \quad (\text{A69})$$

$$\frac{1}{4} \text{Tr}\{L^TL^*H^{s-j-l}\}^* \text{Tr}\{L^\dagger LH^{j+l}\}, \quad (\text{A70})$$

$$\frac{1}{4} \text{Tr}\{H^{s-j-l}\}^* \text{Tr}\{L^\dagger LH^jL^TL^*H^l\}. \quad (\text{A71})$$

Now, we can simplify these expressions by making the following observations: Firstly, s must be even since (i) heuristically, the trace must be real since we are calculating the fidelity (a real quantity) and therefore the prefactor i^s in Eq. (A61) cannot be imaginary, and (ii) formally we prove this in Appendix A 7. Secondly, by symmetry of the binomial expansions, we are free to make the following change of variables:

$$\begin{aligned} j &\rightarrow k-j, \\ l &\rightarrow s-k-l. \end{aligned}$$

For clarity, note that this change of variables does not affect the prefactor

$$(-1)^{s+k-j-l} \rightarrow (-1)^{j+k+l},$$

since, with s even, the ratio of these two terms is always a power of 2 and therefore equal to 1.

As an example to illustrate the effect of this change of variables, for the first term Eq. (A63), the forward and backwards sums are complex conjugates and therefore only the real part can remain (omitting prefactors of the full expression):

$$\sum_{j=0}^k \sum_{l=0}^{s-k} \text{Tr}\{LH^{k-j}LH^{s-k-l}\}^* \text{Tr}\{LH^jLH^l\} \rightarrow \sum_{j=0}^k \sum_{l=0}^{s-k} \text{Tr}\{LH^jLH^l\}^* \text{Tr}\{LH^{k-j}LH^{s-k-l}\} \quad (\text{A72})$$

$$\Rightarrow \sum_{j=0}^k \sum_{l=0}^{s-k} \text{Tr}\{LH^{k-j}LH^{s-k-l}\}^* \text{Tr}\{LH^jLH^l\} = \sum_{j=0}^k \sum_{l=0}^{s-k} \text{Re}\{\text{Tr}\{LH^{k-j}LH^{s-k-l}\}^* \text{Tr}\{LH^jLH^l\}\}. \quad (\text{A73})$$

Similarly, by comparing the remaining terms in Eqs. (A64) to (A71) with their counterparts following the change of variables, it is possible to identify the following sums as complex conjugates of one another:

$$\begin{aligned} \sum_{j=0}^k \sum_{l=0}^{s-k} (\text{A64} + \text{A65}) &= \sum_{j=0}^k \sum_{l=0}^{s-k} 2 \text{Re}\{\text{A64}\}, \\ \sum_{j=0}^k \sum_{l=0}^{s-k} (\text{A66} + \text{A69}) &= \sum_{j=0}^k \sum_{l=0}^{s-k} 2 \text{Re}\{\text{A66}\}, \\ \sum_{j=0}^k \sum_{l=0}^{s-k} (\text{A68} + \text{A70}) &= \sum_{j=0}^k \sum_{l=0}^{s-k} 2 \text{Re}\{\text{A68}\}, \\ \sum_{j=0}^k \sum_{l=0}^{s-k} (\text{A67} + \text{A71}) &= \sum_{j=0}^k \sum_{l=0}^{s-k} 2 \text{Re}\{\text{A67}\}. \end{aligned}$$

Hence, by combining all of these terms into the full expression for $\text{Tr}\{\mathcal{L}[(\mathcal{S})^s, \mathcal{L}]\}$ in Eq. (A61), we obtain the following result of Eq. (67):

$$\begin{aligned} &\text{Tr}\{\mathcal{L}[(\mathcal{S})^s, \mathcal{L}]\} \\ &= \sum_{k=0}^s \sum_{j=0}^k \sum_{l=0}^{s-k} \binom{s}{k} \binom{k}{j} \binom{s-k}{l} (-1)^{s+k-j-l} \times \\ &\quad \times \text{Re} \left[\text{Tr}\{LH^{k-j}LH^{s-k-l}\}^* \text{Tr}\{LH^jLH^l\} \right. \\ &\quad + \frac{1}{2} \text{Tr}\{L^T L^* H^{s-j-l}\}^* \text{Tr}\{L^T L^* H^{j+l}\} \\ &\quad + \frac{1}{2} \text{Tr}\{L^T L^* H^{k-j}L^T L^* H^{s-k-l}\}^* \text{Tr}\{H^{j+l}\} \\ &\quad - \text{Tr}\{LH^{k-j}L^T L^* H^{s-k-l}\}^* \text{Tr}\{LH^{j+l}\} \\ &\quad \left. - \text{Tr}\{L^T L^* H^{k-j}LH^{s-k-l}\}^* \text{Tr}\{LH^{j+l}\} \right]. \quad (\text{A74}) \end{aligned}$$

7. Tracelessness of the Odd-Order Iterated Commutator

Theorem A.3. *Given two operators A and B , the product of B with the iterated commutator of order s , $B[(A)^s, B]$, is traceless for all odd s ,*

$$\forall s = 2k + 1, k \in \mathbb{Z}, \text{Tr}\{B[(A)^s, B]\} = 0. \quad (\text{A75})$$

Proof. We begin with the trace of the binomial expansion of the iterated commutator [41],

$$B[(A)^s, B] = \sum_{k=0}^s (-1)^k \binom{s}{k} B A^{s-k} B A^k \quad (\text{A76})$$

$$\therefore \text{Tr}\{B[(A)^s, B]\} = \sum_{k=0}^s (-1)^k \binom{s}{k} \text{Tr}\{B A^{s-k} B A^k\}. \quad (\text{A77})$$

By symmetry of the binomial expansion $\binom{s}{k} = \binom{s}{s-k}$, and considering s odd $(-1)^{s-k} = -(-1)^k$, we can write the equivalent expansion

$$B[(A)^s, B] = - \sum_{k=0}^s (-1)^k \binom{s}{k} B A^k B A^{s-k} \quad (\text{A78})$$

$$\therefore \text{Tr}\{B[(A)^s, B]\} = - \sum_{k=0}^s (-1)^k \binom{s}{k} \text{Tr}\{B A^k B A^{s-k}\} \quad (\text{A79})$$

$$= - \sum_{k=0}^s (-1)^k \binom{s}{k} \text{Tr}\{B A^{s-k} B A^k\}, \quad (\text{A80})$$

by cyclic permutation of the trace, $\text{Tr}\{CD\} = \text{Tr}\{DC\} \Rightarrow \text{Tr}\{[C, D]\} = 0$. Hence, we have the result for odd s

$$\text{Tr}\{B[(A)^s, B]\} = - \text{Tr}\{B[(A)^s, B]\} \quad (\text{A81})$$

$$\Rightarrow \text{Tr}\{B[(A)^s, B]\} = 0. \quad (\text{A82})$$

□

Appendix B: Gates and Operators

Here we compile additional information and examples regarding the quantum gates and collapse operators used in the main text.

1. Quantum Gates

Given the set of single-qudit gates $U_g \in \{\mathbb{1}_d, X, Z, F\}$ defined in Eqs. (15) to (18), we present them in matrix

form to illustrate their structure. The identity matrix in d dimensions is trivial, and generated by a null control Hamiltonian $H_c = \mathbb{0}_d$, corresponding to no action on the qudit state. The generalized Pauli-X or SHIFT gate $X = \Sigma_x$ is defined as

$$X = \begin{bmatrix} 0 & 1 & 0 & 0 & \cdots & 0 \\ 0 & 0 & 1 & 0 & \cdots & 0 \\ 0 & 0 & 0 & 1 & \cdots & 0 \\ \vdots & \vdots & \vdots & \vdots & \ddots & \vdots \\ 0 & 0 & 0 & 0 & \cdots & 1 \\ 1 & 0 & 0 & 0 & \cdots & 0 \end{bmatrix},$$

which cyclically permutes the basis states, incrementing them all by 1 level. An equivalent formulation is given by the transpose X^T , which cyclically permutes the states downwards,

$$X^T = \begin{bmatrix} 0 & 0 & 0 & \cdots & 0 & 1 \\ 1 & 0 & 0 & \cdots & 0 & 0 \\ 0 & 1 & 0 & \cdots & 0 & 0 \\ 0 & 0 & 1 & \cdots & 0 & 0 \\ \vdots & \vdots & \vdots & \ddots & \vdots & \vdots \\ 0 & 0 & 0 & \cdots & 1 & 0 \end{bmatrix}.$$

The generalized Pauli-Z or CLOCK gate $Z = \Sigma_z$ is defined as

$$Z = \begin{bmatrix} 1 & 0 & 0 & \cdots & 0 \\ 0 & \omega & 0 & \cdots & 0 \\ 0 & 0 & \omega^2 & \cdots & 0 \\ \vdots & \vdots & \vdots & \ddots & \vdots \\ 0 & 0 & \cdots & 0 & \omega^{d-1} \end{bmatrix},$$

where the d -th roots of unity, ω , are also used to define the matrix form of the Quantum Fourier Transform in d dimensions, being the generalisation of the Walsh-Hadamard (superposition) gate,

$$F = \frac{1}{\sqrt{d}} \begin{bmatrix} 1 & 1 & 1 & 1 & \cdots & 1 \\ 1 & \omega & \omega^2 & \omega^3 & \cdots & \omega^{d-1} \\ 1 & \omega^2 & \omega^4 & \omega^6 & \cdots & \omega^{2(d-1)} \\ 1 & \omega^3 & \omega^6 & \omega^9 & \cdots & \omega^{3(d-1)} \\ \vdots & \vdots & \vdots & \vdots & \ddots & \vdots \\ 1 & \omega^{d-1} & \omega^{2(d-1)} & \omega^{3(d-1)} & \cdots & \omega^{(d-1)(d-1)} \end{bmatrix}.$$

Now, we introduce the interpolated X (SHIFT) and Z CLOCK gates, where we raise the X and Z gates to the power $\eta \in [0, 1]$, which allows us to smoothly interpolate the action of the gate(s) between the identity ($\eta = 0$) and the original gate ($\eta = 1$). As an example, consider $\eta = \frac{3d-2}{4d}$ for $d = 2$:

$$X^{0.5} = \frac{1}{\sqrt{2}} \begin{bmatrix} e^{i\frac{\pi}{4}} & e^{-i\frac{\pi}{4}} \\ e^{-i\frac{\pi}{4}} & e^{i\frac{\pi}{4}} \end{bmatrix}.$$

2. Collapse Operators

We present a brief example for the collapse operators of pure dephasing and bit-flip, as defined in Eqs. (19) and (20). In $d = 4$, these are precisely the generalised spin operators J_z and J_x for spin- $\frac{3}{2}$ systems, given by

$$J_z = \frac{1}{2} \begin{bmatrix} 3 & 0 & 0 & 0 \\ 0 & 1 & 0 & 0 \\ 0 & 0 & -1 & 0 \\ 0 & 0 & 0 & -3 \end{bmatrix},$$

and

$$J_x = \frac{1}{2} \begin{bmatrix} 0 & \sqrt{3} & 0 & 0 \\ \sqrt{3} & 0 & 2 & 0 \\ 0 & 2 & 0 & \sqrt{3} \\ 0 & 0 & \sqrt{3} & 0 \end{bmatrix}.$$

Appendix C: Complementary Results

Here, we present further results and investigations that support the findings of the main text.

1. Uniformity of the CUE for Haar-random Unitaries

As noted in Sec. II C, the ability to generate ensembles of well-distributed random matrices for arbitrary qudit dimensions is of fundamental importance to the study of the statistical behaviour of the AGL, particularly regarding the aspect of gate-dependence. Given a qudit of dimension d , we identify the space of all possible quantum gates with the unitary group $\mathbf{U}(d)$ of $d \times d$ unitary matrices, associated to skew-Hamiltonian control terms generated through the matrix exponential map of the Lie algebra $\mathfrak{u}(d)$. Therefore, the aim is to sample from a uniform distribution over this group.

Since \mathbf{U} is a compact, connected Lie group, it has a unique (up to positive scalar multiplication) and operation-invariant measure, referred to as the Haar measure [43]. When normalised to one, it produces a uniform probability measure on \mathbf{U} , with the associated probability space referred to by the name Circular Unitary Ensemble (CUE), as originally introduced by Dyson [44]. Elements of the CUE are thus typically referred to as Haar-random unitary matrices. The properties of these random matrices have been well-studied, particularly in the standard reference text on random matrix theory by Mehta [45], to which we shall refer. For the specific case of the generation of random unitary matrices, we shall refer to the work of Mezzadri [43].

The spectral statistics form the foundation for the study of random matrices, and in particular we shall concern ourselves with the two primary quantities: (1) the eigenvalue distribution (level density), and (2) the

nearest-neighbour eigenvalue (n -level, for $n = 1$) spacing distribution.

Since we are studying unitary matrices whose eigenvalues all lie on the unit circle in the complex plane, $\lambda_j = e^{i\theta_j}$, the eigenvalue distribution is thus the distribution of the complex phases θ_j of the d eigenvalues:

$$-\pi \leq \theta_j < \pi \quad \forall \quad 1 \leq j \leq d. \quad (\text{C1})$$

In the large matrix limit where $d \rightarrow \infty$ the eigenvalue phases will tend towards a uniform distribution on the domain $[-\pi, \pi)$ with probability density $\rho(\theta) = \frac{1}{2\pi}$.

Next, the nearest-neighbour eigenvalue spacing distribution $p(s)$ is obtained by: (1) sorting the spectrum of phases θ_j from smallest to largest, (2) unfolding this spectrum by the factor $\frac{d}{2\pi}$ to normalise the mean spacing to 1, and then (3) taking their successive differences $s_j = \frac{d}{2\pi}(\theta_{j+1} - \theta_j)$, resulting in a list of $d - 1$ elements. This distribution for the unitary ensembles is well approximated by the Wigner Surmise $p_w(s)$,

$$p_w(s) = \frac{32s^2}{\pi^2} e^{-\frac{4s^2}{\pi}}, \quad (\text{C2})$$

where s is taken in the continuous limit of s_j . In the original work of Wigner [46] on the Gaussian Unitary Ensemble (GUE) of random Hamiltonian (Hermitian) matrices, this is the exact analytical form for the case of 2×2 matrices, which applies to very good approximation for large d . Additionally since the GUE and CUE are related functionally, these two distributions become equivalent for both ensembles for large d .

Given our requirements of sampling random matrices uniformly from the unitary group, we note that there exist numerous (PYTHON-based) packages with methods for generating unitary matrices. Some common, but non-exhaustive, examples include: QUTiP [47, 48] (`rand_unitary`, `rand_unitary_haar`, `rand_herm`), CIRQ [49] (`rand_unitary`, `rand_special_unitary`), and BRISTOL [50] (`gen_cue`).

Both QUTiP's `rand_unitary_haar` and CIRQ's `rand_unitary` methods implement precisely the algorithm provided by Mezzadri in [43]. The CIRQ's `rand_special_unitary` method augments the original `rand_unitary` method by normalising the determinant of the randomly generated matrix to 1. The QUTiP's `rand_unitary` method uses the `rand_herm` method to generate a random Hermitian matrix and then computes its unitary equivalent by matrix exponentiation.

We tested each of these different methods by sampling one million eigenvalues in each of 2 matrix size configurations, $d \in \{2, 100\}$ for each method. These two values were chosen to represent the two regimes of large and small matrix dimensions. The number of eigenvalues was chosen such that, for the algorithm of Mezzadri the standard deviation of the mean for the level density of the eigenvalue phases of the $d = 100$ matrices fell below the threshold of 0.001. The number of eigenvalues was kept

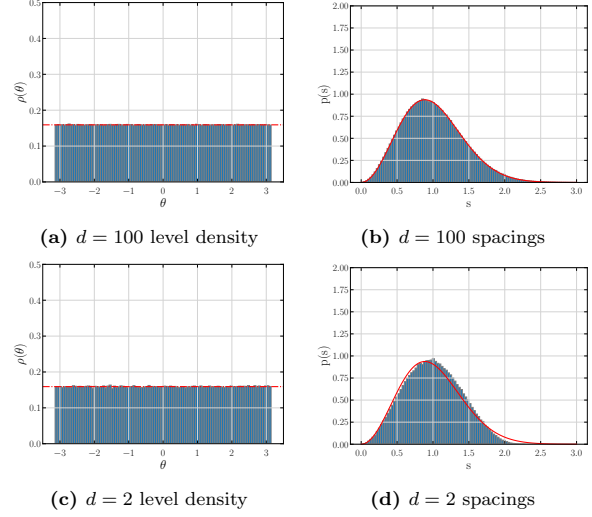


Figure 11: Method `QUTiP.rand_unitary_haar` (and equivalently `CIRQ.rand_unitary`), based on [43].

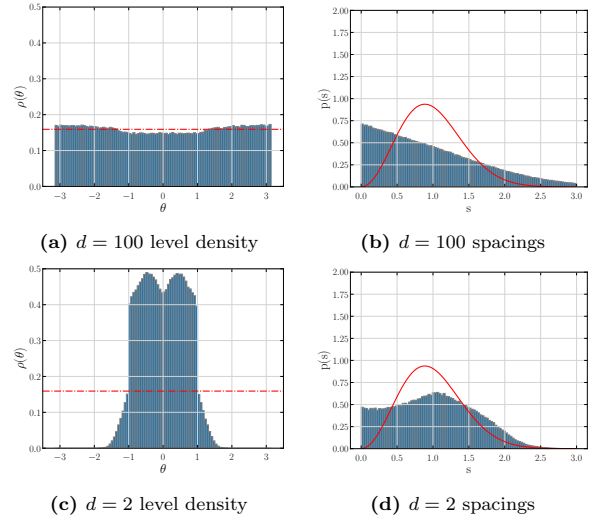


Figure 12: Method `QUTiP.rand_unitary` (and equivalently `QUTiP.rand_herm`).

constant at each dimension by varying the number of quantum gates generated, specifically 500000 and 10000 for $d = 2$ and $d = 4$ respectively.

In Figs. 11 to 14, the simulated data of eigenvalue and spacing distributions (blue) are compared to their analytically expected results (red). We can see that the method of Mezzadri in Fig. 11 performs the best for generating uniformly distributed Haar-random gates. Hence this is our method of choice. However, even for this method the spacing distribution does show reduced accuracy for lower dimensions, despite the level densities remaining

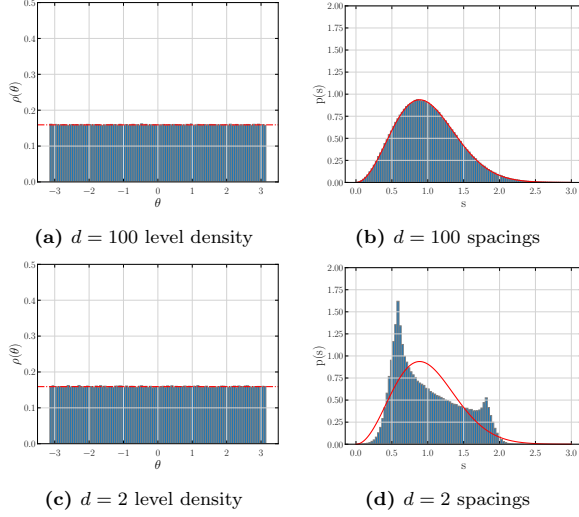


Figure 13: Method BRISTOL.gen_cue

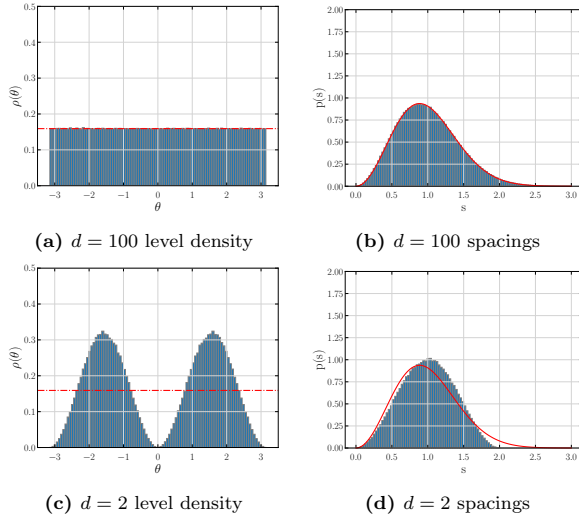


Figure 14: Method CIRQ.rand.special_unitary

uniform. This could be attributed to the fact that the Wigner Surmise is exact for 2×2 Hermitian matrices (but still very accurate for large d), but it is only in the large d limit that the distributions for the CUE are identical to that of the GUE [45]. Thus some deviation is to be expected for small unitary matrices.

The QUTiP.rand.unitary and QUTiP.rand.herm methods in Fig. 12 do not appear suitable for sampling uniformly from the CUE. Indeed, inspection of the sampled matrices showed that approximately 50% of the generated unitary matrices were diagonal. On the other hand, the BRISTOL.gen.cue in Fig. 13 is well optimised for high-dimensional systems but is unsuitable for small

dimensions. Finally, it is interesting to note that the special unitary matrices of CIRQ.rand.special_unitary in Fig. 14 are similarly distributed for large dimension, but show singular behaviour for small d .

2. Distribution of the asymptotic AGIs

We continue our investigations on the different PYTHON methods for generating Haar-random gates, namely: BRISTOL.gen.cue, QUTiP.rand.unitary, QUTiP.rand.unitary.haar, CIRQ.rand.unitary and CIRQ.rand.special_unitary.

In Sec. II C, and Fig. 3 specifically, we discussed the distribution of the plateau values \mathcal{I}^* of the AGI in the large- γt regime. Recall that we refer to these plateau values \mathcal{I}^* at the large- γt limit, $\lim_{\gamma t \gg 1} \mathcal{I} \rightarrow \mathcal{I}^*$. We showed that they must be bounded above and below by Eq. (43) for all gates. We also observed the appearance of two distinct behaviours (\mathcal{I}_{mono}^* and \mathcal{I}_{over}^*) in the sampled Haar-random gates: (1) Monotonic growth of the AGI towards \mathcal{I}^* , and (2) overshoot with a single turning point above \mathcal{I}^* .

We note that, as for all the numerical results in the main text, the QUTiP.rand.unitary.haar method was used to generate the data shown in Fig. 3. We complement this work by repeating these simulations using the remaining methods (for $d = 2$) and also with QUTiP.rand.unitary.haar for $d \in \{2, 4, 8, 16\}$. For each test method and dimension, 100000 gates were generated, their \mathcal{I}^* calculated numerically and their behaviour categorised as either monotonic or overshooting as shown in Table I.

Figures 15 and 16 display the data of these experiments by plotting histograms of the probability densities of the \mathcal{I}^* for each category of gate, \mathcal{I}_{mono}^* in orange and \mathcal{I}_{over}^* in blue, as well as their combined distribution \mathcal{I}_{total}^* in grey. The histograms were normalised such that the area under the curve of $p(\mathcal{I}_{total}^*)$ was equal to 1. The red and black vertical lines show the upper and lower bounds on \mathcal{I}^* , respectively. The dashed blue vertical lines show the expected mean value for each dimension.

Looking closer at Fig. 15, the two CIRQ methods in Figs. 15c and 15d appear to have distributions matching most closely with that of QUTiP.rand.unitary.haar in Fig. 16a, although the normalisation procedure for the special unitary matrices appears to generate a larger proportion of gates with overshoot. It is interesting to note that the BRISTOL.gen.cue method in Fig. 15a generates an increasing number of gates near the expected mean, but only below, with no gates in the range $1 - \frac{1}{d} \leq \mathcal{I}^* \leq 1 - \frac{1}{d+1}$. As mentioned in Appendix C 1, QUTiP.rand.unitary in Fig. 15b generates a large number of diagonal unitary matrices, whose $\mathcal{I}^* = \mathcal{I}_{min}^* = 1 - \frac{2}{d+1}$ are equivalent to that of the identity matrix 1_d .

Figure 16 shows the preferred QUTiP.rand.unitary.haar method for different dimensions $d \in \{2, 4, 8, 16\}$. We note that at each di-

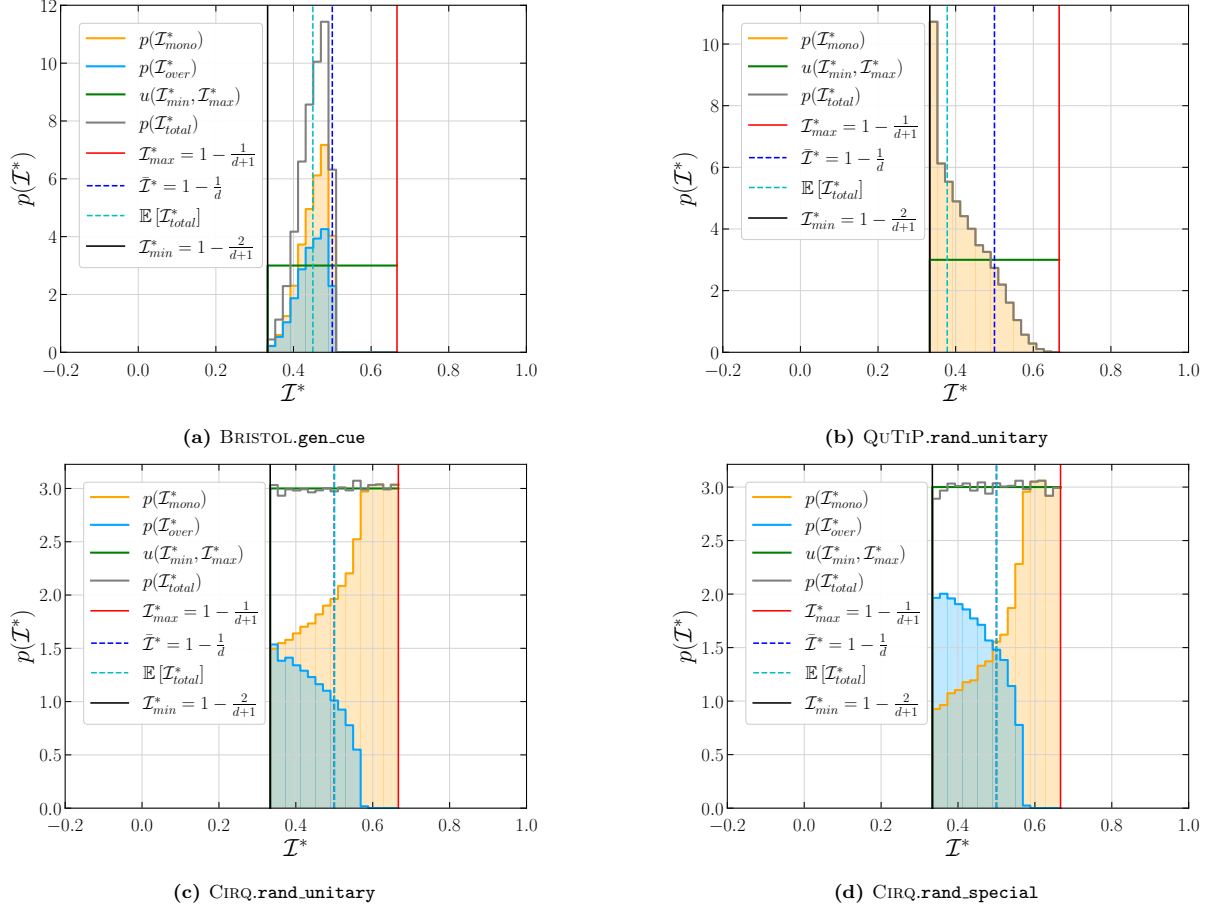


Figure 15: Probability distributions of the AGI plateaus for different gate generation methods. 100000 gates were generated using each of the four methods for $d = 2$: BRISTOL.gen.cue in Fig. 15a, QUTiP.rand.unitary in Fig. 15b, CIRQ.rand.unitary in Fig. 15c and CIRQ.rand.special in Fig. 15d. For each gate, the \mathcal{I}^* was calculated and categorised according to whether the curves were monotonic (orange) or overshooting (blue). The distributions of the counts of \mathcal{I}^* in the domain $[\mathcal{I}_{min}^*, \mathcal{I}_{max}^*]$ (black and red vertical lines, respectively) were binned according to Sturge’s formula $n_{bins} = \log_2(n_{gates} + 1)$ and normalised such that the total distribution $p(\mathcal{I}_{total}^*)$ (grey) had unit area. The mean plateau value $\mathbb{E}[\mathcal{I}_{total}^*]$ (cyan, dotted vertical line), was plotted in comparison with the expected mean $\bar{\mathcal{I}}^* = 1 - \frac{1}{d}$ (blue, dashed vertical line). The green line represents the expected uniform distribution $u(\mathcal{I}_{min}^*, \mathcal{I}_{max}^*)$ in the domains.

mention the computed mean over all sampled \mathcal{I}^* is equal to (within statistical error) the expected mean shown by the dashed blue vertical line, $\bar{\mathcal{I}}^* = 1 - \frac{1}{d}$. However, most striking is the fact that for $d > 2$ the total probability density is no longer uniformly distributed between \mathcal{I}_{min}^* and \mathcal{I}_{max}^* , but becomes increasingly concentrated about the mean.

We remark that this observed behaviour is due to the concentration of measure phenomenon as the dimensionality of the system increases [51, 52]. To understand this, we first demonstrate the following property of the AGI:

Lemma C.1. *The AGI function $\mathcal{I} : \mathbf{U}(d) \rightarrow \mathbb{R}$ is L -Lipschitz continuous with respect to the Frobenius norm $\|A\|_F = \sqrt{\text{Tr}\{A^\dagger A\}}$ over the unitary group $\mathbf{U}(d)$ with*

Lipschitz constant $L = \frac{2}{d+1}$, such that

$$|\mathcal{I}(U) - \mathcal{I}(U')| \leq L \|U - U'\|_F \quad (\text{C3})$$

where $U, U' \in \mathbf{U}(d)$.

Proof. The AGF \mathcal{F} can be written in terms of the process fidelity F as [40]

$$\mathcal{F} = \frac{dF + 1}{d + 1}, \quad (\text{C4})$$

where $F = \frac{1}{d^2} |\text{Tr}\{U^\dagger V\}|^2$ for two unitaries $U, V \in \mathbf{U}(d)$. Then, with $\bar{\mathcal{I}} = 1 - \mathcal{F}$, we have that

$$\mathcal{I} = \frac{d^2 - |\text{Tr}\{U^\dagger V\}|^2}{d(d + 1)}. \quad (\text{C5})$$

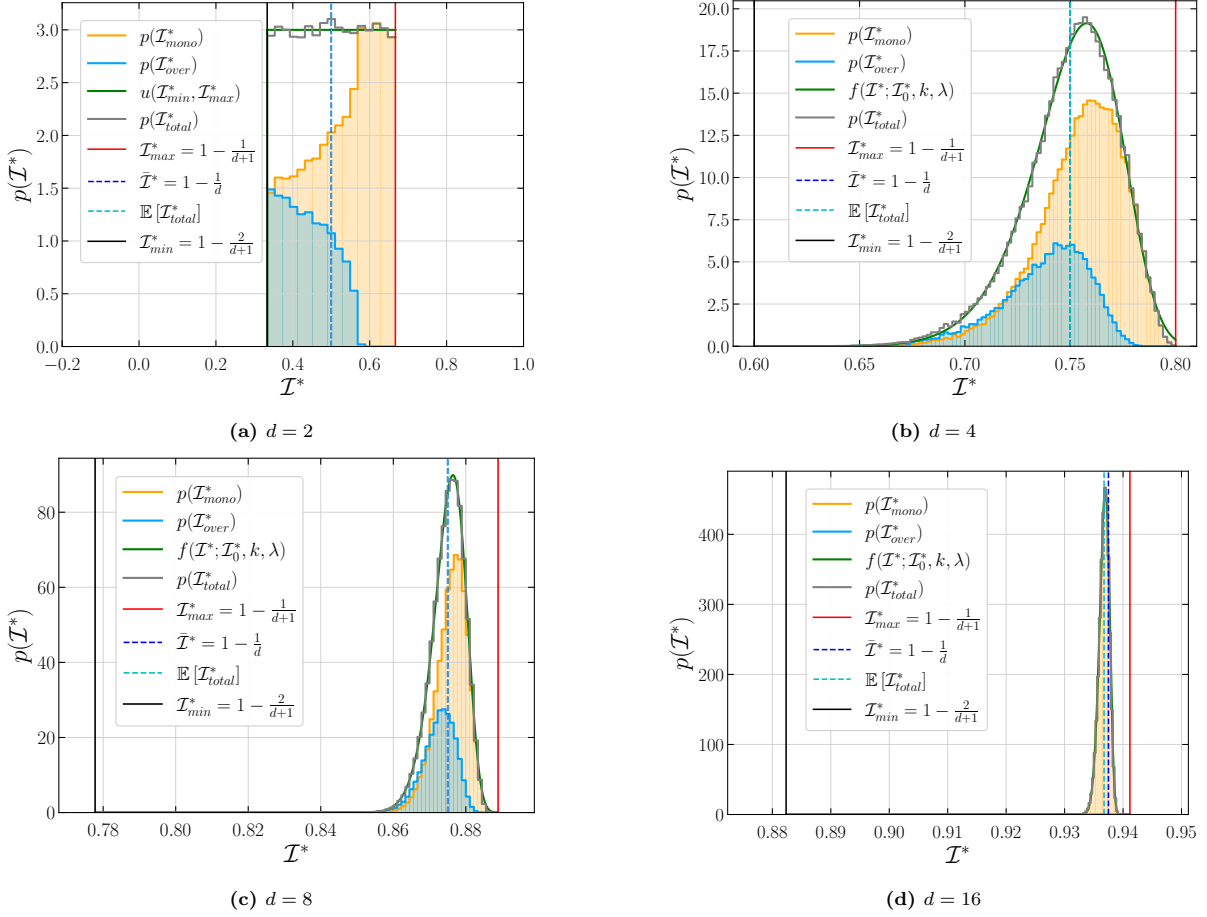


Figure 16: Probability distributions of the AGI plateaus for dimensions $d \in \{2, 4, 8, 16\}$. 100000 gates were generated using the method `QUtiP.rand.unitary.haar` of [43] at each dimension: $d = 2$ in Fig. 16a, $d = 4$ in Fig. 16b, $d = 8$ in Fig. 16c, $d = 16$ in Fig. 16d. For each gate, the \mathcal{I}^* was calculated and categorised according to whether the curves were monotonic (orange) or overshooting (blue). The distributions of the counts of \mathcal{I}^* in the domain $[\mathcal{I}_{min}^*, \mathcal{I}_{max}^*]$ (black and red vertical lines, respectively) were binned according to: Sturge's formula $n_{bins} = \log_2(n_{gates} + 1)$ for $d = 2$, $n_{bins} = 100$ for $d = 4, 8$ and $n_{bins} = 200$ for $d = 16$, due to the increasing concentration of the counts for the larger dimensions. The counts were normalised such that the total distribution $p(\mathcal{I}_{total}^*)$ (grey) had unit area. The mean plateau value $\mathbb{E}[\mathcal{I}_{total}^*]$ (cyan, dotted vertical line), was plotted in comparison with the expected mean $\tilde{\mathcal{I}}^* = 1 - \frac{1}{d}$ (blue, dashed vertical line). The green curve represents the fitted Weibull distributions $f(\mathcal{I}^*; \mathcal{I}_0^*, k, \lambda) = \frac{k}{\lambda} \left(\frac{\mathcal{I}^* - \mathcal{I}_0^*}{\lambda} \right)^{k-1} e^{-\left(\frac{\mathcal{I}^* - \mathcal{I}_0^*}{\lambda} \right)^k}$ in the domain.

Considering the difference, we have that

$$\begin{aligned} |\mathcal{I}(U) - \mathcal{I}(U')| &= \frac{1}{d(d+1)} \left| |\text{Tr}\{U^\dagger V\}|^2 - |\text{Tr}\{U'^\dagger V\}|^2 \right| \\ &= \frac{1}{d(d+1)} \left| |\text{Tr}\{U^\dagger V\}| - |\text{Tr}\{U'^\dagger V\}| \right| \times \\ &\quad \times \left| |\text{Tr}\{U^\dagger V\}| + |\text{Tr}\{U'^\dagger V\}| \right|, \end{aligned} \quad (\text{C6})$$

by difference of squares. Now,

$$\begin{aligned} \left| |\text{Tr}\{U^\dagger V\}| + |\text{Tr}\{U'^\dagger V\}| \right| &\leq |\text{Tr}\{U^\dagger V\}| + |\text{Tr}\{U'^\dagger V\}| \\ &\leq 2d, \end{aligned} \quad (\text{C7})$$

by the Cauchy-Schwartz inequality and since the trace of a unitary is at most d . Similarly,

$$\begin{aligned} \left| |\text{Tr}\{U^\dagger V\}| - |\text{Tr}\{U'^\dagger V\}| \right| &\leq |\text{Tr}\{U^\dagger V\} - \text{Tr}\{U'^\dagger V\}| \\ &\leq \|U^\dagger V - U'^\dagger V\|_F \end{aligned} \quad (\text{C8})$$

$$\leq \|(U - U')^\dagger V\|_F \quad (\text{C9})$$

$$\leq \|U - U'\|_F, \quad (\text{C10})$$

and by unitary invariance of the Frobenius norm. There-

d	Method	\mathcal{I}_{mono}^* (%)	\mathcal{I}_{over}^* (%)	ϵ_{rel} (%)	D_{KL}
2	BRISTOL.gen.cue	59.56	40.44	0.100	0.885
2	QUtIP.rand.unitary	100.00	0.00	0.243	0.438
2	CIRQ.rand.unitary	73.06	26.94	1.02×10^{-3}	5.92×10^{-5}
2	CIRQ.rand.special.unitary	61.66	38.34	6.83×10^{-4}	1.32×10^{-4}
2	QUtIP.rand.unitary.haar	75.51	24.49	2.56×10^{-4}	7.15×10^{-5}
4	QUtIP.rand.unitary.haar	71.24	28.76	4.38×10^{-5}	2.92×10^{-3}
8	QUtIP.rand.unitary.haar	70.21	29.79	1.27×10^{-5}	1.21×10^{-3}
16	QUtIP.rand.unitary.haar	99.95	0.05	7.98×10^{-4}	1.36×10^{-3}

Table I: Proportions of Random Gates with and without Turning Points. 100000 gates were generated for each of the method and dimension pairs shown. The \mathcal{I}_{mono}^* (%) and \mathcal{I}_{over}^* columns show the percentages of gates falling into either of the two categories: (1) monotonic growth, and (2) overshooting behaviour. The column ϵ_{rel} gives the relative error between the measured mean of the overall data $\mathbb{E}(\mathcal{I}_{total}^*)$ and the expected mean $\bar{\mathcal{I}}^* = 1 - \frac{1}{d}$ for the calculated AGI plateau values, given by $\epsilon_{rel} = \left| \frac{\mathbb{E}(\mathcal{I}_{total}^*) - \bar{\mathcal{I}}^*}{\bar{\mathcal{I}}^*} \right|$. The quantity D_{KL} is the Kullback-Leibler divergence measuring the relative entropy between the distribution $p(\mathcal{I}_{total}^*)$ and the reference distribution: $D_{KL}(p(\mathcal{I}_{total}^*) || u(\mathcal{I}_{min}^*, \mathcal{I}_{max}^*))$ for $d = 2$ uniform and $D_{KL}(p(\mathcal{I}_{total}^*) || f(\mathcal{I}^*; \mathcal{I}_0^*, k, \lambda))$ for $d > 2$ Weibull.

fore, substituting these two expressions,

$$|\mathcal{I}(U) - \mathcal{I}(U')| \leq \frac{2}{d+1} \|U - U'\|_F, \quad (C11)$$

and thus \mathcal{I} is Lipschitz with $L = \frac{2}{d+1}$. \square

Now, we can apply this result for \mathcal{I} in conjunction with Levy's Lemma extended to the classical compact group $U(d)$ [53], which we restate here without proof:

Theorem C.1. *Let $f : X \rightarrow \mathbb{R}$ be L -Lipschitz continuous with Lipschitz constant L , and let X be an element of one of the compact classical groups. Then, for each $t > 0$,*

$$\mathbb{P}[|f(X) - \mathbb{E}[f(X)]| \geq t] \leq e^{-\frac{(d-2)t^2}{24L^2}}. \quad (C12)$$

Using our result for \mathcal{I} , we have that

$$\mathbb{P}[|\mathcal{I}(U) - \mathbb{E}[\mathcal{I}(U)]| \geq t] \leq e^{-\frac{(d-2)(d+1)^2 t^2}{96}}. \quad (C13)$$

This therefore confirms our observation of the concentration of measure phenomenon in Fig. 16; it tells us that the probability of observing a gate whose infidelity is further than t from the expectation value of the AGI decays exponentially in the distance t^2 and the dimensionality $(d-2)(d+1)^2$ of the system.

For the case $d = 2$, the exponent is zero and thus the probability is constant for all t and so we see in Fig. 16a that the AGI plateau values are uniformly distributed. However, as $d > 2$ for Figs. 16b to 16d, the \mathcal{I}^* become exponentially concentrated about the mean $\bar{\mathcal{I}}^*$.

This could also account for the fluctuation in the ratios of $\mathcal{I}_{mono}^*/\mathcal{I}_{over}^*$ at different system sizes. However, further work is needed to elucidate the precise reasons for these observations.

3. Power-law behaviour of the saturation points of the AGI

As shown in Fig. 5 in Sec. IID, the saturation points $(\gamma t)^*$ of the AGIs for the interpolated X^η gates were

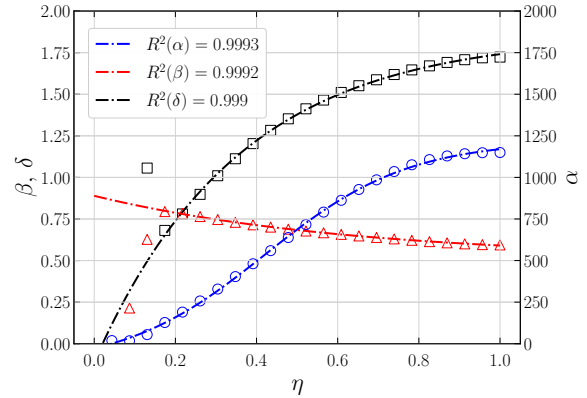


Figure 17: Fitted power-law model parameters as functions of η for the saturation points $(\gamma t)^*$ of the X^η gates. AGIs for X^η with $\eta \in (0, 1]$ for $d \in [2, 12]$. Saturation points $(\gamma t)^*$ were calculated by interpolation and root-finding. A power law model was fitted with parameters $\alpha(\eta)$ (blue, circles), $\beta(\eta)$ (red, triangles), and $\delta(\eta)$ (black, squares) were then fitted to sigmoidal and exponential models (dashed lines) as functions of η .

observed to follow a power-law model described by Eq. (47). The initial analysis was performed for each gate in a range of values $\eta = (0, 1]$ for $d \in [2, 12]$ by: (1) computing the AGIs numerically for a range of γt values in PYTHON using QUtIP's propagator and process fidelity methods, (2) interpolating the AGI curves using SCIPY.interpolate.CubicSpline, and (3) finding the plateau saturation points $(\gamma t)^*$ by root-finding with SCIPY.optimize.root_scalar.

Then, this three-parameter power law model in Eq. (47) was fitted on $(\gamma t)^*$ as a function of d for each η curve by nonlinear least-squares regression using the SCIPY.optimize.curve_fit method. This produced three sets of data for the fitted parameters α , β , γ as functions of η . These three curves were

then themselves fitted to their respective sigmoidal and exponential models in Eqs. (48) to (50), using the same `SciPy.optimize.curve_fit` method. The models showed good agreement with the data, with $R^2(\alpha) = 0.9992$, $R^2(\beta) = 0.9992$ and $R^2(\delta) = 0.9989$.

The fitted data points and resulting models are shown in Fig. 17. We note that the outliers at small values of η (including $\eta = 0$ for the identity gate with constant $(\gamma t)^*$) are due to the near-constant saturation point values of these gates over the range of d , which slowly transition towards more power-law-like behaviour as η increases. For example, for $\eta = 0$ the saturation point is constant in d , giving a horizontal line. Fitting a power-law curve to this dataset was possible but required unrealistic fit parameters like $\alpha \sim 10^{50}$. Nevertheless, this analysis hints at a potential approach for estimating the saturation points based only on the parameter η , without requiring the explicit numerical simulation.

4. Time dependence of the second-order correction to the AGI

As alluded to in Fig. 9 in Sec. II E, the convergence of the second-order (gate-dependent) AGI correction term as a function of t was observed to be linear in Eq. (62). More specifically, the number of iterations s_ε required to reach convergence of two successive terms in the summation Eq. (59) was calculated according to Eqs. (60) and (61).

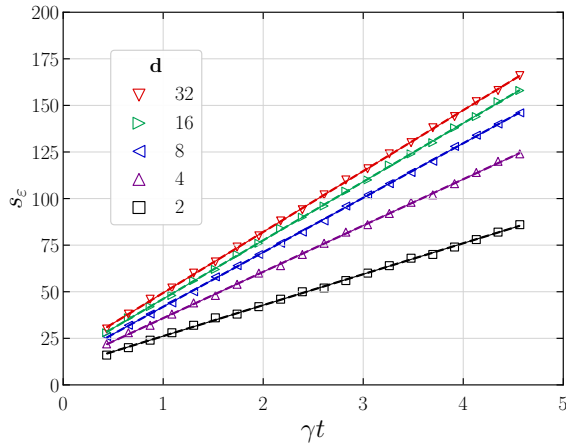


Figure 18: Linear regression fits of the critical order s_ε over gate time t for the X gate. The X gate ($\eta = 1$) was simulated for dimensions $d \in \{2, 4, 8, 16, 32\}$ over gate times $\gamma t \in [0.5, 4.5]$ with $\gamma = 1$ fixed. The second-order gate-dependent correction term was calculated at each t for increasing order s in the summation until convergence between successive terms was obtained at the critical value s_ε . For each d , a linear model was fitted to the data as shown by the dotted lines.

To understand the time-dependence of this, for each of the η and d values shown in Fig. 9, the critical s_ε was computed for a range of times $t \in [0, 5]$ with γ fixed at 1. Interestingly, we can see that in Fig. 18 the s_ε does indeed appear linear in t for each dimension shown for the X gate. This behaviour extends to other η values too. Therefore, a linear least-squares regression was performed on these data points using the `SciPy.optimize.curve_fit`; the resulting fitted models are shown in Fig. 18 alongside the data points, indicating good agreement. The resulting gradients $m = \frac{ds_\varepsilon}{dt}$ for each fitted curve are thus the data shown in Fig. 9.

- [1] O. Ezratty, Perspective on superconducting qubit quantum computing, *The European Physical Journal A* **59**, 94 (2023).
- [2] N. P. De Leon, K. M. Itoh, D. Kim, K. K. Mehta, T. E. Northup, H. Paik, B. S. Palmer, N. Samarth, S. Sangtawesin, and D. W. Steuerman, Materials challenges and opportunities for quantum computing hardware, *Science* **372**, eabb2823 (2021).
- [3] E. Moreno-Pineda, C. Godfrin, F. Balestro, W. Wernsdorfer, and M. Ruben, Molecular Spin Qudits for Quantum Algorithms, *Chemical Society Reviews* **47**, 501 (2018).
- [4] E. Moreno-Pineda and W. Wernsdorfer, Measuring molecular magnets for quantum technologies, *Nature Reviews Physics* **3**, 645 (2021).
- [5] Y. Chi, J. Huang, Z. Zhang, J. Mao, Z. Zhou, X. Chen, C. Zhai, J. Bao, T. Dai, H. Yuan, M. Zhang, D. Dai, B. Tang, Y. Yang, Z. Li, Y. Ding, L. K. Oxenl we, M. G. Thompson, J. L. O'Brien, Y. Li, Q. Gong, and J. Wang, A programmable qudit-based quantum processor, *Nature Communications* **13**, 1166 (2022).
- [6] M. Ringbauer, M. Meth, L. Postler, R. Stricker, R. Blatt, P. Schindler, and T. Monz, A universal qudit quantum processor with trapped ions, *Nature Physics* **18**, 1053 (2022).
- [7] Y. Wang, Z. Hu, B. C. Sanders, and S. Kais, Qudits and High-Dimensional Quantum Computing, *Frontiers in Physics* **8**, 589504 (2020).
- [8] A. Chiesa, F. Petiziol, E. Macaluso, S. Wimberger, P. Santini, and S. Carretta, Embedded quantum-error correction and controlled-phase gate for molecular spin qubits, *AIP Advances* **11**, 025134 (2021).
- [9] F. Petiziol, A. Chiesa, S. Wimberger, P. Santini, and S. Carretta, Counteracting dephasing in Molecular Nanomagnets by optimized qudit encodings, *npj Quantum Information* **7**, 133 (2021).
- [10] H. Miyahara, Y. Chen, V. Roychowdhury, and L.-S. Bouchard, Decoherence mitigation by embedding a logical qubit in a qudit, *Quantum Information Processing* **22**, 278 (2023).
- [11] L. G. Gunderman, Local-dimension-invariant qudit stabilizer codes, *Physical Review A* **101**, 052343 (2020).
- [12] W. Wernsdorfer and M. Ruben, Synthetic Hilbert Space Engineering of Molecular Qudits: Isotopologue Chemistry, *Advanced Materials* **31**, 1806687 (2019).
- [13] Y. Zheng, H. Sharma, and J. Borregaard, Entanglement Distribution with Minimal Memory Requirements Using Time-Bin Photonic Qudits, *PRX Quantum* **3**, 040319 (2022).
- [14] F. Bouchard, R. Fickler, R. W. Boyd, and E. Karimi, High-dimensional quantum cloning and applications to quantum hacking, *Science Advances* **3**, e1601915 (2017).
- [15] N. P. Brusentsov and J. Ramil Alvarez, Ternary Computers: The Setun and the Setun 70, in *Perspectives on Soviet and Russian Computing*, Vol. 357, edited by J. Impagliazzo and E. Proydakov (Springer Berlin Heidelberg, Berlin, Heidelberg, 2011) pp. 74–80, series Title: IFIP Advances in Information and Communication Technology.
- [16] S. Boixo, S. V. Isakov, V. N. Smelyanskiy, R. Babbush, N. Ding, Z. Jiang, M. J. Bremner, J. M. Martinis, and H. Neven, Characterizing quantum supremacy in near-term devices, *Nature Physics* **14**, 595 (2018).
- [17] F. Arute, K. Arya, R. Babbush, D. Bacon, J. C. Bardin, R. Barends, R. Biswas, S. Boixo, F. G. S. L. Brandao, D. A. Buell, B. Burkett, Y. Chen, Z. Chen, B. Chiaro, R. Collins, W. Courtney, A. Dunsworth, E. Farhi, B. Foxen, A. Fowler, C. Gidney, M. Giustina, R. Graff, K. Guerin, S. Habegger, M. P. Harrigan, M. J. Hartmann, A. Ho, M. Hoffmann, T. Huang, T. S. Humble, S. V. Isakov, E. Jeffrey, Z. Jiang, D. Kafri, K. Kechedzhi, J. Kelly, P. V. Klimov, S. Knysh, A. Korotkov, F. Kostritsa, D. Landhuis, M. Lindmark, E. Lucero, D. Lyakh, S. Mandr , J. R. McClean, M. McEwen, A. Megrant, X. Mi, K. Michielsen, M. Mohseni, J. Mutus, O. Naaman, M. Neeley, C. Neill, M. Y. Niu, E. Ostby, A. Petukhov, J. C. Platt, C. Quintana, E. G. Rieffel, P. Roushan, N. C. Rubin, D. Sank, K. J. Satzinger, V. Smelyanskiy, K. J. Sung, M. D. Trevithick, A. Vainsencher, B. Villalonga, T. White, Z. J. Yao, P. Yeh, A. Zalcman, H. Neven, and J. M. Martinis, Quantum supremacy using a programmable superconducting processor, *Nature* **574**, 505 (2019).
- [18] C. Godfrin, A. Ferhat, R. Ballou, S. Klyatskaya, M. Ruben, W. Wernsdorfer, and F. Balestro, Operating Quantum States in Single Magnetic Molecules: Implementation of Grover's Quantum Algorithm, *Physical Review Letters* **119**, 187702 (2017).
- [19] S. Thiele, F. Balestro, R. Ballou, S. Klyatskaya, M. Ruben, and W. Wernsdorfer, Electrically driven nuclear spin resonance in single-molecule magnets, *Science* **344**, 1135 (2014).
- [20] M. Otten, K. Kapoor, A. B. "Ozg"  ler, E. T. Holland, J. B. Kowalkowski, Y. Alexeev, and A. L. Lyon, Impacts of noise and structure on quantum information encoded in a quantum memory, *Physical Review A* **104**, 012605 (2021).
- [21] D. Jankovi , J.-G. Hartmann, M. Ruben, and P.-A. Hervieux, Noisy qudit vs multiple qubits: conditions on gate efficiency for enhancing fidelity, *npj Quantum Information* **10**, 59 (2024).
- [22] M. A. Nielsen and I. L. Chuang, *Quantum computation and quantum information* (Cambridge University Press, Cambridge ; New York, 2000).
- [23] M. A. Nielsen, A simple formula for the average gate fidelity of a quantum dynamical operation, *Physics Letters A* **303**, 249 (2002).
- [24] G. Lindblad, On the generators of quantum dynamical semigroups, *Communications in Mathematical Physics* **48**, 119 (1976).
- [25] V. Gorini, A. Kossakowski, and E. C. G. Sudarshan, Completely positive dynamical semigroups of N -level systems, *Journal of Mathematical Physics* **17**, 821 (1976).
- [26] H.-P. Breuer and F. Petruccione, *The Theory of Open Quantum Systems*, 1st ed. (Oxford University Press Oxford, 2007).
- [27] D. Manzano, A short introduction to the Lindblad master equation, *AIP Advances* **10**, 025106 (2020).
- [28] J. Watrous, *The Theory of Quantum Information*, 1st ed. (Cambridge University Press, 2018).
- [29] I. Bengtsson and K. Życzkowski, *Geometry of Quantum States: An Introduction to Quantum Entanglement*, 1st

- ed. (Cambridge University Press, 2006).
- [30] T. F. Havel, Robust procedures for converting among Lindblad, Kraus and matrix representations of quantum dynamical semigroups, *Journal of Mathematical Physics* **44**, 534 (2003).
- [31] T. A. Loring, Computing a logarithm of a unitary matrix with general spectrum, *Numerical Linear Algebra with Applications* **21**, 744 (2014).
- [32] M. Aïfer and S. Deffner, From quantum speed limits to energy-efficient quantum gates, *New Journal of Physics* **24**, 055002 (2022).
- [33] A. Vourdas, Quantum systems with finite Hilbert space, *Reports on Progress in Physics* **67**, 267 (2004).
- [34] J. Martínez-Carranza, F. Soto-Eguibar, and H. Moya-Cessa, Alternative analysis to perturbation theory in quantum mechanics: Dyson series in matrix form, *The European Physical Journal D* **66**, 22 (2012).
- [35] B. M. Villegas-Martínez, F. Soto-Eguibar, and H. M. Moya-Cessa, Application of Perturbation Theory to a Master Equation, *Advances in Mathematical Physics* **2016**, 1 (2016).
- [36] J. E. Campbell, On a Law of Combination of Operators bearing on the Theory of Continuous Transformation Groups, *Proceedings of the London Mathematical Society* **s1-28**, 381 (1896).
- [37] B. C. Hall, *Lie groups, Lie algebras, and representations: an elementary introduction*, second edition ed., Graduate texts in mathematics No. 222 (Springer, Cham ; New York, 2015) oCLC: ocn910324548.
- [38] B. Collins, S. Matsumoto, and J. Novak, The Weingarten Calculus, *Notices of the American Mathematical Society* **69**, 1 (2022).
- [39] A. Chiesa, E. Macaluso, F. Petiziol, S. Wimberger, P. Santini, and S. Carretta, Molecular Nanomagnets as Qubits with Embedded Quantum-Error Correction, *The Journal of Physical Chemistry Letters* **11**, 8610 (2020).
- [40] M. Horodecki, P. Horodecki, and R. Horodecki, General teleportation channel, singlet fraction, and quasidistillation, *Physical Review A* **60**, 1888 (1999).
- [41] H. Volkin, U. S. N. Aeronautics, S. Administration, and L. R. Center, *Iterated commutators and functions of operators*, NASA technical note (National Aeronautics and Space Administration, 1968).
- [42] J.-G. Hartmann, D. Jankovic, R. Pasquier, M. Ruben, and P.-A. Hervieux, *Code and Data for "Nonlinearity of the Fidelity in Open Qudit Systems: Gate and Noise Dependence in High-dimensional Quantum Computing"* (2024).
- [43] F. Mezzadri, How to generate random matrices from the classical compact groups, *Notices of the American Mathematical Society* **54**, 592 (2007).
- [44] F. J. Dyson, The Threefold Way. Algebraic Structure of Symmetry Groups and Ensembles in Quantum Mechanics, *Journal of Mathematical Physics* **3**, 1199 (1962).
- [45] M. L. Mehta, *Random matrices*, 3rd ed., Pure and applied mathematics series No. 142 (Elsevier, Amsterdam, 2004) oCLC: 253930836.
- [46] E. P. Wigner, Characteristic Vectors of Bordered Matrices With Infinite Dimensions, *The Annals of Mathematics* **62**, 548 (1955).
- [47] J. Johansson, P. Nation, and F. Nori, QuTiP: An open-source Python framework for the dynamics of open quantum systems, *Computer Physics Communications* **183**, 1760 (2012).
- [48] J. Johansson, P. Nation, and F. Nori, QuTiP 2: A Python framework for the dynamics of open quantum systems, *Computer Physics Communications* **184**, 1234 (2013).
- [49] C. Developers, *Cirq* (2023).
- [50] M. Suezen, C. Weber, and J. J. Cerdà, *Spectral Ergodicity In Deep Learning Architectures Via Surrogate Random Matrices* (2017).
- [51] A. Giannopoulos and V. Milman, Concentration Property on Probability Spaces, *Advances in Mathematics* **156**, 77 (2000).
- [52] M. Ledoux, *The concentration of measure phenomenon*, Mathematical surveys and monographs No. Issue 89 (American Mathematical Society, 2001) oCLC: 880580292.
- [53] E. S. Meckes, *The Random Matrix Theory of the Classical Compact Groups*, 1st ed. (Cambridge University Press, 2019).

.1	Proofs for Section 9.5 (Timescales)	374
.2	Proofs for Section 11.1 (The Average Gate Infidelity: Definition and First-Order Approximation)	375
.3	Proofs for Section 12.2 (Perturbative expression of the AGI)	376
.4	Proofs for Section 12.3 (Universal bounds on the AGI for large noise and gate times) .	382
.5	Proofs for Section 13.2 (Quantum Speed Limits)	383
.6	Proofs for Section 14.2 (The T-M sequence in Quantum Computing)	384
.7	Proofs for Section 15.2 (Areas left to explore)	388

CHAPTER F

Proofs of the statements in the main text

.1 Proofs for Section (Timescales)

(Statement: $T_2 \leq 2T_1$)

Proof: Let's show if there is no pure dephasing $T_2 = 2T_1$.

A system with a given T_1 is generally modelled by the following master equation:

$$\rho(t) = E_0(t)\rho(0)E_0(t)^\dagger + E_1(t)\rho(0)E_1(t)^\dagger, \quad (1)$$

with $E_0(t) = \begin{pmatrix} 1 & 0 \\ 0 & e^{-t/2T_1} \end{pmatrix}$ and $E_1(t) = \begin{pmatrix} 0 & \sqrt{1 - e^{-t/T_1}} \\ 0 & 0 \end{pmatrix}$ where E_1 symbolises the possibility of going from $|1\rangle$ to $|0\rangle$ at time t , while E_0 symbolises the possibility of staying as it is at time t . We note that $E_0(t)E_0(t)^\dagger + E_1(t)E_1(t)^\dagger = \mathbb{1}_2$, respecting the condition on the Kraus operators. This leads to the following expression:

$$\rho(t) = \begin{pmatrix} \rho_{00}(0) + \rho_{11}(0)(1 - e^{-t/T_1}) & \rho_{01}(0)e^{-t/2T_1} \\ \rho_{10}(0)e^{-t/2T_1} & \rho_{11}(0)e^{-t/T_1} \end{pmatrix} \quad (2)$$

Where we can verify that $\rho_{11}(t) = \rho_{11}(0)e^{-t/T_1}$ as per the definition of T_1 , but also that $\rho_{01}(t) = \rho_{01}(0)e^{-t/2T_1}$. This concludes that in the absence of any other noise, $T_2 = 2T_1$.

If we add a purely dephasing channel, with characteristic time T_ϕ , then the coherences would decay with $\rho_{01}(t) = \rho_{01}(0)e^{-t/2T_1}e^{-t/T_\phi}$, leading to

$$1/T_2 = 1/2T_1 + 1/T_\phi,$$

proving the inequality.

The Bloch Sphere representations in Fig. 9.8 can also give an intuitive reason for $T_2 = 2T_1$, as longitudinal relaxation also leads to a reduction of the radius of the Bloch Sphere's surface, like for pure dephasing in Fig. 9.10.

(Statement: $|\langle +|\psi(t)\rangle|^2 = \frac{1}{2} \left(1 + \overline{\cos \left(\int_0^t \delta(t') dt' \right)} \right) = \frac{1}{2} (1 + e^{-t/\tau})$)

Proof: We have

$$\begin{aligned} \langle +|\psi(t)\rangle &= \frac{1}{2} \langle +| \left(|0\rangle + \exp \left(-i \int_0^t \delta(t') dt' \right) |1\rangle \right) = \frac{1}{2} \left(1 + \exp \left(-i \int_0^t \delta(t') dt' \right) \right) \\ |\langle +|\psi(t)\rangle|^2 &= \frac{1}{4} \left| 1 + \exp \left(-i \int_0^t \delta(t') dt' \right) \right|^2 = \frac{1}{4} \left(\left(1 + \cos \left(\int_0^t \delta(t') dt' \right) \right)^2 + \sin^2 \left(\int_0^t \delta(t') dt' \right) \right) \\ &= \frac{1}{2} \left(1 + \cos \left(\int_0^t \delta(t') dt' \right) \right). \end{aligned} \quad (3)$$

If we consider δ to be a Gaussian noise of variance σ , then its integral during time t is a 1D Brownian motion, W_t , of variance σt . Moreover, starting from the characteristic function of W_t being $\phi(t) = \mathbb{E}[e^{itW_t}] = e^{-t^2/2}$, one can show that $\mathbb{E}[\cos(W_t)] = e^{-t\sigma/2}$, yielding, for $\sigma = \frac{2}{\tau}$, the final result

$$\mathbb{E}[\langle +|\psi(t)\rangle] = \frac{1}{2} (1 + e^{-t/\tau}). \quad (4)$$

.2 Proofs for Section (The Average Gate Infidelity: Definition and First-Order A

(Statement: *Fluctuation Dissipation Relation for the Infidelity of a perturbed pure state*)

Proof: Substituting (11.3) and (11.2) into (11.6) and (11.5) leads to

$$\mathcal{E}(\rho^*) = \gamma t \left(\frac{1}{2} \text{Tr} \left(\rho^* \{L^\dagger L, \rho^*\} \right) - \text{Tr} \left(\rho^* L \rho^* L^\dagger \right) \right) + \mathcal{O}((\gamma t)^2). \quad (5)$$

The trace being invariant by cyclic permutations and $\rho^{*2} = \rho^*$ leads to the simplification

$$\frac{1}{2} \text{Tr} \left(\rho^* \{L^\dagger L, \rho^*\} \right) = \text{Tr} \left(\rho^* L^\dagger L \right) \equiv \langle L^\dagger L \rangle_*. \quad (6)$$

Moreover

$$\text{Tr} \left(\rho^* L \rho^* L^\dagger \right) = \text{Tr} \left(|\varphi^*\rangle \langle \varphi^*| L |\varphi^*\rangle \langle \varphi^*| L^\dagger \right) \quad (7)$$

$$= \langle L \rangle_* \text{Tr} \left(\rho^* L^\dagger \right) \quad (8)$$

$$= \langle L^\dagger \rangle_* \langle L \rangle_* . \quad (9)$$

Accounting for the above results, one finally obtains

$$\mathcal{E}(\rho^*) = \gamma t \left(\langle L^\dagger L \rangle_* - \langle L^\dagger \rangle_* \langle L \rangle_* \right) + \mathcal{O}((\gamma t)^2), \quad (10)$$

which can be rewritten as (11.7).

(Statement: $\int d\rho \Delta L = \frac{1}{d+1} \text{Tr}(L^\dagger L) - \frac{1}{d(d+1)} |\text{Tr}(L)|^2$)

Proof: First, rewriting $\int d\rho \text{Tr}(\rho M^\dagger M)$ yields

$$\int dU \text{Tr}(U \rho U^\dagger M^\dagger M) = \text{Tr} \left[\left(\int dU U \rho U^\dagger \right) M^\dagger M \right]$$

, where the integration is performed over the uniform Haar measure in the space of unitaries. Using the identity

$$\int dU U X U^\dagger = \frac{\text{Tr}(X) I}{d}$$

valid for any linear operator X , for the special case of ρ pure one obtains

$$\int d\rho \text{Tr}(\rho M^\dagger M) = \frac{1}{d} \text{Tr}(M^\dagger M). \quad (11)$$

Now, rewriting $\int d\rho \text{Tr}(\rho M^\dagger M)$ yields

$$\begin{aligned} \int dU \text{Tr}(U \rho U^\dagger M) &= \\ \sum_{\substack{i,j,k,l \\ m,n,p,q}} \int dU U_{ij} U_{kl} \bar{U}_{mn} \bar{U}_{pq} \rho_{jn} \rho_{\ell q} M_{mi} M_{pk}. \end{aligned}$$

Collins [193] provide formulae to integrate polynomials of unitary matrices

$$\begin{aligned} \int_{U_d} dU U_{ij} U_{k\ell} \bar{U}_{mn} \bar{U}_{pq} = \\ \frac{1}{d^2 - 1} \left[(\delta_{im} \delta_{jn} \delta_{kp} \delta_{\ell q} + \delta_{ip} \delta_{jq} \delta_{km} \delta_{\ell n}) \right. \\ \left. - \frac{1}{d} (\delta_{im} \delta_{jq} \delta_{kp} \delta_{\ell n} + \delta_{ip} \delta_{jn} \delta_{km} \delta_{\ell q}) \right], \end{aligned} \quad (12)$$

which contracting the indices gives

$$\int d\rho |\text{Tr}(\rho M)|^2 = \frac{1}{d(d+1)} \left(\text{Tr}(M^\dagger M) + |\text{Tr}(M)|^2 \right).$$

Finally subtracting Appendix .2 from (11) leads to (11.32).

.3 Proofs for Section (Perturbative expression of the AGI)

(Statement: *See below*)

Proof: To prove that

$$\begin{aligned} \tilde{M}^{(m)}(t) &\equiv \int_0^t \cdots \int_0^{t_{m-1}} \left(\prod_{i=1}^m e^{-S t_i} \mathcal{L} e^{S t_i} \right) dt_m \cdots dt_1 \\ &= t^m \sum_{n_1, \dots, n_m=0}^{\infty} \left(\prod_{i=1}^m \frac{(-t)^{n_i} [(\mathcal{S})^{n_i}, \mathcal{L}]}{n_i! \sum_{j=i}^m (n_j + 1)} \right), \end{aligned} \quad (13)$$

we make use of Campbell's lemma, based on the Baker-Campbell-Hausdorff Formula [207, 208], as stated in (12.30) in the main text,

$$e^X Y e^{-X} = \sum_{n=0}^{\infty} \frac{[(X)^n, Y]}{n!}, \quad (14)$$

with $[(X)^n, Y] = [X, [(X)^{n-1}, Y]]$ and $[(X)^0, Y] = Y$, and proceed with proof by induction.

Base Case: To first-order, $m = 1$,

$$\begin{aligned} \int_0^t e^{-S t_1} \mathcal{L} e^{S t_1} dt_1 &= \int_0^t \sum_{n_1=0}^{\infty} \frac{[(-S t_1)^{n_1}, \mathcal{L}]}{n_1!} dt_1 \\ &= \sum_{n_1=0}^{\infty} \frac{(-1)^{n_1}}{n_1!} [(\mathcal{S})^{n_1}, \mathcal{L}] \int_0^t t_1^{n_1} dt_1 \\ &= t \sum_{n_1=0}^{\infty} \frac{(-t)^{n_1} [(\mathcal{S})^{n_1}, \mathcal{L}]}{n_1! (n_1 + 1)} \\ &= \tilde{M}^{(1)}(t). \end{aligned}$$

Induction Step: Assume that the result in (13) holds at m -th order, and relabel indices

$t, t_1, \dots, t_{m-1} \rightarrow t_1, t_2, \dots, t_m$ and $t \rightarrow t_1$:

$$\begin{aligned}\tilde{M}^{(m)}(t_1) &= \int_0^{t_1} \dots \int_0^{t_m} \left(\prod_{i=2}^{m+1} e^{-S t_i} \mathcal{L} e^{S t_i} \right) dt_{m+1} \dots dt_2 \\ &= t_1^m \sum_{n_2=0}^{\infty} \dots \sum_{n_{m+1}=0}^{\infty} \left(\prod_{i=2}^{m+1} \frac{(-t_1)^{n_i} [(\mathcal{S})^{n_i}, \mathcal{L}]}{n_i! \sum_{j=i}^{m+1} (n_j + 1)} \right).\end{aligned}$$

Then, to order $m + 1$,

$$\begin{aligned}& \int_0^t \tilde{M}^{(m)}(t_1) (e^{-S t_1} \mathcal{L} e^{S t_1}) dt_1 \\ &= \int_0^t \left(t_1^m \sum_{n_2=0}^{\infty} \dots \sum_{n_{m+1}=0}^{\infty} \prod_{i=2}^{m+1} \frac{(-t_1)^{n_i} [(\mathcal{S})^{n_i}, \mathcal{L}]}{n_i! \sum_{j=i}^{m+1} (n_j + 1)} \right) \left(\sum_{n_1=0}^{\infty} \frac{(-t_1)^{n_1} [(\mathcal{S})^{n_1}, \mathcal{L}]}{n_1!} \right) dt_1 \\ &= \sum_{n_2=0}^{\infty} \dots \sum_{n_{m+1}=0}^{\infty} \frac{(-1)^{n_1} [(\mathcal{S})^{n_1}, \mathcal{L}]}{n_1!} \prod_{i=2}^{m+1} \left(\frac{(-1)^{n_i} [(\mathcal{S})^{n_i}, \mathcal{L}]}{n_i! \sum_{j=i}^{m+1} (n_j + 1)} \right) \int_0^t t_1^m t_1^{n_1} \prod_{i=2}^{m+1} t_1^{n_i} dt_1 \\ &= \sum_{n_2=0}^{\infty} \dots \sum_{n_{m+1}=0}^{\infty} \frac{(-1)^{n_1} [(\mathcal{S})^{n_1}, \mathcal{L}]}{n_1!} \prod_{i=2}^{m+1} \left(\frac{(-1)^{n_i} [(\mathcal{S})^{n_i}, \mathcal{L}]}{n_i! \sum_{j=i}^{m+1} (n_j + 1)} \right) \frac{t^{m+1 + \sum_{i=1}^{m+1} n_i}}{m + 1 + \sum_{j=1}^{m+1} n_j} \\ &= t^{m+1} \sum_{n_2=0}^{\infty} \dots \sum_{n_{m+1}=0}^{\infty} \frac{(-t)^{n_1} [(\mathcal{S})^{n_1}, \mathcal{L}]}{n_1! \sum_{j=1}^{m+1} (n_j + 1)} \prod_{i=2}^{m+1} \frac{(-t)^{n_i} [(\mathcal{S})^{n_i}, \mathcal{L}]}{n_i! \sum_{j=i}^{m+1} (n_j + 1)} \\ &= t^{m+1} \sum_{n_2=0}^{\infty} \dots \sum_{n_{m+1}=0}^{\infty} \prod_{i=1}^{m+1} \frac{(-t)^{n_i} [(\mathcal{S})^{n_i}, \mathcal{L}]}{n_i! \sum_{j=i}^{m+1} (n_j + 1)} \\ &= \tilde{M}^{(m+1)}(t),\end{aligned}$$

hence completing the proof by induction.

(Statement: *See below*)

Proof: One can prove that

$$\begin{aligned}\sum_{n_1=1}^{\infty} \sum_{n_2=1}^{\infty} \frac{(-t)^{n_1+n_2} \text{Tr}([(\mathcal{S})^{n_1}, \mathcal{L}][(\mathcal{S})^{n_2}, \mathcal{L}])}{n_1!(n_2+1)!(n_1+n_2+2)} \\ = \sum_{\substack{s=2 \\ s \text{ even}}}^{\infty} \text{Tr}(\mathcal{L} [(\mathcal{S})^s, \mathcal{L}]) \frac{(-t)^s}{(s+2)!}.\end{aligned}\tag{15}$$

by proving the following lemma.

Lemma: Given operators A and B the following binomial sum of the product of iterated commutators at order n and $j - n$ is traceless,

$$\sum_{n=1}^j \binom{j+1}{n} \text{Tr}([(A)^n, B][(A)^{j-n}, B]) = 0.\tag{16}$$

Proof of the lemma: Using $\binom{j+1}{n} = \binom{j+1-1}{n-1} + \binom{j+1-1}{n}$, we have

$$\begin{aligned} & \sum_{n=1}^j \binom{j+1}{n} \text{Tr}([(A)^n, B][(A)^{j-n}, B]) \\ &= \sum_{n=1}^j \binom{j}{n-1} \text{Tr}([(A)^n, B][(A)^{j-n}, B]) + \\ &+ \sum_{n=1}^j \binom{j}{n} \text{Tr}([(A)^n, B][(A)^{j-n}, B]). \end{aligned} \quad (17)$$

Now, for the first term with binomial $\binom{j+1}{n-1}$ and using the change of index $n = n + 1$,

$$\begin{aligned} & \sum_{n=1}^j \binom{j}{n-1} \text{Tr}([(A)^n, B][(A)^{j-n}, B]) \\ &= \sum_{n=0}^{j-1} \binom{j}{n} \text{Tr}([(A)^{n+1}, B][(A)^{j-n-1}, B]) \\ &= \sum_{n=0}^{j-1} \binom{j}{n} \text{Tr}([A, [(A)^n, B]][(A)^{j-n-1}, B]) \\ &= - \sum_{n=0}^{j-1} \binom{j}{n} \text{Tr}([(A)^n, B][(A)^{j-n}, B]), \end{aligned} \quad (18)$$

by cyclic permutation of the trace. This summation is the negation of the second binomial term $\binom{j+1-1}{n}$ for all terms $1 \leq n \leq j-1$. Therefore only the $n=0$ and $n=j$ terms remain. Moreover since $\binom{j}{j} = \binom{j}{0} = 1$, we have that

$$\begin{aligned} & \sum_{n=1}^j \binom{j+1}{n} \text{Tr}([(A)^n, B][(A)^{j-n}, B]) \\ &= \text{Tr}([(A)^j, B]B) - \text{Tr}(B[(A)^j, B]) \\ &= 0. \end{aligned} \quad (19)$$

In our specific case, we have

$$\sum_{n_1=1}^{\infty} \sum_{n_2=1}^{\infty} \frac{(-t)^{n_1+n_2} \text{Tr}([(S)^{n_1}, \mathcal{L}][(S)^{n_2}, \mathcal{L}])}{n_1!n_2!(n_1+n_2+2)(n_2+1)} \quad (20)$$

$$= \sum_{s=0}^{\infty} \sum_{n=0}^{s-2} \frac{(-t)^{s-2} \text{Tr}([(S)^n, \mathcal{L}][(S)^{s-2-n}, \mathcal{L}])}{n!s(s-1-n)!} \quad (21)$$

$$= \sum_{s=0}^{\infty} \frac{(-t)^{s-2}}{s(s-1)!} \sum_{n=0}^{s-2} \binom{s-1}{n} \text{Tr}([(S)^n, \mathcal{L}][(S)^{s-2-n}, \mathcal{L}]). \quad (22)$$

Now, applying the lemma to (22), where we identify $j = s-2$, we have that all terms for $n \geq 1$ are zero, and therefore only the $n=0$ term survives giving the following relation

$$\sum_{n=0}^{s-2} \binom{s-1}{n} \text{Tr}([(S)^n, \mathcal{L}][(S)^{s-2-n}, \mathcal{L}]) = \text{Tr}(\mathcal{L}[(S)^{s-2}, \mathcal{L}]). \quad (23)$$

From this, with a change of index $s - 2 = s$, we can rewrite the full second-order correction as

$$\mathcal{I}^{(2)} = \frac{-(\gamma t)^2}{d(d+1)} \left(\frac{\text{Tr}(\mathcal{L}^2)}{2} + \sum_{s=2}^{\infty} \frac{(-t)^s \text{Tr}(\mathcal{L}[(\mathcal{S})^s, \mathcal{L}])}{(s+2)!} \right), \quad (24)$$

giving the expected result.

Moreover, another useful lemma states

Lemma: Given two operators A and B , the product of B with the iterated commutator of order s , $B[(A)^s, B]$, is traceless for all odd s ,

$$\forall s = 2k + 1, k \in \mathbb{Z}, \text{Tr}(B[(A)^s, B]) = 0. \quad (25)$$

Proof of the lemma: We begin with the trace of the binomial expansion of the iterated commutator [volkin1968iterated],

$$B[(A)^s, B] = \sum_{k=0}^s (-1)^k \binom{s}{k} B A^{s-k} B A^k \quad (26)$$

$$\therefore \text{Tr}(B[(A)^s, B]) = \sum_{k=0}^s (-1)^k \binom{s}{k} \text{Tr}(B A^{s-k} B A^k). \quad (27)$$

By symmetry of the binomial expansion $\binom{s}{k} = \binom{s}{s-k}$, and considering s odd $(-1)^{s-k} = -(-1)^k$, we can write the equivalent expansion

$$B[(A)^s, B] = - \sum_{k=0}^s (-1)^k \binom{s}{k} B A^k B A^{s-k} \quad (28)$$

$$\therefore \text{Tr}(B[(A)^s, B]) = - \sum_{k=0}^s (-1)^k \binom{s}{k} \text{Tr}(B A^k B A^{s-k}) \quad (29)$$

$$= - \sum_{k=0}^s (-1)^k \binom{s}{k} \text{Tr}(B A^{s-k} B A^k), \quad (30)$$

by cyclic permutation of the trace, $\text{Tr}(CD) = \text{Tr}(DC) \implies \text{Tr}([C, D]) = 0$. Hence, we have the result for odd s that

$$\text{Tr}(B[(A)^s, B]) = - \text{Tr}(B[(A)^s, B]) \quad (31)$$

$$\implies \text{Tr}(B[(A)^s, B]) = 0, \quad (32)$$

thus completing the proof.

(Statement: *Operator form of the second order gate-dependent term*)

Proof: Beginning with the binomial expansion of the trace of the iterated commutator [263],

$$\begin{aligned}
 & \text{Tr}(\mathcal{L}[(\mathcal{S})^s, \mathcal{L}]) \\
 &= \sum_{k=0}^s (-1)^k \binom{s}{k} \text{Tr}(\mathcal{L} \mathcal{S}^k \mathcal{L} \mathcal{S}^{s-k}) \\
 &= i^s \sum_{k=0}^s \sum_{j=0}^k \sum_{l=0}^{s-k} \binom{s}{k} \binom{k}{j} \binom{s-k}{l} (-1)^{s+k-j-l} \times \\
 & \quad \times \text{Tr}(\mathcal{L}((H^*)^{k-j} \otimes H^j) \mathcal{L}((H^*)^{s-k-l} \otimes H^l)), \tag{33}
 \end{aligned}$$

where we used the binomial expansion of the expression for \mathcal{S} in terms of H

$$\mathcal{S}^k = i^k \sum_{j=0}^k (-1)^{k-j} \binom{k}{j} (H^*)^{k-j} \otimes H^j. \tag{34}$$

Substituting now the expression for \mathcal{L} in terms of L and expanding algebraically the products of the operator terms in the trace, we obtain the following nine expressions, the sum of which is equivalent to the superoperator trace (omitting the prefactors and summations for convenience):

$$\text{Tr}(LH^{k-j} LH^{s-k-l})^* \text{Tr}(LH^j LH^l), \tag{35}$$

$$-\frac{1}{2} \text{Tr}(LH^{k-j} L^T L^* H^{s-k-l})^* \text{Tr}(LH^{j+l}), \tag{36}$$

$$-\frac{1}{2} \text{Tr}(LH^{s-j-l})^* \text{Tr}(LH^j L^T L^* H^l), \tag{37}$$

$$-\frac{1}{2} \text{Tr}(L^T L^* H^{k-j} LH^{s-k-l})^* \text{Tr}(LH^{j+l}), \tag{38}$$

$$\frac{1}{4} \text{Tr}(L^T L^* H^{k-j} L^T L^* H^{s-k-l})^* \text{Tr}(H^{j+l}), \tag{39}$$

$$\frac{1}{4} \text{Tr}(L^T L^* H^{s-j-l})^* \text{Tr}(L^T L^* H^{j+l}), \tag{40}$$

$$-\frac{1}{2} \text{Tr}(LH^{s-j-l})^* \text{Tr}(L^\dagger LH^j LH^l), \tag{41}$$

$$\frac{1}{4} \text{Tr}(L^T L^* H^{s-j-l})^* \text{Tr}(L^\dagger LH^{j+l}), \tag{42}$$

$$\frac{1}{4} \text{Tr}(H^{s-j-l})^* \text{Tr}(L^\dagger LH^j L^T L^* H^l). \tag{43}$$

Now, we can simplify these expressions by making the following observations: Firstly, s must be even since (i) heuristically, the trace must be real since we are calculating the fidelity (a real quantity) and therefore the prefactor i^s in (33) cannot be imaginary, and (ii) formally we prove this in ???. Secondly, by symmetry of the binomial expansions, we are free to make the following change of variables:

$$\begin{aligned}
 j &\rightarrow k - j, \\
 l &\rightarrow s - k - l.
 \end{aligned}$$

For clarity, note that this change of variables does not affect the prefactor

$$(-1)^{s+k-j-l} \rightarrow (-1)^{j+k+l},$$

since, with s even, the ratio of these two terms is always a power of 2 and therefore equal to 1. As an example to illustrate the effect of this change of variables, for the first term (35), the forward and backwards sums are complex conjugates and therefore only the real part can remain (omitting prefactors of the full expression):

$$\sum_{j=0}^k \sum_{l=0}^{s-k} \text{Tr}(LH^{k-j} LH^{s-k-l})^* \text{Tr}(LH^j LH^l) \rightarrow \sum_{j=0}^k \sum_{l=0}^{s-k} \text{Tr}(LH^j LH^l)^* \text{Tr}(LH^{k-j} LH^{s-k-l}) \quad (44)$$

$$\Rightarrow \sum_{j=0}^k \sum_{l=0}^{s-k} \text{Tr}(LH^{k-j} LH^{s-k-l})^* \text{Tr}(LH^j LH^l) = \sum_{j=0}^k \sum_{l=0}^{s-k} \text{Re}\left\{ \text{Tr}(LH^{k-j} LH^{s-k-l})^* \text{Tr}(LH^j LH^l) \right\}. \quad (45)$$

Similarly, by comparing the remaining terms in (36) to (43) with their counterparts following the change of variables, it is possible to identify the following sums as complex conjugates of one another:

$$\begin{aligned} \sum_{j=0}^k \sum_{l=0}^{s-k} (36 + 37) &= \sum_{j=0}^k \sum_{l=0}^{s-k} 2 \text{Re}\{36\}, \\ \sum_{j=0}^k \sum_{l=0}^{s-k} (38 + 41) &= \sum_{j=0}^k \sum_{l=0}^{s-k} 2 \text{Re}\{38\}, \\ \sum_{j=0}^k \sum_{l=0}^{s-k} (40 + 42) &= \sum_{j=0}^k \sum_{l=0}^{s-k} 2 \text{Re}\{40\}, \\ \sum_{j=0}^k \sum_{l=0}^{s-k} (39 + 43) &= \sum_{j=0}^k \sum_{l=0}^{s-k} 2 \text{Re}\{39\}. \end{aligned}$$

Hence, by combining all of these terms into the full expression for $\text{Tr}(\mathcal{L}[(\mathcal{S})^s, \mathcal{L}])$ in (33), we obtain the expected result

$$\begin{aligned} &\text{Tr}(\mathcal{L}[(\mathcal{S})^s, \mathcal{L}]) \\ &= \sum_{k=0}^s \sum_{j=0}^k \sum_{l=0}^{s-k} \binom{s}{k} \binom{k}{j} \binom{s-k}{l} (-1)^{s+k-j-l} \times \\ &\quad \times \text{Re} \left[\text{Tr}(LH^{k-j} LH^{s-k-l})^* \text{Tr}(LH^j LH^l) \right. \\ &\quad + \frac{1}{2} \text{Tr}(L^T L^* H^{s-j-l})^* \text{Tr}(L^T L^* H^{j+l}) \\ &\quad + \frac{1}{2} \text{Tr}(L^T L^* H^{k-j} L^T L^* H^{s-k-l})^* \text{Tr}(H^{j+l}) \\ &\quad - \text{Tr}(LH^{k-j} L^T L^* H^{s-k-l})^* \text{Tr}(LH^{j+l}) \\ &\quad \left. - \text{Tr}(L^T L^* H^{k-j} LH^{s-k-l})^* \text{Tr}(LH^{j+l}) \right]. \quad (46) \end{aligned}$$

.4 Proofs for Section

(Universal bounds on the AGI for large noise and gate time)

(Statement: $0 \leq \sum_{k=0} |\text{Tr}(E_k)|^2 \leq d$)

Proof: Let M be a completely positive, trace-preserving superoperator, and let E_k be the Kraus operators of M .

In the Kraus representation, using $\text{vec}(M) = \sum_{k=1}^K E_k^* \otimes E_k$, the matrix elements are given, trivially, by

$$M_{ij}^{nm} = \sum_{k=1}^K E_{k,jm}^* E_{k,in}, \quad (47)$$

and, since $\sum_{k=1}^K E_k^\dagger E_k = \mathbb{1}$,

$$\forall n, m, \sum_{i=0}^{d-1} M_{ii}^{nm} = \sum_{k=1}^K \sum_{i=0}^{d-1} E_{k,im}^* E_{k,in} \quad (48)$$

$$= \delta_{nm}. \quad (49)$$

Furthermore, M is trace-preserving,

$$\text{Tr}(M\rho) = \text{Tr}(\rho) \quad (50)$$

$$\text{vec}(\mathbb{1})^T \cdot M \cdot \text{vec}(\rho) = \text{vec}(\mathbb{1})^T \cdot \text{vec}(\rho) \quad (51)$$

$$\therefore \sum_{n=0}^{d-1} M_{ij}^{nn} = \delta_{ij}. \quad (52)$$

Thus, in particular, if $i = j$:

$$\sum_{k=1}^K \sum_{i=0}^{d-1} |E_{k,in}|^2 = 1 \quad (53)$$

$$\iff \sum_{k=1}^K |E_{k,nn}|^2 + \sum_{k, i \neq n} |E_{k,in}|^2 = 1 \quad (54)$$

$$\therefore \forall n, 0 \leq \sum_{k=1}^K |E_{k,nn}|^2 \leq 1 \quad (55)$$

Moreover, since

$$\text{Tr}(M) = \sum_{k, ij} E_{k,jj}^* E_{k,ii} \quad (56)$$

$$= \sum_k |\text{Tr}(E_k)|^2, \quad (57)$$

the trace of M can be equivalently expressed by

$$\text{Tr}(M) = \sum_{i=0}^{d-1} \sum_{j=0}^{d-1} M_{ij}^{ij} \quad (58)$$

$$= \sum_{i=0}^{d-1} M_{ii}^{ii} \quad (59)$$

$$= \sum_{k=1}^K \sum_{i=0}^{d-1} |E_{k,ii}|^2. \quad (60)$$

Therefore, combining this last expression with (55) where each of the d elements $|E_{k,ii}|^2$ are bounded above by 1, it is clear that the sum of all d of them, and thus $\text{Tr}(M)$, must be bounded by d ,

$$0 \leq \sum_k \sum_{i=0}^{d-1} |E_{k,ii}|^2 \leq d, \quad (61)$$

proving the boundedness of \mathcal{F} and \mathcal{I} .

.5 Proofs for Section (Quantum Speed Limits)

(Statement: $\|\log(U)\|$ is minimal up to a factor 2π for $U \in SU(d)$)

Proof: Since $\|\log(e^{i\phi}U)\| = \|\log(U) + \phi\mathbb{1}\| = \|\log(U)\| + |\phi|$, by simple use of the triangle inequality, we have that if $\log(U)$ is traceless, it is not possible to minimize the norm further through a global phase. We then intend to prove that if $U \in SU(d)$, then $\log(U)$ is traceless up to a global phase, multiple of 2π .

To determine whether the trace of the logarithm of a matrix $U \in SU(d)$ is zero, we need to examine the properties of U and its eigenvalues.

Firstly, recall the properties of U . Since $U \in SU(d)$, it is a special unitary matrix, meaning that U is unitary and has a determinant of 1. The unitarity of U implies that $U^\dagger U = I$, where U^\dagger is the conjugate transpose of U and I is the identity matrix.

The eigenvalues of a unitary matrix U lie on the unit circle in the complex plane. Thus, we can write the eigenvalues of U as $\lambda_i = e^{i\theta_i}$, where θ_i are real numbers. Since $U \in SU(d)$, we also have the condition that $\det(U) = 1$. Therefore, the product of the eigenvalues of U is 1:

$$\prod_{i=1}^d \lambda_i = 1.$$

Substituting the form of the eigenvalues, we obtain

$$e^{i \sum_{i=1}^d \theta_i} = 1,$$

which implies

$$\sum_{i=1}^d \theta_i = 2\pi n,$$

where n is some integer.

Now, consider the logarithm of U , denoted by $\log(U)$. The eigenvalues of $\log(U)$ are given by $\log(\lambda_i) = i\theta_i + 2\pi i k_i$, where k_i are integers accounting for the multivalued nature of the complex logarithm. The trace of $\log(U)$ is the sum of its eigenvalues:

$$\text{Tr}(\log(U)) = \sum_{i=1}^d \log(\lambda_i) = i \sum_{i=1}^d \theta_i + 2\pi i \sum_{i=1}^d k_i.$$

Using the earlier result $\sum_{i=1}^d \theta_i = 2\pi n$, we can rewrite this as

$$\text{Tr}(\log(U)) = i(2\pi n) + 2\pi i \sum_{i=1}^d k_i = 2\pi i \left(n + \sum_{i=1}^d k_i \right).$$

Therefore, we see that

$$\text{Tr}(\log(U)) = 2\pi im,$$

where m is an integer given by $m = n + \sum_{i=1}^d k_i$.

In conclusion, the trace of $\log(U)$ is not necessarily zero for $U \in SU(d)$. Instead, it is given by

$$\text{Tr}(\log(U)) = 2\pi im,$$

where m is an integer.

Consider now $e^{-2\pi im}U$, it is still $\in SU(d)$ and $\log(e^{-2\pi im}U) = \text{Tr}(\log(U) - 2\pi im\mathbb{1}) = 0$, so it is not a problem to absorb the factor of $2\pi m$ in the global phase of the gate.

.6 Proofs for Section (The T-M sequence in Quantum Computing)

(Statement: *Property 1.3.1.1*)

Proof: **Proof for σ_z :** (by induction)

- One can easily check that for $N = 2$ it is true. Using $\sigma_z^{(1)} + \sigma_z^{(2)} = \sigma_z \otimes \mathbb{1}_2 + \mathbb{1}_2 \otimes \sigma_z$.

$$\begin{aligned} \langle 0_{TM}^{(2)} | (\sigma_z^{(1)} + \sigma_z^{(2)}) | 0_{TM}^{(2)} \rangle &= \begin{pmatrix} 1 & 0 & 0 & 1 \end{pmatrix} \begin{pmatrix} 2 & 0 & 0 & 0 \\ 0 & 0 & 0 & 0 \\ 0 & 0 & 0 & 0 \\ 0 & 0 & 0 & -2 \end{pmatrix} \begin{pmatrix} 1 \\ 0 \\ 0 \\ 1 \end{pmatrix} = 2 - 2 = 0, \\ \langle 1_{TM}^{(2)} | (\sigma_z^{(1)} + \sigma_z^{(2)}) | 1_{TM}^{(2)} \rangle &= \begin{pmatrix} 0 & 1 & 1 & 0 \end{pmatrix} \begin{pmatrix} 2 & 0 & 0 & 0 \\ 0 & 0 & 0 & 0 \\ 0 & 0 & 0 & 0 \\ 0 & 0 & 0 & -2 \end{pmatrix} \begin{pmatrix} 0 \\ 1 \\ 1 \\ 0 \end{pmatrix} = 0. \end{aligned}$$

- Using the recursive properties of the Thue-Morse sequence,

$$\begin{aligned} \left\langle 0_{TM}^{(N)} \left| \sum_{k=1}^N \sigma_z^{(k)} \right| 0_{TM}^{(N)} \right\rangle &= \left\langle 0_{TM}^{(N-1)} \left| \left\langle 0 \left| \sum_{k=1}^N \sigma_z^{(k)} \right| 0 \right\rangle \right| 0_{TM}^{(N-1)} \right\rangle + \left\langle 0_{TM}^{(N-1)} \left| \left\langle 0 \left| \sum_{k=1}^N \sigma_z^{(k)} \right| 1 \right\rangle \right| 1_{TM}^{(N-1)} \right\rangle \\ &\quad + \left\langle 1_{TM}^{(N-1)} \left| \left\langle 1 \left| \sum_{k=1}^N \sigma_z^{(k)} \right| 0 \right\rangle \right| 0_{TM}^{(N-1)} \right\rangle + \left\langle 1_{TM}^{(N-1)} \left| \left\langle 1 \left| \sum_{k=1}^N \sigma_z^{(k)} \right| 1 \right\rangle \right| 1_{TM}^{(N-1)} \right\rangle \end{aligned}$$

and

$$\begin{aligned} \left\langle 1_{TM}^{(N)} \left| \sum_{k=1}^N \sigma_z^{(k)} \right| 1_{TM}^{(N)} \right\rangle &= \left\langle 1_{TM}^{(N-1)} \left| \left\langle 0 \left| \sum_{k=1}^N \sigma_z^{(k)} \right| 0 \right\rangle \right| 1_{TM}^{(N-1)} \right\rangle + \left\langle 1_{TM}^{(N-1)} \left| \left\langle 0 \left| \sum_{k=1}^N \sigma_z^{(k)} \right| 1 \right\rangle \right| 0_{TM}^{(N-1)} \right\rangle \\ &\quad + \left\langle 0_{TM}^{(N-1)} \left| \left\langle 1 \left| \sum_{k=1}^N \sigma_z^{(k)} \right| 0 \right\rangle \right| 1_{TM}^{(N-1)} \right\rangle + \left\langle 0_{TM}^{(N-1)} \left| \left\langle 1 \left| \sum_{k=1}^N \sigma_z^{(k)} \right| 1 \right\rangle \right| 0_{TM}^{(N-1)} \right\rangle. \end{aligned}$$

Assuming the property holds true for $N - 1$, and since $\sigma_z^{(k)}$ is diagonal, both equations reduce to $\sigma_z^{(1)}$ acting on the added qubit and are equal to:

$$\langle 0 | \sigma_z | 0 \rangle + \langle 1 | \sigma_z | 1 \rangle = 1 - 1 = 0$$

Proof for σ_x and σ_y : Since the effect of $\sigma_x^{(k)}$ is to flip the k^{th} qubit, $\sum_{k=1}^N \sigma_x^{(k)}$ maps $|0_{TM}^{(N)}\rangle \leftrightarrow |1_{TM}^{(N)}\rangle$ which are orthogonal to each other, hence the property is true.

For σ_y , it follows from $\sigma_y = -i\sigma_z\sigma_x$. Therefore, by defining $c_k := 0, 1$ as the state of the k^{th} qubit

$$\begin{aligned} \left\langle 0, 1_{TM}^{(N)} \left| \sum_{k=1}^N \sigma_y^{(k)} \right| 0, 1_{TM}^{(N)} \right\rangle &= -i \left\langle 0, 1_{TM}^{(N)} \left| \sum_{k=1}^N \sigma_z^{(k)} \sigma_x^{(k)} \right| 0, 1_{TM}^{(N)} \right\rangle = -i \sum_{k=1}^N \left\langle 0, 1_{TM}^{(N)} \left| \sigma_z^{(k)} \sigma_x^{(k)} \right| 0, 1_{TM}^{(N)} \right\rangle \\ &= -i \sum_{k=1}^N \left\langle 0, 1_{TM}^{(N)} \left| \sigma_z^{(k)} \sigma_x^{(k)} \right| 0, 1_{TM}^{(N)} \right\rangle = -i \sum_{k=1}^N \langle c_k | \sigma_z | \overline{c_k} \rangle = 0. \end{aligned}$$

(Statement: *Property 1.3.1.2*)

Proof: First, we recall that σ_z is involutory i.e. $(\sigma_z^{(k)})^2 = \mathbb{1}$ and having a $\sigma_z^{(k)}$ appear an odd amount of time is equivalent to it appearing only once. Therefore, we notice

$$\prod_{k \in Z} \sigma_z^{(k)} = \bigotimes_{k \in Z'} \sigma_z^{(k)}$$

with Z' being the ensemble of only one occurrence of the $\sigma^{(k)}$ s that appear an odd amount of times and not the others.

Induction:

- One can check that for $N = 2$, the equality does not hold for $Z' = (\sigma_z^{(1)}, \sigma_z^{(2)})$, but does for

any subset.

$$\left\{ \begin{aligned} \langle 0_{TM}^{(2)} | \sigma_z^{(1)} \otimes \mathbb{1}_2 | 0_{TM}^{(2)} \rangle &= \begin{pmatrix} 1 & 0 & 0 & 1 \end{pmatrix} \begin{pmatrix} 1 & 0 & 0 & 0 \\ 0 & 1 & 0 & 0 \\ 0 & 0 & -1 & 0 \\ 0 & 0 & 0 & -1 \end{pmatrix} \begin{pmatrix} 1 \\ 0 \\ 0 \\ 1 \end{pmatrix} = 1 - 1 = 0 \\ \langle 1_{TM}^{(2)} | \sigma_z^{(1)} \otimes \mathbb{1}_2 | 1_{TM}^{(2)} \rangle &= \begin{pmatrix} 0 & 1 & 1 & 0 \end{pmatrix} \begin{pmatrix} 1 & 0 & 0 & 0 \\ 0 & 1 & 0 & 0 \\ 0 & 0 & -1 & 0 \\ 0 & 0 & 0 & -1 \end{pmatrix} \begin{pmatrix} 0 \\ 1 \\ 1 \\ 0 \end{pmatrix} = 1 - 1 = 0 \\ \langle 0_{TM}^{(2)} | \mathbb{1}_2 \otimes \sigma_z^{(2)} | 0_{TM}^{(2)} \rangle &= \begin{pmatrix} 1 & 0 & 0 & 1 \end{pmatrix} \begin{pmatrix} 1 & 0 & 0 & 0 \\ 0 & -1 & 0 & 0 \\ 0 & 0 & 1 & 0 \\ 0 & 0 & 0 & -1 \end{pmatrix} \begin{pmatrix} 1 \\ 0 \\ 0 \\ 1 \end{pmatrix} = 1 - 1 = 0 \\ \langle 1_{TM}^{(2)} | \mathbb{1}_2 \otimes \sigma_z^{(2)} | 1_{TM}^{(2)} \rangle &= \begin{pmatrix} 0 & 1 & 1 & 0 \end{pmatrix} \begin{pmatrix} 1 & 0 & 0 & 0 \\ 0 & -1 & 0 & 0 \\ 0 & 0 & 1 & 0 \\ 0 & 0 & 0 & -1 \end{pmatrix} \begin{pmatrix} 0 \\ 1 \\ 1 \\ 0 \end{pmatrix} = 1 - 1 = 0 \\ \langle 0_{TM}^{(2)} | \sigma_z^{(1)} \otimes \sigma_z^{(2)} | 0_{TM}^{(2)} \rangle &= \begin{pmatrix} 1 & 0 & 0 & 1 \end{pmatrix} \begin{pmatrix} 1 & 0 & 0 & 0 \\ 0 & -1 & 0 & 0 \\ 0 & 0 & -1 & 0 \\ 0 & 0 & 0 & 1 \end{pmatrix} \begin{pmatrix} 1 \\ 0 \\ 0 \\ 1 \end{pmatrix} = 1 + 1 = 2 \\ \langle 1_{TM}^{(2)} | \sigma_z^{(1)} \otimes \sigma_z^{(2)} | 1_{TM}^{(2)} \rangle &= \begin{pmatrix} 0 & 1 & 1 & 0 \end{pmatrix} \begin{pmatrix} 1 & 0 & 0 & 0 \\ 0 & -1 & 0 & 0 \\ 0 & 0 & -1 & 0 \\ 0 & 0 & 0 & 1 \end{pmatrix} \begin{pmatrix} 0 \\ 1 \\ 1 \\ 0 \end{pmatrix} = -1 - 1 = -2 \end{aligned} \right.$$

Thus the orthogonality for $N = 2$ is conserved since we are dealing with diagonal operators.

- The orthogonality for any N is trivial since the matrices are diagonal. Let's look at $\langle 0_{TM}^{(N)} | \bigotimes_{k \in Z'} \sigma_z^{(k)} | 0_{TM}^{(N)} \rangle - \langle 1_{TM}^{(N)} | \bigotimes_{k \in Z'} \sigma_z^{(k)} | 1_{TM}^{(N)} \rangle$ and use the recursive definition of the states.

We also define $\epsilon^{(k)} = \begin{cases} \sigma_z^{(k)} & \text{if } \sigma_z^{(k)} \in Z' \\ \mathbb{1}_2 & \text{if not} \end{cases}$.

$$\begin{aligned}
& \left\langle 0_{TM}^{(N)} \left| \bigotimes_{k \in Z'} \sigma_z^{(k)} \right| 0_{TM}^{(N)} \right\rangle - \left\langle 1_{TM}^{(N)} \left| \bigotimes_{k \in Z'} \sigma_z^{(k)} \right| 1_{TM}^{(N)} \right\rangle \\
&= \left\langle 0_{TM}^{(N-1)} \left| \left\langle 0 \left| \bigotimes_{k \in Z'} \sigma_z^{(k)} \right| 0 \right\rangle \right| 0_{TM}^{(N-1)} \right\rangle + \left\langle 1_{TM}^{(N-1)} \left| \left\langle 1 \left| \bigotimes_{k \in Z'} \sigma_z^{(k)} \right| 1 \right\rangle \right| 1_{TM}^{(N-1)} \right\rangle \\
&\quad - \left\langle 1_{TM}^{(N-1)} \left| \left\langle 0 \left| \bigotimes_{k \in Z'} \sigma_z^{(k)} \right| 0 \right\rangle \right| 1_{TM}^{(N-1)} \right\rangle - \left\langle 0_{TM}^{(N-1)} \left| \left\langle 1 \left| \bigotimes_{k \in Z'} \sigma_z^{(k)} \right| 1 \right\rangle \right| 0_{TM}^{(N-1)} \right\rangle \\
&= \left\langle 0_{TM}^{(N-1)} \left| \bigotimes_{k \in Z' \setminus \sigma_z^{(N)}} \sigma_z^{(k)} \right| 0_{TM}^{(N-1)} \right\rangle \langle 0 | \epsilon^{(N)} | 0 \rangle + \left\langle 1_{TM}^{(N-1)} \left| \bigotimes_{k \in Z' \setminus \sigma_z^{(N)}} \sigma_z^{(k)} \right| 1_{TM}^{(N-1)} \right\rangle \langle 1 | \epsilon^{(N)} | 1 \rangle \\
&\quad - \left\langle 1_{TM}^{(N-1)} \left| \bigotimes_{k \in Z' \setminus \sigma_z^{(N)}} \sigma_z^{(k)} \right| 1_{TM}^{(N-1)} \right\rangle \langle 0 | \epsilon^{(N)} | 0 \rangle - \left\langle 0_{TM}^{(N-1)} \left| \bigotimes_{k \in Z' \setminus \sigma_z^{(N)}} \sigma_z^{(k)} \right| 0_{TM}^{(N-1)} \right\rangle \langle 1 | \epsilon^{(N)} | 1 \rangle \\
&= \left(\left\langle 0_{TM}^{(N-1)} \left| \bigotimes_{k \in Z' \setminus \sigma_z^{(N)}} \sigma_z^{(k)} \right| 0_{TM}^{(N-1)} \right\rangle - \left\langle 1_{TM}^{(N-1)} \left| \bigotimes_{k \in Z' \setminus \sigma_z^{(N)}} \sigma_z^{(k)} \right| 1_{TM}^{(N-1)} \right\rangle \right) \langle 0 | \epsilon^{(N)} | 0 \rangle \\
&\quad + \left(\left\langle 1_{TM}^{(N-1)} \left| \bigotimes_{k \in Z' \setminus \sigma_z^{(N)}} \sigma_z^{(k)} \right| 1_{TM}^{(N-1)} \right\rangle - \left\langle 0_{TM}^{(N-1)} \left| \bigotimes_{k \in Z' \setminus \sigma_z^{(N)}} \sigma_z^{(k)} \right| 0_{TM}^{(N-1)} \right\rangle \right) \langle 1 | \epsilon^{(N)} | 1 \rangle
\end{aligned}$$

If we assume the property holds for $N-1$, this expression equals to zero

– if $\sigma_z \in Z'$ and $Z' \setminus \sigma_z^{(N)}$ doesn't already contain all the other $\sigma_z^{(k)}$ s.

Since $\epsilon^{(N)} = \sigma_z \Rightarrow \langle 0 | \epsilon^{(N)} | 0 \rangle = -\langle 1 | \epsilon^{(N)} | 1 \rangle$, so we need

$$\left\langle 0_{TM}^{(N-1)} \left| \bigotimes_{k \in Z' \setminus \sigma_z^{(N)}} \sigma_z^{(k)} \right| 0_{TM}^{(N-1)} \right\rangle - \left\langle 1_{TM}^{(N-1)} \left| \bigotimes_{k \in Z' \setminus \sigma_z^{(N)}} \sigma_z^{(k)} \right| 1_{TM}^{(N-1)} \right\rangle = 0$$

or

– if $\sigma_z \notin Z'$ since $\epsilon^{(N)} = \mathbb{1}_2 \Rightarrow \langle 0 | \epsilon^{(N)} | 0 \rangle = \langle 1 | \epsilon^{(N)} | 1 \rangle$.

So, $\left\langle 0_{TM}^{(N)} \left| \bigotimes_{k \in Z'} \sigma_z^{(k)} \right| 0_{TM}^{(N)} \right\rangle - \left\langle 1_{TM}^{(N)} \left| \bigotimes_{k \in Z'} \sigma_z^{(k)} \right| 1_{TM}^{(N)} \right\rangle = 0$ iff E' doesn't contain all $\sigma_z^{(k)}$ s.

A similar argument can be made with $\sigma_y = -i\sigma_z\sigma_x$ using the diagonality of σ_z .

(Statement: *Property 1.3.1.3*)

Proof: For a given integer j ,

$$\left(\sum_{k=1}^N \sigma_z^{(k)} \right)^j = \sum_{j_1 + j_2 + \dots + j_N = j} \frac{j!}{j_1! j_2! \dots j_N!} \prod_{k=1}^N \left(\sigma_{y,z}^{(k)} \right)^{j_k},$$

which is then a state-independent weighted sum of products over ensembles E like in property 2. The ensembles E are then simply partitions of j of size N , and as long as $j < N$, it is not possible for E to contain all $\sigma_z^{(k)}$ s. If $j \geq N$, there exists ensembles E such that the equalities of property 2 do not hold anymore. Therefore property ?? is a consequence of property ??.

(Statement: *Property 1.3.1.4*)

Proof: Since $\sigma_x^2 = 1$, if $k = j$, then the state remains unchanged. If exactly two different qubits are flipped without a relative phase (which is the action of two σ_x operators), the parity of the number of 1's stays unchanged.

(Statement: *Property 1.3.1.3 for qudits*)

Proof: If one works with PTM logical states in a qudit of dimension $d = 2^N$.

$$|1_{\text{TM}}^{(N)}\rangle = \sqrt{\frac{2}{d}} \sum_{k=0}^{d-1} t_k |k\rangle = \sqrt{\frac{2}{d}} \sum_{k \in O(N)} |k\rangle \quad \text{and} \quad |0_{\text{TM}}^{(N)}\rangle = \sqrt{\frac{2}{d}} \sum_{k=0}^{d-1} \bar{t}_k |k\rangle = \sqrt{\frac{2}{d}} \sum_{k \in E(N)} |k\rangle$$

We have that

$$\begin{aligned} \langle 0_{\text{TM}}^{(N)} | J_z^j | 0_{\text{TM}}^{(N)} \rangle &= \sum_{k=0}^{d-1} \left(\frac{d-1-2k}{2} \right)^j \\ &= 2^{-j} \sum_{k \in E(N)} \sum_{l=0}^j \binom{j}{n} 2^l k^l (d-1)^{j-l} \\ &= 2^{-j} \sum_{l=0}^j \binom{j}{n} 2^l \left(\sum_{k \in E(N)} k^l \right) (d-1)^{j-l}, \end{aligned}$$

and similarly,

$$\langle 1_{\text{TM}}^{(N)} | J_z^j | 1_{\text{TM}}^{(N)} \rangle = 2^{-j} \sum_{l=0}^j \binom{j}{n} 2^l \left(\sum_{k \in O(N)} k^l \right) (d-1)^{j-l}.$$

Referring to the discussion about the Prouhet-Tarry-Escott problem, we know that $\sum_{k \in E(N)} k^l = \sum_{k \in O(N)} k^l$, and, therefore $\langle 0_{\text{TM}}^{(N)} | J_z^j | 0_{\text{TM}}^{(N)} \rangle = \langle 1_{\text{TM}}^{(N)} | J_z^j | 1_{\text{TM}}^{(N)} \rangle$. Moreover, J_z is diagonal therefore $\langle 1_{\text{TM}}^{(N)} | J_z^j | 0_{\text{TM}}^{(N)} \rangle = 0$.

.7 Proofs for Section (Areas left to explore)

Bibliography

- [1] Veldhorst, M.; Eenink, H. G. J.; Yang, C. H.; Dzurak, A. S. “Silicon CMOS architecture for a spin-based quantum computer”, *Nature Communications*, 2017, 8:1, 1766.
- [2] Gonzalez-Zalba, M. F.; De Franceschi, S.; Charbon, E.; Meunier, T.; Vinet, M.; Dzurak, A. S. “Scaling silicon-based quantum computing using CMOS technology”, *Nature Electronics*, 2021, 4:12, 872–884.
- [3] Manin, J. I. “Mathematics as Metaphor: Selected Essays of Yuri I. Manin”, *Philosophia Mathematica*, 2008, 17:1, 122–123.
- [4] Benioff, P. “The computer as a physical system: A microscopic quantum mechanical Hamiltonian model of computers as represented by Turing machines”, *Journal of Statistical Physics*, 1980, 22:5, 563–591.
- [5] Feynman, R. P. “Simulating physics with computers”, *International Journal of Theoretical Physics*, 1982, 21:6, 467–488.
- [6] Deutsch, D. “Quantum theory, the Church–Turing principle and the universal quantum computer”, *Proceedings of the Royal Society of London. A. Mathematical and Physical Sciences*, 1985, 400:1818, 97–117.
- [7] Shor, P. W. “Polynomial-Time Algorithms for Prime Factorization and Discrete Logarithms on a Quantum Computer”, *SIAM Journal on Computing*, 1997, 26:5, 1484–1509.
- [8] Grover, L. K. In *Proceedings of the twenty-eighth annual ACM symposium on Theory of computing - STOC '96*, ACM Press: 1996, pp 212–219.
- [9] Lloyd, S. “Universal Quantum Simulators”, *Science*, 1996, 273:5278, 1073–1078.
- [10] Kjaergaard, M.; Schwartz, M. E.; Greene, A.; Samach, G. O.; Bengtsson, A.; O’Keeffe, M.; McNally, C. M.; Braumüller, J.; Kim, D. K.; Krantz, P., et al. “Programming a quantum computer with quantum instructions”, 2020.
- [11] Bruzewicz, C. D.; Chiaverini, J.; McConnell, R.; Sage, J. M. “Trapped-ion quantum computing: Progress and challenges”, *Applied Physics Reviews*, 2019, 6:2, 021314.
- [12] Pogorelov, I. et al. “Compact Ion-Trap Quantum Computing Demonstrator”, *PRX Quantum*, 2021, 2:2, 020343.
- [13] Slussarenko, S.; Pryde, G. J. “Photonic quantum information processing: A concise review”, *Applied Physics Reviews*, 2019, 6:4, 041303.
- [14] Chi, Y.; Huang, J.; Zhang, Z.; Mao, J.; Zhou, Z.; Chen, X.; Zhai, C.; Bao, J.; Dai, T.; Yuan, H., et al. “A programmable qudit-based quantum processor”, *Nature Communications*, 2022, 13:1, 1166.
- [15] Morgado, M.; Whitlock, S. “Quantum simulation and computing with Rydberg-interacting qubits”, *AVS Quantum Science*, 2021, 3:2, 023501.
- [16] Madjarov, I. S.; Covey, J. P.; Shaw, A. L.; Choi, J.; Kale, A.; Cooper, A.; Pichler, H.; Schkolnik, V.; Williams, J. R.; Endres, M. “High-fidelity entanglement and detection of alkaline-earth Rydberg atoms”, *Nature Physics*, 2020, 16:8, 857–861.
- [17] Burkard, G.; Ladd, T. D.; Pan, A.; Nichol, J. M.; Petta, J. R. “Semiconductor spin qubits”, *Reviews of Modern Physics*, 2023, 95:2, 025003.

- [18] Zhang, X.; Li, H.-O.; Cao, G.; Xiao, M.; Guo, G.-C.; Guo, G.-P. “Semiconductor quantum computation”, *National Science Review*, 2019, 6:1, 32–54.
- [19] Arute, F.; Arya, K.; Babbush, R.; Bacon, D.; Bardin, J. C.; Barends, R.; Biswas, R.; Boixo, S.; Brandao, F. G. S. L.; Buell, D. A., et al. “Quantum supremacy using a programmable superconducting processor”, *Nature*, 2019, 574:7779, 505–510.
- [20] First IBM Quantum Data Center in Europe Opens; Will Include IBM’s Most Performant Quantum Systems <https://newsroom.ibm.com/2024-10-01-first-ibm-quantum-data-center-in-europe-opens-will-include-ibms-most-performant-quantum-systems> (accessed 10/02/2024).
- [21] Ezratty, O. “Perspective on superconducting qubit quantum computing”, *The European Physical Journal A*, 2023, 59:5, 94.
- [22] DiVincenzo, D. P. “The Physical Implementation of Quantum Computation”, *Fortschritte der Physik*, 2000, 48:9, 771–783.
- [23] Wang, Y.; Hu, Z.; Sanders, B. C.; Kais, S. “Qudits and High-Dimensional Quantum Computing”, *Frontiers in Physics*, 2020, 8.
- [24] Brusentsov, N. P.; Ramil Alvarez, J. In *Perspectives on Soviet and Russian Computing*, Impagliazzo, J., Proydakov, E., Eds.; Springer Berlin Heidelberg: Berlin, Heidelberg, 2011; Vol. 357, pp 74–80.
- [25] Moreno-Pineda, E.; Wernsdorfer, W. “Measuring molecular magnets for quantum technologies”, *Nature Reviews Physics*, 2021, 3:9, 645–659.
- [26] Thiele, S.; Balestro, F.; Ballou, R.; Klyatskaya, S.; Ruben, M.; Wernsdorfer, W. “Electrically driven nuclear spin resonance in single-molecule magnets”, *Science (New York, N. Y.)*, 2014, 344:6188, 1135–1138.
- [27] Boltyanski, V.; Martini, H.; Soltan, V., *Geometric Methods and Optimization Problems*; Springer Science & Business Media: 2013; 438 pp.
- [28] Pontryagin, L. S., *Mathematical Theory of Optimal Processes*; Routledge: London, 2017; 360 pp.
- [29] Bellman, R.; Bellman, R. E., *Dynamic Programming*; Princeton University Press: 1957; 339 pp.
- [30] Glaser, S. J.; Boscain, U.; Calarco, T.; Koch, C. P.; Köckenberger, W.; Kosloff, R.; Kuprov, I.; Luy, B.; Schirmer, S.; Schulte-Herbrüggen, T.; Sugny, D.; Wilhelm, F. K. “Training Schrödinger’s cat: quantum optimal control: Strategic report on current status, visions and goals for research in Europe”, *The European Physical Journal D*, 2015, 69:12, 279.
- [31] Koch, C. P.; Boscain, U.; Calarco, T.; Dirr, G.; Filipp, S.; Glaser, S. J.; Kosloff, R.; Montangero, S.; Schulte-Herbrüggen, T.; Sugny, D.; Wilhelm, F. K. “Quantum optimal control in quantum technologies. Strategic report on current status, visions and goals for research in Europe”, *EPJ Quantum Technology*, 2022, 9:1, 19.
- [32] Khaneja, N.; Reiss, T.; Kehlet, C.; Schulte-Herbrüggen, T.; Glaser, S. J. “Optimal control of coupled spin dynamics: design of NMR pulse sequences by gradient ascent algorithms”, *Journal of Magnetic Resonance*, 2005, 172:2, 296–305.
- [33] Rutherford, E. “The scattering of alpha and beta particles by matter and the structure of the atom”, *The London, Edinburgh, and Dublin Philosophical Magazine and Journal of Science*, 1911, 21:125, 669–688.
- [34] Gamow, G.; Rutherford, E. “Mass defect curve and nuclear constitution”, *Proceedings of the Royal Society of London. Series A, Containing Papers of a Mathematical and Physical Character*, 1930, 126:803, 632–644.
- [35] Bohr, N.; Wheeler, J. A. “The Mechanism of Nuclear Fission”, *Physical Review*, 1939, 56:5, 426–450.
- [36] Mayer, M. G. “On Closed Shells in Nuclei. II”, *Physical Review*, 1949, 75:12, 1969–1970.
- [37] Haxel, O.; Jensen, J. H. D.; Suess, H. E. “On the ”Magic Numbers” in Nuclear Structure”, *Physical Review*, 1949, 75:11, 1766–1766.
- [38] De Groote, R. P.; Neyens, G. In *Handbook of Nuclear Physics*, Tanihata, I., Toki, H., Kajino, T., Eds.; Springer Nature: Singapore, 2020, pp 1–36.

- [39] Skyrme, T. “The effective nuclear potential”, *Nuclear Physics*, 1958, 9:4, 615–634.
- [40] Vautherin, D.; Brink, D. M. “Hartree-Fock Calculations with Skyrme’s Interaction. I. Spherical Nuclei”, *Physical Review C*, 1972, 5:3, 626–647.
- [41] Ring, P.; Schuck, P., *The nuclear many body problem*, 1. ed., 3. print., study ed; Texts and monographs in physics; Springer: Berlin Heidelberg, 2004; 716 pp.
- [42] Casten, R., *Nuclear Structure from a Simple Perspective*; Oxford University Press: 2000; 484 pp.
- [43] Hartree-Fock-Bogoliubov results based on the Gogny force https://www-phynu.cea.fr/science_en_ligne/carte_potentiels_microscopiques/carte_potentiel_nucleaire_eng.htm (accessed 08/15/2024).
- [44] Gerginov, V.; Calkins, K.; Tanner, C.; McFerran, J.; Diddams, S.; Bartels, A.; Hollberg, L. “Optical frequency measurements of 6s 2S_{1/2}-6p 2P_{1/2} (D1) transitions in Cs133 and their impact on the fine-structure constant”, *Physical Review A*, 2006, 73, 32504.
- [45] Goudsmit, S. “La découverte du spin de l’électron”, *Journal de Physique*, 1967, 28:1, 123–128.
- [46] Dirac, P. A. M. “The quantum theory of the electron”, *Proceedings of the Royal Society of London. Series A, Containing Papers of a Mathematical and Physical Character*, 1928, 117:778, 610–624.
- [47] Casimir, H. B. G. In *On the Interaction between Atomic Nuclei and Electrons*, Casimir, H. B. G., Ed.; Springer Netherlands: Dordrecht, 1936, pp 201–283.
- [48] Christy, R. F.; Kusaka, S. “Electric Quadrupole Moment of the Deuteron”, *Physical Review*, 1939, 55:7, 665–665.
- [49] Ramsey, N. F. “Theory of Molecular Hydrogen and Deuterium in Magnetic Fields”, *Physical Review*, 1952, 85:1, 60–65.
- [50] Bohr, A.; Weisskopf, V. F. “The Influence of Nuclear Structure on the Hyperfine Structure of Heavy Elements”, *Physical Review*, 1950, 77:1, 94–98.
- [51] Rosenthal, J. E.; Breit, G. “The Isotope Shift in Hyperfine Structure”, *Physical Review*, 1932, 41:4, 459–470.
- [52] Engfer, R.; Schneuwly, H.; Vuilleumier, J. L.; Walter, H. K.; Zehnder, A. “Charge-distribution parameters, isotope shifts, isomer shifts, and magnetic hyperfine constants from muonic atoms”, *Atomic Data and Nuclear Data Tables*, 1974, 14:5, 509–597.
- [53] Daum, C., *Muonic atoms and nuclear charge distributions*, 1967.
- [54] The SI, BIPM <https://www.bipm.org/en/measurement-units> (accessed 10/13/2024).
- [55] Wynands, R.; Weyers, S. “Atomic fountain clocks”, *Metrologia*, 2005, 42:3, S64.
- [56] Pla, J. J.; Tan, K. Y.; Dehollain, J. P.; Lim, W. H.; Morton, J. J. L.; Zwanenburg, F. A.; Jamieson, D. N.; Dzurak, A. S.; Morello, A. “High-fidelity readout and control of a nuclear spin qubit in silicon”, *Nature*, 2013, 496:7445, 334–338.
- [57] Harty, T. P.; Allcock, D. T. C.; Ballance, C. J.; Guidoni, L.; Janacek, H. A.; Linke, N. M.; Stacey, D. N.; Lucas, D. M. “High-Fidelity Preparation, Gates, Memory, and Readout of a Trapped-Ion Quantum Bit”, *Physical Review Letters*, 2014, 113:22, 220501.
- [58] Ballance, C. J.; Harty, T. P.; Linke, N. M.; Sepiol, M. A.; Lucas, D. M. “High-Fidelity Quantum Logic Gates Using Trapped-Ion Hyperfine Qubits”, *Physical Review Letters*, 2016, 117:6, 060504.
- [59] Ringbauer, M.; Meth, M.; Postler, L.; Stricker, R.; Blatt, R.; Schindler, P.; Monz, T. “A universal qudit quantum processor with trapped ions”, *Nature Physics*, 2022, 18:9, 1053–1057.
- [60] Butler, P. A.; Nazarewicz, W. “Intrinsic reflection asymmetry in atomic nuclei”, *Reviews of Modern Physics*, 1996, 68:2, 349–421.
- [61] Sajid, M. A. Blocks of the Periodic Table — s-p-d-f Blocks, PSIBERG <https://psiberg.com/blocks-of-the-periodic-table/> (accessed 10/14/2024).
- [62] Greenwood, N. N.; Earnshaw, A., *Chemistry of the elements*, 2nd ed; Butterworth-Heinemann: Oxford ; Boston, 1997; 1341 pp.
- [63] *The rare earth elements: fundamentals and applications*; Atwood, D. A., Ed.; EIC Bks; John Wiley & Sons, Inc: Chichester, West Sussex, United Kingdom Hoboken, 2012, 606 pp.
- [64] SEABORG, G. T. In *Modern Alchemy*, 1951, pp 256–279.

- [65] Gutfleisch, O.; Willard, M. A.; Brück, E.; Chen, C. H.; Sankar, S. G.; Liu, J. P. “Magnetic Materials and Devices for the 21st Century: Stronger, Lighter, and More Energy Efficient”, *Advanced Materials*, 2011, *23*:7, 821–842.
- [66] Ramanantoanina, H.; Urland, W.; García-Fuente, A.; Cimpoesu, F.; Daul, C. “Ligand field density functional theory for the prediction of future domestic lighting”, *Physical Chemistry Chemical Physics*, 2014, *16*:28, 14625–14634.
- [67] Liu, G., *Spectroscopic Properties of Rare Earths in Optical Materials*, 1st ed; Springer Series in Materials Science Ser v.83; Springer Berlin / Heidelberg: Berlin, Heidelberg, 2005; 1 p.
- [68] Eliseeva, S. V.; Bünzli, J.-C. G. “Lanthanide luminescence for functional materials and bio-sciences”, *Chemical Society Reviews*, 2009, *39*:1, 189–227.
- [69] Jordens, A.; Cheng, Y. P.; Waters, K. E. “A review of the beneficiation of rare earth element bearing minerals”, *Minerals Engineering*, 2013, *41*, 97–114.
- [70] Atwood, D. A., *Sustainable Inorganic Chemistry*, 1. Aufl; EIC Books; Wiley: s.l., 2016; 1 p.
- [71] Binnemans, K.; Jones, P. T.; Blanpain, B.; Van Gerven, T.; Yang, Y.; Walton, A.; Buchert, M. “Recycling of rare earths: a critical review”, *Journal of Cleaner Production*, 2013, *51*, 1–22.
- [72] Bethe, H. “Termaufspaltung in kristallen”, *Annalen der Physik*, 1929, *395*:2, 133–208.
- [73] Bethe, H. “Zur Theorie des Zeemaneffektes an den Salzen der seltenen Erden”, *Zeitschrift für Physik*, 1930, *60*:3, 218–233.
- [74] Van Vleck, J. “Valence strength and the magnetism of complex salts”, *The Journal of Chemical Physics*, 1935, *3*:12, 807–813.
- [75] *Advanced inorganic chemistry*, 6th ed; Cotton, F. A., Cotton, F. A., Eds.; Wiley: New York, 1999, 1355 pp.
- [76] Crystal Field Theory, Chemistry LibreTexts [https://chem.libretexts.org/Bookshelves/Inorganic_Chemistry/Supplemental_Modules_and_Websites_\(Inorganic_Chemistry\)/Crystal_Field_Theory/Crystal_Field_Theory](https://chem.libretexts.org/Bookshelves/Inorganic_Chemistry/Supplemental_Modules_and_Websites_(Inorganic_Chemistry)/Crystal_Field_Theory/Crystal_Field_Theory) (accessed 10/14/2024).
- [77] Alessandri, R.; Zulfikri, H.; Autschbach, J.; Bolvin, H. “Crystal Field in Rare-Earth Complexes: From Electrostatics to Bonding”, *Chemistry (Weinheim an Der Bergstrasse, Germany)*, 2018, *24*:21, 5538–5550.
- [78] Jung, J.; Islam, M. A.; Pecoraro, V. L.; Mallah, T.; Berthon, C.; Bolvin, H. “Derivation of Lanthanide Series Crystal Field Parameters From First Principles”, *Chemistry – A European Journal*, 2019, *25*:66, 15112–15122.
- [79] Sessoli, R.; Gatteschi, D.; Caneschi, A.; Novak, M. A. “Magnetic bistability in a metal-ion cluster”, *Nature*, 1993, *365*:6442, 141–143.
- [80] Woodruff, D. N.; Winpenny, R. E. P.; Layfield, R. A. “Lanthanide Single-Molecule Magnets”, *Chemical Reviews*, 2013, *113*:7, 5110–5148.
- [81] Cap, G.; F, O.; D, R.; Nf, C.; Dp, M. “Molecular magnetic hysteresis at 60 kelvin in dysprosocene”, *Nature*, 2017, *548*:7668.
- [82] Hauser, A.; Münzfeld, L.; Uhlmann, C.; Lebedkin, S.; Schlittenhardt, S.; Ruan, T.-T.; Kappes, M. M.; Ruben, M.; Roesky, P. W. “It’s not just the size that matters: crystal engineering of lanthanide-based coordination polymers”, *Chemical Science*, 2024, *15*:4, 1338–1347.
- [83] Curie, P., *Propriétés magnétiques des corps à diverses températures*; Gauthier-Villars et fils: 1895; 148 pp.
- [84] Langevin, P., *Magnétisme et Théorie Des électrons*; Independently Published: 1905; 44 pp.
- [85] Pauling, L. “Nature of the Iron–Oxygen Bond in Oxyhaemoglobin”, *Nature*, 1964, *203*:4941, 182–183.
- [86] Stranski, I. N. “Zur Theorie des Kristallwachstums”, *Zeitschrift für Physikalische Chemie*, 1928, *136U*:1, 259–278.
- [87] Van Vleck, J. H. “Theory of the Variations in Paramagnetic Anisotropy Among Different Salts of the Iron Group”, *Physical Review*, 1932, *41*:2, 208–215.
- [88] Stumpf, H. O.; Pei, Y.; Kahn, O.; Ouahab, L.; Grandjean, D. “A Molecular-Based Magnet with a Fully Interlocked Three-Dimensional Structure”, *Science*, 1993, *261*:5120, 447–449.

- [89] Gatteschi, D.; Sessoli, R.; Villain, J., *Molecular Nanomagnets*; OUP Oxford: 2006; 408 pp.
- [90] Thomas, L.; Lionti, F.; Ballou, R.; Gatteschi, D.; Sessoli, R.; Barbara, B. “Macroscopic quantum tunnelling of magnetization in a single crystal of nanomagnets”, *Nature*, 1996, *383*:6596, 145–147.
- [91] Naoto Ishikawa; Miki Sugita; Tadahiko Ishikawa; T. Ishikawa; Shin-ya Koshihara; Youkoh Kaizu; Youkoh Kaizu “Lanthanide Double-Decker Complexes Functioning as Magnets at the Single-Molecular Level”, *Journal of the American Chemical Society*, 2003, *125*:29, 8694–8695.
- [92] Ishikawa, N.; Sugita, M.; Wernsdorfer, W. “Quantum Tunneling of Magnetization in Lanthanide Single-Molecule Magnets”, *Angewandte Chemie International Edition*, 2005, *44*:19, 2931–2935.
- [93] Bogani, L.; Wernsdorfer, W. “Molecular spintronics using single-molecule magnets”, *Nature Materials*, 2008, *7*:3, 179–186.
- [94] Leuenberger, M. N.; Loss, D. “Quantum computing in molecular magnets”, *Nature*, 2001, *410*:6830, 789–793.
- [95] Ardavan, A.; Rival, O.; Morton, J. J. L.; Blundell, S. J.; Tyryshkin, A. M.; Timco, G. A.; Winpenny, R. E. P. “Will Spin-Relaxation Times in Molecular Magnets Permit Quantum Information Processing?”, *Physical Review Letters*, 2007, *98*:5, 057201.
- [96] Zadrozny, J. M.; Freedman, D. E. “Qubit Control Limited by Spin–Lattice Relaxation in a Nuclear Spin-Free Iron(III) Complex”, *Inorganic Chemistry*, 2015, *54*:24, 12027–12031.
- [97] Wernsdorfer, W. “From micro- to nano-SQUIDS: applications to nanomagnetism”, *Superconductor Science and Technology*, 2009, *22*:6, 064013.
- [98] Romain Vincent; Svetlana Klyatskaya; Mario Ruben; Wolfgang Wernsdorfer; Franck Balestro “Electronic read-out of a single nuclear spin using a molecular spin transistor”, *Nature*, 2012, *488*:7411, 357–360.
- [99] Godfrin, C.; Ferhat, A.; Ballou, R.; Klyatskaya, S.; Ruben, M.; Wernsdorfer, W.; Balestro, F. “Operating Quantum States in Single Magnetic Molecules: Implementation of Grover’s Quantum Algorithm”, *Physical Review Letters*, 2017, *119*:18, 187702.
- [100] Wernsdorfer, W.; Ruben, M. “Synthetic Hilbert Space Engineering of Molecular Qudits: Isotopologue Chemistry”, *Advanced Materials*, 2019, *31*:26, 1806687.
- [101] Kumar, K. S.; Serrano, D.; Nonat, A. M.; Heinrich, B.; Karmazin, L.; Charbonnière, L. J.; Goldner, P.; Ruben, M. “Optical spin-state polarization in a binuclear europium complex towards molecule-based coherent light-spin interfaces”, *Nature Communications*, 2021, *12*:1, 2152.
- [102] Moreno-Pineda, E.; Godfrin, C.; Balestro, F.; Wernsdorfer, W.; Ruben, M. “Molecular Spin Qudits for Quantum Algorithms”, *Chemical Society Reviews*, 2018, *47*:2, 501–513.
- [103] Thiele, S. Read-out and coherent manipulation of an isolated nuclear spin using a single molecule magnet spin transistor, Ph.D. Thesis, Université de Grenoble, 2014.
- [104] Godfrin, C. Quantum information processing using a molecular magnet single nuclear spin qudit, These de doctorat, Université Grenoble Alpes (ComUE), 2017.
- [105] Leuenberger, M. N.; Loss, D.; Poggio, M.; Awschalom, D. D. “Quantum Information Processing with Large Nuclear Spins in GaAs Semiconductors”, *Physical Review Letters*, 2002, *89*:20, 207601.
- [106] Leuenberger, M. N.; Loss, D. “Grover algorithm for large nuclear spins in semiconductors”, *Physical Review B*, 2003, *68*:16, 165317.
- [107] Dieke, G. H.; Crosswhite, H. M. “The Spectra of the Doubly and Triply Ionized Rare Earths”, *Applied Optics*, 1963, *2*:7, 675–686.
- [108] Wybourne, B. G.; Smentek, L., *Optical Spectroscopy of Lanthanides: magnetic and hyperfine interactions*. CRC Press: S.I., 2019.
- [109] Tuszynski, J. A., *Spherical tensor operators: tables of matrix elements and symmetries*; World Scientific: 1990.
- [110] Cowan, R. D., *The Theory of Atomic Structure and Spectra*; University of California Press: 2023; 764 pp.

- [111] Nielson, C.; Koster, G., *Spectroscopic Coefficients for the Pn, Dn, and Fn Configurations*; M.I.T. Press: 1963.
- [112] Condon, E. U.; Odabasi, H., *Atomic Structure*; CUP Archive: 1980; 684 pp.
- [113] Rudzikas, Z., *Theoretical Atomic Spectroscopy*; Cambridge University Press: 2007; 466 pp.
- [114] Judd, B. R., *Operator Techniques in Atomic Spectroscopy*; Princeton University Press: 2014; 302 pp.
- [115] Jucis, A. P.; Savukinas, A. J., *Matematicheskiye osnovi teorii atoma*; Izdat "Mintis": 1973; 479 pp.
- [116] Tuszyński, J. A. "The action of product tensor operators within and between pure and mixed configurations", *The Journal of Chemical Physics*, 1986, 85:7, 3950–3963.
- [117] Watanabe, H., *Operator methods in ligand field theory*; Englewood Cliffs, N.J., Prentice-Hall: 1966; 218 pp.
- [118] Ramanantoanina, H. "A DFT-based theoretical model for the calculation of spectral profiles of lanthanide M4,5-edge x-ray absorption", *The Journal of Chemical Physics*, 2018, 149:5, 054104.
- [119] Van Lenthe, E. The ZORA equation. Ph.D. Thesis, Vrije Universiteit Amsterdam, 1996.
- [120] Ramanantoanina, H.; Urland, W.; Cimpoesu, F.; Daul, C. "The angular overlap model extended for two-open-shell f and d electrons", *Physical Chemistry Chemical Physics*, 2014, 16:24, 12282–12290.
- [121] Suta, M.; Cimpoesu, F.; Urland, W. "The angular overlap model of ligand field theory for f elements: An intuitive approach building bridges between theory and experiment", *Coordination Chemistry Reviews*, 2021, 441, 213981.
- [122] Ramanantoanina, H.; Studniarek, M.; Daffé, N.; Dreiser, J. "Non-empirical calculation of X-ray magnetic circular dichroism in lanthanide compounds", *Chemical Communications*, 2019, 55:20, 2988–2991.
- [123] Ramanantoanina, H.; Daul, C. "A non-empirical calculation of 2p core-electron excitation in compounds with 3d transition metal ions using ligand-field and density functional theory (LFDFT)", *Physical Chemistry Chemical Physics*, 2017, 19:31, 20919–20929.
- [124] DLMP: Chapter 34 3j,6j,9j Symbols <https://dlmf.nist.gov/34> (accessed 08/11/2024).
- [125] Walsh, B. M. In *Advances in Spectroscopy for Lasers and Sensing*, ed. by Di Bartolo, B.; Forte, O., Springer Netherlands: Dordrecht, 2006, pp 403–433.
- [126] Jørgensen, C. K.; Judd, B. R. "Hypersensitive pseudoquadrupole transitions in lanthanides", *Molecular Physics*, 1964.
- [127] Tanaka, M.; Kushida, T. "Interference between Judd-Ofelt and Wybourne-Downer mechanisms in the $\{5\} \mathit{D}_{0} \mathit{F}_{7} \mathit{J}_{J}$ ($J=2,4$) transitions of Sm^{2+} in solids", *Physical Review B*, 1996, 53:2, 588–593.
- [128] Binnemans, K. "Interpretation of europium(III) spectra", *Coordination Chemistry Reviews*, 2015, 295, 1–45.
- [129] Godfrin, C.; Ballou, R.; Bonet, E.; Ruben, M.; Klyatskaya, S.; Wernsdorfer, W.; Balestro, F. "Generalized Ramsey interferometry explored with a single nuclear spin qudit", *npj Quantum Information*, 2018, 4:1, 1–7.
- [130] Ord-Smith, R. J. "The Symmetry Relations of the $12j$ Symbol", *Physical Review*, 1954, 94:5, 1227–1228.
- [131] Lämmerzahl, C. "The pseudodifferential operator square root of the Klein–Gordon equation", *Journal of Mathematical Physics*, 1993, 34:9, 3918–3932.
- [132] Anderson, C. D. "The Apparent Existence of Easily Deflectable Positives", *Science*, 1932, 76:1967, 238–239.
- [133] Gerlach, W.; Stern, O. "Der experimentelle Nachweis der Richtungsquantelung im Magnetfeld", *Zeitschrift für Physik*, 1922, 9:1, 349–352.
- [134] Strange, P., *Relativistic Quantum Mechanics: With Applications in Condensed Matter and Atomic Physics*; Cambridge University Press: Cambridge, 1998.

- [135] Johnson, W. R., *Atomic Structure Theory*; Springer: Berlin, Heidelberg, 2007.
- [136] Michelson, A. A.; Morley, E. W. “On a method of making the wavelength of sodium light the actual and practical standard of length”, *American Journal of Science*, 1887, *s3-34*:204, 427–430.
- [137] Bullis, R. G.; Rasor, C.; Tavis, W. L.; Johnson, S. A.; Weiss, M. R.; Yost, D. C. “Ramsey Spectroscopy of the $2S_{1/2}$ Hyperfine Interval in Atomic Hydrogen”, *Physical Review Letters*, 2023, *130*:20, 203001.
- [138] Boucard, S. Calcul de haute precision d’énergies de transitions dans les atomes exotiques et les lithumoides : corrections relativistes, corrections radiatives, structure hyperfine et interaction avec le cortege electronique residuel, These de doctorat, Paris 6, 1998.
- [139] Hinschberger, Y.; Dixit, A.; Manfredi, G.; Hervieux, P.-A. “Equivalence between the semirelativistic limit of the Dirac-Maxwell equations and the Breit-Pauli model in the mean-field approximation”, *Physical Review A*, 2015, *91*:1, 012101.
- [140] Borie, E.; Rinker, G. A. “The energy levels of muonic atoms”, *Reviews of Modern Physics*, 1982, *54*:1, 67–118.
- [141] Shabaev, V. In *Large Coulomb Systems: Lecture Notes on Mathematical Aspects of QED*, Dereziński, J., Siedentop, H., Eds.; Springer: Berlin, Heidelberg, 2006, pp 275–295.
- [142] Damgaard, J.; Pauli, H.; Pashkevich, V.; Strutinsky, V. “A method for solving the independent-particle Schrödinger equation with a deformed average field”, *Nuclear Physics A*, 1969, *135*:2, 432–444.
- [143] Vautherin, D. “Hartree-Fock Calculations with Skyrme’s Interaction. II. Axially Deformed Nuclei”, *Physical Review C*, 1973, *7*:1, 296–316.
- [144] Flocard, H.; Quentin, P.; Kerman, A.; Vautherin, D. “Nuclear deformation energy curves with the constrained Hartree-Fock method”, *Nuclear Physics A*, 1973, *203*:3, 433–472.
- [145] Stone, N. J. “Table of nuclear magnetic dipole and electric quadrupole moments”, *Atomic Data and Nuclear Data Tables*, 2005, *90*:1, 75–176.
- [146] Bohr, A.; Mottelson, B. R., *Nuclear Structure*; World Scientific: 1998; 500 pp.
- [147] Rowe, D. J., *Nuclear Collective Motion: Models and Theory*; WORLD SCIENTIFIC: 2010.
- [148] *Numerical data and functional relationships in science and technology. Bd. 20: Gruppe 1: Kern- und Teilchenphysik = Group 1: @Nuclear and particle physics Nuclear charge radii / ed.: H. Schopper. Authors: G. Fricke; Fricke, G., Schopper, H., Eds.; Springer: Berlin Heidelberg, 2004; Vol. 20, 385 pp.*
- [149] Pálffy, A. “Nuclear effects in atomic transitions”, *Contemporary Physics*, 2010, *51*:6, 471–496.
- [150] Negele, J. W. “The mean-field theory of nuclear structure and dynamics”, *Reviews of Modern Physics*, 1982, *54*:4, 913–1015.
- [151] Bonneau, L.; Minkov, N.; Duc, D. D.; Quentin, P.; Bartel, J. “Effect of core polarization on magnetic dipole moments in deformed odd-mass nuclei”, *Physical Review C*, 2015, *91*:5, 054307.
- [152] Schwartz, C. “Theory of Hyperfine Structure”, *Physical Review*, 1955, *97*:2, 380–395.
- [153] Bouchiat, M. A.; Bouchiat, C. “I. Parity violation induced by weak neutral currents in atomic physics”, *Journal de Physique*, 1974, *35*:12, 899–927.
- [154] Büttgenbach, S. “Magnetic hyperfine anomalies”, *Hyperfine Interactions*, 1984, *20*:1, 1–64.
- [155] Persson, J. R. “Table of hyperfine anomaly in atomic systems — 2023”, *Atomic Data and Nuclear Data Tables*, 2023, *154*, 101589.
- [156] Hinschberger, Y. Etude théorique des effets relativistes induits par une impulsion lumineuse ultra-rapide dans la matière, These de doctorat, Strasbourg, 2012.
- [157] Hinschberger, Y.; Hervieux, P.-A. “Foldy–Wouthuysen transformation applied to the interaction of an electron with ultrafast electromagnetic fields”, *Physics Letters A*, 2012, *376*:6, 813–819.
- [158] Pritchard, J. R.; Loeb, A. “21 cm cosmology in the 21st century”, *Reports on Progress in Physics*, 2012, *75*:8, 086901.

- [159] Hellwig, H.; Vessot, R. F. C.; Levine, M. W.; Zitzewitz, P. W.; Allan, D. W.; Glaze, D. J. "Measurement of the Unperturbed Hydrogen Hyperfine Transition Frequency", *IEEE Transactions on Instrumentation and Measurement*, 1970, 19:4, 200–209.
- [160] Pointillart, F.; Bernot, K.; Guennic, B. L.; Cador, O. "Isotopic enrichment in lanthanide coordination complexes: contribution to single-molecule magnets and spin qudit insights", *Chemical Communications*, 2023, 59:55, 8520–8531.
- [161] Persson, J. "Muonic Hyperfine Structure and the Bohr-Weisskopf Effect", 2023.
- [162] Crespo López-Urrutia, J. R.; Beiersdorfer, P.; Savin, D. W.; Widmann, K. "Direct Observation of the Spontaneous Emission of the Hyperfine Transition $F = 4$ to $F = 3$ in Ground State Hydrogenlike $H^{165}O^{6+}$ in an Electron Beam Ion Trap", *Physical Review Letters*, 1996, 77:5, 826–829.
- [163] Bonneau, L.; Quentin, P.; Sieja, K. "Ground-state properties of even-even $N=Z$ nuclei within the Hartree-Fock-BCS and higher Tamm–Dancoff approaches", *Physical Review C*, 2007, 76:1, 014304.
- [164] Nielsen, M. A.; Chuang, I. L., *Quantum Computation and Quantum Information: 10th Anniversary Edition*; Cambridge University Press: Cambridge, 2010.
- [165] Figgatt, C.; Maslov, D.; Landsman, K. A.; Linke, N. M.; Debnath, S.; Monroe, C. "Complete 3-Qubit Grover search on a programmable quantum computer", *Nature Communications*, 2017, 8:1, 1918.
- [166] Mandilara, A.; Dellen, B.; Jaekel, U.; Valtinos, T.; Syvridis, D. "Classification of data with a qudit, a geometric approach", *Quantum Machine Intelligence*, 2024, 6:1, 17.
- [167] Chiesa, A.; Petiziol, F.; Macaluso, E.; Wimberger, S.; Santini, P.; Carretta, S. "Embedded quantum-error correction and controlled-phase gate for molecular spin qubits", *AIP Advances*, 2021, 11:2, 025134.
- [168] Petiziol, F.; Chiesa, A.; Wimberger, S.; Santini, P.; Carretta, S. "Counteracting dephasing in Molecular Nanomagnets by optimized qudit encodings", *npj Quantum Information*, 2021, 7:1, 1–10.
- [169] Luis, F. et al. "A dissymmetric [Gd₂] coordination molecular dimer hosting six addressable spin qubits", *Communications Chemistry*, 2020, 3:1.
- [170] Zheng, Y.; Sharma, H.; Borregaard, J. "Entanglement Distribution with Minimal Memory Requirements Using Time-Bin Photonic Qudits", *PRX Quantum*, 2022, 3:4, 040319.
- [171] Bouchard, F.; Fickler, R.; Boyd, R. W.; Karimi, E. "High-dimensional quantum cloning and applications to quantum hacking", *Science Advances*, 2017, 3:2, e1601915.
- [172] Campbell, E. T.; Anwar, H.; Browne, D. E. "Magic-State Distillation in All Prime Dimensions Using Quantum Reed-Muller Codes", *Physical Review X*, 2012, 2:4, 041021.
- [173] Lanyon, B. P. et al. "Simplifying quantum logic using higher-dimensional Hilbert spaces", *Nature Physics*, 2008, 5:2, 134–140.
- [174] Manzano, D. "A short introduction to the Lindblad master equation", *AIP Advances*, 2020, 10:2, 025106.
- [175] Gorini, V.; Kossakowski, A.; Sudarshan, E. C. G. "Completely positive dynamical semigroups of N -level systems", *Journal of Mathematical Physics*, 1976, 17:5, 821–825.
- [176] Lindblad, G. "On the generators of quantum dynamical semigroups", *Communications in Mathematical Physics*, 1976, 48:2, 119–130.
- [177] Kraus, K., *States, Effects, and Operations: Fundamental Notions of Quantum Theory*; Springer Berlin Heidelberg: 1983; 176 pp.
- [178] Havel, T. F. "Procedures for Converting among Lindblad, Kraus and Matrix Representations of Quantum Dynamical Semigroups", *Journal of Mathematical Physics*, 2003, 44:2, 534.
- [179] Andersson, E.; Cresser, J. D.; Hall, M. J. W. "Finding the Kraus decomposition from a master equation and vice versa", *Journal of Modern Optics*, 2007.
- [180] Zhong, W.; Sun, Z.; Ma, J.; Wang, X.; Nori, F. "Fisher information under decoherence in Bloch representation", *Physical Review A*, 2013, 87:2, 022337.

- [181] Chiesa, A.; Macaluso, E.; Petiziol, F.; Wimberger, S.; Santini, P.; Carretta, S. “Molecular Nanomagnets as Qubits with Embedded Quantum-Error Correction”, *The Journal of Physical Chemistry Letters*, 2020, *11*:20, 8610–8615.
- [182] Chen, H.; Borzì, A.; Janković, D.; Hartmann, J.-G.; Hervieux, P.-A. Full- and low-rank exponential Euler integrators for the Lindblad equation, 2024.
- [183] Riesch, M.; Jirauschek, C. “Analyzing the positivity preservation of numerical methods for the Liouville-von Neumann equation”, *Journal of Computational Physics*, 2019, *390*, 290–296.
- [184] Ziolkowski, R. W.; Arnold, J. M.; Gogny, D. M. “Ultrafast pulse interactions with two-level atoms”, *Physical Review A*, 1995, *52*:4, 3082–3094.
- [185] Bidégaray, B.; Bourgeade, A.; Reignier, D. “Introducing Physical Relaxation Terms in Bloch Equations”, *Journal of Computational Physics*, 2001, *170*:2, 603–613.
- [186] Janković, D.; Hartmann, J.-G.; Ruben, M.; Hervieux, P.-A. “Noisy qudit vs multiple qubits: conditions on gate efficiency for enhancing fidelity”, *npj Quantum Information*, 2024, *10*:1, 59.
- [187] Jankovic, D. Source Code for data generation and pulses data for Noisy Qudit vs Multiple Qubits, 2024.
- [188] Jozsa, R. “Fidelity for Mixed Quantum States”, *Journal of Modern Optics*, 1994, *41*:12, 2315–2323.
- [189] Nielsen, M. A. “A simple formula for the average gate fidelity of a quantum dynamical operation”, *Physics Letters A*, 2002, *303*:4, 249–252.
- [190] Qi, J.; Ng, H. K. “Comparing the randomized benchmarking figure with the average infidelity of a quantum gate-set”, *International Journal of Quantum Information*, 2019, *17*:4, 1950031.
- [191] Johnston, N.; Kribs, D. W. “Quantum gate fidelity in terms of Choi matrices”, *Journal of Physics A: Mathematical and Theoretical*, 2011, *44*:49, 495303.
- [192] Abad, T.; Fernández-Pendás, J.; Frisk Kockum, A.; Johansson, G. “Universal Fidelity Reduction of Quantum Operations from Weak Dissipation”, *Physical Review Letters*, 2022, *129*:15, 150504.
- [193] Collins, B.; Matsumoto, S.; Novak, J. “The Weingarten Calculus”, 2021.
- [194] Horodecki, M.; Horodecki, P.; Horodecki, R. “General teleportation channel, singlet fraction, and quasidistillation”, *Physical Review A*, 1999, *60*:3, 1888–1898.
- [195] Ozaeta, A.; McMahon, P. L. “Decoherence of up to 8-qubit entangled states in a 16-qubit superconducting quantum processor”, *Quantum Science and Technology*, 2019, *4*:2, 025015.
- [196] Chen, Y.; Neill, C.; Roushan, P.; Leung, N.; Fang, M.; Barends, R.; Kelly, J.; Campbell, B.; Chen, Z.; Chiaro, B., et al. “Qubit Architecture with High Coherence and Fast Tunable Coupling”, *Physical Review Letters*, 2014, *113*:22, 220502.
- [197] Kjaergaard, M.; Schwartz, M. E.; Braumüller, J.; Krantz, P.; Wang, J. I.-J.; Gustavsson, S.; Oliver, W. D. “Superconducting Qubits: Current State of Play”, *Annual Review of Condensed Matter Physics*, 2020, *11*:1, 369–395.
- [198] Rosenblum, S.; Gao, Y. Y.; Reinhold, P.; Wang, C.; Axline, C. J.; Frunzio, L.; Girvin, S. M.; Jiang, L.; Mirrahimi, M.; Devoret, M. H.; Schoelkopf, R. J. “A CNOT gate between multiphoton qubits encoded in two cavities”, *Nature Communications*, 2018, *9*:1, 652.
- [199] Larrouy, A.; Patsch, S.; Richaud, R.; Raimond, J.-M.; Brune, M.; Koch, C. P.; Gleyzes, S. “Fast Navigation in a Large Hilbert Space Using Quantum Optimal Control”, *Physical Review X*, 2020, *10*:2, 021058.
- [200] Krinner, S. et al. “Realizing repeated quantum error correction in a distance-three surface code”, *Nature*, 2022, *605*:7911, 669–674.
- [201] Chiesa, A.; Roca, S.; Chicco, S.; de Ory, M.; Gómez-León, A.; Gomez, A.; Zueco, D.; Luis, F.; Carretta, S. “Blueprint for a Molecular-Spin Quantum Processor”, *Phys. Rev. Appl.*, 2023, *19*:6, 064060.
- [202] Wu, X.; Tomarken, S. L.; Petersson, N. A.; Martinez, L. A.; Rosen, Y. J.; DuBois, J. L. “High-Fidelity Software-Defined Quantum Logic on a Superconducting Qudit”, *Phys. Rev. Lett.*, 2020, *125*:17, 170502.

- [203] Cao, S.; Bakr, M.; Campanaro, G.; Fasciati, S. D.; Wills, J.; Lall, D.; Shteynas, B.; Chidambaram, V.; Rungger, I.; Leek, P. Emulating two qubits with a four-level transmon qudit for variational quantum algorithms, 2023.
- [204] Hartmann, J.-G.; Janković, D.; Pasquier, R.; Ruben, M.; Hervieux, P.-A. Nonlinearity of the Fidelity in Open Qudit Systems: Gate and Noise Dependence in High-dimensional Quantum Computing, 2024.
- [205] Hartmann, J.-G.; Jankovic, D.; Pasquier, R.; Ruben, M.; Hervieux, P.-A. Code and Data for "Nonlinearity of the Fidelity in Open Qudit Systems: Gate and Noise Dependence in High-dimensional Quantum Computing", version 1.0.0, 2024.
- [206] Villegas-Martínez, B. M.; Soto-Eguibar, F.; Moya-Cessa, H. M. "Application of Perturbation Theory to a Master Equation", *Advances in Mathematical Physics*, 2016, 2016:1, 9265039.
- [207] Campbell, J. E. "On a Law of Combination of Operators bearing on the Theory of Continuous Transformation Groups", *Proceedings of the London Mathematical Society*, 1896, s1-28:1, 381–390.
- [208] Hall, B. C., *Lie groups, Lie algebras, and representations: an elementary introduction*, Second edition; Graduate texts in mathematics 222; Springer: Cham ; New York, 2015; 449 pp.
- [209] Fisher, R. M. Optimal Control of Multi-Level Quantum Systems, Ph.D. Thesis, echnische Univ. Muenchen (Germany). Fakultaet fuer Chemie.
- [210] Bengtsson, I.; Życzkowski, K., *Geometry of Quantum States: An Introduction to Quantum Entanglement*; Cambridge University Press: Cambridge, 2006.
- [211] Eltschka, C.; Huber, M.; Morelli, S.; Siewert, J. "The shape of higher-dimensional state space: Bloch-ball analog for a qutrit", *Quantum*, 2021, 5, 485.
- [212] Aifer, M.; Deffner, S. "From quantum speed limits to energy-efficient quantum gates", *New Journal of Physics*, 2022, 24:5, 055002.
- [213] Dionis, E.; Sugny, D. "Time-optimal control of two-level quantum systems by piecewise constant pulses", *Physical Review A*, 2023, 107:3, 032613.
- [214] D'Alessandro, D., *Introduction to quantum control and dynamics*, 2nd edition; Advances in mathematics series; CRC Press: Boca Raton, 2021.
- [215] Givens, W. "Computation of Plain Unitary Rotations Transforming a General Matrix to Triangular Form", *Journal of the Society for Industrial and Applied Mathematics*, 1958, 6:1, 26–50.
- [216] Murnaghan, F. D. "The orthogonal and symplectic groups", *Commun. Dublin Inst. Adv. Stud.*, 1958, 13, 156.
- [217] Murnaghan, F. D., *The Unitary and Rotation Groups*; Lecture Notes in Applied Mathematics, Vol. 3; Spartan Books, [Washington, D.C., 1962.
- [218] Barenco, A.; Bennett, C. H.; Cleve, R.; DiVincenzo, D. P.; Margolus, N.; Shor, P.; Sleator, T.; Smolin, J. A.; Weinfurter, H. "Elementary gates for quantum computation", *Physical Review A*, 1995, 52:5, 3457–3467.
- [219] DiVincenzo, D. P. "Two-bit gates are universal for quantum computation", *Physical Review A*, 1995, 51:2, 1015–1022.
- [220] Cybenko, G. "Reducing quantum computations to elementary unitary operations", *Computing in Science and Engg.*, 1996, 3:2, 27–32.
- [221] O'Leary, D. P.; Bullock, S. S. "QR factorizations using a restricted set of rotations", *Electronic Transactions on Numerical Analysis*, 2005, 21, 20–27.
- [222] Brennen, G.; O'Leary, D.; Bullock, S. "Criteria for exact qudit universality", *Physical Review A*, 2005, 71:5, 052318.
- [223] Rong, X.; Geng, J.; Shi, F.; Liu, Y.; Xu, K.; Ma, W.; Kong, F.; Jiang, Z.; Wu, Y.; Du, J. "Experimental fault-tolerant universal quantum gates with solid-state spins under ambient conditions", *Nature Communications*, 2015, 6:1, 8748.

- [224] Devra, A.; Prabhu, P.; Singh, H.; Arvind; Dorai, K. “Efficient experimental design of high-fidelity three-qubit quantum gates via genetic programming”, *Quantum Information Processing*, 2018, 17:3, 67.
- [225] Rowland, B.; Jones, J. A. “Implementing quantum logic gates with gradient ascent pulse engineering: principles and practicalities”, *Philosophical Transactions of the Royal Society A: Mathematical, Physical and Engineering Sciences*, 2012, 370:1976, 4636–4650.
- [226] Shapiro, S. “Lagrange and Mayer problems in optimal control”, *Automatica*, 1966, 3:3, 219–230.
- [227] Lutz, K.; Privat, Y. Decoherence control for quantum information, Master Thesis, Université de Strasbourg, 2023.
- [228] Bergounioux, M.; Bourdin, L. “Pontryagin maximum principle for general Caputo fractional optimal control problems with Bolza cost and terminal constraints”, *ESAIM: Control, Optimisation and Calculus of Variations*, 2020, 26, 35.
- [229] Allouche, J.-P.; Shallit, J. In *Sequences and their Applications*, ed. by Ding, C.; Helleseht, T.; Niederreiter, H., Springer London: London, 1999, pp 1–16.
- [230] Kolářínmóde {\textbackslash}checkr{\textbackslash}else ř{\textbackslash}fi, M.; Ali, M. K.; Nori, F. “Generalized Thue-Morse chains and their physical properties”, *Phys. Rev. B*, 1991, 43:1, 1034–1047.
- [231] Prouhet, E. “Memoire sur quelques relations entre les puissances des nombres”, *C. R. Acad. Sci. Paris Ser. I*, 1851, 33, 225.
- [232] Thue, A. “Über unendliche Zeichenreihen”, *Kra. Vidensk. Selsk. Skrifter. I. Mat.-Nat. Kl.*, 1906:7.
- [233] Morse, H. M. “Recurrent geodesics on a surface of negative curvature”, *Transactions of the American Mathematical Society*, 22, 84–100.
- [234] Xiong, L.; Zhang, Y.; Liu, Y.; Zheng, Y.; Jiang, X. “Higher-order topological states in photonic Thue-Morse quasicrystals: Quadrupole insulator and the origin of corner states”, *Physical Review Applied*, 2022, 18:6, 064089.
- [235] Deng, X.-H.; Yuan, R.; Hong, W.-Q.; Ouyang, H. “Tunable filters based on Thue-Morse quasicrystals composed of single-negative materials”, *Physics Procedia*, 2011, 22, 360–365.
- [236] Matarazzo, V.; De Nicola, S.; Zito, G.; Mormile, P.; Rippa, M.; Abbate, G.; Zhou, J.; Petti, L. “Spectral characterization of two-dimensional Thue–Morse quasicrystals realized with high resolution lithography”, *Journal of Optics*, 2010, 13:1, 015602.
- [237] Yang, J.-K.; Noh, H.; Boriskina, S. V.; Rooks, M. J.; Solomon, G. S.; Dal Negro, L.; Cao, H. In *2012 Conference on Lasers and Electro-Optics (CLEO)*, 2012, pp 1–2.
- [238] Nguyen, H. D. A New Proof of the Prouhet-Tarry-Escott Problem, 2014.
- [239] Knill, E.; Laflamme, R. “Theory of quantum error-correcting codes”, *Phys. Rev. A*, 1997, 55:2, 900–911.
- [240] Meenakshisundaram, N.; Lakshminarayan, A. “Multifractal eigenstates of quantum chaos and the Thue-Morse sequence”, *Phys. Rev. E*, 2005, 71:6, 065303.
- [241] Maity, K.; Lakshminarayan, A. “Quantum chaos in the spectrum of operators used in Shor’s algorithm”, *Phys. Rev. E*, 2006, 74:3, 035203.
- [242] Fan, A.; Schmeling, J.; Shen, W. Multifractal Analysis of generalized Thue-Morse trigonometric polynomials, 2022.
- [243] Tóth, L. “Linear Combinations of Dirichlet Series Associated with the Thue-Morse Sequence”, 2022.
- [244] Feiler, C.; Schleich, W. P. “Dirichlet series as interfering probability amplitudes for quantum measurements”, *New Journal of Physics*, 2015, 17:6, 063040.
- [245] Gleisberg, F.; Mack, R.; Vogel, K.; Schleich, W. P. “Factorization with a logarithmic energy spectrum”, *New Journal of Physics*, 2013, 15:2, 023037.
- [246] Feiler, C.; Schleich, W. P. “Entanglement and analytical continuation: an intimate relation told by the Riemann zeta function”, *New Journal of Physics*, 2013, 15:6, 063009.

- [247] Mirzoyan, R.; Kazmierczak, N. P.; Hadt, R. G. “Deconvolving Contributions to Decoherence in Molecular Electron Spin Qubits: A Dynamic Ligand Field Approach”, *Chemistry – A European Journal*, 2021, chem.202100845.
- [248] Mirzoyan, R.; Hadt, R. G. “The dynamic ligand field of a molecular qubit: decoherence through spin–phonon coupling”, *Physical Chemistry Chemical Physics*, 2020, 22:20, 11249–11265.
- [249] C. Kragsskow, J. G.; Mattioni, A.; K. Staab, J.; Reta, D.; M. Skelton, J.; F. Chilton, N. “Spin–phonon coupling and magnetic relaxation in single-molecule magnets”, *Chemical Society Reviews*, 2023, 52:14, 4567–4585.
- [250] Mandelshtam, V. A.; Taylor, H. S. “A low-storage filter diagonalization method for quantum eigenenergy calculation or for spectral analysis of time signals”, *The Journal of Chemical Physics*, 1997, 106:12, 5085–5090.
- [251] Green, T. J.; Sastrawan, J.; Uys, H.; Biercuk, M. J. “Arbitrary quantum control of qubits in the presence of universal noise”, *New Journal of Physics*, 2013, 15:9, 095004.
- [252] Koch, C. P. “Controlling open quantum systems: tools, achievements, and limitations”, *Journal of Physics: Condensed Matter*, 2016, 28:21, 213001.
- [253] Jandura, S.; Pupillo, G. “Time-Optimal Two- and Three-Qubit Gates for Rydberg Atoms”, *Quantum*, 2022, 6, 712.
- [254] Hartmann, J.-G. Hilbert space engineering and optimal control for quantum computing with applications for rare-earth single molecule magnets, Ph.D. Thesis, Université de Strasbourg, 2024.
- [255] Viola, L.; Lloyd, S. “Dynamical suppression of decoherence in two-state quantum systems”, *Physical Review A*, 1998, 58:4, 2733–2744.
- [256] Guéry-Odelin, D.; Ruschhaupt, A.; Kiely, A.; Torrontegui, E.; Martínez-Garaot, S.; Muga, J. G. “Shortcuts to adiabaticity: Concepts, methods, and applications”, *Reviews of Modern Physics*, 2019, 91:4, 045001.
- [257] Wimperis, S. “Broadband, Narrowband, and Passband Composite Pulses for Use in Advanced NMR Experiments”, *Journal of Magnetic Resonance, Series A*, 1994, 109:2, 221–231.
- [258] Chizzini, M.; Crippa, L.; Chiesa, A.; Tacchino, F.; Petiziol, F.; Tavernelli, I.; Santini, P.; Carretta, S. “Molecular nanomagnets with competing interactions as optimal units for qudit-based quantum computation”, *Physical Review Research*, 2022, 4:4, 043135.
- [259] Lidar, D. A.; Chuang, I. L.; Whaley, K. B. “Decoherence-Free Subspaces for Quantum Computation”, *Physical Review Letters*, 1998, 81:12, 2594–2597.
- [260] Johansson, J.; Nation, P.; Nori, F. “QuTiP: An open-source Python framework for the dynamics of open quantum systems”, *Computer Physics Communications*, 2012, 183:8, 1760–1772.
- [261] Suezem, M. Bristol: A Python Package for Random Matrix Ensembles, 2017.
- [262] Srinivasa Rao, K.; Rajeswari, V.; Srinavasa Rao, K., *Quantum theory of angular momentum: selected topics*; Springer [u.a.]: Berlin Heidelberg, 1993; 315 pp.
- [263] Volkin, H.; Aeronautics, U. S. N.; Administration, S.; Center, L. R., *Iterated commutators and functions of operators*; NASA technical note; National Aeronautics and Space Administration: 1968.

PART VII

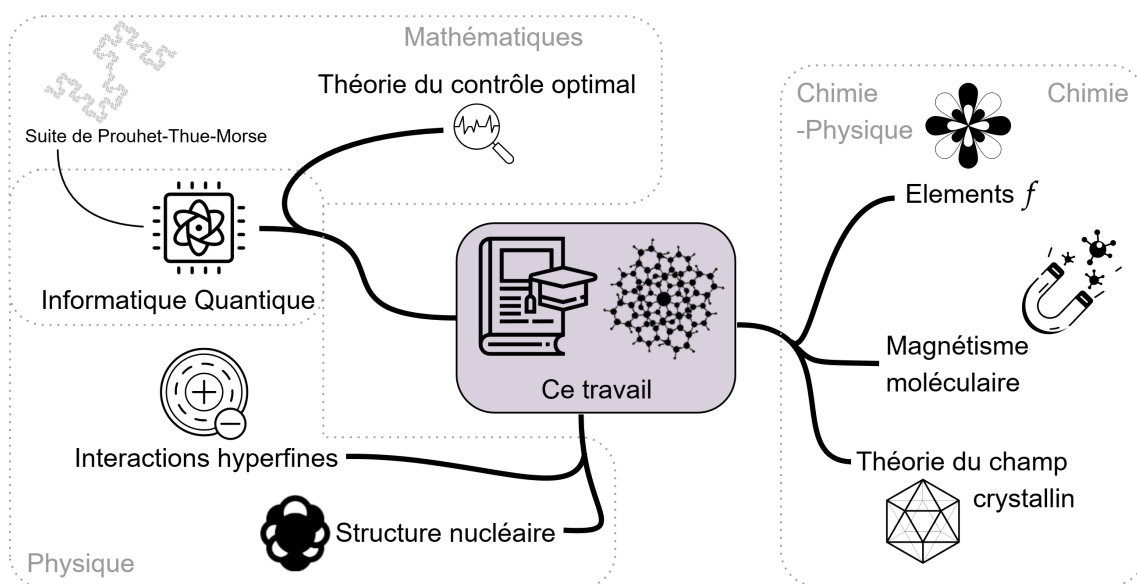
French summarized version

PARTIE 0^F

Introduction en français

Ce chapitre introductif vise à présenter les différents domaines et la manière dont ils se rapportent à cette thèse et à cet effort. Tout d'abord, il introduira le contexte historique et l'état de l'art actuel des différents formalismes. Ensuite, il discutera de la manière dont ces domaines s'entrelacent pour former les bases théoriques utilisées pour les systèmes d'intérêt dans cette étude.

0^F.1 Chemins convergents : Une introduction historique multidisciplinaire



Ce travail se situe à l'intersection de plusieurs domaines : l'informatique quantique, la théorie du contrôle optimal, la structure nucléaire, les interactions hyperfines, les éléments f , la théorie du champ cristallin, et le magnétisme moléculaire. Le développement historique de ces domaines est interconnecté, chacun apportant des idées et des méthodologies uniques qui ont façonné notre compréhension des systèmes quantiques et des matériaux. Cette section offre un bref aperçu de l'évolution de ces disciplines et de leur convergence, dans ce travail, vers l'étude des complexes organiques de lanthanides pour le traitement de l'information quantique.

Informatique quantique

L'évolution de l'informatique quantique est intimement liée à la quête de compréhension et de manipulation des principes fondamentaux du traitement de l'information. Bien que l'informatique classique ait accompli des avancées remarquables, la miniaturisation incessante des transistors approche des limites physiques imposées par la mécanique quantique [1, 2]. Cette convergence imminente a propulsé l'exploration de l'informatique quantique comme un nouveau paradigme tirant parti des propriétés uniques de la mécanique quantique.

Les premières idées d'informatique quantique remontent au début des années 1980. Yuri Manin a d'abord proposé l'idée d'exploiter la mécanique quantique pour le calcul en 1980 [3]. Peu après, Paul Benioff a introduit un modèle quantique de la machine de Turing [4], posant les bases des modèles théoriques d'informatique quantique. Richard Feynman, dans son célèbre article de 1982 *Simulating physics with computers* [5], a déclaré : « La nature n'est pas classique, bon sang, et si vous voulez simuler la nature, vous feriez mieux de la rendre quantique. » David Deutsch a encore fait progresser le domaine en 1985 en proposant le premier modèle d'ordinateur quantique universel [6].

Le développement des algorithmes quantiques a été essentiel pour démontrer les avantages potentiels des ordinateurs quantiques par rapport à leurs homologues classiques. L'algorithme révolutionnaire de Peter Shor en 1994 pour la factorisation de grands nombres et le calcul de logarithmes discrets [7] a montré que les ordinateurs quantiques pouvaient résoudre certains problèmes de manière exponentiellement plus rapide que les ordinateurs classiques. L'algorithme de recherche non structurée de Lov Grover en 1996 a offert une accélération quadratique [8], et les travaux de Seth Lloyd sur les simulateurs quantiques universels [9] ont mis en évidence la capacité des systèmes quantiques à simuler efficacement d'autres systèmes quantiques.

Ces avancées théoriques ont stimulé des recherches intensives sur la mise en œuvre pratique des ordinateurs quantiques. Diverses plateformes physiques ont été explorées, notamment les circuits supraconducteurs [10], les ions piégés [11, 12], les systèmes photoniques [13, 14], les atomes neutres [15, 16], et les boîtes quantiques semi-conductrices [17, 18]. Parmi celles-ci, les qubits supraconducteurs se sont imposés en raison de leur dimensionnement et de leur intégration avec les technologies existantes. Des entreprises comme IBM et Google ont développé des processeurs quantiques supraconducteurs avec des dizaines à des centaines de qubits [19, 20], atteignant des jalons significatifs en termes de temps de cohérence et de fidélité des portes logiques.

Malgré les progrès rapides, des défis techniques majeurs subsistent pour atteindre une informatique quantique universelle et tolérante aux fautes. Des problèmes liés à la décohérence, à la gestion du bruit et à la correction d'erreurs persistent, en particulier à mesure que les systèmes s'agrandissent [21]. Les critères de DiVincenzo [22] définissent les exigences essentielles pour un ordinateur quantique fonctionnel, y compris des qubits extensibles, une initialisation fiable, de longs temps de cohérence, un ensemble universel de portes quantiques, et une lecture efficace des qubits. Répondre à tous ces critères simultanément est une tâche redoutable, et les plateformes actuelles basées sur les qubits (résumées dans Fig. 1) ont souvent du mal à maintenir la cohérence et des opérations de haute fidélité dans des systèmes de grande taille.

Face à ces défis, des approches alternatives comme les qudits—des systèmes quantiques avec plus de deux niveaux—ont suscité un intérêt grandissant. En encodant l'information dans des espaces de Hilbert de dimension supérieure, les qudits peuvent potentiellement améliorer l'efficacité des calculs et réduire la complexité des circuits quantiques [23]. Bien que l'informatique classique se soit finalement standardisée sur des bits binaires, les premiers ordinateurs ont exploré la logique ternaire pour augmenter la capacité de calcul [24]. De même, les qudits offrent un moyen d'encoder plus d'informations par unité physique, ce qui pourrait être avantageux pour le dimensionnement.

Les systèmes de spins nucléaires, en particulier, présentent une voie intéressante en raison de leurs longs temps de cohérence et de leur isolement inhérent du bruit environnemental. L'interaction entre

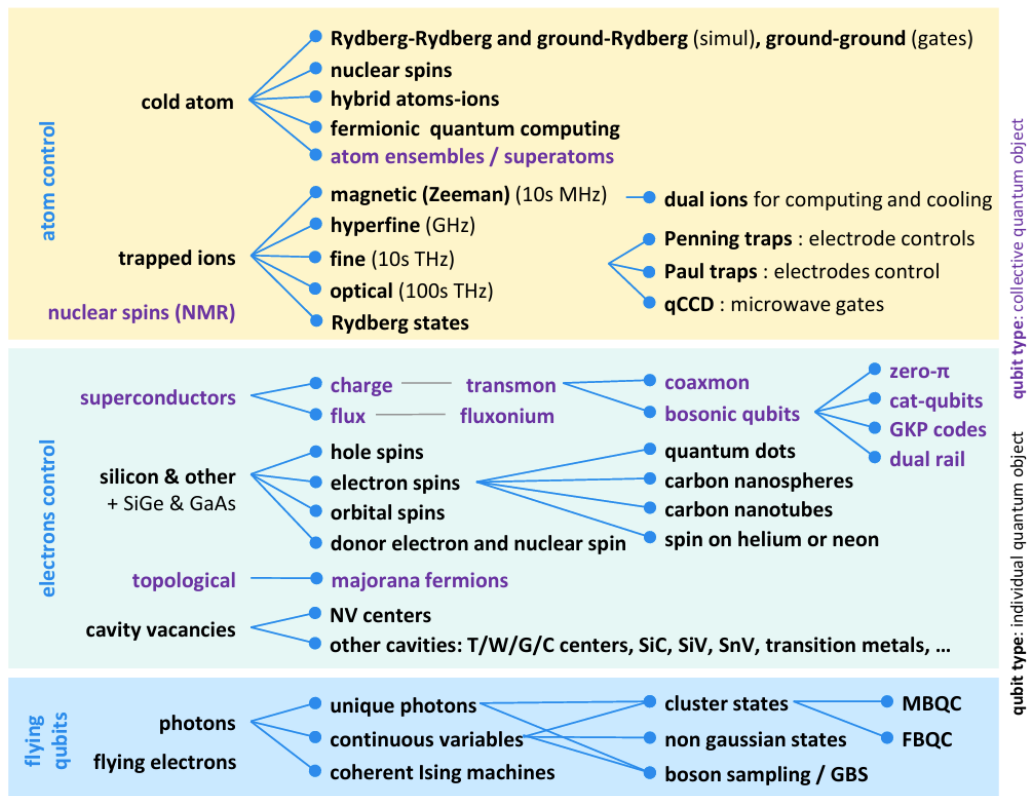


Figure 1: Zoologie approximative des plateformes d'informatique quantique à qubits. Adapté de Ezratty [21].

les degrés de liberté électroniques et nucléaires dans ces systèmes offre des avantages uniques pour le traitement de l'information quantique [25]. Bien que l'isolation forte des spins nucléaires pose des défis pour leur contrôle et leur manipulation, les progrès dans la conception des plateformes et des techniques de contrôle [26] rendent de plus en plus faisable l'exploitation de ces systèmes pour l'informatique quantique.

L'exploration de l'informatique quantique basée sur les qudits représente une stratégie prometteuse pour surmonter certaines des limitations inhérentes aux systèmes basés sur les qubits. En tirant parti des propriétés naturelles des spins nucléaires et des états quantiques de dimension supérieure, il est possible de concevoir des architectures informatiques quantiques plus évolutives et plus robustes. Alors que nous continuons à repousser les limites de la technologie et de la théorie, la convergence de plusieurs disciplines—y compris la physique, la chimie et l'informatique—sera cruciale pour progresser vers la réalisation d'ordinateurs quantiques en pratique.

Théorie du contrôle optimal

La théorie du contrôle optimal est une discipline mathématique centrée sur la recherche de stratégies de contrôle optimisant la performance de systèmes dynamiques. Ses origines remontent au calcul variationnel développé par Euler et Lagrange au XVIIIe siècle, qui a fourni des méthodes pour trouver des fonctions minimisant ou maximisant des fonctionnelles. Cette base a ouvert la voie à la résolution de problèmes d'optimisation plus complexes dans le domaine de l'ingénierie et de la physique.

Au milieu du XXe siècle, des avancées significatives ont eu lieu avec l'introduction du principe du maximum de Pontryagin par Lev Pontryagin et ses collaborateurs en 1956 [27, 28]. Ce principe a offert des conditions d'optimalité nécessaires dans les problèmes de contrôle, permettant de déterminer des lois de contrôle qui conduisent un système d'un état initial à un état final tout en optimisant un critère

de performance donné. À la même époque, Richard Bellman a développé le concept de programmation dynamique, conduisant à la formulation de l'équation de Hamilton-Jacobi-Bellman [29], qui fournit une méthode pour résoudre des problèmes de contrôle en les décomposant en sous-problèmes plus simples.

La théorie du contrôle optimal a été essentielle dans de nombreux domaines comme l'économie, où elle aide à l'allocation des ressources, l'ingénierie aérospatiale pour l'optimisation des trajectoires, et la robotique pour la planification des mouvements. Ces dernières décennies, ses principes ont été appliqués aux systèmes quantiques, donnant naissance au domaine du contrôle quantique. Le contrôle quantique consiste à manipuler les états et dynamiques quantiques pour atteindre des résultats désirés, ce qui est essentiel pour l'informatique quantique et le traitement de l'information quantique [30, 31].

Dans le cadre de l'informatique quantique, la théorie du contrôle optimal est utilisée pour concevoir des impulsions de contrôle qui appliquent des portes quantiques spécifiques sur des qubits avec une haute fidélité. Des techniques comme le *Gradient Ascent Pulse Engineering* (GRAPE) ont été développées pour optimiser les champs de contrôle dans des systèmes aux interactions complexes [32]. Ces méthodes ajustent les paramètres de contrôle de manière itérative afin de maximiser le recouvrement entre les états quantiques souhaités et réels, naviguant ainsi efficacement dans le paysage complexe du contrôle des systèmes quantiques.

À mesure que les systèmes quantiques deviennent plus complexes, en particulier avec l'introduction des qudits qui possèdent des espaces d'état de dimensions plus élevées, l'application de la théorie du contrôle optimal devient de plus en plus cruciale. La complexité du contrôle de tels systèmes nécessite des outils mathématiques sophistiqués pour assurer une manipulation précise tout en atténuant les erreurs dues à la décohérence et aux autres sources de bruit quantique.

L'intégration de la théorie du contrôle optimal avec les technologies quantiques améliore non seulement les performances des opérations quantiques, mais contribue également à surmonter certains des défis liés au dimensionnement rencontrés par les plateformes actuelles d'informatique quantique. En optimisant les stratégies de contrôle, il est possible d'améliorer la fidélité des portes et les temps de cohérence, nous rapprochant ainsi de la réalisation d'ordinateurs quantiques universels et tolérants aux fautes.

Structure nucléaire

L'étude de la structure nucléaire vise à comprendre les propriétés et comportements des noyaux atomiques en examinant les interactions entre protons et neutrons. Ce domaine a considérablement évolué depuis l'expérience de la feuille d'or d'Ernest Rutherford en 1911, qui a conduit à la découverte du noyau atomique [33]. Les travaux de Rutherford ont jeté les bases des modèles ultérieurs qui ont cherché à expliquer la stabilité nucléaire, les énergies de liaison, et d'autres propriétés fondamentales.

Les premiers modèles théoriques, tels que le modèle de la goutte liquide proposé par George Gamow [34], puis raffiné par Niels Bohr et John Archibald Wheeler [35], traitaient le noyau comme une goutte de liquide incompressible. Cette approche macroscopique expliquait avec succès la fission nucléaire et les propriétés globales, mais ne pouvait pas rendre compte des niveaux d'énergie discrets observés dans les expériences. Pour répondre à cela, Maria Goeppert Mayer et J. Hans D. Jensen ont développé indépendamment le modèle en couches nucléaires en 1949 [36, 37], qui considérait des nucléons individuels se déplaçant dans un potentiel moyen. Le modèle en couches a expliqué l'apparition de "nombres magiques" correspondant à des configurations exceptionnellement stables, illuminant l'importance de la mécanique quantique dans les systèmes nucléaires. Ce modèle a valu à ses créateurs le prix Nobel de physique en 1963. À titre illustratif, la Fig. 2 montre les orbites du modèle en couches nucléaires avec leurs numéros quantiques respectifs et l'ordre typique des niveaux.

Comprendre la force nucléaire forte—la force fondamentale responsable de la liaison des protons et des neutrons—s'est révélé crucial en physique nucléaire. La force nucléaire forte est caractérisée par une attraction de courte portée mais extrêmement puissante, surmontant la répulsion électromagnétique entre les protons. Cependant, résoudre directement les équations de la chromodynamique quantique

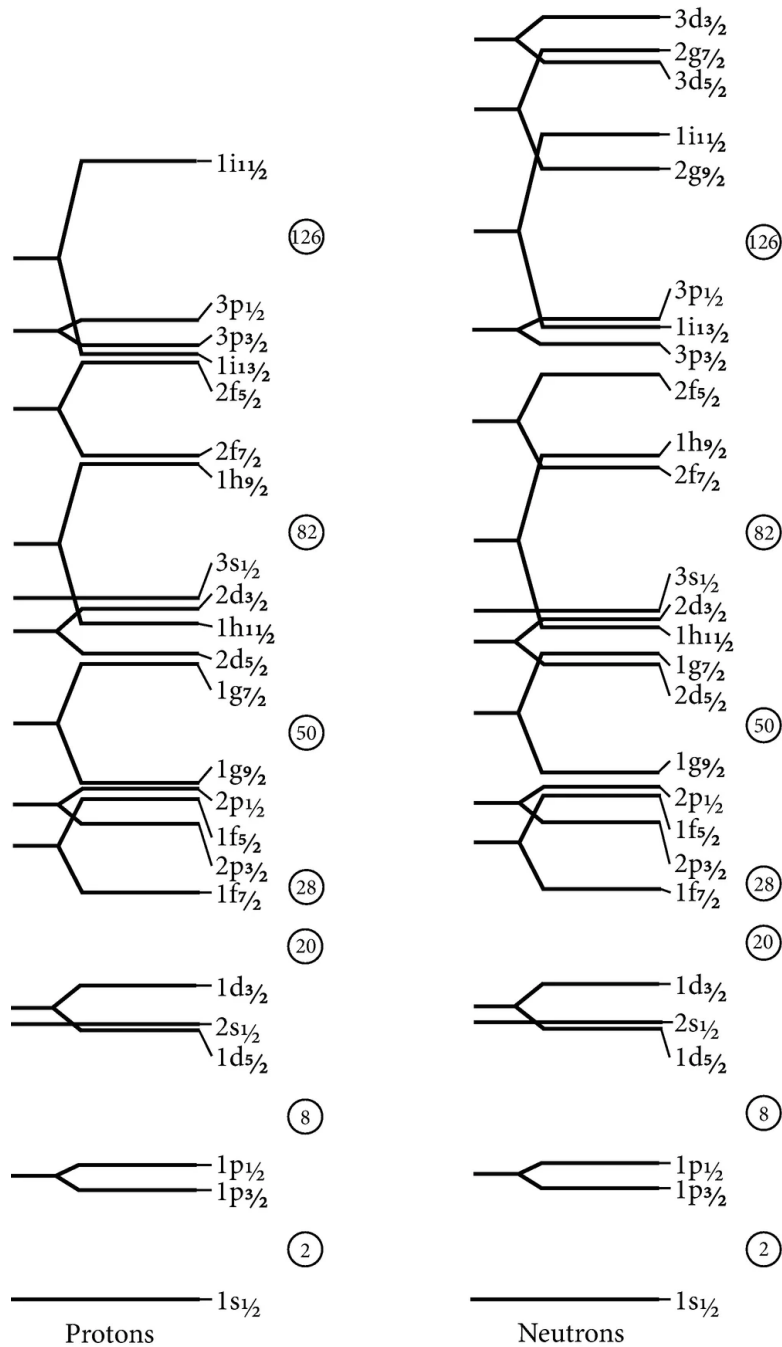


Figure 2: Orbits du modèle en couches nucléaires avec leurs numéros quantiques respectifs et ordre des niveaux typique. Les nombres magiques de protons et de neutrons sont encadrés. Adapté de [38].

(QCD) pour les noyaux est infaisable à l'état actuel sur le plan computationnel en raison de la complexité des interactions à plusieurs corps à basse énergie.

Pour contourner ce défi, des interactions effectives et des modèles phénoménologiques ont été développés. Un exemple notable est l'interaction de Skyrme, introduite par Tony Skyrme en 1958 [39]. L'interaction de Skyrme est une force effective à paramètres utilisée dans le cadre du champ moyen, permettant des calculs simplifiés des propriétés nucléaires tout en capturant les caractéristiques essentielles de la force forte.

La méthode Skyrme-Hartree-Fock (SHF) combine l'interaction de Skyrme avec l'approche de Hartree-

Fock pour modéliser le noyau comme un ensemble de nucléons indépendants se déplaçant dans des champs moyens auto-consistants [40]. Cette méthode prend en compte les cruciaux effets d'échange et de corrélation pour une description précise des systèmes nucléaires. Pour inclure les corrélations de paire essentielles pour les noyaux à couche ouverte, la théorie Hartree-Fock-Bogoliubov (HFB) étend la méthode SHF en incorporant les transformations de Bogoliubov [41].

Les noyaux déformés, en particulier ceux de la série des lanthanides, présentent des déviations significatives par rapport à la symétrie sphérique en raison de leurs configurations à couche ouverte et des interactions fortes entre nucléons [42, 43]. Les modèles SHF et HFB, utilisant des interactions de type Skyrme, ont été essentiels pour prédire et expliquer les propriétés de ces noyaux déformés.

Interactions hyperfines

L'exploration des interactions hyperfines a été une pierre angulaire dans le développement de la physique atomique et nucléaire, fournissant des aperçus fondamentaux sur les structures internes des atomes et des noyaux. Le phénomène a été observé pour la première fois à la fin du XIXe et au début du XXe siècle, lorsque des spectroscopistes ont détecté de petites séparations dans les raies spectrales atomiques allant au-delà de la structure fine expliquée par le couplage spin-orbite des électrons. Ces séparations supplémentaires, appelées structure hyperfine, étaient attribuées aux interactions entre les électrons et le noyau, spécifiquement impliquant les moments magnétiques nucléaires.

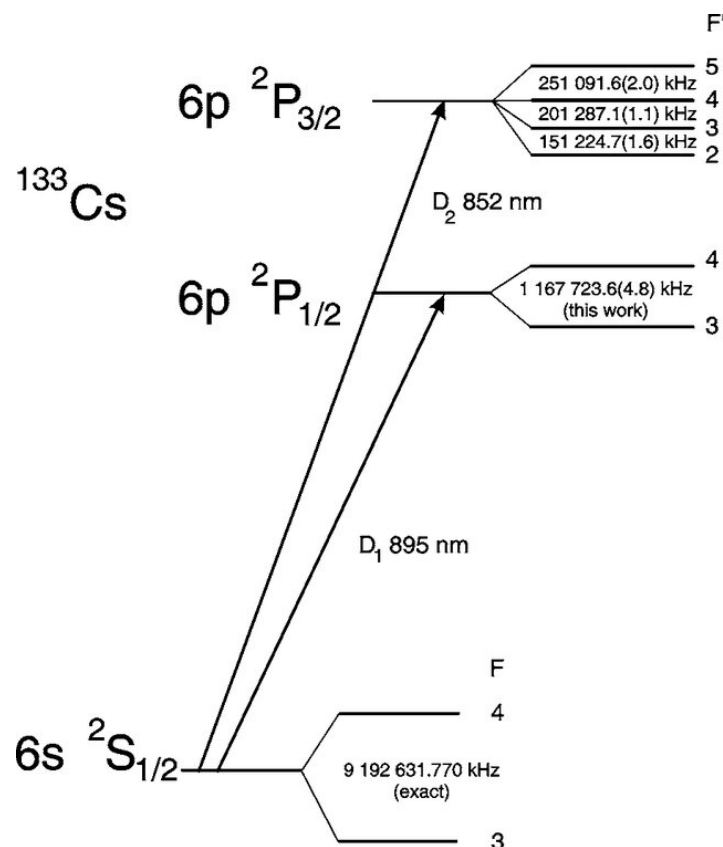


Figure 3: Diagramme des niveaux d'énergie du ^{133}Cs neutre, non à l'échelle. La transition hyperfine entre les états fondamentaux $F = 4$ et $F = 3$ est utilisée comme base pour les horloges atomiques. Adapté de [44].

La compréhension théorique des interactions hyperfines a été considérablement avancée par l'introduction du concept de spin électronique par George Uhlenbeck et Samuel Goudsmit [45]. Leur proposition selon laquelle les électrons possèdent un moment angulaire intrinsèque, ou spin, a été essentielle pour

expliquer les structures fines atomiques. La théorie quantique relativiste de l'électron de Paul Dirac a ensuite fourni un cadre complet intégrant le spin électronique et les moments magnétiques [46], essentiel pour décrire avec précision les phénomènes de structure fine.

Pour expliquer les structures hyperfines, il est devenu nécessaire de considérer le moment dipolaire magnétique nucléaire résultant du spin intrinsèque et du mouvement orbital des protons et neutrons au sein du noyau. L'interaction entre le moment magnétique nucléaire et le champ magnétique produit par les électrons au niveau du noyau conduit à des séparations de niveaux d'énergie observables comme structure hyperfine [47].

À mesure que la précision expérimentale s'est améliorée, il a été découvert que certains noyaux présentaient des séparations hyperfines ne pouvant être entièrement expliquées par des interactions dipolaires magnétiques. En 1939, l'existence du moment quadripolaire électrique nucléaire a été proposée pour traiter ces écarts [48]. Ce moment quadripolaire provient d'une distribution de charge non sphérique au sein de noyaux déformés et interagit avec les gradients de champ électrique générés par les électrons environnants, entraînant des séparations hyperfines supplémentaires [49].

D'autres affinements de la théorie des interactions hyperfines ont inclus des corrections tenant compte de la taille finie et de la structure du noyau. L'effet Bohr-Weisskopf [50] prend en considération la distribution de la magnétisation nucléaire et son impact sur l'interaction hyperfine, ce qui devient particulièrement significatif dans les noyaux lourds où l'hypothèse d'un noyau ponctuel est mal adaptée. La correction de Breit-Rosenthal [51] intègre les effets relativistes et le recouvrement des fonctions d'onde électroniques avec le noyau de taille finie, fournissant des calculs plus précis des structures hyperfines.

Les atomes muoniques ont offert des aperçus précieux sur les interactions hyperfines et les propriétés nucléaires. Dans ces atomes, un électron est remplacé par un muon, un lepton ayant la même charge mais environ 200 fois la masse d'un électron. La proximité accrue du muon par rapport au noyau amplifie la sensibilité aux distributions de charge nucléaire et aux déformations [52]. L'étude des séparations hyperfines dans les atomes muoniques a permis des examens détaillés des tailles et formes nucléaires, ainsi que de la distribution de la magnétisation nucléaire [53].

Les interactions hyperfines ont des applications critiques dans la technologie moderne et la science fondamentale. La transition hyperfine entre les états fondamentaux $F = 4$ et $F = 3$ du césium-133 est utilisée pour définir la seconde dans le Système international d'unités (SI) [54], comme illustré dans la Fig. 3. Les horloges atomiques basées sur cette transition fournissent des standards de fréquence extrêmement stables, essentiels pour les systèmes de positionnement global (GPS), les télécommunications et la mesure du temps avec précision [55].

Dans le domaine de l'informatique quantique, les niveaux hyperfins sont exploités pour leurs longs temps de cohérence et leur robustesse contre la décohérence environnementale. Des systèmes comme le silicium dopé au phosphore utilisent les états de spin nucléaire des atomes de phosphore comme qubits, les interactions hyperfines facilitant l'initialisation et la lecture des états quantiques par couplage avec les spins électroniques [56]. Les ordinateurs quantiques à ions piégés utilisent les états hyperfins d'ions comme le $^{43}\text{Ca}^+$ et le $^{171}\text{Yb}^+$ pour obtenir des opérations quantiques et de l'intrication de haute fidélité nécessaires au traitement de l'information quantique évolutif [57, 58, 59].

Les interactions hyperfines sont également fondamentales dans la recherche en physique nucléaire, notamment pour l'étude des noyaux avec déformation octupolaire — des noyaux présentant des distributions de charge en forme de poire. En analysant les modèles de séparation hyperfine, les chercheurs peuvent déduire la présence de telles formes exotiques, ayant des implications pour la compréhension des symétries fondamentales et des interactions au sein du noyau [60]. Ces études enrichissent notre connaissance de la structure nucléaire et informent les modèles prédisant le comportement nucléaire sous diverses conditions.

En résumé, l'étude des interactions hyperfines a profondément influencé la physique théorique et

appliquée. Depuis les premières observations des séparations de raies spectrales jusqu'à leur utilisation dans les technologies de pointe comme les horloges atomiques et les ordinateurs quantiques, les interactions hyperfines restent un domaine d'étude vital. Elles relient notre compréhension des structures atomiques et nucléaires et facilitent les avancées dans plusieurs disciplines, y compris la métrologie de précision, la science de l'information quantique, et la recherche fondamentale en physique.

Les éléments f

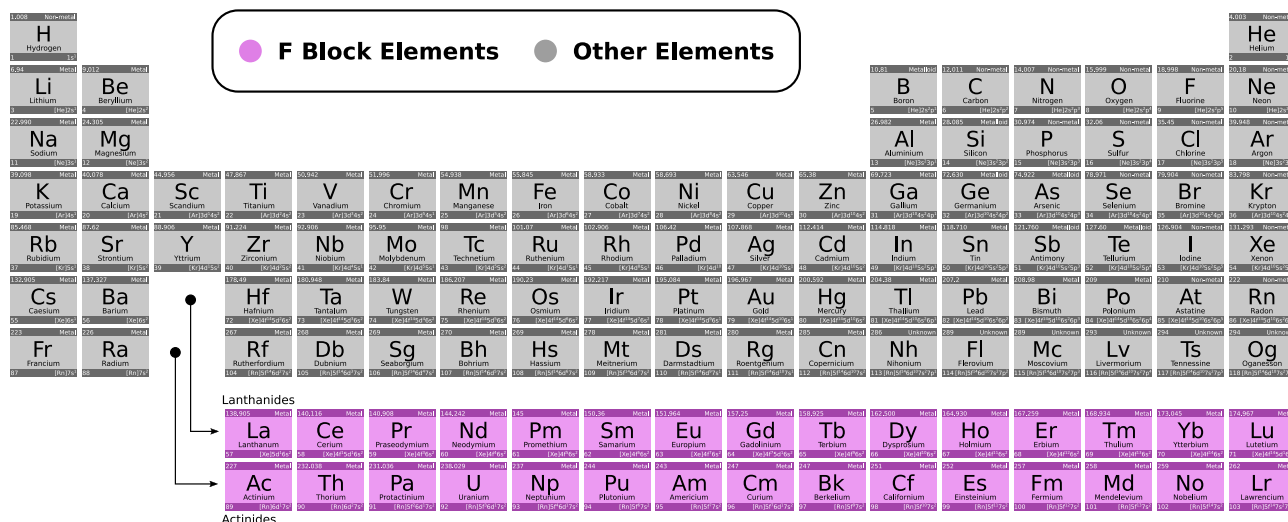


Figure 4: Le bloc f du tableau périodique, englobant les lanthanides et actinides. Adapté de [61].

Les éléments f , représentés dans la Fig. 4, forment un groupe d'éléments occupant les deux rangées en bas du tableau périodique. Cette famille englobe les lanthanides et les actinides, caractérisés par le remplissage progressif des orbitales électroniques $4f$ et $5f$, respectivement. Leur découverte et exploration ont été cruciales pour l'avancement de la chimie inorganique et de la science des matériaux. L'aventure a commencé à la fin du XVIIIe et au début du XIXe siècle avec l'isolement de l'yttrium et du cérium. Cependant, c'est le travail de Carl Gustav Mosander dans les années 1830 et 1840 qui a considérablement enrichi la connaissance des lanthanides avec la découverte du lanthane, de l'erbium, et du terbium [62].

Les lanthanides ont posé un défi considérable aux chimistes en raison de leurs propriétés chimiques similaires, rendant leur séparation et identification difficiles. Un phénomène, souvent appelé « contraction des lanthanides », découle de l'effet d'écrantage des électrons $4f$, et conduit à une diminution progressive des rayons ioniques au sein de la série et donc de propriétés chimiques subtilement différentes entre complexes de lanthanide [63]. Ce dernier, couplé au développement de techniques de séparation avancées, comme l'échange d'ions et l'extraction par solvant au milieu du XXe siècle, a finalement permis l'isolement d'éléments lanthanides purs.

Les actinides, quant à eux, ont gagné en notoriété avec la découverte de l'uranium et du thorium à la fin du XVIIIe et au début du XIXe siècle. La synthèse du neptunium et du plutonium dans les années 1940 a marqué l'expansion de la série des actinides, en grande partie motivée par la recherche sur l'énergie nucléaire et l'armement [64]. Les actinides sont remarquables pour leurs propriétés radioactives et une plus grande variété d'états d'oxydation comparés aux lanthanides, attribuée à la participation des électrons $5f$ dans les liaisons.

Les configurations électroniques uniques des éléments f conduisent à des propriétés magnétiques, optiques et chimiques particulières. Les orbitales f partiellement remplies sont protégées par les électrons extérieurs s et p , conduisant à des bandes d'absorption et d'émission étroites. Leurs électrons de valence se comportent donc comme ceux d'un ion libre, faiblement perturbés par l'environnement.

Cette propriété est exploitée dans divers matériaux et dispositifs luminescents. Le fort couplage spin-orbite et de grands moments magnétiques rendent les éléments f particulièrement intéressants pour les applications en magnétisme, comme nous le verrons bientôt avec le magnétisme moléculaire.

Dans les technologies contemporaines, les lanthanides sont largement utilisés dans plusieurs industries en raison de ces propriétés exceptionnelles. Ils sont des composants critiques dans la production d'aimants permanents à haute résistance, tels que les aimants en néodyme-fer-bore (NdFeB), essentiels dans les moteurs de véhicules électriques, les générateurs d'éoliennes et divers dispositifs électroniques [65]. Le dysprosium et le terbium sont souvent ajoutés à ces aimants pour améliorer leur performance à haute température.

Les lanthanides jouent également un rôle essentiel dans les technologies d'éclairage et d'affichage. L'euprium et le terbium sont des activateurs clés dans les phosphores rouges et verts utilisés dans les lampes fluorescentes et les tubes de télévision couleur [66]. Les lignes d'émission nettes et les hautes efficacités quantiques des ions lanthanides sont exploitées dans les lasers et amplificateurs optiques, notamment dans les systèmes de communication par fibre optique où les fibres dopées à l'erbium amplifient les signaux sur de longues distances [67].

Une revue exhaustive par Bünzli et Eliseeva [68] détaille les applications variées des lanthanides dans les technologies modernes, en mettant l'accent sur leurs rôles dans les sciences des matériaux, l'électronique et la médecine. L'exploration continue de la chimie des éléments f enrichit non seulement notre compréhension fondamentale de ces éléments mais favorise aussi l'innovation dans diverses industries de haute technologie.

Cependant, il convient de noter que l'utilisation généralisée des lanthanides soulève des préoccupations écologiques et géopolitiques. L'extraction et le traitement entraînent souvent des dommages environnementaux, notamment l'érosion des sols, la destruction des habitats et la contamination de l'eau par des sous-produits toxiques comme le thorium radioactif [69]. Cela est aggravé par les faibles concentrations de lanthanides dans les minerais, nécessitant un traitement de grande envergure. Des efforts sont en cours pour développer des pratiques minières durables et des technologies de recyclage pour réduire l'impact environnemental [70], de plus, le recyclage des déchets électroniques gagne de l'attention en tant que complément [71]. Alors que la demande pour les lanthanides augmente avec les technologies vertes, la prise en compte de l'impact environnemental et la garantie d'accessibilité restent cruciales pour un développement et une innovation durables.

En résumé, les éléments f , autrefois considérés comme chimiquement énigmatiques en raison de leurs propriétés similaires et de leurs configurations électroniques complexes, sont devenus indispensables dans la technologie contemporaine. Leurs propriétés magnétiques, optiques et catalytiques sont centrales aux avancées dans les domaines de l'énergie, des communications, de la santé et du développement durable. La recherche continue sur les éléments f promet de débloquent de nouvelles applications et de relever certains des défis critiques auxquels la société moderne est confrontée.

Théorie du champ cristallin

La théorie du champ cristallin (CFT) a été développée au début du XXe siècle pour expliquer les structures électroniques et les propriétés spectrales des complexes de métaux de transition. Les travaux fondamentaux ont été réalisés par Hans Bethe en 1929, qui a introduit le concept de séparation des niveaux du champ cristallin pour décrire comment la dégénérescence des orbitales d des ions métalliques est levée en raison des champs électrostatiques produits par les ligands environnants [72, 73]. John Hasbrouck Van Vleck a ensuite perfectionné la théorie en l'appliquant aux sels paramagnétiques et en expliquant les comportements magnétiques et spectraux des ions de métaux de transition dans différents environnements de coordination [74].

La CFT modélise l'interaction métal-ligand comme une liaison purement ionique où les ligands sont traités comme des charges ponctuelles ou des dipôles qui créent un champ électrostatique, perturbant

les niveaux d'énergie des orbitales d des ions métalliques. Dans un champ octaédrique, par exemple, les cinq orbitales d dégénérées se scindent en deux ensembles : les orbitales t_{2g} de plus basse énergie et les orbitales e_g de plus haute énergie. Cette séparation, connue sous le nom d'énergie de séparation du champ cristallin (Δ_0), et illustrée dans la Fig. 5, explique l'absorption de certaines longueurs d'onde de la lumière, entraînant les couleurs caractéristiques de nombreux complexes de métaux de transition [75].

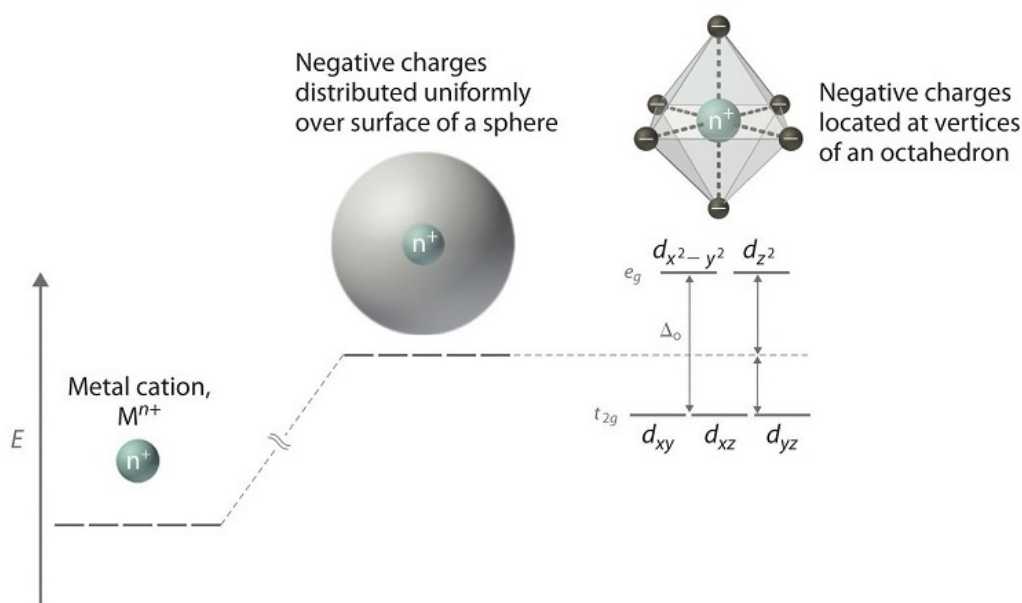


Figure 5: Séparation du champ cristallin des orbitales d dans un champ octaédrique. Les orbitales d dégénérées se scindent en ensembles t_{2g} de plus basse énergie et e_g de plus haute énergie. Adapté de [76].

Bien qu'initialement formulée pour les éléments du bloc d , la CFT a été étendue aux éléments du bloc f — les lanthanides et les actinides — pour prendre en compte leurs propriétés électroniques et magnétiques uniques. En raison de la nature profondément enfouie des orbitales f sous les orbitales extérieures s et p , les effets du champ cristallin dans les éléments f sont généralement plus faibles que dans les métaux de transition mais sont néanmoins cruciaux pour comprendre leur comportement spectroscopique. Les limitations de la modélisation des interactions métal-ligand purement électrostatiques ont conduit au développement de la théorie du champ de ligand (LFT), qui intègre les caractères covalents et considère les orbitales moléculaires dans le cadre de la CFT. La LFT fournit une compréhension plus complète de la liaison et des structures électroniques des composés de coordination, reconnaissant que les interactions métal-ligand ont souvent des contributions covalentes significatives [66, 77, 78].

Dans le domaine du magnétisme moléculaire, la CFT et la LFT sont des outils indispensables pour concevoir des molécules avec des propriétés magnétiques spécifiques. En manipulant l'environnement des ligands autour d'un centre métallique, les chimistes peuvent ajuster la séparation du champ cristallin pour maximiser l'anisotropie magnétique et stabiliser des états de spin particuliers. Ceci est particulièrement important dans le développement d'aimants moléculaires à molécule unique (SMMs), où l'objectif est d'atteindre des températures de blocage élevées et une relaxation magnétique lente [79, 80]. Par exemple, l'augmentation de la séparation axiale du champ cristallin dans les SMMs à base de dysprosium a conduit à des améliorations significatives de l'hystérésis magnétique et des températures de fonctionnement [81].

La compréhension des effets du champ cristallin est également cruciale dans le contexte de l'informatique quantique, notamment lors de l'utilisation de systèmes moléculaires comme qubits ou qudits. Le contrôle précis des niveaux d'énergie électronique par le design de ligands permet de concevoir des

molécules avec des propriétés quantiques voulues, telles que de longs temps de cohérence et des énergies de transition bien définies nécessaires pour la manipulation des qubits [82]. La capacité de moduler le champ cristallin peut conduire à une meilleure performance des qubits de spin moléculaires en minimisant les canaux de décohérence et en augmentant les temps de relaxation du spin. Dans ce travail, nous verrons également comment la symétrie des complexes, via les paramètres du champ de ligand, joue un rôle dans la vitesse d'adressage des qubits moléculaires.

En conclusion, la théorie du champ cristallin a été un concept fondamental en chimie inorganique, fournissant des aperçus critiques sur les structures électroniques et les propriétés des complexes métalliques. Ses applications vont au-delà de l'explication des couleurs et du magnétisme, permettant la conception rationnelle de matériaux pour des technologies avancées, y compris la catalyse, les dispositifs luminescents, et le traitement de l'information quantique. Le perfectionnement continu et l'application de la CFT restent centraux pour les avancées en chimie et en science des matériaux.

Magnétisme moléculaire

Le début du XXe siècle a vu se développer la compréhension fondamentale du magnétisme aux niveaux atomique et moléculaire, avec des contributions significatives de scientifiques comme Pierre Curie et Paul Langevin, qui ont exploré les susceptibilités magnétiques et le paramagnétisme [83, 84]. Le cadre conceptuel pour comprendre les interactions magnétiques dans les molécules a été davantage développé avec l'introduction de la mécanique quantique. Les travaux de Linus Pauling sur la nature de la liaison chimique ont fourni des renseignements sur la manière dont les spins électroniques non appariés contribuent aux propriétés magnétiques des molécules [85]. Le concept des interactions d'échange, où les spins électroniques sur des atomes ou ions adjacents s'influencent mutuellement comme conséquence du principe de Pauli et de la superposition de leur fonction d'onde, est devenu central pour expliquer le couplage magnétique dans les systèmes moléculaires [86].

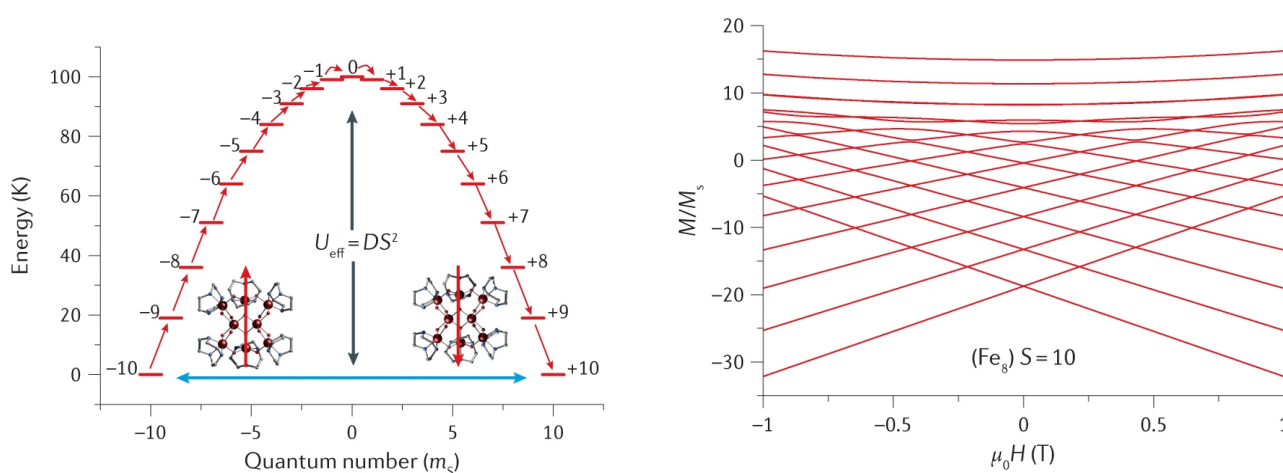
Le magnétisme moléculaire est un domaine qui explore les phénomènes magnétiques au niveau moléculaire, faisant le lien entre la chimie quantique et la physique de la matière condensée. Les origines du magnétisme moléculaire remontent au début du XXe siècle avec l'étude des propriétés paramagnétiques et diamagnétiques des composés de coordination [87]. Cependant, ce n'est que dans la seconde moitié du siècle que des avancées significatives ont été réalisées, grâce au développement de techniques spectroscopiques sophistiquées et à une compréhension plus profonde des structures électroniques.

Le travail fondateur d'Olivier Kahn dans les années 1980 et 1990 a joué un rôle crucial dans l'établissement du magnétisme moléculaire comme une discipline distincte. Les recherches de Kahn se concentraient sur la conception et la synthèse de matériaux moléculaires présentant des comportements magnétiques coopératifs, tels que le ferromagnétisme et l'antiferromagnétisme, par des interactions de superéchange médiées par des ligands pontants [88]. Ce travail a démontré que de l'ordre magnétique pouvait être obtenu dans des systèmes purement moléculaires sans nécessiter les réseaux étendus que l'on trouve dans les matériaux magnétiques traditionnels.

Une découverte marquante dans ce domaine a été l'identification des aimants à molécule unique (SMMs) en 1993 par Dante Gatteschi et Roberta Sessoli [79]. Ils ont rapporté un cluster à base de manganèse, Mn_{12} -acétate, qui présentait une relaxation lente de la magnétisation et une hystérésis magnétique d'origine purement moléculaire à basse température. Ce comportement a été attribué à un état de spin élevé combiné à une anisotropie magnétique significative, résultant en une barrière d'énergie pour l'inversion de la magnétisation — un phénomène précédemment observé uniquement dans les matériaux magnétiques en vrac.

Les SMMs sont caractérisés par une grande multiplicité de spin à l'état fondamental et une anisotropie magnétique significative, menant à une barrière d'énergie pour l'inversion de la magnétisation. Cette barrière permet à la molécule de maintenir son orientation magnétique au fil du temps, une propriété

essentielle pour les applications potentielles en stockage de données à haute densité et en informatique quantique [89]. Le *tunneling* quantique de la magnétisation (QTM) observé dans les SMMs a fourni des preuves expérimentales de phénomènes quantiques macroscopiques dans les systèmes moléculaires [90]. Ces travaux ont conduit aux études de Ishikawa et Wernsdorfer, *et. al.* au début et milieu des années 2000, où ils ont étudié les propriétés magnétiques du TbPc₂, observant une relaxation magnétique lente et le QTM [91, 92].



a) Représentation schématique du diagramme énergétique d'un aimant à molécule unique avec $S = 10$ et une énergie égale à DS^2 , où S est l'état de spin et D est le paramètre de séparation des niveaux à champ nul. L'inversion de la magnétisation se produit via les états m_S (flèches rouges) par absorption de phonons (pour exciter le système de spin au sommet de la barrière) et émission (désexcitation vers le bas de l'autre côté de la barrière). L'inversion de la magnétisation peut également se produire par *tunneling* quantique de la magnétisation à travers la barrière avec les états en résonance.

b) Diagramme de Zeeman pour Fe₈, un aimant à molécule unique avec un état fondamental de $S = 10$. Le *tunneling* quantique de la magnétisation peut se produire pour certaines intersections des états électroniques (m_S), offrant un chemin de relaxation pour la magnétisation.

Figure 6: Exemples de processus de QTM pour deux SMMs différents. Adapté de [25].

La découverte des SMMs a ouvert de nouvelles voies de recherche, avec des implications pour le stockage de données, l'informatique quantique et la spintronique. Les SMMs agissent comme des aimants à l'échelle nanométrique où chaque molécule peut potentiellement stocker un bit d'information, menant au concept de dispositifs de mémoire basés sur les molécules avec une ultra-haute densité proposé par Bogani et Wernsdorfer [93]. Le *tunneling* quantique de la magnétisation observé dans ces systèmes a également offert une plateforme pour étudier des phénomènes quantiques à l'échelle macroscopique.

Dans le contexte de l'informatique quantique, les SMMs représentent une plateforme prometteuse pour les qubits et les qudits en raison de leurs niveaux d'énergie discrets et du potentiel de cohérence quantique, comme proposé par Leuenberger et Loss en 2001 [94]. La capacité de manipuler les états de spin de molécules individuelles à l'aide de stimuli externes, tels que des champs magnétiques ou la lumière, ouvre de nouvelles perspectives pour le traitement de l'information à l'échelle moléculaire. Des défis subsistent pour obtenir de longs temps de cohérence et un contrôle cohérent, mais des stratégies telles que la modification chimique pour réduire les chemins de décohérence et l'intégration des SMMs dans des dispositifs à l'état solide sont activement étudiées [95, 96]. L'une des techniques de mesure les plus populaires pour observer le QTM est l'utilisation de magnétomètres à interférences quantiques supraconductrices (SQUID), capables de mesurer la magnétisation d'un échantillon avec une grande sensibilité et résolution. Avec le développement par Wernsdorfer des nano-SQUIDS en 2009 [97],

affinant les capacités des dispositifs micro-SQUID, la sensibilité accrue a permis la lecture électronique directe des états de spin nucléaire individuels du Tb^{3+} dans TbPc_2 [98], utilisables comme qudits, et sujet de la sous-section suivante.

En résumé, le magnétisme moléculaire a évolué, passant des études fondamentales des propriétés magnétiques des molécules à un domaine dynamique avec des implications technologiques significatives. La découverte et le développement des aimants à molécule unique ont non seulement permis d’approfondir la compréhension des phénomènes magnétiques quantiques, mais ont également ouvert la voie à des applications potentielles en informatique quantique, stockage de données à haute densité et spintronique. Les efforts interdisciplinaires combinant la chimie de synthèse, la modélisation théorique et les techniques de caractérisation avancées promettent de débloquent encore davantage le potentiel des aimants moléculaires dans les années à venir.

0^F.2 Comblent les lacunes grâce aux complexes organiques de lanthanides

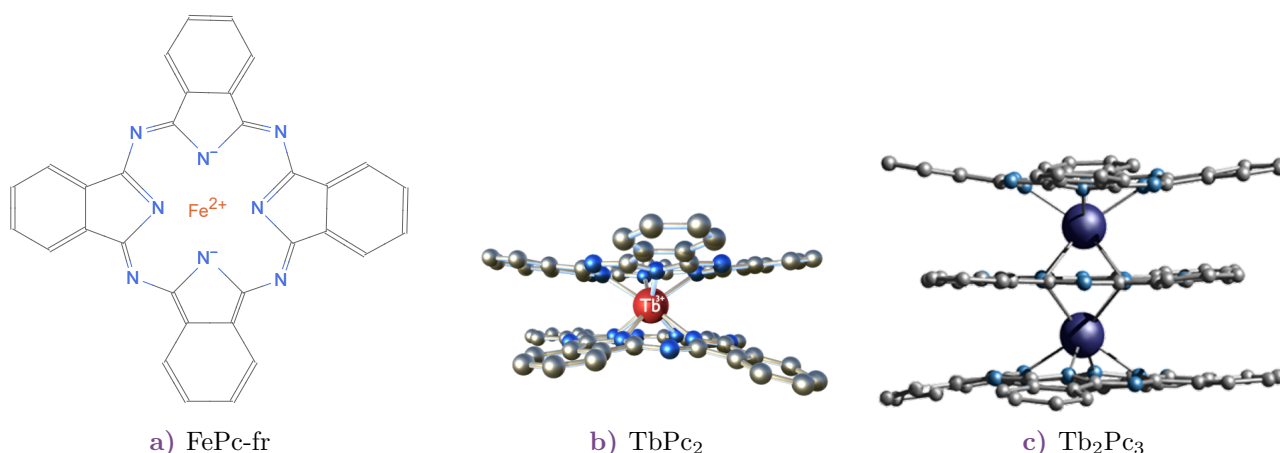


Figure 7: Exemples de complexes moléculaires à base de phtalocyanine, incluant : (a) FePc, (b) TbPc₂ et (c) Tb₂Pc₃.

Les domaines de l’informatique quantique, de la théorie du contrôle optimal, de la structure nucléaire, des interactions hyperfines, des éléments f , de la théorie du champ cristallin et du magnétisme moléculaire sont interconnectés par l’étude des complexes organiques de lanthanides. Dans la collaboration entre les chimistes de notre groupe au KIT et les physiciens du groupe Wernsdorfer à Grenoble, puis au KIT, les états de spin nucléaire des ions de lanthanides, en particulier le dysprosium et le terbium, incorporés dans des aimants à molécule unique ont été étudiés. Les systèmes les plus prometteurs sont les complexes *double-decker* (à deux étages) à base de phtalocyanine (Pc) avec un ion de lanthanide unique (LnPc_2) au centre, notamment TbPc₂ (terbium bis-phtalocyanine, voir Fig. 7 pour des exemples). En 2012, la première lecture électronique directe des états de spin nucléaire du Tb^{3+} dans une molécule unique a été démontrée [98]. Ce travail a été suivi en 2014 par la première démonstration du contrôle électrique d’un spin nucléaire dans une molécule unique, toujours avec la TbPc₂ [26]. Enfin, en 2018, sur le même système, la première implémentation d’un algorithme quantique dans une molécule unique a été réalisée [99].

En 2019, Wernsdorfer et Ruben ont publié une stratégie pour un processeur quantique et évolutif basé sur des qudits utilisant des complexes $\text{Ln}_n\text{Pc}_{n+1}$ [100]. L’idée était d’utiliser la chimie isotopologue pour concevoir et construire l’espace de Hilbert des spins nucléaires des ions de lanthanides. Par exemple, remplacer le ^{159}Tb par du ^{161}Dy ou du ^{163}Dy sélectionné isotopiquement augmenterait le nombre de niveaux nucléaires, et donc la dimension d du qudit. Synthétiser à son tour des phtalocyanines à « multiples étages » augmenterait le nombre d’ions de lanthanides, et donc le nombre de qudits n .

Cela permettrait (i) un dimensionnement linéaire de l'espace de Hilbert avec le choix de l'isotope et (ii) un dimensionnement exponentiel de l'espace de Hilbert d^n avec le nombre de qudits n . Cette thèse vise à explorer les fondements théoriques de ce sujet de recherche et à fournir une feuille de route basée sur des idées théoriques pour le développement d'un processeur quantique moléculaire basé sur des complexes organiques de lanthanides. Ce schéma est illustré dans la Fig. 8.

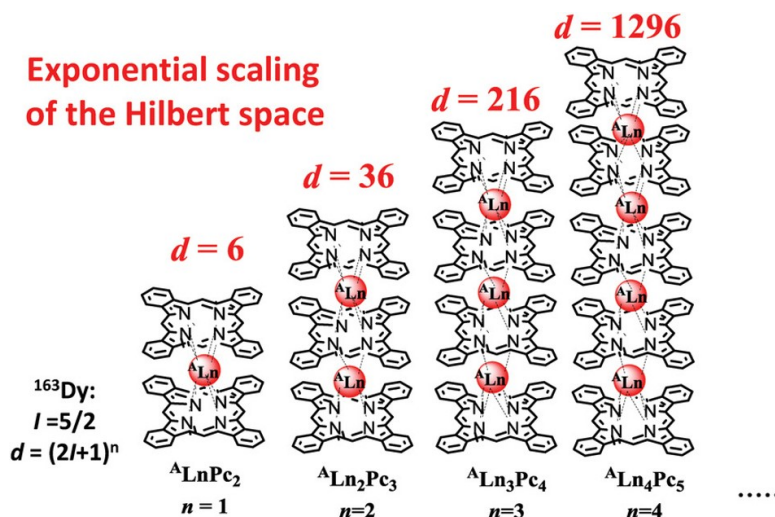


Figure 8: Dimensionnement conceptuel de l'espace de Hilbert des spins qudit $^A\text{Ln}_n\text{Pc}_{n+1}$ ($I = 5/2$) avec l'exemple de $^{163}\text{Dy}_n\text{Pc}_{n+1}$ pour $n = 1-4$ conduisant à une augmentation exponentielle par $d = (2I + 1)^n$. Adapté de [100].

Enfin, le travail de Kumar *et al.* [101], issu d'une collaboration entre notre groupe au KIT et celui de Philippe Goldner à Paris, montre le potentiel des complexes organiques de lanthanides au-delà de l'approche des SMMs, avec la démonstration, dans des complexes binucléaires d'euprémium en cristaux, de transitions de spin nucléaire contrôlées de façon optique plutôt qu'électrique. Cela ouvre également la possibilité d'utiliser les transitions optiques des ions de lanthanides pour déclencher les transitions de spin nucléaire.

Le cas d'école: TbPc_2

Présentons en détail le système physique sur lequel ont été réalisées les expériences précédemment mentionnées, la molécule de TbPc_2 . La molécule de TbPc_2 est un aimant à molécule unique (SMM) composé d'un ion Tb^{3+} coordonné à deux ligands phthalocyanine. Les expériences ont été réalisées à des températures cryogéniques de 1,2 K, où la molécule présente une relaxation magnétique lente en raison de la présence d'une grande barrière d'énergie entre les états fondamental et excité. La molécule est placée sur une surface d'or et connectée à des électrodes en or, formant une jonction de rupture, comme illustré dans la Fig. 9. Les électrons de valence de l'ion central Tb^{3+} sont couplés par interaction d'échange à l'électron délocalisé dans le radical, ce qui est la source des variations de conductance en fonction de l'orientation du spin de type Ising des électrons de valence, qui se révélera plus tard très utile.

Un hamiltonien à échelles multiples

Le hamiltonien du système est composé de plusieurs termes, chacun responsable d'une séparation d'énergie différente du système. Le hamiltonien de champ central H_0 fournit la séparation d'énergie entre les configurations électroniques fondamentales $4f^8$ et excitées $4f^75d^1$. L'état spectroscopique fondamental est alors 7F_6 , dû à la répulsion interélectronique H_{e-e} et au couplage spin-orbite H_{so} . Le champ de ligand H_{LF} divise ensuite le terme 7F_6 en 7 niveaux d'énergie, relativement bien définis en

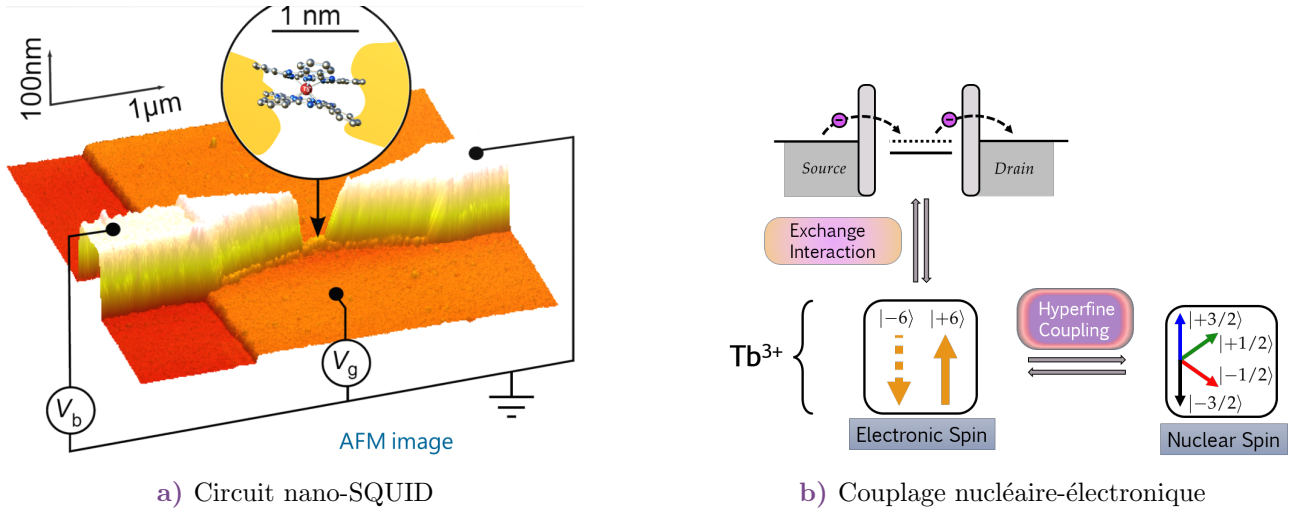


Figure 9: Illustration schématique du dispositif de lecture du spin du TbPc₂. (a) Image AFM colorée d'un SMM TbPc₂ connecté à des électrodes source et de puits en or par des barrières à effet tunnel, dans une jonction de rupture au sommet d'une couche Au/HfO₂. (b) Schéma de la procédure de couplage entre les états de spin nucléaire et électronique de Tb³⁺ via l'interaction hyperfine, puis à l'électron délocalisé du courant tunnel par interaction d'échange. Adapté de [26].

$|M_J|$, la projection du moment angulaire total J sur l'axe de quantification, avec un grand écart d'énergie entre les doublets fondamentaux $M_J = \pm 6$ et le premier doublet excité $M_J = \pm 5$, conduisant à un comportement quasi-Ising de ce doublet à des températures cryogéniques. Enfin, l'interaction hyperfine H_{hf} divise les niveaux en 4 niveaux hyperfins puisque le spin nucléaire de l'ion Tb³⁺ est $I = 3/2$. Les niveaux hyperfins de l'état fondamental $M_J = \pm 6$ sont alors $|4f^8 \ ^7F_6 \ M_J = \pm 6 \ M_I\rangle$, ce qui donne 4 niveaux d'énergie doublement dégénérés, pour chaque paire de $M_J = \pm 6$ et $M_I = \pm 1/2, \pm 3/2$. Les différentes séparations d'énergie sont représentées dans la Fig. 10. Notez les différentes échelles d'énergie des différents termes du hamiltonien, ainsi que leurs origines physiques variées, allant des interactions purement atomiques aux interactions chimiques pour le champ de ligand, et nucléaires pour l'interaction hyperfine.

Note: Ces considérations, et les nombres quantiques indexant chaque état discuté dans la Fig. 10 ne sont valables qu'au premier ordre, car chacun de ces états est un mélange d'autres états, avec un poids majoritaire sur l'état désigné. Les mélanges proviennent des différentes règles de sélection et du fait que tous les termes du hamiltonien ne sont pas diagonaux dans les mêmes bases de nombres quantiques. Cela sera discuté plus en détail dans la Partie I de cette thèse.

L'angle de torsion léger des deux phtalocyanines l'une par rapport à l'autre, faisant légèrement dévier l'environnement de l'ion Tb³⁺ de la symétrie D_{4d} du cristal, conduit à l'apparition de paramètres de champ cristallin B_q^k avec $q \neq 0$ mais avec $q = \pm 4$ (voir Section 3.1.1). Cela conduit, via l'application du théorème de Wigner-Eckart, à des mélanges entre les états avec $\Delta M_J = 4$. Par la théorie des perturbations du troisième ordre, il est possible de montrer qu'un mélange entre les états $M_J = -6$ et $M_J = 6$ est possible, de sorte que des corrections à la fonction d'onde contiendraient des termes de la forme $\langle M_J = +6 | H_{\text{LF}} | M_J = +2 \rangle \langle M_J = +2 | H_{\text{LF}} | M_J = -2 \rangle \langle M_J = -2 | H_{\text{LF}} | M_J = -6 \rangle$, où les dénominateurs ont été négligés. Ce mélange est responsable d'une séparation à champ nul entre les deux doublets, ce qui est à l'origine du *tunneling* quantique de la magnétisation (QTM) observé dans le complexe [26, 99, 102].

En ignorant la structure hyperfine, le diagramme de Zeeman, c'est-à-dire les niveaux d'énergie du

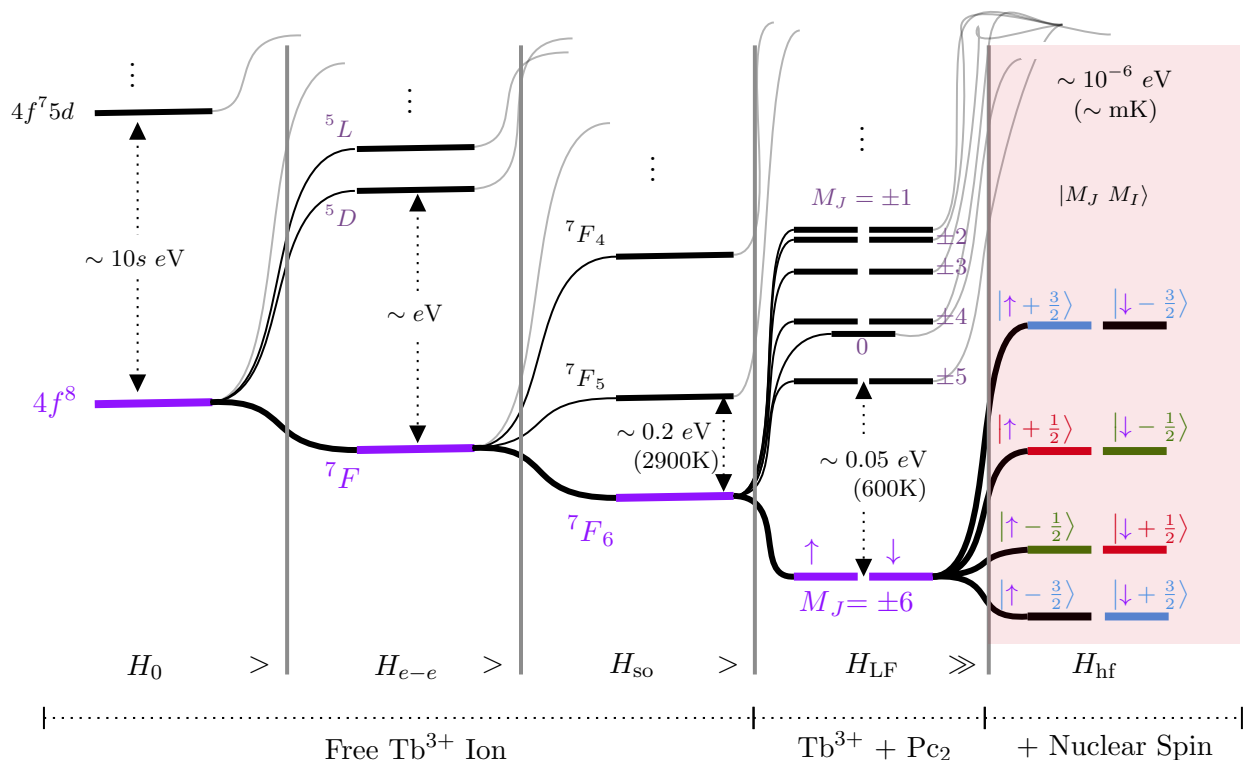


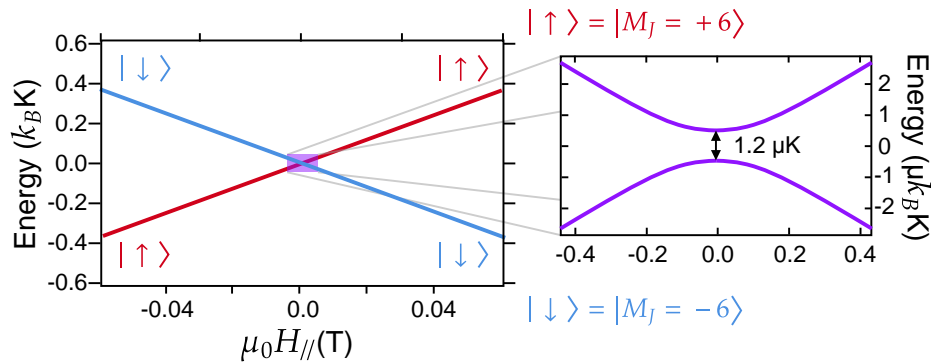
Figure 10: Spectre itératif de chaque terme du hamiltonien de TbPc_2 par ordre décroissant d'amplitude énergétique. L'espace de Hilbert de calcul est étendu par les 4 niveaux hyperfins de l'état fondamental du système. Représenté ici à droite.

système en fonction du champ magnétique, présente alors une intersection évitée entre les deux doublets, autour de $B = 0\text{T}$. Comme représenté dans la Fig. 11a), cet anti-croisement est de l'ordre de $1.2 \times 10^{-6} k_B\text{K}$, ce qui, en se référant à la Fig. 10, est bien inférieur à l'écart énergétique entre les niveaux hyperfins, de l'ordre de $10^{-3} k_B\text{K}$. Cela signifie qu'en tenant compte des niveaux hyperfins du système, il y aura 4 anti-croisements, un pour chaque valeur du spin nucléaire, chacun se produisant à une valeur critique différente du champ magnétique, voir Fig. 11b).

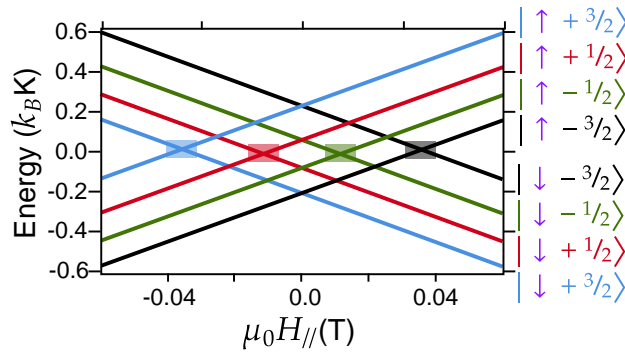
Il est alors possible de lire dans quel état de spin nucléaire se trouve le noyau de terbium en mesurant la valeur du champ magnétique où l'anti-croisement se produit. En balayant le champ magnétique à un taux constant, le spin électronique se renversera à l'anti-croisement, et ce renversement influencera la conductance de la molécule dans son ensemble [103], comme montré dans la Fig. 12. Cela permet de lire l'état de spin nucléaire du noyau de terbium et, à condition de pouvoir manipuler de manière cohérente cet état de spin nucléaire, de l'utiliser comme un qudit avec $d = 4$ niveaux. C'est exactement ce qui a été démontré par Thiele *et al.* en 2014 [26], où ils ont montré qu'il était possible de conduire des oscillations de Rabi, signature de la manipulation cohérente de l'état de spin nucléaire, et de réaliser des portes quantiques sur le spin nucléaire du noyau de terbium. Avec l'utilisation d'un champ électrique AC appliqué à la molécule, il est possible de provoquer des oscillations de Rabi et de réaliser des opérations quantiques sur le spin nucléaire, comme illustré dans la Fig. 12.

Vers un processeur quantique moléculaire

Comme mentionné au début de cette section, Godfrin *et al.* (2017) [99] ont démontré que les temps de cohérence étaient suffisamment longs et les oscillations de Rabi suffisamment cohérentes pour implémenter à la fois la porte de superposition (Hadamard généralisée) et l'algorithme de recherche de



a) Diagramme de Zeeman du doublet fondamental $M_J = \pm 6$, en négligeant la séparation hyperfine. Le anti-croisement entre les deux doublets est mis en évidence. L'énergie de cet anti-croisement est de l'ordre de $1.2 \times 10^{-6} k_B K$.



b) Diagramme de Zeeman du doublet fondamental $M_J = \pm 6$, avec la séparation hyperfine. Les anti-croisements pour chaque valeur du spin nucléaire M_I sont mis en évidence.

Figure 11: Diagramme de Zeeman du doublet fondamental $M_J = \pm 6$, (a) en négligeant la séparation hyperfine, (b) avec la séparation hyperfine. Les niveaux d'énergie sont représentés en unités de $k_B K$, où k_B est la constante de Boltzmann. Le champ magnétique parallèle appliqué $\mu_0 H_{//}$ est donné en Tesla. Adapté de [99].

Grover sur des états de qudit (voir Fig. 13).

Cette expérience s'est inspirée du cadre théorique établi par Leuenberger et Loss, qui, au début des années 2000, ont proposé des méthodes générales pour l'informatique quantique avec de grands spins nucléaires. Ils ont également présenté un exemple spécifique impliquant une nouvelle implémentation de l'algorithme de Grover sur un seul grand qudit [94, 105, 106].

Là où la théorie fait défaut

En discutant cette dernière expérience, il y a principalement quatre points où la théorie actuelle est insuffisante.

L'effet Stark hyperfin

Tout d'abord, l'adressage électrique des transitions de spin nucléaire observé par Thiele *et al.* en 2014 [26]. Il a été démontré que l'application d'un champ électrique continu (DC) à la molécule peut modifier la fréquence de résonance des transitions de spin nucléaire. Un champ électrique de l'ordre

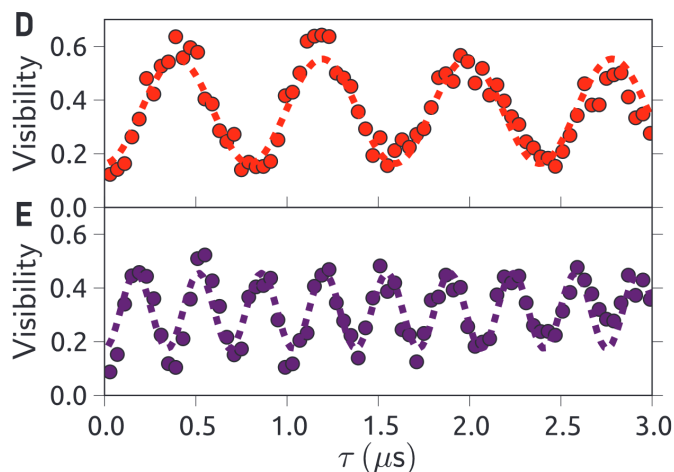
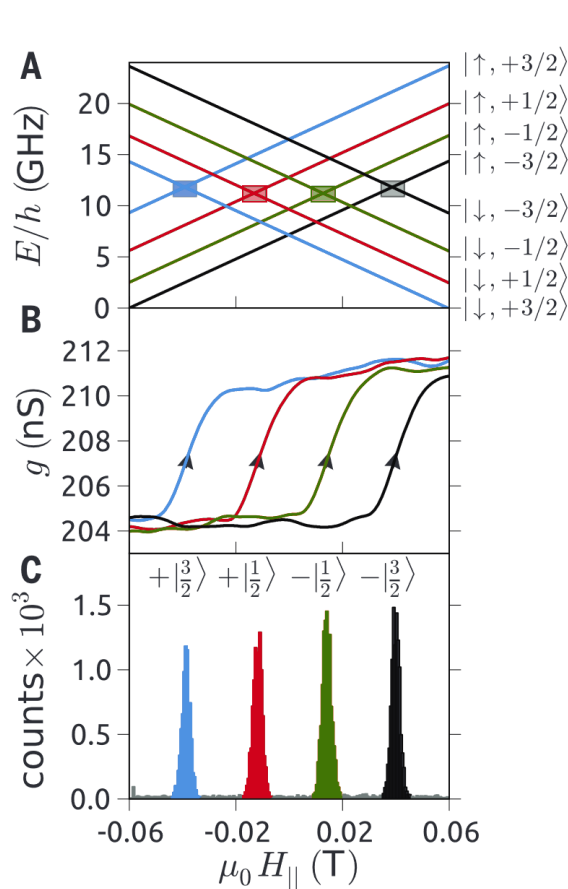


Figure 12: Le panneau A montre le diagramme de Zeeman de la Fig. 11b). Le panneau B montre les sauts de conductance dus à l'inversion magnétique se produisant aux anti-croisements respectifs. Le panneau C montre un histogramme des comptages des inversions magnétiques observées en fonction de la force du champ magnétique. Les panneaux D et E montrent les populations des états intermédiaires subissant des oscillations de Rabi à deux intensités de champ électrique différentes. Adapté de [26].

de $\sim 0.1 \text{ mV}/\text{\AA}$ a été utilisé pour déplacer la fréquence de résonance du spin nucléaire de $\sim 5 \text{ MHz}$. De plus, un champ électrique alternatif (AC) a été utilisé pour entraîner des oscillations de Rabi sur les transitions de spin nucléaire, avec une fréquence de Rabi proportionnelle à l'amplitude du champ électrique AC [103], comme montré dans la Fig. 14, résultat corroboré par Godfrin *et al.* en 2017 [104].

Ce que l'on appelle **l'effet Stark hyperfin** n'est pas encore bien compris, et le cadre théorique actuel manque d'une description adéquate de cet effet. Bien qu'il soit assez certain que cet effet résulte d'une interaction entre l'interaction hyperfine, le champ électrique et le champ de ligand des phtalocyanines, la nature exacte de cette interaction reste floue. Nous proposons d'examiner cet effet en détail dans cette thèse, via une approche atomistique et l'introduction d'opérateurs effectifs obtenus par la théorie des perturbations multiples. Nous montrerons également comment le cadre théorique utilisé peut être appliqué à l'étude des transitions induites par l'interaction hyperfine dans d'autres systèmes, tels que les complexes binucléaires d'euprémium étudiés par Kumar *et al.* [101].

Les portes quantiques sur le spin nucléaire

Bien que Godfrin ait fait des avancées considérables dans le développement d'une plateforme d'informatique quantique basée sur des qudits, l'implémentation de l'algorithme de Grover s'est limitée à trois des quatre états de spin nucléaire du noyau de terbium. Cela a soulevé une question théorique importante concernant l'universalité des qudits : est-il possible d'utiliser les états de spin nucléaire de l'ion de terbium pour implémenter un ensemble universel de portes quantiques, permettant ainsi l'exécution de tout algorithme quantique arbitraire ? Une question subséquente est alors de savoir, étant donné une porte désirée, comment l'implémenter dans le système. Ce point sera abordé dans cette thèse par l'utilisation de la théorie du contrôle optimal et une étude approfondie des hamiltoniens de contrôle du système.

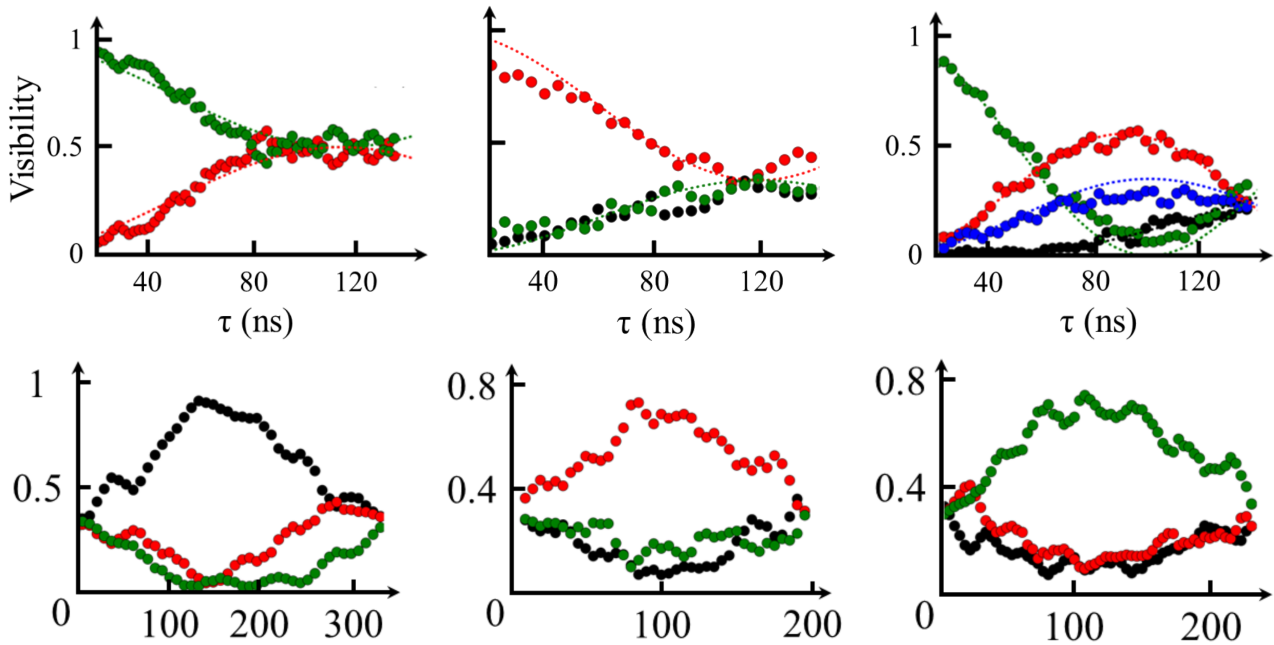


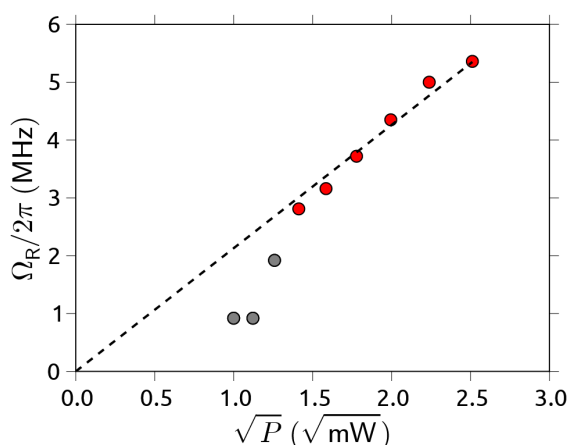
Figure 13: Réalisation expérimentale de l'algorithme de Grover dans TbPc_2 . Chaque graphique montre les populations des états de spin nucléaire individuels de TbPc_2 (représentés en rouge, vert, noir et bleu) en fonction du temps (en ns). La rangée supérieure illustre l'implémentation de la porte de superposition par la transformée de Fourier quantique (QFT) généralisée dans un système qudit avec $d = 4$, où les première, deuxième et troisième colonnes représentent respectivement 2, 3 et les 4 niveaux. La rangée inférieure montre deux cycles de l'opérateur de diffusion de Grover appliqué à l'état marqué (noir à gauche, rouge au centre, et vert à droite), montrant l'amplification de l'amplitude avant de revenir à la superposition originale. Adapté de [99].

La croissance du bruit avec la dimension de l'espace de Hilbert

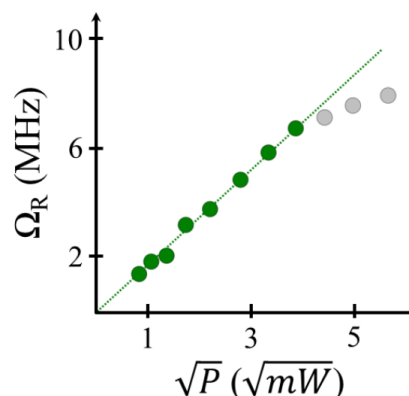
Comme proposé dans [100], l'idée est d'augmenter la dimension de l'espace de Hilbert des spins nucléaires des ions de lanthanides en utilisant la chimie isotopologue. Cela conduira à une augmentation linéaire de la dimension de l'espace de Hilbert d en fonction du choix de l'isotope. Cependant, on peut supposer qu'à mesure que le nombre de niveaux nucléaires augmente, le nombre de canaux d'erreur augmentera également. Cela entraînera une augmentation du bruit avec la dimension de l'espace de Hilbert, et il est important de comprendre comment cette augmentation affectera la performance du processeur quantique. De plus, est-il possible de quantifier une limite supérieure à la dimension du qudit pour rester compétitif par rapport aux plateformes utilisant des qubits, compte tenu du niveau de bruit du système ? Enfin, comment les performances de calcul du système évoluent-elles avec le nombre de qudits ? Ce point sera étudié dans cette thèse par l'utilisation de la théorie des perturbations sur l'équation maîtresse de Lindblad.

Le degré de liberté nucléaire

Enfin, pour revenir à l'ingénierie isotopologique de l'espace de Hilbert suggérée par Wernsdorfer et Ruben [100], il est essentiel de comprendre comment l'ajout d'un proton et d'un neutron pour passer de ^{159}Tb à ^{161}Dy affecte la structure hyperfine afin de passer d'un système à 4 niveaux à un système à 6 niveaux. De plus, les séparations hyperfines de ^{161}Dy et ^{163}Dy sont assez différentes, bien que le nombre de niveaux hyperfins reste identique. Comment une différence de deux neutrons sans charge électrique peut-elle mener à une telle différence dans la structure hyperfine ? Ce point sera étudié dans cette thèse et nécessitera un détour par la structure nucléaire des isotopes des différents lanthanides,



a) Adapté de [103].



b) Adapté de [104].

Figure 14: Fréquence de Rabi $\Omega_R/2\pi$ en fonction de la racine carrée de la puissance micro-onde P du champ électrique entraînant la transition.

des ions fortement chargés et des ions exotiques muoniques.

0^F.3 Plan de la thèse

Cette thèse est divisée en trois parties, chacune abordant un aspect différent des défis théoriques soulignés concernant les interactions hyperfines dans les complexes organiques de lanthanides. Une quatrième partie supplémentaire fournit un aperçu d'un projet parallèle sur l'omniprésence de la séquence de Thue-Morse dans le monde de l'informatique quantique et son lien avec le chaos quantique.

Les lanthanides dans la matière : libres atomiquement mais liés chimiquement

La partie I se concentrera sur le cadre théorique utilisé pour décrire les électrons de valence des systèmes atomiques. En utilisant l'**algèbre de Racah**, nous dériverons formellement les expressions analytiques des éléments de matrice des différents hamiltoniens présentés dans la Fig. 10 et montrerons comment ils peuvent être évalués de manière non empirique à l'aide de codes Hartree-Fock ou DFT. En particulier, nous présenterons la méthode **LFDF**, que nous considérons la plus appropriée dans ce contexte d'ingénierie de l'espace de Hilbert pour les lanthanides. Nous montrerons également comment l'interaction entre l'hyperfine, le champ électrique et le champ de ligand des phtalocyanines peut être décrite à l'aide d'opérateurs effectifs obtenus par une généralisation de la **théorie de Judd-Ofelt** que nous introduirons.

L'interaction hyperfine

La **partie II** se concentrera sur l'interaction hyperfine ainsi que sur la structure nucléaire des différents isotopes de lanthanides. Nous partirons de l'équation de **Dirac** et dériverons l'interaction hyperfine et les **constantes hyperfines** par une perturbation de l'hamiltonien électronique. Nous montrerons ensuite comment la structure interne nucléaire influence les constantes hyperfines des électrons, en calculant les effets de taille finie tels que les corrections de **Bohr-Weisskopf** ou de **Breit-Rosenthal**. Nous approfondirons particulièrement les ions hydrogénoïdes fortement chargés et les **ions muoniques**, et montrerons comment l'électron ou le muon peut être utilisé comme sonde de la structure nucléaire.

■ L'informatique quantique avec les spins nucléaires des lanthanides

La partie III portera sur l'informatique quantique dans les complexes organiques de lanthanides et, plus généralement, les qudits. Nous rappellerons d'abord les notions de base de l'informatique quantique et des systèmes quantiques ouverts, puis les appliquerons aux qudits. Nous nous concentrerons d'abord sur l'effet du bruit sur les qudits via la théorie des perturbations sur **l'équation maîtresse de Lindblad**. Dans un premier chapitre, en utilisant uniquement une approche du premier ordre, nous comparerons les échelles d'infidélités computationnelles entre **qubits et qudits**, et montrerons comment le bruit évolue avec la dimension de l'espace de Hilbert. Dans un second chapitre, nous généraliserons la perturbation à tout ordre et considérerons l'effet de l'hamiltonien et des portes quantiques sur la performance computationnelle à mesure que la durée des opérations et l'amplitude du bruit augmentent. Enfin, dans un dernier chapitre, nous nous concentrerons sur **comment implémenter des portes quantiques au niveau des impulsions** dans le système, et montrerons comment **la théorie du contrôle optimal** peut être utilisée pour raccourcir les temps de porte et réduire ainsi les effets du bruit étudiés dans les chapitres précédents.

■ La séquence omniprésente de Prouhet-Thue-Morse

La partie IV se penchera sur un projet parallèle concernant la **séquence de Prouhet-Thue-Morse**, dont nous avons remarqué l'apparition en testant certaines simulations numériques. Nous souhaitons donc mettre en avant son omniprésence dans le monde de l'informatique quantique. Nous commencerons par introduire la séquence et ses propriétés, puis montrerons comment elle est liée au **chaos quantique** et à la transformation du boullanger quantique. Nous montrerons ensuite comment elle apparaît naturellement de l'interaction de la Transformée de Fourier Quantique avec la transformation d'Hadamard de N qubits. Enfin, nous présenterons son lien avec **la théorie des nombres** et l'hypothèse de Riemann.

PARTIE **I^F**

(Résumé) Les lanthanides dans la matière: libres atomiquement mais liés chimiquement

I^F.1 hamiltonien d'un atome/ion libre

Ce chapitre se concentre sur le calcul des éléments de matrice de l'hamiltonien pour les électrons dans un atome ou un ion libre, en incluant les effets du noyau. La première partie présente l'hamiltonien des électrons, où les effets de l'interaction avec le noyau sont introduits dans la dernière section. L'accent est mis sur la décomposition des fonctions d'onde électroniques en parties radiales et angulaires, ce qui conduit à la séparation des éléments de matrice de l'hamiltonien en une intégrale radiale et un terme dépendant des nombres quantiques angulaires.

Forme générale de l'hamiltonien

L'hamiltonien pour un atome/ion libre est donné par:

$$H = \sum_{i=1}^N \left(-\frac{\hbar^2}{2m} \nabla_i^2 - \frac{Ze^2}{4\pi\epsilon_0 r_i} \right) + \sum_{i<j} \frac{e^2}{4\pi\epsilon_0 r_{ij}} + H_{\text{so}} + H_{\text{hf}},$$

où les termes représentent respectivement l'énergie cinétique des électrons, l'interaction de Coulomb électron-noyau, l'interaction de Coulomb électron-électron, le couplage spin-orbite et le couplage hyperfin.

Résultats pour les électrons non-interagissants dans un potentiel central

L'hamiltonien pour des électrons indépendants dans un potentiel central est:

$$H_0 = \sum_{i=1}^N \left(-\frac{\hbar^2}{2m} \nabla_i^2 - \frac{Ze^2}{4\pi\epsilon_0 r_i} \right),$$

ce qui représente l'énergie de N électrons indépendants sous l'influence d'un noyau central de charge Ze . Les fonctions d'onde résultantes sont similaires à celles des fonctions d'onde de type hydrogène et

sont utilisées pour construire des déterminants de Slater afin de respecter le principe d'exclusion de Pauli.

Couplage des moments angulaires et antisymétrisation

Les moments angulaires totaux du système sont décomposés en moments orbitaux (\vec{L}) et de spin (\vec{S}), ce qui permet deux schémas de couplage : le couplage $L - S$ et le couplage $j - j$. La transition entre ces deux schémas se fait en utilisant des symboles $9 - j$ et des coefficients de Clebsch-Gordan. Les fonctions d'onde doivent être antisymétrisées en raison de la nature fermionique des électrons, et l'antisymétrisation complique les calculs des éléments de matrice.

Termes diagonaux pour la répulsion électronique

L'interaction de répulsion entre électrons est décrite par :

$$H_{e-e} = \sum_{i < j} \frac{e^2}{4\pi\epsilon_0 r_{ij}}.$$

Les éléments de matrice pour cette interaction sont exprimés en termes d'intégrales radiales F_k et de coefficients angulaires f_k . Ces éléments peuvent être simplifiés en utilisant des opérateurs tensoriels unitaires, ce qui réduit le nombre de paramètres nécessaires pour décrire l'interaction.

Couplage spin-orbite

Le couplage spin-orbite, une correction relativiste, est donné par :

$$H_{so} = \sum_{i=1}^N \xi(r_i) \vec{l}_i \cdot \vec{s}_i,$$

où $\xi(r_i)$ est une constante de couplage spin-orbite dépendant du rayon. Ce terme induit un mélange des états L et S et est souvent traité comme une correction plus petite que les interactions électroniques directes.

Interaction hyperfine

Deux types d'interactions hyperfines sont traités :

- **Interaction magnétique hyperfine:** Cette interaction provient du couplage entre le moment magnétique nucléaire et celui des électrons, exprimée par :

$$H_{hf,dip} = \mathcal{A} \sum_i \frac{\vec{N}_i}{r_i^3} \cdot \vec{I},$$

où \vec{N}_i est lié aux moments angulaires électroniques.

- **Interaction quadripolaire électrique hyperfine:** Cette interaction est liée à la déformation non-sphérique du noyau et est décrite par :

$$H_{hf,quad} = \mathcal{B} \sum_i \left(\frac{I(I+1)}{r_i^3} + \frac{3(\vec{r}_i \cdot \vec{I}_i)^2}{r_i^5} \right).$$

Les éléments de matrice sont dérivés pour ces interactions en utilisant des opérateurs tensoriels et des symboles de Wigner, permettant ainsi une description précise des effets hyperfins.

Contribution aux résultats

Les principales contributions de ce chapitre incluent :

- L'introduction et le calcul des éléments de matrice de l'hamiltonien des électrons libres, avec un accent sur la séparation des termes radiaux et angulaires.
- La mise en évidence de la complexité apportée par l'antisymétrisation nécessaire des fonctions d'onde.
- La simplification des calculs par l'utilisation d'opérateurs tensoriels unitaires, ce qui permet de réduire les interactions multielectroniques à un ensemble limité de paramètres.
- La clarification des schémas de couplage angulaire et leur importance pour la classification des niveaux d'énergie des atomes et ions, notamment par l'introduction du couplage spin-orbite et des interactions hyperfines.

Ce travail constitue une base essentielle pour la compréhension des interactions électroniques dans les atomes/ions libres et prépare le lecteur à des discussions plus approfondies sur les effets du ligand et du noyau dans les sections/parties suivantes.

I^F.2 Champ de Ligands

Cette section traite de l'effet des ligands environnants sur la structure électronique de l'atome central, appelé champ de ligands. Il résulte de l'interaction électrostatique entre les électrons des ligands et ceux de l'atome central. Cette théorie est cruciale pour comprendre les propriétés des complexes métalliques de transition, notamment les couleurs observées, ainsi que les propriétés magnétiques et optiques des lanthanides et actinides.

De la théorie du champ cristallin à la théorie du champ de ligands

Théorie du champ cristallin

La théorie du champ cristallin (CFT) est un modèle simplifié qui décrit l'effet des ligands comme des charges ponctuelles disposées de manière régulière autour de l'atome central. La CFT permet de comprendre qualitativement la structure électronique des complexes métalliques de transition, en prenant en compte l'interaction électrostatique entre les charges des ligands et les électrons de l'atome central. Les hypothèses principales incluent : les ligands sont considérés comme des charges statiques, non polarisables et non magnétiques.

L'interaction électrostatique peut être exprimée par l'expansion multipolaire, permettant de définir le potentiel de champ cristallin H_{CF} :

$$H_{CF}(\vec{r}_1 \dots \vec{r}_N) = -|e| \sum_{i=0}^N \sum_{l=0}^{+\infty} \sum_{m=-l}^l (-1)^m V_{-m}^{(l)}(r_i) C_m^{(l)}(\theta_i, \phi_i), \quad (\text{I}^F.1)$$

où $V_m^{(l)}(r)$ représente les coefficients multipolaires, déterminés par la distribution de charge des ligands. La CFT permet de calculer les éléments de matrice du hamiltonien du champ cristallin et de définir les paramètres de champ cristallin B_m^l .

On a alors :

$$B_m^l = (-1)^m \int V_{-m}^{(l)}(r) P_{nl}^2(r) dr, \quad (\text{I}^F.2)$$

où $P_{nl}(r)$ est la fonction radiale de l'orbitale de valence de l'atome central.

Éléments de matrice dans la couche de valence

Les éléments de matrice sont essentiels pour comprendre la structure électronique des complexes et sont donnés par :

$$\langle n\ell^p LSJM_J | H_{CF} | n\ell^p L'S'J'M_{J'} \rangle = \sum_{l,m} (-1)^m \langle n\ell | eV_{-m}^{(l)}(r) | n'\ell' \rangle \langle \ell^p LSJM_J | \sum_{i=0}^p C_m^{(l)}(\theta_i, \phi_i) | \ell^p L'S'J'M_{J'} \rangle. \quad (\text{I}^F.3)$$

La théorie se base sur le théorème de Wigner-Eckart et les règles de sélection associées aux harmoniques sphériques, limitant les termes B_m^l nécessaires pour décrire le système.

Paramètres et symétrie du champ cristallin

La CFT permet de déterminer les paramètres de champ cristallin nécessaires pour caractériser l'effet des ligands. Le nombre de paramètres non nuls dépend de la symétrie des ligands autour de l'atome central. Par exemple, pour une configuration de type d , on dénombre 15 paramètres non nuls, tandis que pour une configuration f , il y en a 28. L'introduction de symétries géométriques des ligands réduit encore le nombre de paramètres indépendants, simplifiant ainsi l'analyse.

Théorie du champ de ligands

La théorie du champ de ligands (LFT) étend la CFT en incluant la covalence des liaisons entre les ligands et l'atome central, ce qui permet de mieux décrire les complexes moléculaires. Contrairement à la CFT, la LFT prend en compte :

- La polarisation des ligands par l'atome central.
- Le chevauchement orbitalaire entre les électrons de l'atome central et ceux des ligands.
- La capacité des ligands à être polarisables.

L'expression du hamiltonien est alors modifiée pour inclure ces effets, avec des paramètres B_m^l redéfinis pour prendre en compte la polarisation et le chevauchement orbitalaire.

Ligand Field DFT (LFDFT)

La LFDFT est une méthode pour calculer les paramètres de champ de ligands à partir de la théorie de la fonctionnelle de la densité (DFT), permettant une modélisation plus précise des complexes, notamment ceux à base de lanthanides. Elle permet d'extraire les fonctions radiales des orbitales de valence en utilisant les orbitales de Kohn-Sham, ce qui conduit à une détermination plus fidèle des paramètres du champ de ligands. Les résultats obtenus par cette méthode montrent un bon accord avec les données expérimentales, confirmant la validité de la LFDFT pour la description des propriétés électroniques complexes.

Résultats principaux

Les résultats montrent que la CFT, bien que simplifiée, permet de comprendre les structures électroniques de base grâce aux calculs des éléments de matrice et des paramètres de champ cristallin B_m^l . Cependant, pour des systèmes plus complexes, comme les complexes de lanthanides, la LFT est nécessaire pour inclure la covalence des liaisons. Les paramètres B_m^l obtenus via LFDFT ont montré une amélioration significative dans la prédiction des propriétés électroniques et magnétiques, notamment grâce à une meilleure prise en compte des contributions du champ de ligands et des interactions inter-électroniques.

complexes. De plus la LFDFT est une méthode computationnellement efficace pour déterminer les paramètres de champ de ligands rapidement, ce qui en fait un outil précieux pour la modélisation de nombreux complexes moléculaires avec de différents lanthanides, champs externes ou géométrie, rapidement.

I^F.3 Interaction de configurations

Symétrie et paramètres de champ cristallin impairs

Dans les sections précédentes, il a été établi que le seul terme du hamiltonien pouvant coupler des configurations électroniques de parités différentes (comme les configurations $4f^n$ et $4f^{n-1}5d$) est le terme de champ cristallin. L'amplitude de ce couplage est déterminée par les éléments de matrice hors-diagonaux, et nécessite la présence de **paramètres de champ cristallin impairs** $B_m^l(n\ell, n\ell')$ avec l impair. Par considération de symétrie, de tels paramètres hors-diagonaux ne sont possibles que dans les complexes sans symétrie d'inversion, car sinon les éléments de matrice s'annulent.

Théorie de Judd-Ofelt et opérateurs effectifs

Aperçu de la théorie de Judd-Ofelt

La théorie de Judd-Ofelt, introduite dans les années 1960 par Brian Judd et George Ofelt, décrit l'intensité des transitions dipolaires électriques des ions des terres rares. Les transitions $f - f$ étant normalement interdites par la parité, cette théorie explique que les transitions sont principalement dues au couplage de l'ion des terres rares avec les ligands via le mélange de configurations. Le hamiltonien total s'écrit :

$$H_{\text{tot}} = H + \varepsilon(PH_{\text{LF}}Q + QH_{\text{LF}}P),$$

où H est le hamiltonien non perturbé de l'ion, H_{LF} le hamiltonien de champ cristallin, et P et Q les opérateurs de projection sur les états du sol et excités, respectivement.

Les fonctions d'onde perturbées du premier ordre sont données par :

$$|\Psi_i\rangle = |\Psi_i^{(0)}\rangle + \varepsilon \sum_{j \neq i} \frac{\langle \Psi_j^{(0)} | QH_{\text{LF}}P | \Psi_i^{(0)} \rangle}{\varepsilon(E_i^{(0)} - E_j^{(0)})} |\Psi_j^{(0)}\rangle,$$

montrant que les termes hors-diagonaux du champ cristallin impairs $B_m^{2t+1}(4f, 5d)$ sont essentiels pour expliquer le mélange de configurations.

Amplitudes de transition et opérateurs effectifs

L'application de la théorie de perturbation permet de réécrire les éléments de matrice du dipôle électrique comme suit :

$$\vec{\Gamma}(i, i') = \langle \Psi_i | \mathbf{D}^{(1)} | \Psi_{i'} \rangle = \langle \Psi_i^{(0)} | \mathbf{D}^{(1)} | \Psi_{i'}^{(1)} \rangle + \text{h.c.}$$

À partir des règles de sélection et en supposant un dénominateur constant pour les énergies excitées, on obtient l'opérateur dipolaire effectif :

$$\tilde{D}_q^A = 2U_\rho^{(A)} \sum_{t=0}^2 \sum_{m=-2t-1}^{2t+1} (-1)^{q+m} B_m^{(2t+1)}(4f, 5d) \begin{pmatrix} A & 1 & 2t+1 \\ \rho & q & m \end{pmatrix} A_{2t+1}^A(4f, 5d) R(4f, 5d).$$

Cette formulation permet de définir des paramètres Judd-Ofelt Ω_λ , simplifiant ainsi l'analyse expérimentale des transitions $4f - 4f$.

Effet Stark hyperfin

Des expériences récentes mentionnées dans l'introduction ont montré que les transitions hyperfines peuvent être modulées par un champ électrique, modifiant les constantes hyperfines des ions. Cela s'explique par le fait que le champ électrique perturbe la constante hyperfine et permet un contrôle Rabi des transitions.

Le hamiltonien de l'effet Stark hyperfin est donné par :

$$H_{\text{hf,dip}} = a(\vec{E})\vec{I} \cdot \vec{J} = a_0\vec{I} \cdot \vec{J} + \delta a(\vec{E})\vec{I} \cdot \vec{J},$$

où $\delta a(\vec{E})$ représente le décalage Stark de la constante hyperfine. En utilisant la théorie de double perturbation, on obtient des opérateurs effectifs expliquant ce couplage, qui dépend directement des paramètres impairs du champ cristallin.

Résultats et implications

Les résultats soulignent deux points principaux :

1. Les transitions $f - f$ peuvent être analysées via des opérateurs effectifs simplifiant considérablement les calculs, avec seulement trois paramètres à ajuster expérimentalement.
2. L'effet Stark hyperfin est directement lié à la présence de paramètres de champ cristallin impairs dont les composantes $m = 0, 1$ ou 2 sont non-nulles, ce qui permet une modulation fine des transitions hyperfines. Cette modulation est cruciale pour des applications dans le contrôle des états de spin nucléaire, et la symétrie du champ cristallin joue un rôle déterminant dans ces processus.

L'effet des paramètres impairs et des symétries de ligands sur ces transitions souligne leur importance pour la compréhension du comportement des ions de terres rares, avec des implications pour des applications en optoélectronique.

PARTIE II^F

(Résumé) L'interaction hyperfine

II^F.1 L'équation de Dirac

L'équation de Dirac, formulée par Paul Dirac en 1928 [46], est une équation d'onde de la mécanique quantique relativiste qui décrit le comportement des fermions de spin-1/2. Elle généralise l'équation de Schrödinger en y intégrant la relativité restreinte. Pour un électron libre, l'équation de Dirac est donnée par :

$$(i\hbar\gamma^\mu\partial_\mu - mc)\psi = 0, \quad (\text{II}^{\text{F}}.1)$$

où γ^μ sont les matrices de Dirac, ∂_μ représente l'opérateur de dérivée à quatre dimensions, m la masse de la particule, c la vitesse de la lumière, et ψ la fonction d'onde de la particule.

Présentation et résultats de l'équation de Dirac

Les matrices de Dirac sont définies par :

$$\gamma^0 = \begin{pmatrix} \mathbb{1} & 0 \\ 0 & -\mathbb{1} \end{pmatrix}, \quad \gamma^i = \begin{pmatrix} 0 & \sigma^i \\ -\sigma^i & 0 \end{pmatrix}, \quad (\text{II}^{\text{F}}.2)$$

où $\mathbb{1}$ est la matrice identité et σ^i sont les matrices de Pauli. L'équation de Dirac peut être développée comme :

$$(c\vec{\alpha} \cdot \vec{p} + mc^2\beta) \psi = i\hbar \frac{\partial}{\partial t} \begin{pmatrix} u \\ v \end{pmatrix}, \quad (\text{II}^{\text{F}}.3)$$

où \vec{p} est l'opérateur impulsion et $\vec{\alpha}$, β sont des matrices définies à partir des matrices de Dirac.

$$\vec{\alpha} = \begin{pmatrix} 0 & \vec{\sigma} \\ \vec{\sigma} & 0 \end{pmatrix}, \quad \beta = \begin{pmatrix} \mathbb{1} & 0 \\ 0 & -\mathbb{1} \end{pmatrix}. \quad (\text{II}^{\text{F}}.4)$$

Les solutions de cette équation prédisent des énergies positives et négatives :

$$E = \pm \sqrt{c^2 p^2 + m^2 c^4}. \quad (\text{II}^{\text{F}}.5)$$

Les solutions d'énergie positive correspondent à l'électron, tandis que les solutions d'énergie négative, initialement considérées comme non physiques, furent interprétées par Dirac comme représentant le positron, l'antiparticule de l'électron. Cette prédiction théorique de l'existence des antiparticules fut confirmée expérimentalement en 1932 par Carl Anderson [132]. L'équation permet également de décrire le spin intrinsèque de l'électron, déjà mis en évidence par l'expérience de Stern-Gerlach en 1922 [133].

Inclusion de champs externes : Le cas de l'ion monoélectronique

L'équation de Dirac peut être étendue pour inclure l'interaction d'un électron avec des champs externes via le principe de couplage minimal. Cela implique de remplacer l'opérateur impulsion \vec{p} par $\vec{p} - e\vec{A}(\vec{r}, t)$, où $\vec{A}(\vec{r}, t)$ est le potentiel vecteur et $e < 0$ la charge de l'électron. L'équation devient alors :

$$(c\vec{\alpha} \cdot (\vec{p} - e\vec{A}) + \beta mc^2 + e\phi) \psi = i\hbar \frac{\partial}{\partial t} \psi, \quad (\text{II}^F.6)$$

où ϕ est le potentiel scalaire.

En considérant un ion monoélectronique, l'interaction se réduit à un champ électrique coulombien. Pour un noyau ponctuel, l'équation de Dirac se simplifie en :

$$\left(c\vec{\alpha} \cdot \vec{p} + \beta mc^2 - \frac{Ze^2}{4\pi\epsilon_0 r} \right) \psi = i\hbar \frac{\partial}{\partial t} \psi. \quad (\text{II}^F.7)$$

Les solutions permettent de décrire les fonctions d'onde radiales sous la forme :

$$\psi_{n\kappa, m_j}(\vec{r}) = \frac{1}{r} \begin{pmatrix} i P_{n\kappa}(r) \chi_{\kappa, m_j} \\ Q_{n-\kappa}(r) \chi_{-\kappa, m_j} \end{pmatrix}, \quad (\text{II}^F.8)$$

où $P_{n\kappa}$ et $Q_{n-\kappa}$ sont des fonctions radiales, et χ_{κ, m_j} sont les fonctions propres du spin.

Énergies Propres et Structure Fine

Les énergies propres résultantes pour un ion monoélectronique sont données par :

$$E_{n\kappa} = \frac{mc^2}{\sqrt{1 + \frac{\alpha^2 Z^2}{\gamma + n - |\kappa|}}}, \quad (\text{II}^F.9)$$

avec $\gamma = \sqrt{\kappa^2 - (Z\alpha)^2}$. En développant cette expression en termes de la constante de structure fine α , on obtient :

$$E_{n\kappa} = mc^2 - \frac{Z\alpha^2}{2n^2} mc^2 - \frac{Z^2\alpha^4}{2n^3} \left(\frac{1}{|\kappa|} - \frac{3}{4n} \right) mc^2 + \mathcal{O}(\alpha^6). \quad (\text{II}^F.10)$$

Le terme proportionnel à α^4 correspond à la correction relativiste de premier ordre connue sous le nom de correction de structure fine, observée expérimentalement dans les atomes d'hydrogène. La structure fine est un effet relativiste modélisable via un hamiltonien effectif dans l'équation de Schrödinger.

Au-Delà de l'Équation de Dirac

L'équation de Dirac constitue un outil puissant pour la description des fermions de spin-1/2, mais elle ne permet pas de rendre compte des interactions complexes impliquant plusieurs particules. Pour cela, la théorie quantique des champs, et en particulier l'électrodynamique quantique (QED), est nécessaire. La QED inclut des effets tels que l'énergie d'auto-interaction de l'électron et la polarisation du vide, lesquels influencent les niveaux d'énergie des ions hautement chargés [138]. Les corrections relativistes supplémentaires ne seront cependant pas abordées dans ce travail, l'équation de Dirac restant l'outil principal pour l'étude des interactions hyperfines des ions hydrogéoïdes dans les chapitres suivants.

II^F.2 Le noyau fini

Corrections de masse

Jusqu'à présent, le noyau était supposé infiniment massif, mais en réalité, il a une masse finie M_N . La correction la plus simple est le déplacement (de masse) normal (NMS), qui prend en compte la masse

réduite de l'électron et du noyau en substituant

$$m = m_e \rightarrow \mu = \frac{m_e M_N}{m_e + M_N}, \quad (\text{II}^F.11)$$

où M_N est la masse du noyau. Cela implique de résoudre l'équation de Dirac avec la masse réduite de l'électron, ajustant ainsi les énergies et les fonctions d'onde.

Pour les atomes multi-électroniques, il est nécessaire de considérer le déplacement (de masse) spécifique (SMS), qui représente un effet de polarisation de masse et peut être modélisé par un hamiltonien effectif :

$$H_{\text{SMS}} = -\frac{\hbar^2}{M_N} \sum_{i < j} \vec{\nabla}_i \cdot \vec{\nabla}_j. \quad (\text{II}^F.12)$$

Un traitement plus rigoureux et relativiste nécessite l'équation de Bethe-Salpeter ou une description complète en électrodynamique quantique (QED) [140, 141].

Ions muoniques

Les ions muoniques sont des atomes où au moins un électron est remplacé par un muon, une particule de même charge mais de masse 207 fois supérieure. Le muon forme des atomes muoniques malgré sa durée de vie limitée ($2,2\mu\text{s}$). La masse importante du muon impose de considérer la masse réduite du système muon-noyau :

$$\mu = \frac{m_\mu M_N}{m_\mu + M_N}, \quad (\text{II}^F.13)$$

où m_μ est la masse du muon. Les niveaux d'énergie et fonctions d'onde peuvent alors être calculés en résolvant l'équation de Dirac avec cette masse réduite.

La distribution de charge nucléaire : Monopôle et quadripôle

Le noyau n'est pas une particule ponctuelle mais possède une taille finie et une distribution de charge potentiellement asymétrique. La densité de charge nucléaire $\rho(\vec{R})$ peut être calculée ab initio par la résolution de l'équation de Schrödinger pour les nucléons, souvent via des interactions effectives comme l'interaction de Skyrme.

L'interaction effective de Skyrme et méthode Hartree-Fock

L'interaction de Skyrme modélise la force nucléaire en tenant compte des propriétés à courte portée et dépendantes de la densité des nucléons. En utilisant la méthode Hartree-Fock (HF), où les nucléons se déplacent dans un champ moyen, on obtient les densités locales des noyaux, utiles pour calculer des moments multipolaires. Le modèle HF avec interaction de Skyrme permet de traiter des noyaux avec des symétries axiales, par exemple pour décrire les déformations quadripolaires.

Moments quadripolaire et densités de charge

Le potentiel électrique monopolaire du noyau est donné par :

$$\phi_0^{(0)}(r) = \frac{1}{4\pi\epsilon_0 r} \int_{R=0}^r \rho(\vec{R}) d^3\vec{R} + \frac{1}{4\pi\epsilon_0} \int_{R=r}^{+\infty} \frac{\rho(\vec{R})}{R} d^3\vec{R}, \quad (\text{II}^F.14)$$

et représente la contribution de la charge interne et externe. Pour un noyau déformé, le moment quadripolaire est traité perturbativement, permettant de dériver un hamiltonien effectif quadripolaire.

Le potentiel électrique quadripolaire est donné par :

$$\phi_0^{(2)}(r) = \frac{1}{4\pi\epsilon_0 r^3} \int_{R=0}^r \rho(\vec{R})(3z^2 - r^2) d^3\vec{R} + \frac{1}{4\pi\epsilon_0} \int_{R=r}^{+\infty} \frac{\rho(\vec{R})(3z^2 - r^2)}{R^3} d^3\vec{R}, \quad (\text{II}^F.15)$$

Les potentiels quadripolaires et monopolaires peuvent être calculés à partir des densités de charge issues de modèles comme HFBCS et sont essentiels pour décrire des noyaux avec des formes non sphériques.

Distribution de courants nucléaires : Moment magnétique dipolaire

Le noyau a également un moment magnétique dipolaire dû au mouvement et au spin des protons et neutrons. Les courants de spin et de convection contribuent au moment dipolaire :

$$\vec{m}(\vec{R}) = \frac{1}{2} \vec{R} \wedge \vec{j}(\vec{R}), \quad (\text{II}^F.16)$$

où $\vec{j}(\vec{R})$ est la densité de courant nucléaire. Le moment magnétique global peut être déterminé par l'intégration de $\vec{m}(\vec{R})$ sur le volume nucléaire. Les distributions obtenues montrent une forte polarisation du noyau par les neutrons non appariés, comme observé pour ^{161}Dy et ^{163}Dy .

Autres effets nucléaires

D'autres effets influencent les niveaux d'énergie atomiques, comme :

- **la violation de la parité** : Interaction faible entre électrons et noyau, mélangeant états de parité différente.
- **la polarisation nucléaire** : Transition virtuelle du noyau induisant des décalages d'énergie des électrons atomiques.
- **l'interactions électrons-noyaux** : Mécanismes comme l'Excitation Nucléaire par Capture d'Électrons (NEEC) affectant les transitions atomiques.

Ces effets, bien que non abordés en détail ici, sont essentiels pour des études métrologiques précises de la structure hyperfine.

Résumé

Ce chapitre traite de la complexité ajoutée par la prise en compte d'un noyau fini, à la fois en termes de masse, de taille et de courants. Les corrections de masse incluent le déplacement de masse normal et spécifique, tandis que les ions muoniques nécessitent une masse réduite spécifique. Les moments monopolaire et quadripolaire décrivent les distributions de charge nucléaire, et la théorie HFBCS permet de modéliser ces phénomènes efficacement. Enfin, les courants magnétiques et les effets de polarisation soulignent l'importance des propriétés dynamiques des nucléons, toutes ces corrections contribuant à une compréhension plus complète des interactions hyperfines et de la structure des ions hydrogénoïdes étudiés.

II^F.3 Constantes hyperfines

Dans ce chapitre, nous présentons les corrections aux niveaux d'énergie atomiques dues aux multipôles magnétiques et électriques du noyau au-delà du monopôle. Ces interactions définissent les constantes hyperfines, utilisées pour caractériser les séparations d'énergie des niveaux atomiques causées par les champs nucléaires de plus haut ordre.

Constante hyperfine dipolaire

L'effet du potentiel vecteur dipolaire magnétique du noyau sur l'électron peut être exprimé par un terme de hamiltonien effectif dans l'équation de Dirac. Le hamiltonien est donné par :

$$H_{\text{hf,dip}} = -ec\vec{\alpha} \cdot \vec{A}(\vec{r}). \quad (\text{II}^{\text{F}}.17)$$

L'énergie de correction due au hamiltonien dipolaire est obtenue par théorie de perturbation du premier ordre, et en utilisant le théorème de Wigner-Eckart, on obtient :

$$W_{\text{hf,dip}} = \frac{a}{2}K, \quad (\text{II}^{\text{F}}.18)$$

où $K = F(F+1) - I(I+1) - J(J+1)$ et a est défini par :

$$a = ec \frac{\mu_0}{2\pi} \frac{\kappa_a}{I j_a(j_a+1)} \int_0^{+\infty} P_{n_a \kappa_a}(r) Q_{n_a \kappa_a}(r) f_{\text{M},0}(r) dr, \quad (\text{II}^{\text{F}}.19)$$

pour un ion à un électron, de plus en l'absence de pénétration nucléaire ($r \gg R$), a peut être simplifié par :

$$a_{\text{n.p.}} = ec \frac{\mu_0}{2\pi} \frac{M_z^{(1)}}{I} \frac{\kappa_a}{j_a(j_a+1)} \int_0^{+\infty} \frac{1}{r^2} P_{n_a \kappa_a}(r) Q_{n_a \kappa_a}(r) dr. \quad (\text{II}^{\text{F}}.20)$$

Constante hyperfine quadripolaire

L'interaction quadripolaire hyperfine est définie par le potentiel quadripolaire nucléaire :

$$H_{\text{hf,quad}} = e\phi_{\text{quad}}(\vec{r}), \quad (\text{II}^{\text{F}}.21)$$

avec $\phi_{\text{quad}}(\vec{r}) = \frac{1}{4\pi\epsilon_0} C_0^{(2)}(\theta, \phi) f_{\text{Q},0}(r)$.

L'énergie de correction quadripolaire est donnée par :

$$W_{\text{hf,quad}} = \frac{b}{2} \frac{3K(K+1) - 4j_a(j_a+1)I(I+1)}{2I(2I-1)2j_a(2j_a-1)}, \quad (\text{II}^{\text{F}}.22)$$

où b est défini pour un électron par :

$$b = \frac{|e|}{4\pi\epsilon_0} \frac{2j_a-1}{j_a+1} \int_0^{+\infty} f_{\text{Q},0}(r) (P_{n_a \kappa_a}^2(r) + Q_{n_a \kappa_a}^2(r)) dr. \quad (\text{II}^{\text{F}}.23)$$

L'anomalie hyperfine

L'anomalie hyperfine est quantifiée par :

$$\Delta_B^A = \frac{{}^{(A)}a}{{}^{(B)}a} \frac{{}^{(B)}M_z^{(1,\text{spec})}/{}^{(B)}I}{{}^{(A)}M_z^{(1,\text{spec})}/{}^{(A)}I} - 1. \quad (\text{II}^{\text{F}}.24)$$

Elle est principalement due aux effets de la distribution finie de charge et de courant du noyau, modélisés par les corrections de Breit-Rosenthal et de Bohr-Weisskopf :

$$\epsilon_{\text{BR}} = 1 - \frac{a_{\text{p.d.}}}{a_{\text{pt}}}, \quad \epsilon_{\text{BW}} = 1 - \frac{a_{\text{f.d.}}}{a_{\text{p.d.}}}. \quad (\text{II}^{\text{F}}.25)$$

L'anomalie totale est alors donnée par :

$$\Delta_B^A \approx \epsilon_{\text{BR}}^{(B)} + \epsilon_{\text{BW}}^{(B)} - \epsilon_{\text{BR}}^{(A)} - \epsilon_{\text{BW}}^{(A)}. \quad (\text{II}^{\text{F}}.26)$$

Limite non-relativiste et terme de contact de Fermi

La limite non-relativiste de la constante hyperfine dipolaire a pour un noyau dipolaire ponctuel peut être exprimée par le terme de contact de Fermi :

$$a_{\text{n.p.}}^{\text{Fermi}} = \frac{2e\hbar}{3m} \frac{M_z^{(1)}}{I} \frac{\mu_0}{4\pi} |\psi_{ns}(0)|^2. \quad (\text{II}^{\text{F}}.27)$$

Pour les ions hydrogénoïdes, $|\psi_{ns}(0)|^2 = 4 \frac{Z^3}{n^3 a_0^3}$, et donc :

$$a_{\text{n.p.}}^{\text{Fermi}} = \frac{8e\hbar}{3m} \frac{M_z^{(1)}}{I} \frac{\mu_0}{4\pi} \frac{Z^3}{n^3 a_0^3}. \quad (\text{II}^{\text{F}}.28)$$

Cette approximation est valide pour des systèmes faiblement relativistes où les effets de couplage spin-orbite sont négligeables.

Constantes hyperfines en milieu solide

En présence d'un environnement, comme dans les solides, les valeurs des constantes hyperfines peuvent être modifiées par le champ cristallin et d'autres interactions externes. Les états propres sont alors majoritairement décrits dans une base découplée $|JM_J IM_I\rangle$ et les constantes hyperfines sont ajustées selon la combinaison linéaire des états.

Les expressions des hamiltoniens effectifs demeurent pertinentes, mais il est nécessaire de prendre en compte la diagonalisation complète du hamiltonien atomique, y compris les effets de champ cristallin, pour obtenir les séparations d'énergie exactes et des constantes effectives ajustées par des mesures expérimentales.

II^F.4 L'électron/muon comme sonde nucléaire : ions hydrogénoïdes de Dy

Cette section explore l'utilisation de l'équation de Dirac pour les électrons et les muons en présence d'un noyau, permettant de résoudre numériquement les fonctions d'onde et de calculer les niveaux d'énergie. Ces calculs aident à évaluer la précision des modèles nucléaires en comparant les résultats théoriques aux données expérimentales. Les isotopes étudiés ici sont les deux isotopes naturellement abondants de dysprosium avec un spin nucléaire non nul : ^{161}Dy et ^{163}Dy .

Fonctions d'onde des électrons et muons dans les ions de type hydrogène

Les fonctions d'onde radiales relativistes pour les états $1s_{1/2}$ et $2p_{1/2}$ des électrons et muons dans $^{163}\text{Dy}^{65+}$ montrent des différences significatives aux alentours de la région nucléaire. Les fonctions d'onde des muons pénètrent davantage le noyau par rapport aux électrons.

Niveaux d'énergie des ions de type hydrogène

Les calculs des niveaux d'énergie pour les électrons et muons montrent que la taille finie du noyau réduit les énergies des états. Les résultats révèlent que les décalages énergétiques sont plus prononcés pour les muons, pouvant atteindre 40% pour les états $1s_{1/2}$, contre seulement 0.02% pour les électrons. Ainsi, les décalages d'énergie dus à la distribution de charge finie sont utiles pour discriminer différents modèles nucléaires, surtout dans le cas des ions muoniques.

Constantes hyperfines et anomalies

L'étude se poursuit avec le calcul des corrections de Breit-Rosenthal (BR) et de Bohr-Weisskopf (BW) sur les constantes hyperfines. Les corrections BR dues à la taille finie du noyau sont plus significatives pour les muons que pour les électrons, atteignant jusqu'à 100% pour les états $s_{1/2}$ des muons. Les corrections BW, qui tiennent compte de la pénétration des fonctions d'onde dans le noyau, montrent également des contributions importantes des courants de spin neutroniques.

Les anomalies hyperfines entre ^{161}Dy et ^{163}Dy sont également étudiées, et on observe que les anomalies pour les ions muoniques sont beaucoup plus marquées (jusqu'à 10^{-1}) par rapport aux anomalies électroniques (10^{-4}). Ces anomalies peuvent être exploitées pour différencier les isotopes.

Anomalie hyperfine quadripolaire

L'étude des constantes hyperfines quadripolaires montre que les décalages quadripolaires sont beaucoup plus importants pour les muons que pour les électrons (jusqu'à 50% pour les états $p_{3/2}$ muoniques). Par conséquent, les anomalies quadripolaires sont mesurables pour les muons et non pour les électrons, avec des valeurs atteignant 10^{-3} pour les muons.

Exemples supplémentaires : $^{159}\text{Tb}^{64+}$ et $^{165}\text{Ho}^{66+}$

Les densités de charge et de courant des noyaux de ^{159}Tb et ^{165}Ho sont présentées pour illustrer l'application du modèle à d'autres éléments lanthanides. Les calculs montrent que la déformation prolata du noyau de ^{165}Ho est plus marquée que celle des autres isotopes étudiés. Les densités de courants montrent des contributions polarisées par le proton non apparié dans ces noyaux, inversement à ce qui est observé pour le Dy.

Les constantes hyperfines de $^{165}\text{Ho}^{66+}$ sont comparées à des données expérimentales disponibles pour valider les modèles. En ajustant les résultats théoriques avec les valeurs expérimentales des moments dipolaires magnétiques, une précision inférieure à 1% est atteinte, confirmant la validité du modèle malgré quelques ajustements nécessaires.

Conclusion

Les résultats montrent que l'étude des corrections hyperfines et des anomalies entre isotopes, particulièrement avec des muons, permet de discriminer efficacement les modèles nucléaires. Les corrections BR et BW, ainsi que les anomalies hyperfines, sont de bons indicateurs pour la validation des descriptions de la structure nucléaire, offrant une approche prometteuse pour améliorer la compréhension des propriétés nucléaires à travers l'interaction avec des particules chargées lourdes comme le muon.

PARTIE III^F

(Résumé) Informatique Quantique avec des spins nucléaire de lanthanides

III^F.1 Des bits aux qubits aux qudits

Définition et représentation des qubits

Un **qubit** est l'unité fondamentale de l'information quantique, pouvant être en superposition des états classiques $|0\rangle$ et $|1\rangle$. Mathématiquement, il est représenté comme $|\psi\rangle = \alpha|0\rangle + \beta|1\rangle$, avec α et β des nombres complexes tels que $|\alpha|^2 + |\beta|^2 = 1$.

Les qubits peuvent aussi être représentés par une matrice densité :

$$\rho = \begin{pmatrix} \rho_{00} & \rho_{01} \\ \rho_{10} & \rho_{11} \end{pmatrix},$$

où $\rho_{00} + \rho_{11} = 1$ et $\rho_{01} = \rho_{10}^*$. La représentation par sphère de Bloch permet de visualiser les états des qubits en tant que points sur une sphère unitaire.

Intrication

Les qubits peuvent être **intriqués**, créant des états où les qubits ne peuvent être décrits indépendamment. Cela permet d'exploiter une croissance exponentielle de l'espace de Hilbert et est la base de nombreux algorithmes quantiques.

Portes quantiques

Les **portes quantiques** sont des opérateurs unitaires qui manipulent les qubits. Certaines portes classiques comme les matrices de Pauli (X , Y , Z) et la porte de Hadamard (H) agissent sur un seul qubit, tandis que d'autres, comme la porte CNOT, agissent sur plusieurs qubits et peuvent créer de l'intrication.

Les portes quantiques doivent être implémentées physiquement, nécessitant des séquences de contrôle adaptées et précises, surtout pour des technologies comme les qubits supraconducteurs ou les ions

piégés.

Algorithmes quantiques

Les **algorithmes quantiques** exploitent la superposition et l'intrication pour effectuer des calculs de manière plus efficace que les algorithmes classiques. Parmi eux, l'algorithme de **Shor** permet de factoriser des entiers de manière exponentiellement plus rapide que les méthodes classiques, tandis que l'algorithme de **Grover** offre une accélération quadratique pour des problèmes de recherche non structurée.

Qudits

Les **qudits** généralisent les qubits en ayant plus de deux niveaux (d niveaux). Un qudit peut être dans une superposition de d états de base, ce qui permet une représentation d'information plus dense et la réduction de la complexité des circuits quantiques. Les portes pour qudits sont des matrices unitaires de dimension $d \times d$, et les plateformes quditiques offrent souvent des avantages tels qu'une meilleure robustesse aux décohérences et des capacités de correction d'erreur améliorées.

Échelles de temps : T_1, T_2, T_2^*

L'efficacité des systèmes quantiques dépend de leur capacité à maintenir des états cohérents sur des périodes de temps significatives, décrites par les constantes T_1 , T_2 , et T_2^* :

- **Temps de relaxation longitudinale T_1** : mesure le temps nécessaire pour qu'un qubit retourne à son état fondamental après avoir été excité.
- **Temps de décohérence transverse T_2** : décrit la perte de cohérence quantique due à la déphasing entre états.
- **Temps de déphasage total T_2^*** : inclut toutes les sources de déphasage, y compris celles dues aux interactions externes, et est souvent plus court que T_2 .

Ces échelles de temps influencent directement les taux d'erreur et la viabilité des calculs quantiques, car elles définissent la période pendant laquelle les qubits peuvent être manipulés avant de perdre leur cohérence.

Conclusion

Le chapitre introduit les concepts clés du traitement de l'information quantique, en commençant par la description des qubits et des qudits, et en couvrant les portes quantiques, les algorithmes célèbres et les défis liés aux échelles de temps des qubits. Ces fondements sont essentiels pour comprendre le potentiel et les limites actuelles des technologies quantiques.

III^F.2 Systèmes quantiques ouverts avec bruit markovien

L'équation de Lindblad

Pour modéliser les dynamiques temporelles d'un système quantique interagissant avec un environnement, l'équation de **Lindblad** est une approche clé. Si l'on suppose une dynamique markovienne, l'évolution du système peut être exprimée par un générateur \mathcal{L} satisfaisant :

$$\frac{d\rho}{dt} = \mathcal{L}[\rho], \quad \rho(t) = e^{\mathcal{L}t}[\rho(0)].$$

\mathcal{L} doit vérifier plusieurs propriétés :

1. Se réduire à $-i[H, \cdot]$ en l'absence de bruit (équation de Von-Neumann).
2. Préserver la trace, assurant que $\text{Tr}(\rho) = 1$.
3. Garantir la positivité et la **complète positivité** pour éviter les incohérences dans les systèmes composés.

L'équation de Lindblad peut être exprimée comme :

$$\frac{d\rho}{dt} = -i[H, \rho] + \sum_{k=1}^K \gamma_k \left(L_k \rho L_k^\dagger - \frac{1}{2} \{L_k^\dagger L_k, \rho\} \right),$$

où H est le hamiltonien et $\{L_k\}$ sont des opérateurs de dissipation.

Représentation alternative : opérateurs de Kraus

Une autre manière de modéliser le bruit est d'utiliser les **opérateurs de Kraus**, qui représentent le bruit comme un processus discret :

$$\rho \rightarrow \sum_{k=1}^K E_k \rho E_k^\dagger.$$

Les représentations de Lindblad et de Kraus sont équivalentes, et l'une peut être transformée en l'autre via une approche par superopérateurs.

Lien avec les échelles de temps T_1 et T_2

Les canaux d'erreurs correspondant aux échelles de temps T_1 (relaxation longitudinale) et T_2 (déphasage pur) peuvent être modélisés par des opérateurs de Lindblad ou de Kraus spécifiques. Par exemple, le canal de déphasage pur peut être représenté par un opérateur de Lindblad :

$$L_1 = \sqrt{\frac{2}{T_2}} \sigma_z,$$

et son équation d'évolution :

$$\frac{d\rho}{dt} = -i[H, \rho] + \frac{2}{T_2} \left(\sigma_z \rho \sigma_z - \frac{1}{2} \{\sigma_z^2, \rho\} \right).$$

Défis numériques pour résoudre l'équation de Lindblad

La résolution numérique de l'équation de Lindblad est complexe en raison des coûts computationnels élevés (manipulation de d^{2N} nombres complexes). De plus, les méthodes standard, comme Runge-Kutta explicite, ne préservent pas toujours les propriétés essentielles telles que la positivité et la conservation de la trace.

Pour surmonter ces défis, des méthodes d'intégration exponentielle, comme les intégrateurs de **Euler exponentiels en rang complet (FREE)** et en **bas rang (LREE)**, ont été développées en collaboration avec des mathématiciens de l'Université normale de Chongqing et de l'Université de Würzburg. Nous les présentons dans notre preprint **Full- and low- rank exponential Euler integrators for the Lindblad equation** soumis pour publication dans SIAM Journal on Scientific Computing [182]. Ces méthodes garantissent la positivité et la conservation de la trace, tout en améliorant l'efficacité computationnelle. Le LREE, en particulier, réduit la complexité en utilisant des approximations de rang réduit, ce qui est crucial pour les simulations de grands systèmes.

Les expériences numériques montrent que ces nouvelles méthodes surpassent les solveurs standard de la librairie QuTip en termes de maintien de la positivité, notamment en présence de dissipation, tout en offrant des avantages computationnels significatifs pour les systèmes de grande dimension.

Conclusion

Le chapitre explore les différentes façons de modéliser les systèmes quantiques ouverts avec bruit markovien, en mettant l'accent sur l'équation de Lindblad et les opérateurs de Kraus. Les nouvelles méthodes numériques proposées pour résoudre ces équations représentent des avancées significatives pour la simulation de systèmes quantiques complexes, tout en assurant des résultats physiquement valides.

III^F.3 Qudit bruyant vs. plusieurs qubits : approche du premier ordre

Ce chapitre est basé sur notre article **Noisy Qudit vs Multiple Qubits : Conditions on Gate Efficiency for Enhancing Fidelity** qui a été publié dans npj Quantum Information [186], le code et les données utilisés dans l'étude ont été rendus publics [187].

Introduction

Dans ce chapitre, nous étudions la dynamique des systèmes quantiques en présence de bruit, en se concentrant sur les qudits, systèmes quantiques à d niveaux. Nous examinons l'influence du bruit sur les performances computationnelles des qudits et comparons ces résultats avec des systèmes de qubits multiples ayant un nombre équivalent de niveaux. L'objectif est de comprendre comment le bruit affecte les qudits et de déterminer dans quelles conditions ils peuvent surpasser les qubits.

Infidélité moyenne de porte (AGI) : définition et approximation du premier ordre

Pour étudier les effets du bruit, on se base sur l'équation maîtresse de Lindblad :

$$\frac{d\rho}{dt} = -i[H, \rho] + \sum_{k=1}^K \gamma_k \left(L_k \rho L_k^\dagger - \frac{1}{2} \{ L_k^\dagger L_k, \rho \} \right),$$

où $\rho(t)$ est la matrice de densité du système, H le hamiltonien et L_k des opérateurs d'effondrement dit de "collapse" décrivant le bruit. Pour de faibles amplitudes de bruit ($\gamma t \ll 1$), on peut approximer l'évolution de ρ par :

$$\rho(t) = \rho^* - \gamma t M + \mathcal{O}((\gamma t)^2),$$

où ρ^* est l'état cible sans bruit. L'infidélité \mathcal{E} d'une opération quantique peut alors être exprimée par :

$$\mathcal{E}(\rho^*) = \gamma t \Delta_* L + \mathcal{O}((\gamma t)^2),$$

où $\Delta_* L$ représente une relation fluctuation-dissipation.

Comparaison qudits vs. qubits : différences de comportement de l'AGI

En comparant un qudit avec un ensemble de qubits, on obtient deux expressions distinctes pour l'infidélité moyenne de porte (AGI). Pour un qudit sous déphasage pur :

$$\overline{\mathcal{E}}(\mathcal{E}_z) = \frac{\gamma t}{12} d(d-1) + \mathcal{O}((\gamma t)^2),$$

et pour n qubits sous déphasage pur :

$$\overline{\mathcal{E}}(\mathcal{E}_z) = \frac{\gamma t}{4} \frac{n 2^n}{2^n + 1} + \mathcal{O}((\gamma t)^2).$$

Ces résultats montrent que l'infidélité moyenne pour les qudits croît de façon quadratique avec la dimension d , alors que pour un ensemble de qubits, elle croît linéairement avec le nombre de qubits $n = \log_2(d)$.

Condition pour la supériorité des qudits

Il est possible de déterminer dans quelles conditions un qudit peut surpasser des qubits en termes de robustesse au bruit :

$$\frac{\overline{\mathcal{E}_d(\mathcal{E}_z)}}{\overline{\mathcal{E}_{b,n}(\mathcal{E}_z)}} = \frac{t_{b,n}/T_{2,b}}{t_d/T_{2,d}} > \frac{d^2 - 1}{3n}.$$

Pour qu'un qudit soit avantageux, le ratio des temps de porte en unités de temps de décohérence doit être supérieur à un certain seuil, dépendant du nombre de niveaux du qudit.

Validation numérique et applications

Des simulations numériques ont validé les comportements théoriques de l'AGI, en confirmant que les qudits peuvent offrir des performances supérieures aux ensembles de qubits pour des valeurs appropriées des paramètres de bruit et de temps de porte. Par exemple, un qudit de dimension $d = 8$ pourrait surpasser trois qubits si son temps de décohérence est au moins sept fois supérieur à celui des qubits.

En explorant des plateformes actuelles comme les qubits supraconducteurs et les qudits à base de spins nucléaires, il a été montré que certains qudits, avec leurs caractéristiques actuelles, peuvent bénéficier d'un avantage face aux plateformes mutliqubit, notamment pour des dimensions allant jusqu'à $d = 40$.

Scalabilité et connectivité des qudits

L'analyse de la scalabilité des réseaux de qudits et de qubits a révélé que, dans certaines architectures, comme les réseaux en grille 2D ou 1D, les qudits permettent de maintenir une meilleure connectivité tout en réduisant la complexité des interactions. Par exemple, un réseau de N qudits peut être plus efficace qu'un réseau de $n = \log_2(N)$ qubits, surtout dans des architectures où la connectivité entre les qubits est restreinte.

Conclusion

Les qudits offrent une alternative prometteuse aux qubits pour des applications quantiques nécessitant des dimensions de Hilbert élevées. Ils permettent une densité d'information accrue et peuvent présenter une meilleure tolérance au bruit dans certains contextes. Toutefois, leur supériorité dépend fortement des conditions physiques, notamment des temps de porte et des temps de décohérence, ainsi que de la topologie de la connectivité des qubits. Leur nombre accru de niveau impose une exigence plus élevée sur l'amplitude du bruit et la durée des portes logique, de manière à compenser le nombre accru de canaux d'erreur. Les résultats de ce chapitre fournissent des bases analytiques et numériques pour évaluer et exploiter cet avantage potentiel dans les futures plateformes de calcul quantique.

III^F.4 Qudit bruyant : Au-delà de l'approche du premier ordre

Ce chapitre résume notre article **Nonlinearity of the Fidelity in Open Qudit Systems: Gate and Noise Dependence in High-dimensional Quantum Computing**, soumis à publication dans Quantum et disponible en prépublication sur arXiv [204]. Le code et les données utilisés sont accessibles sur Zenodo [205].

Les simulations numériques présentées dans la Section 11.2 ont montré que la fidélité moyenne d'un qudit soumis à une décohérence pure se comporte de manière linéaire en fonction de l'intensité du bruit γt pour de faibles valeurs de γt . Cependant, pour des valeurs plus élevées, cette linéarité se dégrade, indiquant l'importance des termes d'ordre supérieur dans le développement limité de la fidélité moyenne. Ce chapitre explore cette déviation par une approche perturbative, permettant d'examiner l'influence du bruit pour différents types de canaux.

Équation de Lindblad sous forme de superopérateur

L'équation de Lindblad peut être formulée en termes de superopérateurs :

$$\frac{d\rho}{dt} = \mathcal{S}[\rho] + \mathcal{D}[\rho], \quad (\text{III}^{\text{F}}.1)$$

où $\mathcal{S}[\rho] = -i[H(t), \rho]$ représente l'évolution unitaire et $\mathcal{D}[\rho]$ la partie dissipative. Le canal quantique décrivant l'évolution devient :

$$\rho(t) = \mathcal{E}(t)[\rho(0)] = \mathcal{T} \exp \left(\int_0^t (\mathcal{S}(t') + \mathcal{D}) dt' \right) [\rho(0)]. \quad (\text{III}^{\text{F}}.2)$$

Forme perturbative de la fidélité moyenne

Par une expansion perturbative, on développe le superopérateur \mathcal{E} en puissances de γ sous la forme :

$$\mathcal{E} = e^{\mathcal{S}t} + e^{\mathcal{S}t} \sum_{m=1}^{\infty} \gamma^m \left(\int_0^t \cdots dt_1 \right). \quad (\text{III}^{\text{F}}.3)$$

L'expression perturbative de la fidélité moyenne est alors :

$$\overline{\mathcal{F}}(\mathcal{E}, \mathcal{U}) = \frac{\text{Tr}(\mathcal{U}^\dagger \circ \mathcal{E}) + d}{d(d+1)}. \quad (\text{III}^{\text{F}}.4)$$

Résultats de l'approche perturbative

L'étude révèle que la fidélité moyenne présente des corrections de second ordre dépendantes du bruit, confirmées par l'équation suivante :

$$\overline{\mathcal{E}}^{(2)}(\mathcal{E}, \mathcal{U}) = -\frac{(\gamma t)^2}{d(d+1)} \left[\frac{\text{Tr}(\mathcal{L}^2)}{2} + \sum_{s=2}^{\infty} \frac{(-t)^s \text{Tr}(\mathcal{L}[(\mathcal{S})^s, \mathcal{L}])}{(s+2)!} \right]. \quad (\text{III}^{\text{F}}.5)$$

Le terme d'ordre le plus bas sensible à la dépendance au bruit et aux portes est :

$$-\frac{\gamma^2 t^4}{24d(d+1)} \text{Tr}(\mathcal{L}[\mathcal{S}, [\mathcal{S}, \mathcal{L}]]). \quad (\text{III}^{\text{F}}.6)$$

Exemple de déphasage pur et correction d'erreurs

En cas de déphasage pur avec $L = J_z$, le terme de second ordre se simplifie en :

$$\text{Tr}(\mathcal{J}_z^2) = \frac{d^2(3 - 5d^2 + 2d^4)}{120}. \quad (\text{III}^{\text{F}}.7)$$

De plus, il est possible d'obtenir des expressions pour les corrections d'ordre supérieur, non pas en termes de superopérateurs, mais en termes d'opérateurs, la forme, bien que moins utile analytiquement, permet des avantages numériques significatifs pour les grandes dimensions.

Bornes universelles pour la fidélité

Des simulations intensives ont révélé que la fidélité moyenne atteint des plateaux aux valeurs maximales et minimales définies par :

$$\mathcal{I}_{\max}^* = 1 - \frac{1}{d+1}, \quad (\text{III}^{\text{F}}.8)$$

$$\mathcal{I}_{\min}^* = 1 - \frac{1}{d}, \quad (\text{III}^{\text{F}}.9)$$

$$\mathcal{I}_{\text{mean}}^* = 1 - \frac{2}{d+1}. \quad (\text{III}^{\text{F}}.10)$$

Conclusion et implications

L'étude montre que l'extension de la dimension du qudit au-delà des corrections de premier ordre est cruciale pour améliorer les performances en présence de bruit significatif. L'approche superopératoire permet de traiter efficacement ces extensions, et les résultats obtenus offrent un cadre solide pour la conception de systèmes de calcul quantique en haute dimension. Pour des détails supplémentaires, consulter [204].

III^F.5 Génération optimale de portes

Les chapitres précédents ont montré que lorsque la dimension augmente, la fidélité computationnelle des opérations diminue, et une quantité importante, la figure de mérite γt , a été identifiée. Ce produit de la force du bruit et du temps de porte est crucial pour déterminer la dimension optimale du système pour une force de bruit et un temps de porte donnés. Afin d'améliorer la performance d'un système de qudits, que ce soit en augmentant la dimension d ou en améliorant la fidélité des portes, il est nécessaire d'améliorer cette figure de mérite pour contrer la déphasage pur. Une possibilité est de réduire le bruit en optimisant le système, ou bien de réduire le temps de porte t . Ce chapitre se concentre sur cette dernière option, en optimisant le processus de génération de portes pour réduire le temps de porte.

Approximation de l'onde tournante et référentiel en rotation

Nous considérons un système à d niveaux dans le référentiel du laboratoire évoluant avec l'hamiltonien :

$$H_{\text{lab}} = H_0 + u(t)H_c, \quad (\text{III}^F.11)$$

où H_0 est l'hamiltonien libre, diagonal dans la base computationnelle, de valeurs propres $\{\omega\}$, et H_c est l'hamiltonien de contrôle. En décomposant $u(t)$ en série de Fourier et en passant au référentiel en rotation via la transformation unitaire $R(t)$, on simplifie l'analyse pour éliminer les oscillations de haute fréquence. Cette transformation permet de traiter chaque transition entre états comme un système à deux niveaux, facilitant ainsi l'étude des contrôles.

Le passage au référentiel en rotation mène à l'hamiltonien simplifié :

$$H_{\text{rot}}(t) = \sum_{n' > n} \Omega_{n,n'}(t) \cos(\phi_{n,n'}(t)) \sigma_{n,n'}^x + \Omega_{n,n'}(t) \sin(\phi_{n,n'}(t)) \sigma_{n,n'}^y, \quad (\text{III}^F.12)$$

avec $\Omega_{n,n'}(t)$ et $\phi_{n,n'}(t)$ représentant les amplitudes et phases des champs de contrôle. Cette représentation facilite l'optimisation des séquences de contrôles nécessaires pour réaliser les opérations quantiques désirées.

Résultats principaux

Hamiltonien dans le référentiel en rotation Un des résultats clefs est la possibilité de formuler l'hamiltonien de contrôle sous forme d'une combinaison de termes dépendant des amplitudes et phases de contrôles, simplifiant la manipulation des systèmes multi-niveaux en les traitant comme des rotations dans des sous-espaces à deux niveaux. Cela permet de visualiser les champs de contrôle comme des rotations sur la sphère de Bloch des sous-espaces à deux niveaux.

Vitesse quantiques limites (QSL) Les vitesses quantiques limites (QSL) définissent le temps minimal requis pour transférer un état initial vers un état final ou pour réaliser une porte unitaire donnée. Pour un système à deux niveaux, la QSL pour un transfert état-à-état est :

$$\tau_{\text{QSL}}^{\text{état}} = \frac{\theta}{\|H\|}, \quad (\text{III}^{\text{F}}.13)$$

où θ est l'angle de rotation sur la sphère de Bloch et $\|H\|$ la norme de l'hamiltonien. Cette limite peut être généralisée aux systèmes à d niveaux en définissant la QSL de la porte comme le temps minimal requis pour transformer simultanément tous les états initiaux en leurs états finaux correspondants. La QSL d'une porte unitaire G pour un qubit est donnée par :

$$\tau_{\text{QSL}}^{\text{porte}}(G) = \frac{\|\log(G)\|}{\|H\|}. \quad (\text{III}^{\text{F}}.14)$$

Décomposition par rotations de Givens (GRD) La méthode GRD permet de décomposer un opérateur unitaire cible en une séquence de rotations élémentaires appelées rotations de Givens. Ces rotations facilitent la génération exacte des portes quantiques pour des systèmes à plusieurs niveaux, en particulier pour des systèmes où les transitions entre états sont limitées.

Optimisation par GRAPE et PMP L'algorithme GRAPE optimise les champs de contrôle pour maximiser la fidélité d'une porte cible. En utilisant le gradient ascendant, il ajuste les contrôles à chaque étape pour se rapprocher de la solution optimale.

Algorithme MAGICARP En complément, le Principe du Maximum de Pontryagin (PMP) fournit une condition nécessaire pour optimiser les contrôles. Ensemble, ces méthodes permettent de trouver des champs de contrôle qui minimisent le coût énergétique ou le temps nécessaire pour implémenter une porte. L'algorithme MAGICARP combine les principes du PMP avec le gradient ascendant pour itérer vers la solution optimale en utilisant une structure auto-itérative basée sur les informations obtenus du PMP. Cette approche offre un cadre prometteur pour générer des portes optimales, surtout lorsque les contrôles sont contraints.

Coût énergétique et temps optimal Le coût énergétique total pour implémenter une opération quantique est donné par :

$$C[H] = \int_0^T \|H_{\text{rot}}(t)\| dt, \quad (\text{III}^{\text{F}}.15)$$

et la durée minimale de l'opération est déterminée par l'optimisation des champs de contrôle maximaux permis. Le principe fondamental est que la réduction du coût énergétique et la minimisation du temps d'opération dépendent de la gestion fine des contrôles dans le référentiel en rotation .

Conclusion et perspectives Ce chapitre présente des méthodes pour générer des portes optimales en optimisant les temps de porte via une approche rigoureuse basée sur la physique des systèmes quantiques et la théorie du contrôle. Les résultats obtenus montrent que les techniques de simplification par le référentiel en rotation , combinées à des approches numériques et analytiques comme GRAPE et MAGICARP, peuvent grandement améliorer les performances des systèmes de qudits. Ces avancées ouvrent la voie à des applications plus efficaces en calcul quantique, où la minimisation des temps de porte est cruciale pour réduire les effets de la décohérence et maximiser la fidélité des opérations.

PARTIE IV^F

(Résumé) La séquence omniprésente de Prouhet-Thue-Morse

IV^F.1 La séquence omniprésente de Prouhet-Thue-Morse

Ce chapitre explore les applications de la séquence de Prouhet-Thue-Morse (PTM) en informatique quantique, mettant en avant sa beauté mathématique et son utilité pratique. Nous avons démontré que cette séquence joue un rôle crucial dans la correction d'erreurs quantiques, la conception de mémoires quantiques résistantes au bruit, ainsi que dans l'analyse du chaos quantique. La séquence PTM apparaît naturellement dans les systèmes à interactions de type Ising X - X , permettant ainsi une codification robuste des états de mémoire quantique.

Propriétés et Définitions Multiples de la Séquence PTM

La séquence PTM est définie par plusieurs approches : de manière explicite, par itération ou récursion. Les termes de la séquence suivent une structure auto-similaire, représentée mathématiquement par :

$$t_n = \left(\sum_{k=0}^{\infty} \left\lfloor \frac{n}{2^k} \right\rfloor \right) \bmod 2$$

où t_n est le n -ème terme de la séquence, calculé comme la somme des chiffres binaires de n . Une propriété notable de la séquence est sa capacité à résoudre le problème de Prouhet-Tarry-Escott : la somme des puissances k -èmes des indices avec un $t_n = 0$ (ensemble $E(N)$) est égale à celle des indices avec $t_n = 1$ (ensemble $O(N)$), pour $k < N$.

États PTM dans les Systèmes Quantique et Correction d'Erreurs

Nous définissons les *états logiques PTM* d'un système de N qubits comme suit :

$$|0_{\text{TM}}^{(N)}\rangle = \frac{1}{\sqrt{2^{N-1}}} \sum_{e \in E(N)} |(e)_2\rangle, \quad |1_{\text{TM}}^{(N)}\rangle = \frac{1}{\sqrt{2^{N-1}}} \sum_{o \in O(N)} |(o)_2\rangle.$$

Les propriétés de ces états montrent qu'ils respectent les conditions de Knill-Laflamme, ce qui les rend utiles pour détecter des erreurs de phase jusqu'à un certain nombre d'erreurs sur un seul qubit. Un circuit de correction d'erreurs quantique, adapté pour ces états, permet ainsi de corriger une inversion de phase unique sans préparation préalable de l'état.

Interactions X - X et Mémoire Quantique Résistante au Bruit

Les états PTM se révèlent être des états propres d'interactions de type Ising X - X , ne subissant qu'un simple déphasage global, ce qui en fait des candidats idéaux pour l'encodage de mémoire quantique. En particulier, les interactions X - X dans une chaîne de spins permettent de préserver les états de mémoire quantique dans un environnement de bruit magnétique le long des axes y ou z , offrant une robustesse aux déphasages dans ces directions.

Lien avec le Chaos Quantique et la Transformée de Fourier Quantique

Nous avons montré que la transformée de Walsh-Hadamard est intimement liée à la suite de PTM et combinée à la transformée de Fourier quantique (QFT), l'image des états de bases à N qubits exhibent des propriétés multifractales et auto-similaires, offrant un cadre pour étudier le chaos quantique et potentiellement pour concevoir des états propres approximatifs de la transformation du boulanger quantique.

Applications en Théorie des Nombres

La séquence PTM présente aussi des relations intéressantes avec des fonctions analytiques en théorie des nombres. Notamment, la séquence PTM intervient dans des formules générant des séries de Dirichlet, permettant d'exprimer la fonction ζ de Riemann. Par un état initial spécifique et une interaction non linéaire d'oscillateurs logarithmiques, on peut obtenir la valeur de $\zeta(s)$ par des mesures d'amplitudes de corrélation, reliant ainsi l'informatique quantique à la théorie analytique des nombres.

Conclusion

Les résultats obtenus montrent que la séquence PTM, au-delà de son intérêt théorique, est d'une grande utilité pratique pour la correction d'erreurs, la résistance au bruit en mémoire quantique, et l'étude du chaos quantique. Elle fait ainsi le lien entre l'informatique quantique et des domaines tels que la physique et les mathématiques pures. L'interdisciplinarité entre ces disciplines, rendue possible grâce à la séquence PTM, constitue un levier pour exploiter pleinement les potentiels de l'informatique quantique, renforçant notre compréhension de la structure mathématique des systèmes quantiques.

PARTIE **V^F**

Conclusion en français – Aperçu et Perspectives

V^F.1 État de l'art actuel

Une boîte à outils théorique pour la conception de qubits à base de lanthanides

Tout au long de ce travail, nous avons développé une boîte à outils théorique complète visant à la conception non empirique de qubits moléculaires à base de lanthanides. L'une de nos principales réalisations a été de démontrer que le cadre théorique atomique — particulièrement adapté aux lanthanides dans les matériaux — peut être efficacement appliqué pour prédire les structures électroniques des complexes de lanthanides. Nous avons notamment proposé que la méthode de Théorie de Champ de Ligand DFT (LFDFT) s'avère extrêmement utile pour effectuer un étalonnage rapide et quantitatif de divers environnements moléculaires. En combinant des calculs DFT rapides avec des calculs de fonction d'onde obtenus grâce à l'entiereté de la forme matricielle de l'hamiltonien atomique, cette méthode nous permet d'obtenir avec précision les niveaux d'énergie hyperfins des ions de lanthanides dans différents environnements de ligands et orientations de champs externes. Cette approche computationnelle puissante peut servir d'outil robuste pour prédire les symétries spécifiques, les compositions de ligands et les combinaisons métal-ligand permettant d'obtenir les niveaux d'énergie hyperfins souhaités. Elle permet également d'identifier les propriétés importantes nécessaires ou améliorant la réponse aux champs électriques ou lumineux, cruciales pour les applications en traitement de l'information quantique.

En explorant systématiquement l'espace des paramètres des conceptions moléculaires sans recourir aux méthodes empiriques souvent coûteuses en laboratoire, nous pouvons adapter les propriétés des qubits basés sur les lanthanides pour répondre à des exigences spécifiques, effectuant ainsi des expériences *in-silico*. Cette capacité accélérerait significativement le développement de matériaux avancés à base de lanthanides pour le traitement de l'information quantique. Globalement, notre travail établit une base théorique solide qui soutient la conception rationnelle et efficace de systèmes moléculaires à base de lanthanides pour une utilisation dans le traitement de l'information quantique.

Un guide pratique pour les implémentations QIP dans les complexes Ln-moléculaires

Ce travail jette également les bases pour l'implémentation pratique de portes quantiques universelles à un seul qubit, un défi important rencontré lors des précédentes expériences. Nous avons exploré diverses méthodes pour concevoir des impulsions permettant d'implémenter les portes quantiques souhaitées de

manière contrôlée et précise. En utilisant la théorie du contrôle optimal, nous avons démontré qu'il est possible de trouver des séquences d'impulsions optimales qui réalisent l'implémentation de ces portes avec une grande fidélité.

De plus, nous avons montré que les performances computationnelles des qudits sont extrêmement sensibles aux augmentations de la dimensionnalité du système, et nous avons quantifié ce comportement d'échelle. Cette sensibilité rend essentiel de réduire la durée des impulsions pour éviter l'accumulation d'erreurs au fil du temps, ce qui peut gravement affecter les performances. Pour répondre à ce problème, nous avons introduit la Méthode pour la Construction Auto-Itérative et le Raffinement d'Impulsions basées sur le Principe Maximum de Pontryagin et le Gradient ascendant (MAGICARP). Cette méthode hybride repose sur le Principe du Maximum de Pontryagin pour déterminer la forme mathématique de l'impulsion optimale en temps et utilise des techniques de gradient ascendant pour trouver les paramètres optimaux pour que l'impulsion implémente la porte logique souhaitée. Un avantage important de la méthode MAGICARP est que le nombre de paramètres d'optimisation dépend uniquement de la dimension du système, et non du nombre d'impulsions de contrôle ou du nombre de pas de discrétisation dans le temps.

Dans l'ensemble, nos contributions offrent une voie pratique vers la réalisation de portes quantiques universelles à un seul qudit, abordant les défis clés liés à la conception et à l'optimisation d'impulsions dans les systèmes quantiques de haute dimension. Cette avancée profite non seulement aux efforts expérimentaux de notre groupe, mais a également des implications plus larges pour le domaine du traitement de l'information quantique. Le contrôle efficace des systèmes de qudits est essentiel pour le développement de technologies quantiques évolutives, et notre travail contribue de manière significative à cet objectif en offrant des solutions innovantes à des problèmes auparavant insolubles.

En appliquant systématiquement ces méthodes, nous pouvons accélérer le développement de dispositifs quantiques exploitant les espaces d'états de dimension plus élevée des qudits. Cela ouvre de nouvelles voies pour des calculs et des simulations quantiques plus complexes, pouvant potentiellement conduire à des percées dans des domaines tels que la cryptographie quantique, la correction d'erreurs quantiques et les algorithmes quantiques. Notre recherche sert donc de tremplin essentiel vers la prochaine génération de technologies quantiques, où la précision du contrôle et la dimensionnalité des systèmes jouent un rôle déterminant dans les performances et les capacités.

Structure nucléaire et hyperfine des lanthanides

Notre exploration de la physique nucléaire à basse énergie a mis en évidence le potentiel d'utiliser des ions de lanthanides hautement chargés et muoniques pour tester des modèles nucléaires de noyaux fortement déformés. Nous avons notamment calculé les corrections de Bohr-Weisskopf et Breit-Rosenthal pour divers isotopes de lanthanides, ^{159}Tb , ^{161}Dy , ^{163}Dy et ^{165}Ho . Ces résultats ont été comparés à des résultats expérimentaux pour évaluer le modèle. Ces calculs ont apporté des informations précieuses sur les noyaux paires-impairs et impairs-paires, révélant la complexité et la diversité des propriétés nucléaires exhibées par les lanthanides malgré des changements minimes dans leurs compositions en nucléons.

La complexité et la variation observées des propriétés nucléaires rendent les lanthanides particulièrement intéressants pour l'exploration isotopique au sein de cette famille d'éléments. En manipulant leurs propriétés nucléaires et électriques par variation isotopique, nous pouvons optimiser l'espace de Hilbert des qudits pour des applications en traitement de l'information quantique. Cette capacité de réglage fin des propriétés au niveau nucléaire offre une voie prometteuse pour améliorer les performances et l'évolutivité des systèmes quantiques à base de qudits.

De plus, nos résultats suggèrent que l'exploitation des caractéristiques uniques des isotopes de lanthanides pourrait améliorer les modèles nucléaires, en particulier pour les noyaux fortement déformés comme c'est le cas des lanthanides. En comblant l'écart entre la physique nucléaire, la physique atomique et la chimie quantique, nous ouvrons de nouvelles possibilités pour la conception et le contrôle

des systèmes quantiques à l'intersection de ces disciplines.

Dans l'ensemble, notre détour par la physique nucléaire à basse énergie a enrichi notre compréhension de l'interaction complexe entre la structure nucléaire et le traitement de l'information quantique. Cela souligne l'importance des approches interdisciplinaires dans le traitement des défis scientifiques complexes et ouvre la voie à des recherches futures qui pourraient encore optimiser les propriétés des qudits. En explorant les variations isotopiques des lanthanides, nous pouvons continuer à affiner nos modèles et techniques, contribuant finalement à l'avancement de la physique nucléaire et de l'informatique quantique.

V^F.2 Axes de recherche futurs

Étude ab-initio de la décohérence

Dans notre modèle actuel, l'incorporation des ligands et des champs externes est purement statique, ce qui limite notre capacité à comprendre pleinement les propriétés dynamiques des ions de lanthanides dans une matrice environnementale. L'introduction d'éléments dépendants du temps dans le modèle fournirait des informations supplémentaires sur ces dynamiques. Cette amélioration peut être obtenue en étendant les approches perturbatives utilisées dans ce travail pour inclure la théorie des perturbations dépendante du temps. Une telle extension permettrait de capturer l'évolution du système dans le temps, offrant une compréhension plus complète des interactions en jeu.

Par ailleurs, les dynamiques du champ de ligands peuvent être incorporées en faisant progresser la théorie du champ de ligands au-delà de son cadre statique. En incluant le couplage spin-phonon par un développement limité au premier ordre des paramètres du champ de ligands par rapport au mouvement nucléaire des ligands [247, 248, 249], nous pouvons prendre en compte les interactions entre les spins électroniques et les vibrations du réseau. Cette méthode devrait être considérée comme une priorité pour les recherches futures, car elle fournirait des informations précieuses sur les échelles de temps T_1 (relaxation spin-réseau) et T_2 (relaxation spin-spin) des qudits nucléaires. La compréhension de ces processus de relaxation est cruciale pour les applications en traitement de l'information quantique, où la décohérence peut significativement affecter les performances.

De plus, l'incorporation des dynamiques dépendantes du temps dans notre modèle serait extrêmement bénéfique pour l'étude des propriétés optiques des lanthanides. Au-delà de la capacité du modèle statique à calculer les amplitudes de transition, une approche dynamique pourrait nous permettre de prédire les largeurs de raie des transitions interdites f - f . Ces transitions sont d'un intérêt particulier en raison de leurs caractéristiques spectrales pointues et de leurs applications potentielles dans les dispositifs optiques et les technologies quantiques. Une meilleure compréhension des largeurs de raie améliorerait notre capacité à concevoir des matériaux à base de lanthanides avec des propriétés optiques spécifiques.

En étendant notre cadre théorique pour inclure les effets dépendants du temps et les champs de ligands dynamiques, nous ouvrons la voie à une compréhension plus profonde des systèmes à base de lanthanides. Cette avancée contribue non seulement à la science fondamentale de ces matériaux complexes, mais elle facilite également la conception de nouveaux composés avec des propriétés sur mesure pour des applications spécifiques dans l'informatique quantique, la photonique et les sciences des matériaux. Un modèle aussi complet nous permettrait de manipuler les propriétés nucléaires et électriques de manière plus efficace, optimisant l'espace de Hilbert des qudits et pouvant potentiellement conduire à des percées dans les réalisations expérimentales de traitement de l'information quantique en haute dimension.

En résumé, aller au-delà des modèles statiques pour intégrer des dynamiques dépendantes du temps et des interactions spin-phonon promet d'importants progrès dans notre compréhension théorique et nos capacités pratiques. Cela ouvre de nouvelles voies pour explorer les comportements complexes

des ions de lanthanides et concevoir des matériaux capables de répondre aux exigences rigoureuses des technologies quantiques de nouvelle génération. Cette approche s'aligne avec les objectifs plus larges de notre recherche, visant à combler les écarts entre les prédictions théoriques et les réalisations expérimentales, contribuant en fin de compte au développement de systèmes quantiques plus efficaces et évolutifs.

Étude approfondie de l'effet de la composition et de la géométrie des ligands

Dans notre recherche, le formalisme de l'opérateur effectif développé pour l'effet Stark hyperfin et les transitions optiques induites par l'interaction hyperfine a fourni des informations précieuses sur les conditions imposées aux paramètres du champ de ligand dans les expressions analytiques des opérateurs effectifs. Auparavant, nous avons abordé ces conditions en termes de règles de sélection simples dérivées de l'algèbre de Racah. Cependant, mener une étude approfondie de ces règles de sélection, ainsi qu'une évaluation plus quantitative des divers termes dans le hamiltonien effectif, pourrait fournir des informations particulièrement utiles sur les exigences spécifiques pour le champ de ligand. Une telle analyse pourrait également élucider l'importance relative de certaines contributions de rang impair par rapport à d'autres.

Approfondir l'étude des règles de sélection des opérateurs effectifs nous permettrait de mieux comprendre comment différents paramètres du champ de ligand influencent les interactions hyperfines et les transitions optiques dans les complexes de lanthanides. En évaluant quantitativement les contributions de chaque terme dans le hamiltonien effectif, nous pourrions identifier quels paramètres sont les plus critiques pour obtenir les propriétés souhaitées dans le système. Cette approche est similaire aux informations fournies par la théorie de Judd-Ofelt lors de son introduction, qui a significativement amélioré notre compréhension des transitions dipolaires électriques dans les ions terres rares en prenant systématiquement en compte les contributions des opérateurs tensoriels de différents rangs.

Une étude aussi complète affinerait non seulement nos modèles théoriques, mais elle guiderait également la conception pratique de nouveaux matériaux avec des propriétés adaptées au traitement de l'information quantique et à d'autres applications avancées. En comprenant les rôles spécifiques des différents paramètres du champ de ligand et la signification des opérateurs tensoriels de rang impair, nous pourrions optimiser l'environnement du champ de ligand pour améliorer certaines réponses au champ électrique hyperfin ou aux transitions optiques. Cette optimisation est cruciale pour améliorer les performances et l'évolutivité des qubits moléculaires en informatique quantique.

De plus, cette analyse plus approfondie pourrait révéler des effets subtils non apparents lors d'une simple observation des règles de sélection. Elle pourrait notamment montrer comment de petits changements dans la géométrie ou la composition du ligand peuvent avoir des impacts significatifs sur les interactions hyperfines en raison de la dépendance sensible à certains paramètres du champ de ligand. De telles informations seraient inestimables pour les expérimentateurs cherchant à synthétiser de nouveaux composés aux propriétés précisément contrôlées.

L'extension de notre investigation pour inclure un examen détaillé des règles de sélection et une évaluation quantitative des termes du hamiltonien effectif est donc très prometteuse. Elle enrichirait notre compréhension de l'interaction entre les champs de ligands et les interactions hyperfines, tout comme la théorie de Judd-Ofelt a enrichi notre connaissance des transitions optiques dans les éléments des terres rares. Cette avancée contribuerait finalement au développement de stratégies plus efficaces pour la conception de systèmes quantiques à base de lanthanides, repoussant les limites de ce qui est réalisable dans le traitement de l'information quantique en haute dimension.

Calcul de la structure hf des ions multiélectroniques dans des molécules/cristaux

Notre méthodologie pour le calcul des termes de contact de Fermi et des constantes hyperfines dans les complexes de lanthanides s'est jusqu'à présent principalement concentrée sur les systèmes à électron

unique (ou à muon unique), où les effets de corrélation électronique sont relativement simples à gérer. Cependant, étendre cette méthodologie aux systèmes multiélectroniques présente un défi majeur en raison de la complexité accrue des interactions électron-électron. Malgré ces défis, développer des méthodes précises pour le calcul des constantes hyperfines dans les systèmes multiélectroniques est crucial pour une compréhension complète des interactions hyperfines dans les complexes de lanthanides, qui impliquent généralement plusieurs électrons dans les orbitales $4f$ et parfois $6s$.

Intégrer les hamiltoniens hyperfins exacts — au-delà de leur forme traditionnelle effective dans un multiplet donné J — dans le hamiltonien atomique de l'ion de lanthanide dans le champ de ligand serait particulièrement avantageux et permettrait de tenir compte du mélange de multiplets et même de configurations. Cette approche nous permettrait de calculer l'effet Stark hyperfin et les transitions optiques induites par l'interaction hyperfine avec une plus grande précision grâce à la diagonalisation exacte du hamiltonien complet. Cependant, la diagonalisation exacte de ces grands hamiltoniens peut être exigeante en termes de calcul et peut ne pas être réalisable pour les systèmes avec un grand nombre d'électrons.

Pour surmonter cet obstacle computationnel, nous pouvons employer des méthodes de diagonalisation partielle plus rapides et moins gourmandes en ressources [250]. Ces techniques permettent d'obtenir uniquement les énergies des doublets hyperfins de l'état fondamental et éventuellement les vecteurs propres correspondants sans avoir besoin de calculer tout le spectre du hamiltonien. Par exemple, des algorithmes itératifs comme la méthode de Lanczos ou l'algorithme de Davidson peuvent trouver efficacement quelques valeurs et vecteurs propres extrémaux de grandes matrices creuses, ce qui les rend bien adaptés à nos objectifs.

Appliquer ces méthodes de diagonalisation partielle serait particulièrement utile pour étudier l'effet Stark hyperfin en présence de champs électriques externes. En effectuant des diagonalisations successives du hamiltonien pour différentes valeurs de l'intensité et des orientations du champ électrique, nous pouvons évaluer quantitativement comment les niveaux d'énergie hyperfins se déplacent en réponse au champ. De plus, l'analyse de la composition des vecteurs propres fournit des informations précieuses sur les décalages Stark attendus, améliorant notre compréhension de la réponse du système aux perturbations externes.

Le développement de nos méthodes de calcul pour traiter les systèmes multiélectroniques et l'intégration des hamiltoniens hyperfins exacts approfondira notre compréhension des interactions hyperfines dans les complexes de lanthanides. Cette avancée améliorera de manière significative notre capacité à prédire et à contrôler les propriétés de ces complexes pour des applications en traitement de l'information quantique et dans d'autres technologies avancées. De plus, ces méthodes améliorées pourraient faciliter la conception de nouveaux matériaux à base de lanthanides avec des propriétés optimisées pour des applications spécifiques, contribuant ainsi à l'avancement des technologies quantiques.

Une méthodologie pour explorer l'espace chimique des isotopologues

Bien que nous ayons proposé un modèle pour explorer l'espace chimique des compositions et des géométries de ligands — dans le but d'ajuster les propriétés électriques et hyperfines des qudits à spin nucléaire dans les complexes organiques de lanthanides — nous n'avons pas encore eu l'occasion de mener une étude aussi exhaustive. Explorer cet espace chimique est crucial car les variations de composition et de géométrie des ligands peuvent influencer considérablement la structure électronique des complexes de lanthanides, affectant ainsi les performances et la cohérence des qudits. Comprendre ces influences est essentiel pour optimiser la conception des systèmes de qudits pour les applications en traitement de l'information quantique.

La prochaine étape logique consiste à utiliser la méthodologie développée pour mener une étude approfondie de différents ligands, en considérant divers types de déformations structurales. Par exemple, dans le cas de TbPc_2 , nous pourrions étudier comment la modification des angles de torsion

entre les plans de phtalocyanine, l'introduction de déviations par rapport à la coplanarité des deux phtalocyanines, l'altération des longueurs de liaison et d'autres modifications structurelles affectent les propriétés des qudits. De plus, explorer différentes compositions de ligands nous permettrait d'évaluer comment les variations chimiques influencent la structure électronique et les interactions hyperfines. Une telle étude complète fournirait des informations précieuses sur la manière dont des modifications spécifiques des ligands peuvent être employées pour ajuster les propriétés des qudits de lanthanides.

L'efficacité computationnelle de la méthode LFDFT rend cette exploration extensive réalisable. Cette méthode peut rapidement fournir des paramètres de champ de ligand pour une géométrie et une composition données, nous permettant de passer en revue une large gamme de configurations de ligands en relativement peu de temps. Couplée à notre capacité à obtenir un hamiltonien atomistique pour le complexe étudié — qui peut également intégrer des champs externes — nous pouvons effectuer des simulations détaillées des structures électroniques et hyperfines. La combinaison de ces capacités nous permet d'explorer systématiquement les effets des différentes modifications de ligand sur les propriétés des qudits, accélérant ainsi la découverte de conceptions optimales de ligands.

En outre, mener une étude combinée qui exploite à la fois les résultats de la diagonalisation exacte et l'approche de l'opérateur effectif — maintenant accessible grâce à notre connaissance des paramètres de champ de ligand impairs — offrirait de multiples avantages. Premièrement, elle servirait de vérification de cohérence pour la méthode de l'opérateur effectif, garantissant qu'elle donne des résultats en accord avec la diagonalisation exacte plus intensive en calcul. Deuxièmement, elle nous permettrait de comprendre empiriquement l'interaction entre les différents termes dans le hamiltonien effectif et le rôle des paramètres spécifiques du champ de ligand. En évaluant quantitativement les contributions des différents termes du hamiltonien, nous pourrions identifier quelles interactions sont les plus significatives et comment elles sont influencées par les modifications du ligand. Cette compréhension plus approfondie guiderait la conception rationnelle de nouveaux complexes de lanthanides avec des propriétés de qudit optimisées.

En résumé, bien que nous ayons posé les bases théoriques pour l'exploration de l'espace chimique des compositions et des géométries de ligands, l'application pratique de cette méthodologie à une étude complète reste une direction future importante. En tirant parti de l'efficacité computationnelle de la méthode LFDFT et en la combinant avec des analyses détaillées de hamiltoniens, nous pouvons explorer systématiquement comment les modifications de ligand influencent les propriétés des qudits de lanthanides. Cette approche promet de révéler de nouvelles informations sur les principes de conception des systèmes de qudits.

Évolutivité de la performance computationnelle avec un nombre accru de qudits

Notre recherche a comparé la performance computationnelle — en termes d'Infidélité Moyenne de Porte (AGI) — d'un système à qudit unique avec celle d'un système multi-qubit de même dimension d'espace de Hilbert. Nous avons observé que sous une décohérence pure, l'AGI des systèmes à qudit unique augmente de manière quadratique avec le nombre de niveaux d , tandis que l'AGI des systèmes multi-qubit augmente de manière linéaire avec le nombre de qubits, c'est-à-dire de façon logarithmique avec la dimension de l'espace de Hilbert. Au premier ordre, cette évolution de l'AGI est proportionnelle au rapport entre le temps de porte et le temps de décohérence — la figure de mérite. Cette différence fondamentale dans l'évolution montre comment la décohérence affecte davantage les systèmes à qudit unique que les systèmes multi-qubit à mesure que la dimension de l'espace de Hilbert augmente.

Nous avons également brièvement abordé le cas des systèmes multi-qudits, où les qudits peuvent offrir des avantages en termes de connectivité et de réduction du nombre de portes non locales par rapport aux systèmes à qubits. Cette réduction du besoin de portes non locales peut assouplir les exigences en matière de temps de porte, permettant potentiellement aux systèmes de qudits de rivaliser avec les systèmes multi-qubits en termes d'AGI. La capacité de réaliser un nombre réduit de portes non locales réduit l'impact de la décohérence, ce qui pourrait compenser les inconvénients de l'augmentation

quadratique de l'AGI dans les systèmes de qudits.

Cependant, une étude plus détaillée sur la manière dont la performance computationnelle évolue avec le nombre de qudits est nécessaire pour mieux comprendre les avantages et les limitations potentielles des systèmes de qudits par rapport aux systèmes de qubits. Une telle analyse devrait examiner des facteurs tels que le graphe de connectivité entre les qudits et le nombre d'hamiltoniens de contrôle locaux et non locaux disponibles pour l'implémentation des portes. Ces facteurs supplémentaires, ainsi que l'évolution des taux d'erreur et des durées d'implémentation des portes comme fonction de ces facteurs, sont essentiels pour obtenir une compréhension nuancée des compromis impliqués dans le dimensionnement en nombre des systèmes de qudits pour les applications de calcul quantique.

En menant une enquête approfondie sur ces facteurs, nous pourrions déterminer les conditions pour lesquelles les systèmes multi-qudits pourraient surpasser les systèmes multi-qubits, notamment en termes d'AGI et d'efficacité des portes. Cette analyse fournirait des informations précieuses sur l'évolutivité du calcul quantique basé sur les qudits et aiderait à identifier les approches les plus prometteuses pour implémenter des portes quantiques performantes dans des systèmes pratiques.

En résumé, bien que notre comparaison initiale ait révélé des différences importantes dans le dimensionnement de l'AGI entre les systèmes de qudits et de qubits, des recherches supplémentaires sont nécessaires pour explorer pleinement le potentiel des qudits. En étudiant les effets de la connectivité du système, le nombre d'hamiltoniens de contrôle, et d'autres contraintes pratiques, nous pourrions développer une compréhension plus complète des compromis impliqués dans la mise à l'échelle des systèmes de qudits et identifier des stratégies optimales pour leur mise en œuvre dans les applications de calcul quantique.

Quantification de l'optimalité de l'implémentation d'une porte de qudit

Dans notre recherche, nous avons développé une méthodologie complète pour concevoir des séquences d'impulsions optimales afin d'implémenter des portes quantiques universelles à un seul qudit. En utilisant la théorie du contrôle optimal et en appliquant la Méthode pour la Construction Auto-Itérative et le Raffinement d'Impulsions basées sur le Principe Maximum de Pontryagin et le Gradient ascendant (MAGICARP), nous avons démontré qu'il est possible de trouver des séquences d'impulsions à haute fidélité permettant de réaliser les opérations de porte souhaitées avec un minimum d'erreurs.

Cependant, quantifier l'optimalité de ces séquences d'impulsions demeure une question ouverte. Bien que nous puissions utiliser le coût optimal — spécifiquement, la durée minimale pour un système contrôlé de manière maximale — pour un ensemble non contraint d'hamiltoniens de contrôle, comme référence pour mesurer l'optimalité d'une porte implémentée en utilisant un nombre réduit d'hamiltoniens de contrôle (moins de $d^2 - 1$), cette approche ne fournit pas de valeur définitive pour le coût optimal lorsqu'on implémente la porte avec un nombre restreint d'hamiltoniens de contrôle.

Comme discuté, dans les systèmes quantiques de dimension d , le nombre de générateurs indépendants du groupe unitaire $SU(d)$ est $d^2 - 1$. Ainsi, disposer de tous les $d^2 - 1$ hamiltoniens de contrôle correspond à une contrôlabilité totale sans contraintes. Cependant, dans les implémentations pratiques, il est souvent difficile de disposer d'un si grand nombre d'hamiltoniens de contrôle en raison de limitations physiques. Par conséquent, comprendre comment implémenter de manière optimale des portes quantiques avec un ensemble réduit d'hamiltoniens de contrôle revêt une grande importance.

D'après les résultats de nos simulations, nous avons observé des comportements compatibles avec l'existence d'une durée minimale possible pour l'implémentation de la Transformée de Fourier Quantique (QFT) en utilisant un nombre d'hamiltoniens de contrôle inférieur à $d^2 - 1$. Concrètement, à mesure que le nombre d'hamiltoniens de contrôle disponibles diminue par rapport au nombre total possible $d^2 - 1$, la durée minimale requise pour implémenter la porte avec une haute fidélité tend à augmenter. Ce comportement suggère que l'optimalité des séquences d'impulsions est étroitement liée au nombre d'hamiltoniens de contrôle disponibles pour l'implémentation.

Une étude approfondie de cette durée minimale en fonction du nombre d'hamiltoniens de contrôle et du graphe de connectivité des niveaux de qudit impliqués par les contrôles fournirait des informations précieuses sur l'optimalité de nos séquences d'impulsions. Le graphe de connectivité représente les transitions permises entre les niveaux de qudit facilitée par les hamiltoniens de contrôle. En analysant comment différentes configurations de connectivité influencent les durées minimales réalisables pour les portes, nous pourrions identifier les schémas de contrôle les plus efficaces.

Une telle étude devrait être menée parallèlement à une analyse détaillée de la stabilité numérique et des propriétés de convergence de la méthode MAGICARP, car ces facteurs peuvent considérablement impacter l'optimalité et la praticabilité des séquences d'impulsions obtenues. De plus, cette analyse pourrait fournir une compréhension plus approfondie du paysage d'optimisation et de ses éventuels écueils, ce qui serait inestimable pour la conception de séquences d'impulsions plus robustes et efficaces.

En comprenant la relation entre le nombre d'hamiltoniens de contrôle, le graphe de connectivité, et la durée minimale réalisable pour les portes, nous pourrions acquérir une meilleure compréhension des compromis liés à l'implémentation rapide de portes quantiques universelles pour les qudits. Ces connaissances nous permettraient de concevoir des séquences d'impulsions plus efficaces qui optimisent l'utilisation des ressources sans compromettre la fidélité des portes.

Cette analyse approfondie de l'optimalité nous permettrait finalement d'optimiser la conception des séquences d'impulsions non seulement pour la fidélité, mais aussi pour l'efficacité et la praticité, qui sont des facteurs cruciaux dans la réalisation des technologies de calcul quantique. En relevant les défis associés aux hamiltoniens de contrôle contraints et en comprenant les limitations imposées par les systèmes physiques, nous pourrions nous rapprocher de l'implémentation de portes quantiques rapides et fiables dans des contextes expérimentaux.

Vers l'informatique quantique à qudit robuste aux bruits et la correction d'erreurs

Dans notre recherche, nous avons mis l'accent sur le développement de séquences d'impulsions optimales pour l'implémentation de portes quantiques universelles rapides à un seul qudit. Bien que ces portes soient essentielles pour effectuer des calculs quantiques, elles sont intrinsèquement vulnérables à diverses sources de bruit, y compris la décohérence, les imperfections de contrôle et les fluctuations environnementales. Parmi celles-ci, la décohérence markovienne est efficacement minimisée par le contrôle optimal temporel, comme discuté dans ce travail. Cependant, d'autres sources de bruit, telles que les imperfections de contrôle et les fluctuations environnementales, peuvent introduire des erreurs importantes qui dégradent la fidélité des opérations de porte. De plus, on pourrait avancer que le contrôle temporel optimal, par sa nature même, manque de redondance et peut donc être plus sensible aux erreurs de contrôle et au bruit environnemental par rapport à d'autres stratégies de contrôle.

Pour relever ces défis, des techniques de contrôle quantique optimal peuvent être employées pour concevoir des séquences d'impulsions intrinsèquement robustes au bruit, améliorant ainsi la fiabilité et les performances des systèmes de calcul quantique à base de qudits. Une approche courante pour obtenir une résilience au bruit consiste à intégrer directement cette robustesse dans la fonction de coût à optimiser. Par exemple, la robustesse aux erreurs de contrôle ou aux fluctuations des paramètres du système peut être intégrée dans le problème d'optimisation, permettant à la séquence d'impulsions résultante de tolérer des écarts par rapport aux conditions idéales sans compromettre significativement la fidélité de la porte. Cela peut se faire en utilisant une fonction de coût robuste prenant en compte les variations des paramètres du système au cours du processus d'optimisation [251, 252, 253].

Dans le travail doctoral de mon collègue Jean-Gabriel Hartmann, une enquête détaillée sur la robustesse au bruit des séquences d'impulsions générées via la Décomposition en Rotations de Givens (GRD) et la Conception d'Impulsions par Ascension de Gradient (GRAPE) a été réalisée, quantifiant leur robustesse naturelle, c'est-à-dire sans optimisation de la robustesse, aux erreurs de contrôle et au bruit markovien [254].

En plus d'incorporer la robustesse au bruit dans la fonction de coût, il existe d'autres stratégies pour améliorer la résilience des portes quantiques au bruit. Par exemple, les techniques de découplage dynamique, qui impliquent l'application d'impulsions soigneusement synchronisées pour moyenniser les effets du bruit environnemental, peuvent être utilisées pour atténuer l'impact des fluctuations lentes et du bruit basse fréquence [255]. Une autre approche consiste à utiliser des techniques de contrôle robustes aux erreurs, telles que les "raccourcis vers l'adiabacité", qui permettent de réaliser des opérations quantiques rapides et à haute fidélité tout en étant moins sensibles au bruit [256].

De plus, des séquences d'impulsions composites, qui combinent plusieurs impulsions imparfaites de manière à ce que leurs erreurs se compensent, peuvent être utilisées pour améliorer la robustesse aux imperfections de contrôle [257]. Ces méthodes sont particulièrement efficaces pour réduire les erreurs systématiques dans les champs de contrôle, les rendant utiles dans les systèmes où de telles imperfections sont une source dominante de bruit.

En résumé, bien que notre objectif actuel ait été de minimiser la décohérence par le contrôle optimal temporel, il est nécessaire d'explorer des stratégies supplémentaires pour renforcer la robustesse des portes de qudit contre d'autres sources de bruit. L'incorporation de la résilience au bruit dans la fonction de coût et l'utilisation d'autres stratégies de réduction des erreurs telles que le découplage dynamique et les impulsions composites sont des avenues prometteuses pour améliorer la fidélité et la fiabilité des systèmes de calcul quantique basés sur les qudits.

Enfin, nous avons également exploré des propositions de qubits logiques dont les erreurs sont corrigées et qui sont implémentés dans des qudits physiques [167, 258], et nous avons effectué une étude qualitative de la dimensionnalité optimale pour un taux de bruit donné. Cependant, notre investigation s'est concentrée sur les codes binomiaux comme méthode pour intégrer les qubits dans les qudits pour la correction d'erreurs. Bien que cette approche présente des avantages prometteurs, elle n'est pas la seule technique disponible pour implémenter des qudits corrigés d'erreurs [168].

Une possibilité prometteuse pour de futures recherches serait de mener une étude détaillée pour déterminer la dimensionnalité exacte optimale des qudits pour un taux de bruit donné. Une telle étude fournirait des informations précieuses sur les compromis entre l'ajout de redondance par le biais des niveaux supplémentaires du qudit et l'augmentation associée des taux d'erreur. Par exemple, bien que les qudits plus grands offrent plus de degrés de liberté pour encoder des qubits logiques et implémenter la correction d'erreurs, ils sont également plus susceptibles au bruit, comme cela a été discuté plusieurs fois dans cette thèse. Identifier le "point idéal" de la dimension où le qudit peut offrir le meilleur équilibre entre la redondance et la résilience au bruit est essentiel pour réaliser un calcul quantique à base de qudits corrigé d'erreurs.

Notons également que l'utilisation de sous-espaces libres de décohérence dans les systèmes de qudits pourrait protéger les informations logiques de certains types de bruit, offrant une alternative à la correction d'erreurs quantiques traditionnelle [259]. Ces techniques pourraient exploiter les symétries du système pour encoder des qubits logiques de manière à supprimer naturellement certains canaux d'erreurs. Explorer la faisabilité et les performances des sous-espaces libres de décohérence dans les systèmes de qudits serait une direction de recherche passionnante pour l'avenir.

Pour pleinement tirer parti de ces avantages, une analyse complète de la performance des différentes méthodes de correction d'erreurs pour les qudits sous des modèles de bruit réalistes est nécessaire. Cette analyse devrait non seulement étudier la capacité de correction d'erreurs des divers codes, mais aussi examiner comment les différents taux et types de bruit (comme la dépolarisation, la décohérence de phase, ou l'amortissement d'amplitude) affectent la performance de la correction d'erreurs pour les qudits. En optimisant la dimensionnalité des qudits et le choix du code de correction d'erreurs, nous pourrions identifier les configurations les plus efficaces pour implémenter un calcul quantique tolérant aux fautes avec des qudits.

*"Au fond, j'crois qu'la Terre est ronde
Pour une seule bonne raison
Après avoir fait l'tour du monde
Tout c'qu'on veut, c'est être à la maison"*

*– Deep down, I believe the Earth is round
For one sole good reason
After one has been around the world
All one wants is to be home,
Orelsan*

"大事にしいや。夢は目覚めればいつか消える"

*– Treasure the experience. Dreams fade away after you wake up,
Hitoha Miyamizu – 君の名は。*

"A tremendous feeling of peace came over him. He knew that at last (...) it was now all, finally, over."
— **Douglas Adams**, *Mostly Harmless*

Denis Janković
Hyperfine Interactions in Lanthanide-Organic Complexes for Quantum Information Processing

Abstract: This thesis integrates quantum computing, optimal control theory, nuclear structure, hyperfine interactions, f-elements, crystal field theory, and molecular magnetism, focusing on lanthanide-organic complexes, particularly TbPc₂, as potential molecular quantum processors. The research begins with a theoretical overview, highlighting the convergence of these fields and the role of lanthanide chemistry. Key properties of lanthanides are analyzed, including their atomic and ionic states, ligand field interactions, and responses to external fields. Detailed discussions cover non-interacting electrons, Coulomb repulsion, spin-orbit coupling, and hyperfine coupling, as well as the transition from crystal field theory to ligand field theory and the capabilities of ligand field DFT. The hyperfine interaction is examined through the Dirac equation, incorporating relativity into the Schrödinger equation. Topics include mass corrections, muonic atoms, and hyperfine constants. Quantum computing with nuclear spins in lanthanides is explored, introducing qubits, qudits, quantum gates, algorithms, and relevant timescales. Optimal gate generation is investigated, aiming to develop efficient qudit gates, with TbPc₂ as a practical example. The Prouhet-Thue-Morse sequence is analyzed for its properties and applications in quantum computing. The thesis concludes with future research directions, including decoherence studies, effects of ligand composition, hyperfine constant calculations, and qudit gate optimization.

Keywords: *Quantum Computing, Qudit, AGI, Optimal Control, Lanthanides, Hyperfine Interaction, Ligand Field Theory, TbPc₂.*

Résumé: Cette thèse intègre l'informatique quantique, la théorie du contrôle optimal, la structure nucléaire, les interactions hyperfines, les éléments-f, la théorie du champ cristallin et le magnétisme moléculaire, en se concentrant sur les complexes organiques de lanthanides, en particulier TbPc₂, en tant que processeurs quantiques moléculaires potentiels. La recherche commence par un aperçu théorique, mettant en évidence la convergence de ces domaines et le rôle de la chimie des lanthanides. Les propriétés clés des lanthanides sont analysées, y compris leurs états atomiques et ioniques, les interactions du champ des ligands et les réponses aux champs externes. Les discussions détaillées couvrent les électrons non interactifs, la répulsion coulombienne, le couplage spin-orbite et le couplage hyperfin, ainsi que la transition de la théorie du champ cristallin à la théorie du champ de ligands et les capacités de la DFT du champ de ligands. L'interaction hyperfine est examinée à travers l'équation de Dirac, intégrant la relativité dans l'équation de Schrödinger. Les sujets incluent les corrections de masse, les atomes muoniques et les constantes hyperfines. L'informatique quantique avec des spins nucléaires dans les lanthanides est explorée, en introduisant les qubits, qudits, portes quantiques, algorithmes et échelles de temps pertinentes. La génération optimale de portes est étudiée, visant à développer des portes qudits efficaces, avec TbPc₂ comme exemple pratique. La suite de Prouhet-Thue-Morse est analysée pour ses propriétés et applications en informatique quantique. La thèse se termine par des orientations de recherche future, y compris des études de décohérence, les effets de la composition des ligands, les calculs des constantes hyperfines et l'optimisation des portes qudits.

Mots-clés : *Informatique Quantique, Qudit, AGI, Contrôle Optimal, Lanthanides, Interaction Hyperfine, Théorie du Champ de Ligand, TbPc₂.*

Zusammenfassung: Diese Dissertation integriert Quantencomputing, optimale Steuerungstheorie, Kernstruktur, Hyperfeinwechselwirkungen, f-Elemente, Kristallfeldtheorie und molekularen Magnetismus, mit einem Schwerpunkt auf Lanthanid-organischen Komplexen, insbesondere TbPc₂, als potenzielle molekulare Quantenprozessoren. Die Forschung beginnt mit einem theoretischen Überblick, der die Konvergenz dieser Felder und die Rolle der Lanthanidchemie hervorhebt. Wichtige Eigenschaften von Lanthaniden werden analysiert, einschließlich ihrer atomaren und ionischen Zustände, Ligandenfeldwechselwirkungen und Reaktionen auf externe Felder. Detaillierte Diskussionen umfassen nicht interagierende Elektronen, Coulomb-Abstoßung, Spin-Bahn-Kopplung und Hyperfein-Kopplung sowie den Übergang von der Kristallfeldtheorie zur Ligandenfeldtheorie und die Fähigkeiten der Ligandenfeld-DFT. Die Hyperfeinwechselwirkung wird anhand der Dirac-Gleichung untersucht, wobei die Relativität in die Schrödinger-Gleichung integriert wird. Themen sind Massenkorrekturen, muonische Atome und Hyperfeinkonstanten. Quantencomputing mit Kernspins in Lanthaniden wird untersucht, wobei Qubits, Qudits, Quantengatter, Algorithmen und relevante Zeitskalen eingeführt werden. Optimale Gattergenerierung wird erforscht, mit dem Ziel, effiziente Qudit-Gatter zu entwickeln, wobei TbPc₂ als praktisches Beispiel dient. Die Prouhet-Thue-Morse-Folge wird hinsichtlich ihrer Eigenschaften und Anwendungen im Quantencomputing analysiert. Die Dissertation schließt mit zukünftigen Forschungsrichtungen, einschließlich Dekohärenzstudien, Auswirkungen der Ligandenzusammensetzung, Berechnungen der Hyperfeinkonstanten und Optimierung der Qudit-Gatter.

Schlüsselwörter: *Quantencomputing, Qudit, AGI, Optimale Steuerung, Lanthanide, Hyperfeinwechselwirkung, Ligandenfeldtheorie, TbPc₂.*